DTIC
ELECTE
JUL 0 2 1991
S
C
D

DOT/FAA/CT-88/8-1

FAA Technical Center
Atlantic City International Airport
N.J. 08405

Aircraft Icing Handbook
Volume 1 of 3

March 1991

U.S. Department of Transportation
Federal Aviation Administration

91-03901

‖‖‖‖‖‖‖‖‖‖‖‖‖‖‖‖‖‖‖‖‖‖‖

NOTICE

This document is disseminated under the sponsorship of the U. S. Department of Transportation in the interest of information exchange. The United States Government assumes no liability for the contents or use thereof.

The United States Government does not endorse products or manufacturers. Trade or manufacturers' names appear herein solely because they are considered essential to the objective of this report.

411784

1. Report No.	2. Government Accession No.	3. Recipient's Catalog No.
DOT/FAA/CT-88/8-1		

4. Title and Subtitle		5. Report Date
Aircraft Icing Handbook - Volume 1 of 3		March 1991
		6. Performing Organization Code

7. Author(s) A. Heinrich, R. Ross, G. Zumwalt, J. Provorse, V. Padmanabhan, J. Thompson, J. Riley	8. Performing Organization Report No.
	DOT/FAA/CT-88/8-1

9. Performing Organization Name and Address	10. Work Unit No. (TRAIS)
Gates Learjet Corporation 8220 W. Harry Wichita, KS 67277	
	11. Contract or Grant No.
	DTFA03-85-C-00007

12. Sponsoring Agency Name and Address	13. Type of Report and Period Covered
Department of Transportation Federal Aviation Administration Technical Center Atlantic City International Airport, NJ 08405	Final Report February 1985-March 1991
	14. Sponsoring Agency Code
	ACD 230

15. Supplementary Notes
FAA Technical Monitor, E. E. Schlatter Flight Safety Research Branch ACD 230

16. Abstract

The design and validation of adequate aircraft ice protection has evolved into a specialized and technically complex area where many engineering disciplines are involved; namely, aeronautical, electrical, mechanical, electronics, chemical simulations, mathematical modeling, airframe/engine systems design, atmospheric physics, and meteorology. Research advances in any one discipline have a direct effect on updating the procedural technology used in the design and validation of ice protection configurations, equipment, and systems. Periodically the Federal Aviation Administration (FAA) provides documentation to assist regulatory certification teams and industry design engineers in standardizing testing and validating procedures. Examples of such documentation are "Engineering Summary of Airframe Icing Technical Data," FAA Report No. ADS-4 dated December 1968, and "Engineering Summary of Powerplant Icing Technical Data," FAA Report No. RD-77-76 dated July 1977. Although most of the information contained in these reports is still valid, some is outdated, and more usable information is now available through recent research and experience. Therefore, this work was directed towards developing an updated and more comprehensive combined version of Report ADS-4 and RD-77-76 that includes reference material on ground and airborne icing facilities, simulation procedures, and analytical techniques. This document represents all types and classes of aircraft and is intended as a working tool for the designer and analyst of ice protection systems. (25)

17. Key Words	18. Distribution Statement
Aircraft Icing, Ice Protection, Atmospheric Icing, Icing Certification, Icing Measurements, De-Icing Systems, Anti-Icing, Helicopter Icing	Document is available to the U. S. public through National Technical Information Service, Springfield, Virginia.

19. Security Classif. (of this report)	20. Security Classif. (of this page)	21. No. of Pages	22. Price
Unclassified.	Unclassified.	386	

Form DOT F 1700.7 (8-72)   Reproduction of completed page authorized

PREFACE

This document, FAA Technical Report No. DOT/FAA/CT-88/8, produced in three volumes, is the final report of a program conducted by the Gates Learjet Corporation of Wichita, Kansas, to develop an updated comprehensive multi-volume engineering handbook on aircraft icing. The work effort was directed towards producing a combined version of Federal Aviation Administration (FAA) Technical Reports Number ADS-4 (airframe icing) and RD-77-76 (engine icing), which would include reference material on ground and airborne icing facilities, simulation procedures, and analytical techniques and represent all types and classes of aircraft. The program was sponsored by the FAA Aircraft Icing Program, Flight Safety Research Branch, at the FAA Technical Center, Atlantic City International Airport, New Jersey. Mr. Ernest Schlatter, Research Meteorologist, was the Technical Monitor for the FAA Technical Center. Dr. James T. Riley and Mr. Charles O. Masters of the FAA's Aircraft Icing Program were instrumental in the completion of this document following the retirement of Mr. Schlatter.

Work was performed under the coordination of Mr. A.M. Heinrich, Project Director. Technical support was provided by Mr. Richard Ross of Ross Aviation Associates, Sedgwick, Kansas; Dr. Glen Zumwalt of Wichita State University, Wichita, Kansas; Mr. John Provorse of Cedar Hill Industries, El Dorado, Kansas; and Dr. Viswa Padmanabhan of the Gates Learjet Corporation.

Additional subcontractor contribution to the handbook was provided by the following companies and academic institutions:

Aeromet, Inc., Tulsa, Oklahoma
Beech Aircraft Corporation, Wichita, Kansas
Boeing Vertol Company, Ridley Park, Pennsylvania
Douglas Aircraft Company, Long Beach, California
Ideal Research, Inc., Rockville, Maryland
Kohlman Aviation, Lawrence, Kansas
Ohio State University, Columbus, Ohio
Pratt and Whitney Aircraft Group, East Hartford, Connecticut
Rosemount Inc., Burnsville, Minnesota
Rohr Aircraft Industries, Inc., Chula Vista, California
Sikorsky Aircraft Company, Stratford, Connecticut
Sverdrup Technology, Inc., Tullahoma, Tennessee
Wichita State University, Wichita, Kansas

An additional contractor contribution to the handbook was provided by Mr. James Thompson of Thompson Enterprises, Arlington, Virginia.

Appreciation is gratefully extended for the assistance and material provided by personnel of the B.F. Goodrich Company, Akron, Ohio; Fluidyne Engineering Corporation, Minneapolis, Minnesota; National Research Council (NRC), Ottawa, Canada; NASA Lewis Research Center,

iv

INTRODUCTION

The formation of ice on aircraft has been a concern since the early days of aviation. There are three basic forms of ice accumulation on aircraft: rime ice, glaze (clear) ice, and frost. Mixtures of rime and glaze ice are common. Ice on the airframe decreases lift and increases weight, drag, and stalling speed. In addition, the accumulation of ice on the exterior moveable surfaces affects the control of the aircraft. If ice begins to form on the blades of a propeller or helicopter rotor, its propulsion efficiency is decreased and further power is demanded of the engine to maintain flight. The overall effect on the aircraft is loss of aerodynamic efficiency, engine power, proper control surface operation, brake and landing gear operation, outside vision, proper flight instrument indications, and, in the extreme, loss of radio communication due to antenna shielding or damage. Certain areas of the aircraft's outer surfaces, sometimes even critical surfaces, may be damaged when impacted by shed ice. Engine ingestion of the shed ice and subsequent damage or engine failure is another cause for concern. Early aircraft were often forced down due to ice accretion on wings, empennage, and propellers. If the aircraft was undamaged, the ice was cleared and the aircraft continued on its flight. Eventually, pneumatic-boot de-icers were developed followed by fluid, hot air and electric ice protection systems. Both the number of instrument rated pilots and the number of rotorcraft and general aviation aircraft equipped for flight into icing environments have increased dramatically in recent years. Transport category and corporate aircraft are continually advancing in aerodynamic designs and striving for more fuel efficient engines and propellers. As the requirements change, so do the requirements for modifying contemporary ice protection systems. Therefore, to improve and optimize ice protection capabilities, there is a need for research and development of de-icing/ anti-icing systems and analysis procedures. Present research is concentrating in the areas of electro-impulse, improved pneumatics, electro-thermal, fluid freezing point depressant, microwave, and icephobic ice protection systems. The design and successful certification of these systems depend upon adequate documentation, including advantages and limitations.

The intent of this report is to provide a technical reference handbook which can be used by airframe, powerplant, and test flight engineers as a guide in design, analysis, test, and certification of ice protection systems. Previous FAA technical reports were developed to serve the needs of airframe (reference 1-1) and powerplant (reference 1-37) ice protection system design engineers. This Handbook contains much of these documents and in addition more contemporary and updated information as a result of recent research investigations and experience.

Users of this Handbook should keep in mind that the overall subject of atmospheric icing and ice protection systems is a highly complex technical field in which unresolved questions and puzzling phenomena continue to be researched by industry, universities, and the government.

Recent available research and test results have been incorporated in order to make the analytical and test procedures as up-to-date as possible. The incorporation of such recent advances in technology during the preparation of this handbook has required examination of past and present procedures, as well as field experience. In these procedures, simplifying assumptions are required to make analyses possible, imperfect simulations are required, and demonstration tests are not always sufficiently specific or well correlated. Thus, engineering judgement must be used to provide the conservativeness required in design, analysis, and test to compensate for uncertainties. It is expected that there will be future FAA updates to this Handbook on a periodic basis as a result of continuing research and development in the field. These updates will be incorporated through subsequent loose-leaf addenda as they become available and as directed by the Federal Aviation Administration.

The Handbook is organized into nine major Chapters as follows:

CHAPTER I
FLIGHT IN ICING

CHAPTER 1
SECTION 1.0
THE ICING ATMOSPHERE

CHAPTER I - FLIGHT IN ICING
CONTENTS
SECTION 1.0 THE ICING ATMOSPHERE

LIST OF TABLES

LIST OF FIGURES

SYMBOLS AND ABBREVIATIONS

Symbol	Description
AFGL	Air Force Geophysics Laboratory
AGL	Above Ground Level
ASL	Above Sea Level
°C	Degrees Celsius
deg	Degrees
FAA	Federal Aviation Administration
FAR	Federal Aviation Regulation
°F	Degrees Fahrenheit
ft	Foot (or feet)
g/m^3	Grams Per Cubic Meter
ICAO	International Civil Aviation Organization
km	Kilometer
L^{-1}	Per liter
LWC	Liquid Water Content
m	Meter
mi	Statute mile
mm	Millimeter (one thousandth of a meter)
MRI	Meteorology Research Incorporated
MVD	Median Volumetric Diameter
NACA	National Advisory Committee for Aeronautics
NASA	National Aeronautics and Space Administration
n mi	Nautical mile
NRL	U.S. Naval Research Laboratory
OAT	Outside Air Temperature
μm	Micron (micro meter)
USAF	U.S. Air Force

GLOSSARY

adiabatic process - A thermodynamic change of state of a system in which there is no transfer of heat or mass across the boundaries of the system. In an adiabatic process, compression always results in heating, expansion in cooling.

airmass - A widespread body of air, the properties of which can be identified as having been established while that air was situated over a particular region of the earth's surface, and undergoing specific modifications while in transit away from the source region.

altocumulus (Ac) - A mid-level (6500 - 20,000 ft.) stratiform cloud, white or gray, or a combination thereof. Appears as laminae, rounded masses or rolls. Some turbulence and small amounts of icing.

altostratus (As) - A mid-level (6500 - 20,000 ft.) stratiform cloud appearing either as a gray or bluish (never white) sheet or layer of striated, fibrous, or uniform appearance. May totally cover the sky and extend over an area of several thousand square miles with a vertical extent from several hundred to thousands of feet.

cirrocumulus (Cc) - A high level (20,000 - 30,000 ft) thin stratiform cloud appearing as a white patch of cloud without shadows, composed of very small elements in the form of waves or ripples. Usually ice crystals but may contain highly supercooled water droplets. Some turbulence and icing.

cirrostratus (Cs) - A high level (20,000 - 30,000 ft.) stratiform ice-crystal cloud appearing as a whitish veil or sheet usually fibrous but can be smooth. Often totally covers the sky. Often produces halo phenomenon. No turbulence and little if any icing.

cirrus (Ci) - A high level (20,000 - 30,000 ft.) thin, stratiform ice crystal cloud. Larger ice crystals often trail downward in wisps called "mare's tails". Detached cirriform elements in the form of feather-like white patches or narrow bands have little turbulence or airframe icing. Dense bands however contain turbulence.

clear ice - a glossy, clear, or translucent ice formed by relatively slow freezing of large supercooled droplets. The large droplets spread out over the airfoil prior to complete freezing, forming a sheet of clear ice. Although clear ice is expected mostly with temperatures between 32 and 14 degrees Fahrenheit, it does occur at temperatures as cold as -13 degrees Fahrenheit.

conditional instability - The state of a column of air in the atmosphere when its temperature lapse rate is less than the dry-adiabatic lapse rate but greater than the saturation-adiabatic lapse rate.

cumuliform cloud - descriptor of cumulus family clouds, the principal characteristic of which is vertical development in the form of rising mounds, domes or towers.

cumulonimbus (Cb) - Cumuliform cloud type with extreme vertical development occurring as individual cells or as a broad band with only individual tops discernable. Thunderstorm cloud. May have dense boiling "cauliflower" top or dense cirrus "anvil" top. Bases 1000 to 5000 ft. solid growth to 30,000 ft. normal, 70,000 extreme. Hail, severe turbulence, airframe and powerplant icing.

cumulus (Cu) - Cumuliform cloud in the form of individual detailed elements which have flat bases and dome-shaped tops. Humilis type have little vertical development or turbulence and no significant icing and are called fair-weather cumulus. Congestus type shows towering vertical development with billowing cauliflower tops. Showers, strong turbulence and clear icing. Bases 1000 to 3000 ft., tops 15,000 - 20,000 ft.

dry adiabatic lapse rate - The rate of decrease of temperature with height of a parcel of dry air lifted adiabatically through an atmosphere in hydrostatic equilibrium.

freezing level - The lowest altitude in the atmosphere, over a given location, at which the air temperature is 32 degrees Fahrenheit; the height of the 32 degree Fahrenheit constant temperature surface.

graupel - See snow pellets.

horizontal extent - The horizontal distance of an icing encounter.

hydrostatic equilibrium - The state of a fluid whose surfaces of constant pressure and constant mass (or density) coincide and are horizontal throughout.

ice pellets - Type of precipitation consisting of transparent or translucent pellets of ice 5 millimeters or less in diameter.

icing encounter - A series of icing events consecutively penetrated until an interruption of more than some selected distance is experienced.

icing event - A portion of a subfreezing cloud over which the cloud properties are approximately constant.

light icing - The rate of accumulation that may create a hazard if flight is prolonged in this environment. Occasional use of de-icing/anti-icing equipment removes/prevents accumulation.

liquid water content - The total mass of water contained in all the liquid cloud droplets within a unit volume of cloud. Units of LWC are usually grams of water per cubic meter of air (g/m^3).

mean effective diameter (MED) - The droplet diameter which divides the total water volume present in the droplet distribution in half, i.e., half the water volume will be in larger drops and half the volume in smaller drops. The value is calculated based on an assumed droplet distribution.

median volumetric diameter (MVD) - The droplet diameter which divides the total water volume present in the droplet distribution in half, i.e., half the water volume will be in larger drops and half the volume in smaller drops. The value is obtained by actual drop size measurements.

micron (μm) - One millionth of a meter.

mixed cloud - A subfreezing cloud composed of snow and/or ice particles as well as liquid droplets.

moderate icing - The rate of accumulation is such that even short encounters become potentially hazardous and use of de-icing/anti-icing equipment or diversion from the area and/or altitude is necessary.

nimbostratus (Ns) - A low level (<6500 ft.) stratiform cloud, gray or dark colored and often with a ragged base and a diffused appearance due to almost continuous drizzle, rain, snow, or ice pellets. Little turbulence but can create serious icing problems.

rime ice - A rough, milky, opaque ice formed by the instantaneous freezing of small, supercooled droplets as they strike the aircraft. Rime ice usually occurs at temperatures colder than about +15° F., although it has been observed at somewhat warmer temperatures.

saturation adiabatic lapse rate - The rate of decrease of temperature with height of an air parcel lifted in a saturation adiabatic process.

saturation adiabatic process - An adiabatic process in which the air is maintained at saturation by the evaporation or condensation of water substance, the latent heat being supplied by or to the air, respectively.

severe icing - The rate of accumulation is such that de-icing/anti-icing fails to reduce or control the hazard requiring immediate diversion from the area and/or altitude.

sleet - See ice pellets.

snow grains - Precipitation in the form of very small (generally < 1 mm) white opaque particles of ice, the solid equivalent of drizzle. Snow grains resemble snow pellets except are smaller, harder and have a more flattened appearance.

snow pellets - Precipitation consisting of white, opaque, approximately round (diameter of 2 to 5 mm) ice particles which have a snowlike structure. Also known as graupel, soft hail, or tapioca snow.

stability - The stability of an atmosphere in hydrostatic equilibrium with respect to vertical displacements. The criterion for stability is that the displaced parcel be subjected to a buoyant force opposite to its displacement, e.g., that a parcel displaced upward be colder than its new environment.

stratiform clouds - Low, middle, or high level layer clouds, characterized by extensive horizontal rather than vertical development.

stratocumulus (Sc) - A low level (< 6500 ft.) stratiform cloud ranging from white or gray repetitive masses or rolls to low, ragged, dark clouds. Some turbulence and serious icing with distance.

stratus (St) - A low level (< 6500 ft.) stratiform cloud with a uniform, gray, sheet-like appearance resembling fog. No turbulence but can create serious icing due to distance.

subsidence inversion - A temperature inversion produced by the adiabatic warming of a layer of subsiding air. This inversion is enhanced by vertical mixing in the air layer below the inversion.

trace icing - Ice becomes perceptible. The rate of accumulation is slightly greater than the rate of sublimation. It is not hazardous, even though de-icing/anti-icing equipment is not used, unless encountered for an extended period of time.

I.1.0 THE ICING ATMOSPHERE

I.1.1 INTRODUCTION

The design of ice protection systems depends upon a knowledge of icing characteristics. This section defines the prevailing types of icing conditions in the atmosphere and provides the latest, accepted information used in the design of ice prevention and removal systems. The data and information presented updates, where necessary, that presented in the 1964 FAA publication "Engineering Summary of Airframe Icing Technical Data (ADS-4)" (reference 1-1). Much of the data is obtained from National Advisory Committee for Aeronautics statistical icing reports which include icing encounters by commercial, military, and icing research aircraft. Some foreign data is also included.

The National Advisory Committee for Aeronautics and cooperating groups conducted research on natural icing conditions for a period of many years. Early work was performed by specially equipped research aircraft using a rotating multicylinder to measure icing intensity. Later data were obtained by mounting icing rate meters on commercial and military aircraft, thus obtaining icing data related to routine flight operations. These data (reference 1-2 to 1-17) form the major part of icing statistical data and is the basis for most U.S., Canadian, British commercial, and military design criteria. For this reason, the significant results of the various reports are presented in this section as figures 1-1, 1-2, 1-12, 1-13 and 1-22 through 1-38 plus table 1-1.

Additional data has been solicited and is presented at both very low and very high altitudes to supplement the NACA data that is confined, for the most part, to altitudes of 3000 to 22,000 feet (1 to 7 km). These additional data are presented in table 1-2 and figures 1-3 to 1-11 and 1-14 to 1-21. Discussion of the figures and tables is presented.

The terminology used in the succeeding portions of the report may be unfamiliar and deserves some explanation. The cloud liquid water content is expressed in grams of liquid water per cubic meter of air, and includes only the water in supercooled droplet form (it does not include the water in vapor form). Typical ranges of values are 0.1 to 0.8 g/m^3 for layer type clouds, and 0.2 to 2.5 g/m^3 for cumulus clouds. Individual cloud droplets are typically between 2 and 50 microns in diameter. Larger droplets can occur, but require special circumstances to form. Any droplets larger than about 100μm tend to precipitate out. MVD's are generally less than 35 μm, but values as large as 100 μm have been reported (reference 1-33). Freezing rain may involve droplets as large as 1,000 microns, or one millimeter. As a measure of central tendency and for design purposes, the aggregate cloud droplet distribution is expressed as a median volume diameter (MVD) value; i.e., half the volume of water in a given sample is contained in drops larger than the quoted value, and half in drops smaller. Cloud temperature may vary from -40 °F to 32 °F (-40 to 0 °C). At colder temperatures, ice crystals predominate and supercooled water droplets rarely exist. The horizontal extent used for design purposes may vary from 1 to 300 nautical miles for layer type clouds (stratiform), or 0.2 to 5 nautical miles for cumuliform clouds.

1.1.2 SUPERCOOLED CLOUDS

Accretion of ice on aircraft surfaces in flight is a result of the tendency of cloud droplets to remain in a liquid state at temperatures below freezing. This condition is referred to as supercooling. The amount and shape of ice accreted is dependent on outside air temperature, cloud liquid water content, droplet size, airspeed and horizontal extent of the icing conditions. Additionally, the likelihood of supercooling increases as droplet size decreases and droplet purity increases. Supercooled clouds are common and have been observed at temperatures as low as -40 °F (-40 °C) (reference 1-18). Supercooled clouds are unstable and can change phase from liquid to solid rapidly with the addition of ice crystals, ice nuclei, or with agitation.

1.2.1 Cloud Types

In discussing aircraft icing, cloud types are placed into two general classifications; stratiform (layer type clouds) and cumuliform (clouds with vertical development). Fog differs from clouds only in that the base of fog is at earth's surface while clouds are above the surface. Freezing fog consists of supercooled droplets that freeze upon contact with exposed objects. Accretion may result in the form of rime or glaze ice (reference 1-19).

1.2.1.1 Stratiform Clouds

Icing in stratiform clouds is normally in the middle to lower level clouds below 10,000 feet (3 km). Stratiform clouds are quite stable leading to the formation of clouds with extensive coverage plus the existence of clouds at different altitudes, i.e., multiple layers of clouds which may or may not be similar in content and are commonly encountered with total thicknesses on the order of 6500 feet (2 km).

The high level stratiform clouds (above 20,000 feet) are composed of ice crystals which do not contribute to airframe icing but should be considered for engine icing. These clouds, known as cirrus (Ci), cirrocumulus (Cc), and cirrostratus (Cs), are distinguished by their light, white transparent appearance (figure 1-39).

The middle level stratiform clouds between 6500 and 20,000 feet (2 km and 6 km) are important to the icing environment since they have both solid and liquid water content. These clouds may be very thin but can extend over large areas up to thousands of square miles. These cloud types, known as altocumulus (Ac) and altostratus (As), are distinguished from the cirrus cloud types by the darker color being gray to bluish but never white.

The lower level stratiform clouds normally below 6500 feet (2 km) are important to the icing environment because of the LWC and because of the horizontal extent. The area covered is not as extensive as some of the middle level clouds; however, the LWC is greater. These cloud types are known as stratocumulus (Sc), stratus (St), and nimbostratus (Ns) and are characterized by the white to gray appearance with darker patches (figure 1-39). The nimbo-stratus clouds also have non-

uniform bases which are usually diffused due to precipitation. These clouds also have little or no electrical activity or hail.

Variation of cloud properties with altitude for a specific stratus cloud is shown in figure 1-1. Within low level stratiform clouds, free air temperature decreases with altitude, but liquid water content (LWC) increases, reaching a maximum at or near the top of the cloud. This is in agreement with adiabatic lifting theory (figure 1-2 and reference 1-29), which predicts an increase in LWC as cloud temperature (and capacity to hold water in vapor form) decreases. Droplet diameter also increases (in the statistical sense) with increasing altitude. In middle level stratiform clouds, there is not such a regular dependence of LWC and MVD on height above cloud base. Thus in As, and Ac, there can be varying altitudes of icing severity (references 1-33, 1-34, 1-35). Flight in layer clouds can result in icing conditions of long duration, and form the criteria most often used for design of ice protection systems for such airframe components as wings, empennage, propellers, windshields, etc. The intensity of icing generally ranges from light to moderate with maximum values occurring in the upper portions of the cloud. Both rime and glaze icing are observed in stratiform clouds. The main hazard results from the great horizontal extent of some cloud decks (figure 1-9 to 1-11). Stratiform clouds (figures 1-3 to 1-8) are characterized by moderate liquid water contents with a maximum value of 1.1 g/m^3. Icing in these clouds is most frequently rime.

1.2.1.2 Cumuliform Clouds

The cumuliform clouds, of which cumulonimbus is the best known, are important to the icing environment because of their rapid development and large LWC which, due to the adiabatic lifting process, may be in a supercooled state. Cumuliform clouds, which develop vertically first, are characterized by flat bases at the lifting condensation level and sometimes flat tops if vertical motion is suppressed by the presence of an inversion. These clouds are often referred to as fair weather cumulus, since they tend to persist in a fairly constant state in good weather. These clouds can, however, develop into cumulus congestus, still of the same cumulus cloud type (Cu), which has a large vertical development and may include the cauliflower or tower aspect. Both of these cloud formations are characterized by the fact that they do not contain ice crystals. This accompanies the further development into the final cloud type, cumulonimbus (Cb). The formation of ice crystals is in fact a signal that the change has or is being accomplished. The cumulonimbus clouds may produce rain and/or various forms of frozen precipitation and have displays of thunder and lightning. This gives it the classic name "thunderhead" (figure 1-39).

Cumuliform clouds cover less area horizontally than do stratiform clouds. Icing is variable and dependent on the stage of development of the individual cloud. Intensities may range from light, in small supercooled cumulus, to moderate or severe in cumulus congestus and cumulonimbus clouds. Although icing may occur at all levels above the freezing level in a building cumulus, it is most intense in the updrafts.

Cumuliform clouds (figures 1-12 to 1-18) are characterized by short duration exposures to typically high liquid water contents of up to 2.5 g/m³, or up to 6-8 g/m³ for large tropical Cb's. Typical median volume diameters range from 9 to 50 microns. The maximum water content of a cloud containing only a single cell is likely to be at the cloud center at a height above the freezing level as shown in figure 1-12 (reference 1-21). Droplet size and LWC tend to increase with cloud height as shown in figure 1-13 and figure 1-40. The drop sizes quoted are mean volume values (see glossary). Measurements shown in figure 1-12 and 1-13 are for two separate typical cumulus cells. Other cumulus clouds may have greater or smaller LWC and drop size values, or may be composed of multiple cells rather than single cells. The horizontal extent averages from two to six nautical miles (3.7 - 11 kilometers) (figures 1-9, 1-10, 1-11) for a single cloud but may be greater in convective cloud lines or clusters and areas where convective clouds are imbedded in stratiform clouds. Icing in these clouds is usually clear or a mixture of clear and rime ice.

1.2.2 Variations with Altitude

The analysis of United States flight data, primarily from reference 1-20 for clouds under 10,000 feet, indicates that icing conditions become most serious in the winter months at altitudes of 7000 to 9000 feet (2130 to 2170 meters) above ground level (AGL). Maximum observed LWC's are 1.7 g/m³ for convective clouds and 1.1 g/m³ for layer clouds. Above 10,000 ft the maximum LWC appears to decrease (figure 1-19) in wintertime clouds. This decrease is, however, somewhat uncertain due to insufficient data on convective clouds with the low bases and the large vertical extent required to produce supercooled LWC's greater than 1.5 g/m³ above 8000 feet (2440 meters). Consideration should be given to the fact that most data have been collected during the winter months when icing is of greater concern and convective clouds occur less frequently. Large tropical cumulonimbus clouds, which can attain great vertical development, have LWC values to 6-8 g/m³.

A secondary area of concern occurs at an altitude range of 4,000 to 6,000 feet (1.2 - 2 km) AGL and near 2,000 feet (0.6 km) AGL. The 4,000 to 6,000 feet AGL layer corresponds to typical upper limits of the turbulent mixing layer in many wintertime situations. The base of the subsidence inversion in this altitude range blocks vertical development of the stratus or stratocumulus that forms underneath as a result of turbulent mixing (reference 1-20).

Flight data comparing altitude with horizontal extent reinforces the comparison of LWC and altitude for serious icing conditions. These data show a peak over the 3,000 to 5,000 feet (1 - 1.5 km) AGL range and a second sharper peak near 8,000 feet (2.4 km) AGL (figure 1-20). These horizontal extents for layer clouds indicate that the top of the turbulent mixing layer in wintertime stratus-forming conditions lies between 3,000 to 5,000 feet AGL. Convective cloud icing encounters are shorter than layer cloud encounters. Convective encounters peak at altitudes of around 6,000 and 8,000 feet (1.8 - 2.4 km) AGL (figure 1-21) during the winter (reference 1-20).

Icing encounters occur less frequently at higher altitudes (up to 22,000 feet (7 km) where the minimum observed icing temperature is -22 °F (-30 °C) (figure 1-33). Encounters above 22,000 feet are rare. This is due to the fact that LWC decreases with decreasing temperature (figures 1-23 and 1-24). When encountered, icing is likely to be classified as "light" (reference 1-1).

Note that for stratiform clouds the maximum LWC compares favorably with a theoretical limit based on two-thirds the LWC of a 3,000-ft. cloud, calculated by adiabatic lifting theory (figure 1-2). (For a detailed discussion and equations on adiabatic lifting theory, see reference 1-29.) The data for cumulus clouds shows less correlation between LWC and temperature. In both cases, however, no icing was found below -15 °F. The minimum temperature usually referenced for the existence of supercooled cloud (water) droplets is -40 °F. At extremely low temperatures, virtually all water is converted to ice crystals, therefore icing is not likely to be a problem (see Section I.1.3 for cautionary note). There is a general relationship of LWC decreasing with temperature (figures 1-3, 1-4, 1-5) although a definite correlation has not been established (figures 1-25, 1-26). Little data exists for certain areas of the distribution.

The probability of exceeding specific values of maximum LWC or drop size, is shown in figures 1-27 and 1-28. The plots are in terms of exceedance probability; i.e., the probability that the given parameter will be equalled or exceeded. A probability of 10 percent, for example, means that the given parameter will be exceeded in one out of 10 icing encounters. For layer type clouds, the liquid water content for 10 percent exceedance is 0.5 to 0.6 g/m³, whereas it is 1.18 g/m³ for cumuliform clouds. For the same probability, the mean effective drop diameter is 18 to 21 microns, and the maximum 23 to 27 microns. The temperature for this same probability level is 5° to -4 °F (-15 to -20 °C), depending on the particular data source.

Because of the horizontal variations of cloud structure, the average LWC for a long-duration encounter is substantially lower than the average for short-duration encounters. This is shown in figure 1-30, where the maximum value for a 40-mi. encounter is 0.8 g/m³, whereas for 200 miles, it is 0.3 g/m³. This variation is also shown in figure 1-31 in dimensionless form. For cumuliform clouds, the LWC for a six-mile cloud is 0.85 of the water content for a three-mile cloud. For layer clouds, the LWC for a 40-mile distance is 0.64 of that for a 10-mile distance, and at 150 miles is only 0.32 of the 10 mile value. The probability of encountering icing conditions in excess of specific distances is shown in figure 1-32. From these data, it can be seen that 90 percent of all encounters are for a distance of less than 53 nautical miles, and 99 percent are less than 123 nautical miles. These variations of LWC with distance are of interest primarily for predicting the amount of ice accumulation on unprotected components for various flight conditions.

As shown in figure 1-33, low-level stratiform icing rarely occurs below 0 °F. At higher levels (up to 22,000 ft.), the minimum icing temperature is -22 °F (-30 °C). The icing envelope for cumuliform clouds is somewhat more narrow than for stratiform clouds, as shown in figure 1-34. The minimum altitude for cumuliform clouds is 4,000 ft., and the maximum (for these data) is 24,000 ft. The temperature range is more restricted for cumuliform clouds at a given altitude than for stratiform

I 1-5

clouds. The icing envelopes shown here were used as a basis for the FAR 25 transport category airworthiness requirements.

For some types of icing studies, it may be convenient to define an average or most probable icing temperature versus altitude (figure 1-36). At sea level, the most probable icing temperature is 26 °F (-3 °C) decreasing to -11 °F (-24 °C) at 20,000 ft. At the higher altitudes (16,000 to 24,000 ft.), the probable icing temperature is very close to the ICAO Standard Atmosphere temperature.

The probability of encountering icing when flying in clouds is of particular interest. It may be seen in figure 1-37 that at ambient temperatures of 14 to 32 °F (-10 to 0 °C) (where icing is encountered most frequently) about 40 percent of the flights through clouds will result in ice accumulation. At lower temperatures, the frequency of icing in clouds is much lower; about six percent at -22 °F (-30 °C).

1.2.3 Variations with Season

The summer or warm season months create large warm air masses which can contain large amounts of water vapor. The high temperatures can also create temperature instability leading to strong convective up-drafts which in turn cause cumuliform cloud formations which have relatively high LWC values. These formations can create very severe local icing encounters.

The winter or cool season with large cold air masses contain much less water vapor due to the lower temperatures. The cool air masses create more stable temperature environments leading to the creation of stratiform cloud systems instead of the cumuliform systems of the warmer season. The lower freezing temperature of winter, however, leads to the increased likelihood of aircraft icing encounters (reference 1-2) plus the time in the cloud formation can be extensive, thus creating a critical icing environment.

1.2.4 Variations with Geography

Cloud data for the continental United States have been grouped by NACA (reference 1-11 and 1-20) into three geographical regions: Eastern United States, Plateau, and Pacific Coast (figure 1-38). The boundary between the Eastern and Plateau is the eastern border of Montana, Wyoming, Colorado and New Mexico while the boundary between the Plateau and Pacific Coast is the eastern border of Washington, Oregon and California.

Areas of greatest icing concern in the United States are the Great Lakes, coastal areas, and mountainous regions, although cold fronts with freezing rain and/or other icing condition can occur in most areas. The Great Lakes and coastal areas, particularly near the Gulf Stream, enhance the possibility of encountering high values of liquid water content due to the "lake effect" phenomenon. Large bodies of water add moisture add heat to the lower layers of a cold airmass. This induces instability, resulting in convection. Forced lifting of air on the windward side of mountainous areas (orographic effect) cause the air to cool and clouds to form if there is adequate moisture. If the air is stable, the clouds will be stratiform. If it is conditionally unstable, convection will occur and

cumulus clouds will form. The Appalachian and Pacific Coast mountains cause significant orographic effects. A warm, moist maritime influence may greatly enhance this effect along the higher Pacific Coast ranges (reference 1-20).

1.2.5. Cloud Liquid Water Content

Liquid water content (LWC) is the most important factor in aircraft icing. However, the concept of droplet critical diameter must be understood before the importance of liquid water as the primary contributor to aircraft icing, over temperature and drop size distribution, can be accepted. (See Section 1 1.2.6)

In a recent study on clouds under 10,000 feet AGL, supercooled LWCs as high as 1.7 g/m^3 in convective clouds and 1.1 g/m^3 in layer clouds have been reported (reference 1-20). Theoretically, convective clouds may have LWCs greater than 1.7 g/m^3 below 10,000 feet if the bases are warm and occur below 4000 feet AGL, but none were found. In this study only 4 cases of LWCs greater than 1.4 g/m^3 were found and in this group, horizontal extents were less than 5 miles, MVDs were less than 22 microns, and temperatures were warmer than -10° C. LWCs of less than 1.1 g/m^3 observed in 99% of the data and less than 0.6 g/m^3 in 95% of the data for all cloud types.

The largest LWCs occur in cumulus and cumulonimbus clouds, generally from 100 to 300 nautical miles behind a cold front, in maritime air masses, or in areas of orographic lifting. In the United States, supercooled convective clouds are rarely observed at altitudes below 3000 feet AGL, except in mountainous areas.

1.2.6 Cloud Droplet Size Distribution

Cloud water droplet sizes are not uniform but extend over a range of droplet diameters, called a distribution. The total liquid water content can be calculated if the number of droplets (concentration) are grouped by droplet size diameters. In most cases, the entire distribution can be represented adequately by the median volume droplet diameter (MVD). That is, one-half of the mass volume of water in the cloud (sample) is contained in drops larger than the MVD value, and half in drops smaller. However, in some cases, particularly for clouds where the MVD is small and the distribution of particle sizes varies widely from the median, it may be desirable to model the entire range of droplet sizes. This is imperative for obtaining more precise ice accretion rates because of the critical dropsize diameter concept (reference 1-36). This concept recognizes that for a given component of an aircraft, drops less than a certain diameter will remain in the freestream and not impinge on the component. Therefore, the liquid water contained in these smaller drops will not contribute to ice accretion. Each component (size) has it's own critical dropsize diameter. The FAR 25, App. C, design envelopes were developed with this concept in mind and cloud droplet concentrations with MVD's less than 15 microns were ommitted from the design envelopes.

Langmuir & Blodgett (reference 1-23) developed a theoretical family of drop size distributions based on percentages of LWC. These are traditionally used for estimating the rate of water

impingement on an airfoil (See table 1-1). Some researchers have reported (reference 1-35) that the Langmuir distributions are not too representative of real cloud droplet distributions.

1.1.3 ICE CRYSTALS

Ice crystals are various macroscopic crystalline formations with a basic hexagonal symmetry although, depending on the condition of temperature and vapor pressure, the simple hexagonal pattern may be almost undiscernible. Ice crystals are common in the atmosphere with the high clouds (>20,000 feet) being formed almost entirely of ice crystals.

Ice crystals are created by the formation of a crystalline structure about microscopic nuclei or by the freezing of very small supercooled droplets. The median concentration is 114 crystals/ft^3 (4/liter) with 15% of the measured concentrations less than 7.1/ft^3 (0.25/liter) and 15% greater than 2860/ft^3 (100/liter) (reference 1-20).

It is believed that the co-existence of ice crystals and supercooled water drops is only a transitory stage as the cloud progresses to a pure ice crystal cloud.

Ice crystals alone do not constitute a critical airframe icing problem but should be considered in air compressor systems, total pressure probes, and engine and/or inlet systems where extreme bends or flow reversals exist.

1.1.4 SNOW

Snow is formed by the crystallization (sublimation) of water vapor at temperatures below freezing. This process creates ice crystals which combine to form snowflakes, the optimum temperature being just below freezing. Snow can be said to dry out the air since any supercooled water present with snow will have a greater vapor pressure than the snow, thus a mass water transfer will take place from droplets to the ice particle (snow). This growth mechanism is called the Bergeron process after the Swedish meteorologist who first suggested the process (reference 1-29).

Cold (dry) snow by itself is not critical to airframe icing but in combination with supercooled droplets (mixed conditions) or at temperatures only slightly below freezing (wet snow) can create conditions where ice accretion is extremely rapid. For engine and/or inlet systems, the same caution applies to snow as to ice crystals. Care should be exercised during taxiing in snow since snow can collect and freeze on lifting surfaces and significantly change the aircraft performance and stall characteristics.

1.1.5 MIXED CONDITIONS

Many encounters are of a mixed media consisting of ice crystals and/or snow in combination with supercooled water droplets. The mixed cloud condition is basically an unstable condition and is extremely temperature dependent and may change quite rapidly. This condition can be very critical from an icing standpoint because the aggregate of impinging ice crystal/snow and water droplet can

adhere rapidly and roughly to the airframe, causing significant reduction in aircraft performance (reference 1-24 and 1-27).

I.1.6 FREEZING RAIN

Freezing rain is precipitating supercooled water droplets (usually not colder that about 25° F.) which freeze upon impact with the ground or any exposed surface. The temperature of the impacted surface must initially be below freezing. Droplet sizes are large, approximately 1,000 microns in diameter, and liquid water contents average 0.15 g/m³. Normally, freezing rain occurs in the altitude range 0 to 5,000 feet (0 - 1.5 km) ASL and is associated with a melting layer or inversion (i.e., increasing air temperature with height) (reference 1-25). In general, pilots are cautioned to avoid flying in freezing rain conditions because rapid ice accretion on all surfaces results in rapid reduction of aircraft performance and loss of windshield visibility.

I.1.7 FREEZING DRIZZLE

Although formed by a different process, the primary difference from (freezing) rain is a smaller drop size, nominally 200 - 500 microns. Drizzle forms by the coalescence and freezing of cloud droplets and has the appearance of fog except that the slightly larger droplets are affected by gravity and settle slowly to the ground, remelting into water. Freezing drizzle occurs when the drizzle (very small) droplets fall through a layer of below freezing tempeature, supercool, and freeze upon impact with aircraft or the ground (reference 1-25).

Glaze icing is major concern in both freezing rain and freezing drizzle. Care should be exercised both in-flight and taxiing since glaze ice can collect quite rapidly on all surfaces even during short exposures.

I.1.8 HAIL

Hail is small balls or chunks of ice with diameters of 0.2 to 3 inches that are developed within cumulonimbus clouds. Hail commonly are spherical in shape with concentric layers of alternately clear and opaque ice resulting from the freezing of rain drops during successive updrafts and downdrafts within the cumulonimbus cloud.

The largest size hailstones and greatest frequency of occurrence in a mature cell is usually between 10,000 and 30,000 feet, but encounters of hail can occur in clear air outside the storm cell (reference 1-29).

Hail can also include other forms of frozen precipitation with differing origins. Snow pellets are white, opaque spheroidal-shaped ice particles with diameters generally 0.1 to 0.2 inches (2 to 5 mm). Snow pellets are also known as soft hail or graupel. The smaller form of ice (<1 mm) and of a somewhat flattened shape is known as snow grains.

Ice pellets are another form of solid frozen precipitation but, unlike snow pellets, are transparent or translucent spheroidal shapes with diameters generally less than 5 mm. These normally originate

as rain or melted snow flakes which are frozen by a cold air layer near the ground. They are also known as sleet. The term "sleet" has colloquially been used to refer to a mixture of snow and rain.

Hail in itself will not create an icing hazard. It can, however, create structure damage from impact of the larger hail and/or surface erosion from the smaller particles.

I.1.9 SLEET

Sleet is technically the same as ice pellets but is commonly thought of as snow pellets or snow grains described in Section I.1.8.

I.1.10 SUPERCOOLED FOG (ICE FOG)

Supercooled fog is identical to a supercooled cloud except for altitude. Supercooled fog can have the same effect as freezing drizzle. Ice fog has been used interchangeably with supercooled fog but technically represents a fog composed of ice crystals normally in the order of 12 to 20 microns.

Cautions for ground icing are described in Sections I.1.7 and I.1.11.

I.1.11 FROST

Frost is a thin layer of crystalline ice that forms on exposed surfaces when the temperature of these surfaces drops below 32 °F (0 °C) even though OAT may be above freezing. Ice deposition occurs when air with a below-freezing dewpoint becomes saturated as a result of nighttime radiational cooling. Frost formation may also occur when a cold aircraft in flight enters an area of warm, moist air or supersaturated air. Frost is a deceptive form of icing that affects the lift/drag ratio and causes early airflow separation (reference 1-26).

I.1.12 REFERENCES

1-1 Bowden, D.T., et. al., "Engineering Summary of Airframe Icing Technical Data," FAA Technical Report ADS-4, General Dynamics/Convair, San Diego, California, 1964.

1-2 Lewis, W., "Icing Properties of Non-Cyclonic Winter Stratus Clouds," NACA TN 1391, 1947.

1-3 Jones, A. R. and Lewis, William, "Recommended Values of Meteorological Factors to be Considered in the Design of Aircraft Ice-Prevention Equipment," NACA TN 1855, March 1949.

1-4 Lewis, W., "Icing Zones in a Warm Front System with General Precipitation," NACA TN 1392, 1947.

1-5 Lewis, W., "A Flight Investigation of the Meteorological Conditions Conducive to the Formation of Ice on Airplanes," NACA TN 1393, 1947.

1-6 Lewis, W., Kline, D. B., and Steinmetz, C. P., "A Further Investigation of the Meteorological Conditions Conducive to Aircraft Icing," NACA TN 1424, 1947.

1-7 Kline, D. B., "Investigation of Meteorological Conditions Associated with Aircraft icing in Layer-Type Clouds for 1947-48 Winter," NACA TN 1793, 1949.

1-8   Lewis, W. and Hoecker, W. H. ,Jr., "Observations of Icing Conditions Encountered in Flight During 1948," NACA TN 1904, 1949.

1-9   Hacker, P. T. and Dorsch, R. G., "A Summary of Meteorological Conditions Associated with Aircraft Icing and a Proposed Method of Selecting Design Criterions for Ice Protection Equipment, NACA TN 2569, 1951.

1-10   Kline, C. B. and Walker, J.A., "Meteorological Analysis of Icing Conditions Encountered in Low Altitude Stratiform Clouds," NACA TN 2306, 1951.

1-11   Lewis, W. and Bergrun, N. R., "A Probability Analysis of the Meteorological Factors Conducive to Aircraft Icing in the United States," NACA TN 2738, 1952.

1-12   Perkins, P. J., Lewis, W., and Mulholland, D. R., "Statistical Study of Aircraft Icing Probabilities at the 700 and 500 Millibar Levels Over Ocean Area in the Northern Hemisphere, "NACA TN 3984, 1957.

1-13   Perkins, P. J., "Preliminary Survey of Icing Conditions Measured During Routine Transcontinental Airline Operation," NACA RM E52J06, 1952.

1-14   Perkins, P. J., "Statistical Survey of Icing Data Measured in Scheduled Airline Flights over the United States and Canada from November 1951 to June 1952," NACA RM E55F28a, 1955.

1-15   Neel, C. B., "A Heated-Nire, Liquid-Water Content Instrument and Results of Initial Flight Tests in Icing Conditions, "NACA RM A54123, 1955.

1-16   Perkins, P. J., "Summary of Statistical Icing Cloud Data Measured Over United States and North Atlantic, Pacific, and Arctic Oceans During Routine Aircraft Operations," NASA Memo 1-19-59E, 1959.

1-17   Perkins, P. J., "Icing Frequencies Experienced During Climb and Descent by Fighter-Interceptor Aircraft," NACA TN 4314, , July 1958.

1-18   Glass, M., et. al., "Water, Precipitation, Clouds and Fog: Chapter 16, 1983 Revision, Handbook of Geophysics and Space Environments," AFGL-TR-83-0181, Air Force Geophysics Laboratory, Hanscom AFB, MA, 1983.

1-19   Huschke, R. E., et. al., "Glossary of Meteorology," Third Printing, American Meteorological Society, Boston, MA, 1980.

1-20   Jeck, R. K., "A New Data Base of Supercooled Cloud Variables for Altitudes up to 10,000 Feet AGL and the Implications for Low Altitude Aircraft Icing," DOT/FAA/CT-83-21, NRL Report 8738, Washington, D.C., 1983.

1-21   Zaitsev, V. A., "Liquid Water Content and Distribution of Drops in Cumulus Clouds," National Research Council of Canada, Technical Translation TT-395, Ottawa, 1953.

1-22   Masters, C. 0., "A New Characterization of Supercooled Clouds Below 10,000 Feet AGL," DOT/FAA/CT-83-22, Washington, D.C., 1983.

1-23   Langmuir, I., et. al., "A Mathematical Investigation of Water Droplet Trajectories," AAFTR 5418, February 1946.

1-24 Sand, W. R., et. al., "Icing Conditions Encountered by a Research Aircraft," Journal of Climate and Applied Meteorology, Vol. 23, No. 10, 1984.

1-25 Lewis, W., "Review of Icing Criteria in Aircraft Ice Protection" Report of Symposium of April 28 - 30, 1969, DOT/FAA Flight Standards Service, Washington, D.C., 1969.

1-26 "Aerographer's Mate 1 and C", Naval Education and Training Support Command Manual No. NAVEDTRA 10362-B, Government Printing Office, Washington, D.C., 1974.

1-27 Cooper, W. A., et. al ., "Effects of Icing on Performance of a Research Airplane," Journal of Aircraft, Vol. 21, No. 9, 1984.

1-28 "Airworthiness Standards: Transport Category Airplanes," Appendix C, U.S. Department of Transportation, Federal Aviation Administration, Federal Aviation Regulations, FAR Part 25, Washington, D.C., 1974.

1-29 Miller, A. and Thompson, J.C., "Elements of Meteorology," Charles E. Merrill Publishing Co., Columbus, Ohio, 1975.

1-30 Bowditch, N., "American Practical Navigator, "U.S. Navy, Hydrographic Office, 1966.

1-31 Borovikov, A.M., et. al., "Cloud Physics," Translated from Russian, Israel Program for Scientific Translations Ltd., Jerusalem, 1963.

1-32 Blair, T.A. and Fite, R.C., "Weather Elements," Prentice-Hall Inc., Inglewood Cliffs, NJ, 1965.

1-33 Hoffmann, H.E., "Icing Degree Moderate to Severe: If and Where in Clouds," Proceedings; 16th Congress of the International Council of the Aeronautical Sciences, 1988.

1-34 Hoffman, H.E.; Roth, R., "Liquid Water Content, Median Volume Diameter, and Temperature in Dependence on the Height above the Cloud Base for different Types of Clouds", 10th International Cloud Physics Conference, Preprints, Vol. 1, 1988.

1-35 Hoffman, H.E., et. al., "A Documentation of Cloud Physical Parameters of Vertical Soundings in Stratiform Clouds," German Aerospace Research Establishment Report, 1989.

1-36 Neel, Carl B., Jr., et. al., "The Calculation Of The Heat Required For Wing Thermal Ice Prevention In Specified Icing Conditions", NACA TN 1472
December, 1947.

1-37 Pfeifer, G.D. and Maier, G.P, "Engineering Summary of Powerplant Technical Data," Report Number FAA-RD-77-76, July 1977.

TABLE 1-1. LANGMUIR AND BLODGETT DROPLET SIZE DISTRIBUTIONS (REFERENCE 1-23)

Total LW in Each Size Group %	Distribution(s) of			avg. dia. MVD	
	A	B	C	D	E
5	1.00	0.56	0.42	0.31	0.23
10	1.00	0.72	0.61	0.52	0.44
20	1.00	0.84	0.77	0.71	0.65
30	1.00	1.00	1.00	1.00	1.00
20	1.00	1.17	1.26	1.37	1.48
10	1.00	1.32	1.51	1.74	2.00
5	1.00	1.49	1.81	2.22	2.71

Column A represents the highly unlikly distribution where all drops have the same size diameter equal to the MVD (monodispersion).

Columns B thru E represents distributions with increasing ranges of drop diameter sizes about the MVD value of central tendency.

Example subjecting MVD 20 to a B distribution:

5 % of the LWC is contained in drops of 11.2 microns diameter (20 x 0.56).

   i.e.:   5% of the LWC is contained in drops
           whose diameter averages 56% of the MVD.

10 % of the LWC is contained in drops of 14.4 microns diameter (20 x 0.72).

20 % of the LWC is contained in drops of 16.8 microns diameter (20 x 0.84).

30 % of the LWC is contained in drops of 20.0 microns diameter (20 x 1.00).

20 % of the LWC is contained in drops of 23.4 microns diameter (20 x 1.17).

10 % of the LWC is contained in drops of 26.4 microns diameter (20 x 1.32).

5 % of the LWC is contained in drops of 29.8 microns diameter (20 x 1.49).

100 %

NOTE: Langmuir & Blodgett developed this theoretical family of drop size distributions related to percentages of LWC. They are traditionally used for estimating the rate of water impingement on an airfoil. However some researchers have reported (reference 1-35) that the Langmuir distributions are not too representative of real cloud droplet distributions.

TABLE 1-2. GEOGRAPHICAL DISTRIBUTION* OF AVAILABLE MODERN DATA OVER THE CONTERMINOUS UNITED STATES (Reference 1-20)

LAYER CLOUDS

	Pacific Region	Plateau Region	Eastern Region
Max LWC (g/m^3)	1.1	0.3	0.6
Avg LWC (g/m^3)	0.2	0.1	0.2
Max MVD (microns)	32.0	19.0	30.0
Avg MVD (microns)	18.0	13.0	12.0
Min MVD (microns)	7.0	6.0	3.0
Avg OAT (°F)	24.8	10.4	12.2
Min OAT (°F)	21.2	5.0	-13.0

CONVECTIVE CLOUDS

	Pacific Region	Plateau Region	Eastern Region
Max LWC (g/m^3)	1.7	-	1.2
Avg LWC (g/m^3)	0.4	-	0.5
Max MVD (microns)	32.0	-	21.0
Avg MVD (microns)	19.0	-	15.0
Min MVD (microns)	13.0	-	9.0
Avg OAT (°F)	17.6	-	21.2
Min OAT (°F)	1.4	-	15.8

*Geographical Regions are shown in Figure 1-38

TABLE 1-3. CONVERSION FACTORS

1000 microns	= 1.0 millimeter
1 nautical mile	= 1.852 kilometer
	= 1.1508 statute mile
	= 6076.103 feet
1 liter	= 1.06 quart
	= 0.26 gallons
1 gram	= 0.035 ounces
1 cubic meter	= 35.0 cubic feet
	= 1.3 cubic yards

TEMPERATURE CONVERSION

0 degrees Celsius	= 32 degrees Fahrenheit
-40 degrees Celsius	= -40 degrees Fahrenheit
$°C = 5/9 \, (°F - 32)$	$°F = 9/5 \, °C + 32$
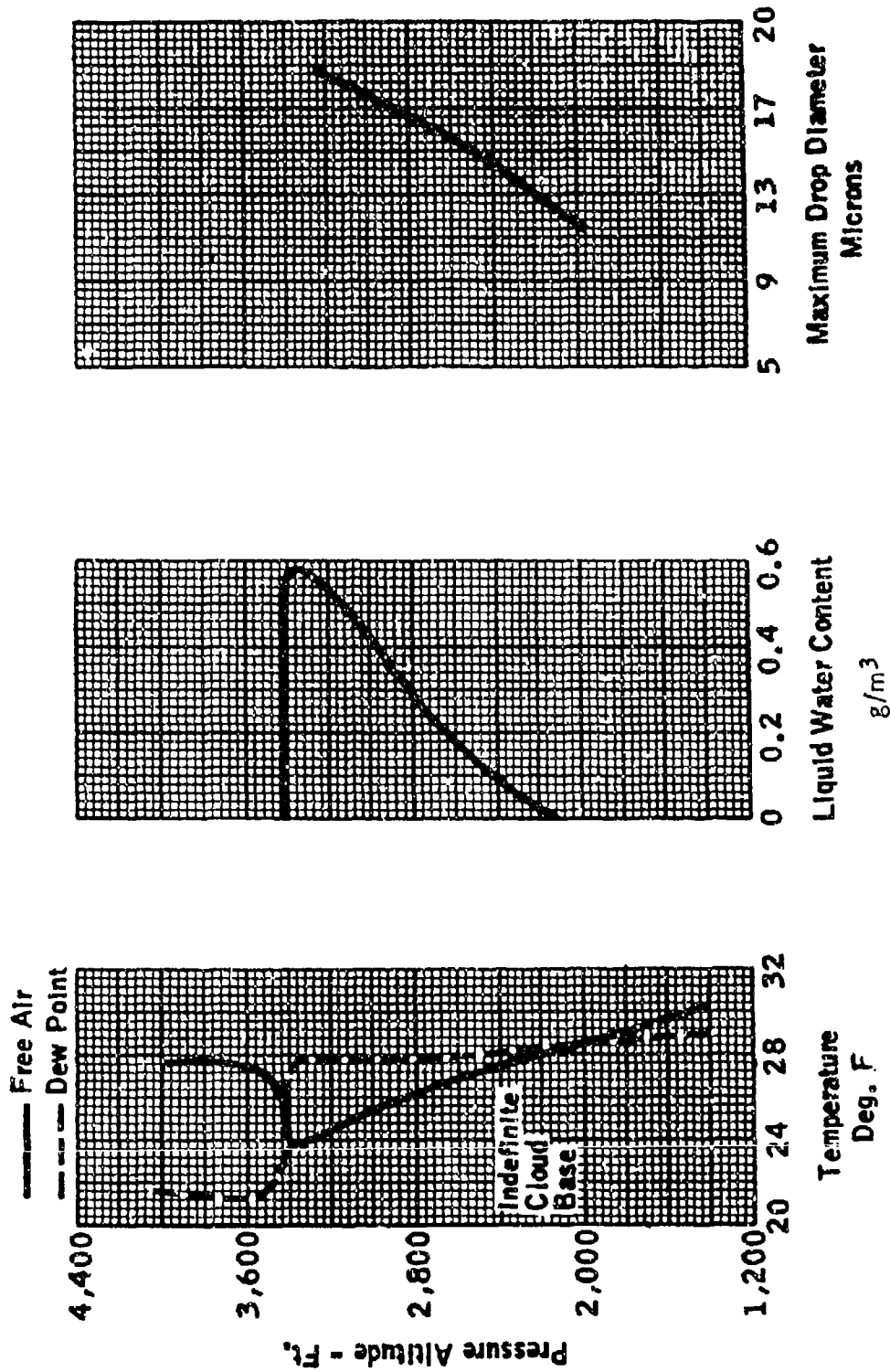
FIGURE 1-1. PROPERTIES OF A TYPICAL NON-CYCLONIC STRATUS CLOUD FROM FIGURE 3a. (REFERENCE 1-2)
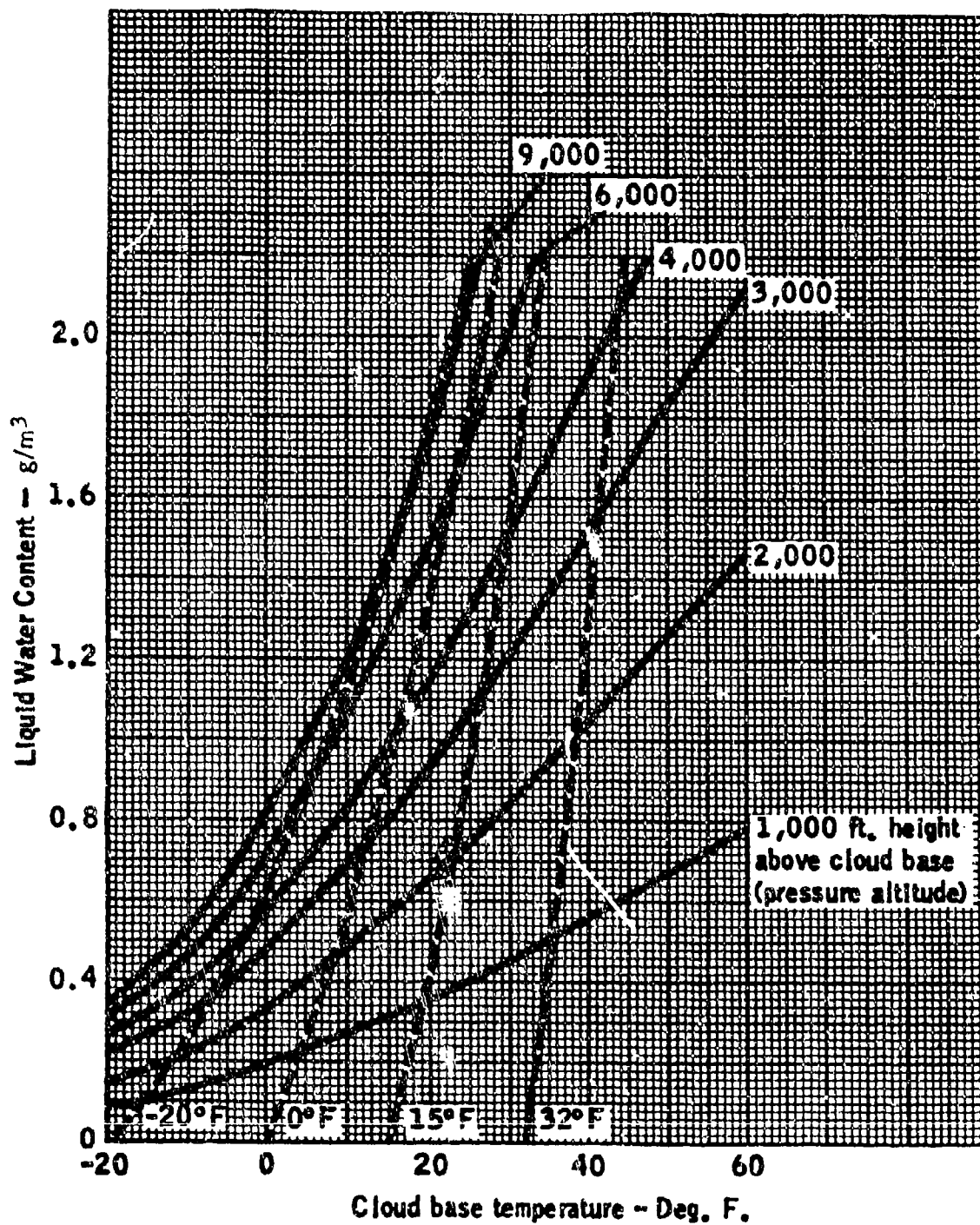
FIGURE 1-2.   THEORETICAL LIQUID WATER CONCENTRATION IN CLOUDS FORMED BY
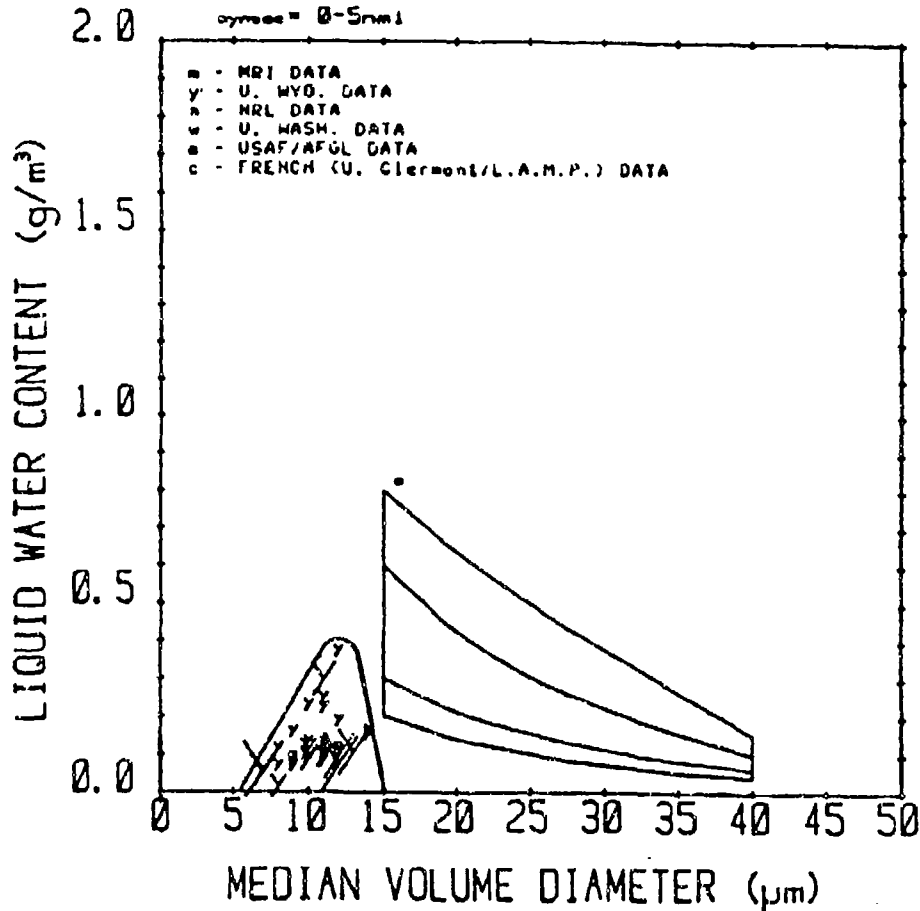ADIABATIC LIFTING (CLOUD BASE AT 948 FT. PRESSURE ALTITUDE).
(DATA FROM REFERENCE 1-2)
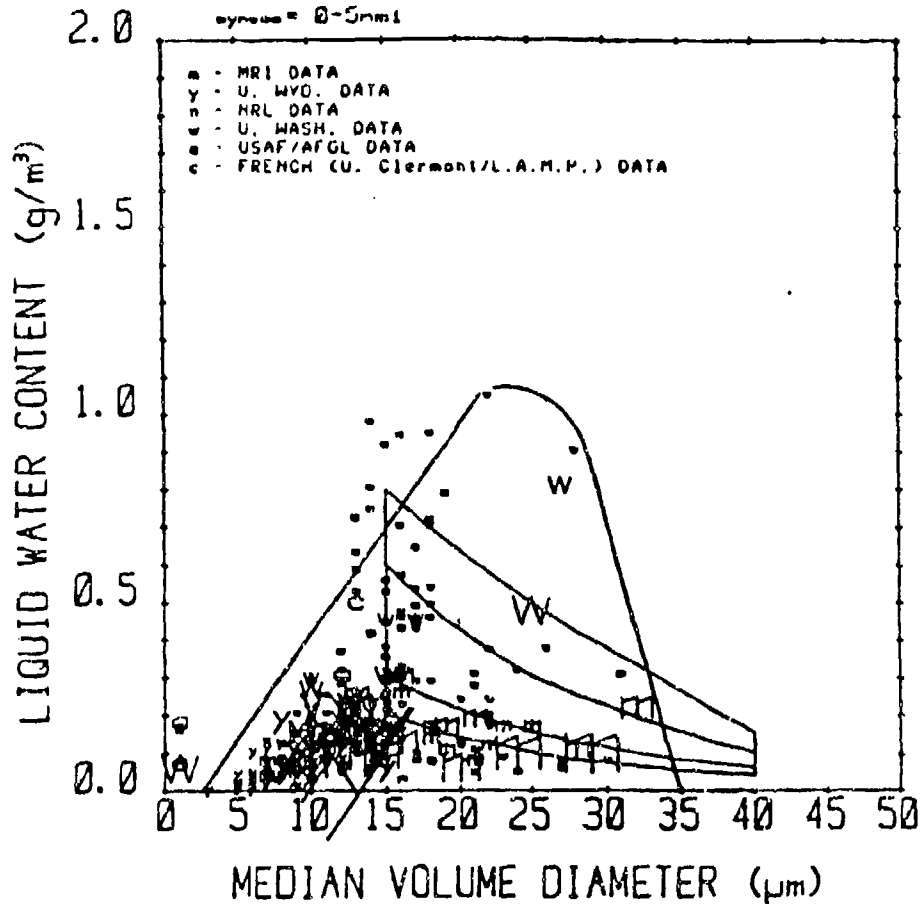
FIGURE 1-3. SCATTERPLOT OF OBSERVED LWC, MVD COMBINATIONS IN THE MODERN DATA FOR LAYER CLOUDS UP TO 10,000 FEET AGL AND FOR CLOUD TEMPERATURES FROM 14 TO 32 DEGREES FAHRENHEIT. The various plotting symbols represent various data sources as indicated in the key. The size of each plotted symbol is proportional to its weight (i.e., the observed horizontal extent of the associated icing event) as shown by the scale above the graph. The center of each plotted symbol corresponds to the average (and approximately constant) value of LWC and MVD observed during the icing event. Values of LWC for which no MVD measurements are available are plotted arbitrarily at 1 micron MVD. A total of 1,320 data miles is represented in this graph. The Continuous Maximum envelope from Figure 1 of FAR-25, Appendix C, is superimposed for comparison. The other smooth curve is the observed, apparent limit to the Continental U.S. data for this temperature interval. (Reference 1-20.)

I 1-18
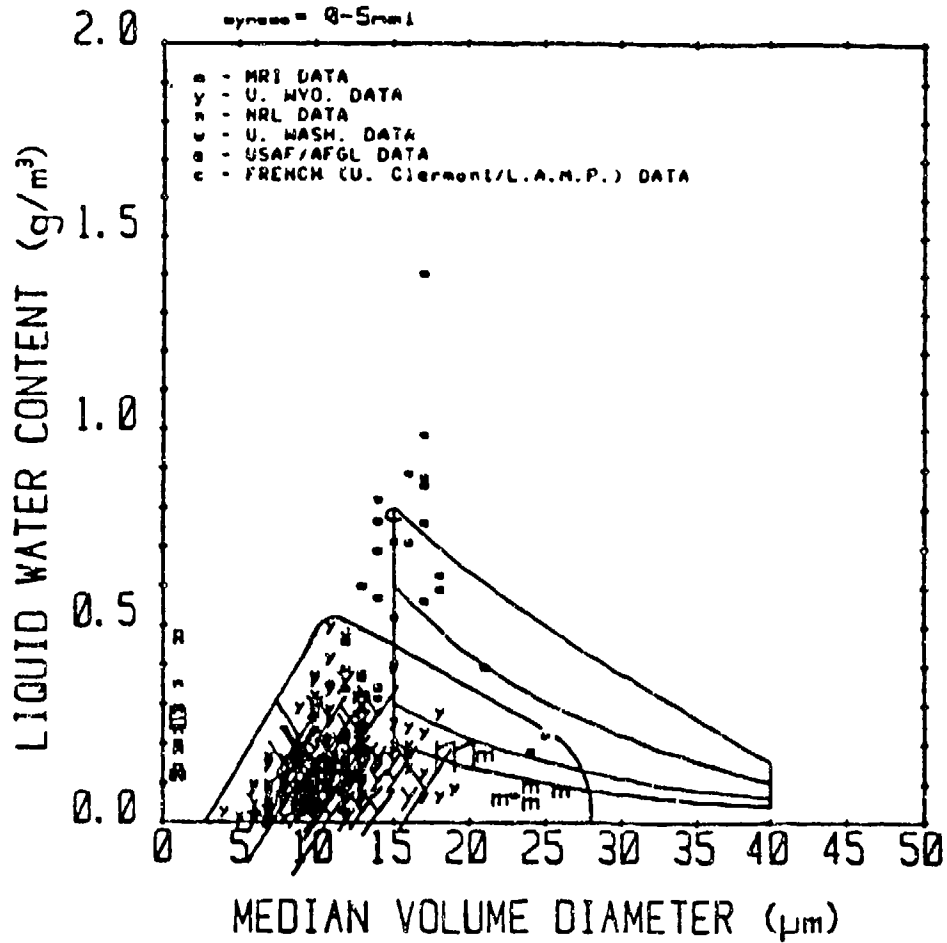
FIGURE 1-4. SCATTERPLOT OF OBSERVED LWC, MVD COMBINATIONS IN THE MODERN DATA FOR LAYER CLOUDS UP TO 10,000 FEET AGL AND FOR CLOUD TEMPERATURES FROM -4 TO 14 DEGREES FAHRENHEIT. The various plotting symbols represent various data sources as indicated in the key. The size of each plotted symbol is proportional to its weight (i.e., the observed horizontal extent of the associated icing event) as shown by the scale above the graph. The center of each plotted symbol corresponds to the average (and approximately constant) value of LWC and MVD observed during the icing event. Values of LWC for which no MVD measurements are available are plotted arbitrarily at 1 micron MVD. A total of 1,180 data miles is represented in this graph. The Continuous Maximum envelope from Figure 1 of FAR-25, Appendix C, is superimposed for comparison. The other smooth curve is the observed, apparent limit to the Continental U.S. data for this temperature interval. (Reference 1-20.)

mynwac = 20-25nmi
mynwac = 15-20nmi
mynwac = 10-15nmi
mynwac = 5-10nmi
mynwac = 0-5nmi

m - MRI DATA
y - U. WYO. DATA
n - NRL DATA
w - U. WASH. DATA
a - USAF/AFGL DATA
c - FRENCH (U. Clermont/L.A.M.P.) DATA

LIQUID WATER CONTENT (g/m³)

MEDIAN VOLUME DIAMETER (μm)

FIGURE 1-5. SCATTERPLOT OF OBSERVED LWC, MVD COMBINATIONS IN THE MODERN DATA FOR LAYER CLOUDS UP TO 10,000 FEET AGL AND FOR CLOUD TEMPERATURES FROM -22 TO -4 DEGREES FAHRENHEIT. The various plotting symbols represent various data sources as indicated in the key. The size of each plotted symbol is proportional to its weight (i.e., the observed horizontal extent of the associated icing event) as shown by the scale above the graph. The center of each plotted symbol corresponds to the average (and approximately constant) value of LWC and MVD observed during the icing event. Values of LWC for which no MVD measurements are available are plotted arbitrarily at 1 micron MVD. A total of 174 data miles is represented in this graph. The Continuous Maximum envelope from Figure 1 of FAR-25, Appendix C, is superimposed for comparison. The other smooth curve is the observed, apparent limit to the Continental U.S. data for this temperature interval. (Reference 1-20.)

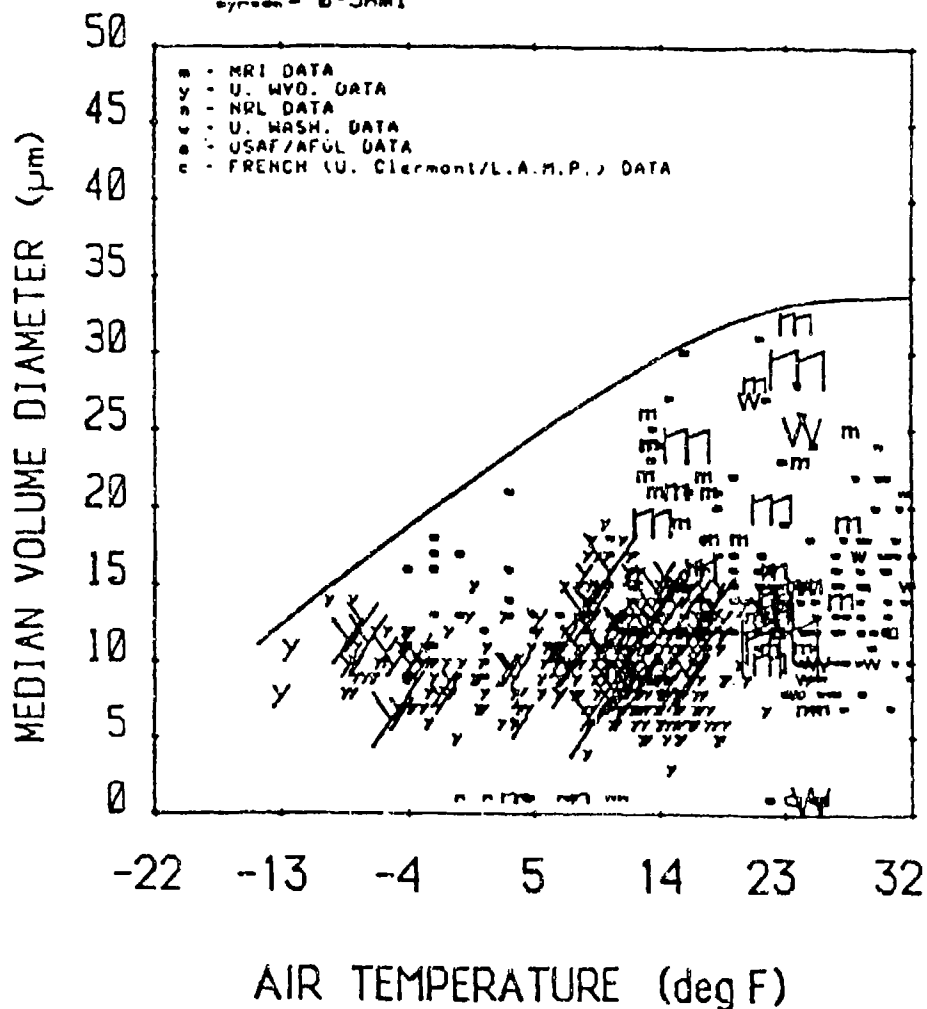FIGURE 1-6. SCATTERPLOT OF ICING EVENT TEMPERATURES VS. ALTITUDE FOR MODERN DATA FROM SUPERCOOLED LAYER CLOUDS UP TO 10,000 FEET AGL. The various plotting symbols represent various data sources as indicated in the key. The size of each symbol is proportional to its statistical weight (i.e., the observed horizontal extent of the associated icing event) as shown by the scale above the graph. The center of each plotted symbol corresponds to the average (and approximately constant) value of altitude and OAT observed during the icing event. A total of 2,660 data miles is represented in this graph. (Reference 1-20.)
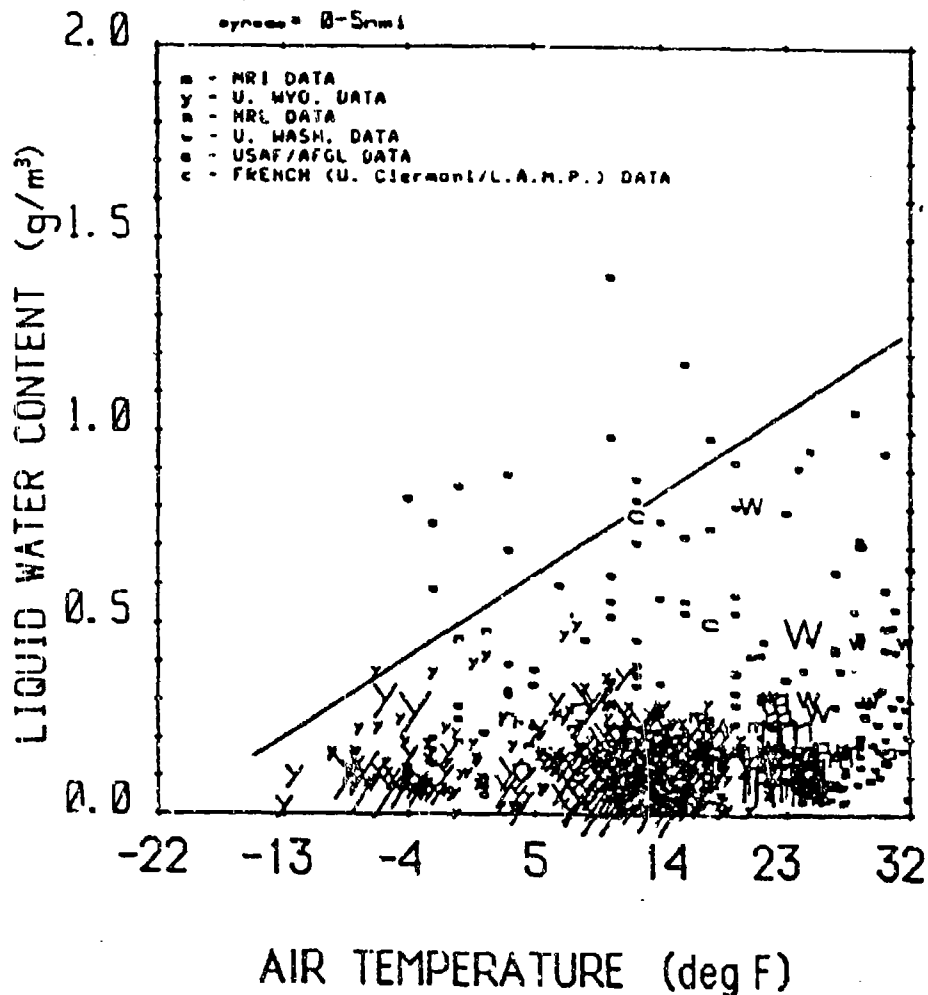
FIGURE 1-7. SCATTERPLOT OF LWC VS. OAT FOR MODERN DATA FROM SUPERCOOLED LAYER CLOUDS UP TO 10,000 FEET AGL. The various plotting symbols represent various data sources as indicated in the key. The size of each symbol is proportional to its statistical weight (i.e., the observed horizontal extent of the associated icing event) as shown by the scale above the graph. The center of each plotted symbol corresponds to the average (and approximately constant) value of LWC and OAT observed during the icing event. The solid line represents the apparent upper limit to LWC as a function of temperature for Continental U.S. supercooled layer clouds below 10,000 feet AGL. The position of the line is based on the maximum LWC values in the combined original data (presented in Reference 1-1) and modern data sets. A total of 2,660 data miles is represented in this graph. (Reference 1-20.)

FIGURE 1-8. SCATTERPLOT OF MVD VS. OAT FOR MODERN DATA FROM SUPERCOOLED LAYER
CLOUDS UP TO 10,000 FEET AGL. The various plotting symbols represent various
data sources as indicated in the key. The size of each symbol is proportional
to its statistical weight (i.e., the observed horizontal extent of the associ-
ated icing event) as shown by the scale above the graph. The center of each
plotted symbol corresponds to the average (and approximately constant) value
of MVD and OAT observed during the icing event. The solid line bounding the
data points represents the apparent upper limit to MVD as a function of temp-
erature for Continental U.S. supercooled layer clouds below 10,000 feet AGL.
The position of the line at temperatures above 5 degrees Fahrenheit is based
on the maximum MVDs from both the original data (presented in Reference 1-1)
and modern data sets. A total of 2,660 data miles is represented in this
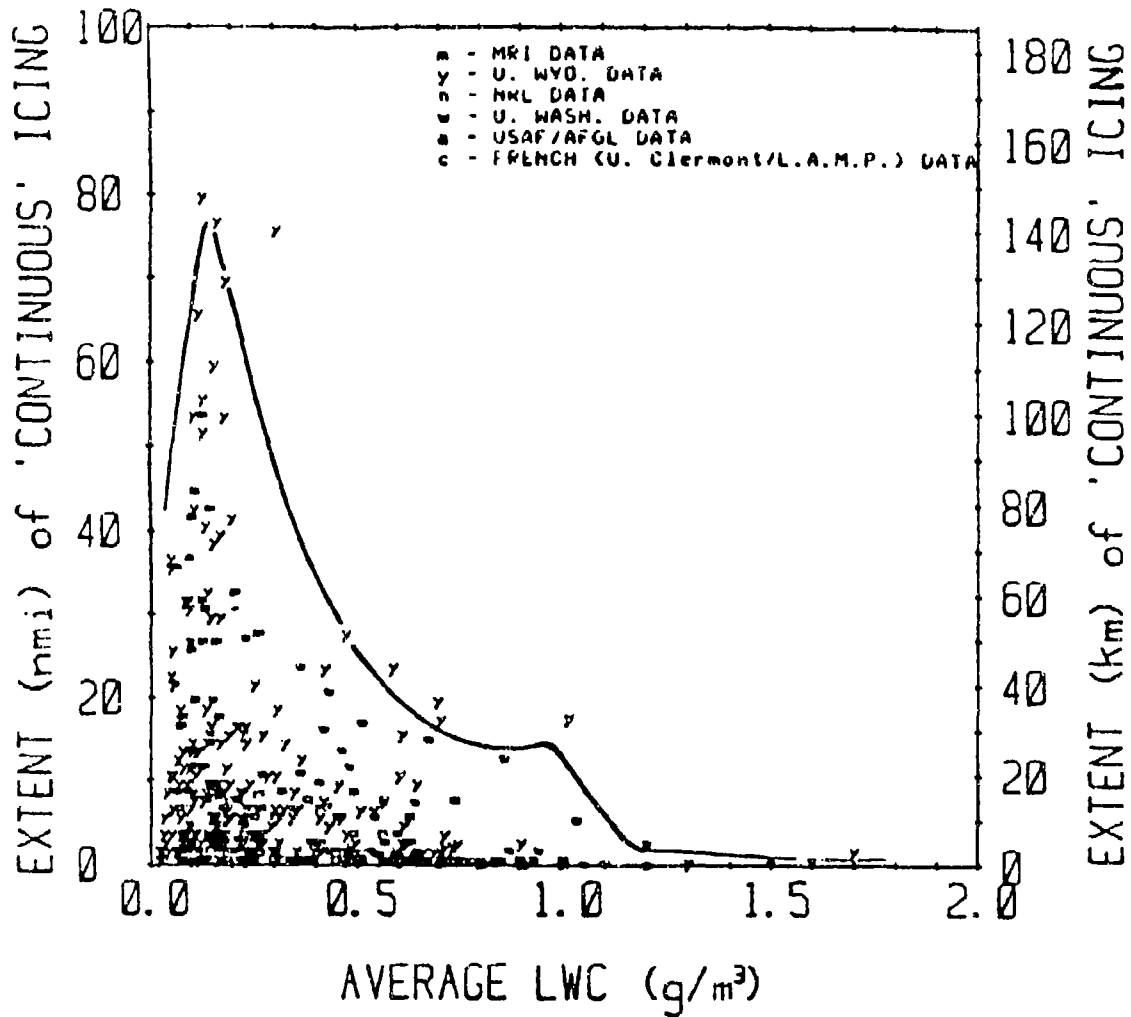graph. (Reference 1-20.)
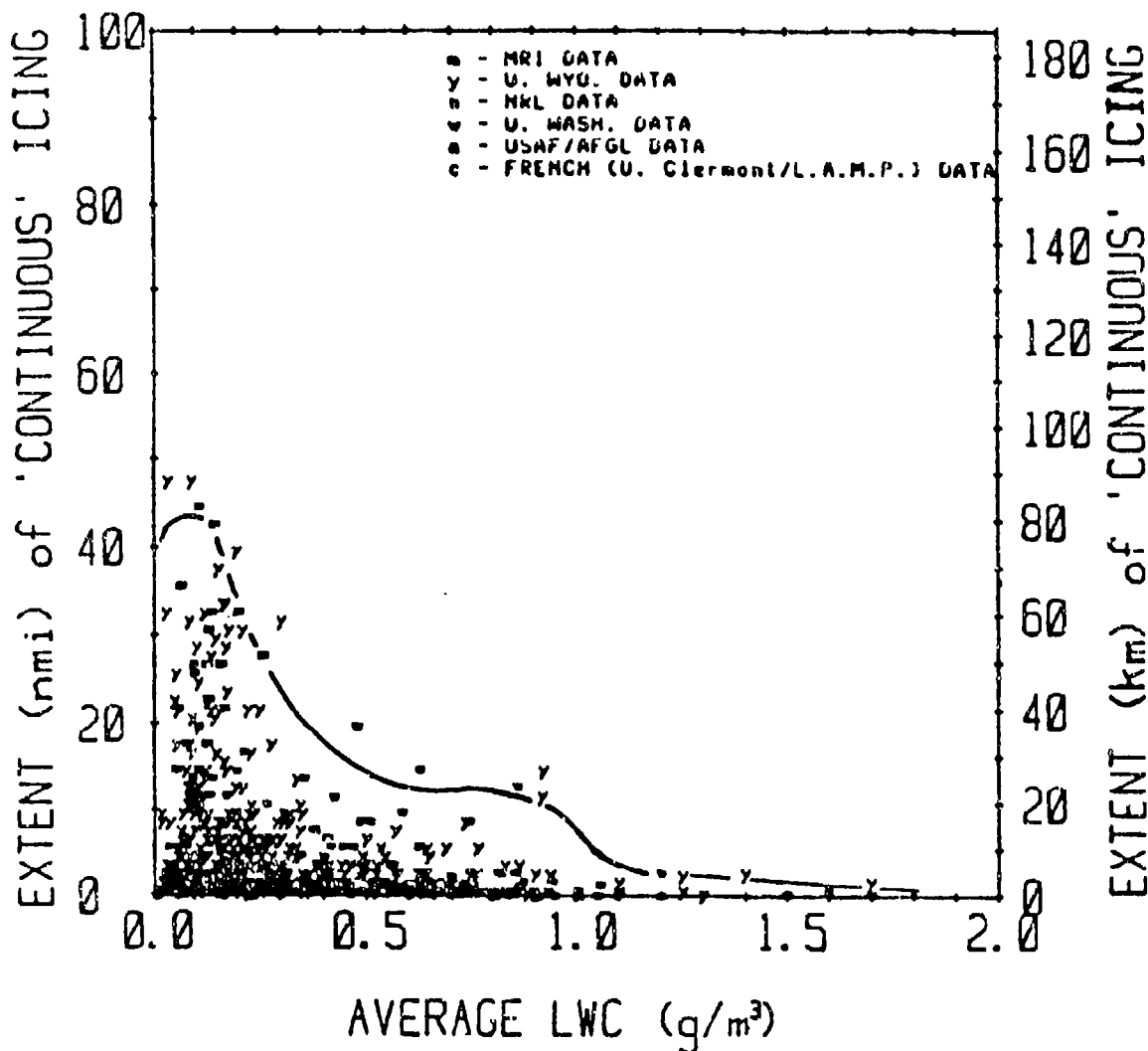
FIGURE 1-9. SCATTERPLOT OF MODERN OBSERVED HORIZONTAL EXTENTS OF ENTIRE ICING ENCOUNTERS VS. AVERAGE LWC OVER THE ENCOUNTER. In this figure an icing encounter is defined as a series of one or more icing events traversed consecutively until a cloud gap of 1 nautical mile or more is reached. The horizontal extent of the encounter is the sum of the horizontal extents of the component icing events but does not include the extent of permissible cloud gaps. Data are for all supercooled cloud types at altitudes up to 10,000 feet AGL and for all observed cloud temperatures below 32 degrees Fahrenheit. A total of 3,645 data miles is represented in this graph. The different plotting symbols represent different data sources as indicated in the key. The curved line is the 99th percentile of horizontal extent for these encounters as a function of average LWC. (Reference 1-20.)
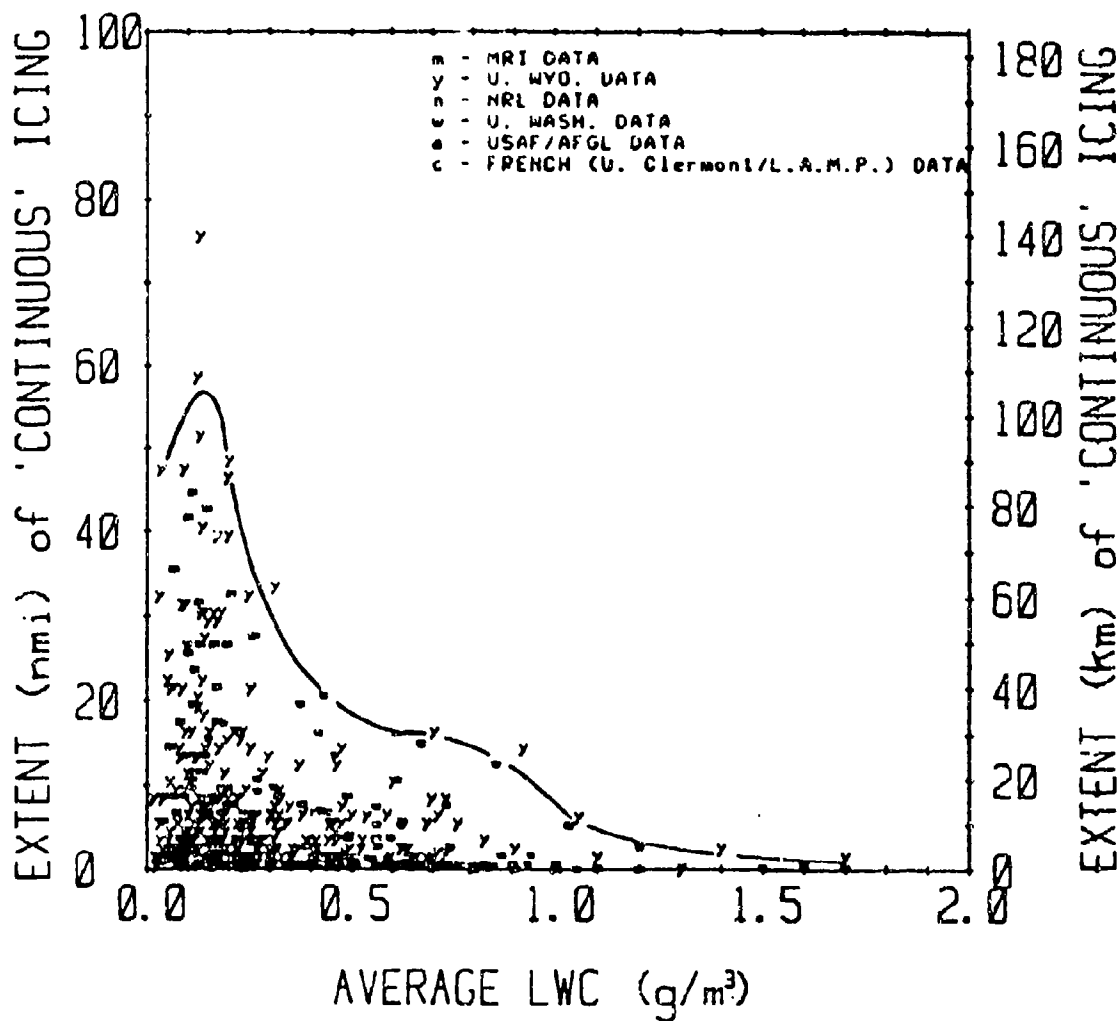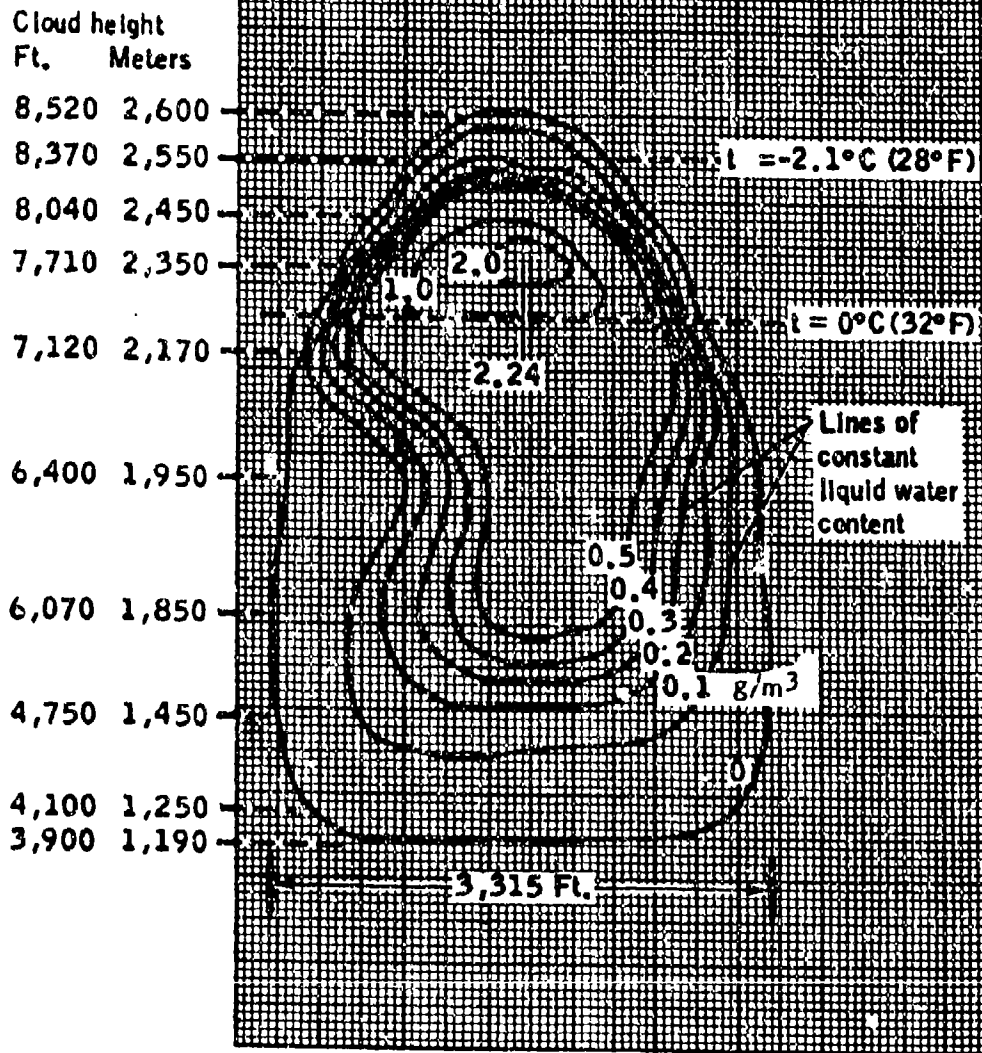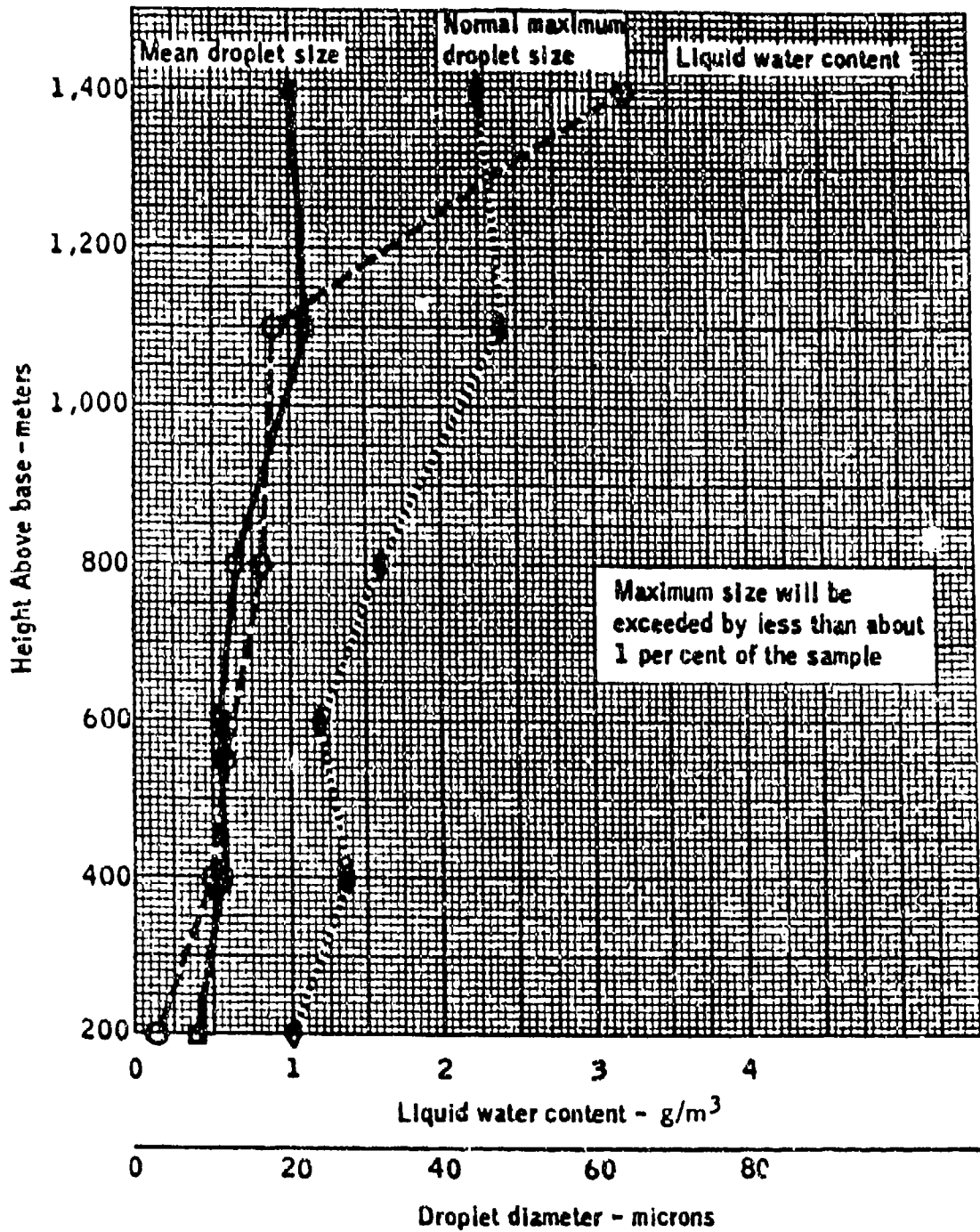
FIGURE 1-10. SCATTERPLOT OF MODERN OBSERVED HORIZONTAL EXTENTS OF ENTIRE ICING ENCOUNTERS VS. AVERAGE LWC OVER THE ENCOUNTER. In this figure, an icing encounter is defined as a series of one or more icing events traversed consecutively until a cloud gap of 3 nautical miles or more is reached. The horizontal extent of the encounter is the sum of the horizontal extents of the component icing events but does not include the extent of permissible cloud gaps. Data are for all supercooled cloud types at altitudes up to 10,000 feet AGL and for all observed cloud temperatures below 32 degrees Fahrenheit. A total of 3,645 data miles is represented in this graph. The different plotting symbols represent different data sources as indicated in the key. The curved line is the 99th percentile of horizontal extent for these encounters as a function of average LWC. (Reference 1-20.)

FIGURE 1-11. SCATTERPLOT OF MODERN OBSERVED HORIZONTAL EXTENTS OF ENTIRE ICING ENCOUNTERS VS. AVERAGE LWC OVER THE ENCOUNTER. In this figure, an icing encounter is defined as a series of one or more icing events traversed consecutively until a cloud gap of 10 nautical miles or more is reached. The horizontal extent of the encounter is the sum of the horizontal extents of the component icing events but does not include the extent of permissible cloud gaps. Data are for all supercooled cloud types at altitudes up to 10,000 feet AGL and for all observed cloud temperatures below 32 degrees Fahrenheit. A total of 3,645 data miles is represented in this graph. The different plotting symbols represent different data sources as indicated in the key. The curved line is the 99th percentile of horizontal extent for these encounters as a function of average LWC. (Reference 1-20.)

Cloud height

Ft.   Meters

8,520 2,600
8,370 2,550 — t = -2.1°C (28°F)
8,040 2,450
7,710 2,350
           2.0
           1.0
7,120 2,170 — t = 0°C (32°F)
           2.24
                              Lines of
                              constant
                              liquid water
6,400 1,950   content
                          0.5
                          0.4
6,070 1,850   0.3
                          0.2
                          0.1 g/m³
4,750 1,450

4,100 1,250   0
3,900 1,190
                    3,315 Ft.

DISTRIBUTION OF LIQUID WATER

FIGURE 1-12.   PROPERTIES OF TYPICAL CUMULUS CONGESTUS CLOUDS - LWC,
DROP SIZE, TEMPERATURE, VERTICAL AND HORIZONTAL DIMENSIONS   (REFERENCE 1-21)

DROPLET SIZE AND LIQUID WATER CONTENT

FIGURE 1-13. PROPERTIES OF TYPICAL CUMULUS CONGESTUS CLOUDS - LWC, DROP SIZE, TEMPERATURE, VERTICAL AND HORIZONTAL DIMENSIONS (REFERENCE 1-21)
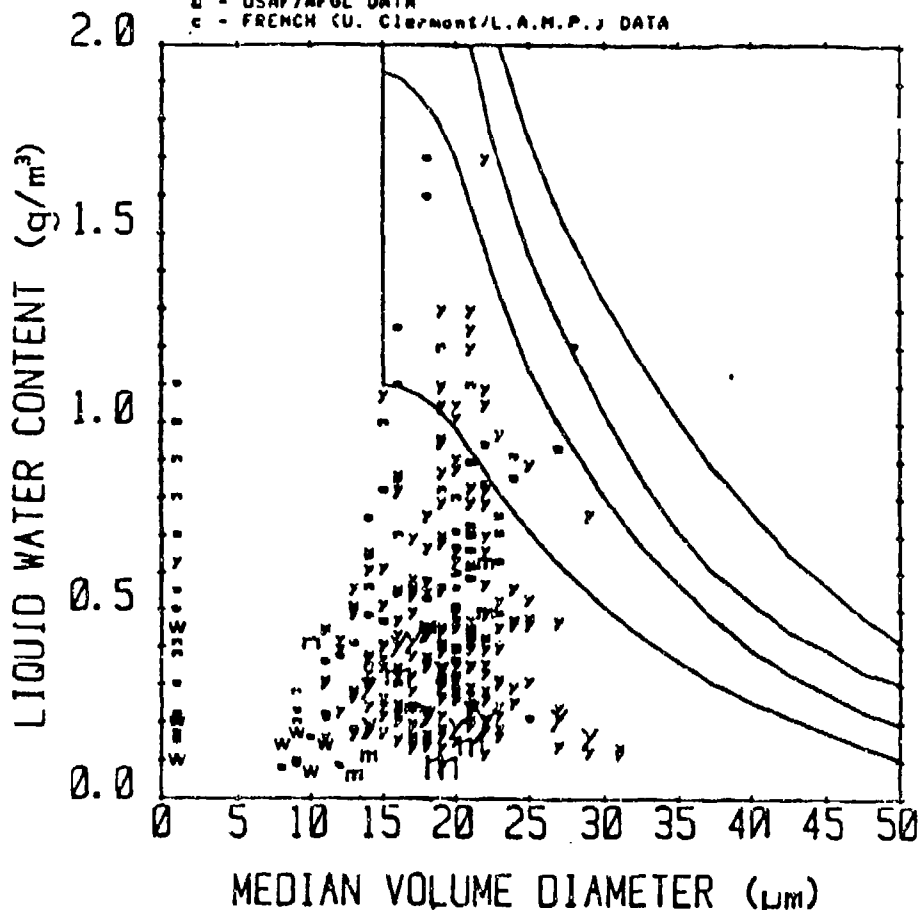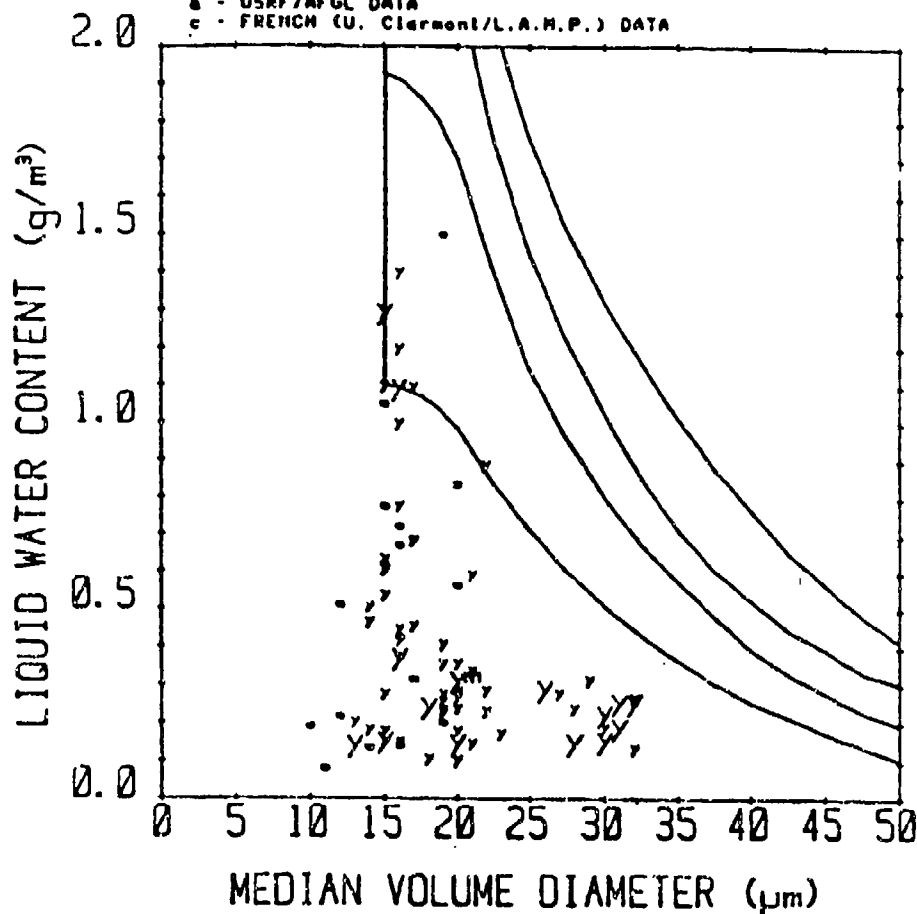
FIGURE 1-14. SCATTERPLOT OF OBSERVED LWC, MVD COMBINATIONS IN THE MODERN DATA FOR CONVECTIVE CLOUDS UP TO 10,000 FEET AGL AND FOR CLOUD TEMPERATURES FROM 14 TO 32 DEGREES FAHRENHEIT. The various plotting symbols represent various data sources as indicated in the key. The size of each plotted symbol is proportional to its weight (i.e., the observed horizontal extent of the associated icing event) as shown by the scale above the graph. The center of each plotted symbol corresponds to the average (and approximately constant) value of LWC and MVD observed during the icing event. Values of LWC for which no MVD measurements are available are plotted arbitrarily at 1 micron MVD. A total of 734 data miles is represented in this graph. The Intermittent Maximum envelope from Figure 4 of FAR-25, Appendix C, is superimposed for comparison. (Reference 1-20.)

FIGURE 1-15. SCATTERPLOT OF OBSERVED LWC, MVD COMBINATIONS IN THE MODERN DATA FOR CONVECTIVE CLOUDS UP TO 10,000 FEET AGL AND FOR CLOUD TEMPERATURES FROM -4 TO 14 DEGREES FAHRENHEIT. The various plotting symbols represent various data sources as indicated in the key. The size of each plotted symbol is proportional to its weight (i.e., the observed horizontal extent of the associated icing event) as shown by the scale above the graph. The center of each plotted symbol corresponds to the average (and approximately constant) value of LWC and MVD observed during the icing event. Values of LWC for which no MVD measurements are available are plotted arbitrarily at 1 micron MVD. A total of 244 data miles is represented in this graph. The Intermittent Maximum envelope from Figure 4 of FAR-25, Appendix C, is superimposed for comparison. (Reference 1-20.)
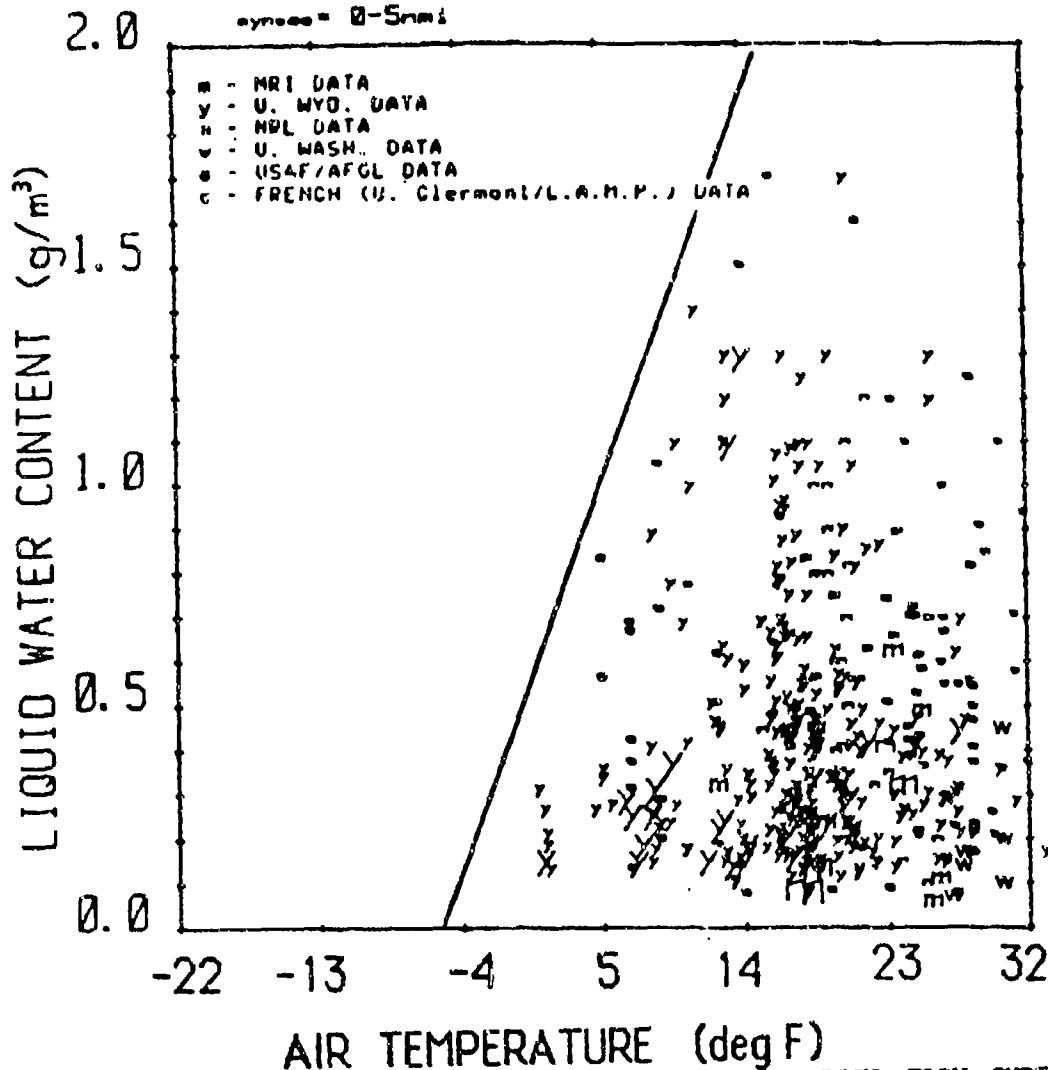
I 1-30
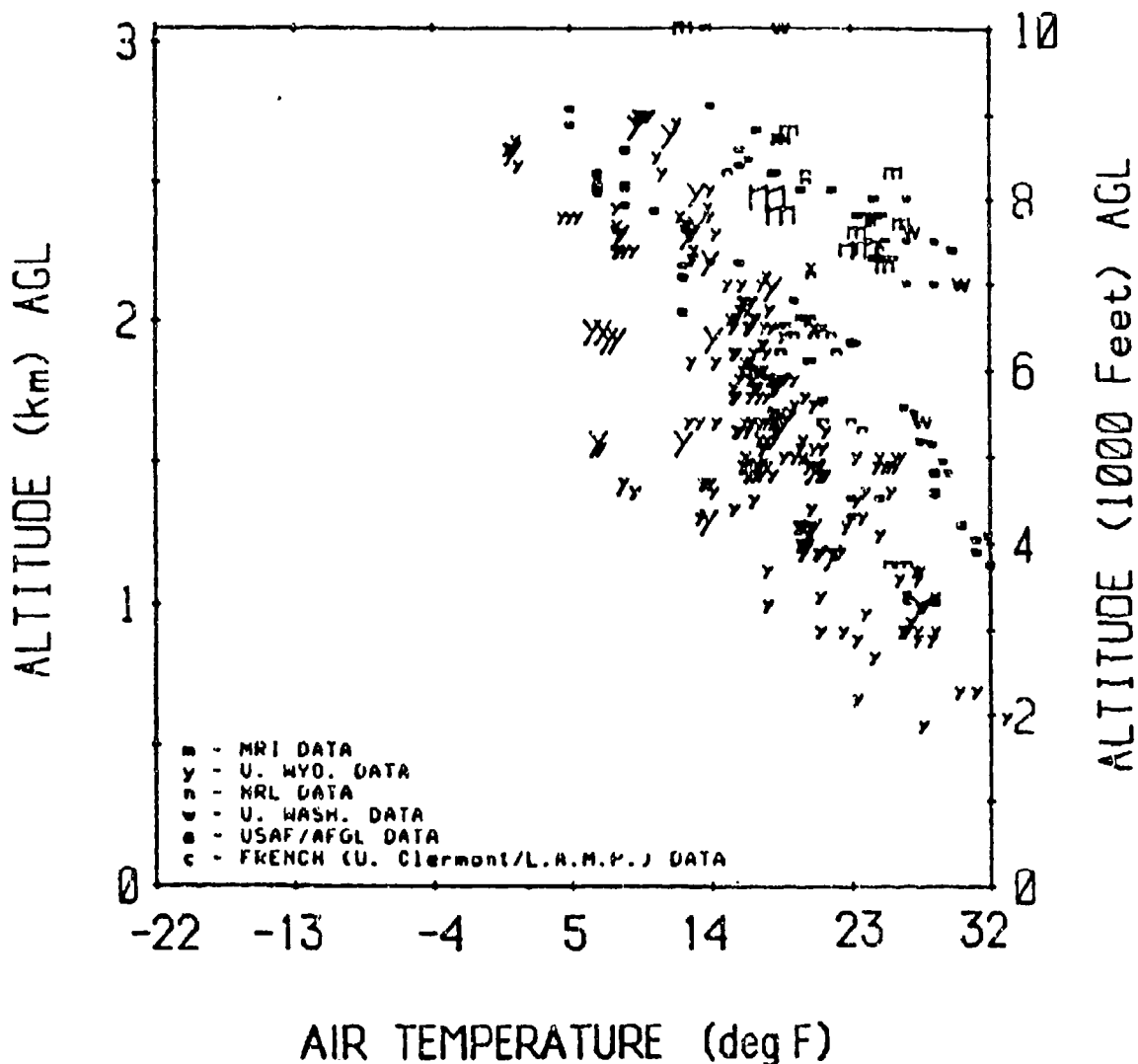
FIGURE 1-16. SCATTERPLOT OF ICING EVENT TEMPERATURES VS. ALTITUDE FOR MODERN DATA FROM SUPERCOOLED CONVECTIVE CLOUDS UP TO 10,000 FEET AGL. The various plotting symbols represent various data sources as indicated in the key. The size of each symbol is proportional to its statistical weight (i.e., the observed horizontal extent of the associated icing event) as shown by the scale above the graph. The center of each plotted symbol corresponds to the average (and approximately constant) value of altitude and OAT observed during the icing event. A total of 980 data miles is represented in this graph. (Reference 1-20.)
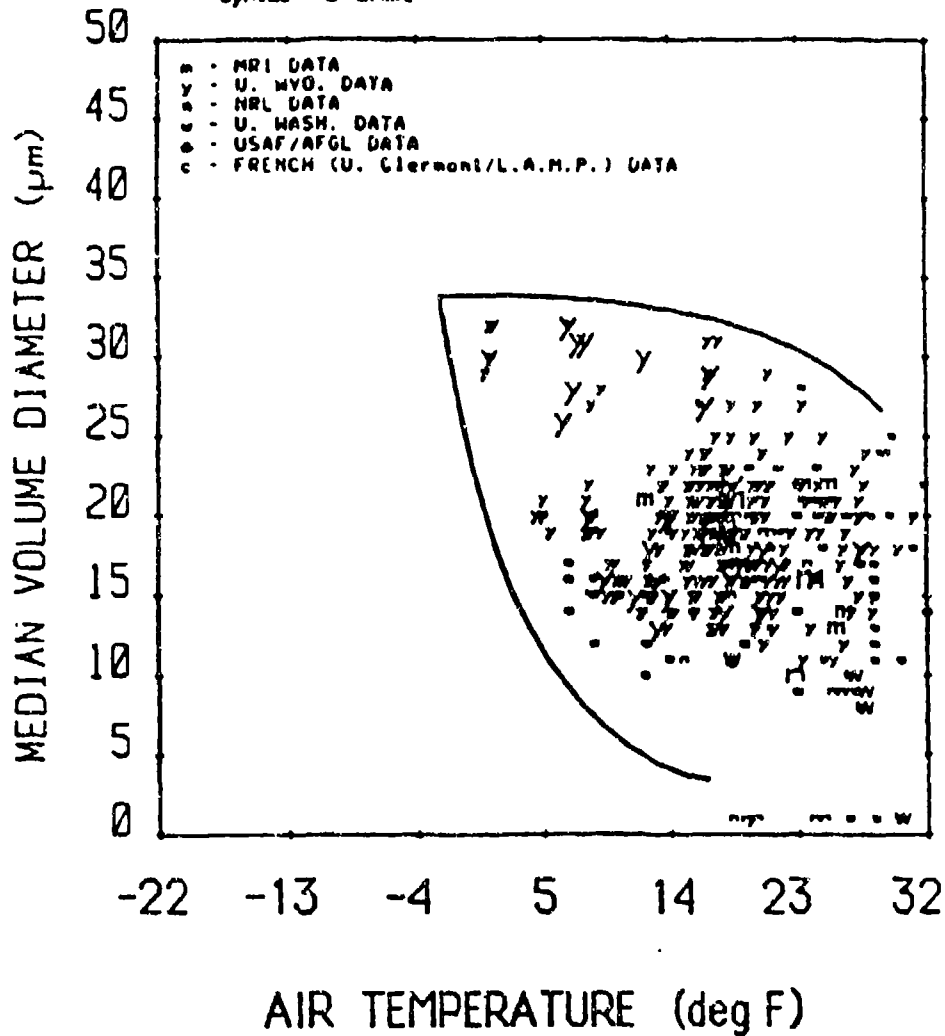
I 1-31

FIGURE 1-17. SCATTERPLOT OF LWC VS. OAT FOR MODERN DATA FROM SUPERCOOLED CONVECTIVE CLOUDS UP TO 10,000 FEET AGL. The various plotting symbols represent various data sources as indicated in the key. The size of each symbol is proportional to its statistical weight (i.e., the observed horizontal extent of the associated icing event) as shown by the scale above the graph. The center of each plotted symbol corresponds to the average (and approximately constant) value of LWC and OAT observed during the icing event. The solid line bounding the data points the apparent upper limit to LWC as a function of temperature for Continental U.S. supercooled convective clouds below 10,000 feet AGL. The position of the line is based on the maximum LWC values in the combined original data (presented in Reference 1-1) and modern data sets. A total of 980 data miles is represented in this graph. (Reference 1-20.)

$m\acute{y}nwac = 20\text{-}25nmi$
$m\acute{y}nwac = 15\text{-}20nmi$
$m\acute{y}nwac = 10\text{-}15nmi$
$m\acute{y}nwac = 5\text{-}10nmi$
$\circ y n \infty = 0\text{-}5nmi$

m : MRI DATA
y : U. MYO. DATA
a : NRL DATA
w : U. WASH. DATA
a : USAF/AFGL DATA
c : FRENCH (U. Clermont/L.A.M.P.) DATA

MEDIAN VOLUME DIAMETER (µm) — 50 45 40 35 30 25 20 15 10 5 0

AIR TEMPERATURE (deg F) — -22 -13 -4 5 14 23 32

FIGURE 1-18. SCATTERPLOT OF MVD VS. OAT FOR MODERN DATA FROM SUPERCOOLED CON-VECTIVE CLOUDS UP TO 10,000 FEET AGL. The various plotting symbols represent various data sources as indicated in the key. The size of each symbol is proportional to its statistical weight (i.e., the observed horizontal extent of the associated icing event) as shown by the scale above the graph. The center of each plotted symbol corresponds to the average (and approximately constant) value of MVD and OAT observed during the icing event. The solid line bounding the data points the apparent upper limit to MVD as a function of temperature for supercooled layer clouds below 10,000 feet AGL. The position of the line is based on the extreme MVD values in both the original data (presented in Reference 1-1) and modern data sets. The data points plotted at 1 micron MVD are those for which the MVD values are actually unknown. A total of 980 data miles is represented in this graph. (Reference 1-20.)
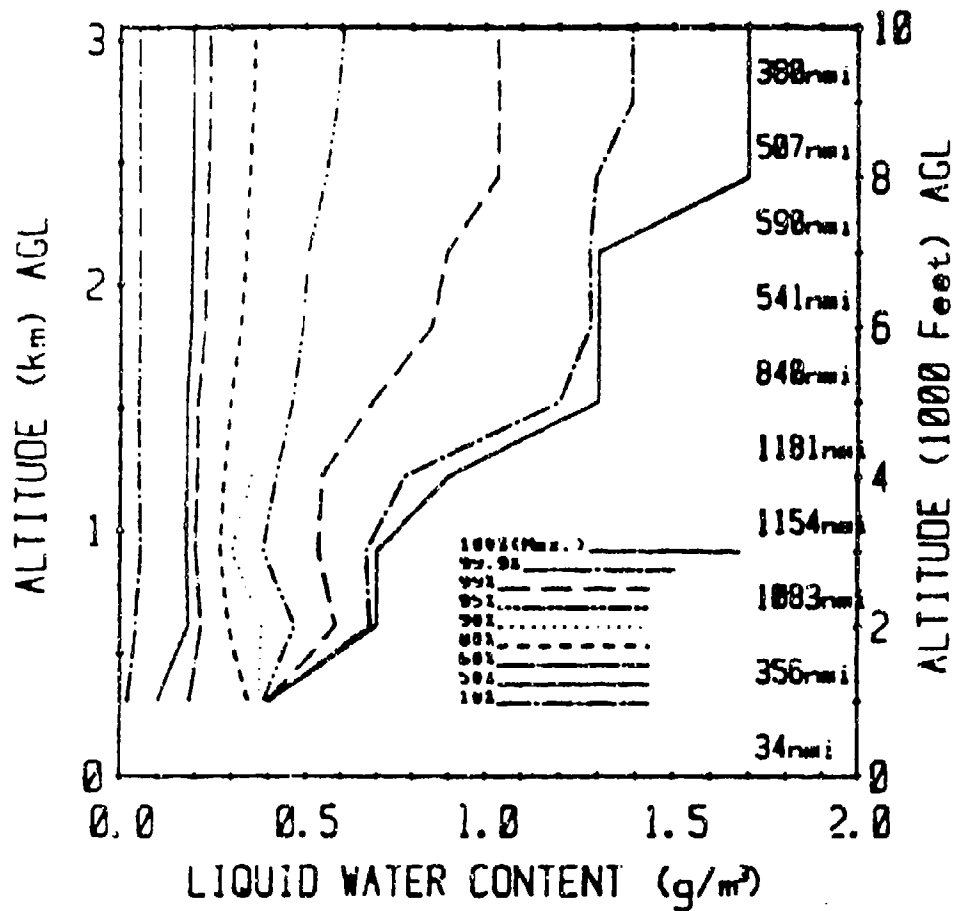
FIGURE 1-19. CUMULATIVE VARIATION WITH ALTITUDE FOR SUPERCOOLED LWC FROM ALL CLOUD TYPES AS RECORDED IN THE ENTIRE CONUS DATA BASE. At each 1000 ft. level the nth percentile curves indicate the value of LWC that was unexceeded in n% of the data miles accumulated at all altitudes below the specified level. The right-hand column of numbers gives the number of data miles recorded within each 1000 ft. interval. A total of 6,660 data miles is represented in this figure. (Reference 1-20.)
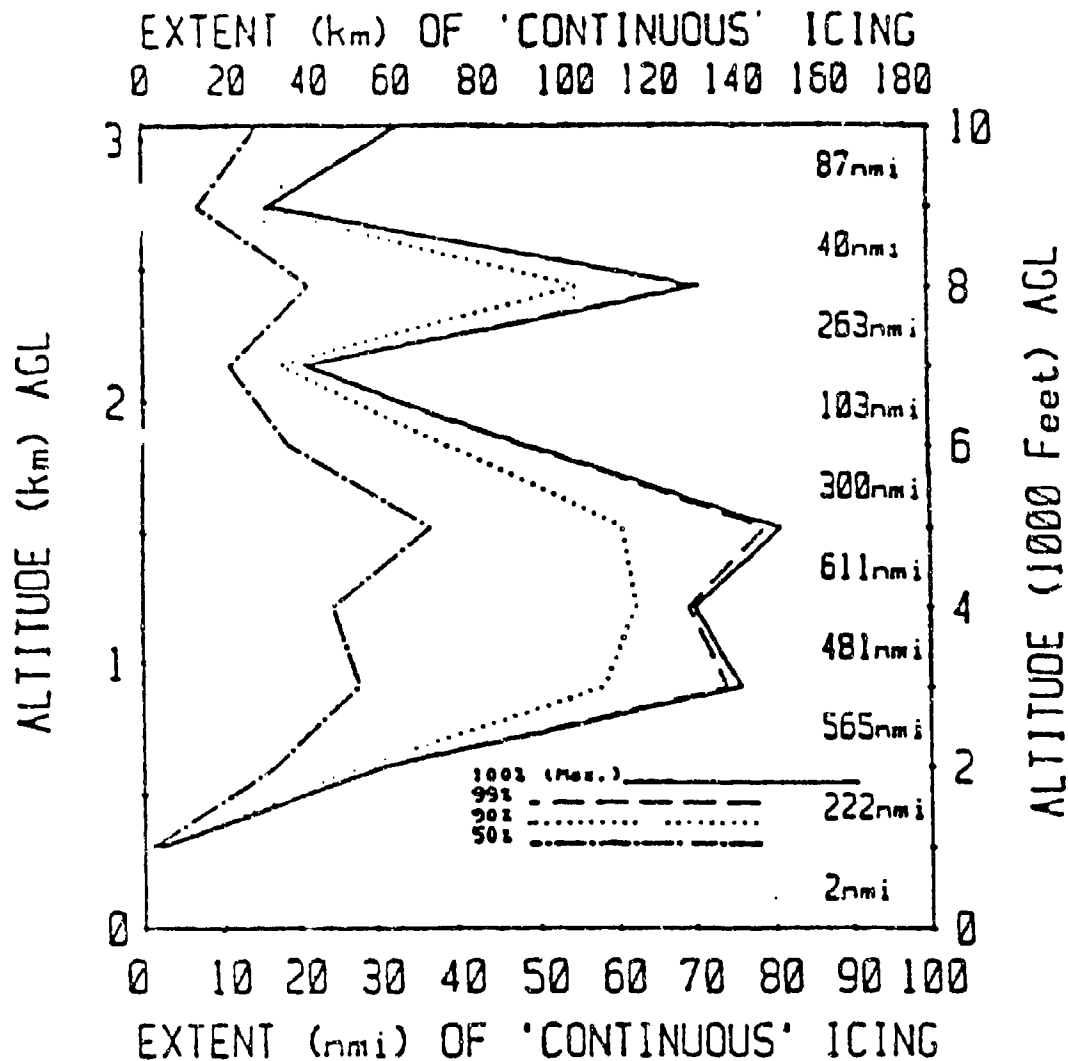
I 1-34

EXTENT (km) OF 'CONTINUOUS' ICING

EXTENT (nmi) OF 'CONTINUOUS' ICING

FIGURE 1-20. ALTITUDE VARIATION OF HORIZONTAL EXTENTS OF EXTENDED ICING
ENCOUNTERS IN LAYER CLOUDS AS OBSERVED IN THE MODERN DATA. An extended
encounter is a series of consecutive icing events added together sequentially
until a gap of some specified duration (3 nautical miles for this case) is
reached. At each 1,000 foot level, the nth percentile curves indicate the
horizontal extent which was unexceeded in n percent of the extended encounters
within the 1,000 foot altitude interval immediately below. The right-hand
column of numbers give the number of data miles contributing within each 1,000
foot interval. A total of 2,675 data miles is represented in this figure.
(Reference 1-20.)

I 1-35
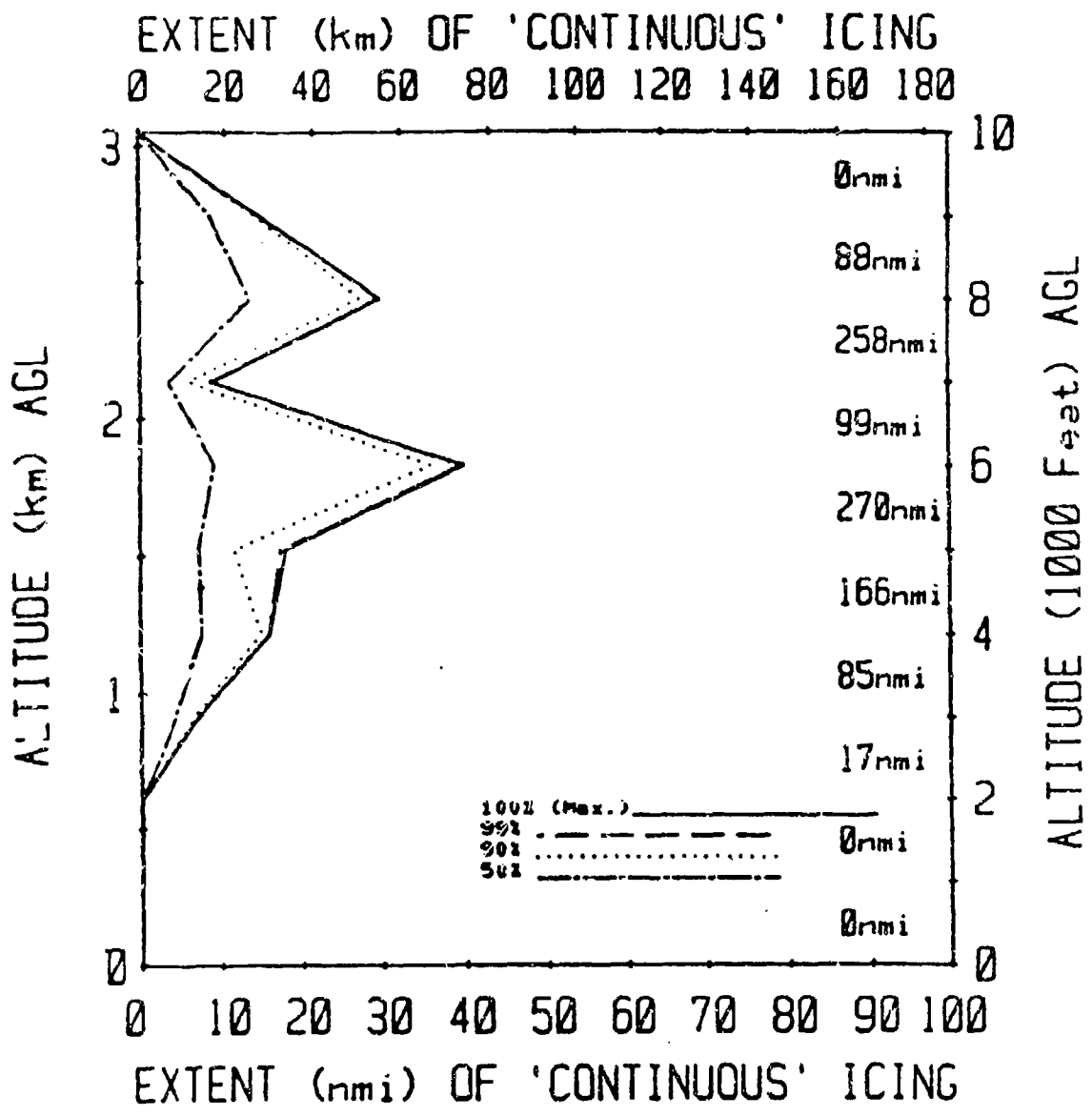
FIGURE 1-21. ALTITUDE VARIATION OF HORIZONTAL EXTENTS OF EXTENDED ICING ENCOUNTERS IN CONVECTIVE CLOUDS AS OBSERVED IN THE MODERN DATA. An extended encounter is a series of consecutive icing events added together sequentially until a gap of some specified duration (3 nautical miles for this case) is reached. At each 1,000 foot level the nth percentile curves indicate the horizontal extent which was unexceeded in n percent of the extended encounters within 1,000 foot altitude interval immediately below. The right-hand column of numbers give the number of data miles contributing within each 1,000 foot interval. A total of 985 data miles is represented in this figure. (Reference 1-20.)

I 1-36
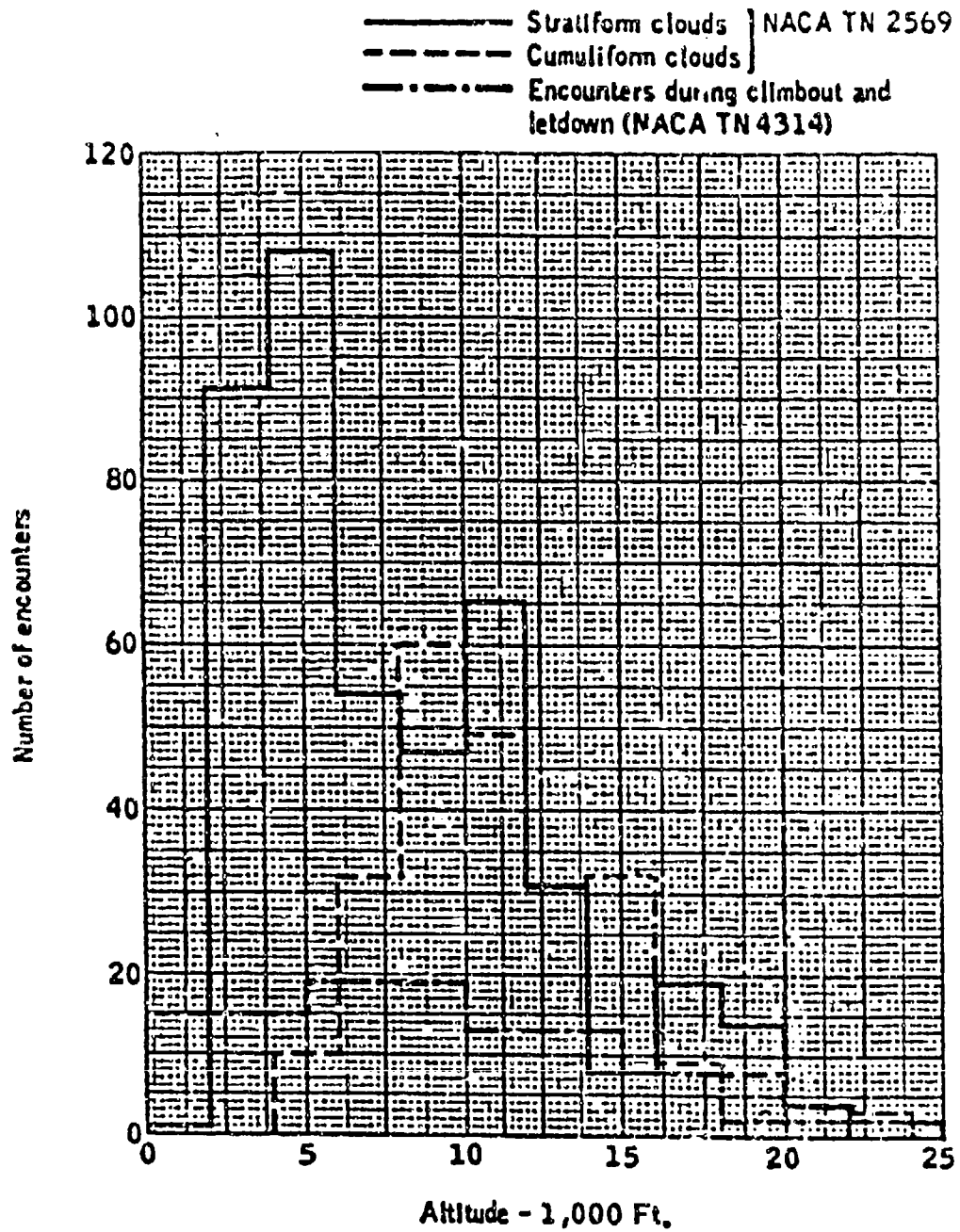
FIGURE 1-22.   ICING ENCOUNTER FREQUENCY VERSUS ALTITUDE   (REFERENCE 1-1)
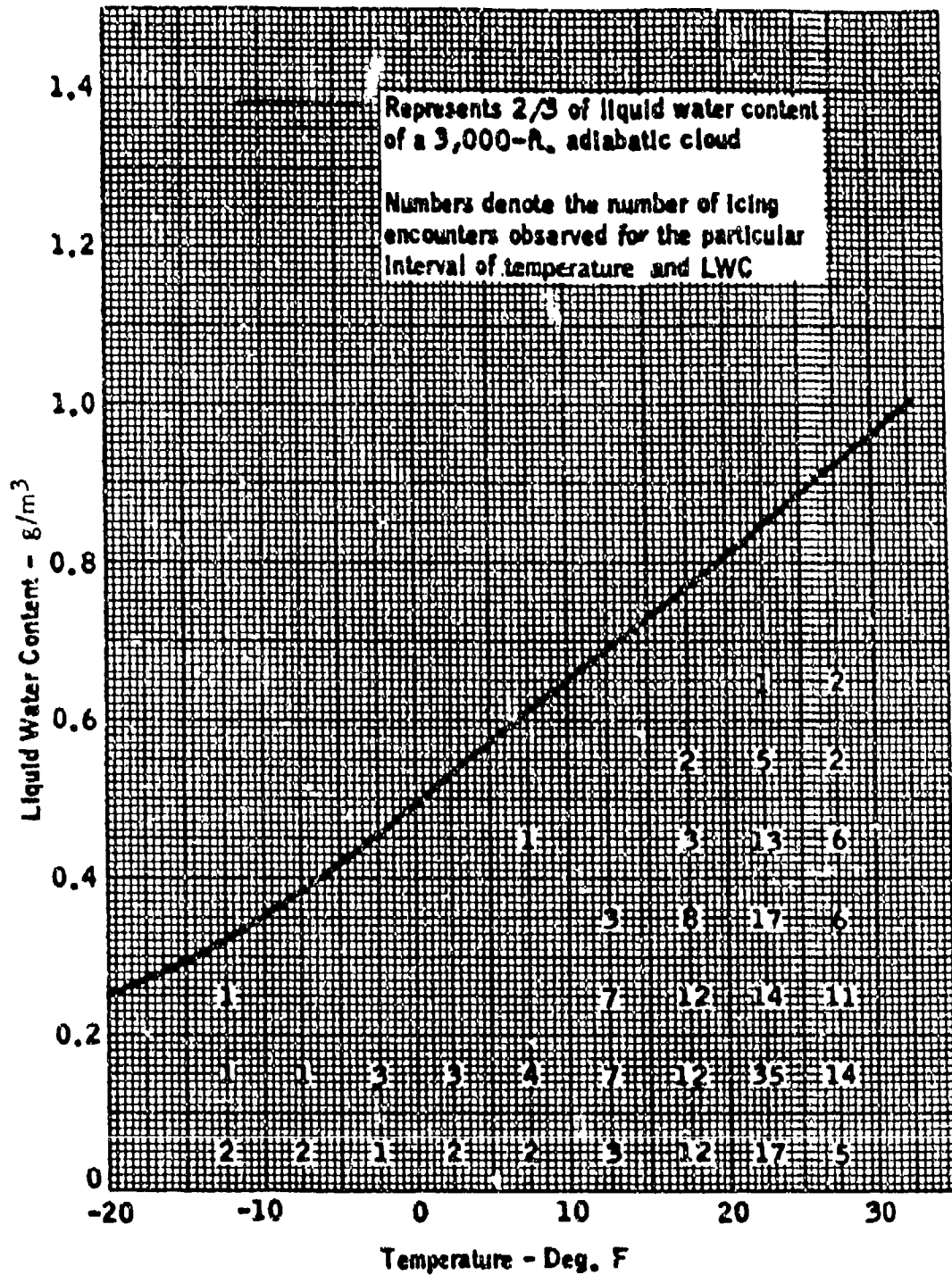
FIGURE 1-23. LWC VERSUS TEMPERATURE - STRATUS CLOUDS (REFERENCES 1-5 & 1-6)

I 1-38
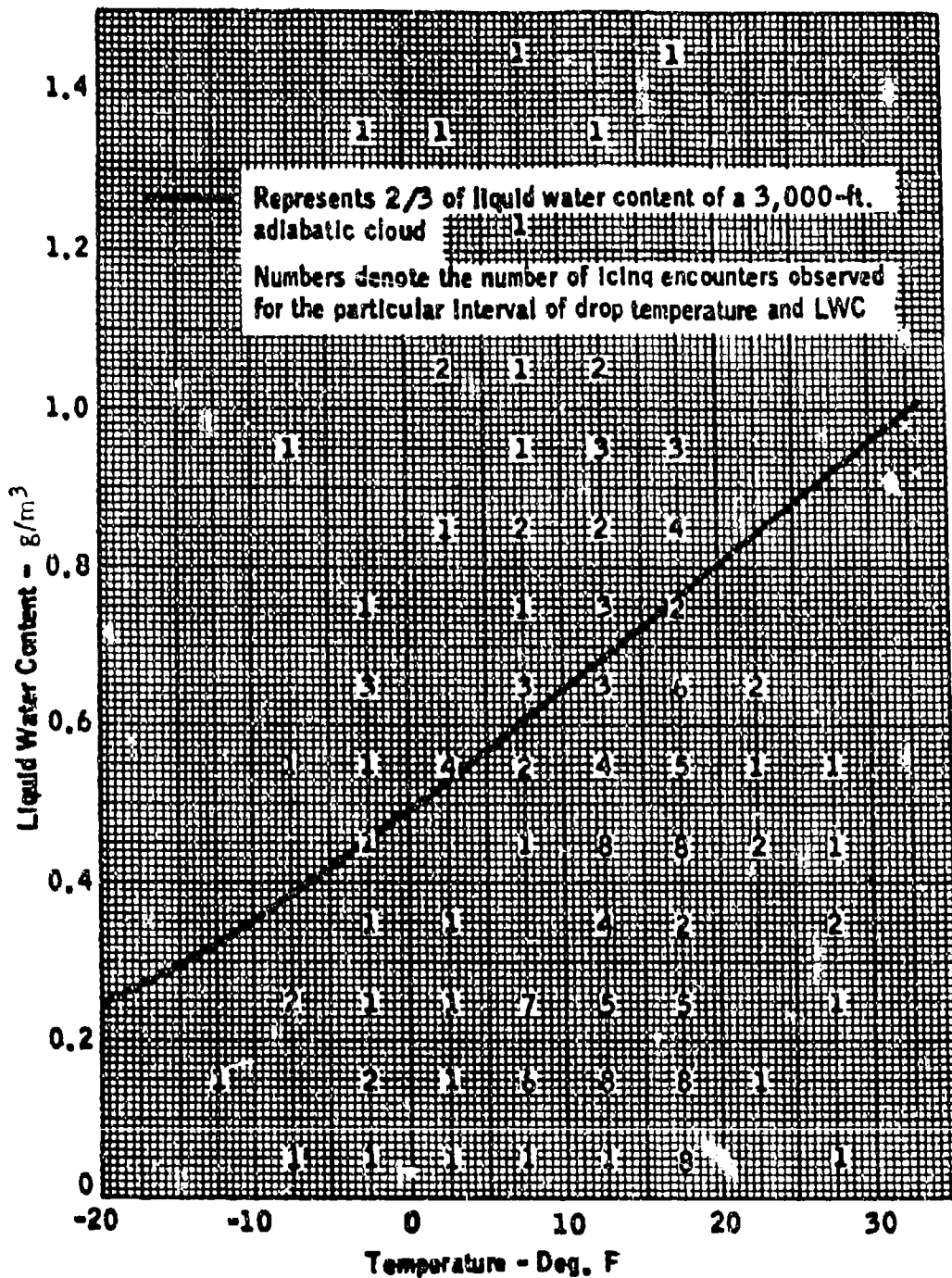
FIGURE 1-24.   LWC VERSUS TEMPERATURE - CUMULUS CLOUDS   (REFERENCES 1-5 & 1-6)
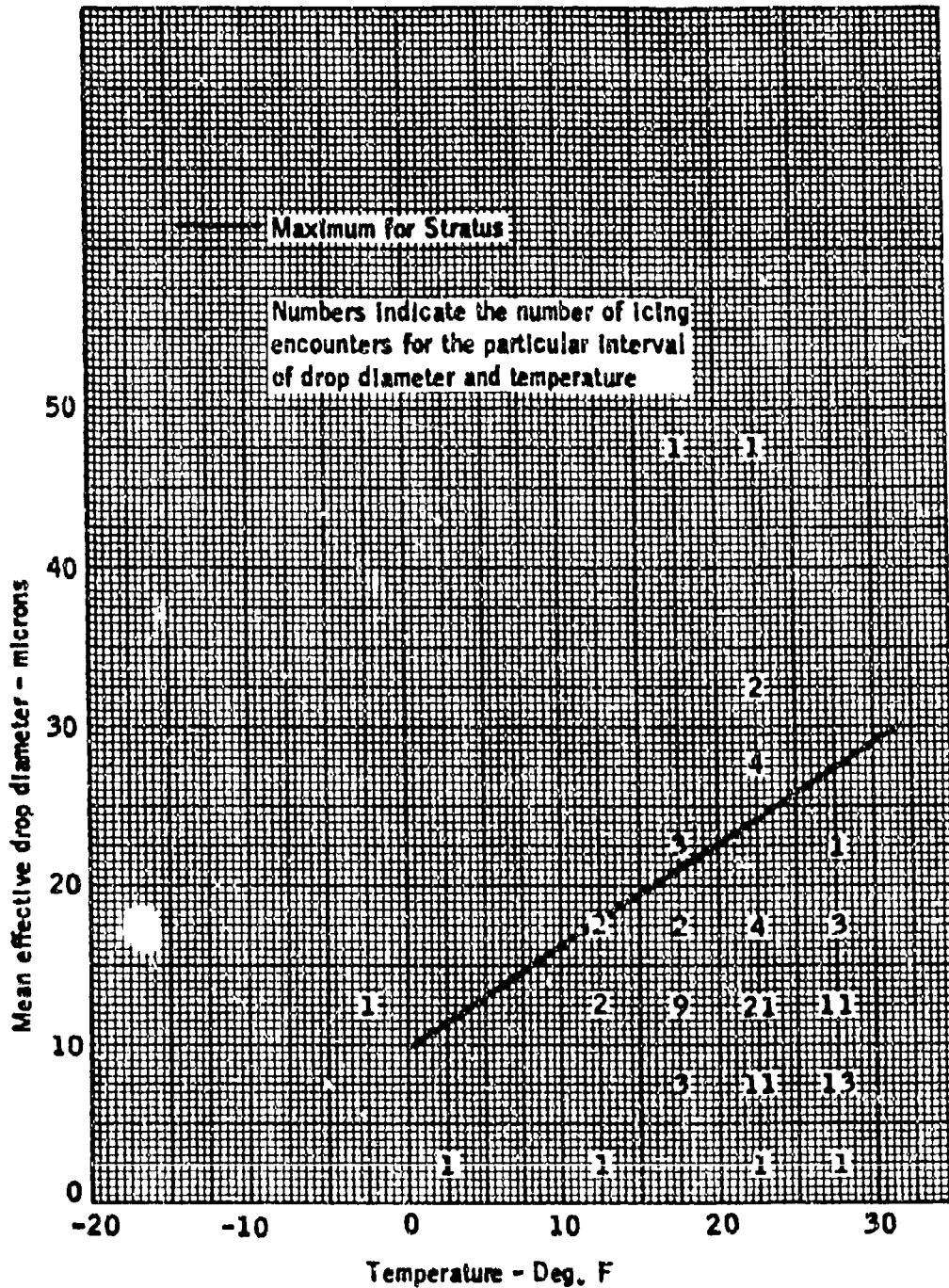
FIGURE 1-25.   DROPLET DIAMETER VERSUS TEMPERATURE - STRATUS CLOUDS
(REFERENCE 1-5)

1 1-40
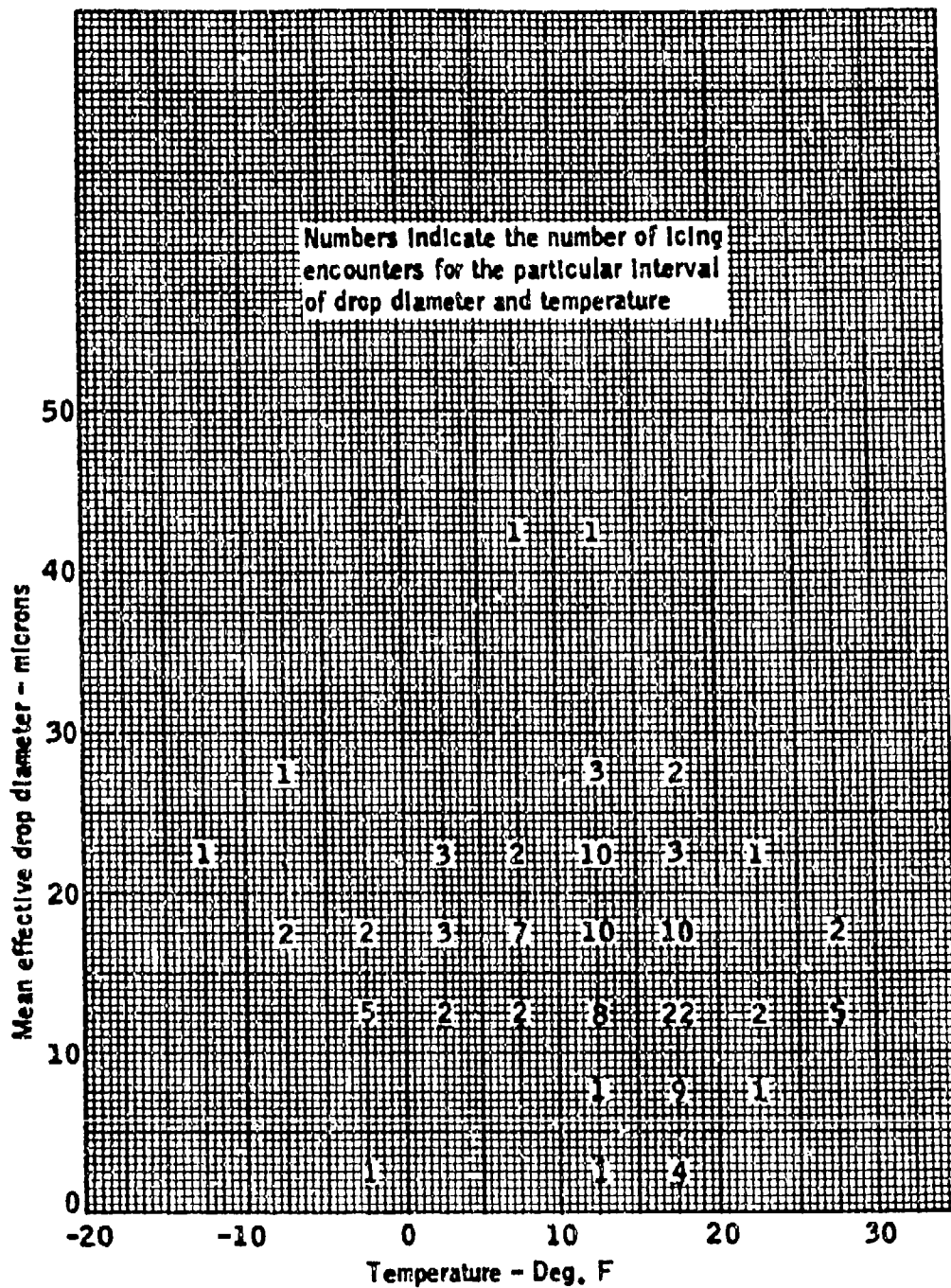
FIGURE 1-26. DROPLET DIAMETER VERSUS TEMPERATURE - CUMULUS CLOUDS
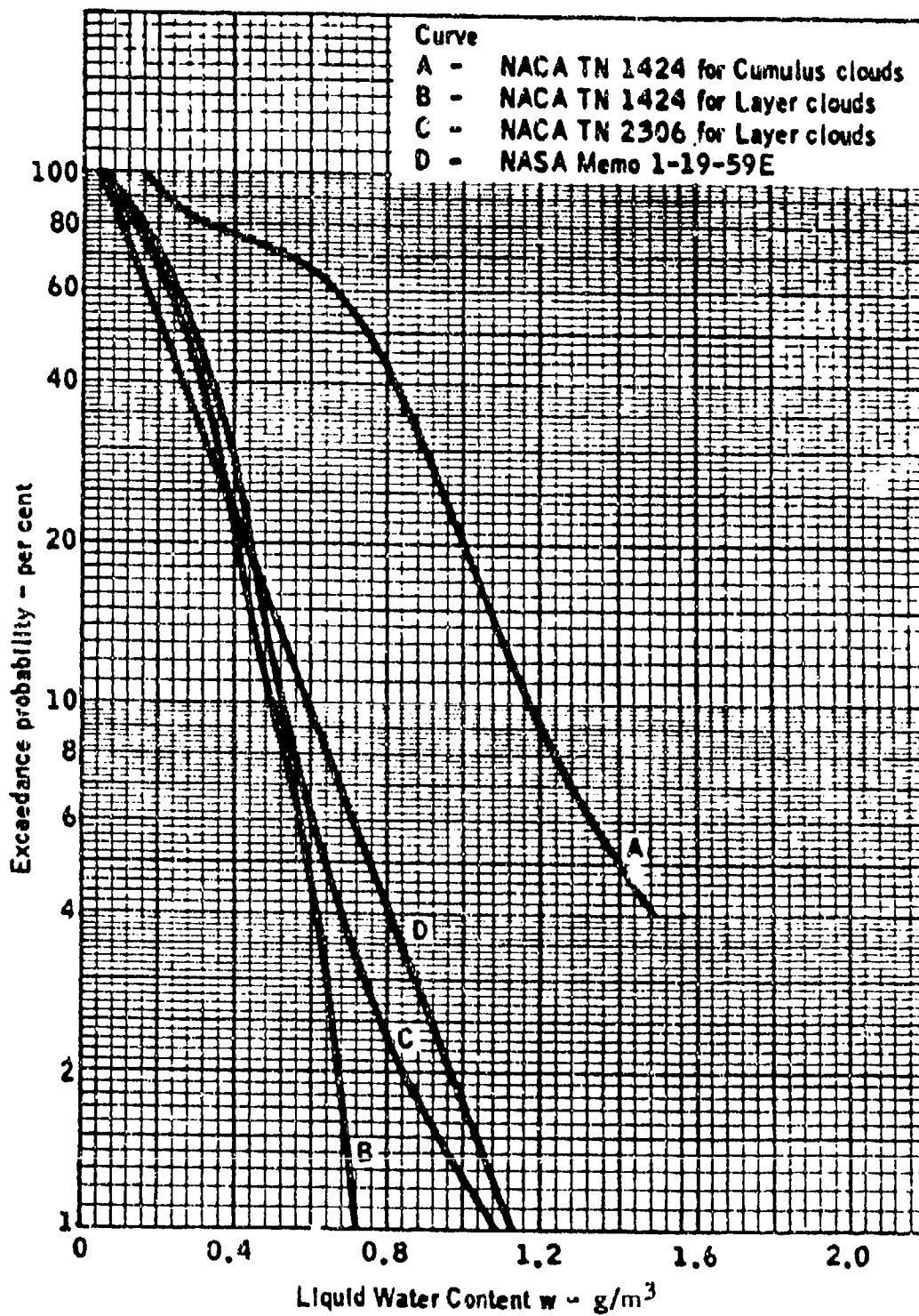(REFERENCE 1-5)

I 1-41

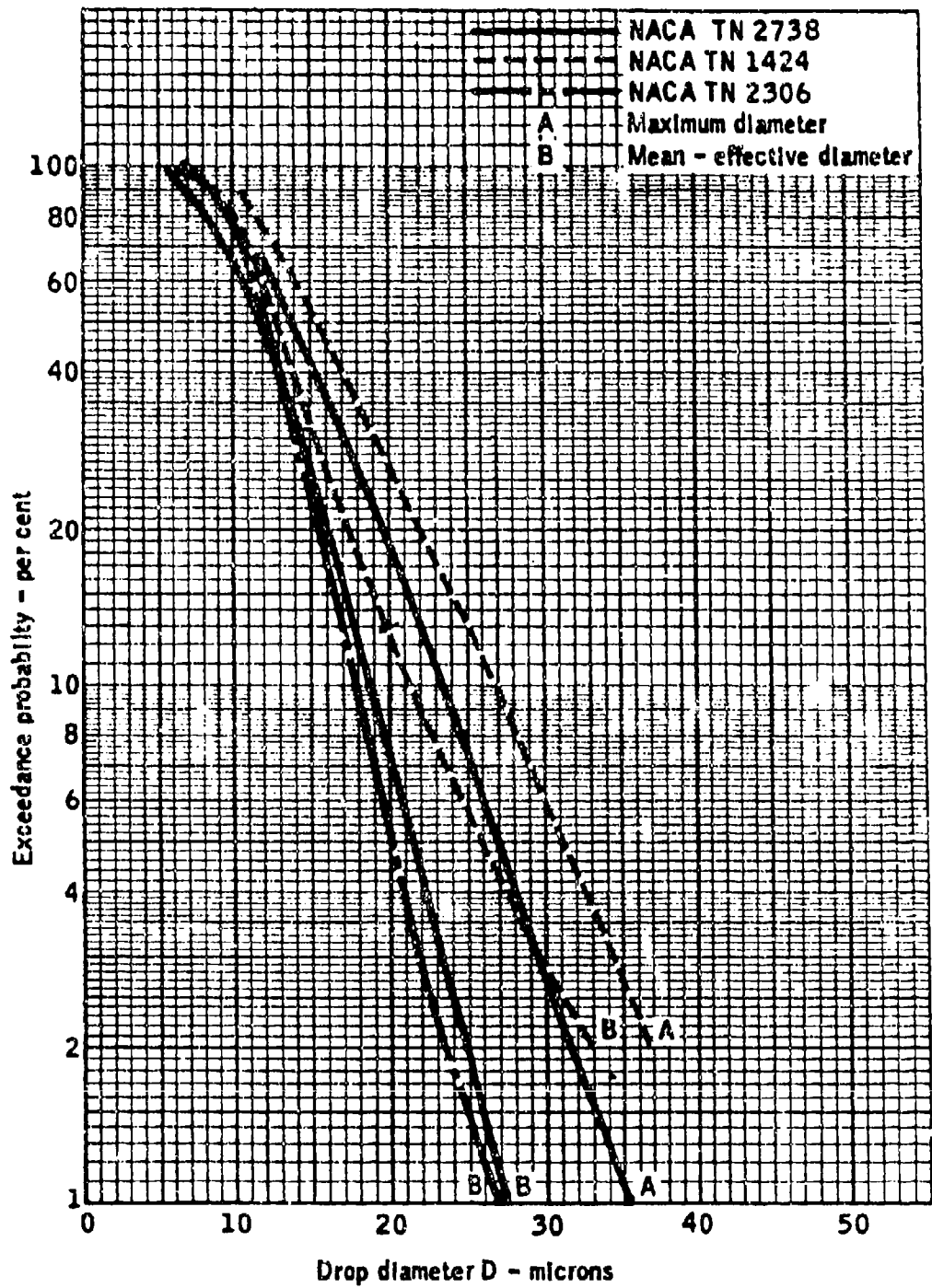FIGURE 1-27. EXCEEDANCE PROBABILITY FOR MAXIMUM LWC
(REFERENCES 1-6, 1-10 AND 1-16)

FIGURE 1-28. EXCEEDANCE PROBABILITY FOR DROP DIAMETER
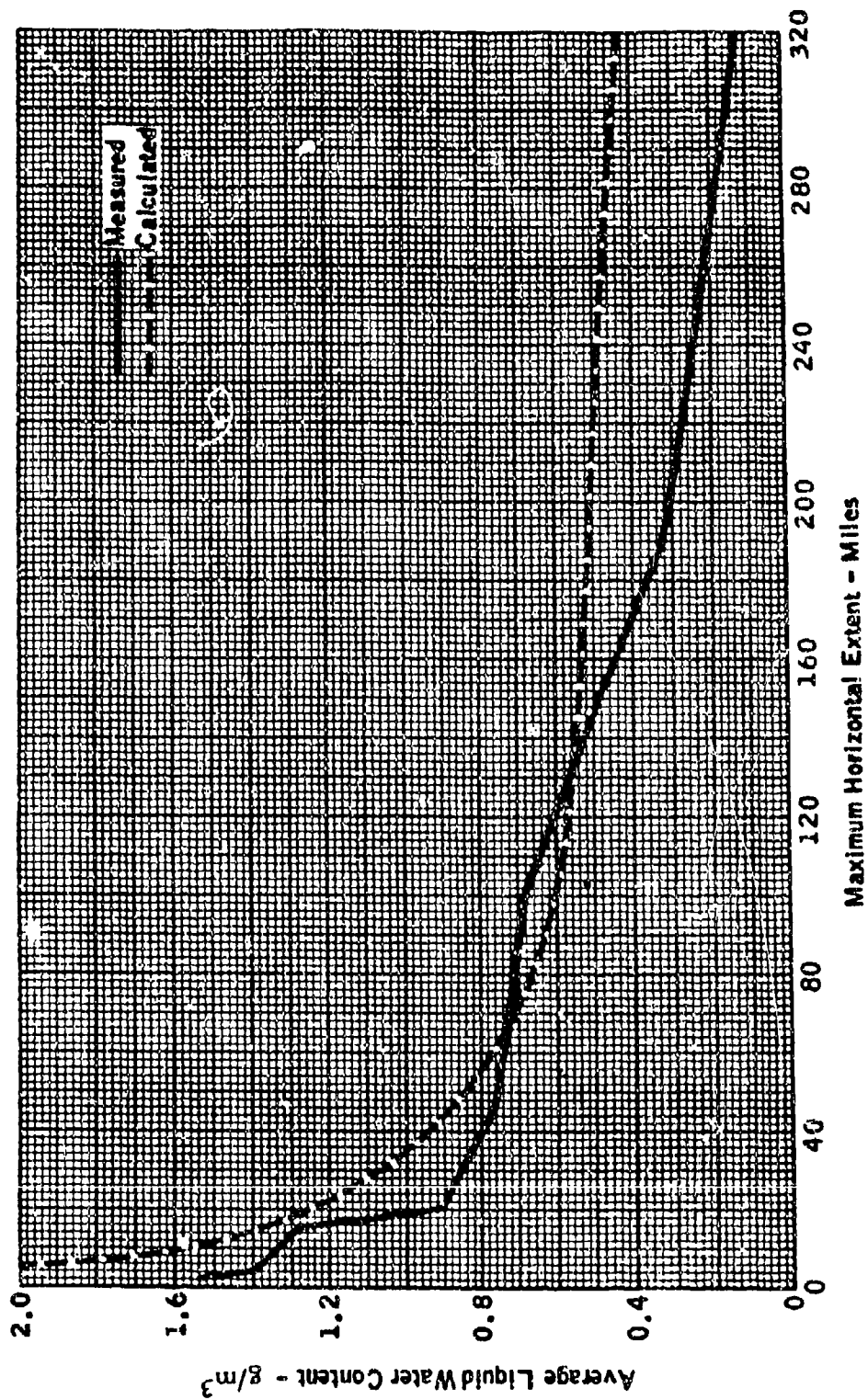(REFERENCES 1-6, 1-10 AND 1-11)
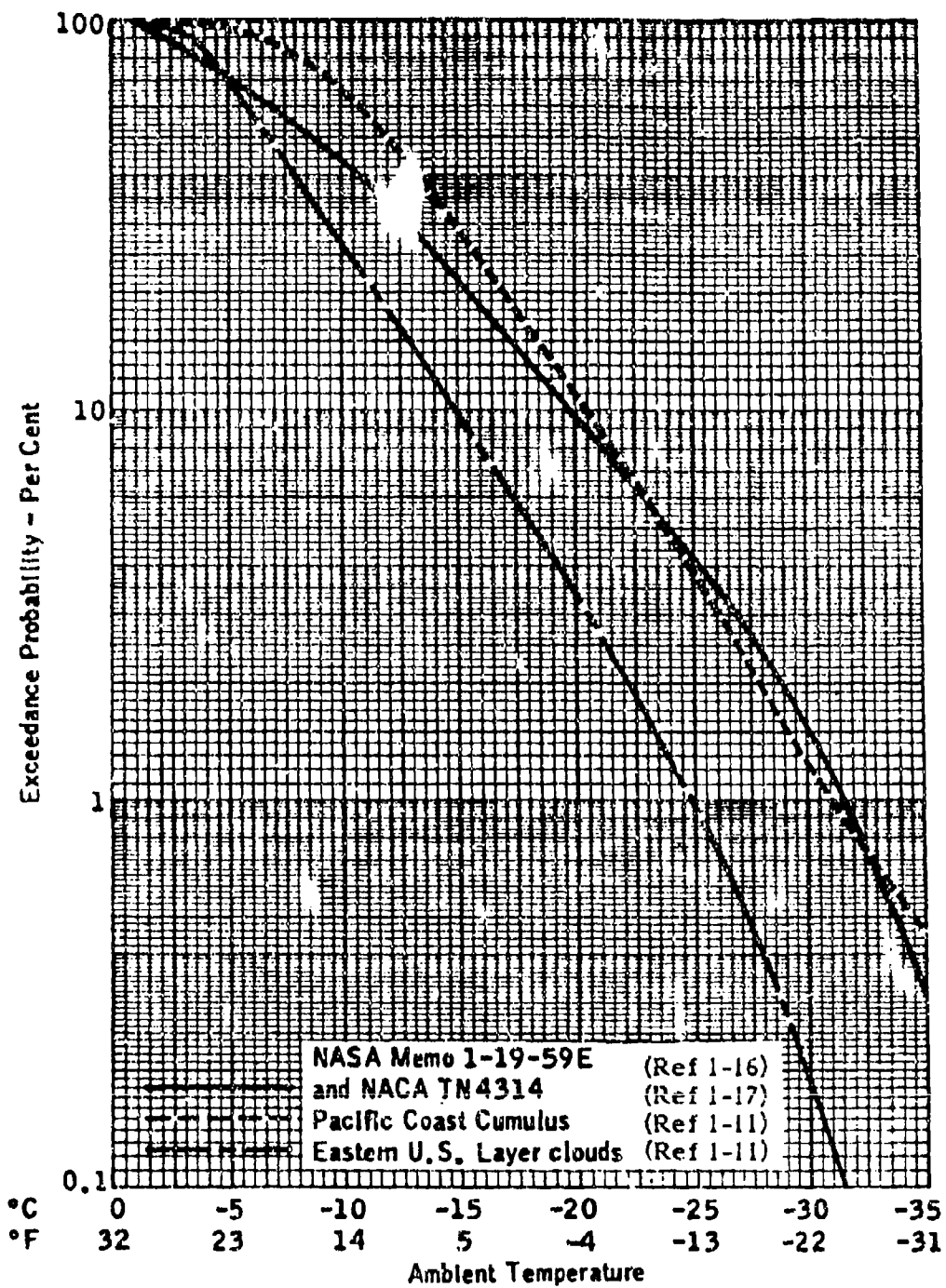
FIGURE 1-29.   PROBABILITY OF CLOUD ICING TEMPERATURE
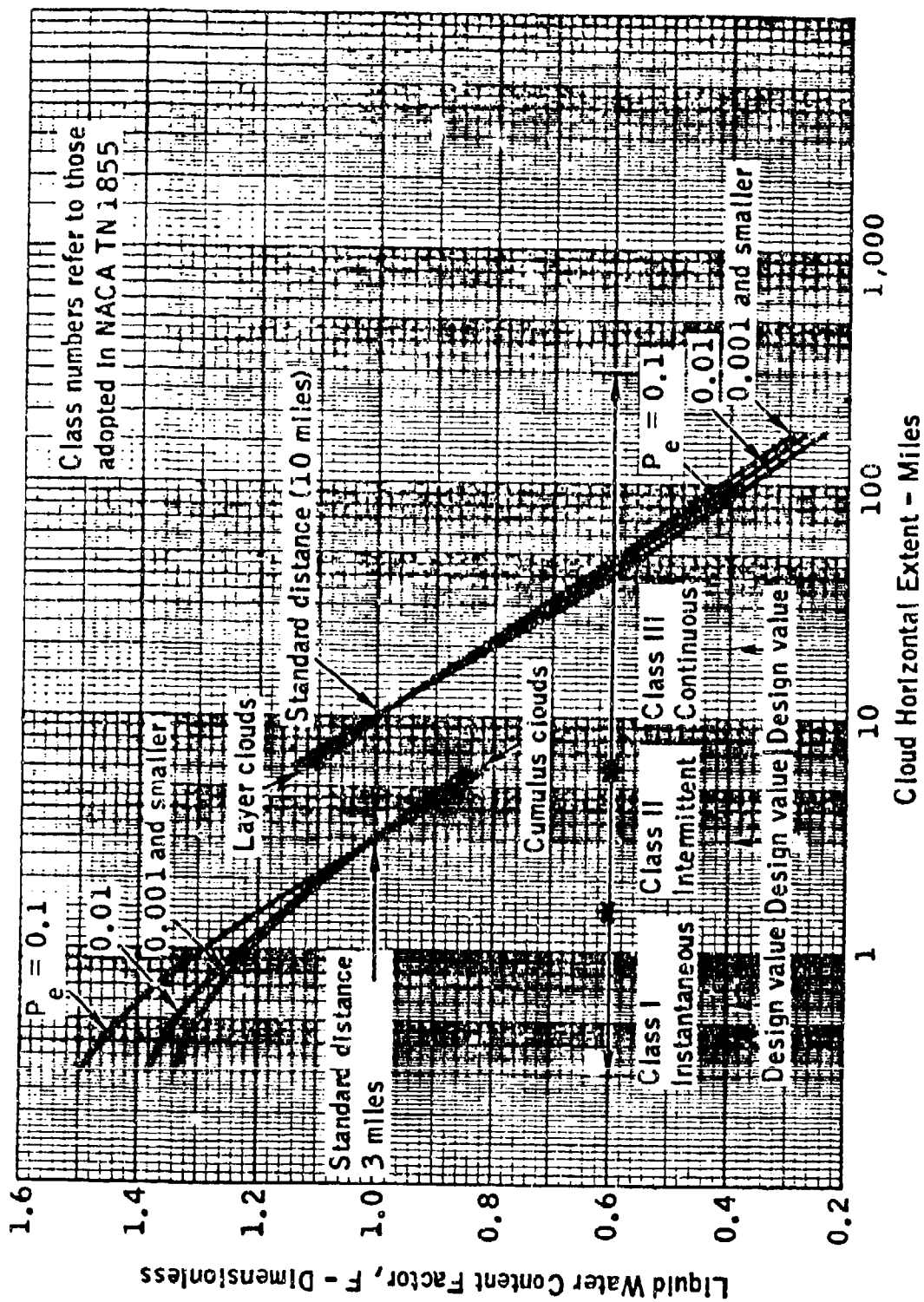
FIGURE 1-30. LWC VERSUS HORIZONTAL EXTENT (REFERENCE 1-9)

FIGURE 1-31. VARIATION OF LWC FACTOR, F, WITH CLOUD HORIZONTAL EXTENT FOR VARIOUS EXCEEDANCE PROBABILITIES (REFERENCE 1-11)
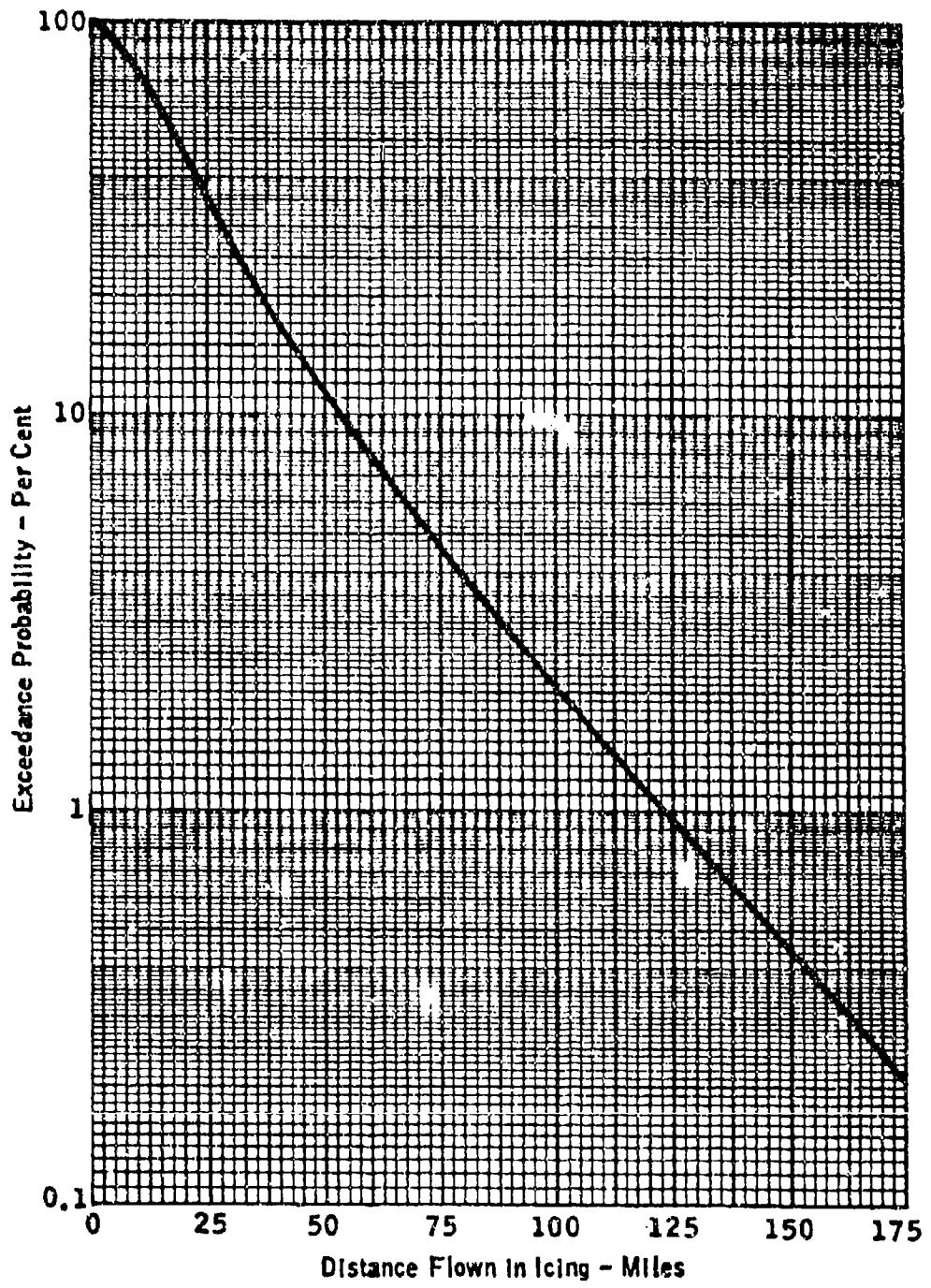
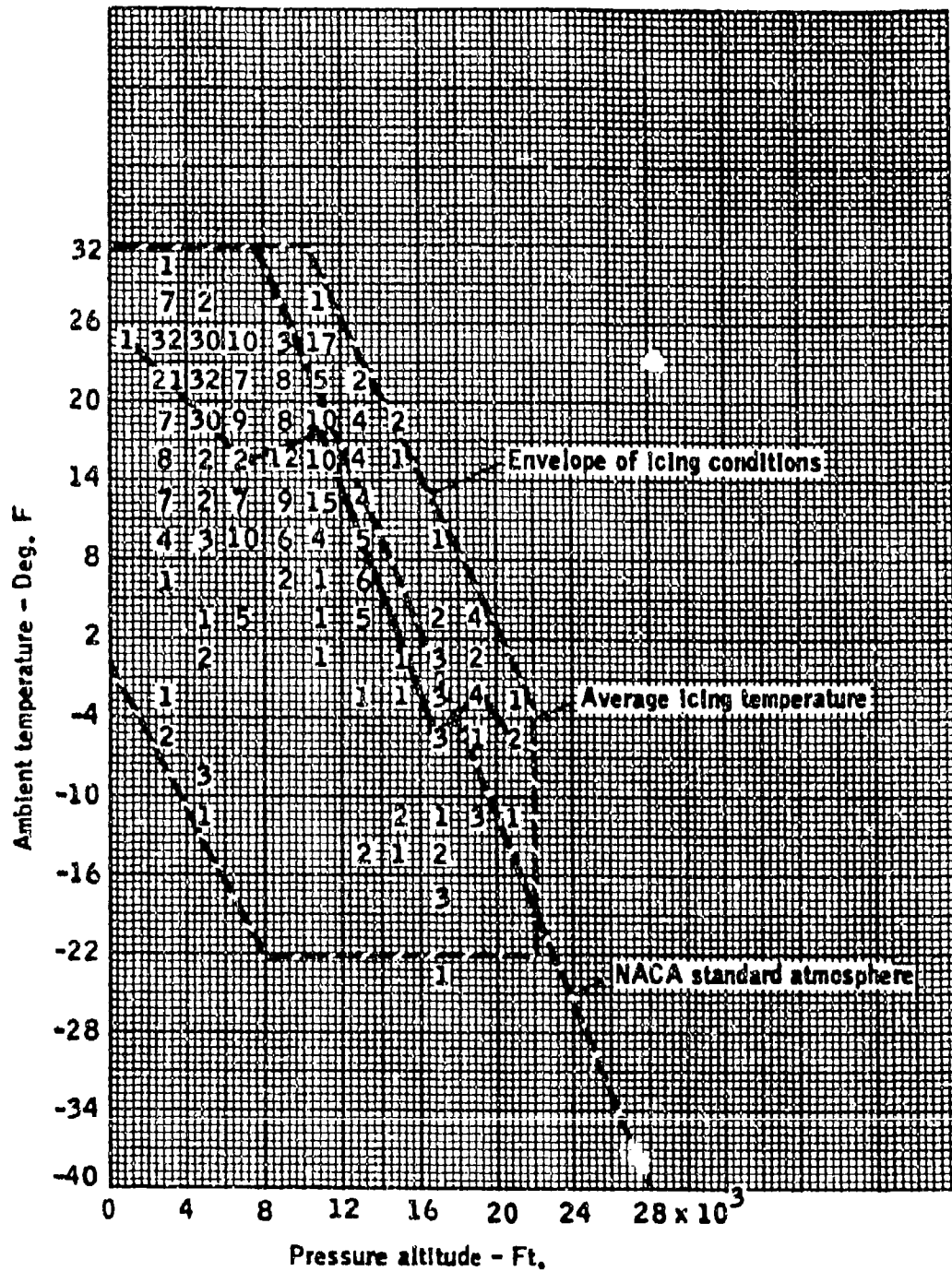FIGURE 1-32. PROBABILITY CURVE OF DISTANCE FLOWN IN ICING (REFERENCE 1-16)

FIGURE 1-33. FREQUENCY DISTRIBUTION OF ICING ENCOUNTERS IN STRATIFORM CLOUDS FOR INCREMENTS OF TEMPERATURE AND ALTITUDE (REFERENCE 1-9)
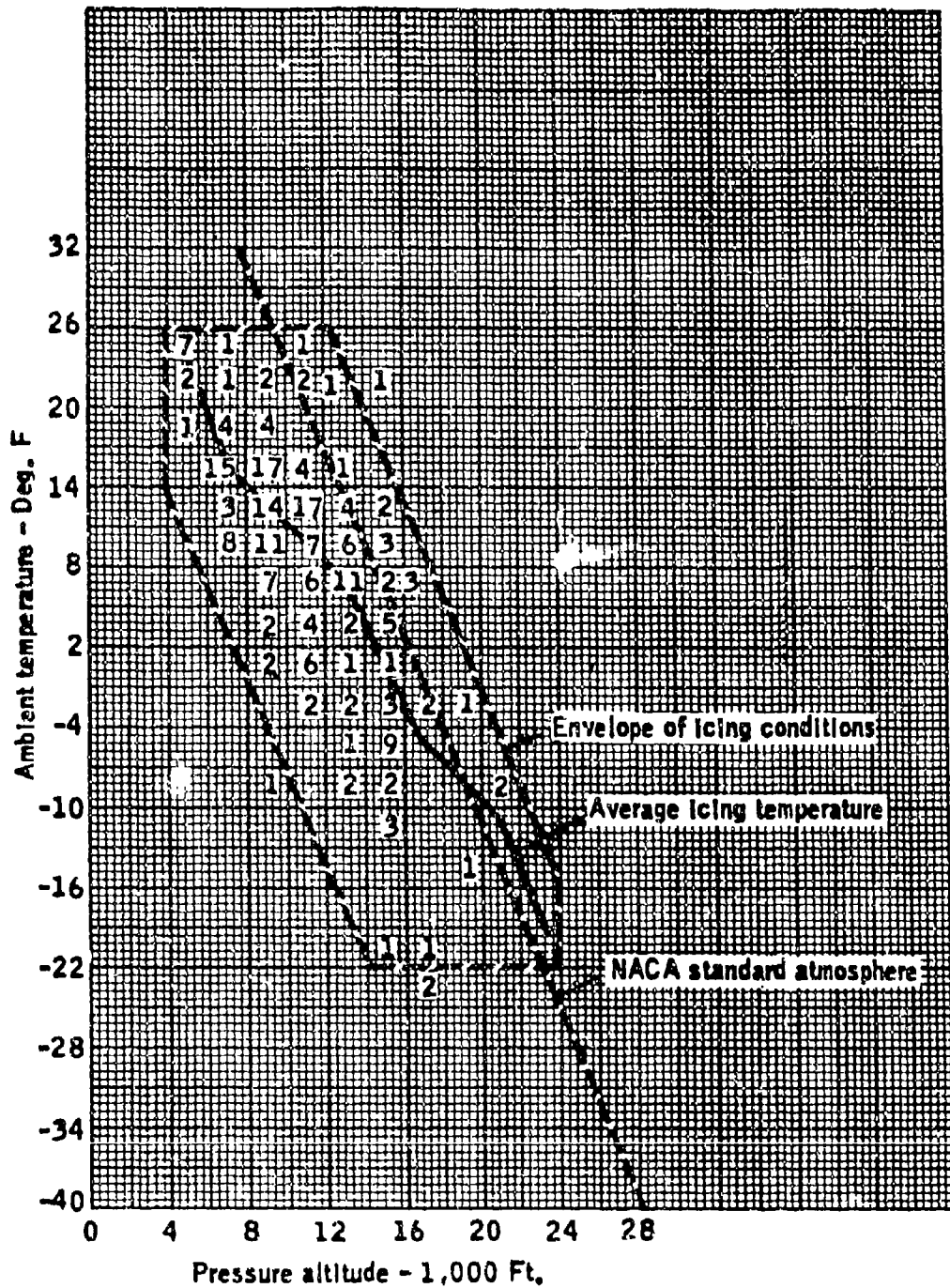
1 1-48

FIGURE 1-34. FREQUENCY DISTRIBUTION OF ICING ENCOUNTERS IN CUMULIFORM
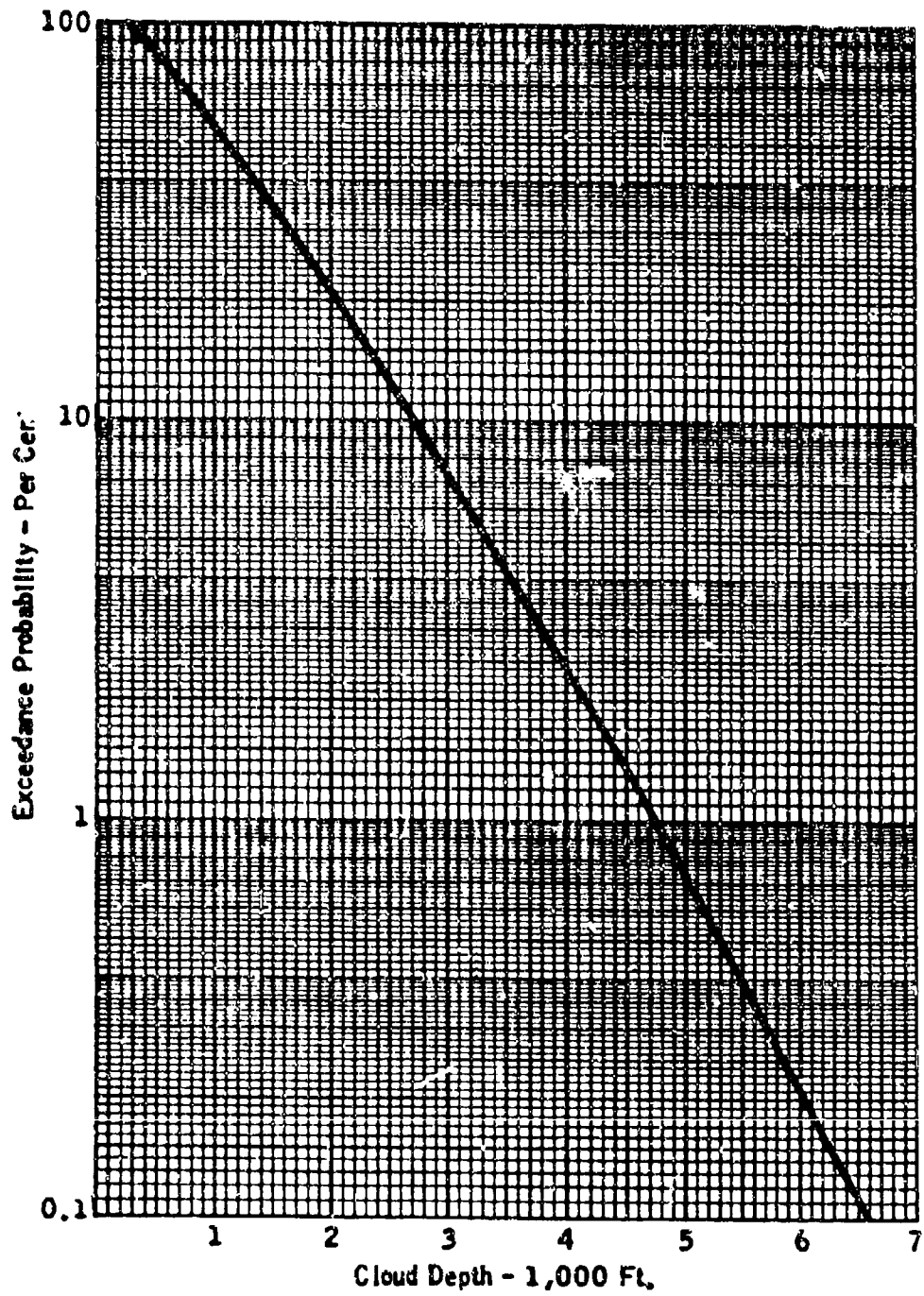CLOUDS FOR INCREMENTS OF TEMPERATURE AND ALTITUDE (REFERENCE 1-9)

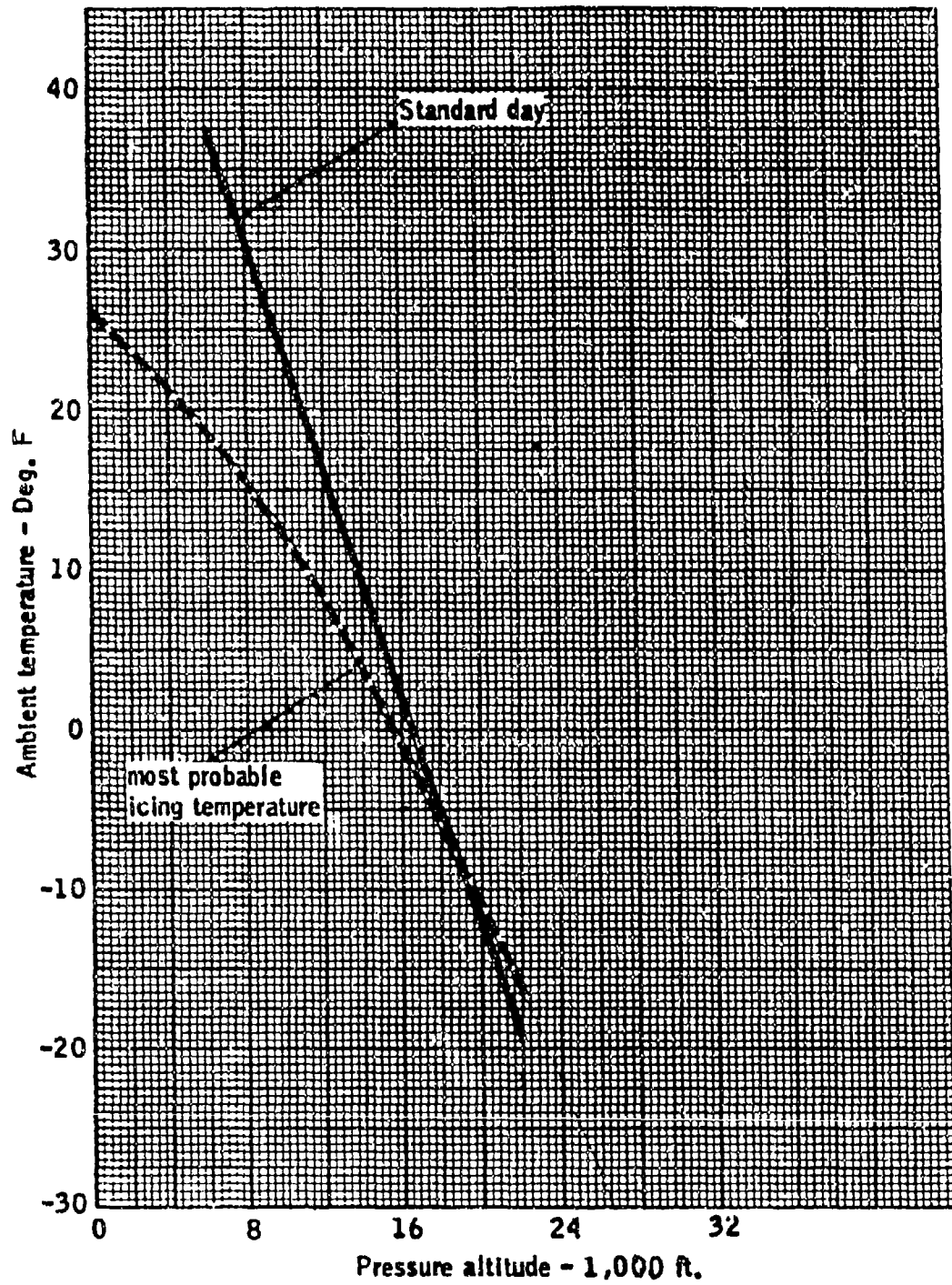FIGURE 1-35. CLOUD DEPTH PROBABILITY FOR LAYER TYPE CLOUDS (REFERENCE 1-16)

I 1-50

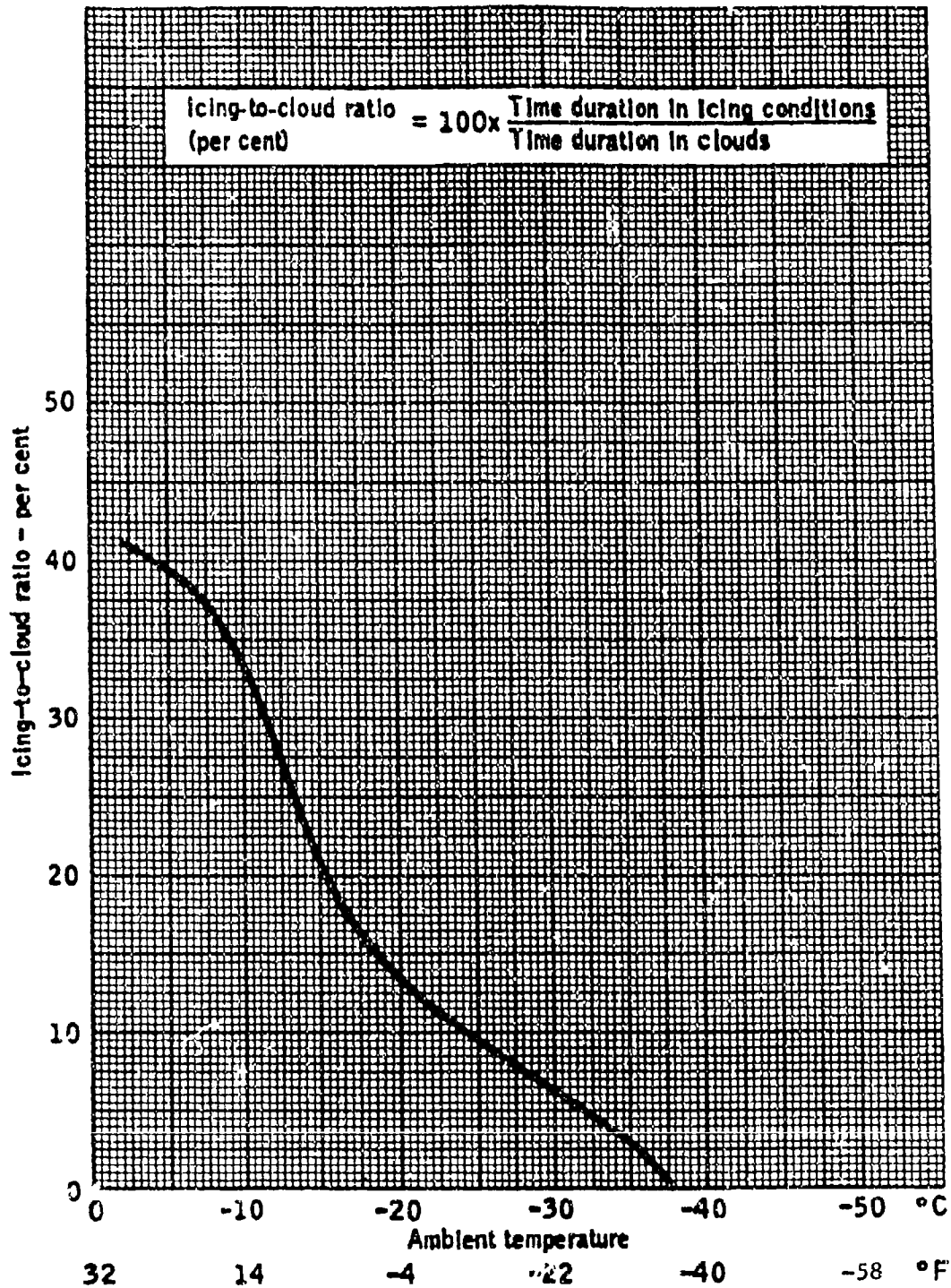FIGURE 1-36. MOST PROBABLE ICING TEMPERATURE VERSUS ALTITUDE (REFERENCE 1-9)

I 1-51

FIGURE 1-37. AVERAGE RELATION OF ICING-TO-CLOUD RATIO TO AMBIENT
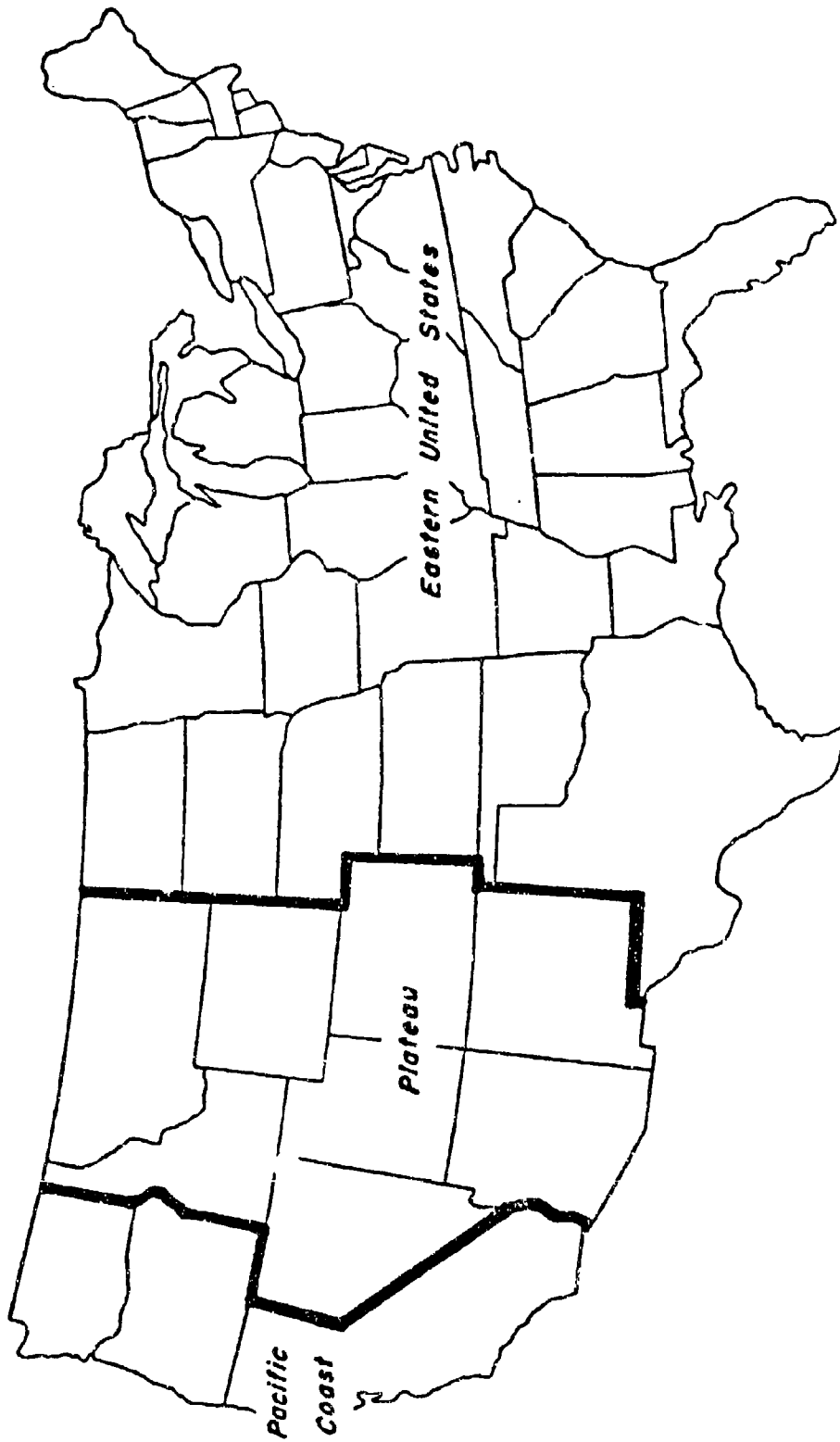TEMPERATURE (REFERENCE 1-12)

I 1-52

FIGURE 1-38. MAP OF THE UNITED STATES SHOWING APPROXIMATE BOUNDARIES OF AREAS USED IN THE GEOGRAPHICAL CLASSIFICATION OF ICING DATA (REFERENCE 1-20)
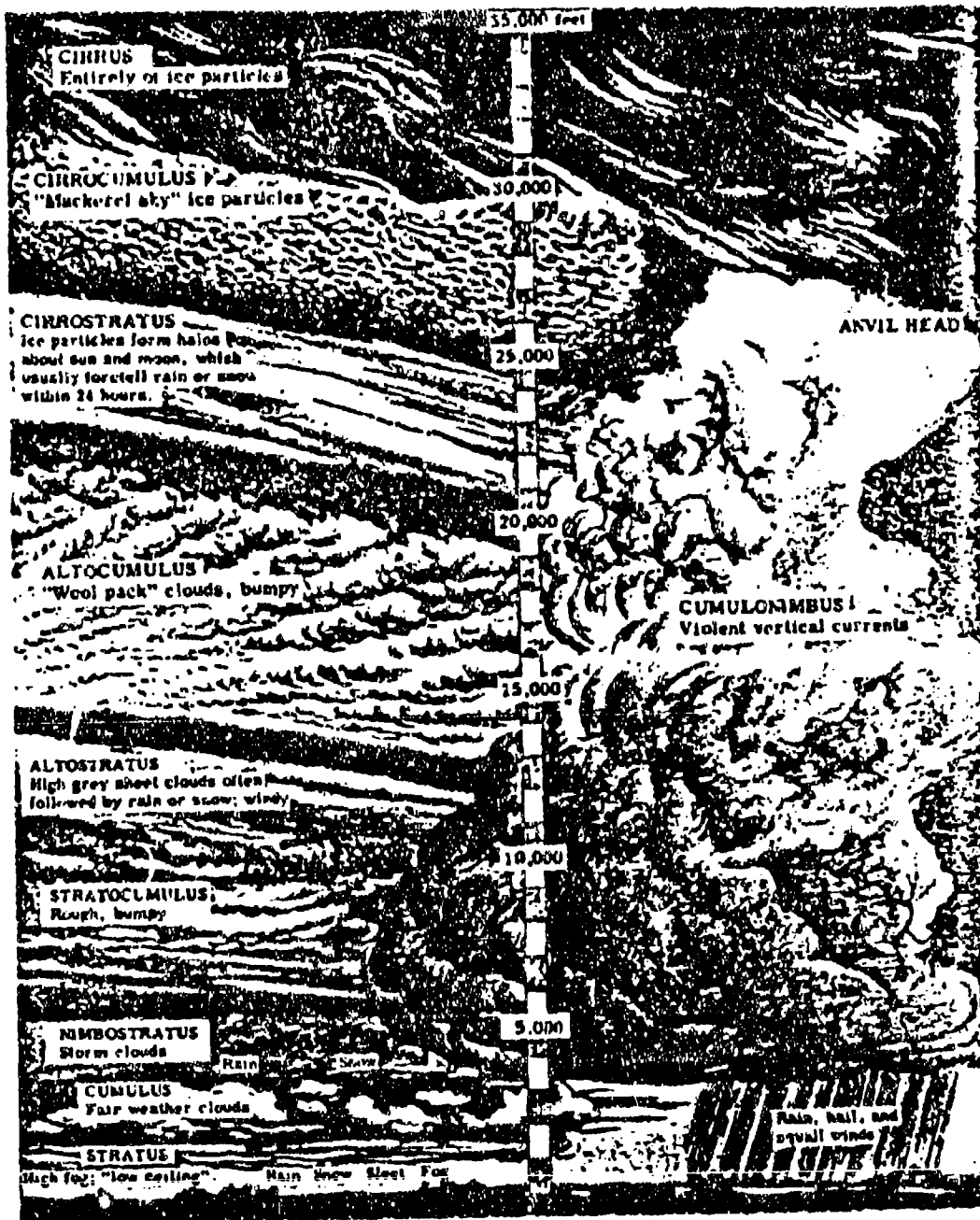
FIGURE 1-39. A GENERALIZED VERTICAL ARRANGEMENT OF CLOUD TYPES
(FROM ATMOSPHERE AND WEATHER CHARTS, REFERENCE 1-32)
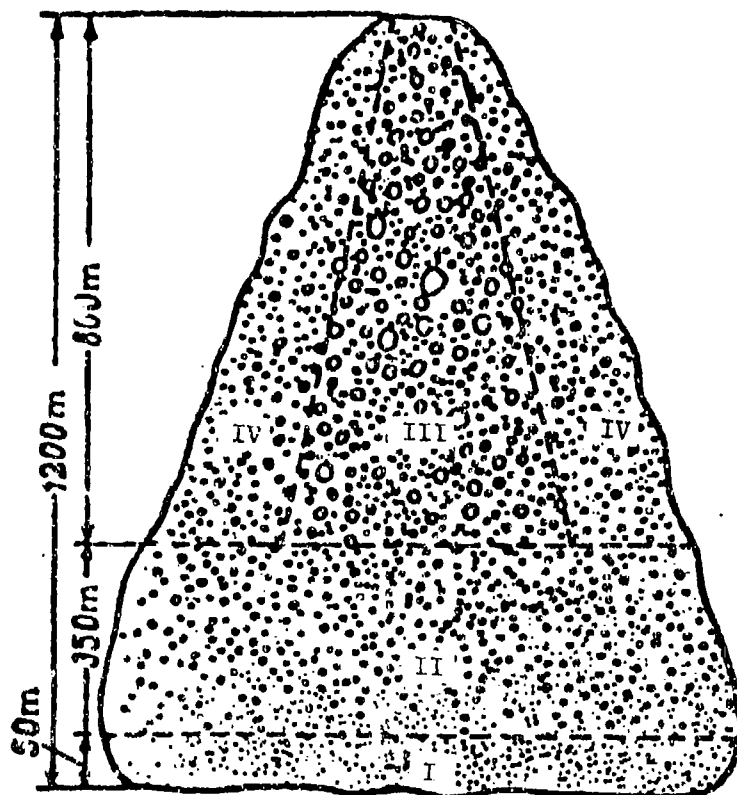
FIGURE 1-40. DIAGRAM OF DROPLET DISTRIBUTION IN CUMULUS CLOUD. I-Zone of newly formed droplets; II-zone of droplet growth due to condensation and coalescence; III-zone of the largest droplets growing mainly due to coalescence; IV-peripheral zone of fractional evaporation of droplets. The heights shown are heights above cloud base. (Reference 1-31.)

CHAPTER I
SECTION 2.0
AIRCRAFT ICE ACCRETION

CHAPTER I - FLIGHT IN ICING
CONTENTS
SECTION 2.0 AIRCRAFT ICE ACCRETION

LIST OF TABLES

LIST OF FIGURES

LIST OF FIGURES (CONTINUED)

LIST OF FIGURES (CONTINUED)

SYMBOLS AND ABBREVIATIONS

Symbol	Description
A	Area (ft^2)
A_C	Accumulation parameter, dimensionless
AFFDL	Air Force Flight Dynamics Laboratory
AGARD	Advisory Group for Aerospace Research and Development
AIAA	American Institute of Aeronautics and Astronautics
c	Airfoil chord length (ft)
°C	Degrees Celsius
C_D	Drag coefficient of aircraft or arbitrary body, dimensionless
C_d	Drag coefficient of airfoil, dimensionless
C_L	Lift coefficient of airfoil or arbitrary body, dimensionless
C_l	Lift coefficient of airfoil, dimensionless
C_m	Moment coefficient of airfoil, dimensionless
CR	Contractor Report
$dv/d\delta$	Derivative of the volume with respect to the droplet diameter δ
E (or E_M)	Total impingement or collection efficiency for an airfoil or body, dimensionless
°F	Degrees Fahrenheit
g/m^3	Grams per cubic meter
h	Projected height of a body, ft or dimensionless, or
	Pressure altitude, or
	Heat transfer coefficient
K	Droplet inertia parameter, dimensionless
K_0	Modified droplet inertia parameter, dimensionless
KIAS	Knots Indicated Air Speed
ℓ	Ice thickness (airfoil chords)
LWC	Liquid water content (g/m^3)
m	Mass of water impingement per unit span for an icing encounter, lbm/ft. span
$\dot{m}$	Rate of water impingement per unit span per unit time, lbm/min-ft. span

SYMBOLS AND ABBREVIATIONS (CONTINUED)

Symbol	Description
MVD	Median volume diameter (μm)
n	Freezing fraction, dimensionless
NACA	National Advisory Committee for Aeronautics
NASA	National Aeronautics and Space Administration
NRC	National Research Council (Canada)
°R	Degrees Rankine
Re	Freestream droplet Reynolds number, dimensionless
Re_l	Local relative droplet Reynolds number, dimensionless
S	Surface distance variable
SAE	Society of Automotive Engineers
T	Temperature (°F)
TM	Technical Memorandum
TN	Technical Note
TR	Technical Report
USAAEFA	United States Army Aviation Engineering Flight Activity
V	Velocity, knots
WADC	Wright Air Development Center
$\vec{x}$	Droplet position vector
Y_U	Y-coordinate in freestream of upper tangent trajectory
Y_L	Y-coordinate in freestream of lower tangent trajectory
ΔY_0	$\Delta Y_0 = Y_U - Y_L$; "freestream impingement width"

Symbol	Description
α	Angle of attack (degrees)
β	Local impingement efficiency at a location on an airfoil or body, dimensionless
δ	Droplet diameter (μm)
μ	Viscosity (slugs/ft.-sec.)
ρ_a	Density of air (slugs/ft^3)
ρ_a	Density of ice (slugs/ft^3)
ρ_w	Density of water (slugs/ft^3)
τ	Icing time (duration of encounter), minutes

Subscripts

a	Air
i	Ice
l	Local
L	Lower surface
med	For the median volume droplet diameter
max	Maximum
s	Static condition
U	Upper surface
w	Water
∞	Denotes freestream conditions

Superscripts

(-)	Indicates impingement terms computed over a droplet spectrum
(.)	Derivative with respect to time

GLOSSARY

flux - Rate of flow per unit area.

impingement efficiency curve (ß-curve) - A plot of the local impingement parameter ß versus the surface distance parameter S for an airfoil or other two-dimensional object.

liquid water content (LWC) - The total mass of water contained in all the liquid cloud droplets within a unit volume of cloud. Units of LWC are usually grams of water per cubic meter of air (g/m^3).

median volumetric diameter (MVD) - The droplet diameter which divides the total water volume present in the droplet distribution in half; i.e., half the water volume will be in larger drops and half the volume in smaller drops. The value is obtained by actual drop size measurements.

micron (µm) - One millionth of a meter.

stagnation point - The point on a surface where the local free stream velocity is zero. It is also the point of maximum collection efficiency for a symmetric body at zero degrees angle of attack.

ß-curve - See "impingement efficiency curve."

I.2.0 AIRCRAFT ICE ACCRETION

I.2.1 INTRODUCTION

Ice may form at various locations on an aircraft when the aircraft is flying in a supercooled cloud, that is, a cloud whose droplets are below 0 °C in temperature. If cloud droplets impinge on a surface and then freeze, ice is said to accrete and the ice that forms is called an accretion. Whether or not ice accretes, and the type, amount, shape, and extent of the ice if it does accrete, depend upon atmospheric variables such as air temperature, cloud liquid water content, droplet size, and aircraft variables such as airspeed, rotary forces, exposure time, component size and geometry, and component skin temperature. These matters are discussed in Section 2, "Physics of Ice Accretion."

Section 3, "Aerodynamic Penalties Due to Icing," addresses loss of lift and increase in drag of airfoils and deterioration in aircraft performance due to ice accretion. Specific icing effects on engines as well as icing problems of helicopters are also discussed.

The information presented here is useful for both unprotected and protected surfaces. Aerodynamic penalties resulting from the presence of the ice can be significant for any unprotected surfaces and also for surfaces protected by de-icing systems, since these systems allow some ice build-up between ice sheds. Although anti-icing systems allow little or no ice build-up, they still require for their design such information as droplet impingement limits and mass flux.

Ice forms on aircraft not only in supercooled clouds but also under certain other conditions, particularly freezing rain. However, only ice accretion in supercooled clouds will be addressed in this section.

Since computer codes to predict droplet impingement, ice accretion and performance degradation are addressed in Chapter IV, Section 2, they will not be discussed here. Only fundamentals will be covered with enough experimental and theoretical data to illustrate the ideas and to aid engineers in the preliminary design stage.

An "icing correlation" is an equation based upon experimental data which is used to estimate some quantity of interest in the study of aircraft icing, such as the increase in drag of an airfoil resulting from ice accreted under given atmospheric and flight conditions. It is usually based on data taken in an icing tunnel, and thus depends on the calibration of that tunnel. If it involves airfoils, it will depend on the airfoils included in the study. For these reasons, although a number of "icing correlations" will be mentioned in this section, none will be given in equation form. Many icing correlations are based on thorough and well done studies and can be very useful, but they should not be used by an engineer until he has consulted the studies themselves to judge if they are applicable to the problem and data that he is addressing, considering especially the calibration of his facility and of that used for the study. The inclusion of such correlations in a handbook, where limitations of space preclude a thorough discussion, could result in their misuse.

1.2.2 PHYSICS OF ACCRETION

The physics of ice accretion is divided here into three subtopics. The f..., droplet impingement, has been the most fully developed mathematically and also possesses a large data bank of experimental results. The second, ice accretion, concerns what happens to the liquid water after it impinges on a surface (e.g., does it run back, and if so, under what conditions?) and the nature of the ice accretion that results. Although much progress has been made in this area, fundamental problems remain. The third, ice adhesion, concerns mainly the strength of forces holding accreted ice to a surface and how they are affected by variables such as temperature. Some useful information is available, mainly of an experimental nature.

2.2.1 Droplet Impingement

If an aircraft is flying through a supercooled cloud, droplets will strike some of the aircraft surfaces. Viewed from the perspective of a coordinate system attached to the aircraft, the droplets approach the aircraft and either hit it or fly by. The path followed by a particular droplet is called a droplet trajectory. If the trajectory intersects an aircraft surface, the droplet is said to impinge upon that surface. The impingement properties of the various aircraft surfaces are of central importance to any discussion of aircraft icing.

In this chapter, much of the discussion pertains to two cases, both two-dimensional: an airfoil, representative of a wing cross section, and a cross section of a circular cylinder. The reason for this concentration is that these cases have been the most intensively investigated, both experimentally and computationally. Furthermore, the definitions used in these cases generalize in a fairly straightforward way to more complex two-dimensional geometries as well as to three-dimensional geometries. (The computational requirements tend to increase dramatically, however.) A good deal of very valuable three-dimensional work, both experimental and computational, has been done in the last few years, and this will also be surveyed.

2.2.1.1 Droplet Trajectory Equation

(Section 2.2.1.1 and 2.2.1.2 are based primarily on reference 2-1, which draws heavily on the basic treatment of droplet trajectories presented in reference 2-2.)

The liquid water content of supercooled clouds rarely exceeds 1.0 grams of liquid water per cubic meter of air. This means that a cloud is rarely more than one-millionth liquid water by volume. Due to this low concentration of water droplets in the freestream, the flow may be considered uncoupled, meaning that the influence of the droplets on the flowfield can be neglected.

Supercooled water droplets in the atmosphere usually have diameters of less than 60 microns and experience Reynolds numbers small enough to permit their treatment as essentially spherical. (Although this is the universal computational practice, it has been argued that a droplet experiencing large accelerations in the vicinity of an ice accretion may assume a non-spherical shape which would alter its coefficient of drag and hence its trajectory (reference 2-3).)

Consider the trajectory of a single droplet approaching a body. The droplet trajectory equation is obtained by applying Newton's Second Law, $\vec{F} = m\vec{a}$, to the droplet. This equation can be expressed as

$$m \frac{d^2 \vec{x}}{dt^2} = \vec{P} + \vec{M}_a + m\vec{g} + \vec{B} + \vec{D} \qquad (2-1)$$

where x is the position vector of the droplet, t is time (the acceleration $\vec{a}$ is of course equal to the second derivative of x with respect to time), $\vec{P}$ is the pressure gradient term, $\vec{M}_a$ is the apparent mass term, $m\vec{g}$ is the gravity force or "settling" term, $\vec{B}$ is the Bassett (unsteady) history force, and $\vec{D}$ is the drag force. The forces $\vec{P}$ and $\vec{M}_a$ are ordinarily neglected because the density of the particle (water droplet) is much greater that of the fluid (air) and the force mg can be neglected because of the very small mass of supercooled water droplets.

The force $\vec{B}$ accounts for the deviation of the flow pattern around the particle from that of steady state and represents the effect of the history of the motion on the instantaneous force (reference 2-4). It is essentially a correction to the drag term for an accelerating sphere. An accelerating sphere experiences a lower drag coefficient since it takes the flowfield some finite time to respond to the changing velocity and droplet Reynolds number. The term is significant if the particle density is of the same order as that of the fluid (which is not the case here), or if the particle experiences "large" accelerations. Droplets experience their largest accelerations when in the leading edge region of an airfoil, and the accelerations are larger yet if "glaze horns" are present. Norment (reference 2-5), using the work of Keim (reference 2-6) and Crowe (reference 2-7), has argued that for the icing problem the accelerations experienced by the droplets are not large enough for the Bassett term to be significant. Lozowski and Oleskiw (reference 2-8) included the Bassett term in the droplet trajectory equation used in their droplet trajectory and impingement code (Chapter IV, Section 2). They state that their results suggest that "in most cases ... the term may be ignored without severely affecting the accuracy of the calculations" (reference 2-8, p. 11). The Bassett force will be neglected in the rest of this discussion.

The drag term, D, can be expressed as

$$\vec{D} = \frac{1}{2} \rho \, C_D \, S \left| \vec{u} - \frac{d\vec{x}}{dt} \right| \left(\vec{u} - \frac{d\vec{x}}{dt} \right) \tag{2-2}$$

$\vec{u}$ is the local flowfield velocity vector, S is the cross sectional area of the sphere (or the projected frontal area of the sphere), and C_D is the drag coefficient. Note that the drag is evaluated using the velocity of the droplet with respect to the local airstream; this is sometimes called the "slip velocity."

All the terms on the right hand side of equation 2-1 other than D are now dropped and equation 2-2 is used to substitute for D; this yields

$$\frac{d^2\vec{x}}{dt^2} = \frac{3}{4} \frac{\rho_a \, C_D}{\delta \, \rho_w} \left| \vec{u} - \frac{d\vec{x}}{dt} \right| \left(\vec{u} - \frac{d\vec{x}}{dt} \right) \tag{2-3}$$

where the equation has been divided by the mass m of the droplet, δ is the droplet diameter, and

ρ_a is the droplet density and ρ_w is the air density.

A standard drag curve (figure 2-1) for a sphere has been established by bringing together experimental results from many sources (reference 2-9). Only a limited range of this curve need be fit for supercooled water droplets, since the relevant droplet Reynolds numbers rarely exceed 500. A number of different fits are available, some of which are discussed in reference 2-1.

2.2.1.2 Modified Droplet Inertia Parameter

Equation (2-3) will now be nondimensionalized in order to introduce the inertia parameter K and modified inertia parameter K_0 (both further discussed in Chapter IV, Section 2). Letting x and y be the components of the vector $\vec{x}$, define the nondimensional variables $x^* = x/c$, $y^* = y/c$, $t^* = t/(c/V_\infty)$, where c is a characteristic length, t is time, and V_∞ is the freestream airspeed. If the asterisks are suppressed after the equation is suitably rearranged, the nondimensional equation is

$$\frac{d^2\vec{x}}{dt^2} = \frac{1}{K} \frac{C_D \, Re_l}{24} \left(\vec{u} - \frac{d\vec{x}}{dt} \right) \tag{2-4}$$

Now $\vec{x}$ is the dimensionless droplet position vector, $\vec{u}$ is the dimensionless local flowfield velocity vector, t is nondimensional time, Re_l is the local relative droplet Reynolds number given by

$$Re_l = \frac{\rho_a \, \delta \left| \vec{u} - \frac{d\vec{x}}{dt} \right|}{\mu_a} \tag{2-5}$$

(μ_a is the viscosity of air) and K is the droplet inertia parameter given by

$$K = \frac{1}{18} \frac{\delta^2 \, V_\infty \, \rho_w}{c \, \mu_a} \qquad (2\text{-}6)$$

It can be seen from equation (2-4) that the trajectory depends upon K and $C_D Re_l/24$. But $C_D Re_l/24$ can be shown (reference 2-2) to depend approximately upon Re, the free stream droplet Reynolds number which is given by

$$Re = \frac{\rho_a \, V_\infty \, \delta}{\mu_a} \qquad (2\text{-}7)$$

Therefore the droplet trajectory depends approximately upon Re and K only.

Langmuir and Blodgett (reference 2-2) combined Re and K into a single parameter K_0, referred to as the modified inertia parameter, as follows:

$$K_0 = K\left(\frac{\lambda}{\lambda_s}\right) \qquad (2\text{-}8)$$

The quantity in brackets, referred to as the range parameter, is the ratio of the trajectory distance of a droplet in still air, with an initial Reynolds number of Re and gravity neglected, divided by the trajectory distance if the drag is assumed to obey Stokes law. Using numerical methods, they obtained a graph giving the range parameter as a function of Re (figure 2-2).

Bragg (reference 2-10) has interpreted K_0 by rewriting Equation 2-4 as

$$[\frac{K}{C_D \, Re_l/24}] \, \frac{d^2\vec{x}}{dt^2} = \vec{u}' - \frac{d\vec{x}}{dt} \qquad (2\text{-}9)$$

If some suitable average of the term in brackets on the left can be found over the entire trajectory, the droplet path becomes a function of just this single variable. Under typical icing conditions K_0 can be interpreted as such an average. Bragg also derived the following expression:

$$K_0 = 18 \, K \, [Re^{-2/3} - \frac{\sqrt{6}}{Re} \, Arctan \, \frac{Re^{1/3}}{\sqrt{6}}] \qquad (2\text{-}10)$$

Equation 2-10 is shown in reference 2-1 to be within 1 percent of Langmuir's calculated values until Re approaches 1000 (much larger than the values for supercooled cloud droplets), where Langmuir's values diverge.

The approximate similarity parameter K_0 has been introduced here because of its wide use in icing calculations. As shall be seen, it greatly simplifies the presentation of droplet impingement data. K_0 will be further discussed in Chapter IV, Section 2, where ice scaling is addressed and where experimental and computational evidence will be presented in support of the use of K_0.

K_0 can be interpreted as relating the importance of droplet inertia to the importance of droplet drag forces. For small values of K_0, drag predominates and the droplet tends to follow the flow streamlines until very close to the body. If K_0 is small enough ($\approx .005$), the droplet acts approximately as a flow tracer. For large values of K_0, droplet inertia predominates and the droplet departs considerably from the flow streamlines as the body is approached. If K_0 is large enough (≈ 1.0), the droplet trajectory is approximately a straight line. Figure 2-3 shows trajectories for two droplets, one with a diameter of 5 μm and $K_0 = .011$ and the other with a diameter of 50 μm and $K_0 = .467$. The trajectories were computed with the computer code LEWICE, which is discussed in Chapter IV, Section 2. The droplet trajectories initially coincide four chord lengths in front of the airfoil (not shown in the figure) but diverge dramatically in the vicinity of the airfoil due to the large difference in K_0 between the two drops.

Bragg (reference 2-10) has derived another trajectory similarity parameter, $\overline{K}$, for which he has given a theoretical justification but which, nonetheless, has not as yet been widely adopted by other workers. K_0 and K are closely related and, in fact, differ by a constant factor if a simple drag law is used in deriving K_0. Bragg shows that $\overline{K}$ is given approximately by

$$K = \frac{1}{18}\left(\frac{\rho_w{}^3 \, \delta^6 \, U}{c^3 \, \mu_a{}^2 \, \rho_a}\right)^{\frac{1}{3}}$$

(2-11)

It follows that since K_0 approximates $\overline{K}$, K_0 is approximately proportional to $\delta^{5/3}$, to $U^{1/3}$, and to $1/c$.

Figure 2-4 illustrates graphically values assumed by K_0 under the range of MVDs and velocities that would ordinarily be experienced by a general aviation aircraft. The bottom panel is for a chord size representative of a full scale wing and the middle panel is for a chord size representative of a full scale horizontal stabilizer, both for a general aviation aircraft, while the top panel is for a chord size (6 inches) representative of an airfoil model. (Much research has been done with models of approximately this size, although larger models are generally preferred in tunnels which can accommodate them.)

Comparison among the three panels shows that K_0 is a strong function of chord size. In fact, the largest value of K_0 for a full scale wing is approximately equal to the smallest value of K_0 for the model. Examination of any one of the three panels shows that K_0 varies strongly with MVD but much more weakly with aircraft velocity. All these observations are in accordance with equation 2-11. The reader may find it useful to refer back to this figure when studying the graphs presented later in which the impingement parameters E and β_{max} (defined in the next section) are presented as functions of K_0.

Figure 2-5 is constructed in the same manner, but using typical maximum droplet diameters rather than MVDs. It is interesting to note that the contrast among the three panels is now more pronounced due to the strong sensitivity of K_0 to droplet diameter. Now the largest values of K_0 even

for a full scale horizontal stabilizer are substantially smaller than the smallest values of K_0 for the model. This figure may be useful in interpreting the later graphs in which the impingement parameters S_U and S_L (defined in the next section) are presented as functions of K_0.

Example 2-1

An example of the calculation of K_0 for an airfoil is now presented.

Airfoil:	$c = 3.1$ foot chord - NACA 0012
Flight Speed:	$V = 200$ kt (230.16 mph)
Altitude:	$h = 10,000$ ft (pressure altitude)
Ambient Temperature:	$T = 15\ °F = 474.7\ °R$
Droplet Size:	$d = 20$ microns

First find the air density and viscosity.

From the pressure altitude, $P = 1455.6$ psf (10.109 psi). Solve for the air density using

$$\rho_a = \frac{P}{RT}$$

$$\rho_a = \frac{1455.6}{1716(474.7)} = .001787\ \frac{slug}{ft^3}$$

For viscosity, one can use the approximate relation $\mu_a = 7.136 \times 10^{-10}\ T$:

$$\mu_a = 7.136 \times 10^{-10}(474.7) = .3387 \times 10^{-6}\ \frac{slug}{ft\text{-}s}$$

Now calculate Re and K.

In these units Re is given by:

$$Re = 5.537 \times 10^{-6}\ \frac{\rho_a Vd}{\mu_a}$$

Thus

$$Re = 5.537 \times 10^{-6}\ \frac{.001787(200)\,20}{.3387 \times 10^{-6}} = 116.$$

For K in these units:

$$K = 1.958 \times 10^{-12}\ \frac{\rho_a\ \delta^2\ U}{c\ \mu_a}$$

Thus

$$K = 1.958 \times 10^{-12} \left[\frac{(1)\ (20)^2\ 200}{5.58\ (.3387 \times 10^{-6})} \right] = .1492$$

I 2-7

If Langmuir and Blodgett's graphical method is used, the problem is completed by using figure 2-2, which shows that for Re = 116.8 the range parameter is approximately equal to .332.
Then

$$K_0 = K\left(\frac{\lambda}{\lambda_s}\right) = (.332)(.1492) = .0495$$

Alternately, if Bragg's result is used, calculate K_0 using Equation 2-9:

$$K_0 = 18(.1492)\left[(116.8)^{-2/3} - \frac{\sqrt{6}}{116.8}\ \text{Arctan}\ \frac{(116.8)^{1/3}}{\sqrt{6}}\right] = .050$$

Summarizing this procedure for the usual case where the aircraft geometry, flight speed, pressure altitude, droplet size, and temperature are known:

1) From a standard atmospheric table obtain P from the pressure altitude, h.

2) Calculate the density:

$$\rho_a = \frac{P}{1716(459.6 + T)}\ \frac{\text{slugs}}{\text{ft}^3} \tag{2-12}$$

3) Calculate the viscosity:

$$\mu_a = 7.1358 \times 10^{-10}(T + 459.67)\ \frac{\text{slugs}}{\text{ft-sec}} \tag{2-13}$$

4) Solve for the droplet freestream Reynolds number:

$$Re = 5.537 \times 10^{-6}\ \frac{\rho_a\ V\ d}{\mu_a} \tag{2-14}$$

5) Solve for the droplet inertia parameter:

$$K = 1.958 \times 10^{-12}\ \frac{\rho_w\ d^2 V}{c\ \mu_a} \tag{2-15}$$

6) Use Re and K to calculate the modified inertia parameter using either equation 2-8 and figure 2-2 or else using equation 2-10.

2.2.1.3 Droplet Impingement Parameters

Several impingement parameters can be defined to characterize the impingement properties of an airfoil or cylinder with respect to the cloud it encounters.

Figure 2-6 illustrates the definition of the impingement parameters S_U, S_L, ΔY_0, h, and E for an airfoil in a supercooled cloud. Let S denote arc length measured along the airfoil surface. It is conventional to take S = 0 at the leading edge, and that is done here (although the reader should note that it is sometimes convenient to take S = 0 at the stagnation point instead). S is defined to be positive on the upper surface and negative on the lower surface. S_U and S_L are defined to be the upper and lower limits of droplet impingement on the airfoil and are determined by the upper and lower tangent droplet trajectories. Define a Y-axis that is perpendicular to the freestream velocity and far enough in front of the airfoil (at least several chords) so that the flow is essentially undisturbed by the presence of the airfoil; then the droplet trajectories can be taken initially to be parallel to one another and to the freestream flow lines. The droplet trajectory which strikes the airfoil at its leading edge intersects the Y-axis at a point which is taken to be Y = 0. The upper tangent trajectory intersects the Y-axis at a point Y_U and the lower tangent droplet trajectory intersects it at a point Y_L. Let $\Delta Y_0 = Y_U - Y_L$; refer to this as the "freestream impingement width." Let h be the projected frontal height of the airfoil; note that this is a function of angle of attack. The total impingement (or collection) efficiency E is defined as the ratio of the freestream impingement width ΔY_0 to the projected frontal height h, i.e.,

$$E = \frac{\Delta Y_0}{h} \tag{2-16}$$

E is the proportion of liquid mass crossing the Y-axis within the frontal projection of the airfoil and ultimately striking the airfoil.

In equation (2-16), E is a dimensionless quantity, but ΔY_0 and h are not. However, it is customary to nondimensionalize the latter two quantities by dividing them by the chord length c. A different notation is not ordinarily introduced for nondimensional ΔY_0 and h; in instances where the meaning may not be clear from the context, it is explicitly noted if the dimensional or nondimensional quantity is meant. Tables and graphs are available giving nondimensional ΔY_0 and h as functions of K_0 and angle of attack α for some airfoils. Nondimensional ΔY_0 can be interpreted as follows: consider a segment of the Y-axis of length equal to one chord and centered at the projected position of the airfoil leading edge. ΔY_0 is the proportion of liquid mass crossing the Y-axis within the segment which ultimately strikes the airfoil.

Figure 2-7 illustrates the definition of the local impingement (or collection) efficiency ß at an arbitrary point P on the airfoil. Let P lie between the points of impact on the airfoil surface of two droplet trajectories. The mass of water droplets between the two trajectories a distance δY_0 apart in the free stream (at the Y-axis) is distributed over a length δS on the airfoil surface. Letting

δS approach 0 in such a way that P always falls between the impact points of the two trajectories, the local impingement efficiency β at P is defined in the limit by the derivative

$$\beta = \frac{dY_0}{dS} \qquad (2\text{-}17)$$

The maximum value assumed by β anywhere on the airfoil surface is denoted by β_{max}. Note also that

$$\Delta Y_0 = \int_{S_L}^{S_U} \beta \, ds \qquad (2\text{-}18)$$

The impingement efficiency curve or β-curve is a plot of β on the vertical axis versus S on the horizontal axis. This is illustrated in figure 2-8. The β-curve can be calculated numerically as follows: First, find the upper and lower tangent trajectories. These are ordinarily approximated numerically by finding upper and lower trajectories which pass within a small prescribed distance ϵ of the airfoil without actually striking it. Second, calculate a set of trajectories between the upper and lower trajectories (figure 2-9). There is a Y value and associated S value for each trajectory. Third, fit a Y vs. S curve to the points (S, Y), as shown in figure 2-10. Fourth, approximate the derivatives to the Y vs. S curve at a set of points; these derivatives are the βs. Fifth, fit a β-curve to the points (S, β). Some researchers omit step three and simply approximate β_i for (S_i, Y_i) by the ratio $(Y_{i+1} - Y_i)/(S_{i+1} - S_i)$, and then fit the β-curve to the points (S_i, β_i).

As noted, equations 2-16 and 2-17 are for the two-dimensional planar case. The local impingement efficiency, β, can be calculated for the three-dimensional case by considering a three-dimensional tube of water droplets starting at infinity with some area, A, perpendicular to the freestream, and impinging on a body over some surface area, A_s. Then, the local impingement efficiency, β, is the limit, as A_S approaches zero, of A divided by A_s:

$$\beta = \lim_{A_S \to 0} \frac{A}{A_S} \qquad (2\text{-}19)$$

Discussions of three-dimensional impingement calculations can be found in references 2-11 and 2-5.

Example 2-2

This example illustrates the estimation of the impingement parameters E, β_{max}, h, S_U and S_L using graphical data (reference 2-12). The graphical data is all presented with K_0 as the independent variable. Much data is available in this form.

The conditions of Example 2-1 for a NACA 0012 airfoil are assumed; thus $K_0 = 0.050$. It also is assumed for simplicity that the angle of attack, α, is 0 degrees. From figure 2-11, E, the total impingement efficiency, is found to be 0.230 for these conditions. So 23 percent of the water in the

projected frontal area of the airfoil, with height $h = .120c$ (found using figure 2-12), impinges on the airfoil. The maximum impingement efficiency for $K_0 = 0.50$ and $\alpha = 0$ degrees is found in figure 2-13 to be $\beta_{max} = 0.69$. At $\alpha = 0$ degrees, the upper and lower limits of impingement are identical. From figure 2-14 at $K_0 = 0.050$, $S_U = S_L = .0435$. Therefore, water droplets will impinge on the airfoil leading edge only back approximately 4 percent of chord. (Note that this example assumes a "monodispersed" cloud, that is, a cloud in which all the droplets are of the same size. More realistic approaches are discussed in the following section.)

2.2.1.4 Droplet Size Distribution Effects

The discussion thus far has proceeded as though clouds consisted of droplets of a single size ("monodispersed" clouds). All actual clouds, whether in the atmosphere or the wind tunnel, possess a spectrum of droplet sizes. This is taken into account in the definition of β and E by integrating over the droplet spectrum. In calculations with experimental data, this leads to taking averages weighted by volume, with the droplet spectrum represented by a histogram. Terms computed over the droplet spectrum are sometimes indicated by writing a bar above them.

$$\bar{\beta}(S) = \int_{\delta_{min}}^{\delta_{max}} \beta(\delta,S) \ \frac{dv}{d\delta} \ d\delta \qquad (2-20)$$

Here $\bar{\beta}$ is called the droplet spectrum local impingement (or collection) efficiency at the surface position specified by S. The phase "droplet spectrum" is ordinarily suppressed, since this is the meaning carried by the bar; some authors use the term "overall" rather than "droplet spectrum." The integral limits are the minimum and maximum droplet diameter in the cloud. In general, a droplet size distribution is described by v, the cumulative volume of water in the cloud as a function of droplet diameter, δ. In equation 2-20, the derivative of this curve, $dv/d\delta$, appears. It is a function of the droplet size, δ, and, of course, the assumed cloud droplet distribution. Usually β and $dv/d\delta$ are not known as continuous functions of δ and equation 2-20 is then represented as a summation

$$\bar{\beta}(S) = \sum_{i=1}^{N} \beta(\delta_i,S) \ \Delta v_i \qquad (2-21)$$

Equation 2-21 is summed over N discrete droplet sizes representing the midpoints of N droplet size bins. (For example, $\delta_i = 6.5 \ \mu m$ for a bin for droplets with diameters from 5 to 8 μm.)

The droplet spectrum (or overall) impingement (or collection) efficiency E for an airfoil or body is defined in a similar way for a droplet size distribution:

$$E = \frac{1}{h} \int_{\delta_{min}}^{\delta_{max}} \Delta Y_0 \ (\delta) \ \frac{dv}{d\delta} \ d\delta \qquad (2-22)$$

I 2-11

Here $\Delta Y_0(\delta)$ is the initial Y difference for the tangent trajectories for a droplet of diameter δ. As in the case of β, one usually knows $\Delta Y_0(\delta)$ for a discrete number of droplet sizes. Equation 2-22 can therefore be written as the sum

$$E = \frac{1}{h} \sum_{i=1}^{N} \Delta Y_0(d_i) \; \Delta v_i \qquad (2\text{-}23)$$

Note that a droplet spectrum (or overall) $\overline{\Delta Y_0}$ may also be defined as

$$\overline{\Delta Y_0} = E \; h \qquad (2\text{-}24)$$

The limits of impingement depend not on the entire droplet spectrum but only on the largest droplets present in the spectrum. Let δ_{max} denote the largest drop diameter present in the spectrum (or the midpoint of the bin containing the largest droplets), and let $K_{0,max}$ denote the modified inertia parameter calculated using δ_{max}. The maximum limits of impingement may be found from plots of S_U and S_L as a function of $K_{0,max}$ and angle of attack α.

Example 2-3

This example is a repetition of Example 2-2 except that this time the impingement parameters will be found using the entire droplet spectrum. It is assumed that the droplet median volume diameter (MVD) is 20 μm (the droplet size used in Example 2-2) and the cloud droplet spectrum can be represented by a Langmuir D distribution. The droplet sizes representing the seven size bins in the distribution are calculated using table 1-1 (discussed in Section 1.2.6). Table 2-1 sł s the droplet sizes δ, the proportion Δv of total droplet volume associated with each δ, and also the values of Re, K, and K_0 for each δ. Usi ig these values of K_0 and figure 2-11, a value $E(\delta)$ is associated with each δ, as shown in the third column of table 2-2. Note that equation 2-23 can also be written as

$$E = \sum_{i=1}^{N} E_i(d_i) \; \Delta v_i \qquad (2\text{-}25)$$

Thus $\overline{E}$ is calculated as an average value of the $E(\delta)$ weighted by volume using the Δv's. Table 2-2 shows that a value $\overline{E} = 0.24$ is obtained, little different from the value $E = 0.23$ for the MVD. This is well within the accuracy of reading numbers from the figure.

Considering this droplet size distribution and using equation 2-21, $\overline{\beta}$ can be calculated for a surface length location of $S = 0$ (stagnation point). For the special case of a symmetric airfoil at zero degrees angle of attack, where $\overline{\beta}_{max}$ occurs at $S = 0$ for all K_0, equation 2-21 can be used directly to determine $\overline{\beta}_{max}$. In table 2-2 the calculation of $\overline{\beta}$ at $S = 0$ is summarized in the last two columns. Here again the value of $\overline{\beta} = 0.66$ is close to the value for the MVD droplet size, where $\beta = 0.69$.

The maximum limits can be found from $K_{0,max}$ and figure 2-14. For the 44.4 micron droplet size, $K_{0,max} = 0.2463$ and from the figure $S_U = S_L = 0.13$, or 13 percent of the chord length.

I 2-12

Estimates of the size of a pneumatic ice protection boot have been made by using an MVD of 20 microns and twice that diameter (40 microns) to determine the maximum extent of significant droplet catch. This comes to about 10% of the airfoil chord on the critical upper surface. Ten percent coverage of the upper surface is consistent with statistical measurements of upper surface icing made in the USSR (reference 2-13).

Comparison of Example 2-2 and 2-3 suggests that, except for the limits of impingement, impingement parameters calculated using the MVD may give a reasonably good approximation to those calculated over an entire droplet distribution. This property of the MVD supplies the main justification for its wide use as the "representative" droplet size for a supercooled cloud in the study of aircraft icing. The error introduced in impingement calculations by its use rather than use of the full droplet spectrum is discussed in reference 2-14 and 2-15.

2.2.1.5 Approximate Two-dimensional Icing Formulas

Several approximate two-dimensional icing formulas are presented in this section. In these formulas, the symbols β, E and ΔY_0 for calculations with the MVD are used. If the corresponding quantities for the droplet spectrum are available, then bars are simply put over these quantities.

The formulas are approximate primarily for two reasons. First, freestream and ambient quantities are used throughout. Second, impingement parameters are for a clean body. As ice accretes, the shape of a body changes and with it the flow field and impingement parameters. For example, if the conditions were glaze and the duration long, a large glaze ice shape would actually accrete and some of the formulas here would give poor approximations. The formulas are most reliable for rime conditions or short durations.

Let $\dot{m}$ denote the water impingement rate per unit span in lbm/min-ft. span; then m is given by

$$\dot{m} = 6.322 \times 10^{-3} \ V_\infty \ (LWC) \ c \ E \ h \qquad (2-26)$$

where V_∞ is the freestream velocity in knots, LWC is the liquid water content in g/m^3, c is the chord length in feet, E is the total collection efficiency (dimensionless), and h is the dimensionless projected height of the body. E and h would be found from a table or graph. Note that although E is a two-dimensional quantity, it may be used in a strip-theory type approach across the wing span as long as the sweep and induced angles of attack are taken into account.

Multiplying $\dot{m}$ by the duration τ of an icing encounter in minutes yields the mass m of water impingement per unit span, lbm/ft. span, for the encounter:

$$m = \dot{m} \ \tau \qquad (2-27)$$

A useful dimensionless term called the accumulation parameter, A_C, is introduced here. Its primary use is in the area of scaling, and it is more fully discussed in Chapter IV, Section 2. It is given by

$$A_c = \frac{LWC \ (V_\infty) \ \tau}{\rho_{ice} \ c} \qquad (2-28)$$

where ρ_{ice} is the density of ice. Using the units of the variables as defined in the

"Symbols and Abbreviations" and Example 2-4, A_C can be calculated using the following equation (reference 2-1):

$$A_c = 1.013 \times 10^{-4} \ \frac{LWC \ (V_\infty) \ \tau}{\rho_{ice} \ c} \qquad (2-29)$$

If the value of ß is known at a point on the surface, the local ice thickness in chords may be approximated by

$$l = A_c \ \beta \qquad (2-30)$$

This equation assumes that the ice growth is normal to the surface, so it is most accurate in the stagnation region and for blunt bodies. The maximum ice thickness in chords is given by

$$l_{max} = A_c \ \beta_{max} \qquad (2-31)$$

For a cylinder or symmetric airfoil at 0° angle of attack, $\beta_{max} \approx \beta_0$, the impingement efficiency at the stagnation point; this may be available from a table or graph. Even for non-symmetric airfoils at 0° angle of attack, $\beta_{max} \approx \beta_0$.

The cross sectional area of an ice accretion can be approximated by

$$A = A_c \ E \ h = A_c \ \Delta Y_0 \qquad (2-32)$$

where A is in units of chord length squared. This formula permits the interpretation of the ice cross-section as a transformed rectangle of length ΔY_0 and width A_C.

Example 2-4

The mass of ice accretion on the NACA 0012 section will be calculated. Using the same flight conditions as Example 2-1, and the droplet size distribution and value from Example 2-3:

Airfoil:	c = 3.1 foot (37.2 in) chord NACA 0012
Flight Speed:	V = 200 knot
Airfoil Projected Height:	h = .12 at α = 0 deg.
Liquid Water Content:	LWC = 0.5 g/m^3
Collection Efficiency:	$\overline{E}$ = .24
Maximum Impingement Efficiency:	$\overline{\beta}_{max}$ = .66
Icing Time:	τ = 5 minutes

Using equation 2-26 the mass of impinging water per unit span per unit time is given by:

$$\dot{m} = 6.3222 \times 10^{-3}(200)(0.5)(3.1)(.24)(.12) = 0.056 \text{ lbm/min-ft. span}$$

Then for a five minute icing encounter (equation 2-27)

$$m = .056(5) = 0.282 \text{ lbm/ft. span}$$

Calculating the accumulation parameter from equation 2-29 gives:

$$A_c = 1.013 \times 10^{-4}\frac{(200)(.5)(5)}{(.8)(3.1)} = 0.0204$$

Note that the density of the ice is assumed to be 0.8 g/cm^3, implying a rime accretion. The maximum ice thickness is approximated from equation 2-31 as

$$l_{max} = 0.0204(.66) = 0.0135 \text{ c, } c = \text{airfoil cord}$$

Thus the maximum ice growth is approximately 1.4 percent of the airfoil chord length, or about (.0135)(37.2) = .50 inches.

The cross sectional area of the ice in square chords, from equation 2-32, is

$$A = (.0204)(.24)(.12) = .0204(.0288) = 5.9 \times 10^{-4} \text{ c}^2$$

The area in feet is given by

$$A = 5.9 \times 10^{-4} (3.1)^2 = 5.7 \times 10^{-3} \text{ ft}^2$$

which is equal to about 0.82 in^2.

I 2-15

2.2.1.6 Compressibility Effects on Droplet Impingement

The droplet impingement characteristics of a body in a flow at high subsonic Mach number may differ from those in a flow at low Mach number. Brun, Serafini and Gallagher (reference 2-16) performed numerical calculations of the droplet impingement on a cylinder at $M = 0.4$ and compared these results to incompressible data of reference 2-17. The result of the calculations, performed over a K_0 range from 0.2 to .66, was a reduction in E, but never by more than 3 percent. The compressible and incompressible curves, shown in the lower right area of figure 2-15, are barely distinguishable from one another.

More recent data on a NACA 0012 airfoil at $\alpha = 0$ degrees and Mach numbers from 0 to 0.8 are also shown in figure 2-15. These data are from references 2-12 and 2-18, with most of the compressible data coming from the latter reference, where a compressible flowfield and a compressible form of the trajectory equation are employed. Figure 2-15 indicates that compressibility effects are greater for lower values of K_0; this presumably is due to the greater sensitivity of the droplets to flowfield changes at these lower K_0's. The effect of compressibility is to reduce E and also S_U and S_L (not shown). These limited studies suggest that design using the incompressible droplet impingement data may be conservative.

2.2.1.7 Droplet Impingement Data

In this section, a selection of droplet impingement data, both theoretical and experimental, will be presented. Refer to Sections 2.2.1.1 - 2.2.1.4 for definitions and uses of the data. Figure 2-16 gives the projected height of several airfoils as a function of angle of attack. Also note that table 2-3 provides the characteristic length used to calculate K_0 for the various bodies. This table is important since the characteristic length used in the calculation of K_0 is a matter of convention and the conventional choice is not always obvious. For example, for a cylinder the radius is used, whereas one might have expected the diameter, by analogy with the use of the chord for an airfoil.

Experimental Data

In the 1950's, the NACA carried out an extensive experimental program to provide impingement information for airfoils and other geometries. Their method required a wind tunnel with spray system and consisted of seven steps:

1. Put dye in the spray system.
2. Put strips of blotter paper at strategic locations on an airfoil, aircraft component, or other geometric object.
3. Expose the object to the spray for a fixed time interval.
4. Remove the strips and place each in a separate container of water.
5. Wait until approximately all the dye in the paper has dissolved in the water. (This could take weeks.)

6. Expose the container to a ray of light. The amount by which the light was shifted was used to determine the amount of dye in the container (called colorimetric analysis).

7. By considering the original locations of the strips, deduce the regions and pattern of impingement.

The test program was mainly confined to a representative sample of airfoils.

Probably the most used of the NACA data are that due to Gelder, Smyers, and von Glahn (reference 2-19) on several two-dimensional airfoils. The data presented here are mostly from that reference but some are also from references 2-20 and 2-21. The form of these figures follows that of reference 2-22. Figures 2-17 to 2-20 present collection efficiency versus K_0 for several bodies. Droplet limits of impingement are given in figures 2-21 to 2-27.

How was one to determine the impingement pattern for an airfoil not tested by the NACA? Before droplet trajectory and impingement codes were developed, one approach was to try to "match" the untested airfoil to one that had been tested and then "extrapolate" the impingement pattern (reference 2-22).

By the early 1980's, many airfoils very different from those of the 1950's were in use or soon to be in use; for such airfoils, the "matching" procedure mentioned above was especially problematical. Furthermore, a need was recognized for impingement information on engine inlets and other three-dimensional configurations.

In conjunction with the need for new information, new technological possibilities also arose. First, the use of laser spectroscopy and microcomputers made it theoretically possible to carry out steps (5) through (7) above in a manner requiring much less time and human labor. Second, and potentially even more important, the availability of powerful computers and efficient numerical algorithms held out the promise of the development of computer codes for the computation of impingement patterns. The goal of the experimental program would be to produce a data bank of sufficient variety and complexity to test and evaluate computer codes. Once a code were validated or calibrated using the bank of experimental data, it could be used to compute the impingement pattern for appropriate configurations not in the data bank. There would no longer be any need for the difficult matching procedure.

A program was established in 1984 to exploit the possibilities mentioned above; the work has been done by Wichita State University (WSU) and Boeing Military Aircraft Company (BMAC) under contract to NASA Lewis Research Center with support from Federal Aviation Administration. Reference 2-15 thoroughly describes the methodology developed and the results obtained for the first set of models tested. The two-dimensional models included were a cylinder, NACA 65_2015 airfoil, MS(1)-0317 airfoil, and three ice shapes (figures 2-28 and 2-29). The cylinder and NACA 65_2015 airfoil were chosen so that results obtained with the new methodology could be compared with data from NACA tests in the 1950's. The MS(1)-0317 airfoil was chosen as a representative of the modern family of supercritical airfoils which is used by some high speed

aircraft. An axisymmetric inlet (tested at 0° and 15° angle of attack) and Boeing 737-300 inlet (figures 2-30 and 2-31) were chosen as representative of modern inlet designs.

Blotter strips typically 1.5 inches wide and of various length, depending on the model being tested, were attached to the forward facing (upstream) surface of the model at strategic locations. Figure 2-32 shows an example of blotter strip locations for the Boeing 737-300 engine model.

The impingement data given in reference 2-15 is in the form of impingement efficiency curves (ß-curves). (Note that the sign convention followed for surface distance s in this report (positive on the bottom and negative on the top) is the opposite of that used earlier in this section.) Just a small sample of data will be presented here. Figure 2-33 is for the circular cylinder, figure 2-34 for the NACA 65_2015 airfoil, and figure 2-35 for the MS(1)-0317 airfoil for an MVD of 16.45 μm and an airspeed of approximately 81 m/s. In addition to the experimental ß-curves, each of these figures also includes for comparison a "theoretical" ß-curve calculated by the Boeing 2D/axisymmetric droplet trajectory and impingement code (see Chapter IV, section 2). Figure 2-36 is for the large glaze ice shape of figure 2-29 for an MVD of 20.36 μm and, again, an airspeed of approximately 81 m/s.

Figure 2-37 shows the highlight marks and surface distance convention and figure 2-38 shows the positions of the blotter strips for the axisymmetric inlet. The ß-curve at the $\Theta = 0°$ position appears in figure 2-39. Figure 2-40 shows the highlight marks and surface distance convention and figure 2-41 shows the positions of the blotter strips for four different test conditions the 737-300 inlet. The ß-curve at the $\Theta = 0°$ position appears in figure 2-42. In addition to the experimental ß-curves each of these figures also includes for comparison a "theoretical" ß-curve calculated this time by the Boeing 3D droplet trajectory and impingement code (see Chapter IV, section 2).

The surface coordinates and surface ß values for many of the tests are available in digital form. This constitutes a valuable data bank for the evaluation and validation of droplet trajectory and impingement codes. Contact NASA Lewis Research Center to learn how to acquire data.

A second set of models has also been tested and a report on the results is due in 1992. This second set included a 2D model of an NLF(1)-0414F (natural laminar flow) airfoil, a 30° swept wing with MS(1)-0317 airfoil section, a NACA 0012 wing tip with 30° sweep angle, and a Boeing 747 engine inlet. Reference 2-23 surveys some of the results which will be included in this report.

Theoretical Data

Figures 2-43 to 2-46 present a summary of theoretical data for droplet impingement on bodies other than airfoils. These data are presented as a function of K_0 and are calculated assuming a monodispersed droplet size distribution. These results are from early NACA research references 2-24 to 2-32), since more recent calculations have focused on airfoils.

While several droplet impingement computer codes currently exist, few detailed studies of droplet impingement characteristics have been conducted using these codes. One exception is reference 2-33, where theoretical droplet impingement characteristics of 30 low and medium speed airfoils are reported. For each airfoil, a table is given including values of h for several values of α (e.g., $\alpha =$

-4°, 0°, 4°, 8°) and values of E, β_{max}, Y_0, S_U and S_L for several values of α and K_0 (e.g., α = -4°, 0°, 4°, 8°, and K_0 = .01, .05, .1, .5, 1.0). These tables can be used to approximate impingement parameters for arbitrary values of α and K_0 through interpolation, to compare impingement properties of two or more airfoils, and also to search for trends or patterns in the impingement parameters as a function of airfoil characteristics such as thickness, camber, and radius of curvature.

Figures 2-48 to 2-59 present a selection of results from reference 2-33: computed values of E, β_{max}, S_U and S_L are shown as a function of K_0 for three airfoil angles of attack. These figures are constructed using the tables discussed in the previous paragraph. Six airfoils from the thirty in the study were selected for the figures (figure 2-47). The NACA 0012 airfoil has been widely used in aircraft icing research during the 1980's. A number of airplanes have airfoils from the NACA 23 series, to which the NACA 23012 belongs. The NACA 63-415 is a "classic" NACA laminar flow airfoil. The NACA 64-109 has been used on the empennage of several general aviation airplanes. The LS(1)0417 and MS(1)0313 are perhaps the most widely used of the "modern" laminar flow airfoils. In summary, the NACA 64-109 and NACA 0012 would be used for the empennage but not for a wing; the other four airfoils would be used for a wing.

Use of figures 2-48 through 2-53 will be illustrated by discussing their use for MVD of 20 μm, an airspeed between 100 and 220 knots, and a chord size of 5.58 feet (representative of an airfoil section for a wing of a full scale general aviation aircraft). As seen from figure 2-4, a value of $K_{0,MVD} \approx$ .02 roughly corresponds to these conditions. Thus in examining figures 2-48 (α = 0°), 2-49 (α = 4°), and 2-50 (α = 8°) for E, one focuses on the lower left hand corner of the graphs. There is very little variation in this region among the airfoils and E is approximately equal to .10 or less for all of them in this region. Note that there is relatively little variation among the airfoils in these figures for **all** values of K_0, the curves for the NACA 64-109 being the ones that most stand out. The NACA 64-109 is the thinnest of the airfoils with a thickness of 9 percent of chord, all the rest having a thickness of at least 12 percent of chord.

In examining figures 2-51 (α = 0°), 2-52 (α = 4°), and 2-53 (α = 8°) for β_{max}, one notes more variation among the airfoils, with the curves for the NACA 64-109 quite different from those for the others. For $K_{0,MVD} \approx$ .02, β_{max} is in the vicinity of .40 for all airfoils except the NACA 64-109, where it is in the vicinity of .60. Note also that there is a tendency of β_{max} to decrease with increasing α. As noted in Chapter IV, Section 2, accurate calculation of β_{max} for such a value of K_0 is a computational challenge, particularly at higher angles of attack. Thus some of the variation among the airfoils in these figures is certainly numerical; how much is not known.

Use of figures 2-54 through 2-59 will be illustrated by discussing their use for a maximum droplet diameter of 45 μm (which approximately corresponds to the maximum diameter for a Langmuir D distribution with an MVD of 20 μm), along with an airspeed between 100 and 220 knots and a chord size of 5.58 feet, as before. As seen from figure 2-5, a value of $K_{0,max} \approx$ .1 roughly corresponds to these conditions. Figure 2-54 indicates that all the airfoils have an S_L value of about .10 or less at these conditions at α = 0°. The figure shows relatively little variation among the airfoils.

I 2-19

Figures 2-55 ($\alpha = 4°$) and 2-56 ($\alpha = 8°$) show a dramatic upward shift in the curves as one would expect, since the impingement on the lower surface will greatly increase as the angle of attack is increased.

In examining figures 2-57 ($\alpha = 0°$), 2-58 ($\alpha = 4°$), and 2-59 ($\alpha = 8°$) for S_U, one notes considerably more variation among the airfoils that was the case for S_L. This is perhaps to be expected, since as the angle of attack is increased, what little impingement occurs on the upper surface will presumably be quite sensitive to the shape of the airfoil. For $K_{0,Max} \approx .1$, S_U is in the vicinity of .07 for all airfoils at $\alpha = 0°$ (figure 2-57), in the vicinity of .01 at $\alpha = 4°$ (figure 2-58), and still in the vicinity of .01 (although somewhat smaller) at $\alpha = 8°$ (figure 2-59). Accurate calculation of S_U for such a value of K_0 is also a computational challenge, particularly at higher angles of attack, so some of the variation among the airfoils in these figures is also numerical.

Comparison of Impingement Properties of a Circular Cylinder and a NACA 0012

Using figures 2-43 and 2-44 for a circular cylinder along with figures 2-11 and 2-13 for the NACA 0012, it is possible to compare the impingement properties of a blunt or bluff body (the cylinder) with those of a streamlined body (the NACA 0012 airfoil). The diameter of the cylinder is taken to be equal to the chord of the airfoil. For illustrative purposes, a very small airfoil model will be assumed, with a chord size of 5 cm. As indicated in table 2-3, K_0 is computed using radius (rather than diameter) for a cylinder while it is computed using chord for an airfoil. Assume that conditions are such that $K_0 = .2$ for the airfoil; then $K_0 = .1$ for the cylinder.

On the other hand, according to figures 2-43 and 2-13, $\beta_{max} \approx .30$ for the cylinder and $\beta_{max} \approx .78$ for the airfoil. According to equation 2-31, it follows that, for a small rime accretion, the ice thickness at the stagnation point would be about two and a half times greater for the airfoil. According to figures 2-44 and 2-11, $E \approx .05$ for the cylinder and $E \approx .37$ for the airfoil. Recall that $E = \Delta Y_0/h$. For the cylinder, the projected frontal length h is equal to the diameter of the cylinder which, nondimensionalized by the diameter itself, is simply equal to 1; hence $\Delta Y_0 = (.05)(1) = .05$ (dimensionless). For the NACA 0012 airfoil at $\alpha = 0°$, h is equal to the airfoil thickness which, nondimensionalized by the chord, is equal to .12; hence $(.78)(.12) = .044$ (dimensionless). Assume the accreted ice is directly proportional to the impinging mass (which should be approximately true for a rime accretion with no water loss due to splashing or shedding). Then, according to equation 2-26, the mass of accreted ice is directly proportional to ΔY_0, and so more ice will accrete on the cylinder than on the airfoil. This apparent contradiction is resolved when it is realized that far less mass impinges on the cylinder than on the airfoil relative to their respective projected frontal areas.

Note also that impingement curves for cylinders have different general shapes than those for airfoils. An airfoil impingement curve is often narrow and peaked in the stagnation region and for most conditions has a region that is distinctly concave upward. A cylinder impingement curve is not peaked in the stagnation region and the entire curve is concave down or only slightly concave upward toward the limits of impingement.

2.2.1.8 Surface Geometry Effects

As is clear from the data of section 2.2.1.7, the geometry of a body affects the droplet impingement parameters. The effect of the overall size of the body is well known and is reflected in the value of K_0. As the characteristic length of the body decreases, K_0 increases and as a result E, β_{max}, S_U and S_L all increase.

For airfoils, Bragg (references 2-12, 2-33, and 2-34) has studied the effect of geometry on droplet impingement. Several airfoil geometry terms were considered, including: maximum thickness and its location, maximum camber and its location, and leading edge radius. One of the strongest relationships found was that between the airfoil leading edge radius and the maximum impingement efficiency. In figure 2-61, β_{max} is plotted versus leading edge radius for the thirty airfoils of reference 2-33. (Points for four airfoils are indicated by solid symbols and labeled; see figure 2-60 for profiles.) Data are plotted for two angles of attack and three modified inertia parameters. Note that at $K_0 = .01$ (within the "typical" range for a wing section of a general aviation aircraft - see figure 2-4) there is a strong relationship between leading edge radius and β_{max}. For an airfoil with leading edge radius of 0.8 percent chord and $K_0 = .01$, β_{max} is approximately 0.5, but drops to around 0.25 for a leading edge radius of 2.0 percent chord. Also note that the dependence decreases markedly with increasing K_0 and that β_{max} decreases slightly with increasing angle of attack for each value of K_0. Finally, note that variation in β_{max} for a particular value of the leading edge radius arises from other characteristics of the airfoils, since they differ in more than leading edge radius.

Another relationship is that between airfoil maximum thickness and collection efficiency, E. In figure 2-62, E is plotted as a function of maximum thickness for all thirty airfoils and for four K_0's. For all K_0's shown, E decreases as the airfoil thickness increases. However, the effect becomes less pronounced with decreasing K_0 and for $K_0 = .01$ is quite slight (note also that E < .10 for all airfoils for this condition). Figure 2-62 indicates that thicker airfoils (and bodies in general) are less efficient droplet collectors with respect to the width h of their projected frontal area. This does not mean, however, that thicker airfoils accrete less mass of ice. Figure 2-63 shows ΔY_0 as a function of airfoil maximum thickness for the same conditions as figure 2-62. Here the opposite relationship is seen, that is, ΔY_0 increases as airfoil thickness increases, the effect being very pronounced for large K_0 (although non-existent for $K_0 = .01$). Since $E = \Delta Y_0/h$, it follows that E decreases with increasing airfoil thickness because h increases faster than ΔY_0. But since mass of ice accreted is directly proportional to ΔY_0, it is essentially independent of airfoil thickness for $K_0 = .01$ and increases with increasing airfoil thickness for larger K_0.

2.2.2 Ice Accretion

2.2.2.1 Types of Ice

The terms "rime" and "glaze" are used in several different senses when discussing aircraft icing. The most common usages are outlined below.

A portion of ice which is opaque and milky white in color is called rime; a portion of clear (transparent) ice is called glaze. Glaze ice is harder (denser) than rime ice. Rime ice is similar to the ice forming on refrigerator coils due to condensation while glaze ice is similar to refrigerator ice cubes.

The term "ice accretion" refers to ice which has accreted on any airframe component during flight (or in an icing tunnel). An ice accretion which is completely opaque and milky-white is called a rime ice accretion. An ice accretion which is completely clear; or clear in the stagnation region and opaque in the regions well aft of the bulk of the ice is called a glaze ice accretion.

The cross-sectional shape of an ice accretion which has formed on a wing or tail is called an airfoil ice accretion shape. A rime ice accretion often has a spearhead or streamlined shape tending to conform to the shape of the airfoil, and this shape is called a rime ice accretion shape. A glaze ice accretion often has a single- or double-horned shape (depending on angle of attack), and this shape is called a glaze ice accretion shape.

Thus the term rime may refer to (1) the entire ice accretion if it is completely rime (opaque) in composition, (2) the opaque portion of an ice accretion consisting of both opaque and clear ice, or (3) the shape of the ice accretion if it possesses a spearhead or streamlined shape. The term glaze may refer to (1) the entire ice accretion if it is completely clear in composition (2) a clear region of ice on an ice accretion consisting of both opaque and clear ice or (3) the shape of the ice accretion if it is single- or double-horned. One must determine the meaning from the context.

These different usages can be confusing; for example, an ice accretion which is entirely rime in composition may not have a streamlined or spearhead shape; indeed, it may appear to have horns. Similarly, an ice accretion which is entirely or mainly glaze in composition may not have the single- or double-horned shape; a great variety of shapes is possible for ice accretions which are glaze in composition, particularly if they are formed when the ambient temperature is near the freezing point. Nonetheless, in a discussion of ice accretion shapes, the term rime means the idealized streamlined shape, while the term glaze means the single- or double-horned shape.

The terms intermediate and mixed are used interchangeably although intermediate is perhaps preferred to avoid confusion with the phrase "clouds of mixed conditions" which indicates clouds consisting of both ice crystals and supercooled water droplets. When referring to the composition of an ice accretion, intermediate indicates that the accretion is neither entirely rime nor glaze but has rime patches slightly aft of the glaze ice portion. When referring to shape, there is no commonly accepted meaning. (Reference 2-22 uses the term "intermediate ice accretion" to refer to an ice

accretion which is a combination of glaze and rime ice; glaze in the forward areas, rime in the aft areas and no horns.)

To further complicate the picture, ice accretions may have rime fingers aft of the bulk of the accretion.

How are rime and glaze ice formed in flight? Rime ice forms when the supercooled droplets in the cloud freeze on impact with the aircraft surface; trapped air gives the ice its milky-white appearance. In the glaze case, the droplets do not freeze on impact (except, perhaps, far aft); instead, they either coalesce with other droplets to form much larger liquid surface drops or else they merge with a liquid film on the surface. In either case, when the water freezes, no air is trapped and the ice is essentially transparent. Both rime and glaze ice may form simultaneously on different regions of the same surface or on different size components.

Why is a streamlined shape common for airfoil ice accretions which are entirely rime in composition? This is simply because essentially all the droplets freeze on impact, causing the ice accretion to grow into the freestream as a forward extension of the airfoil.

Why do the ice accretions that are entirely glaze in composition, or predominately glaze merging with some rime slightly aft, tend to develop characteristic single or double horn shapes? The formation of the horns is sometimes ascribed to water running back on the wing from the stagnation region and then freezing in the area where the horns form. (This "runback" is not to be confused with water which runs back from a thermally protected region and freezes aft of the region, which is also called "runback.") However, other, more complicated, explanations have also been advanced and conclusive experimental evidence in favor of any single explanation does not exist.

Under what conditions do rime and glaze ice accretions form? This depends on the thermodynamics of the surface in question, specifically on all the factors that contribute significantly to the energy balance equation. In general order of importance, these are ambient temperature adjusted for the dynamic heating effects of airspeed and air density (altitude), liquid water content (LWC), and droplet size. Rime accretions tend to form for low temperatures, low LWC's, and small droplet sizes, while glaze ice tends to form for temperatures close to (but below) freezing, high LWC's, and large droplet sizes. Unfortunately, even this very general statement does not cover conditions which sometimes occur. For example, rime accretions can form in the presence of large LWC's and droplet sizes if the temperature is low enough and can also form at temperatures rather close to freezing if the LWC is very low (so that there is very little water to freeze). Similarly, glaze accretions can form for quite low temperatures if the LWC is sufficiently large. The key question is whether the component skin surface temperature is low enough to freeze all incoming droplets on impact. Another obstacle to useful generalization is dependence on surface geometry. Under identical ambient conditions, a rime accretion might form or a glaze accretion might form depending upon the size and shape of the airfoil or component in question.

Table 2-4 summarizes in very general terms the conditions which tend to be associated with rime and glaze ice. In general, anything which tends to lower the energy of the icing process increases the likelihood of rime ice forming.

Photographs of rime and glaze ice accretions are shown in figures 2-64 and 2-65. Ice is difficult to photograph and while many photographs exist, few provide the details which can be found by observing an actual ice shape. Detailed tracings of ice cross-sections are shown in figure 2-66.

When a wing is swept back, crossflow in the spanwise direction occurs and ice shapes show regular three-dimensional variations. For glaze accretions, the ice shape has periodic peaks and valleys along the span. The shapes appear as almost separate cup-shaped accretions stacked spanwise down the airfoil leading edge with their ends bowed toward the wing tip. The segmented "notchings" result in a shape that has been likened to a "lobster tail." The "lobster tail" shape is shown in figure 2-67a and 2-67b.

Icing tests in the Canadian National Research Council's (NRC) High Speed Icing Wind Tunnel have identified glaze ice characteristics which occur at high Mach number. In figure 2-68, three types of glaze ice are shown as identified in reference 2-35. Beak ice forms on airfoils at high subsonic Mach numbers in the region of low pressure on the leading edge upper surface. This is the upper peak of a double horn shape which freezes due to the additional local cooling in the suction peak. The rounded glaze ice shown occurs quite often in rotor airfoil testing and is usually referred to as an intermediate or mixed ice accretion.

The term "icing limit" or "icing boundary" is sometimes used to denote the temperature below which ice will form on a body and above which it will not. This icing limit temperature is highly dependent on the size and shape of the body as well as the ambient and flight conditions. Various correlations have been advanced for the icing limit temperature.

Recent tests by Flemming and Lednicer (reference 2-35) have defined icing boundaries for rotor airfoils operating from Mach numbers of 0.20 to 0.80. In figure 2-69, the icing boundary temperature is shown for a liquid water content of 0.35, 0.66 and 1.2 g/m^3. Here the regions are labelled for no ice accretion, beak ice, glaze or wet growth, and rime ice or dry growth. These data were based on ice accretion experiments in the NRC High Speed Icing Tunnel using rotor airfoils of chord length 2.69 to 6.38 inches. These icing boundaries were also found to be a function of airfoil angle of attack (reference 2-35). Based on this work, Flemming and Lednicer developed an approximate equation for the temperature for the onset of ice on an airfoil. Their results are all based on ice accretions measured in the High Speed Icing Tunnel and may provide guidance as to the ice boundaries for similar airfoils under similar icing conditions. The interested reader is referred to reference 2-35, with the usual cautions on the use of icing correlations.

2.2.2.2 Effect of Flight Parameters and Atmospheric Conditions on Ice Shapes

As already discussed, the combination of flight parameters and cloud properties will determine the type of ice accreted by a particular body. In this section, the effect of these properties will be surveyed using ice tracings taken from wind tunnel experiments.

A study by Olsen, Shaw, and Newton (reference 2-36) conducted in the NASA Lewis Icing Research Tunnel documented the effect of tunnel conditions on ice shapes. For these tests, a NACA 0012 airfoil section of 0.53 m chord was used. Measurements were made of the ice shapes and the resultant section drag coefficient. The ice shapes obtained from ice tracings will be considered here, and the drag coefficients will be discussed in a later section.

In figure 2-70, ice shapes are shown as functions of time and angle of attack. The top ice shapes are for basically glaze accretions, T = 18 °F (-8 °C), and the lower shapes are rime with T = -15 °F (-26 °C). For the rime cases, the effect of time on ice growth is approximately linear, i.e., the ice thickness at a given point on the airfoils increases linearly with time. This is true since the droplets freeze on impact and the ice accretion rate does not vary greatly with time. For the glaze ice shapes, ice thickness does not increase linearly with time. Note particularly the horn which forms rapidly between the 2 and 5 minute tracings in cases A, B, and C. The effect of angle of attack is similar in all cases. As would be expected from the droplet impingement results, the orientation of the ice shapes shifts toward the lower surface as the angle of attack is increased. In the glaze accretions there seems to be a tendency for ice horns to become more severe with increased angle of attack.

The effect of total temperature on ice accretion shapes is shown in figure 2-71. As the air temperature is increased, the ice shape changes from a rime shape at -15 °F (-26 °C) to an intermediate shape, then glaze, and finally, at T = 32 °F (0 °C), no ice accretes at all. The bottom tracings are for a considerably higher airspeed which produces a distinctive double horn shape at a fairly low temperature. The upper tracings never really develop a large double horn shape, although an upper surface horn does develop at about 23 to 28 °F (-5 to -2 °C).

Figure 2-72 shows the effect of droplet size on ice shapes. Here four different MVDs were used at six different tunnel conditions. All the data were taken with the NACA 0012 airfoil at four degrees angle of attack. The most noticeable effects of increasing droplet size are to increase the size of the ice accretion and move the glaze ice horn further back. As the droplet size increases, the overall collection efficiency, E, increases, which means more mass of water impinges plus an increase in the droplet impingement limits. The increased droplet size also tends to make more of the ice glaze in nature, due to the increased amount of mass striking the airfoil. This can be seen most clearly in cases A and F.

2.2.2.3 Ice Shape Correlations

Several researchers have developed correlations to attempt to predict ice shape parameters for given icing conditions. These correlations are based primarily on tunnel data. While these correlations

may be acceptable over the airfoils and data used to develop them, no general correlation has been developed which has proved to be reliable over a wide range of airfoils and icing conditions. An engineer wishing to use one of these correlations should study the report where it appears to determine if it is suited to the problem he is confronting. While no "universal" correlations are available, one of the following may be useful depending on the application.

Gray (reference 2-37) developed correlations for ice shapes based on NACA icing data. These correlations are for the ice height and angle above the chord line of the upper surface horn of a glaze ice shape; they depend upon droplet impingement parameters, freestream conditions and airfoil angle of attack. They were based on low-speed results and a large portion of the data was on the very thin NACA 65A004 airfoil. Wilder presents correlations for ice height and angle for both glaze ice horns and also stagnation point growth in reference 2-38. These correlations are based on Boeing tests in the NASA Icing Research Tunnel and are for a fairly limited range of conditions and airfoil types. Flemming and Lednicer (reference 2-35) have developed a correlation for ice height as a result of their experiments in the NRC High Speed Icing Wind Tunnel. These results are for helicopter sections and include high subsonic Mach numbers.

2.2.2.4 Physical Modeling of Ice Accretion Process

The physical modeling of aircraft icing consists of (1) the modeling of the trajectories and impingement of the supercooled water droplets and (2) the modeling of the behavior of the liquid water formerly in the droplets once it is on a surface of the aircraft. Part (1) has been presented above; the basic assumptions and equations go back to reference 2-2 and are widely accepted; discussion centers on the formulation of numerical procedures. Part (2), which will now be discussed, remains controversial. There exists what might be called a "standard computational model" which is incorporated in various forms in a number of computer codes, the most widely used of which is probably LEWICE (reference 2-39), developed under the direction of NASA Lewis Research Center. However, a number of questions have been raised as to how accurately this model actually depicts the surface behavior of the liquid water. NASA-Lewis (reference 2-40) has initiated efforts to "formulate either changes to the existing model or an alternate model in order to see if ice shape predictions can be improved." (However, LEWICE can presently give useful ice shape predictions for a fairly wide range of conditions when used in conjunction with an appropriate roughness correlation; see the discussion in Chapter IV, Section 2.) This section begins with a presentation of the standard computational model; this is followed by a brief survey of the major criticisms of that model.

The standard model assumes that if air temperature is not low enough for impinging droplets to freeze upon impact, then the droplets are absorbed into a thin water film which flows away from the stagnation line (or point). As it flows, it is cooled mainly by convection to the airstream until it freezes, thus gradually changing the surface shape.

This model is formulated computationally by dividing the airfoil surface into segments, and associating a control volume with each segment. The water entering a control volume has two sources: (1) water droplets impinging on the surface segment; (2) water "running back" from an adjacent control volume closer to the stagnation point. (This "run back" water consists of all water which entered the adjacent control volume but did not freeze.) An energy balance analysis is applied to each control volume to determine the freezing fraction n, the fraction of the incoming water which freezes for that control volume. If n = 1, then all incoming water freezes. If n < 1, then a fraction 1-n does not freeze. This water will in turn run back into the adjacent control volume further away from the stagnation point.

The mass and energy balance analyses for a given control volume will now be presented in some detail. The energy balance analysis was given its classic formulation by Messinger (reference 2-41), whose work drew on earlier work by Tribus (reference 2-42). The presentation and notation used here is based on reference 2-43.

The mass balance for a control volume on the surface can be formulated as follows (figure 2-73). Let M''_{Imp} denote the mass flux per unit time due to impinging water droplets, $M''_{Run\ in}$ and $M''_{Run\ out}$ denote mass flow per unit area per unit time into and out of the control volume due to liquid run back, and M''_{Ice} denote the mass of ice formed per unit area per unit time. Then the mass balance for the control volume is:

$$\dot{M}''_{Ice} = \dot{M}''_{Imp} + \dot{M}''_{Run\ in} - \dot{M}''_{Run\ out} \qquad (2\text{-}33)$$

The term M''_{Imp} is given by:

$$\dot{M}''_{Imp} = V_\infty\ LWC\ \beta \qquad (2\text{-}34)$$

V_∞ is the freestream velocity. However, if the local velocity at the edge of the boundary layer is available, that velocity should be used rather than the freestream velocity. This procedure is followed, for example, in the ice accretion code LEWICE. β is the local collection efficiency for the control volume.

It is convenient to define a term $M''_{Incoming}$ by:

$$\dot{M}''_{Incoming} = \dot{M}''_{Imp} + \dot{M}''_{Run\ in} \qquad (2\text{-}35)$$

Then the freezing fraction n for the control volume is defined by:

$$n = \frac{\dot{M}''_{Ice}}{\dot{M}''_{Incoming}} \quad (2\text{-}36)$$

where M''_{Ice} is the incoming mass which freezes.

The energy balance for a control volume on the surface can be formulated as follows (figure 2-74). First, the main heat source terms (those that release heat into the control volume) are given.

Let Q''_{Freeze} denote the freezing of the incoming water. Then

$$\dot{Q}''_{Freeze} = n\, M_{Incoming}\, L_f \quad (2\text{-}37)$$

where L_f is the heat of fusion.

Let $Q''_{Aero\ Heat}$ denote the aerodynamic heating. Then

$$\dot{Q}''_{Aero\ Heat} = h_c\, r_c\, V_\infty^2 / 2 C_{P_{air}} \quad (2\text{-}38)$$

where h_c is the local heat transfer coefficient, r_c is a recovery factor, and $C_{P_{air}}$ is the specific heat of air.

Let $Q''_{Droplet\ K.\ E.}$ denote the kinetic energy of the incoming droplets. Then:

$$\dot{Q}''_{Droplet\ K.E.} = M_{Imp}\, V_\infty^2 / 2 \quad (2\text{-}39)$$

Let $Q''_{Ice\ Cool}$ denote the cooling of the ice to the surface temperature T_{Surf}. Then

$$\dot{Q}''_{Ice\ Cool} = n\, M_{Ice}\, (T_f - T_{Surf}) \quad (2\text{-}40)$$

where T_f is the ice/water equilibrium temperature (32 °F). Note that if $n < 1$, $T_{Surf} = T_f$ and so this term equals 0.

Define Q''_{Source} by:

$$\dot{Q}''_{Source} = \dot{Q}''_{Freeze} + \dot{Q}''_{Aero\ Heat} + \dot{Q}''_{Droplet\ K.E.} + \dot{Q}''_{Ice\ Cool} \quad (2\text{-}41)$$

Next, the main heat sink terms (those that remove heat from the control volume) are given. Let Q''_{Conv} denote the convective cooling term. Then

$$\dot{Q}''_{conv} = h_c (T_{Surf} - T_\infty) \qquad (2\text{-}42)$$

where T_∞ is the freestream temperature. If the local temperature at the edge of the boundary layer is available, that temperature should be used in this term rather than the freestream temperature. This is also done in LEWICE.

Let $Q''_{Drop\ Warm}$ denote the droplet warming term. Then

$$\dot{Q}''_{Drop\ Warm} = M_{Imp} C_w (T_f - T_\infty) \qquad (2\text{-}43)$$

where C_{Water} is the specific heat of water.

Let Q''_{Evap} denote the heat loss due to evaporation. There are a variety of formulations of this term. The approach of reference 2-44 is used here. Let M''_{Evap} denote the evaporative mass flux per unit time. This term is sufficiently small to be neglected in the mass balance. It is given by

$$\dot{M}''_{Evap} = g\ \Delta B \qquad (2\text{-}44)$$

where g is the mass transfer coefficient and ΔB is the evaporative driving potential dependent on the vapor concentration difference between the surface and the edge of the boundary volume. These quantities are given by:

$$g = \frac{h_c}{C_{P_{air}}} \left(\frac{Pr}{Sc}\right)^{.667} \qquad (2\text{-}45)$$

$$\Delta B = \frac{B_1}{B_2} \qquad (2\text{-}46)$$

$$B_1 = \frac{P_{v Surf}}{T_{Surf}} - \left(\frac{P_T}{P_S}\right) \frac{P_{v\infty}}{T_T} \qquad (2\text{-}47a)$$

$$B_2 = \frac{1}{0.622} \frac{P_T}{T_T} - \frac{P_{v Surf}}{T_{Surf}} \qquad (2\text{-}47b)$$

Pr is the Prandtl number, Sc is the Schmidt number, $P_{v,surf}$ is the vapor pressure at the surface, $P_{v,0}$ is the free stream vapor pressure (or at the edge of the boundary layer, if available), P_T and T_T are free stream total pressure and temperature (or at the edge of the boundary layer, if available), and .0622 is the ratio of the molecular weight of water to that of dry air.

The heat loss due to evaporation is now given by:

$$\dot{Q}''_{Evap} = \dot{M}''_{Evap} \, L_v \qquad (2\text{-}48)$$

L_v is the heat of vaporization.

If the freezing fraction is equal to 1 and the surface temperature T_{Surf} is to be computed, then Q''_{Evap} should be replaced by the heat loss due to sublimation, denoted by Q''_{Subl}. This is given by

$$\dot{Q}''_{Subl} = \dot{M}''_{Subl} \, L_S \qquad (2\text{-}49)$$

where M''_{Subl} denotes the mass flux due to sublimation per unit time and L_S denotes the heat of sublimation. In some programs, M''_{Subl} is computed using the same formulas as M''_{Evap}.

Define Q''_{Sink} by:

$$\dot{Q}''_{Sink} = \dot{Q}''_{Conv} + \dot{Q}''_{Drop\ Warm} + \dot{Q}''_{Evap} \qquad (2\text{-}50)$$

The energy balance equation is:

$$\dot{Q}''_{Source} + \dot{Q}''_{Sink} = 0 \qquad (2\text{-}51)$$

The control volume freezing fraction is calculated as follows: Assume that the equilibrium temperature, T_{surf}, is T_f. With this assumption, all quantities in the energy balance except n can be evaluated. Now solve for n. If the calculation yields a value of n between 0 and 1 inclusive, the calculation is complete. If n is calculated to be larger than 1, assume that n = 1 and that the excess over 1 was because T_{surf} is actually smaller than T_f. So set n equal to 1 in the energy balance equation, which is now solved iteratively (since several quantities depend on T_{surf}) for T_{surf}. If n is calculated to be smaller than 0, similar reasoning leads to setting n equal to 0 and solving iteratively for T_{surf}, which will now be larger than T_f.

A major source of uncertainty in calculating n using this equation arises from the uncertainty in the computation of the heat transfer coefficient h. If n is calculated in the stagnation region of a cylinder, it is common to use the heat transfer correlation for a smooth cylinder (given, for example, in reference 2-45). If n is to be calculated in the stagnation region of an airfoil, the same correlation is sometimes used with radius equal to the radius of curvature of the airfoil. As the ice accretes, the shape changes and the surface roughness also changes, perhaps increasing dramatically. This can have a profound effect on the heat transfer coefficient.

Airfoil ice accretion codes must include an algorithm to calculate the heat transfer coefficient over the entire airfoil (See Chapter IV, Section 2). If it is a time-stepping code such as LEWICE, it must be able to calculate the heat transfer coefficient for an iced airfoil. An integral boundary layer method is typically used (See references 2-39 and 2-46). These methods generally include roughness terms, but a standard method for describing ice roughness has not yet been developed. NASA Lewis has conducted experiments to determine heat transfer coefficient distributions for ice shapes (references 2-47, 2-48). This data is essential to evaluate heat transfer coefficient algorithms. It appears that all existing algorithms introduce substantial uncertainty into the calculation.

Dependence of freezing fraction on meteorological and flight variables

The dependence of the freezing fraction n on meteorological and flight variables in the standard computational model will now be illustrated by calculations at the stagnation line of a circular cylinder of diameter 20 cm. The calculations were done using a program that is a modification of the one discussed in reference 2-44. This program uses the heat transfer coefficient correlation for a clean cylinder from reference 2-45. If these calculations were done for a different geometry, or with a different program, or using a different heat transfer coefficient correlation, the numerical values would certainly change, but the general relationships illustrated would be much the same.

Two "baseline conditions" are specified:

Condition	Ambient Temperature T_∞ (°C)	LWC g/m^3	Droplet Diameter δ (μm)	Freestream Velocity V_∞ (m/s)
a.	-26	.7	20	70
b.	-6	.1	20	70

These were chosen because both have a freezing fraction of approximately .9 and both permit the variation of each of the four parameters individually, driving the value of n toward 0.

(It must be emphasized here that the following results indicate the magnitude of the freezing fraction along the stagnation line only. The unfrozen water may run back (or "slide" back in the form of large surface drops) from the stagnation line and eventually freeze somewhere on the cylinder. This is discussed further in the next section.)

Starting with condition (a), n was calculated for several increasing values of T_∞ terminating with -2 °C (figure 2-75a) and then the same procedure was followed starting with condition (b), again terminating with T_∞ = -2 °C (figure 2-75b). The figures illustrate that n decreases linearly with increasing T_∞. Note that figure 2-75a, with a relatively large LWC of .7 and starting from a low temperature of -26 °C, exhibits a much slower rate of decrease in n than does figure 2-75b, which has a LWC of .1 and starts from a much higher temperature of -6 °C.

Table 2-5a shows the relative contributions to the energy balance of the main heat source and heat sink terms for condition (a) as t_{∞} increases. For the source terms, the relative contribution of the droplet freezing term falls dramatically as the freezing fraction approaches 0 and this results in a larger relative contribution of the aerodynamic heating term. For the sink terms, the contributions are relatively constant. Table 2-5b for condition (b) shows that because LWC = .1 the relative contribution of the droplet freezing term is smaller at all temperatures and the relative contribution of the aerodynamic heating term is correspondingly larger. For the sink terms, the contributions are again relatively constant.

Next, n was calculated for increasing values of LWC starting from both conditions (a) and (b). The shape of the resulting curves in figures 2-76a and 2-76b can be explained as followed: By solving the energy balance equation for n under the assumption that $T_{Surf} = 0$ °C one obtains an expression for n of the form

$$ n = C_1 + \frac{C_2}{LWC} \tag{2-52} $$

where C_1 and C_2 are constants. Thus n approaches the value C_1 asymptotically as LWC increases. Figures 2-76a and 2-76b display this relationship. Note that for $T_{\infty} = -26$ °C (condition a) the value of C_1 is approximately .4 while for $T_{\infty} = -6$ °C (condition b) the value of C_1 is approximately .1. Note also that in figure 2-76b, starting from a small initial value of LWC = .1 g/m^3, the freezing fraction n falls very rapidly at first, going from approximately .9 to approximately .3 for LWC = .4 g/m^3.

Table 2-6a shows the relative contributions to the energy balance of the main heat source and heat sink terms for condition (a) as LWC increases. For the source terms, since n always exceeds .4 as LWC goes from .7 to 5 g/m^3, a lot of water is being frozen, so droplet freezing is dominant for all values of LWC. As to the sink terms, the droplet warming term becomes increasingly important as LWC increases since increasing quantities of water impinge on the surface and warm from $T_{\infty} = -26$ °C to 0 °C. Table 2-6b for condition (b) shows a pattern similar to that of table 2-6a for both the source and sink terms.

Figures 2-77a and 2-77b were calculated starting from conditions a and b respectively, this time increasing the droplet diameter from 20 μm to 80 μm. The curves somewhat resemble the LWC curves just discussed. The reason for this is that as the droplet diameter increases from 20 to 40 to 60 to 80 μm, the collection efficiency at the stagnation point increases from approximately .4 to .7 to .8 to .85 (note the decline in the rate of increase). This increases the amount of liquid water in the stagnation region, so the effect is similar to simply increasing LWC. The droplet size effect is not as pronounced as the LWC effect because of the declining rate of increase in the collection efficiency as the droplet diameters become large.

Tables 2-7a and 2-7b show the relative contributions to the energy balance of the main heat source and heat sink terms for conditions (a) and (b) as δ increases. The trends are similar to those

shown in tables 2-6a and 2-6b for increasing LWC, the reason being that increasing the droplet size has the effect of increasing the liquid water impacting the surface.

Finally, figures 2-78a and 2-78b illustrate the approximately linear decrease in n as the freestream airspeed V_∞ is increased from 70 m/s to 130 m/s for both conditions a and b. This is primarily the effect of aerodynamic heating. However, note that the dependence of n on V_∞ is more complicated than its dependence on the other variables. As V is increased, the collection efficiency increases and the contributions of the convective cooling and evaporation terms change, since both depend on the heat transfer coefficient h, and the calculation of h depends on V_∞. Note that n falls much more rapidly in figure 2-78b, which corresponds to the warmer temperature condition.

Tables 2-8a and 2-8b show the relative contributions to the energy balance of the main heat source and heat sink terms for conditions (a) and (b) as V_∞ increases. For the source terms, the relative contribution of the aerodynamic heating increases steadily in importance for both conditions (a) and (b) as V_∞ increases. Note, however, that it makes a much larger percentage contribution for condition (b), which has the smaller LWC of .1. As to the sink terms, comparison of the tables shows that the relative contribution of the droplet warming term is much smaller for the smaller LWC (condition (b)), with the convective and, especially, evaporative terms larger at its expense. For both tables, the relative contributions of the sink terms are nearly constant as V_∞ increases.

Figures 2-81 to 2-83 (reference 2-49) are based upon an analysis published in 1952 using the freezing fraction concept developed by Messinger (reference 2-41). The plots show an estimate of the freezing fraction for the stagnation line of a two-inch diameter cylinder in a cloud of 15 micron droplets at a 5,000 foot (1.5 km) altitude for LWCs of 0.2 g/m^3, 0.5 g/m^3, and 1.0 g/m^3. Freezing fraction lines are shown as a function of ambient temperature and true airspeed. These lines would undoubtedly shift if a different model were used. However, the general relationships and trends would remain the same, and it is to illustrate these that the figures are reproduced here. Note that the threshold temperature between types of ice (n = 0, n = .66 and n = 1.0) decreases both with increasing airspeed and with increasing liquid water content. The choice of n = .66 as a boundary between glaze and "intermediate" ice is arbitrary.

Criticisms of the Model

Criticism of this model has focused primarily on the runback assumption, not on the control volume energy balance analysis. Reference 2-50 did investigate the possibility that the control volume analysis should include an extra term heat source which would be proportional to the film thickness. However, it was concluded on the basis of an order of magnitude analysis that such a term would not have a major effect on the computation of the freezing fraction.

Much of the recent discussion of the need for revision of the model grew out of close-up movies (and stop action photographs) of the icing process made in the Icing Research Tunnel at the NASA Lewis Research Center (reference 2-51). The movies show surface phenomena at several positions on a symmetrical wooden airfoil immersed in a cloud in the tunnel. The airfoil had a 11.4 cm chord,

a 12 cm span, and a cylindrical leading edge of 1.9 cm radius. Tunnel runs were conducted for a range of airspeeds (50 to 320 km/hr), air temperatures (above freezing down to -25 °C), and cloud conditions. Material from the films was selected to produce a single film showing some of the most important and interesting results (reference 2-52).

The following discussion of the picture that emerged from these films is based on reference 2-53. It is convenient to begin with the results at air temperatures above freezing, since these reveal the surface phenomena without the influence of freezing (figure 2-79a). Large surface drops (beads) are formed from the cloud droplets impacting the surface of the airfoil. When these drops are large enough, they start to move downstream. The lower the airspeed, the larger the drops before they start to move. As they move downstream, the larger drops apparently shed, since only smaller drops are observed on the surface downstream. The film sequences apparently do not show any flowing film of liquid; all liquid transport is through the movement of large drops.

When the above-freezing experiment was performed over a rough artificial ice surface, the same surface behavior was observed except that the surface drops grew larger before they moved.

For below-freezing temperatures and aircraft airspeeds (figure 2-79b), surface liquid transport is again confined to the movement of large drops (the biggest of which were observed at low airspeeds.) However, even the large drops move only in a region near the stagnation line and only during a short initial transient phase. The size of the region of large drop movement and the length of the initial transient phase both tend to increase with increasing sub-freezing temperatures and with decreasing airspeed. The stagnation region initially has a thin water film; away from the stagnation line, this film gives way to very large stationary drops on top of ice hills. The width of the thin-film region decreases with time, and increases somewhat with decreasing temperature. Refer to figures 2-80a and 2-80b for stop action photographs from the film.

The film of reference 2-53 has now been viewed by a large number of researchers. Two aspects of the picture sketched above are sometimes discussed. First, is it true that any large surface drops which are observed to move after the initial phase are in fact shed? Second, is it true that the thin water film in the region of the stagnation line does not contribute to any runback?

Reference 2-54 attempts to explain the existence of stationary surface drops (which this reference refers to as beads) in terms of contact angle and contact angle hysteresis. It is observed that the liquid beads were often surrounded by regions of otherwise dry surfaces. The strong temperature dependence of contact angle behavior indicates the potential importance of thermal gradients on the ice surface. Small variations in surface temperature could restrict the mobility of water and be the cause of the stable nature of surface water beads. A cold dry surface would impose a barrier to water flow away from a bead.

Based on the experimental observations of ice formation in the glaze ice regime, a Multi-Zone model, in which the accreting ice surface is divided into two or more discrete zones with varying surface roughness and water behavior, has been proposed by Hansman and his associates (references 2-55, 2-56, and 2-57). In the simplest version, the surface is divided into two zones, the smooth

zone and the rough zone. In the smooth zone, corresponding to the region observed to be centered about the stagnation point, the surface is smooth and uniformly wet with a thin water film. In the rough zone, corresponding to the region found downstream of the smooth zone, the surface was observed to be considerably rougher.

The standard computational model of aircraft icing does not account for any splashing of the impinging cloud droplets. Reference 2-50 presents an order of magnitude argument that splashing must occur and reference 2-58 presents a scaling argument that it must occur. Direct experimental evidence bearing on this question is apparently lacking. The films and photographs discussed above would not reveal splashing droplets (which would be very small) even if they were present. If splashing does occur, it could be important because of loss of mass and also possibly because of the effect of the small splashing droplets on the boundary layer.

2.2.3 Adhesive Properties of In-Flight Ice

The detailed physics of how ice adheres to an aircraft surface is not well understood. However, a limited amount of experimental data is available which provides some insight into ice adhesion properties. A better understanding of ice adhesion would be very useful in the design of new de-icing systems since many of these work by breaking the bond between the ice and the surface.

Measurements have been made of ice adhesion to a variety of materials using various methods. Two types of ice have been used; bulk and "impact" or accreted ice. Bulk ice results from freezing a large mass of ice, similar to an ice cube. Impact ice is formed in flight or in an icing wind tunnel from supercooled water droplets impacting a surface at flight speed or wind tunnel airspeed.

Several studies have focused on determining the adhesion by measuring the shear force required to remove the ice. Stallabrass and Price (reference 2-59) made ice adhesion measurements with accreted ice on a surface which was clean by operational standards. In figure 2-84, a comparison of their data to that of Raraty and Tabor (reference 2-60) is shown. This figure indicates that ice adhesion can be very sensitive to surface contamination and also demonstrates a linear relationship between adhesion and ambient temperature (although not all the curves shown could be called linear). Adhesion strength is zero at zero degrees Celsius and increases linearly as the temperature decreases below freezing. Loughborough and Haas (reference 2-61) also found an approximately linear relation for several materials and tabulated its slope for those materials, table 2-9. Note, however, that their measurements were taken using bulk ice. Stallabrass and Price (reference 2-59) found that accreted ice on metals had low adhesion values compared to that of bulk ice. This may be due to the reduced contact area resulting from the non-uniformity of the ice accreted.

NASA Lewis Research Center (reference 2-62) has, in recent years, supported an effort to study the structural properties of ice formed in flight (impact ice). The objectives include the measurement and analysis of three basic mechanical properties of impact ice: (1) tensile (e.g., Young's modulus), (2) shear (adhesion); and (3) peeling. References 2-63, 2-64, and 2-65 report on this work. Only the results on adhesion will be discussed here.

The work reported in reference 2-64 included experimental studies of the dependence of adhesive shear strength on several parameters. Adhesive shear strength was found to be statistically independent of the thickness of the ice and of the substrate tested (aluminum, steel, neoprene). The adhesive shear strength increased slightly with both wind velocity and droplet size, resulting in a relationship between adhesive shear strength and droplet momentum (figure 2-85). No relationship was found between adhesive shear strength and either tunnel air temperature or interface temperature below 25 °F (-4 °C). However, between 25 °F (-4 °C) and 32 °F (0 °C) a linear drop in adhesive shear strength as a function of interface temperature was observed (figure 2-86). (These results contradict results reported above for the lower temperature range. This may be related to the size of the samples employed in the studies; the sample used in the work of reference 2-64 was collected over several weeks and was very large; a certain amount of day-to-day variation was observed.) Tests on surface roughness indicated that this is a significant variable affecting adhesive strength. All the data showed a great deal of scatter. This statistical variation from one test to another appears to be a real phenomenon which must be accounted for in the design of ice protection systems that depend on ice shedding for their operation (2-62).

In the work reported in reference 2-66, finite element modeling of the rotating ice-airfoil system was used as the basic tool to study the tensile and shear stresses at the interface between impact ice and a metal airfoil surface. In reference 2-67, a statistical analysis of adhesive shear strength data was undertaken using the Weibull distribution. In reference 2-68, it is shown that in the analysis of stresses of impact ice accreted on aerodynamic surfaces, aerodynamic loading can be neglected for Mach numbers less that .45 but must be considered at higher speeds, particularly at a high angle of attack.

I.2.3 AERODYNAMIC PENALTIES DUE TO ICING

Structural icing of aircraft components, if not removed by ice protection systems, can cause serious aerodynamic penalties and/or structural damage from shed ice. Ice accretion on the lifting surfaces such as wings, tails, rotors and propellers can greatly increase the drag and reduce the lift. Ice accretion on non-lifting components such as nacelles, struts, landing gear, antennas, hinges, etc., results in lesser aerodynamic penalties. Aerodynamic penalties are usually much more serious than the added weight due to the ice and can decrease the ability of the aircraft to complete its mission, thereby leading to a safety hazard.

The aerodynamic effect of ice accretion can be separated into effects due to surface roughness and effects due to a change in body shape. That is, one can think of an ice accretion as the gross ice shape plus the surface roughness of the ice. Both the ice shape and surface roughness reduce lift, increase drag, and change the pitching moment in most cases. In the following sections, these effects will be discussed primarily with respect to airfoils. Several two-dimensional tests of airfoils with ice accretion have been made under various conditions and these data will provide the basis for this discussion. Some flight test results are also available and will be presented.

2.3.1 Wing and Tail Effects

Typical effects of ice accretion on airfoils are shown in figure 2-87. The most important effect of ice accretion on the lift of wing and tails is the reduction of $C_{L_{max}}$; reduction of 40 percent for a glaze ice shape is not unusual. Rime ice may actually increase $C_{L_{max}}$ if accreted at high angle of attack, but the performance at low C_L is very poor. Depending on the particular ice accretion, a shift in the angle of attack for zero lift may also occur. This may be a result of the ice shape changing the airfoil camber or of a thickening of the boundary layer as a result of the added roughness. The drag performance of a typical airfoil with rime and glaze ice is also shown in the figure. Drag rise varies greatly from almost no increase to increases of 500 percent or more in some cases. "Typical" drag increases might be on the order of 100 percent for rime ice and 200 to 300 for glaze ice.

2.3.1.1 Empirical Results

For very streamlined rime ice shapes the drag rise at low angle of attack is due primarily to an increase in surface roughness. Thus data on the affects of surface roughness is relevant. Bragg (reference 2-1) has compiled airfoil roughness data as it affects drag and the results are plotted in figure 2-88. These curves were faired through quite a collection of data, most of which was at a Reynolds number of at least 6 million in incompressible flow. These curves may provide a rough estimate of the drag rise due to streamlined rime ice. The data on which the curves are based is not icing data. A roughness height for ice is not easily measured and is rarely available. However, experience indicates that in using these curves a roughness height, k/c, of 0.001 works well in many cases. The curves show that different types or families of airfoils are affected differently by roughness. These differences may be related to the amount of laminar flow the clean airfoil experiences. To apply this data in a very approximate way to a non-NACA airfoil, one might select the NACA family in which the airfoils have minimum drag coefficients similar to that of the non-NACA airfoil.

For the effect of roughness on $C_{L_{max}}$, Brumby (reference 2-69) has compiled a large amount of wind tunnel and flight data and obtained the curve fits shown in figure 2-89. Again, the data used are not icing data, although a small amount of data for simulated icing roughness is included. The data are for wings with high-lift devices retracted; the effects of various forms of wing surface roughness differ depending on whether trailing edge flaps or leading edge devices are used. No Reynolds number effects have been included, because ice acts as a boundary layer trip and aerodynamic results are fairly insensitive to Reynolds numbers. The curve for localized spanwise disturbance at the leading edge may provide a very rough estimate of the reduction in $C_{L_{max}}$ for small rime ice shapes accreted at low angles of attack.

Empirical expressions to predict lift and drag penalties due to rime ice accretion have been developed. Unfortunately all of these empirical methods demonstrate low accuracy when applied

over a wide range of conditions. The reader is referred to the discussion of icing correlations in I.2.1, Introduction.

One method developed to estimate the increase in C_D due to rime ice on NACA airfoils is presented in reference 2-1. The increase in C_D is correlated with roughness height non-dimensionalized by chord, the product A_CE of the accumulation parameter and the overall collection efficiency, and a constant, I, which depends on the NACA family to which the airfoil belongs. One equation is used if $A_CE < .004$ and another equation is used if $.004 \leq A_CE < .035$. To use this method for a non-NACA airfoil, the reference recommends selecting the constant, I, for the NACA family in which the airfoils have minimum drag coefficients similar to that of the non-NACA airfoil. This method works best if the ice is accreted near the airfoil design C_L. A difficulty with the method is the determination of what value to use for the roughness height.

For large glaze ice accretions, roughness effects are not significant aerodynamically compared to the effect of the gross ice shape (reference 2-70). Figure 2-90 (reference 2-71) shows a measured separation bubble behind the upper surface horn of a glaze ice shape. These measurements were taken on a NACA 0012 airfoil with an ice shape which simulated an actual ice accretion measured in the NASA Icing Research Tunnel. Due to the severe adverse pressure gradient as the flow attempts to pass around the upper surface horn, the flow separates, forming a large separation bubble. This bubble will reattach at low angles of attack causing some lift loss, but, more significantly, a large drag rise. Some change in pitching moment may also occur. At higher angles of attack the flow does not reattach, causing a large reduction in $C_{L_{max}}$. For this airfoil and ice shape the clean drag coefficient at $\alpha = 0$ degrees was 0.0070; this increased to 0.0320 (about 350% increase) with the ice shape. More than a 100% reduction in $C_{L_{max}}$ was also measured.

The size and shape of the ice horns on a glaze ice shape are the most important features with regard to the resulting airfoil aerodynamics. The ice horns act as spoilers and their height and location must be known if their effect on the airfoil aerodynamics is to be accurately evaluated. Unfortunately, existing ice shape correlation methods are not reliable for a wide range of airfoils and icing conditions (Section 2.2.2.3). Furthermore, while much progress is being made in predicting glaze ice shapes using computer models, these predictions are not always accurate enough for detailed flowfield calculations. Even if the ice shape is accurately predicted, the computation of airfoil aerodynamics with large separation zones can be a challenging computational task.

Gray (reference 2-37) used an empirical method for the prediction of glaze ice accretions as a starting point in the development of an empirical equation to predict airfoil drag rise due to ice accretion. While Gray's correlation has been perhaps the most widely used of the existing correlations for airfoil drag rise due to icing, and it has given reasonably good agreement for some data sets, the accuracy of its predictions is sometimes not within acceptable bounds. Figure 2-91, from reference 2-36, illustrates such a case. The figure compares drag changes due to icing for a NACA 0012 measured in the NASA Lewis Icing Research Tunnel with those predicted by Gray's correlation for the same experimental conditions. The poor agreement is not really unusual for this empirical

correlation, or indeed for any existing empirical correlation, when applied to data other than than used in its development.

Correlations for airfoil aerodynamics derived specifically for the rotor case are discussed in a later section.

2.3.1.2 Experimental Results

In recent years, the use of simulated ice shapes made of plastic and wood has increased as a means to obtain aerodynamic data on airfoils with ice. Instrumentation and testing is considerably simpler than for an airfoil with an actual ice accretion. Here a small sample of the available simulated ice data will be discussed as well as some aerodynamic data on airfoils with actual ice.

Reference 2-36 studied the effect of various parameters on ice accretion shape and airfoil drag coefficient. These data were taken in the NASA Icing Research Tunnel on a NACA 0012 airfoil. Figures 2-92 and 2-93 show the airfoil drag as a function of total temperature and droplet size, respectively. The ice shapes for these tests can be found in figures 2-71 and 2-72. The lower total temperatures in figure 2-92 correspond to rime ice accretions. The airfoil drag coefficient is about .020 at -22 °F (-30 °C), which is approximately 200 percent larger than the coefficient for a clean airfoil. As the temperature rises, glaze ice begins to form and a large drag increase, due to the separation aft of the ice horns, is seen. This drag increase reaches a maximum near 23 °F (-5 °C), where C_D is approximately an order of magnitude larger than the value for a clean airfoil; then the drag increase drops to zero as the "no-ice-limit" near 32 °F (0 °C) is reached. Figure 2-93 shows that the drag rise increases as the droplet size increases. Increasing droplet size increases the collection efficiency and, therefore, the total mass of ice accreted. As more liquid water impacts the surface, the freezing fraction falls (glaze conditions) and the ice accretion may become more glaze in nature. Here cases A and E are glaze shapes with large horns as can be seen in figure 2-72; therefore, the drag is great. Reference 2-36 also shows that the airfoil drag tends to increase for both rime and glaze shapes with increasing LWC and for increasing airspeeds.

Using simulated shapes, Ingelman-Sundberg, Trunov and Ivaniko (reference 2-72) studied the effect of ice accretions on a large transport wing. Figure 2-94 presents the lift and drag performance they obtained for a NACA 65A215 airfoil with various simulated ice shapes. Maximum lift is plotted for various ice shapes for three flap positions. For comparison, the drag is also given for the zero degree flap case where $C_L = 0.2$. Ingelman-Sundberg, et. al. also studied the effect of ice accretion on a complex transport wing in the approach configuration. These results are shown in figures 2-95 and 2-96. The maximum lift coefficient is reduced for all ice simulations tested. Not only is $C_{L_{max}}$ reduced, but due to the loss in efficiency of the flap system, the entire C_L vs. α curve is shifted. The airfoil drag is shown as a function of C_L in figure 2-96. Here, as expected, large drag increases are seen, especially at the higher lift coefficients.

Bragg, et. al. (references 2-73 and 2-74), studied the effect of ice accretions on a general aviation wing with a flap system. In figures 2-97 and 2-98 the lift and drag performance of a NACA 63A415

wing section with simulated ice is shown. With the exception of the generic glaze ice shape, the shapes are based on ice accretions in the NASA Icing Research Tunnel (reference 2-75). These data were acquired on an actual section of an aircraft wing and tested at Re ≈ 4.7 x 10^6 and M = 0.15. Maximum lift penalties with no flap deflection, figure 2-97, are small for the rime shapes. Actually the rime ice, Rime-7, was accreted at an angle of attack of 6.6 degrees and increases $C_{L_{max}}$. The glaze ice does present a serious C_L penalty. Drag values are plotted in figure 2-98 and show the large drag penalties with glaze ice. In figure 2-99, the maximum lift for several ice shapes and flap deflections is shown. The NACA 63A415 section was equipped with a single slotted Fowler flap for these tests. Note that although the rime ice shape induces only a small decrease in $C_{L_{max}}$ at δ_f = 0°, the wing suffers a much larger lift penalty at the higher flap deflections.

Reference 2-76 describes an investigation in the NASA Lewis Icing Research Tunnel of the ice accretion patterns and performance characteristics of a multi-element airfoil model in several configurations. The model used was an 0.18 scale model of a Boeing 737-200 ADV wing section with chord length of 18 inches and span of 60 inches. The configurations employed in the study are shown in figure 2-100. Configuration (a) corresponds to a cruise condition while (b) (1° flap configuration), (c) (5° flap configuration), and (d) (15° flap configuration) correspond to various stages of approach.

The test procedure was as follows. First, the force coefficients versus angle of attack α were determined for the clean airfoil. Second, an icing encounter was simulated and force balance measurements were taken during the encounter to record changes that occurred. Third, force coefficients versus α were determined for the iced airfoil. In cases where frost accreted (a tunnel effect - see Chapter IV, Section 1) the force coefficients were determined with and without the frost.

Figure 2-101 shows the ice shape and results for a cruise configuration. The ice accretion produced a premature stall (figure 2-101a) and increased drag (figure 2-101b). The drag values are larger over the entire range of α, while the lift is not much affected until near $C_{L_{max}}$. The moment coefficient (figure 2-101c) changes from being nearly constant below stall speed to being a linearly increasing function of α to stall. Figure 2-101b shows a nonlinear increase in drag with respect to time, approximating a one-third or one-fourth power law. The lift values did not change much with time due to the low angle of attack at which the ice was accreted. These lift and drag affects were characteristic of all the runs done in the cruise configuration. The moment coefficient did not follow a consistent pattern for these runs.

Figure 2-102 shows results for a 1 flap configuration. The ice shape for all the runs in this configuration tended to be on the upper surface of the leading edge slat. Note that the lift curve (figure 2-102a) has a "flat top" indicating that stall would occur early but might not be as severe as for the other configurations.

Figure 2-103a, shows a distinguishing characteristic of the clean airfoil in the 5° flap configuration, namely a sharp drop in the lift at approximately α ≈ 15°. The same phenomenon is observed for the iced airfoil (a mixed accretion), but at a smaller value of α. However, figure 2-104a shows a more gradual change in the lift curve for the iced airfoil (a rime condition). The authors

suggest the following explanation. The rime iced lift curve of figure 2-104a is characteristic of trailing edge stall. This suggests that the mixed ice shape of figure 2-103 retained a small separation bubble which eventually "burst" for higher values of α. The rime ice of figure 2-104 may have tripped the boundary layer and prevented the formation of the leading edge separation bubble.

Figure 2-105 shows results for a 15° flap configuration. Note the ice deposition patterns on the lower surface.

The effect of ice on an aircraft empennage is very similar to that on the main wing. The horizontal and vertical tail are, however, usually of smaller chord and therefore better ice collectors. The ice shapes are then larger (relative to the chord of the accreting body) and the aerodynamic penalties more severe. Perhaps even more important is the effect of the ice on the aircraft stability, control and handling characteristics. This will be discussed briefly in Section 2.3.5. Ingelman-Sundberg and Trunov (reference 2-77) studied the effect of ice on a three-dimensional tail section with a NACA 64A-909 airfoil. Their results show that a thin airfoil with small leading edge radius is less severely affected by ice. This is due to the already low $C_{L_{max}}$ of these sections resulting from a leading edge stall. By modifying the leading edge to increase the $C_{L_{max}}$ of the 64A-009 section, the effect of ice on $C_{L_{max}}$ with ice was approximately the same with or without the leading edge modification. Information on hinge moments and stick forces will be presented in Section 2.3.5.

This section has emphasized empirical methods and experimental results. Theoretical methods are being developed and important improvements in these methods are being made. The current state-of-the-art in analytical methods will be presented in Chapter IV, Section 2.4.0.

2.3.2 Propellers

Propeller blade sections accrete ice and suffer a loss in aerodynamic performance in much the same way as wing and tail sections do. Propeller blades have a small chord and operate at a high effective velocity, thus greatly increasing the collection efficiency and mass of ice (relative to chord size) accreted. Due to the large centrifugal forces, ice shedding, particularly near the propeller blade tip, is a major consideration in any propeller blade icing analysis.

Little experimental work on propeller blade icing aerodynamics has been conducted in recent years. Propellers for aircraft which are certified for flight into icing conditions are usually protected, and apparently little work has been done to determine the effects of ice on propeller performance. However, some analytical work conducted specifically on the analysis of propellers in icing conditions is reported in reference 2-78. The method uses an airfoil icing correlation and a propeller aerodynamics code to predict icing effects on propeller performance. Miller (reference 2-79) used the Bragg, Gray and Fleming correlations with a computer code for comparison of propeller performance, checking against the Neel and Bright flight test data discussed in the following paragraph. This code produced realistic thrust and power coefficients, especially when the radial icing extent was known and input to the code.

Perhaps the best propeller icing data are the results of Neel and Bright (reference 2-80). Flight

tests were conducted with one propeller of a twin-engine aircraft allowed to collect ice and the other propeller kept ice-free. Ice thicknesses of up to one inch on the blade were measured. The spanwise extent of ice was from zero to 95 percent. Efficiency losses were less than 10 percent in most cases, with losses of 15 to 20 percent possible in some situations.

The analysis of ice effects on moving surfaces adds an additional dimension to the icing problem. Two components of motion can be important to this analysis. The first is rotational motion, which produces Mach number (and hence total temperature) variation across the blade span, and introduces centrifugal forces to shed ice. The second component of motion is present for a helicopter rotor but not for a propeller: the variation of blade angle during a revolution. This motion increases the chordwise extent of ice and may result in the operation of rotor blade sections into stall for a greater than normal portion of the rotor disk. Therefore, the calculation of the effects of icing on a rotor is, in general, more complicated than for a propeller. The propeller problem can be viewed as a special case of the rotor problem.

The analysis of propeller icing requires the determination of the local angle of attack and Mach number along the blade. For a propeller (at small aircraft angle of attack), the Mach number and blade angle of attack are not functions of rotational position. Photographs have not shown any evidence of ice beyond 99% of the span of the blade. Correlation work performed to date appears to substantiate the use of two-dimensional wind tunnel airfoil data in propeller calculations, although only limited data is available for correlation (reference 2-79).

2.3.3 Powerplant

Aircraft powerplants may suffer performance and/or physical damage due to icing in three broad categories:

1) Structural damage due to ice shedding.

2) Engine flow distribution causing stall and flameout.

3) Icing over of instrumentation necessary for engine operation.

For reciprocating engines, the amount of air intake is small and the internal icing problems are primarily related to carburetor icing. However, for gas turbines a large amount of air intake is required and, therefore, a large volume of supercooled water droplets is ingested. This sometimes leads to serious icing problems on the spinner for fans, or on the front bearing housing for non-fan, inlet guide vanes and the first row of compressor vanes and stator blades. Instrumentation for turbine engines is located toward the forward and aft parts of the engine to determine the pressure/temperature differential through the engine. This differential is extremely important since the power setting is based on these readings. The forward location can be susceptible to icing. It has been speculated that a malfunction of this gage could have been one of the factors in the disastrous

"14th Street Bridge" accident in Washington, D.C. in 1982. Since these components are usually equipped with ice protection, this effect on vehicle performance will not be discussed here but their protection must not be ignored.

2.3.3.1 Nacelles

Nacelle icing is the primary cause of aerodynamic performance loss in powerplants. In addition, since the possibility exists that any ice that forms on engine inlet lips may be ingested, these surfaces are normally ice protected to lessen the problem of ice ingestion into the engine. Reference 2-81 provides approximate methods for predicting droplet impingement on engine surfaces, but the report is focused on the design of ice protection systems, not the resulting loss in aerodynamic efficiency. Reference 2-82 presents measurements of engine cowl icing effects on aircraft performance. On the twin engine aircraft used, the engine cowling ice caused an aircraft drag increase of 10 percent over the clean aircraft drag. For this case, the aircraft was flown for over 40 minutes in an icing cloud with LWC = 0.4 g/m^3 and a median droplet size of 17 microns. Sufficient data do not exist upon which to base any empirical approach to performance loss due to nacelle icing.

2.3.3.2 Engines

Penalties due to ice accretion on engine components are discussed for two distinct types of gas turbine engines - the turbofan with no add-on anti-icing system, and the small gas turbine (turboprop) engine equipped with an inertial separation anti-icing system in the cowl air inlet duct. Experience has shown that the relative magnitude of freezing fraction, hence ice shape, resulting from the thermodynamic ice accretion process is a major parameter in correlating engine response to icing. In general, warmer temperatures and higher liquid water content yield a lower freezing fraction which results in non-aerodynamic shaped glaze ice. Colder temperatures and lower liquid water content result in a higher freezing fraction which produces more aerodynamic shaped rime ice. The former typically produces more blockage of the compressor inlet airflow.

2.3.3.2.1 Aerodynamics of Ice Accumulation for the Turbofan Engine

The main items of concern on a turbofan are the inlet lip and spinner. The first row of stators are not of as great concern. Although the engine can stand shedding to some extent, flameout can occur if shedding occurs at low power settings such as may be experienced during a descent or holding pattern.

2.3.3.2.2 Turboprop Engine Inertial Separator Intake Losses

An inertial separator anti-icing system that has been in use since 1965 is described in detail in reference 2-83. It is based on the principle of momentum separation of liquid and solid particles from the engine intake air, exhausting them out through a bypass duct. Figure 2-106 shows a schematic of the configuration. A "chin"-type inlet at the front is connected to the compressor intake

I 2-43

located at the rear of the engine by a relatively long duct. This duct accommodates the inertial anti-icing system which is comprised of several articulating vanes that are actuated to the icing mode positions, thereby setting up the desired inertial separator flow field. Vane 1 accelerates the inlet flow and icing elements downward, increasing the particles' momentum. The compressor intake air turns upwards behind Vane 1 while the bypass air and particles of higher momentum are dumped overboard through the bypass duct. The only hardware in this system having active icing protection is the inlet cowl lip, which has a pneumatic de-icer. The standard compressor intake screen prevents any detached ice formations from entering the compressor.

Certification testing on this engine simulated long duration icing encounters to show the effects on engine operation of cumulative ice buildup on the unprotected inertial separator hardware. Figure 2-107 shows intake pressure loss versus time for the most severe icing run of the certification program on this system. The icing parameters of this particular run were the Icing Condition 1 of reference 2-85, a glaze ice condition. The icing facility used was of the bypassing type with the specified condition being set in the tunnel upstream of the engine inlet with a 282 mph approach velocity. Thus, the engine inlet dynamic pressure was also simulated. The data shows an initial pressure loss increase of 18 percent within two minutes due to icing blockage of the screen in vane 2. Thereafter the loss continued to increase gradually until it reached 82 percent during take-off power setting at the end of the run. That increase of intake pressure loss due to ice build-up had no significant effect on the engine in meeting take-off power requirements. From the preceding and other tests, which included icing environments of both ice and snow particles, it was concluded that the inertial separation anti-icing system would protect the engines against any icing environment likely to be encountered.

2.3.4 Helicopter Rotors

Ice accretion on rotorcraft has serious effects on vehicle performance and handling characteristics. Much of this effect is due to the icing of the main rotor. A rotor in forward flight not only experiences the variation in icing conditions as a function of radial location, but also experiences a wide range of angles of attack and Mach numbers as the rotor blade rotates. In the most general case, this periodicity in Mach number and angle of attack must be considered. Helicopter rotor sections, like propeller sections, have relatively small chords and move at relatively high velocity; thus the amount of ice that accretes relative to chord size is potentially large.

Most of our knowledge of helicopter rotor icing has resulted from flight test data. Much of these data were taken in ground based spray rigs with the helicopter in hover. However, a study sponsored by NASA (reference 2-35) reports a detailed study of rotor airfoil icing conducted in the NRC High Speed Icing Tunnel. Some of these results are presented here.

One of the interesting features of rotor airfoil icing is the variation of Mach number and angle of attack with azimuth. Mach number could not be varied in the icing tunnel in a manner to simulate the rotor flowfield. Angle of attack, however, could be varied a maximum of 9° using an oscillating

rig. Selected icing conditions were repeated for the airfoil oscillating sinusoidally at a frequency of 5 Hz with an amplitude of $\pm 4.5°$. Ice was accreted on both an airfoil with oscillating angle of attack and on an airfoil with a constant angle of attack (using the mean oscillation). The lift, drag and pitching moment for the two shapes were then evaluated at several constant values of angle of attack. The effect of ice on lift and pitching moment was nearly the same for ice shapes accreted for constant and oscillating angles of attack. The effect of oscillation on drag was significant (figure 2-108). While the data show an appreciable amount of scatter, the trend of reduced drag penalty for an oscillating ice shape compared to a constant angle of attack shape is evident.

During the test (reference 2-35), nine subscale rotor airfoil sections were tested over a wide range of conditions. The effect of LWC, angle of attack and Mach number on rotor airfoil icing are shown in figures 2-109 to 2-111. In figure 2-110 the angle of attack is the angle at which the ice was accreted and the forces and moments were measured. Noteworthy in figure 2-110 is the effect of Mach number on the ΔC_d vs. α curves.

Based on these icing wind tunnel data, correlations for lift, drag and moment increment with ice accretion were developed (reference 2-35). As with other icing correlations which cover a wide range of conditions, the error between prediction and experiment is often large. The trends predicted by these equations are usually good, but the absolute values may be significantly in error. For the drag increment due ice accretion, a rime equation and a glaze equation were given. Both equations include the relative velocity seen by the blade section and a term with the helicopter forward velocity meant to account for the airfoil oscillation. The equation for glaze ice includes the airfoil leading edge radius and maximum thickness. An expression for the change in pitching moment is also given.

A comparison between the correlation and some of the experimental data is shown in figure 2-112. In this case, ΔC_m is predicted unusually well but ΔC_l and particularly ΔC_d are not well predicted. This level of agreement between experiment and correlation is not unusual.

Ice shedding was found to be a problem during this experiment, even though it was a two-dimensional test with no centrifugal forces. At warmer temperatures, after a certain amount of ice has accreted, the ice feathers and frost often break away, reducing the aerodynamic penalty. A reduction in the drag penalty due to this effect was observed to be as much as 59 percent after 20 minutes. On an actual rotor, ice shedding may occur in this way but the predominant shedding mechanism is the centrifugal force. Furthermore, Korkan (reference 2-78) showed analytically that the ice nearest the tip causes the greatest reduction in aerodynamic performance of the rotor.

Several studies of the effect of ice on helicopter rotors in flight (references 2-86 to 2-90) have been made. By far the most serious effect of rotor blade icing is an increase in profile drag. This drag increase requires a higher engine power to maintain flight conditions. The change in collective pitch setting required is negligible. This suggests that the effect of reduced airfoil lift on the blade performance is small. Lift effects will, however, be important in cases where blade stall occurs due to a reduction in $C_{L_{max}}$ due to the ice. Figure 2-113 (reference 2-87) shows the effect on several parameters with time in an icing cloud. These data were taken on a Sikorsky H045-2

helicopter. Note the increase in average power required between the beginning and the end of the encounter. As discussed, little change is seen in the collective pitch.

As previously stated, the most important parameter for rotor icing is often the radial extent of the ice accretion. This is often difficult to measure in flight due to ice shedding. Figure 2-114 from reference 2-91 shows the extent of icing as a function of static air temperature for a UH1H helicopter in hover. As expected, as the static air temperature decreases, the outer extent of icing moves toward the tip. At -4 °F (-20 °C) air temperature, the blades accrete ice in hover to between 80 and 90 percent of the span.

Current methods for estimating the effect of ice on helicopter rotors, both in hover and forward flight, are primarily computational. These involve using a combination of empirical and numerical data to predict two-dimensional rotor airfoil performance which is then fed into a rotor performance computer code. These methods idealize a complex problem which is in reality a three-dimensional flow problem and can be extremely complex in accounting for all the variations. It is a field where more detailed research is needed.

In hovering flight or for a tilt rotor in the propeller mode, the calculation of ice accretion on a rotorcraft is identical to that of a propeller. However, with a standard "edgewise" rotor in normal level flight, the angle of attack and Mach number vary around the rotor disc. The chordwise extent of ice is a function of the minimum and maximum angle of attack and Mach number as illustrated in figures 2-115a and 2-115b for a SA 13112 airfoil (reference 2-92). Studies to date both in France and the United States have used the mean angle of attack and Mach number to determine ice accretion characteristics, and have used local conditions to approximate the incremental lift, drag, and pitching moment characteristics. Reference 2-35 provides information that indicates that airfoil angle of attack oscillation has little effect on airfoil section incremental lift and pitching moment, but substantially reduces the drag increment (figures 2-116a and 2-116b).

2.3.5 Vehicle Performance and Flight Control Characteristics

Helicopter performance with ice was discussed in Section 2.3.4; however, some additional comments on flight control will be made (references 2-86 and 2-87). The rate of descent is increased in an autorotation due to ice accretion. Since the rotor drag is greatly increased, the rotor speed is reduced which leads to the high descent rate. An increase in descent rate of up to 30 percent has been observed. Unsymmetrical ice shedding on the rotor leads to low frequency vibration of the helicopter. The most severe vibration occurs when the ice sheds unsymmetrically on the tail rotor. Overall handling characteristics present no major problem in normal flight conditions. Increased throttle settings are needed to overcome the additional rotor drag. Since early blade stall can occur due to the rotor ice, any rapid maneuvers should be avoided.

Perhaps the most serious fixed wing aircraft control problem due to ice accretion are those related to the horizontal tail. This is due to the ice accretion decreasing the surface's $C_{L_{max}}$ and thus limiting the available tail down load. If the tail must operate in a region near $C_{L_{max}}$, large stick force changes may occur due to an altered airfoil pressure distribution.

The most complete discussions of this problem can be found in the work of Ingelman-Sundberg and Trunov (references 2-72 and 2-93). In reference 2-73 a wind tunnel study was conducted on three-dimensional tailplane models (including elevators) with simulated ice shapes. First, tailplanes using a NACA 64A-009 airfoil section were used. This section has a very small leading edge radius and therefore its aerodynamic performance was not seriously affected by the ice accretions. These tailplanes were then modified by changing the leading edge to simulate a NACA 0012. Figure 2-117 shows the lift and elevator hinge moment coefficients for this tailplane configuration and several ice simulations. With the modified leading edge, the tailplane suffers a large $C_{L_{max}}$ penalty, and, near stall, a large nose down change in hinge moment coefficient occurs. Thus, for tailplanes with airfoils optimized for good $C_{L_{max}}$ when the tailplane must operate at high lift coefficients (large downloads), ice can have a severe effect on aircraft longitudinal control.

As can be seen from figure 2-117 a large and sudden change in C_H occurs when the tailplane, with ice, begins to stall. Wing flaps aggravate this situation by changing the downwash field at the tail, thus changing the required elevator deflection to trim the aircraft. Trunov and Ingelman-Sundberg (reference 2-93) identify three classes of tailplane ice problems. In the first case, enough elevator is available to provide the tail download; however, the pilot experiences unusually large stick forces. Changes may also occur in the stick force per g. The second case is characterized by such large stick forces that the pilot cannot overcome them. The aircraft pitches nose down at a rapid rate. In the third case, the available elevator deflection is not sufficient to maintain trim loads with ice present. The aircraft pitches nose down at a rapid rate requiring proper pilot action to regain control.

The problem of horizontal tail icing should be carefully considered during the aircraft design. Aircraft least sensitive to tail icing problems are those such that (1) the tail incidence is adjustable, (2) the tail $C_{L_{max}}$ is low due to the airfoil section used, or (3) the tail is designed not to require large C_Ls. Flap deflection should be carefully analyzed or tested for its affect on the iced tail performance. Many aircraft manufacturers suggest limiting flap deflection on aircraft when tail icing is suspected. Ice may affect the aircraft stability and control in other ways. It is anticipated that ice accretion on the vertical surface could affect the rudder performance. This would be most likely to occur when maximum rudder power is needed in an engine-out case. Tailplane icing may also affect the longitudinal stability. Karlsen and Sandberg (reference 2-94) have performed a simulation of aircraft stability with tailplane ice. They found a lack of pitch response to strong downward vertical gusts and unstable oscillations in pitch when elevator control is applied to correct for glideslope tracking errors.

Since the overall degradation of aircraft performance with ice has not been discussed, some brief comments will be made here. One of the earliest experimental studies of the performance of aircraft with ice accretion is that of Preston and Blackman (reference 2-82). They used selective de-icing of the various aircraft components to determine the drag increment due to each. In figure 2-118 the percent drag increase due to these components is shown. This research was conducted using a B-25 aircraft. It is important to note that a large percentage of the drag rise is from non-lifting surfaces. Unlike wing sections, little data is available on the drag rise due to ice accretion on these components.

In Leckman's 1971 paper (reference 2-95), he presents a method for predicting the effect of ice on subsonic aircraft performance. He demonstrates the procedure for a Cessna Centurion and a Super Skymaster. First, ice shapes are estimated using impingement data, then the drag penalties are estimated and a drag build-up procedure is performed. Table 2-10 gives the percent drag increase for the various components.

Leckman used experimental data from the NASA Icing Research Tunnel to estimate the drag increase of the flying surfaces. Table 2-10 represents a continuous maximum icing encounter where $T = 17$ °F, MVD $= 20$ μm, LWC $= 0.46$ g/m^3 and the icing encounter was 20 miles in length. The percentages above correspond to a total drag increase of $\Delta C_D = .0550$ for the Centurion and $\Delta C_D = .0630$ for the Super Skymaster. These calculations are compared to experimental data for the Super Skymaster. Performance with maximum continuous ice is compared to natural icing flight test results in figure 2-119 (reference 2-95).

Other studies have used similar methods to predict aircraft performance degradation with ice accretion. While the basic method is the same as Leckman's, a component build-up method for the drag, these studies computerized the procedure (references 2-96 and 2-97). These programs also made use of the drag correlations discussed earlier to predict wing and empennage drag rise. These codes, therefore, suffer the same inaccuracies as the correlations, but do provide an easy way to predict trends. A major problem is the estimation of the drag from the miscellaneous items as in table 2-10. A large portion of the drag can come from nacelle, fuselage, antenna, landing gear, etc. This is especially true on a "dirty" airplane, i.e., one with a large amount of parasitic drag. At this time, the percentage drag increase due to these non-lifting components must be estimated on the basis of flight tests or previous experience.

Little flight test data was available in the open literature prior to 1983 which could be used to verify calculation methods. In that year, NASA Lewis initiated an icing flight test program using the NASA Icing Research Aircraft (a Twin Otter), which has generated much useful information (references 2-98 and 2-99). One part of the program has been to measure the effect of ice on aircraft performance. After accreting the ice in steady flight, the aircraft exited the clouds to conduct an aircraft performance flight test. Figure 2-120 shows the measured aircraft drag polar for various degrees of de-icing. Note the changed slope of the C_D versus C_L^2 curve with the aircraft completely iced. Also note the large portion of the drag penalty still remaining after the wings and empennage were de-iced. Propeller and engine inlet heaters were on at all times during the flight. This flight

was conducted at $T = 25 °F$ $(-4 °C)$, LWC $= 0.31$ g/m^3, icing time $= 26$ minutes, MVD $= 13$ μm, airspeed $= 125$ KIAS and 6,000 feet (1829 meters) altitude. In figure 2-121, the thrust horsepower versus airspeed information for this flight are shown along with the single-engine power available. This illustrates the critical flight condition of single-engine operation of a twin-engine airplane with ice accretion.

References 2-100, 2-101, and 2-102 describe the results of more recent research with the NASA Icing Research Aircraft.

I.2.4 REFERENCES

2-1   Bragg, M. B., "Rime Ice Accretion and Its Effect on Airfoil Performance," Ph.D. dissertation, The Ohio State University, 1981, and NASA CR 165599, March 1982.

2-2   Langmuir, I. and Blodgett, K., "A Mathematic Investigation of Water Droplet Trajectories," AAFTR 5418, February 1946.

2-3   Norment, unpublished.

2-4   Rudinger, G., "Flow of Solid Particles in Gases," ADARDograph No. 222, 1967, pp. 55-86.

2-5   Norment, H.G., "Calculation of Water Drop Trajectories to and About Arbitrary Three-Dimensional Bodies in Potential Airflow," NASA CR 3291, 1980.

2-6   Keim, S. R., "Fluid Resistance to Cylinders in Accelerated Motion," J. Hydraulics Div. Proc. Amer. Soc. Civil Eng., Vol 6, 1956, paper 1113.

2-7   Crowe, C. T.; Nicholls, J. A.; and Morrison, R. B., "Drag Coefficients of Inert and Burning Particles Accelerating in Gas Streams," Ninth Symposium (Int'l) on Combustion, Academic Press, 1963, pp. 395-405.

2-8   Lozowski, E. P. and Oleskiw, M. M., "Computer Modeling of Time-Dependent Rime Icing in the Atmosphere," CRREL 83-2, Jan. 1983.

2-9   Schlichting, H., Boundary Layer Theory, McGraw Hill, New York, 4th Edition, 1960.

2-10   Bragg, M. B., "A Similarity Analysis of the Droplet Trajectory Equation," AIAA Journal, Vol. 20, No. 12, December 1982, pp. 1681-1686.

2-11   Kim, J.J., "Particle Trajectory Computation on a 3-Dimensional Engine Inlet," NASA CR 175023 (DOT-FAA-CT-86-1), January 1986.

2-12   Bragg, M. B. and Gregorek, G. M., "An Analytical Evaluation of the Icing Properties of Several Low and Medium Speed Airfoils," AIAA Paper No. 83-109, January 1983.

2-13   Trunov, O., "Icing of Aircraft and the Means of Preventing It," English Translation, FTD-M7-65-490, p. 105, 1965.

2-14   Chang, H-P; Frost, W; Shaw, R. J.; and Kimble, K. R., "Influence of Multidrop Size Distribution on Icing Collection Efficiency," AIAA-83-0100, paper presented at the 21st Aerospace Sciences Meeting, Jan. 1983.

2-15   Papadakis, M.; Elangovan, R.; Freund, Jr., G. A.; Breer, M.; Zumwalt, G. W.; and Whitmer, L., "An Experimental Method for Measuring Water Droplet Impingement Efficiency on Two- and Three-Dimensional Bodies," NASA CR 4257, DOT/FAA/CT-87/22, November 1989.

2-16   Brun, Rinaldo J., Serafini, John S. and Gallagher, Helen M., "Impingement of Cloud Droplets on Aerodynamic Bodies as Affected by Compressibility of Air Flow Around the Body," NACA TN 2903, March 1953.

2-17   Brun, R. J. and Mergler, H. W., "Impingement of Water Droplets on a Cylinder in an Incompressible Flow Field and Evaluation of Rotating Multicylinder Method for

Measurement of Droplet Size Distribution, Volume Median Droplet Size, and Liquid Water Content," NACA TN 2904.

2-18   Gent, R. W., "Calculation of Mater Droplet Trajectories About An Aerofoil in Steady, Two-Dimensional, Compressible Flow," RAE TR 84060, June 1984.

2-19   Gelder, T. F., Smyers Jr., W. H., and von Glahn, U. H., "Experimental Droplet Impingement on Several Two-Dimensional Airfoils with Thickness Ratios of 6 to 16 Percent," NACA TN 3839, December 1956.

2-20   Lewis, J. P. and Ruggeri, R. S., "Experimental Droplet Impingement on Four Bodies of Revolution," NACA TN 4092, December 1957.

2-21   Gelder, T. F., Lewis, J.P., and Koutz, S.L., "Icing Protection for a Turbojet Transport Airplane: Heating Requirements, Methods of Protection, and Performance Penalties," NACA TN 2866, 1953.

2-22   Bowden, D. T., Gensemer, A. E. and Skeen, C. A., "Engineering Summary of Airframe Icing Technical Data," FAA ADS-4, March 1964.

2-23   Papadakis, M.; G. A.; Breer, M.; Craig. N.; and Bidwell, C., "Experimental Water Droplet Impingement Data on Modern Aircraft Surfaces,' AIAA-91-0445, paper presented at the 29th Aerospace Sciences Meeting, Jan. 1991.

2-24   Hacker, P. T., Brun, R. J. and Boyd, B., "Impingement of Droplets in 90-degree Elbows with Potential Flow," NACA TN 2999, September 1953.)

2-25   Hacker, P. T., Saper, P.G. and Kadow, C. F., "Impingement of Droplets in 60° Elbows with Potential Flow," NACA TN 3770, October 1956.

2-26   Brun, R. J. and Vogt, D. E., "Impingement of Cloud Droplets on 36.5 Percent Thick Joukowski Airfoil at Zero Angle of Attack and Discussion of Use as Cloud Measuring Instrument in Dye-Tracer Technique," NACA TN 4035, September 1957.

2-27   Dorsch, R. G., Brun, R. J. and Gregg, J. L., "Impingement of WaterDroplets on an Ellipsoid with Fineness Ratio 5 in Axisymmetric Flow," NACA TN 3099, March 1954.

2-28   Brun, R. J. and Dorsch, R. G., "Impingement of Water Droplets on an Ellipsoid with Fineness Ratio 10 in Axisymmetric Flow," NASA TN 3147, May 1954.

2-29   Dorsch, R. G., Saper, P. G. and Kadow, C. F., "Impingement of Water Droplets on a Sphere," NASA TN 3587, November 1955.

2-30   Torgeson, W. L. and Abramson, A. E., "A Study of Heat Requirements for Anti-Icing Radome Shapes with Dry and Wet Surfaces," WADC TR 53-284, September 1953.

2-31   Brun, R. J., Lewis, W., Perkins, P. J. and Serafini, J. S., "Impingement of Cloud Droplets on a Cylinder and Procedure for Measuring Liquid-Water Content and Droplet Sizes in Supercooled Clouds by Rotating Multicylinder Method," NACA Report 1215, (supersedes NACA TN 2903, TN 2904 and RM E53D23).

2-32   Lewis, W. and Brun, R. J., "Impingement of Water Droplets on a Rectangular Half Body in a Two-Dimensional Incompressible Flow Field," NACA TN 3658, February

1956.

2-33   Bragg, M. B., "An Incompressible Droplet Impingement Analysis of Thirty Low and Medium Speed Airfoils," NASA Contractor's Report, to be published.

2-34   Bragg, M. G., "The Effect of Geometry on Airfoil Icing Characteristics," AIAA Journal of Aircraft, Vol. 21, No. 7, July 1984, pp. 505-511.

2-35   Flemming, R. J. and Lednicer, D. A., "High Speed Ice Accretion on Rotorcraft Airfoils," NASA CR 3910, 1985.

2-36   Olsen, W., Shaw, R. and Newton, J., "Ice Shapes and the Resulting Drag Increase for a NACA 0012 Airfoil ," NASA TM 83556, 1983.

2-37   Gray, Vernon H., "Prediction of Aerodynamic Penalties Caused by Ice Formations on Various Airfoils," NASA TN-D-2166, 1964.

2-38   Wilder, R. W. "A Theoretical and Experimental Means to Predict Ice Accretion Shapes for Evaluating Aircraft Handling and Performance Characteristics," AGARD-AR-127, 1978, pp. 5-1 to 5-20.

2-39   Ruff, G. A. and Berkowitz, B. M., "Users Manual for the NASA Lewis Ice Accretion Prediction Code (LEWICE)," NASA CR 185129.

2-40   Shaw, R. J., "NASA's Aircraft Icing Analysis Program," NASA TM 88791, Sept. 1986.

2-41   Messinger, B. L., "Equilibrium Temperature of an Unheated Surface as a Function of Airspeed," Journal of Aeronautical Sciences, January 1953 (Vol. 20, No. 1).

2-42   Tribus, M.V., et. al., "Analysis of Heat Transfer over a Small Cylinder in Icing Conditions on Mount Washington," American Society of Mechanical Engineers Transactions, Vol. 70, 1949, pp. 871-876.

2-43   Kirby, M.S. and Hansman, R.J., "An Experimental and Theoretical Study of the Ice Accretion Process During Artificial and Natural Icing Conditions," NASA CR 182119 (DOT/FAA/CT-87/17), 1988.

2-44   Ruff, G.A., "Analysis and Verification of the Icing Scaling Equations," AEDC-TR-85-30, Vol. 1, November 1985.

2-45   Kreith, F., Principles of Heat Transfer, Intext Educational Publishers, New York, 1973, third edition.

2-46   Makkonen, L., "Heat Transfer and Icing of a Rough Cylinder," Cold Regions Science and Technology, Vol. 10, 1985, pp. 105-116.

2-47   Van Fossen, G. J.; Simoneau, R. J.; Olsen, W. A.; and Shaw, R. J., "Heat Transfer Distributions around Nominal Ice Accretion Shapes Formed on a Cylinder in the NASA Lewis Icing Research Tunnel," NASA TM 83557, Jan. 1984.

2-48   Poinsatte, P. E.; Van Fossen, G. J.; and DeWitt, K. J., "Convective Heat Transfer Measurements from a NACA 0012 Airfoil in Flight and in the NASA Lewis Icing Research Tunnel," NASA TM 102448, Jan. 1990.

2-49   Dickey, T.A., "An Analysis of the Effects of Certain Variables in Determining the

Form of an Ice Accretion," AEL 1206, (presented at Mt. Washington Spring Planning Conference, April 1952, Aeronautical Engineering Laboratory, Naval Air Experimental Station, May 29, 1952.)

2-50   Bilanin, A.J., "Proposed Modifications to Ice Accretion/Icing Scaling Theory," AIAA-88-0203, paper presented at the 26th Aerospace Sciences Meeting, Jan. 1988.

2-51   Olsen, W.A., Jr.; Walker, E.D.; and Sotos, R.G., "Microscopic High Speed Movies Showing the Droplet Freezing Process of Icing," AIAA-84-0019, paper presented at the 22nd Aerospace Sciences Meeting, Jan. 1984.

2-52   Olsen, W., Walker, E., and Sotos, E., Close-up Movies of the Icing Process on the Leading Edge of an Airfoil, "NASA Lewis Research Center Movie C-313, 1985.

2-53   Olsen, W. and Walker, E., "Experimental Evidence for Modifying the Current Physical Model for Ice Accretion on Aircraft Surfaces," NASA TM 87184, May 1986.

2-54   Hansman, R.J. and Turnock, S.R., "Investigation of Surface Water Behavior During Glaze Ice Accretion," AIAA Journal of Aircraft, Vol. 26, No. 2, Feb. 1989, pp. 140-147.

2-55   Hansman, R.J.; Yamaguchi, K.; Berkowitz, B.; and Potapczuk, M., "Modeling of Surface Roughness Effects on Glaze Ice Accretion," AIAA-89-0734, paper presented at the 27th Aerospace Sciences Meeting, Jan. 1989.

2-56   Yamaguchi, K. and Hansman, R.J., "Heat Transfer on Accreting Ice Surfaces," AIAA-90-0200, paper presented at the 28th Aerospace Sciences Meeting, Jan. 1990.

2-57   Yamaguchi, K. and Hansman, R.J., "Deterministic Multi-Zone Ice Accretion Modeling," AIAA-91-0265, paper presented at the 29th Aerospace Sciences Meeting, Jan. 1991.

2-58   Bilanin, A.J., "Problems in Understanding Aircraft Icing Dynamics," AIAA-89-0735, paper presented at the 27th Aerospace Sciences Meeting, Jan. 1989.

2-59   Stallabrass, J. R. and Price, R. D., "On the Adhesion of Ice to Various Materials," Canadian Aeronautics and Space Journal, September 1963, pp. 199-204.

2-60   Raraty, L. E. and Tabor, D., "The Adhesion and Strength Properties of Ice," Proceedings of the Royal Society, Vol. XXA245, No. 1241, June 1958, pp. 184-201.

2-61   Loughborough, D. L. and Haas, E. G., "Reduction of the Adhesion of Ice to De-Icer Surfaces," Journal of the Aeronautical Sciences, March 1946, pp. 126-134.

2-62   Reinmann, J. J.; Shaw, R. J.; and Ranaudo, R. J., "NASA's Program on Icing Research and Technology," NASA TM 101989, May 1989.

2-63   Scavuzzo, R. J.; Chu, J. L.; and Lam, P.D., "Development of a Composite Technique in the Determination of the Tensile Strength of Impact Ices," Proceedings of 3rd International Workshop on the Atmospheric Icing of Structures, May 1986.

2-64   Scavuzzo, R. J. and Chu, J. L., "Structural Properties of Impact Ices Accreted on Aircraft Structures," NASA CR 179580, Jan. 1987.

2-65   Scavuzzo, R. J.; Chu, J. L.; and Brikmanis, C. K., "Adhesive Peel Strength of Artificial Ice," Proceedings of the 4th International Conference on Atmospheric Icing of Structures, 1988.

2-66   Scavuzzo, R. J.; Chu, M. L.; and Kellackey, C. J., "Impact Ice Stresses in Rotating Airfoils," AIAA-90-0198, paper presented at the 28th Aerospace Sciences Meeting, Jan. 1990.

2-67   Kellackey, C. J.; Chu, M. L.; Scavuzzo, R. J., "Statistical Structural Analysis of Rotor Impact Ice Shedding," AIAA-91-0663, paper presented at the 29th Aerospace Sciences Meeting, Jan. 1991.

2-68   Scavuzzo, R. J.; Chu, M. L.; and Ananthaswamy, V., "Influence of Aerodynamic Forces in Ice Shedding," AIAA-91-0664, paper presented at the 29th Aerospace Sciences Meeting, Jan. 1991.

2-69   Brumby, Ralph E., "Wing Surface Roughness, Cause and Effect," DC Flight Approach, January 1979, pp. 2-7.

2-70   Bragg, M. B., Gregorek, G. M. and Shaw, R. J., "Wind Tunnel Investigation of Airfoil Performance Degradation Due to Icing," AIAA Paper No. 82-0582, presented at the 12th Aerodynamic Testing Conference, Williamsburg, Virginia, March 22-24, 1982.

2-71   Bragg, M. B. and Coirier, W. J., "Detailed Measurements of the Flow Field in the Vicinity of an Airfoil with Glaze Ice," AIAA-85-0409, paper presented at the 23rd Aerospace Sciences Meeting, Jan. 1985.

2-72   Ingleman-Sundberg, M., Trunov, O. K. and Ivaniko, A., "Methods for Prediction of the Influence of Ice on Aircraft Flying Characteristics," a joint report from the Swedish-Soviet Working Group on Flight Safety, 6th Meeting, 1977.

2-73   Bragg, M. B., Zaguli, R. J. and Gregorek, G. M., "Wind Tunnel Evaluation of Airfoil Performance Using Simulated Ice Shapes," NASA CR 167960, November 1982.

2-74   Zaguli, R. J., Bragg, M. B. and Gregorek, G. M., "Results of an Experimental Program Investigating the Effects of Simulated Ice on the Performance of the NACA 63A415 Airfoil with Flap," NASA CR 168288, Jan. 1984.

2-75   Shaw, R. J., Sotos, R. G. and Solano, F. R., "An Experimental Study of Airfoil Icing Characteristics," NASA TM 82790, Jan. 1982.

2-76   Potapczuk, M. G. and Berkowitz, B. M., "An Experimental Investigation of Multi-Element Airfoil Ice Accretion and Resulting Performance Degradation," AIAA-89-0752, paper presented at the 27th Aerospace Sciences Meeting, Jan. 1989.

2-77   Ingelman-Sundberg, M. and Trunov, O. K., "Wind Tunnel Investigation of the Hazardous Tail Stall Due to Icing" a joint report from the Swedish-Soviet Working Group on Flight Safety, Report No. JR-2, 1979.

2-78   Korkan, K. D., Dadone, L. and Shaw, R. J. "Performance Degradation of Propeller Systems Due to Rime Ice," AIAA Journal of Aircraft, Vol. 21, No. 1, Jan. 1984, pp.

44-49.

2-79   Miller, T. L., "Analytical Determination of Propeller Performance Degradation Due to Ice Accretion," NASA CR 175092, 1986.

2-80   Neel, C. B. and Bright, L. G., "The Effect of Ice Formations on Propeller Performance," NACA TN 2212, 1950.

2-81   Pfeifer, G. D. and Maier, G. P., "Engineering Summary of Powerplant Icing Technical Data," Report No. FAA-RD-77-76, 1977.

2-82   Preston, G. M. and Blackman, C. C., "Effect of Ice Formations on Airplane P-erformance in Level Cruising Flight," NACA TN 1598, 1948.

2-83   Grabe, W. and Tedstone, D, "Icing Tests on a Small Gas Turbine With Inertial Separation Anti-Icing System," AGARD Conference Proceedings No. 236 on Icing Test For Aircraft Engines, London, United Kingdom, 3-4 April 1978, AGARD-CP--236.

2-84   Lozowski, E. P., Stallabrass, J. R., and Hearty, P. F., "The Icing of an Unheated Non-Rotating Cylinder in Liquid Water Droplet - Ice Crystal Clouds." National Research Council of Canada Report, LTR-LT-96, February 1979.

2-85   "Aircraft Ice Protection," U.S. Department of Transportation, Federal Aviation Administration, Advisory Circular, AC 20-73, April 21, 1971.

2-86   Stallabrass, J. R., "Icing Flight Trials of a Bell HTL-4 Helicopter," LR-197, National Aeronautical Establishment of Canada, Ottawa, Canada, 1957.}

2-87   Stallabrass, J. R., "Icing Flight Trials of a Sikorsky HO45-2 Helicopter," LR-219, National Aeronautical Establishment of Canada, Ottawa, Canada, 1958.}

2-88   Hanks, M. L., Higgins, L. B. and Diekmann, V. L., "Artificial and Natural Icing Tests, Production UH-6OA Helicopter - Final Report," USAAEFA Project No. 79-19, 1980.

2-89   Abbott, W. Y. et. al. [JR: Give all authors], "Evaluation of UH-1H Hover Performance Degradation Caused by Rotor Icing," USAAEFA Project No. 82-12, Final Report, 1983.

2-90   Lee, J. D. and Shaw, R. J., "The Aerodynamics of Rotor Blades with Ice Shapes Accreted in Hover and in Level Flight," paper presented at the 41st Annual Forum of the American Helicopter Society, Ft. Worth, Texas, May, 1985.

2-91   Flemming, R. J., Shaw, R. J. and Lee, J.D., "The Performance Characteristics of Simulated Ice on Rotor Airfoils," paper presented at the 41st Annual Forum of the American Helicopter Society, Ft. Worth, Texas, May 1985.

2-92   "Rotorcraft Icing - Progress and Potential," AGARD Advisory Report No. 223, Sept. 1986.

2-93   Trunov, O. K. and Ingelman-Sundberg, M., "On the Problem of Horizontal Tail Stall Due to Ice," a joint report from the Swedish-Soviet Working Group on Flight Safety, Report No. JR-3, 1985.

2-94 Karlsen, L. K. and Salberg, A., "Digital Simulation of Aircraft Longitudinal Motions With Tailplane Ice," XXTH Aero Report 55, Dept. of Aeronautics, The Royal Institute of Technology, Stockholm, Sweden, 1983.

2-95 Leckman, P. R., "Qualification of Light Aircraft for Flight in Icing Conditions," Society of Automotive Engineers Paper No. 710394, 1971.

2-96 Jackson, G. C., "AEROICE: A Computer Program to Evaluate the Aerodynamic Penalties Due to Icing," Technical Memorandum AFFDL-79-91-WE, Air Force Flight Dynamics Laboratory, 1979.

2-97 Bragg, M. B. and Gregorek, G. M., "Predicting Aircraft Performance Penalties Due to Ice Accretion," SAE Paper 830742, 1983.

2-98 Ranaudo, R. ,J.; Mikkelsen, K. L.; McKnight, R. C. and Perkins, P. J. Jr., "Performance Degradation of a Typical Twin Engine Commuter Type Aircraft in Measured Natural Icing Conditions," NASA TM 83564 and AIAA-84-0179, 1984.

2-99 Mikkelsen, K. L., McKnight, R. C., Ranaudo, R. J. and Perkins, P. J. Jr., "Icing Flight Research: Aerodynamic Effects of Ice and Ice Shape Documentation with Stereo Photography," NASA TM 86906 or AIAA-85-0468,1985.

2-100 Mikkelsen, K. L.; Juhasz, N.; Ranaudo, R. J.; McKnight, R. C.; Freedman, R.; and Greissing, J., "In-Flight Measurements of Wing Ice Shapes and Wing Section Drag Increases Caused by Natural Icing Conditions," NASA TM 87301, April 1986.

2-101 Ranaudo, R. ,J.; Mikkelsen, K. L.; McKnight, R. C.; Ide, R. F.; Reehorst, A. L.; Jordan, J. L.; Schinstock, W. C.; and Platz, S. J., "The Measurement of aircraft Performance and Stability and Control after Flight Through Natural Icing Conditions," NASA TM 87265, April 1986.

2-102 Ranaudo, R. ,J.; Batterson, J. G.; Reehorst, A. L.; Bond, T. H.; and O"Mara, T. M., "Determination of Longitudinal Aerodynamic Derivatives Using Flight Data from an Icing Research Aircraft," NASA TM 101427, Jan. 1989.

TABLE 2-1. DROPLET PARAMETERS FOR THE LANGMUIR D DISTRIBUTION

δ	Δv	Re	K	K_0
6.2	.05	36.24	.0143	.00726
10.4	.10	60.79	.0403	.0173
14.2	.20	83.00	.0752	.0288
20.0	.30	116.9	.1492	.0501
27.4	.20	160.15	.2800	.0825
34.8	.10	203.41	.4517	.120
44.4	.05	259.52	.7353	.1749

TABLE 2-2. CALCULATION OF $\overline{E}$ AND $\overline{B}$ (S=0)

K_0	$\triangle v$	E	$E \cdot \triangle v$	$\beta(S=0)$	$\beta(S=0) \cdot \triangle v$
.00726	.05	.04	.002	.10	.005
.0173	.10	.09	.009	.43	.043
0288	.20	.14	.028	.63	.126
.0501	.30	.23	.069	.69	.207
.0825	.20	.32	.064	.77	.154
.120	.10	.40	.040	.80	.080
.1749	.05	.49	.024	.85	.0425
			-------		-------
			$\overline{E} = .24$		$\overline{\beta}(S=0) = .66$

TABLE 2-3. CHARACTERISTIC LENGTHS FOR SEVERAL BODIES FOR CALCULATION OF K_c

BODY	CHARACTERISTIC LENGTH	DATA SOURCE
Airfoil	Chord, c	All airfoil data
Cylinder	Radius, D/2	NACA Rpt. 1215 (Reference 2-32)
Ribbons	Half width, b/2	AAFTR 5418 (Reference 2-2)
Semi-infinite rectangle	Half width	NACA TN 3658 (Reference 2-32)
Ellipsoids (10%, 20%) A/B = 10, 5	Body length, L_{el}	NACA TN 3099 (Reference 2-27) NACA TN 3147 (Reference 2-28)
Ellipsoids (A/B = 2, 3, 5)	Half body length, $L_{el}/2$	WADC TR 53-284 (Reference 2-30)
Cones	Cone length	WADC TR 53-284 (Reference 2-30)
Elbow	Arbitrary length, L_{eb} proportional to elbow size[*]	NACA TN 2999, (Reference 2-24) NACA TN 3770 (Reference 2-25)

[*] Elbow entrance width is $L_{eb}/4$, so that L_{ab} = 4 x entrance width

TABLE 2-4. ICE ACCRETION CHARACTERISTICS

Characteristic	Rime	Glaze
Air Temperature	Low	Near Freezing
Liquid Water Content	Low	High
Aircraft speed	Low	High
Droplet Size	Small	Large
Ice Color	Opaque	Clear or Translucent
Ice Density	Low	Near 1 g/cc
Ice Shape	Streamlined	Double Horn

TABLE 2-5. PERCENTAGE CONTRIBUTIONS OF MAIN TERMS IN ENERGY BALANCE FOR INCREASING T_∞ FOR A CIRCULAR CYLINDER WITH DIAMETER 20 CM

(a) LWC = .7 g/m^3, Droplet Diameter δ = 20 μm, V_∞ = 70 m/s

Percentage contribution of

| | | Heat Source Terms | | | Heat Sink Terms | | |
T_∞ °C	n	Aerodynamic Heating	Droplet Freezing	Droplet Kinetic Energy	Convective Cooling	Evaporative Cooling	Droplet Warming
-26	.90	5	94	1	48	15	36
-20	.70	6	93	1	47	18	35
-14	.49	8	91	1	46	21	33
-8	.27	14	84	2	44	24	32
-2	.03	53	38	9	44	25	31

(b) LWC = .1 g/m^3, Droplet Diameter δ = 20 μm, V_∞ = 70 m/s

Percentage contribution of

| | | Heat Source Terms | | | Heat Sink Terms | | |
T_∞ °C	n	Aerodynamic Heating	Droplet Freezing	Droplet Kinetic Energy	Convective Cooling	Evaporative Cooling	Droplet Warming
-6	.93	24	75	1	60	34	6
-4	.53	36	63	1	59	35	6
-2	.10	73	25	2	60	34	6

TABLE 2-6. PERCENTAGE CONTRIBUTIONS OF MAIN TERMS IN ENERGY BALANCE FOR INCREASING LWC FOR A CIRCULAR CYLINDER WITH DIAMETER 20 CM

(a) $T_\infty = -26$ °C, Droplet Diameter $\delta = 20$ μm, $V_\infty = 70$ m/s

Percentage contribution of

| | | Heat Source Terms | | | Heat Sink Terms | | |
LWC g/m³	n	Aerodynamic Heating	Droplet Freezing	Droplet Kinetic Energy	Convective Cooling	Evaporative Cooling	Droplet Warming
0.7	.90	5	95	1	48	15	36
0.8	.83	4	95	1	46	14	40
0.9	.78	4	95	1	44	14	42
1.0	.73	4	95	1	42	13	45
2.0	.54	3	96	1	29	9	62
3.0	.47	2	96	2	22	7	71
4.0	.44	2	97	2	18	6	77
5.0	.42	1	97	2	15	5	80

(b) $T_\infty = -6$ °C, Droplet Diameter $\delta = 20$ μm, $V_\infty = 70$ m/s

Percentage contribution of

| | | Heat Source Terms | | | Heat Sink Terms | | |
LWC g/m³	n	Aerodynamic Heating	Droplet Freezing	Droplet Kinetic Energy	Convective Cooling	Evaporative Cooling	Droplet Warming
0.1	.93	24	75	1	60	34	6
0.4	.28	21	77	2	51	29	21
0.7	.19	18	79	3	44	25	32
1.0	.15	16	80	4	39	22	40
1.3	.14	14	82	4	34	19	46
1.6	.12	13	82	5	31	18	51
1.9	.11	12	83	5	28	16	56
2.2	.11	11	84	6	26	15	59
2.5	.10	10	84	6	24	14	62
2.8	.10	9	85	6	23	13	65

TABLE 2-7. PERCENTAGE CONTRIBUTIONS OF MAIN TERMS IN ENERGY BALANCE FOR INCREASING DROPLET DIAMETER δ FOR A CIRCULAR CYLINDER WITH DIAMETER 20 CM

(a) $T_\infty = -26$ °C, LWC $= .7$ g/m^3, $V_\infty = 70$ m/s

Percentage contribution of

		Heat Source Terms			Heat Sink Terms		
δ μm	n	Aerodynamic Heating	Droplet Freezing	Droplet Kinetic Energy	Convective Cooling	Evaporative Cooling	Droplet Warming
20	.90	5	95	1	48	15	36
40	.68	4	95	1	39	12	48
60	.64	3	95	1	37	11	52
80	.62	3	96	1	35	11	54

(b) $T_\infty = -6$ °C, LWC $= .1$ g/m^3, $V_\infty = 70$ m/s

Percentage contribution of

		Heat Source Terms			Heat Sink Terms		
δ μm	n	Aerodynamic Heating	Droplet Freezing	Droplet Kinetic Energy	Convective Cooling	Evaporative Cooling	Droplet Warming
20	.93	24	75	1	60	34	6
40	.60	24	76	1	58	33	10
60	.52	23	76	1	57	32	11
80	.49	23	76	1	56	32	12

12-63

TABLE 2-8. PERCENTAGE CONTRIBUTIONS OF MAIN TERMS IN ENERGY BALANCE FOR INCREASING V_∞ FOR A CIRCULAR CYLINDER WITH DIAMETER 20 CM

(a) $T_\infty = -26\ °C$, LWC $= .7\ g/m^3$, Droplet Diameter $\delta = 20\ \mu m$

Percentage contribution of

V_∞ m/s	n	Heat Source Terms			Heat Sink Terms		
		Aerodynamic Heating	Droplet Freezing	Droplet Kinetic Energy	Convective Cooling	Evaporative Cooling	Droplet Warming
70	.90	5	95	1	48	15	36
80	.82	6	93	1	46	14	39
90	.76	7	92	1	45	14	42
100	.71	8	90	2	43	13	44
110	.67	10	88	2	42	13	46
120	.62	11	86	3	40	12	48
130	.59	13	84	4	39	11	49

(b) $T_\infty = -6\ °C$, LWC $= .1\ g/m^3$, DROPLET DIAMETER $\delta = 20\ \mu m$

Percentage contribution of

V_∞ m/s	n	Heat Source Terms			Heat Sink Terms		
		Aerodynamic Heating	Droplet Freezing	Droplet Kinetic Energy	Convective Cooling	Evaporative Cooling	Droplet Warming
70	.93	24	75	1	60	34	6
80	.74	32	67	1	60	33	7
90	.58	40	58	1	60	32	8
100	.44	50	48	2	60	32	8
110	.31	61	37	2	60	30	9
120	.19	72	25	3	60	30	10
130	.08	85	11	3	61	29	10

TABLE 2-9. TEMPERATURE DEPENDENCE OF ADHESION (REFERENCE 2-61)

Material	Temperature Slope (lbs. per Sq. In. per °C)
Ice	0.0
Steel	-7.4
Copper	-5.0
Aluminum	-8.8
Glass (96% silica)	-4.5
Polyethylene	-5.8
Rubber	-6.0
Silicone treated rubber	-0.4

TABLE 2-10. COMPONENT PERCENTAGE DRAG INCREASE

Component	Icing Drag Contribution, Percent	
	Centurion	Super Skymaster
Wing	59	38
Horizontal Stabilizer	15	5
Vertical Stabilizer	6	8
Wing Struts	--	25
Misc. (engine cowls, nose antenna, etc.)	20	24
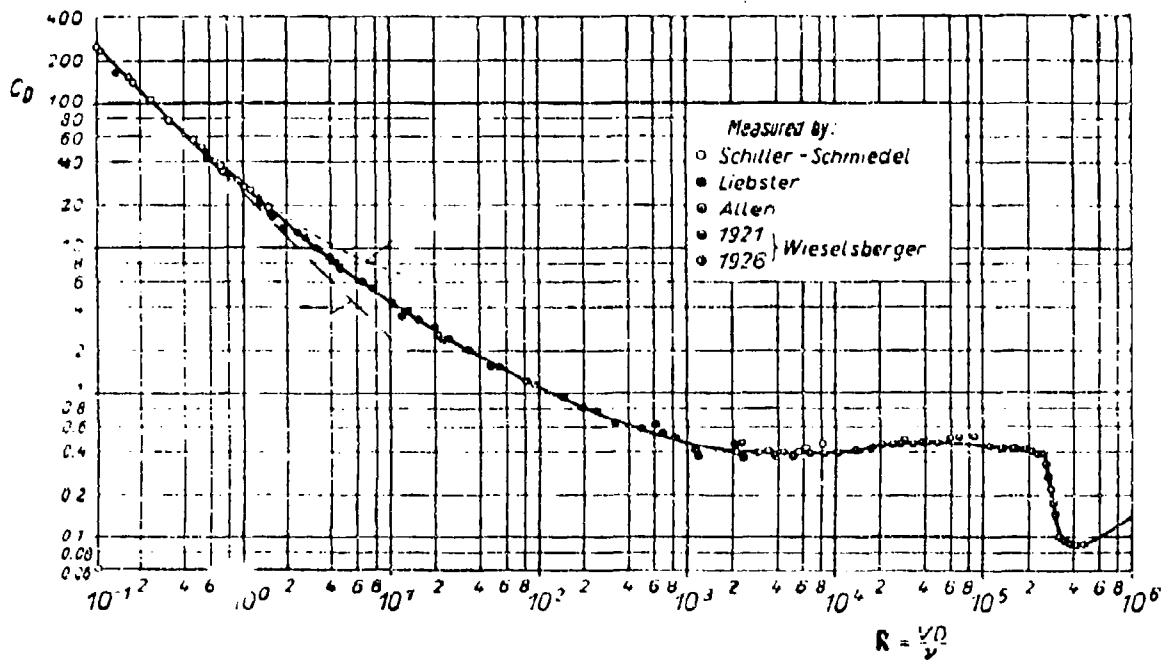
FIGURE 2-1.   DRAG COEFFICIENT FOR SPHERES AS A FUNCTION OF
REYNOLDS NUMBER (REFERENCE 2-9)
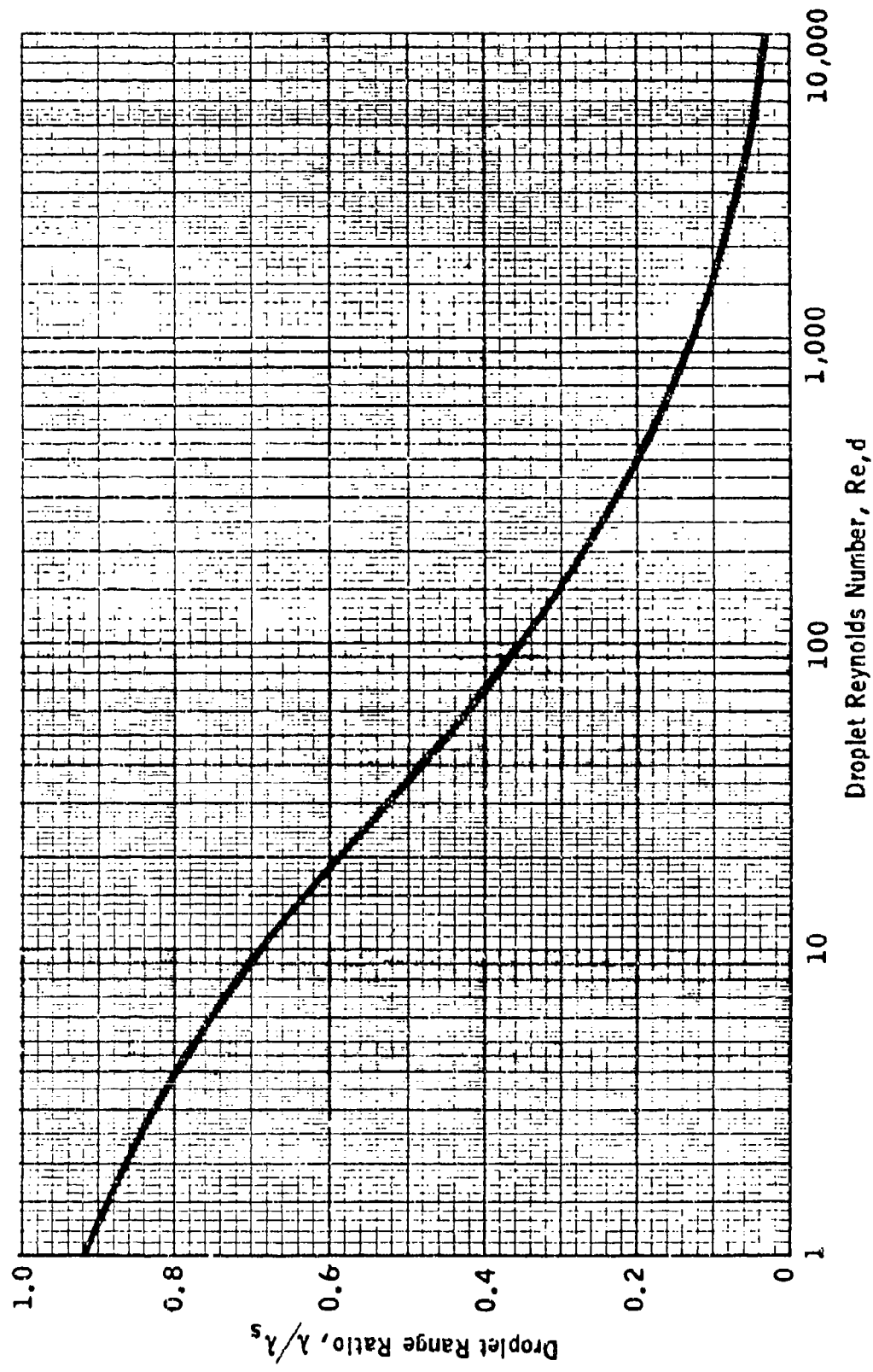
FIGURE 2-2. DROPLET RANGE RATIO AS A FUNCTION OF DROPLET REYNOLDS NUMBER (REFERENCE 2-22)

NACA 0012			CHORD (M) .3		V (M/S.) 70.00
T (SEC) 0.00		P (KPA) 90.75			TEMP (C) -12.60
LWC (G/M^3) 0.50		H (%) 100.00			DD (MIC) 5.00

$\delta = 5 \ \mu m \quad K_o = 0.011$

$\delta = 50 \ \mu m \quad K_o = 0.467$
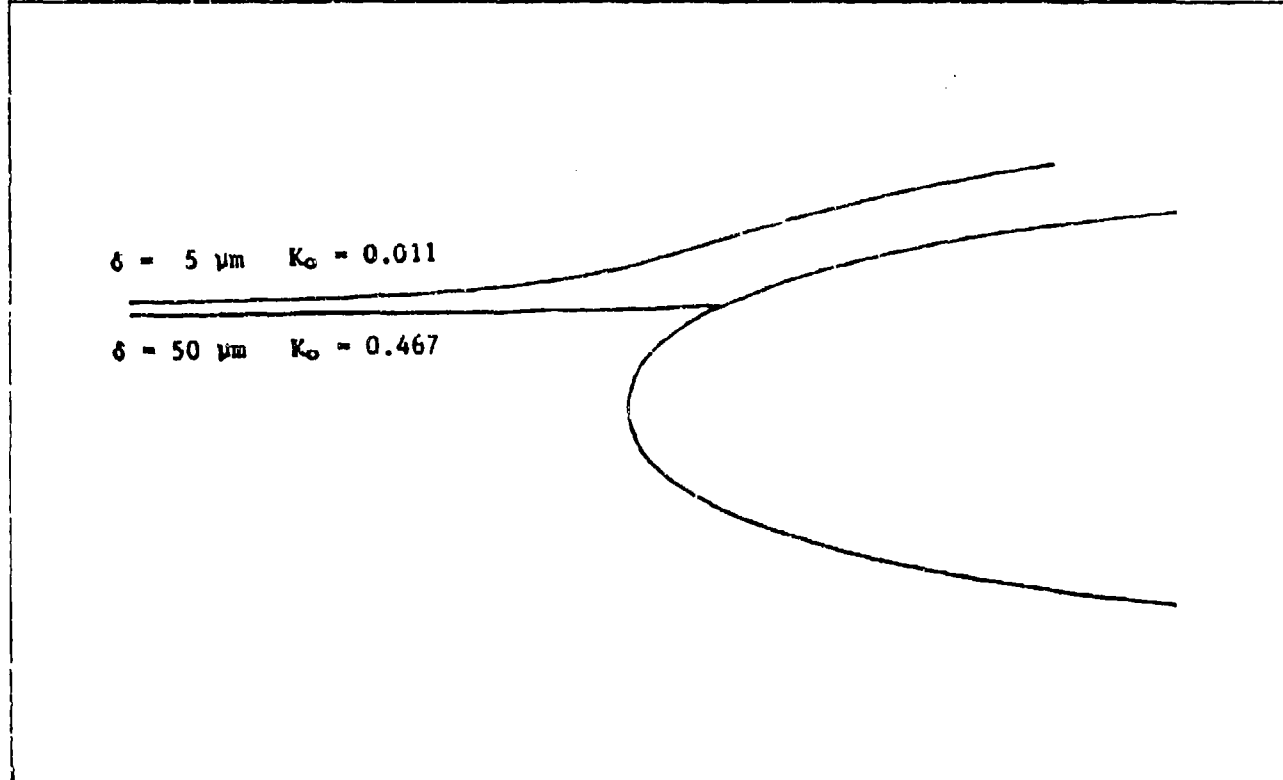
FIGURE 2-3. COMPARISON OF DROPLET TRAJECTORIES
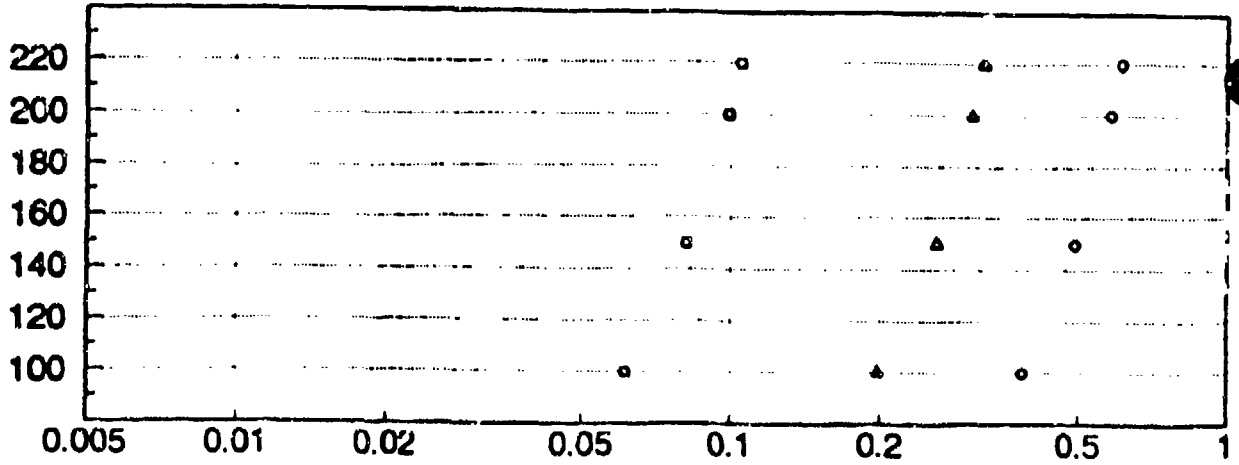
I 2-69
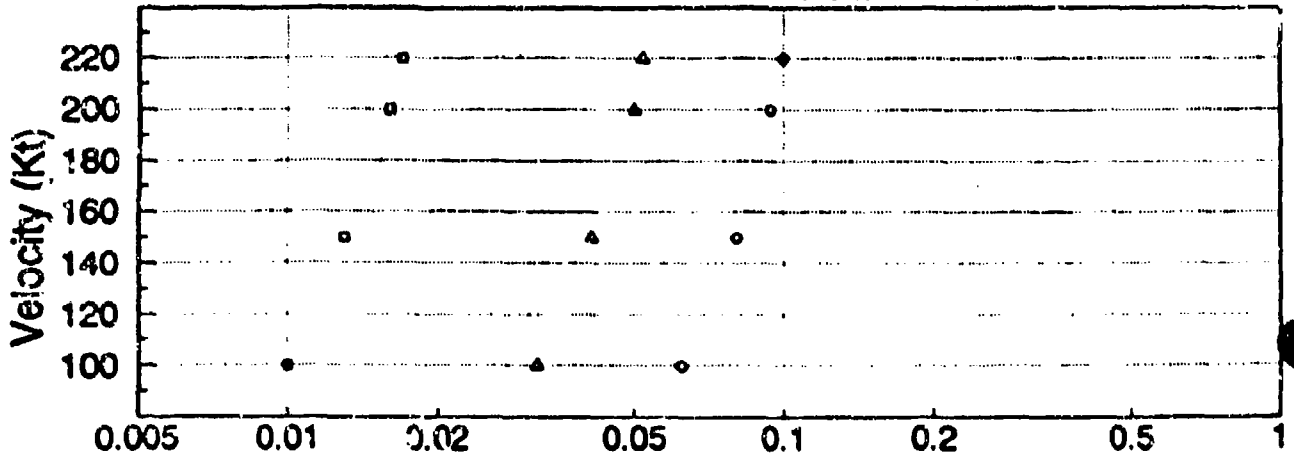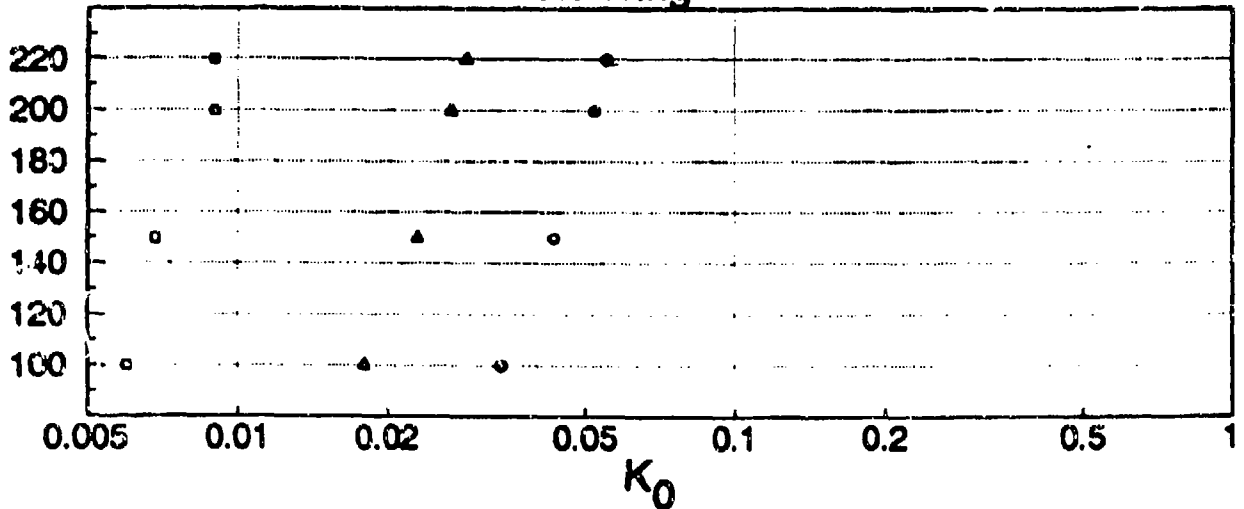
FIGURE 2-4. K_0 BASED ON MVD FOR SEVERAL CHORD SIZES
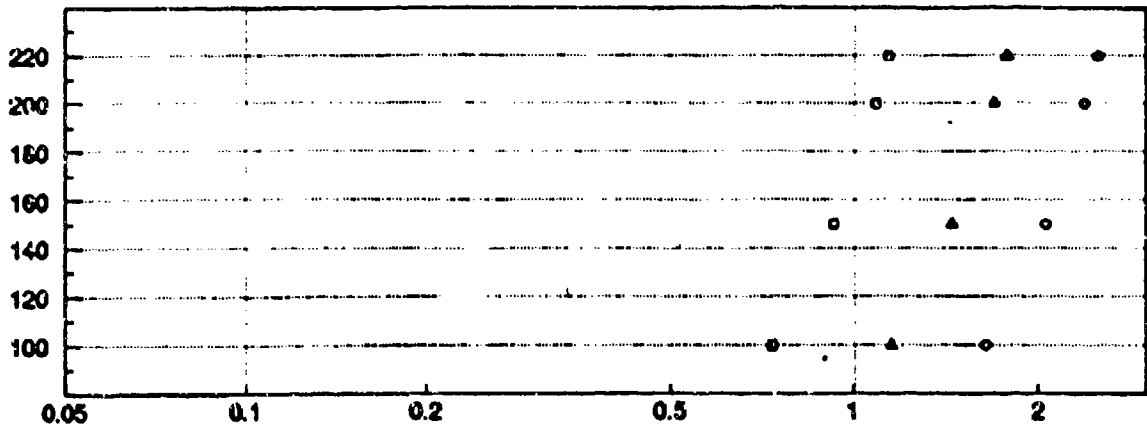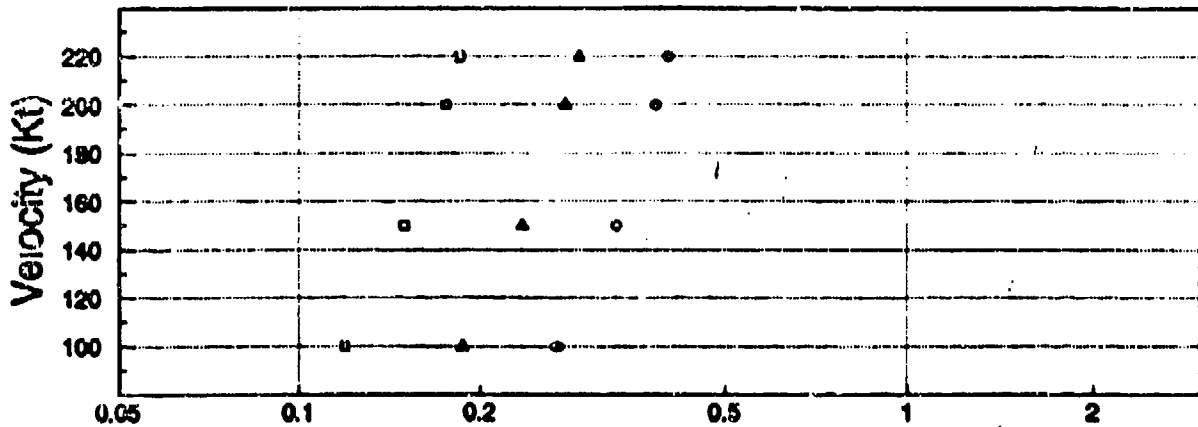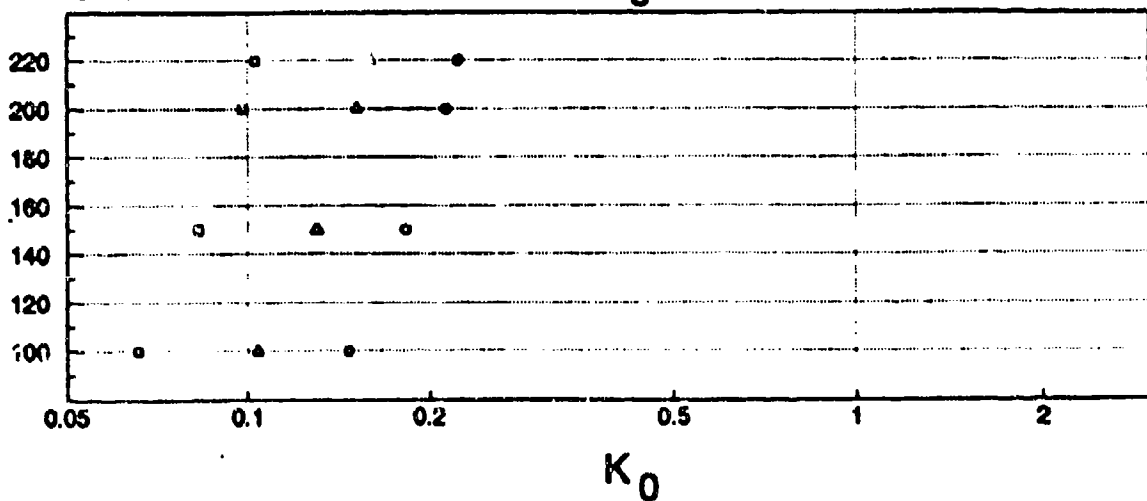
FIGURE 2-5. K_0 BASED ON DIAM$_{MAX}$ FOR SEVERAL CHORD SIZES

a)

Freestream Vector

Y-axis

Y_U

ΔY_O O

Y_L

S_U

$S = 0$

S_L

h

$E = \Delta Y_O / h$

b)
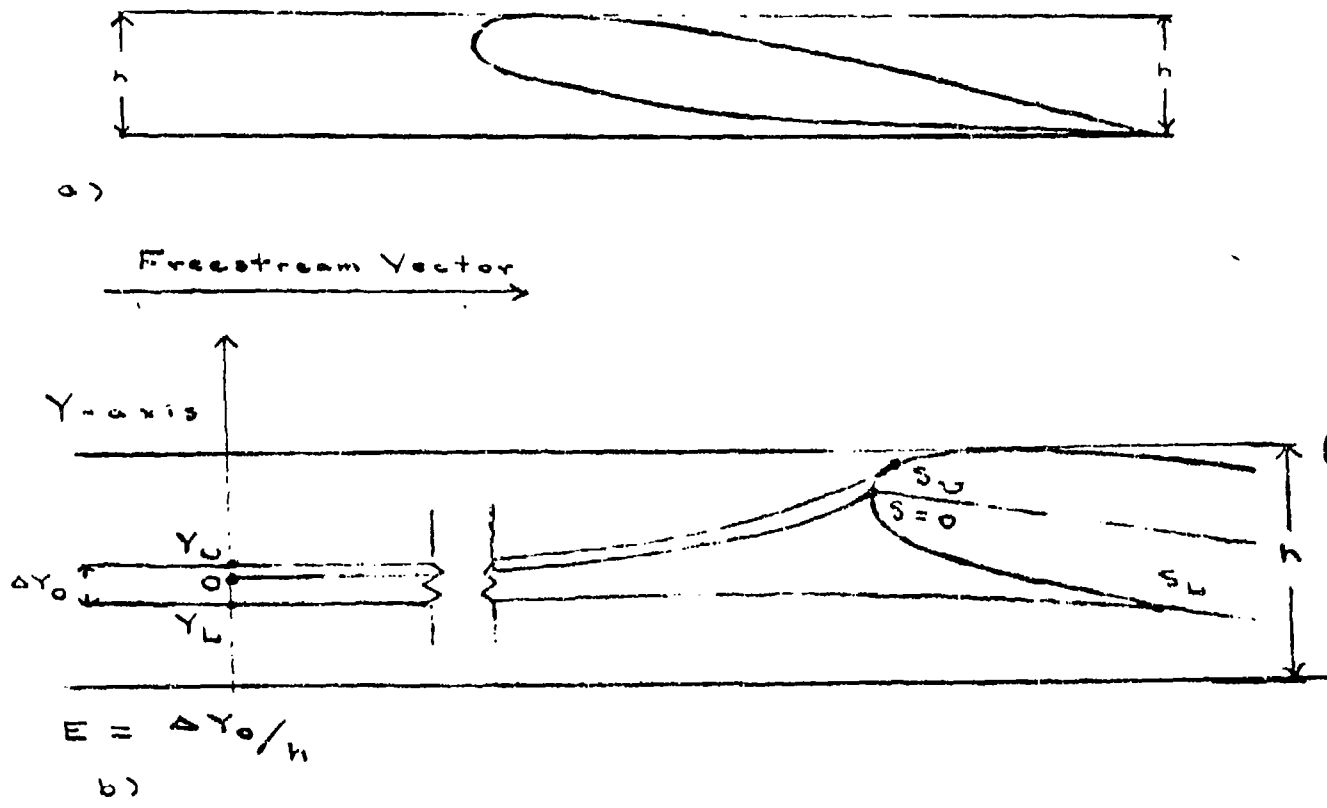
FIGURE 2-6.   DEFINITION OF DROPLET IMPINGEMENT PARAMETERS
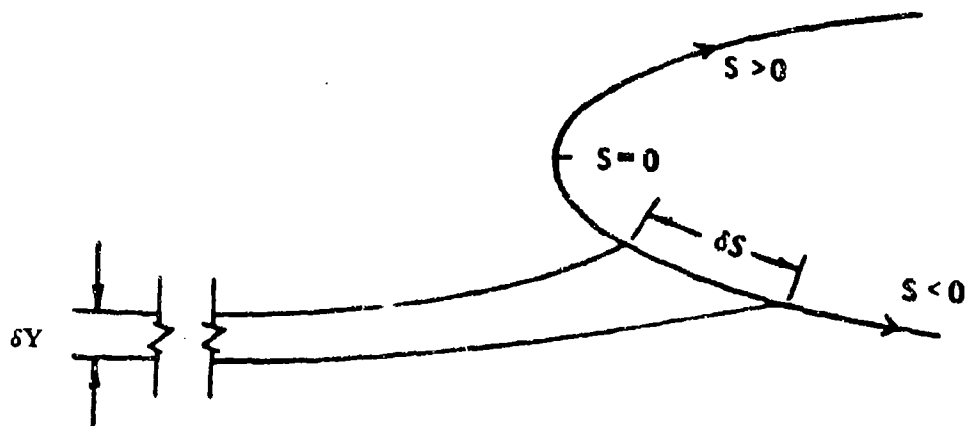
$$\beta = \lim_{\delta S \to 0} \frac{\delta Y}{\delta S} = \frac{dY}{dS}$$

FIGURE 2-7. DEFINITION OF LOCAL IMPINGEMENT EFFICIENCY PARAMETER β
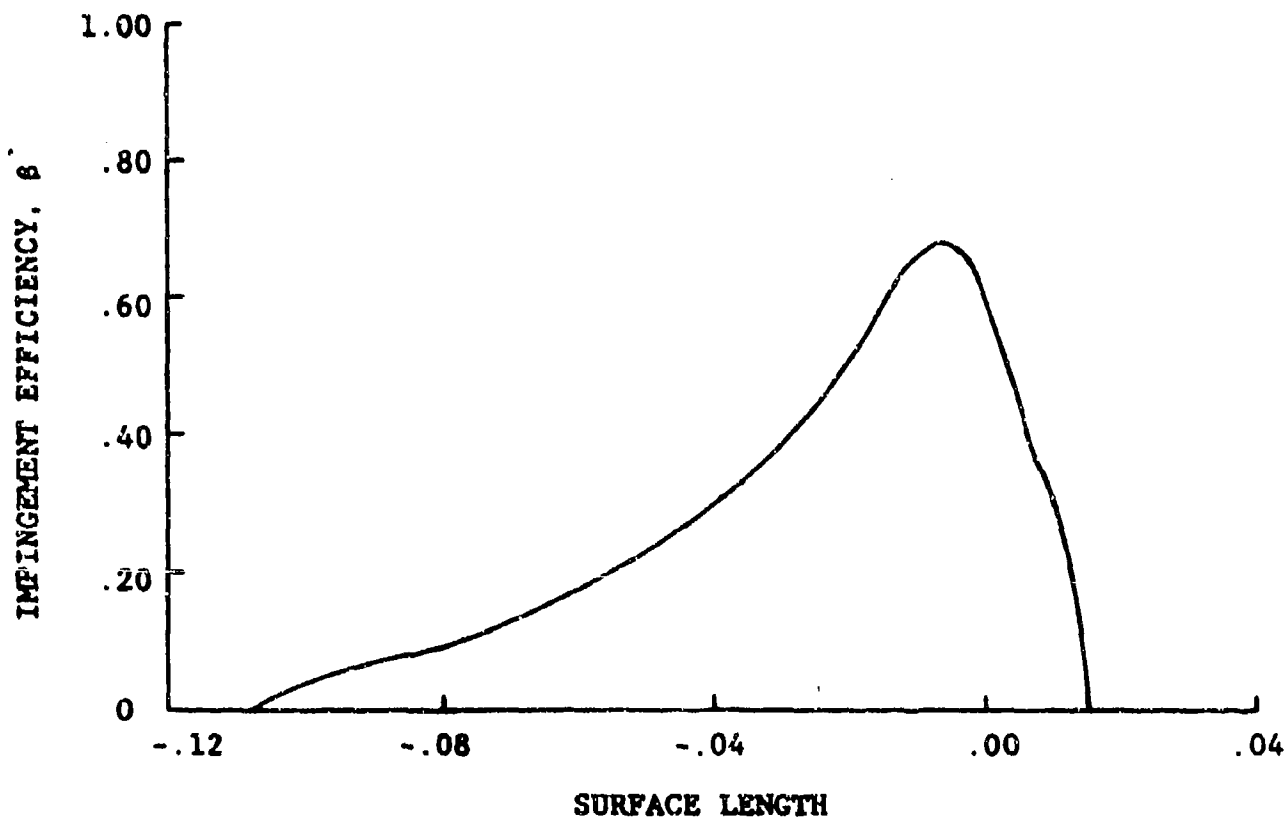
FIGURE 2-8. EXAMPLE OF IMPINGEMENT EFFICIENCY CURVE (β-CURVE)

I 2-73
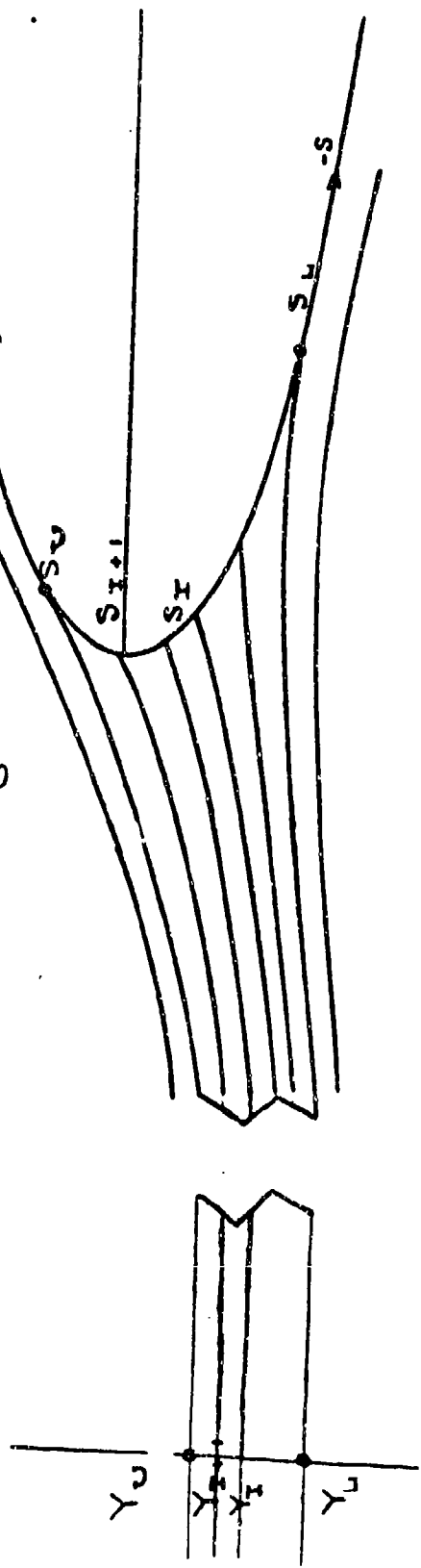
FIGURE 2-9. NUMERICAL CALCULATION OF β-CURVE
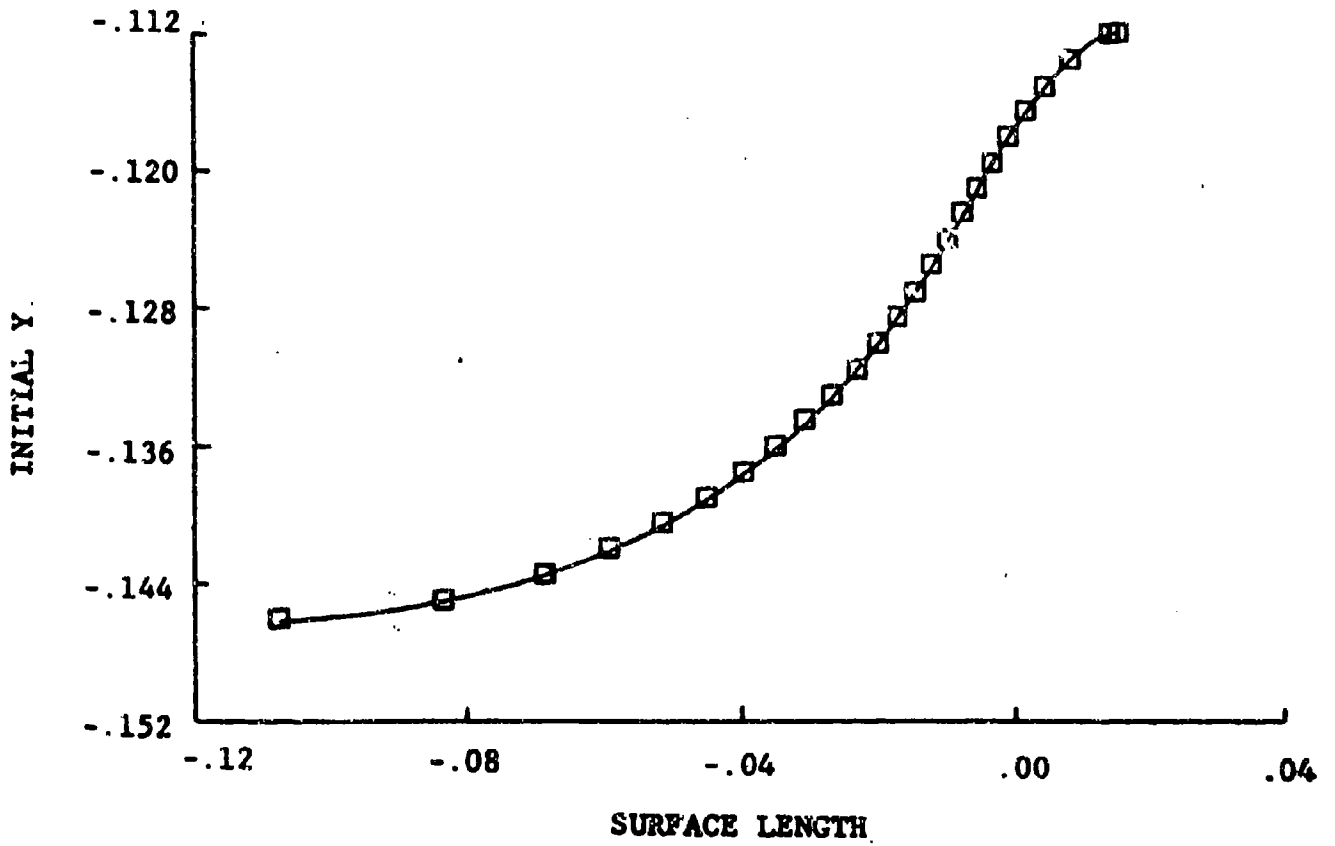
FIGURE 2-10.   EXAMPLE OF Y VS. S CURVE

I 2-75
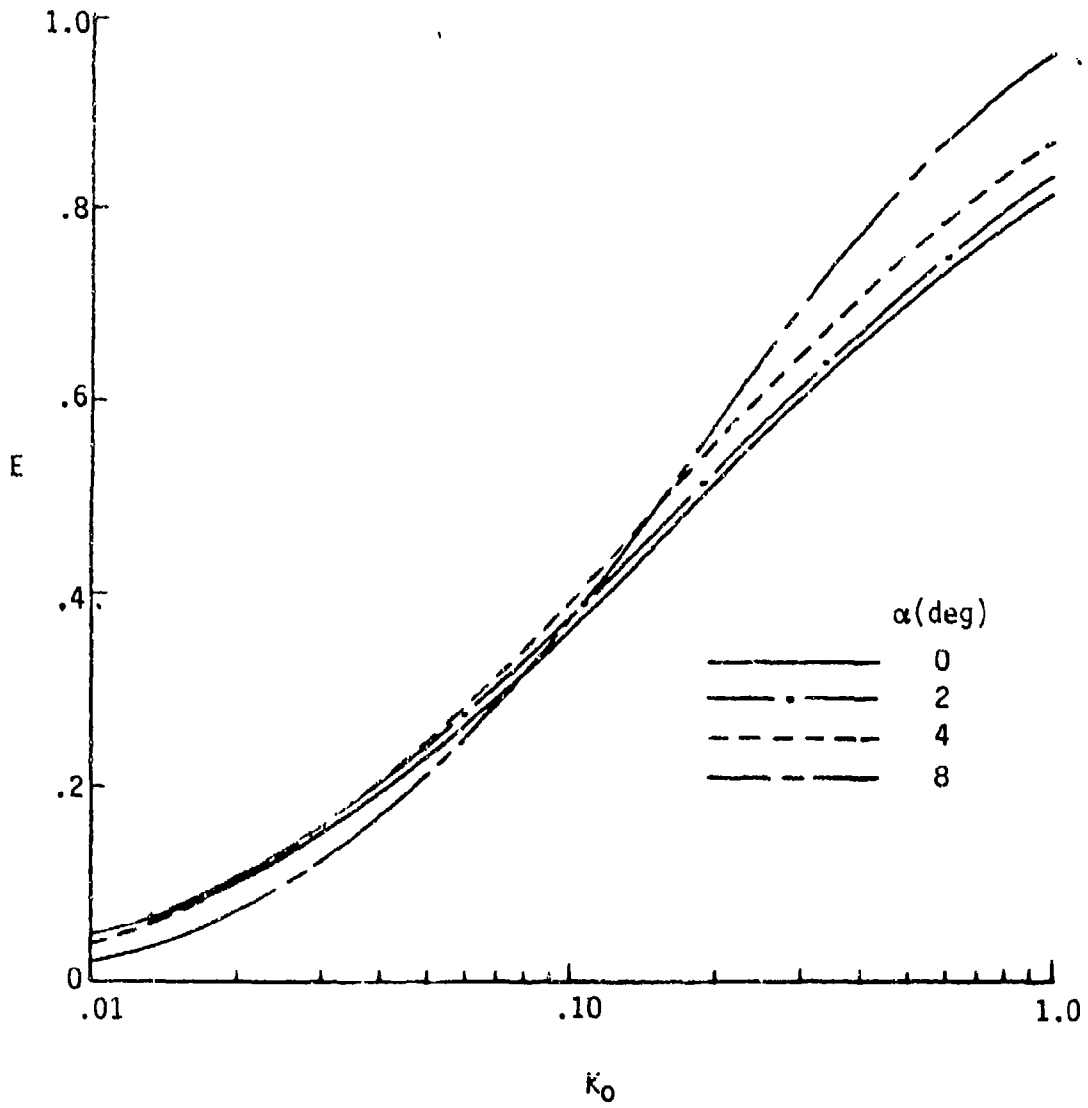
FIGURE 2-11. TOTAL COLLECTION EFFICIENCY OF A NACA 0012 AIRFOIL

I 2-76
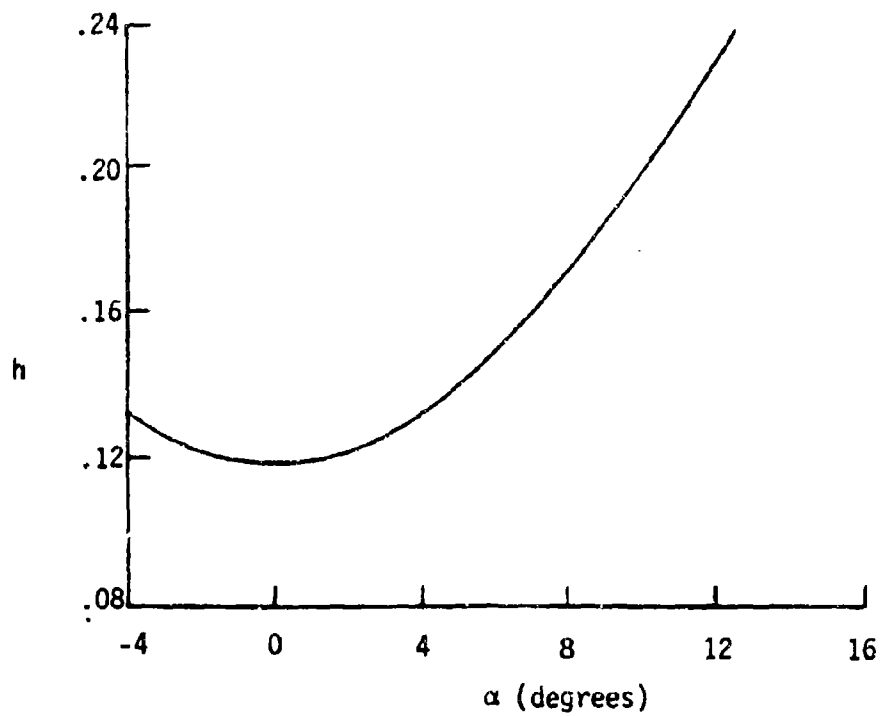
FIGURE 2-12.   NACA 0012: H (NONDIMENSIONAL) VS. ANGLE OF ATTACK

I 2-77
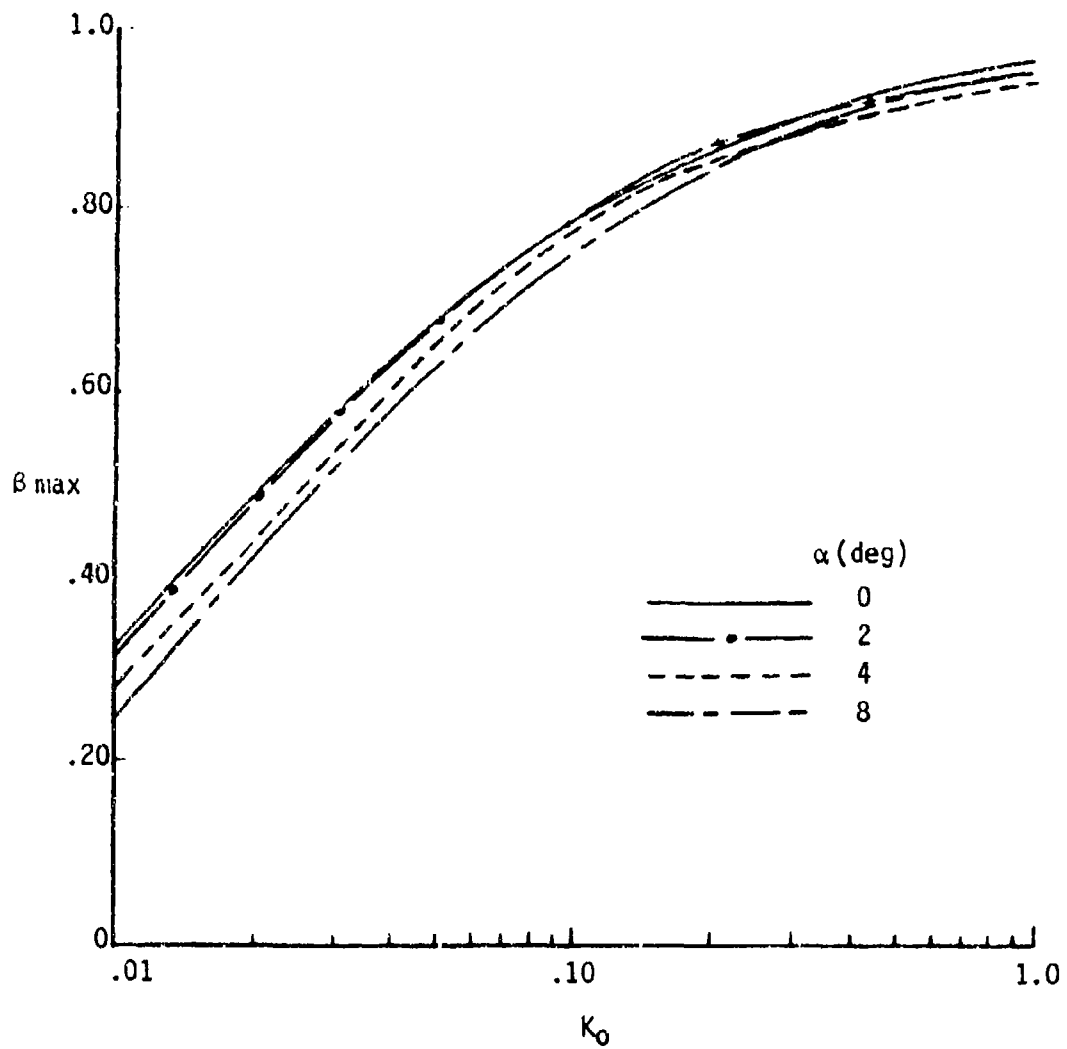
FIGURE 2-13. MAXIMUM IMPINGEMENT EFFICIENCY FOR A NACA 0012 AIRFOIL

I 2-78
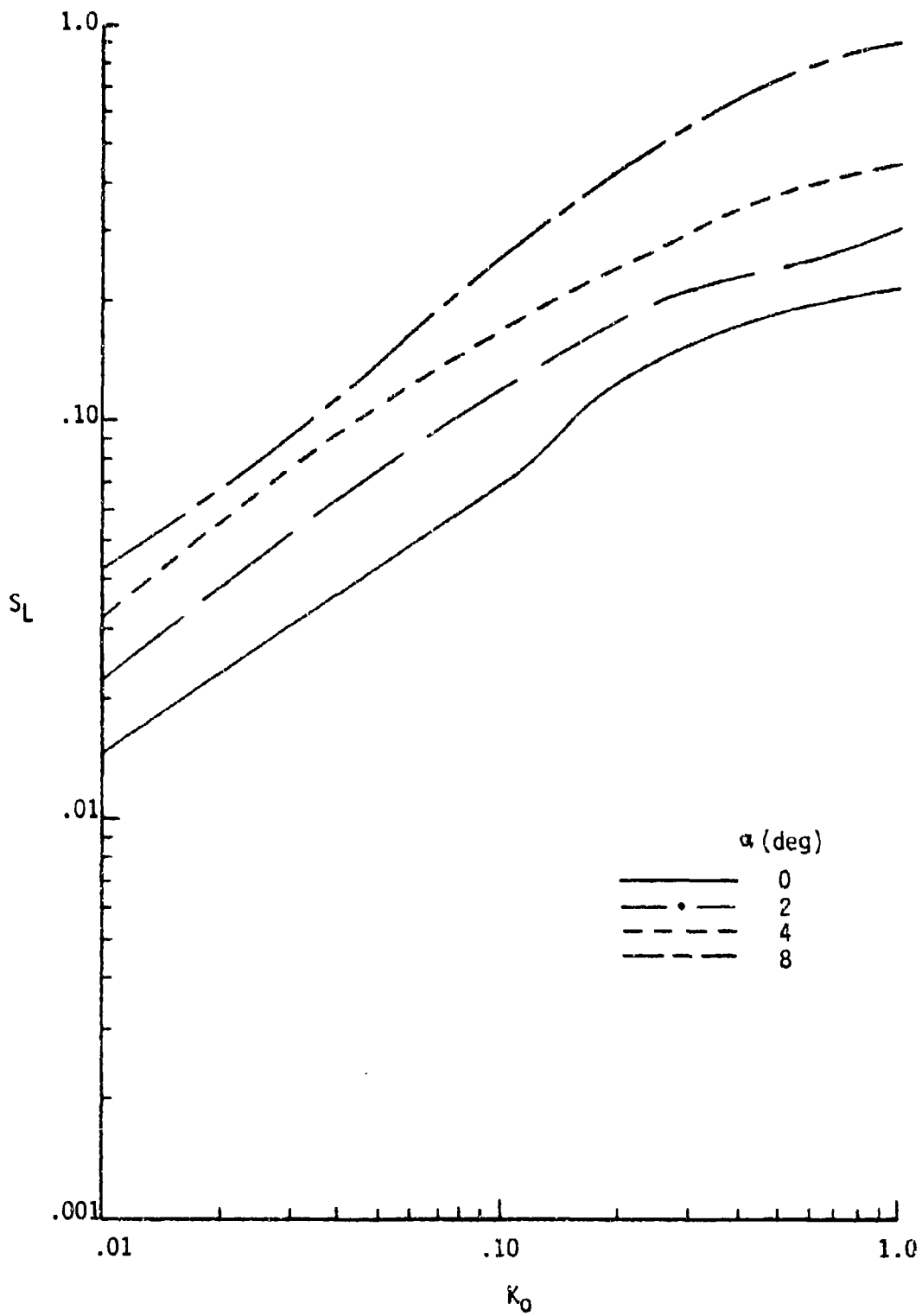
FIGURE 2-14.   LOWER SURFACE IMPINGEMENT LIMIT FOR A NACA 0012
AIRFOIL
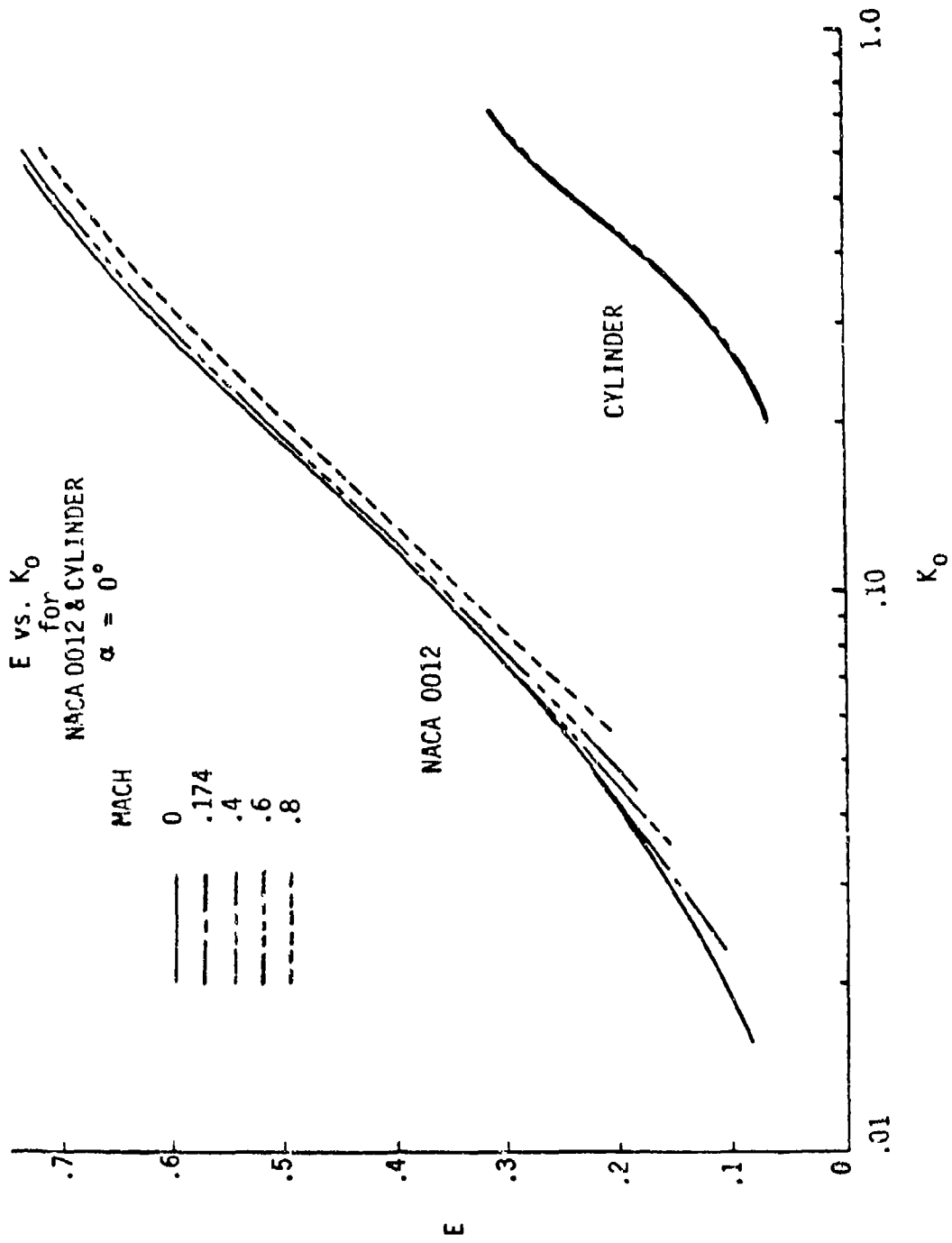
FIGURE 2-15. COMPRESSIBLE DROPLET IMPINGEMENT DATA ON A NACA 0012 AIRFOIL AND A CYLINDER
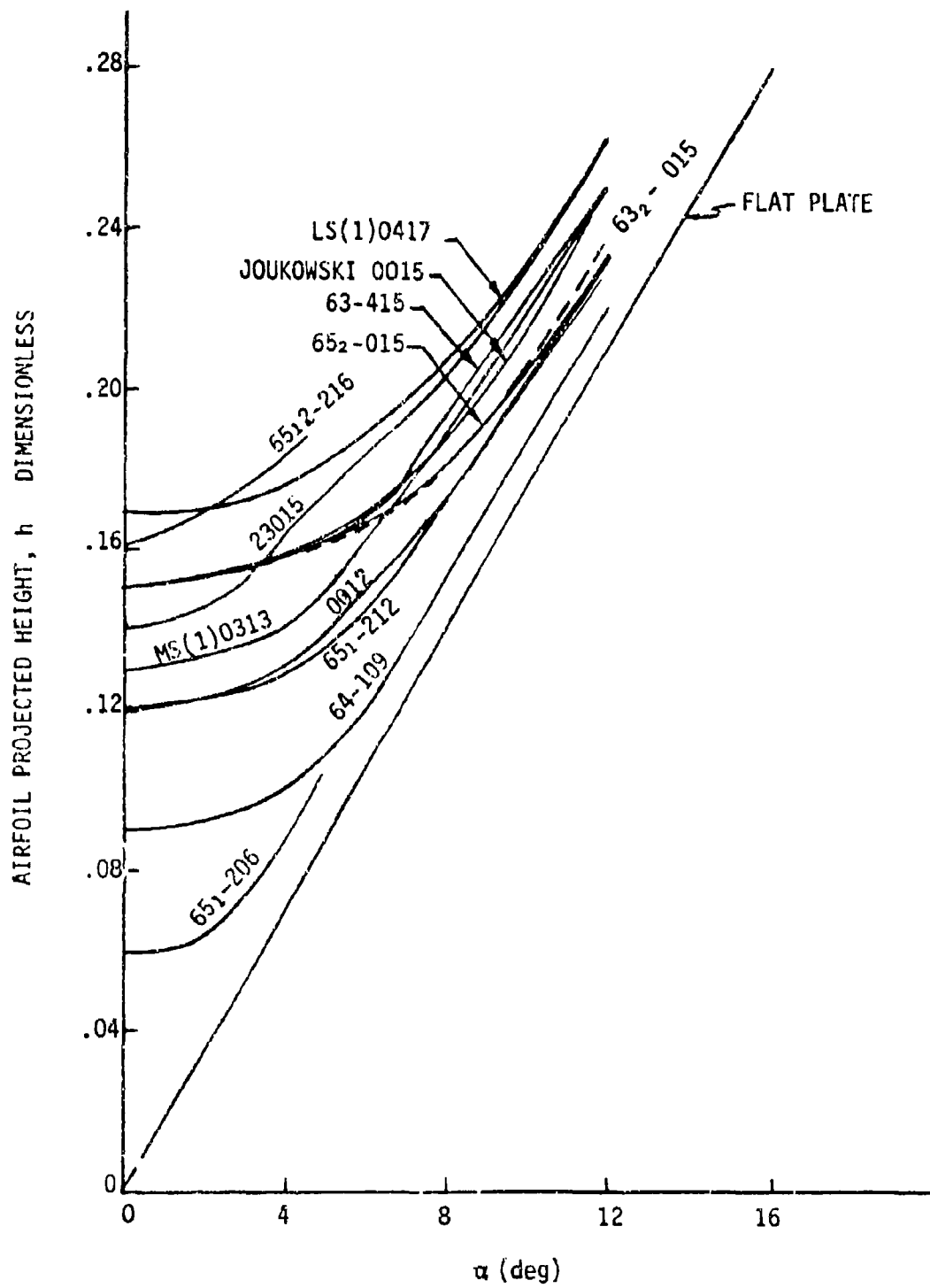
FIGURE 2-16. PROJECTED HEIGHT (DIMENSIONLESS) OF SEVERAL AIRFOILS
PLOTTED VERSUS ANGLE OF ATTACK

I 2-81
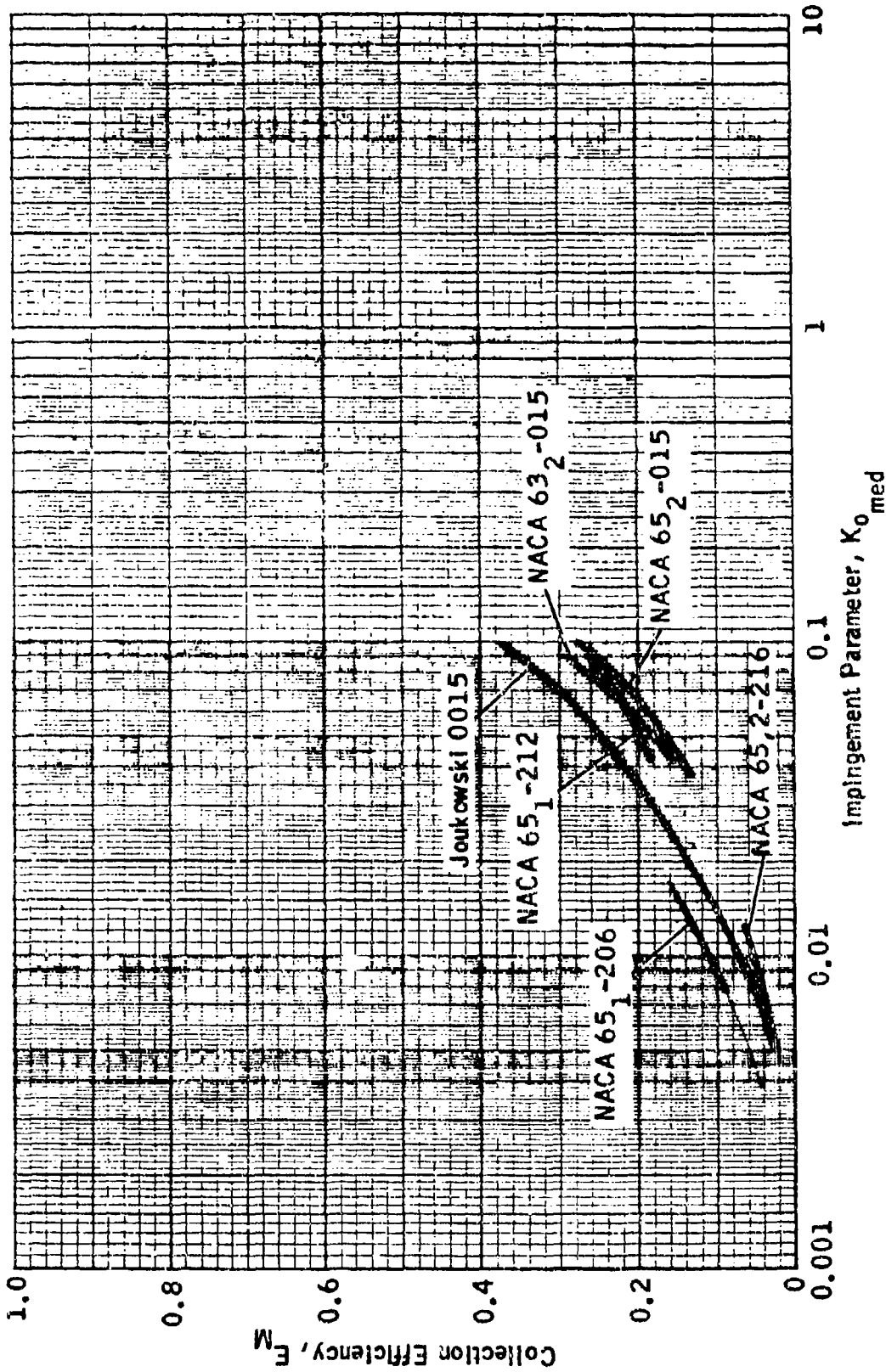
FIGURE 2-17. COLLECTION EFFICIENCY VERSUS $K_{o_{med}}$ FOR AIRFOILS - EXPERIMENTAL DATA
AT 0° ANGLE OF ATTACK
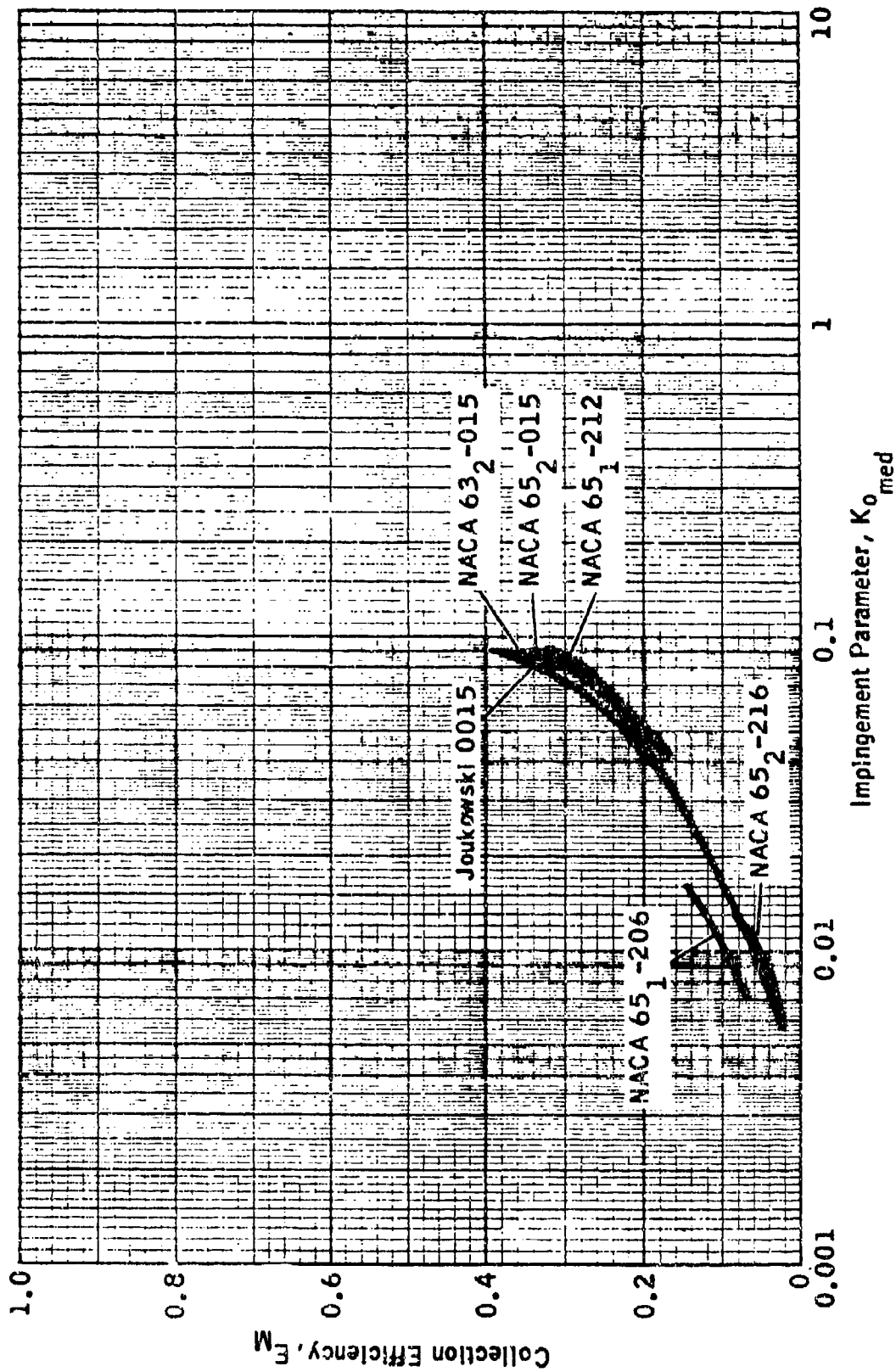
FIGURE 2-18. COLLECTION EFFICIENCY VERSUS Ko_{med} FOR AIRFOILS -EXPERIMENTAL DATA

FOR 4° ANGLE OF ATTACK
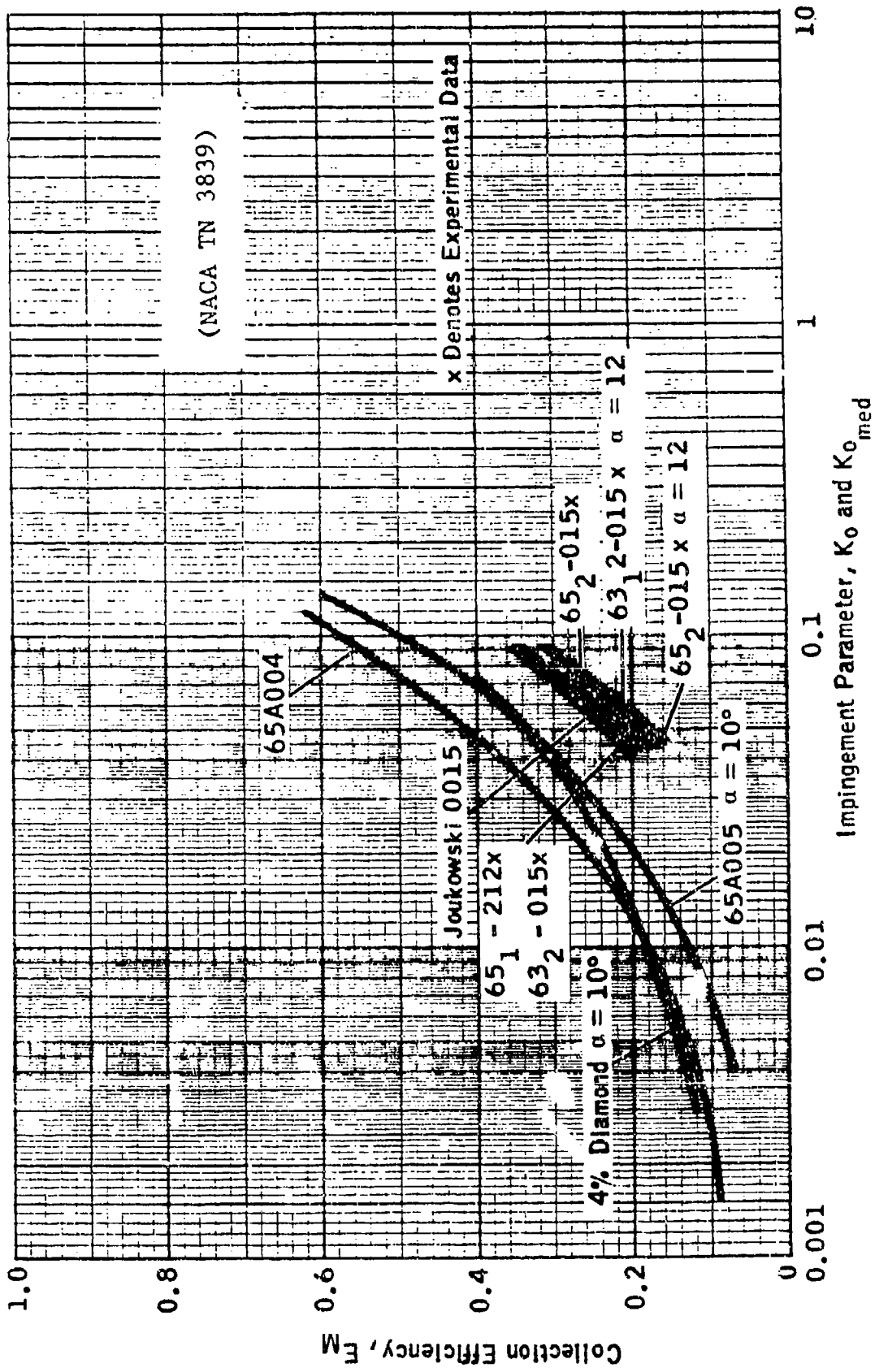
FIGURE 2-19. COLLECTION EFFICIENCY VERSUS K_0 FOR AIRFOILS – EXPERIMENTAL DATA FOR 8° ANGLE OF ATTACK
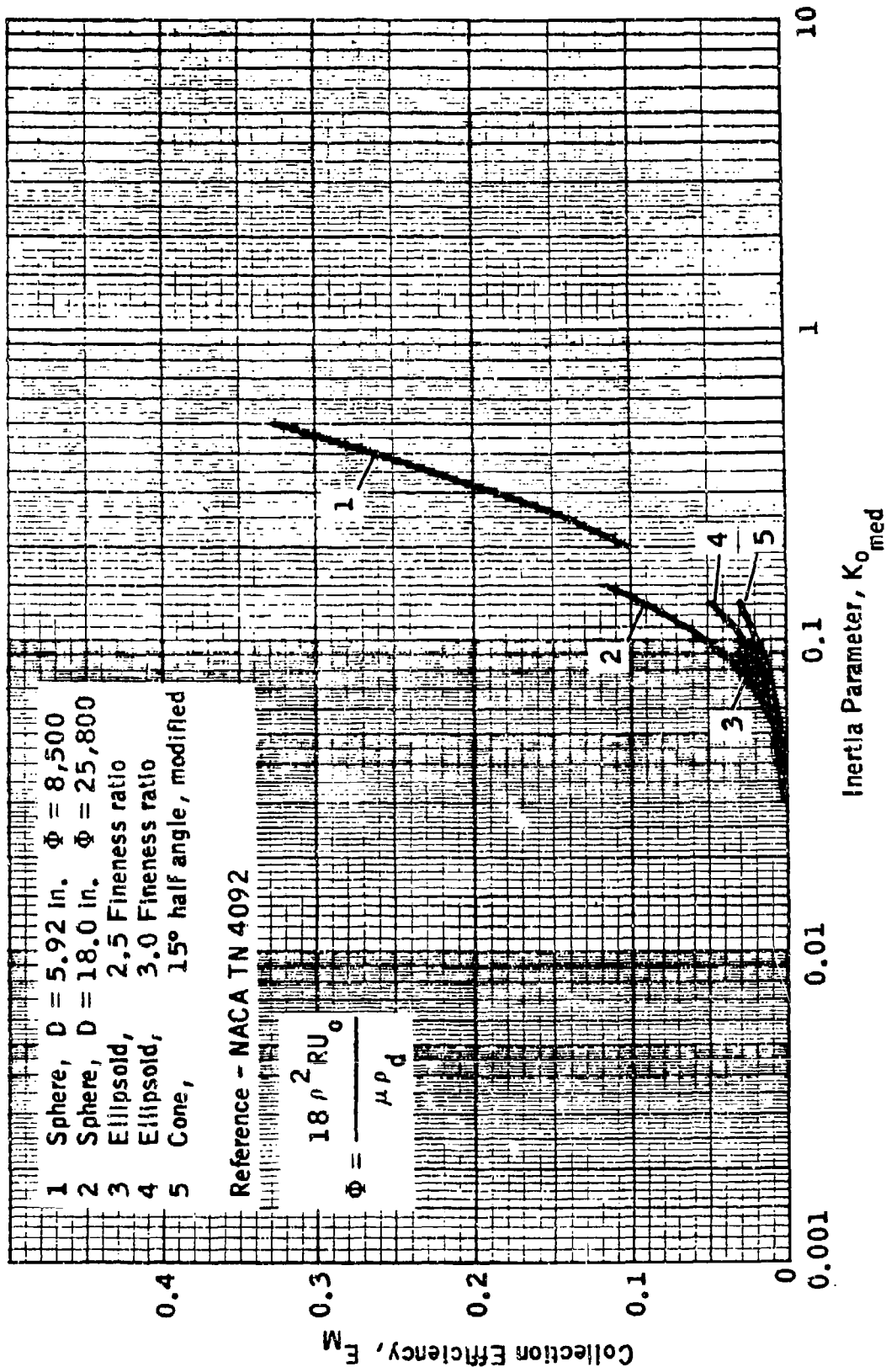
FIGURE 2-20. COLLECTION EFFICIENCY VERSUS $K_{o_{med}}$ FOR GEOMETRIC BODIES - EXPERIMENTAL DATA FOR 0° ANGLE OF ATTACK

The following labels appear within the figure:

Inertia Parameter, $K_{o_{med}}$

Collection Efficiency, E_M

1	Sphere,	D = 5.92 in.	Φ = 8,500	
2	Sphere,	D = 18.0 in.	Φ = 25,800	
3	Ellipsoid,	2.5 Fineness ratio		
4	Ellipsoid,	3.0 Fineness ratio		
5	Cone,	15° half angle, modified		

Reference - NACA TN 4092

$$\Phi = \frac{18 \rho^2 R U_o}{\mu \rho_d}$$
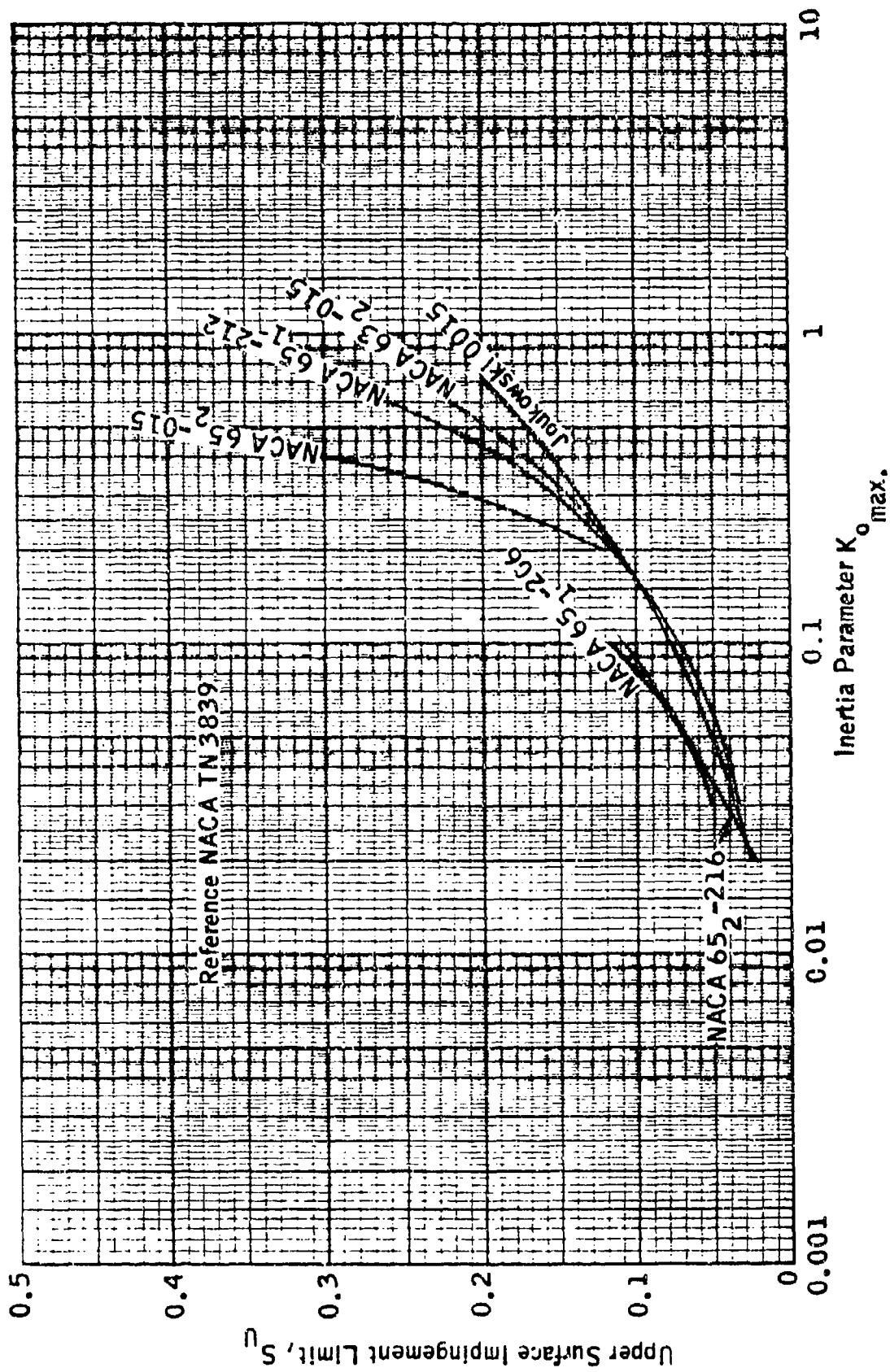
FIGURE 2-21. UPPER SURFACE IMPINGEMENT LIMITS FOR SEVERAL AIRFOILS AT 0° ANGLE OF ATTACK (EXPERIMENTAL DATA)
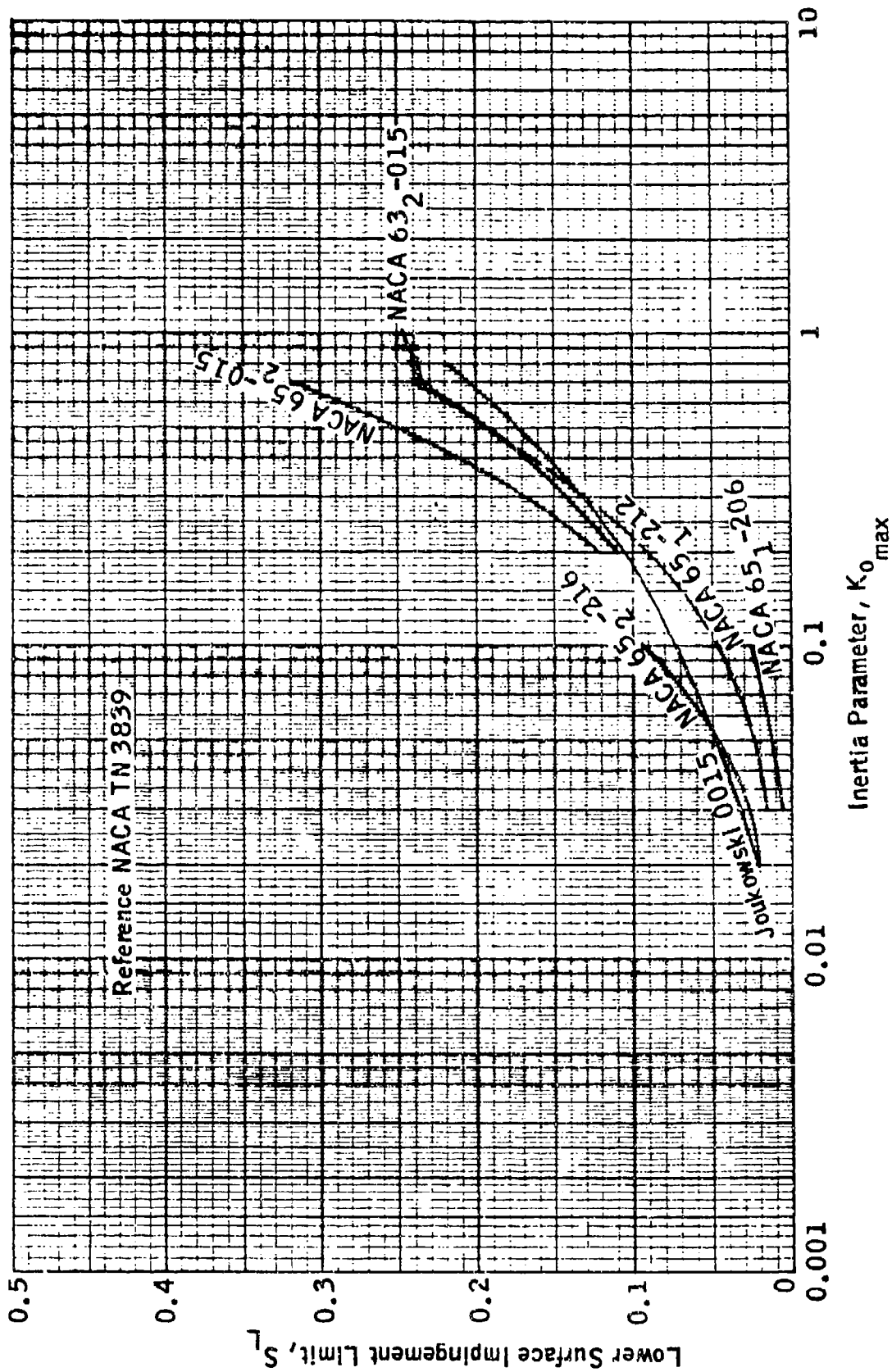
FIGURE 2-22. LOWER SURFACE IMPINGEMENT LIMITS FOR SEVERAL AIRFOILS AT 0° ANGLE OF ATTACK
(EXPERIMENTAL DATA)

FIGURE 2-23. UPPER SURFACE IMPINGEMENT LIMITS FOR SEVERAL AIRFOILS AT 4° ANGLE OF ATTACK
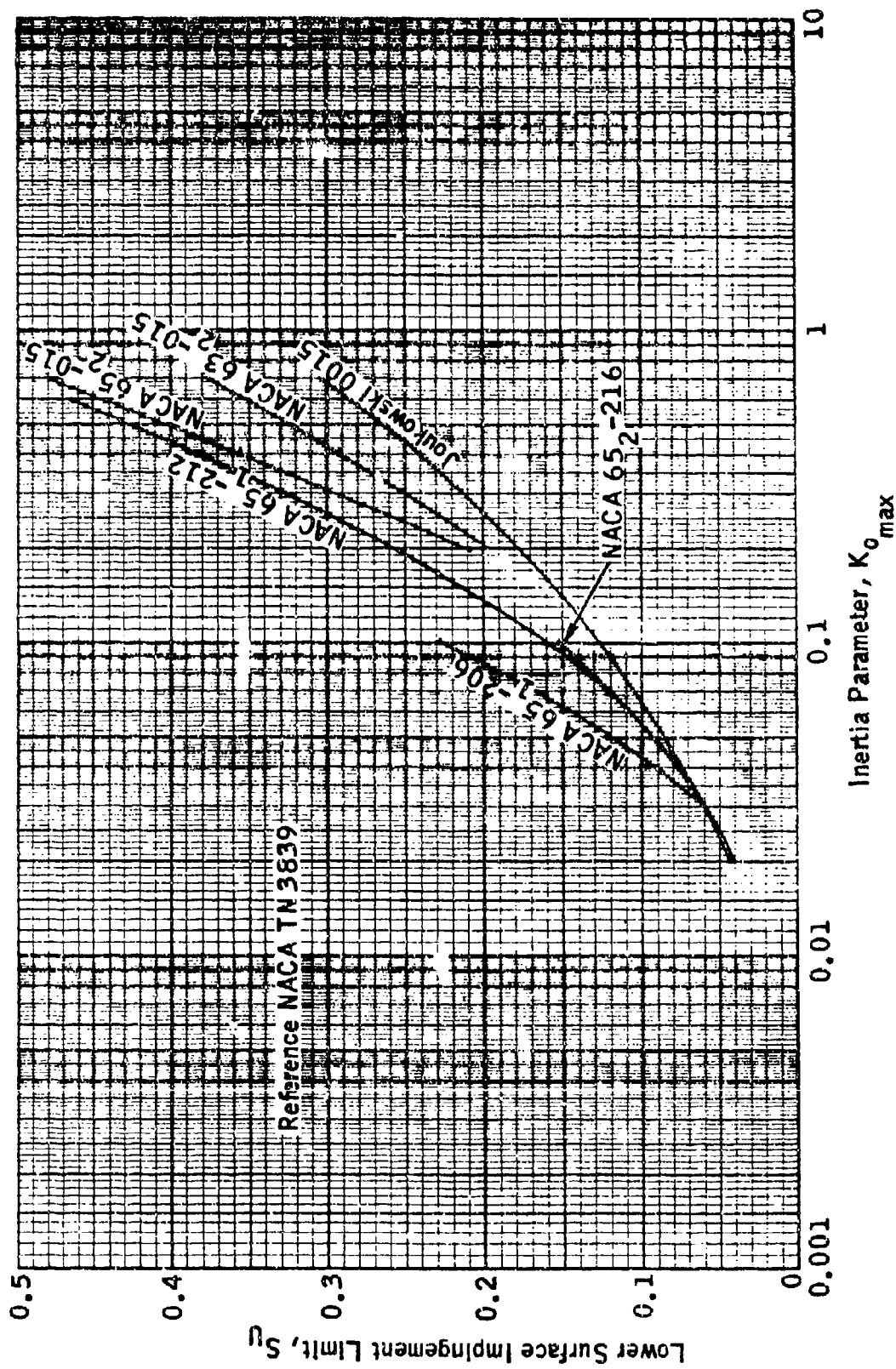
(EXPERIMENTAL DATA)

FIGURE 2-24. LOWER SURFACE IMPINGEMENT LIMITS FOR SEVERAL AIRFOILS AT 4° ANGLE OF ATTACK (EXPERIMENTAL DATA)
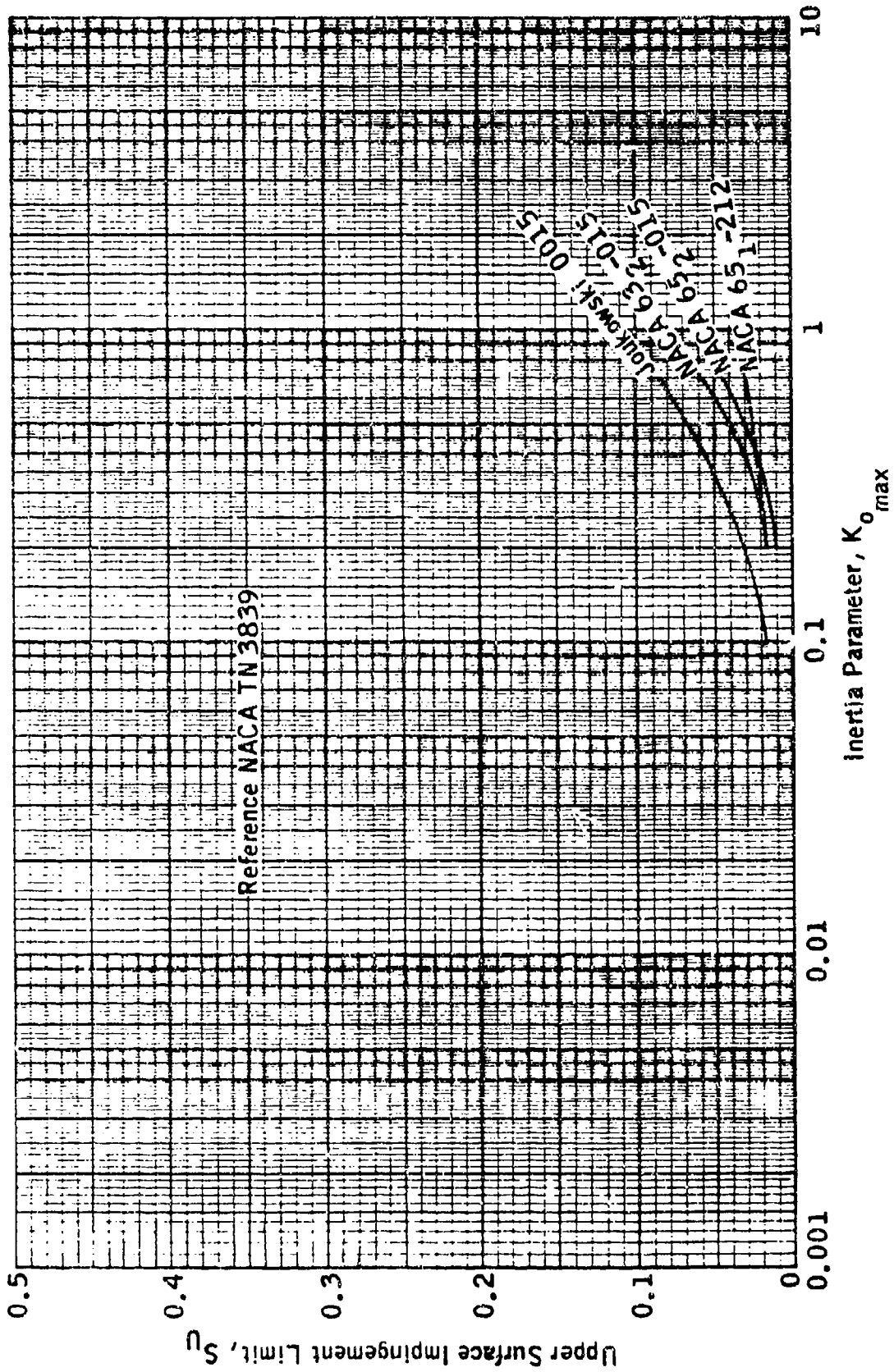
FIGURE 2-25. UPPER SURFACE IMPINGEMENT LIMITS FOR SEVERAL AIRFOILS AT 8° ANGLE OF ATTACK (EXPERIMENTAL DATA)
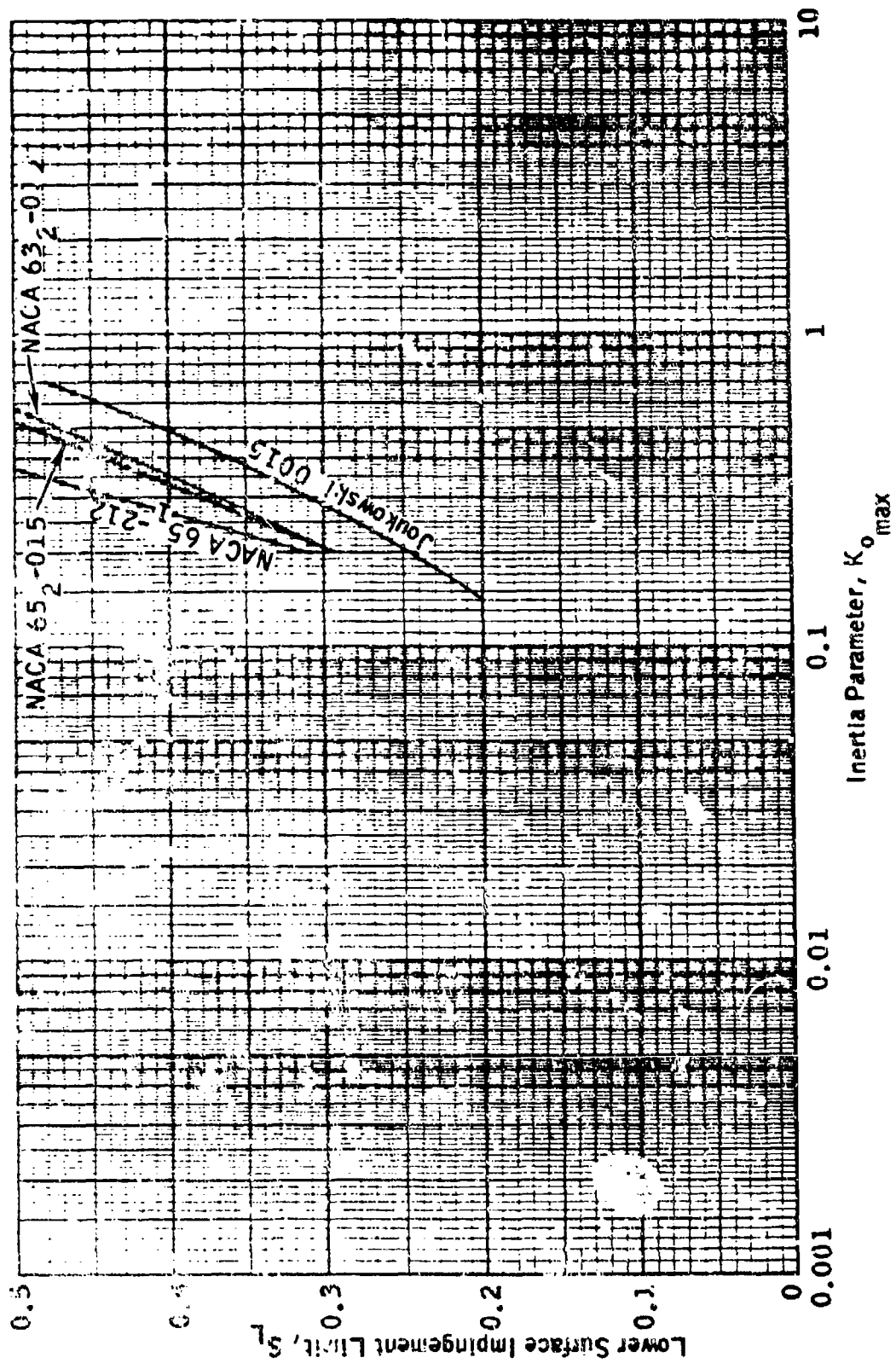
FIGURE 2-26. LOWER SURFACE IMPINGEMENT LIMITS FOR SEVERAL AIRFOILS AT 8° ANGLE OF ATTACK (EXPERIMENTAL DATA)
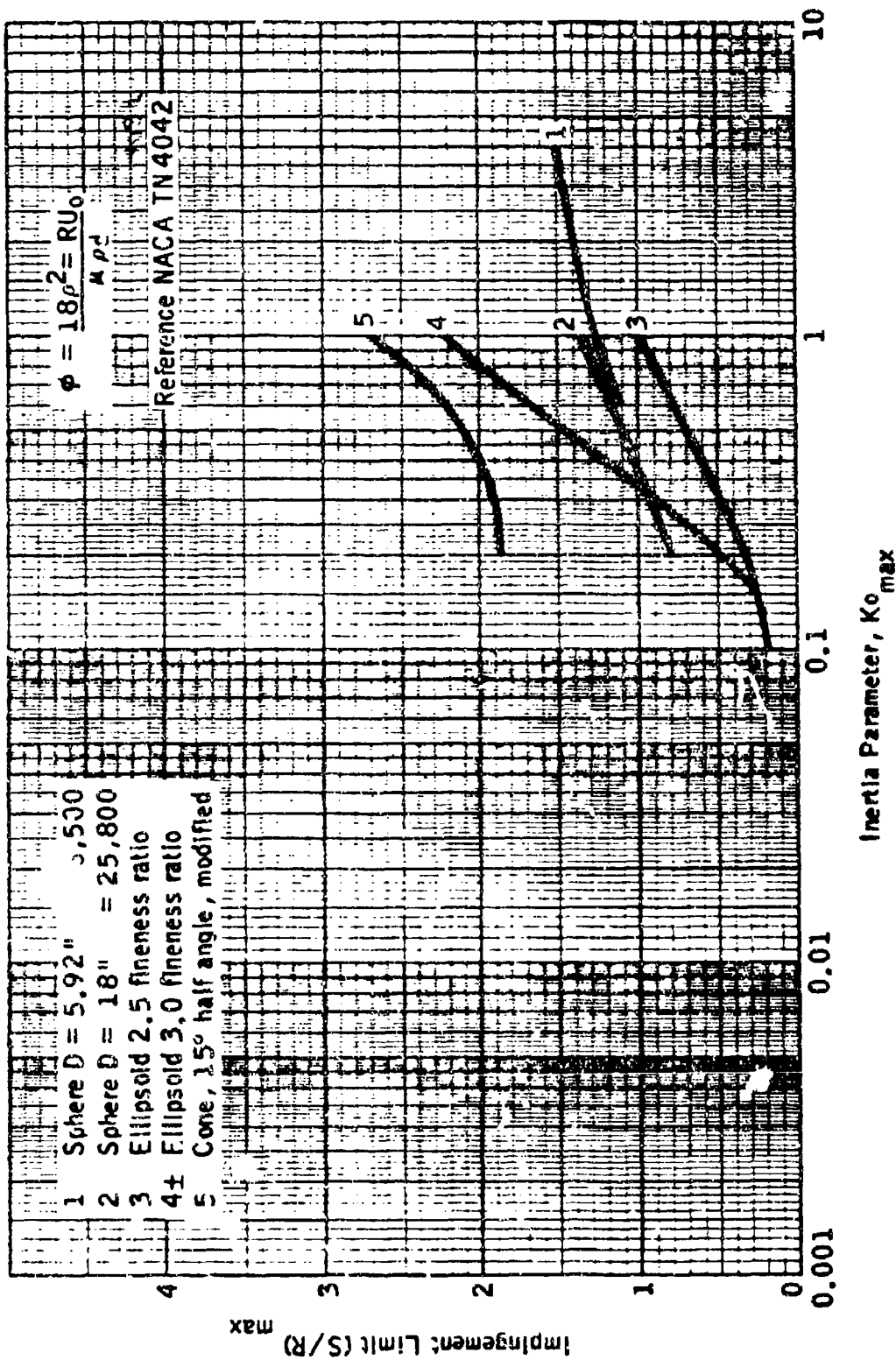
FIGURE 2-27. IMPINGEMENT LIMITS FOR SEVERAL BODIES OF REVOLUTION AT 0° ANGLE OF ATTACK
(EXPERIMENTAL DATA)
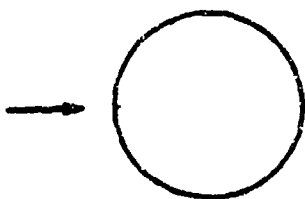
(A) 4 INCH CYLINDER
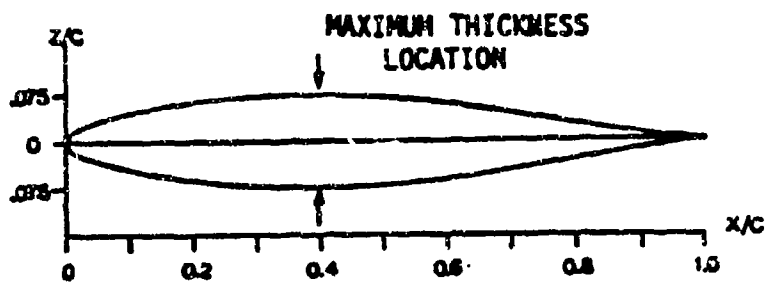
(B) 65₂015 AIRFOIL
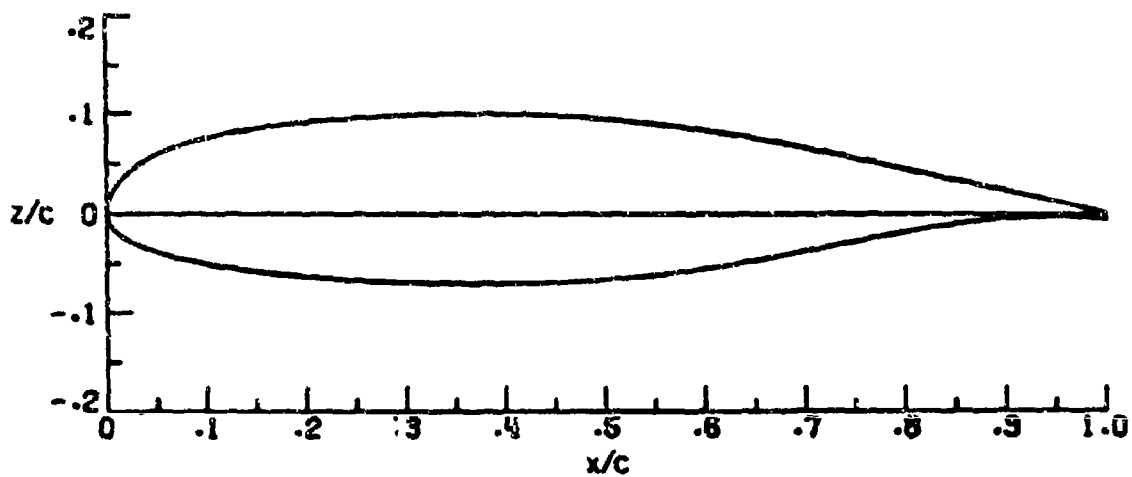
(C) MS(1)-0317 SUPERCRITICAL AIRFOIL

FIGURE 2-28. TWO-DIMENSIONAL "CLEAN" MODEL SECTIONS
(REFERENCE 2-15)

I 2-93

LARGE GLAZE ICE

RIME ICE

SMALL GLAZE ICE

1 INCH
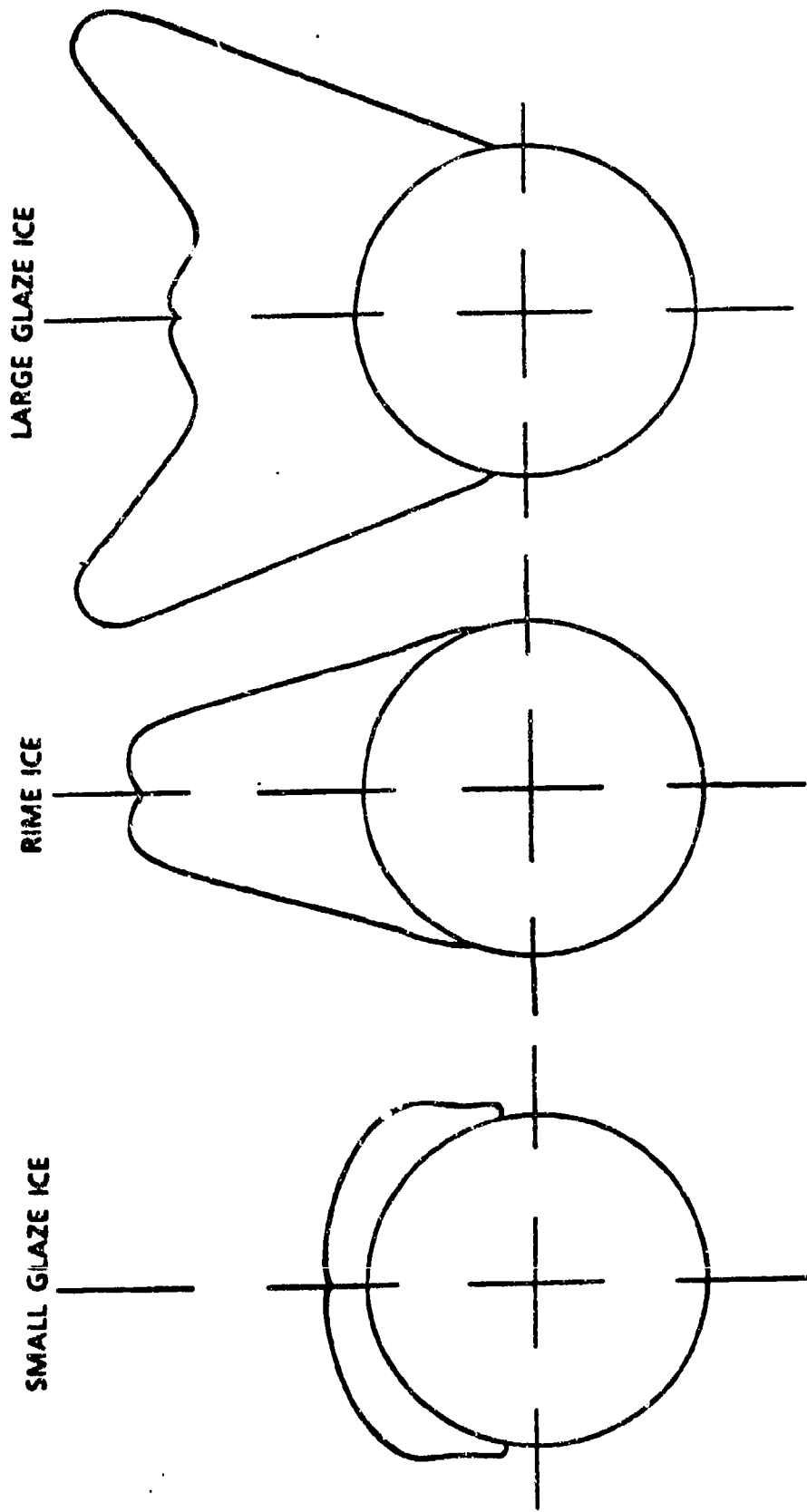
FIGURE 2-29. "ICED" CYLINDER SECTIONS (REFERENCE 2-15)
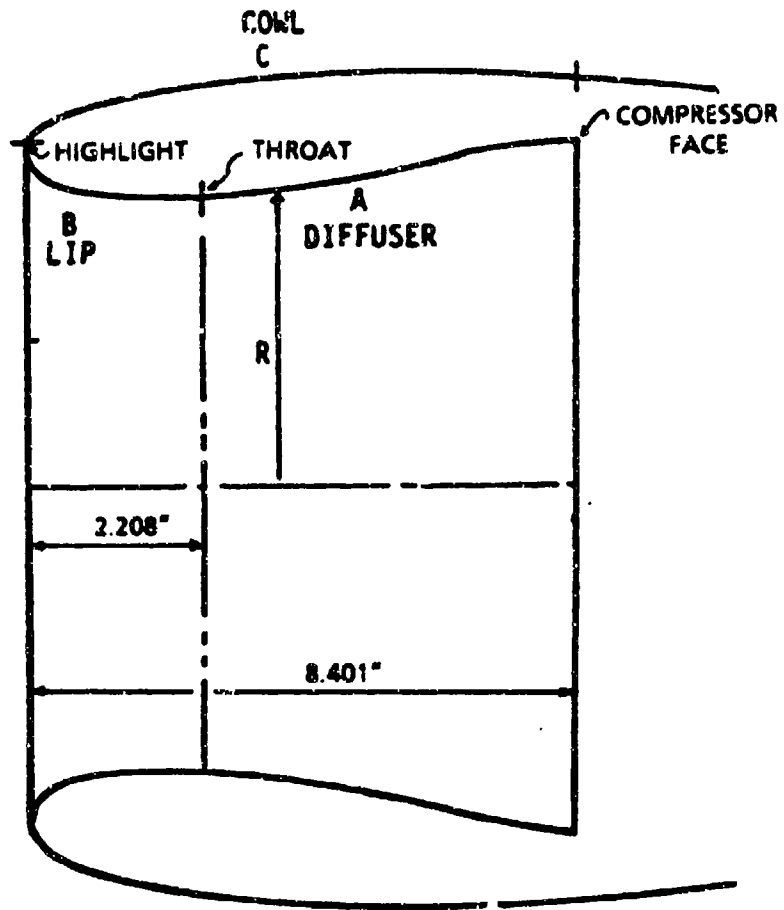
FIGURE 2-30. AXISYMMETRIC INLET (REFERENCE 2-15)

SEC A-A
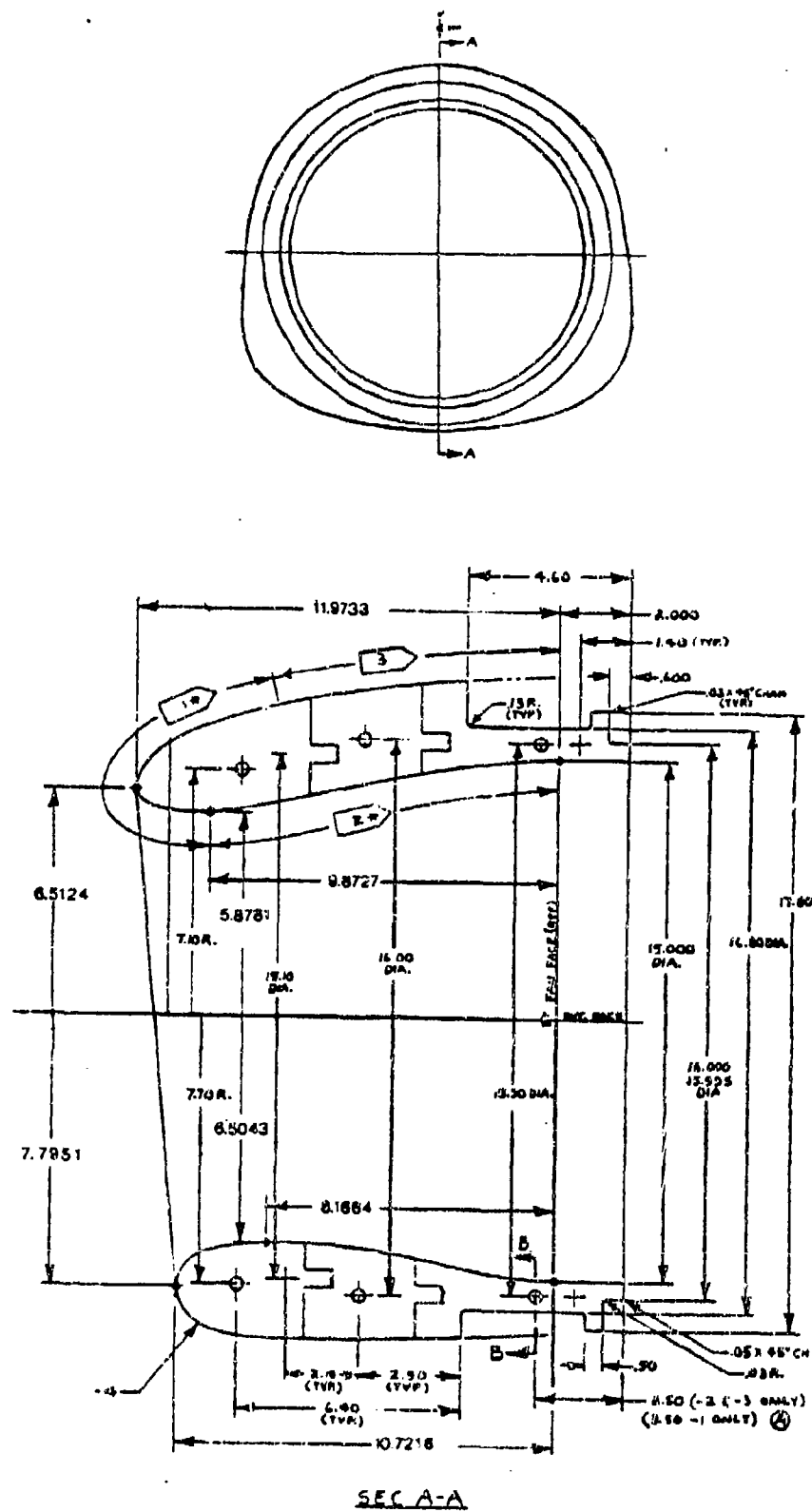
FIGURE 2-31.   BOEING 737-300 INLET (REFERENCE 2-15)

FIGURE 2-32. BLOTTER STRIP LOCATIONS ON BOEING 737-300 INLET
FOR $\alpha = 0°$ AND $\alpha = 15°$ TESTS (REFERENCE 2-15)

I 2-97

TEST RUN ID: 091585-5C.6C8-4IN-CYL 4 INCH CYLINDER
TRUE AIR SPEED   =   81.02 m/s   (181.22 mph)
TUNNEL TOTAL TEMP   =   8.2 C   (46.7 F)
TUNNEL STATIC PRESSURE   =   95.65 kPa   (13.88 psia)
AIR/WATER PRESSURE RATIO   =   0.80
COLLECTOR EFFICIENCY   =   0.86
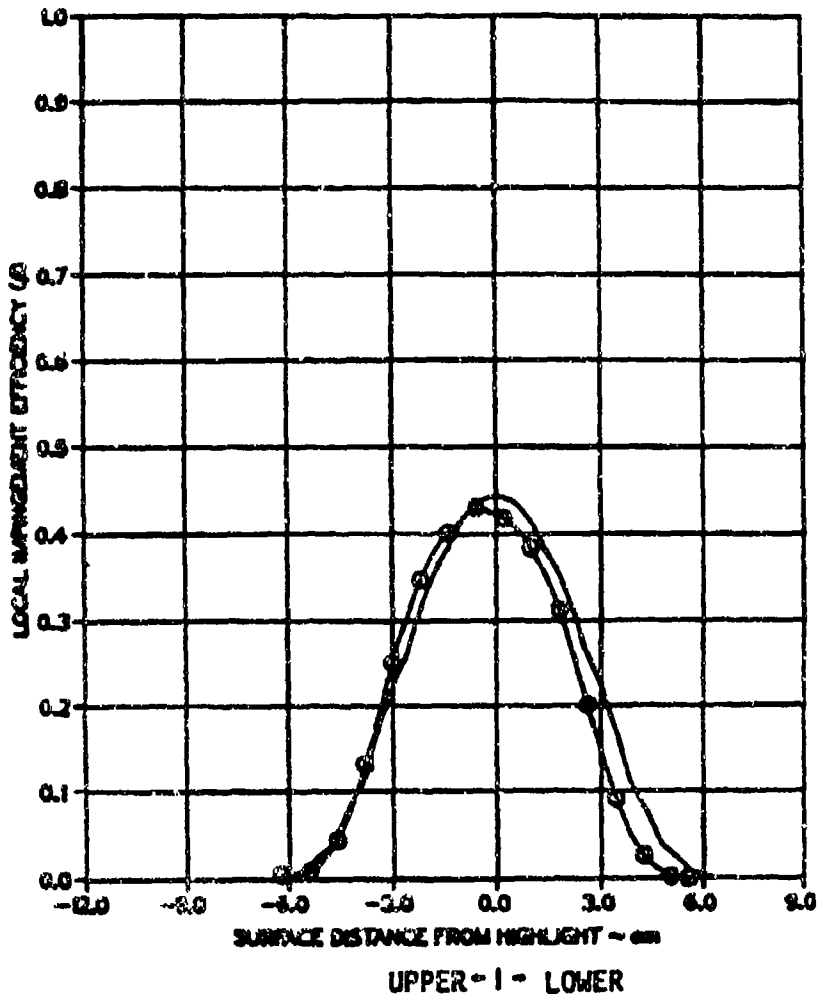
MVD = 16.45 MICRONS

FIGURE 2-33.   IMPINGEMENT EFFICIENCY CURVES (EXPERIMENTAL AND
               COMPUTATIONAL) FOR A 4-INCH CYLINDER (REFERENCE 2-15)

TRUE AIR SPEED   =   81.55 m/s   (182.40 mph)
TUNNEL TOTAL TEMP   =   9.4 C   (49.0 F)
TUNNEL STATIC PRESSURE   =   94.48 kPa   (13.71 psia)
AIR/WATER PRESSURE RATIO   =   0.80
COLLECTOR EFFICIENCY   =   0.86

O   TEST DATA
―― THEORY
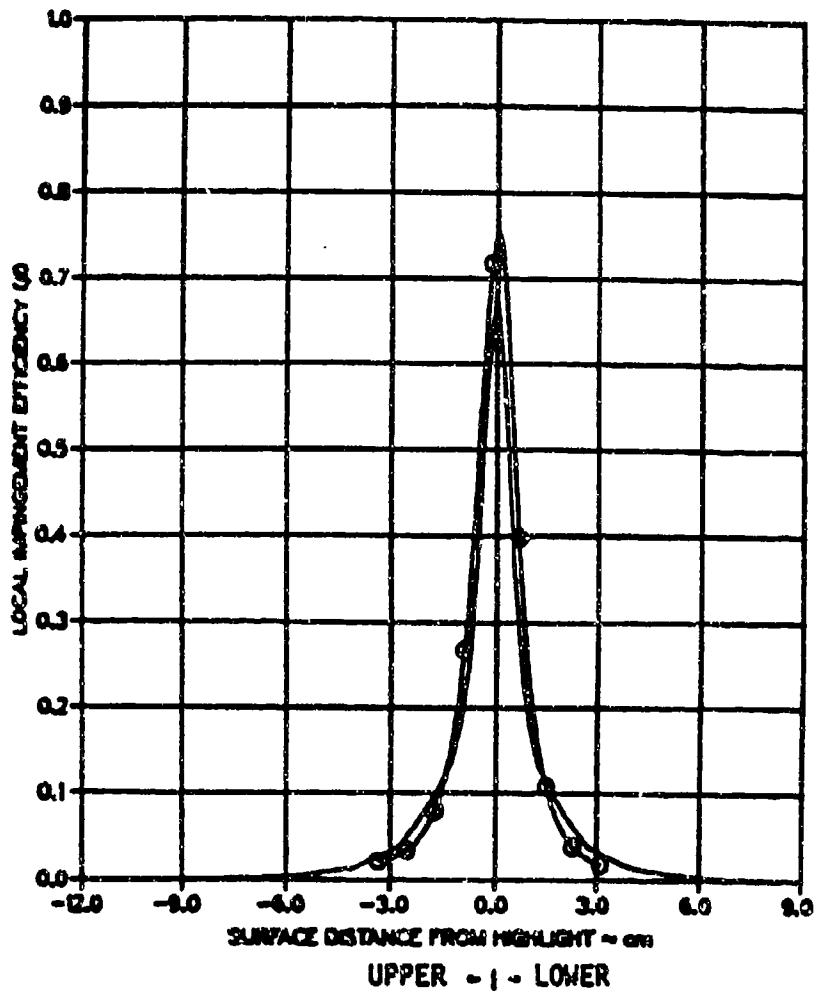
MVD = 16.45 MICRONS

FIGURE 2-34.   IMPINGEMENT EFFICIENCY CURVES (EXPERIMENTAL AND
COMPUTATIONAL) FOR A NACA 65$_2$015 AIRFOIL AT $\alpha = 0°$
(REFERENCE 2-15)

TEST RUN ID: 092685-4,5,6%C-SUP-0 SUPERCRITICAL AIRFOIL
TRUE AIR SPEED   = 81.13 m/s   (181.47 mph)
TUNNEL TOTAL TEMP   = 9.8 C   (49.6 F)
TUNNEL STATIC PRESSURE   = 94.48 kPa   (13.71 psia)
AIR/WATER PRESSURE RATIO   = 0.80
COLLECTOR EFFICIENCY   = 0.86

O TEST DATA
——— THEORY
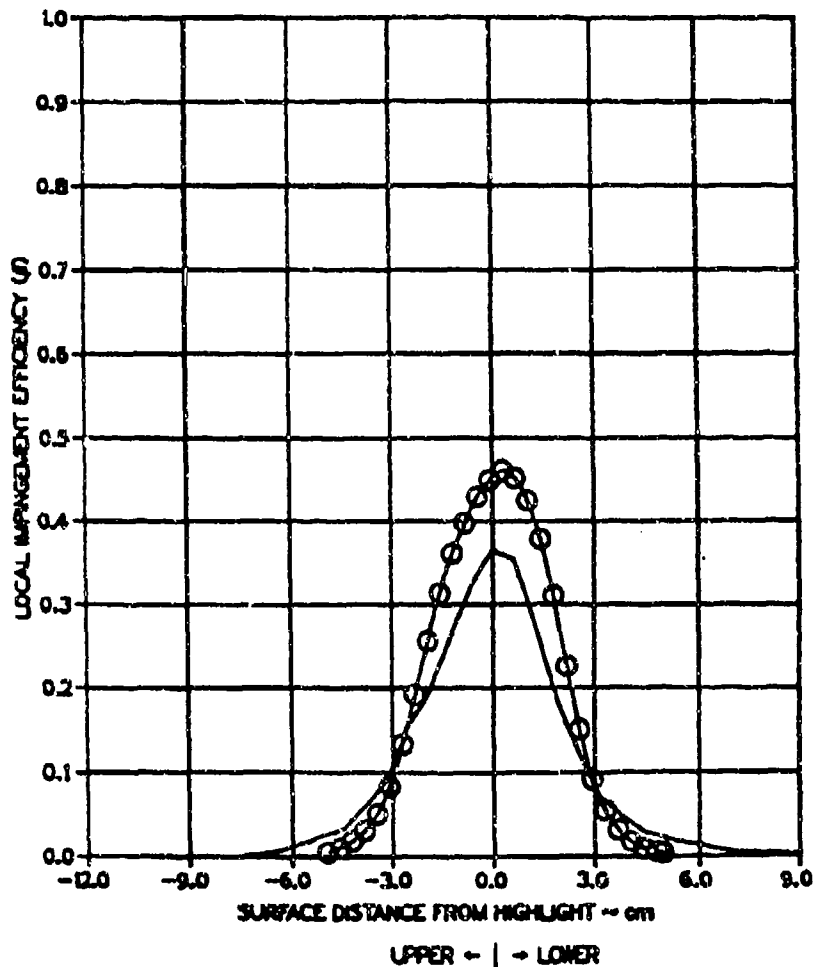
MVD = 16.45 MICRONS

FIGURE 2-35. IMPINGEMENT EFFICIENCY CURVES (EXPERIMENTAL AND
COMPUTATIONAL) FOR A MS(1)-0317 AIRFOIL AT α = 0°
(REFERENCE 2-15)

I 2-100
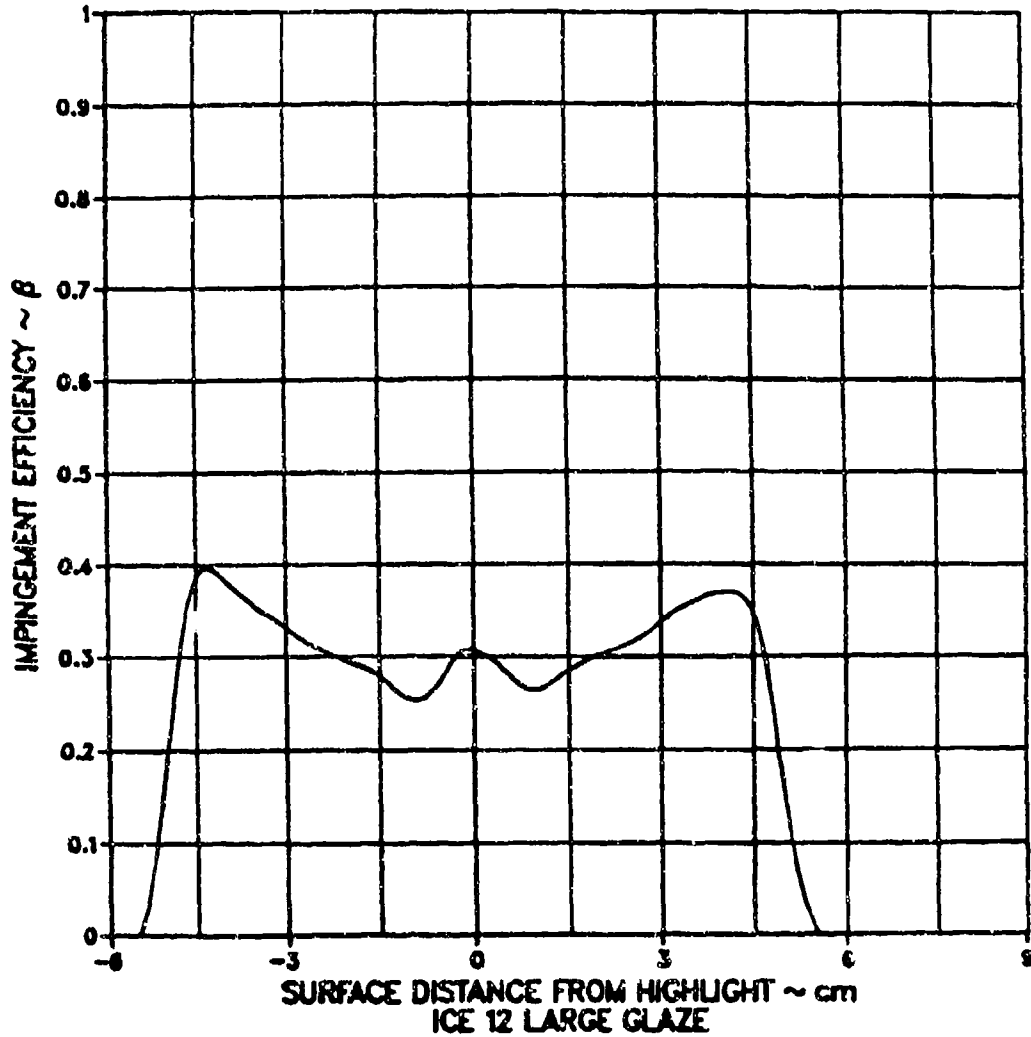
MVD = 20.36 MICRONS

FIGURE 2-36.   IMPINGEMENT EFFICIENCY CURVE (EXPERIMENTAL) FOR A
                2-INCH CYLINDER WITH GLAZE ICE (REFERENCE 2-15)
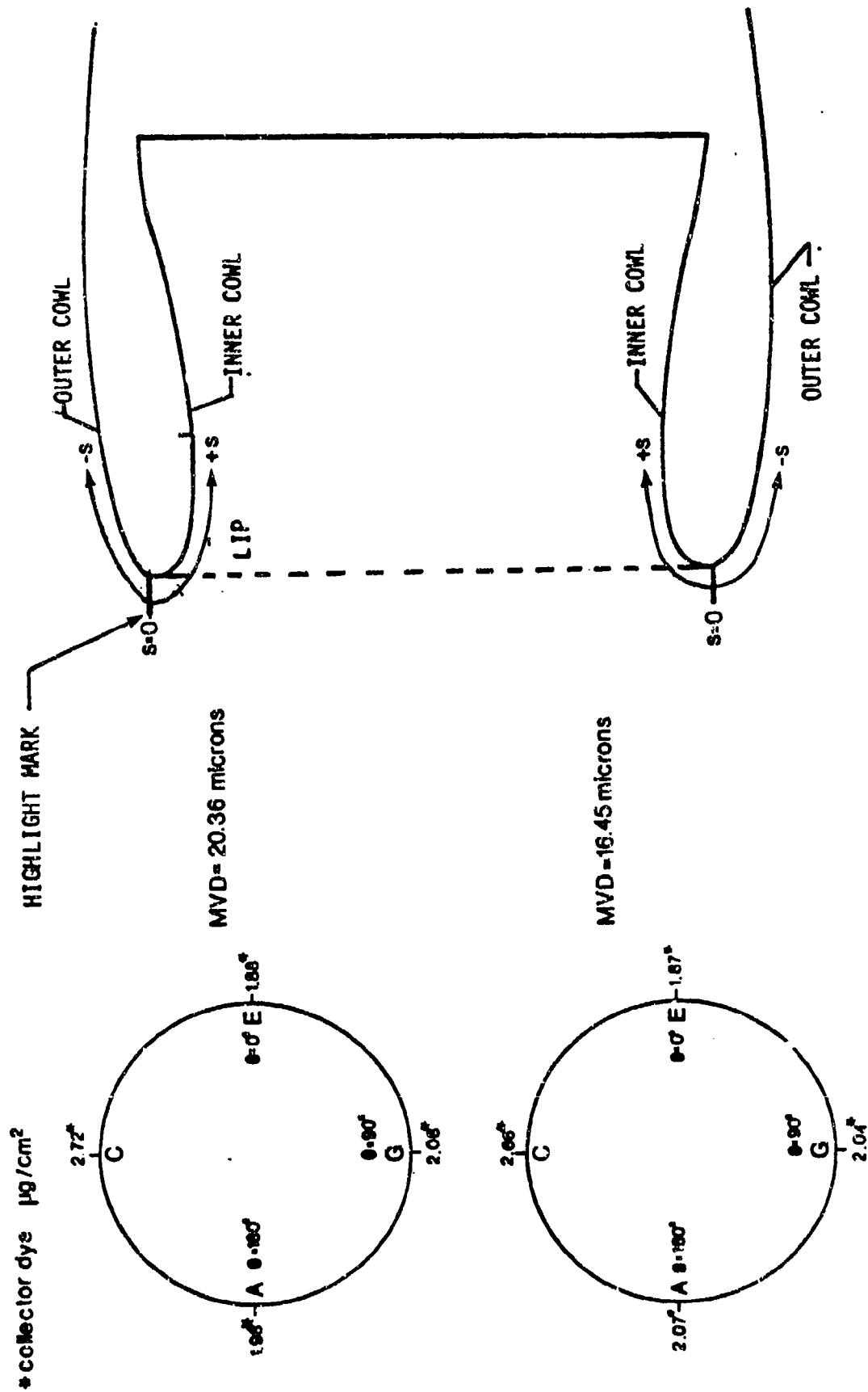
FIGURE 2-37. BLOTTER STRIP LOCATIONS, REFERENCE COLLECTOR DYE MASS, HIGHLIGHT MARK AND SURFACE DISTANCE CONVENTION FOR AXISYMETRIC INLET AT α = 0° (REFERENCE 2-15)

* COLLECTOR DYE μg/cm^2
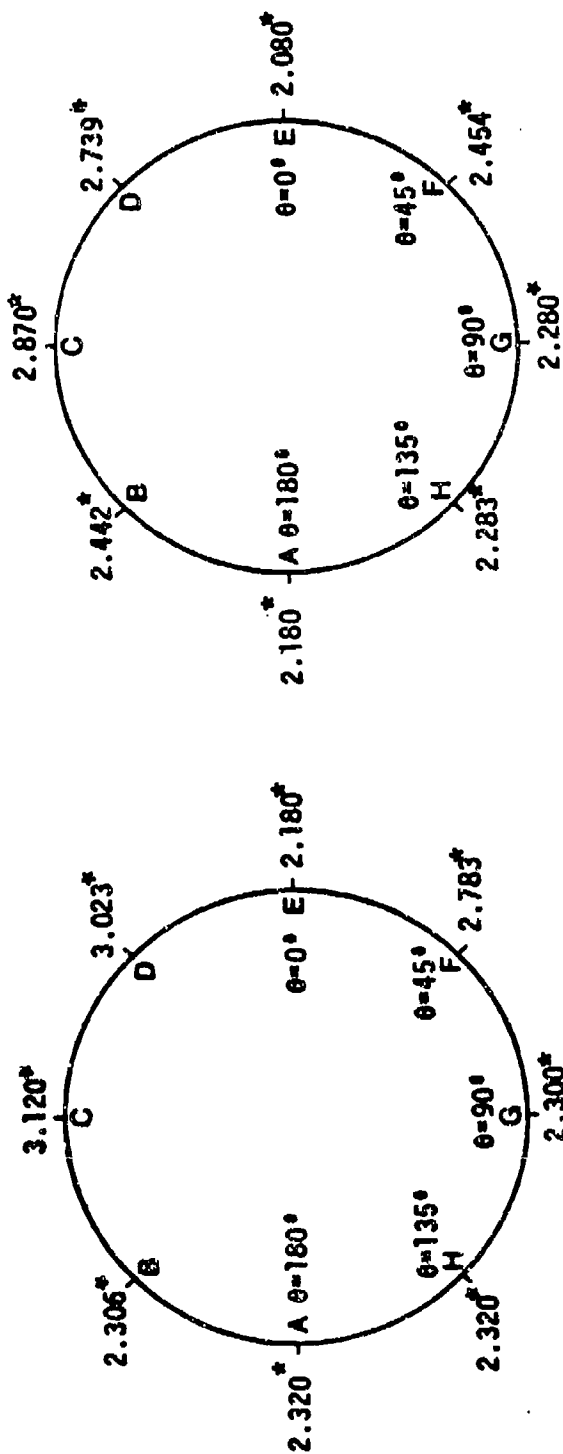
MVD = 16.45 microns

MVD = 20.36 microns

FIGURE 2-38. BLOTTER STRIP LOCATIONS FOR AXISYMMETRIC INLET AT α = 15 (REFERENCE 2-15)

TEST RUN ID: 082185-1,2,3E-AXI-15 AXISYMMETRIC INLET
TRUE AIR SPEED   = 76.98 m/s   (172.19 mph)
TUNNEL TOTAL TEMP   = 10.4 C   (50.7 F)
TUNNEL STATIC PRESSURE   = 95.44 kPa   (13.85 psia)
AIR/WATER PRESSURE RATIO   = 0.65
COLLECTOR EFFICIENCY   = 0.89

☐ TEST DATA
── THEORY

17A

LOCAL IMPINGEMENT EFFICIENCY (β)

SURFACE DISTANCE FROM HIGHLIGHT ~ cm

(POSITIVE S VALUES ON INNER SURFACE)
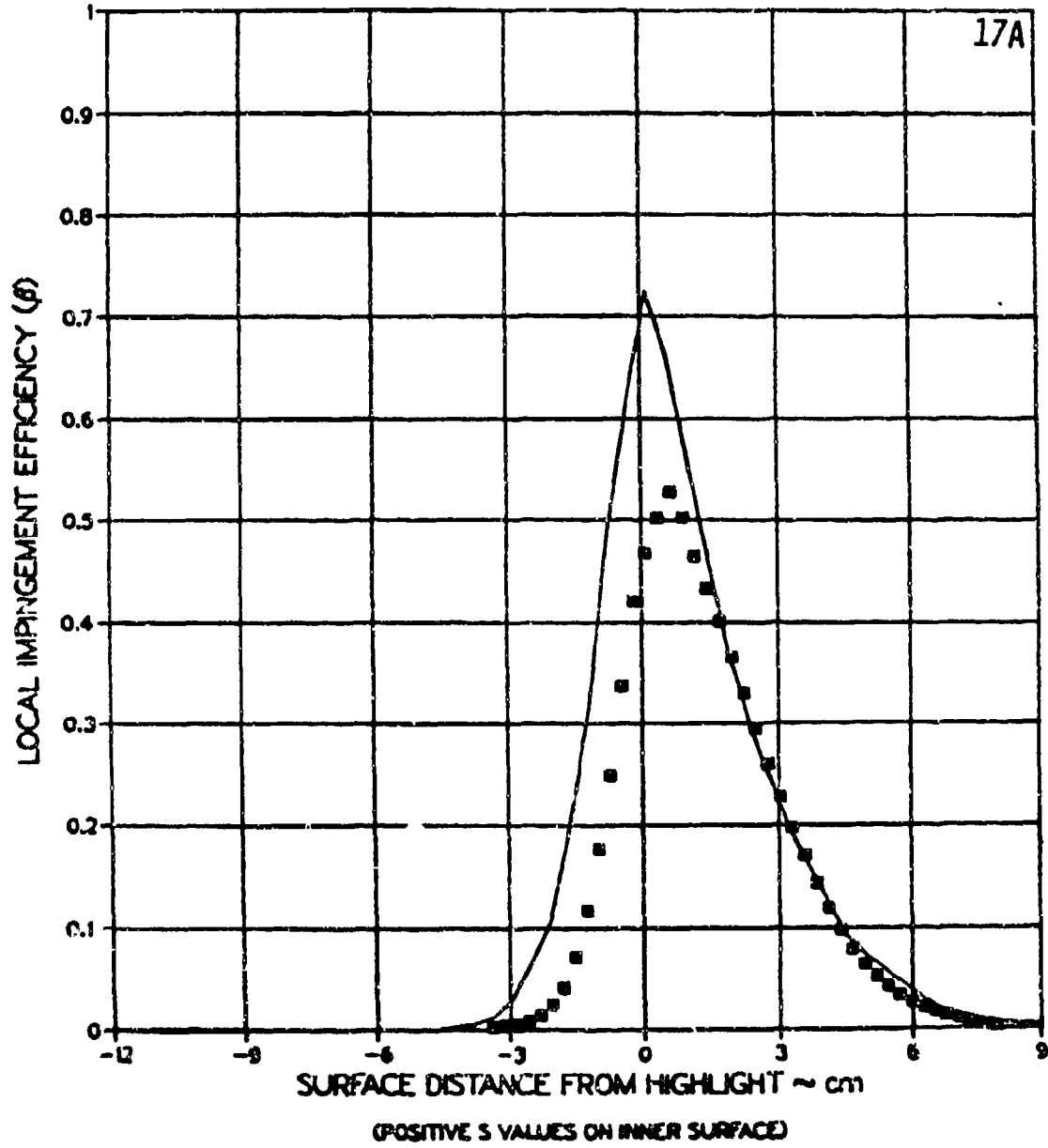
(A1) MVD = 20.36 MICRONS,   MASS FLOW = 22.96 LBM/SEC.   θ = 0°

FIGURE 2-39. IMPINGEMENT EFFICIENCY CURVES (EXPERIMENTAL AND
COMPUTUTATIONAL) AT θ = 0° FOR AXISYMMETRIC INLET AT
α = 15° (REFERENCE 2-15)

I 2-104
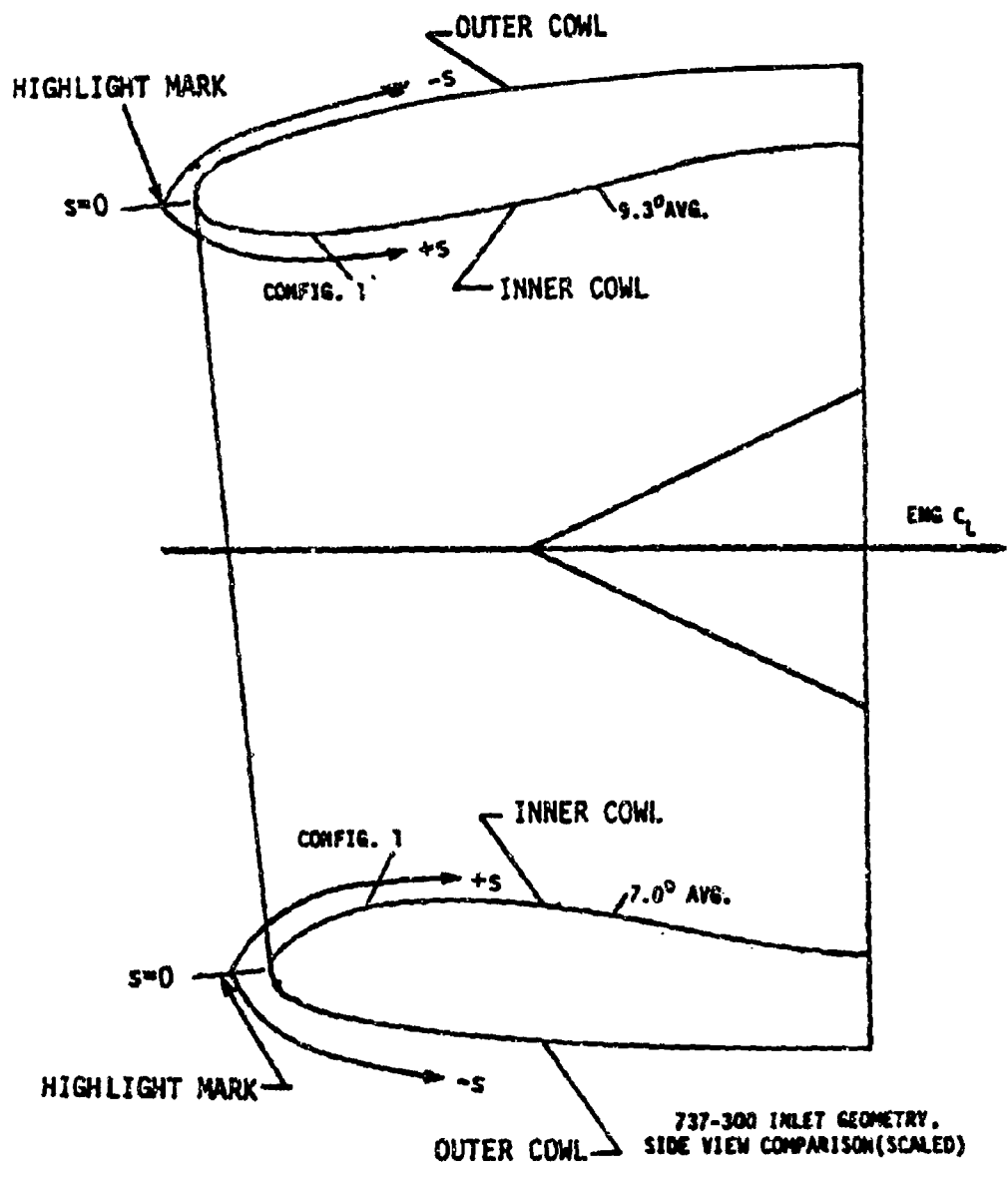
FIGURE 2-40. HIGHLIGHT MARK AND SURFACE DISTANCE CONVENTION FOR
BOEING 737-300 INLET (REFERENCE 2-15)

I 2-105
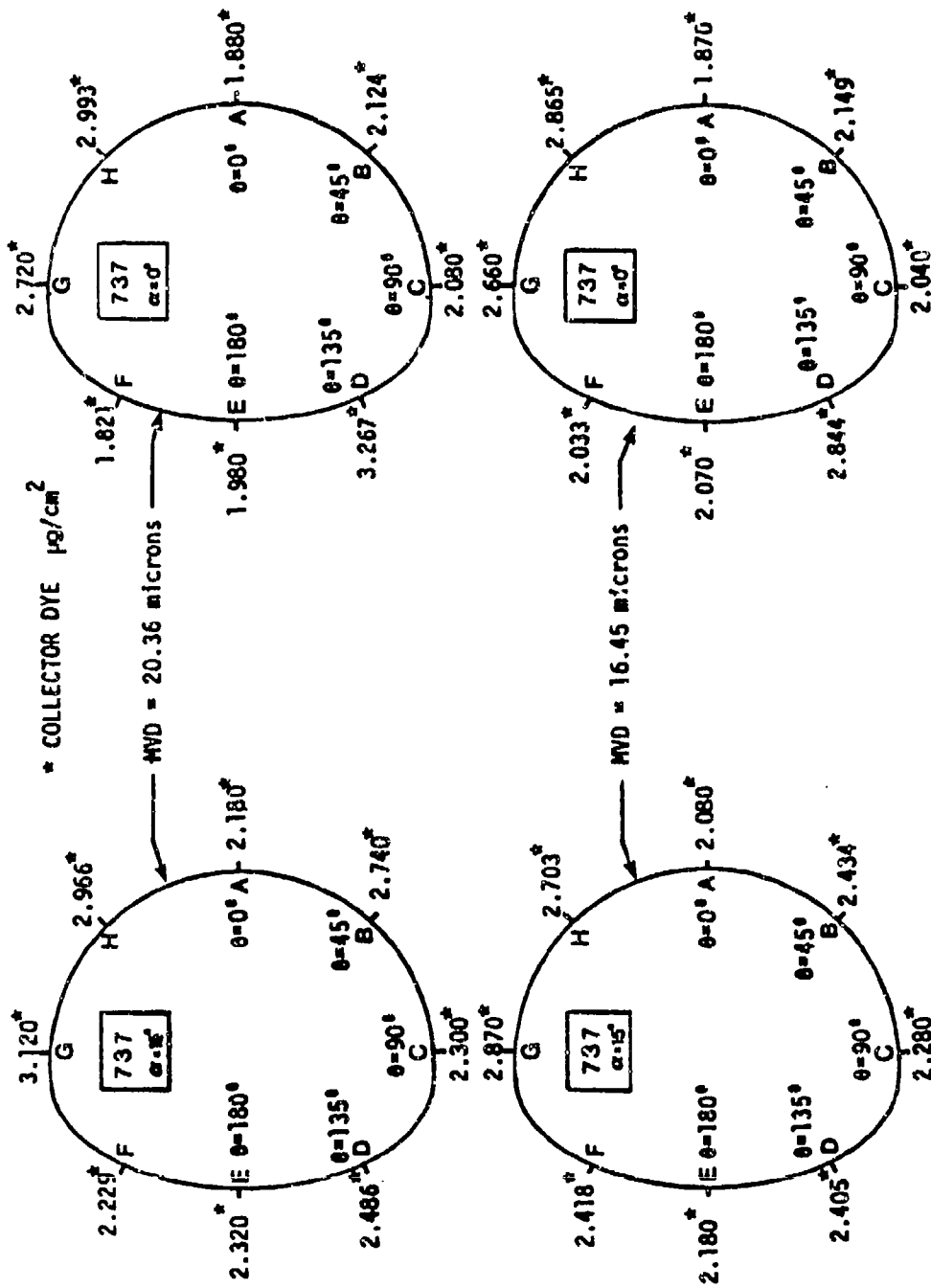
FIGURE 2-41. BLOTTER STRIP LOCATIONS AND REFERENCE COLLECTOR DYE MASS FOR BOEING 737-300 INLET (REFERENCE 2-15)

MVD = 20.36 MICRONS,   MASS FLOW = 22.96 LBM/SEC

FIGURE 2-42.   IMPINGEMENT EFFICIENCY CURVES (EXPERIMENTAL AND
COMPUTATIONAL) AT θ = 0° FOR BOEING 737-300 INLET
AT α = 0° (REFERENCE 2-15)
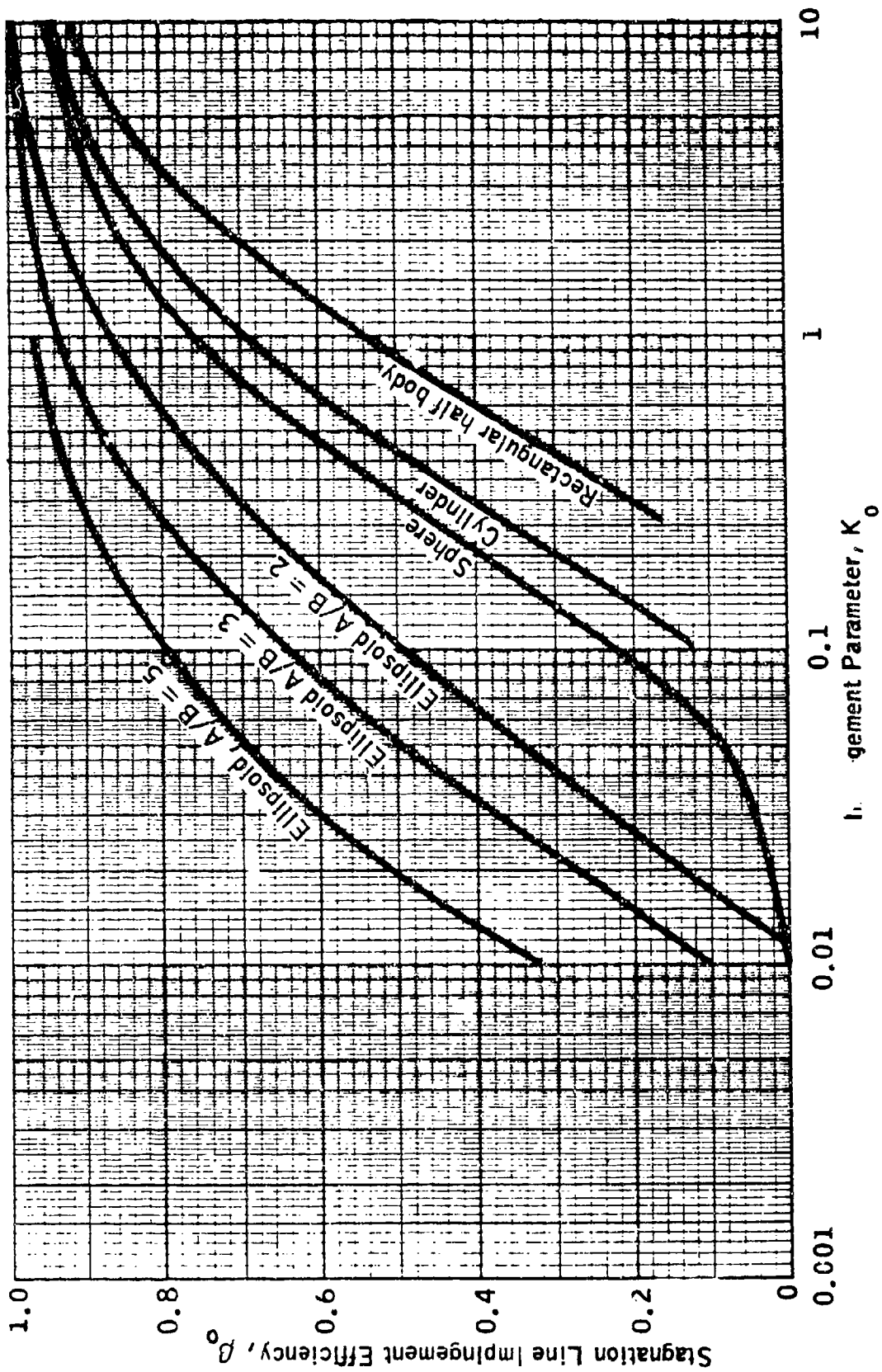
FIGURE 2-43. IMPINGEMENT EFFICIENCY AT THE STAGNATION LINE FOR SEVERAL BODIES
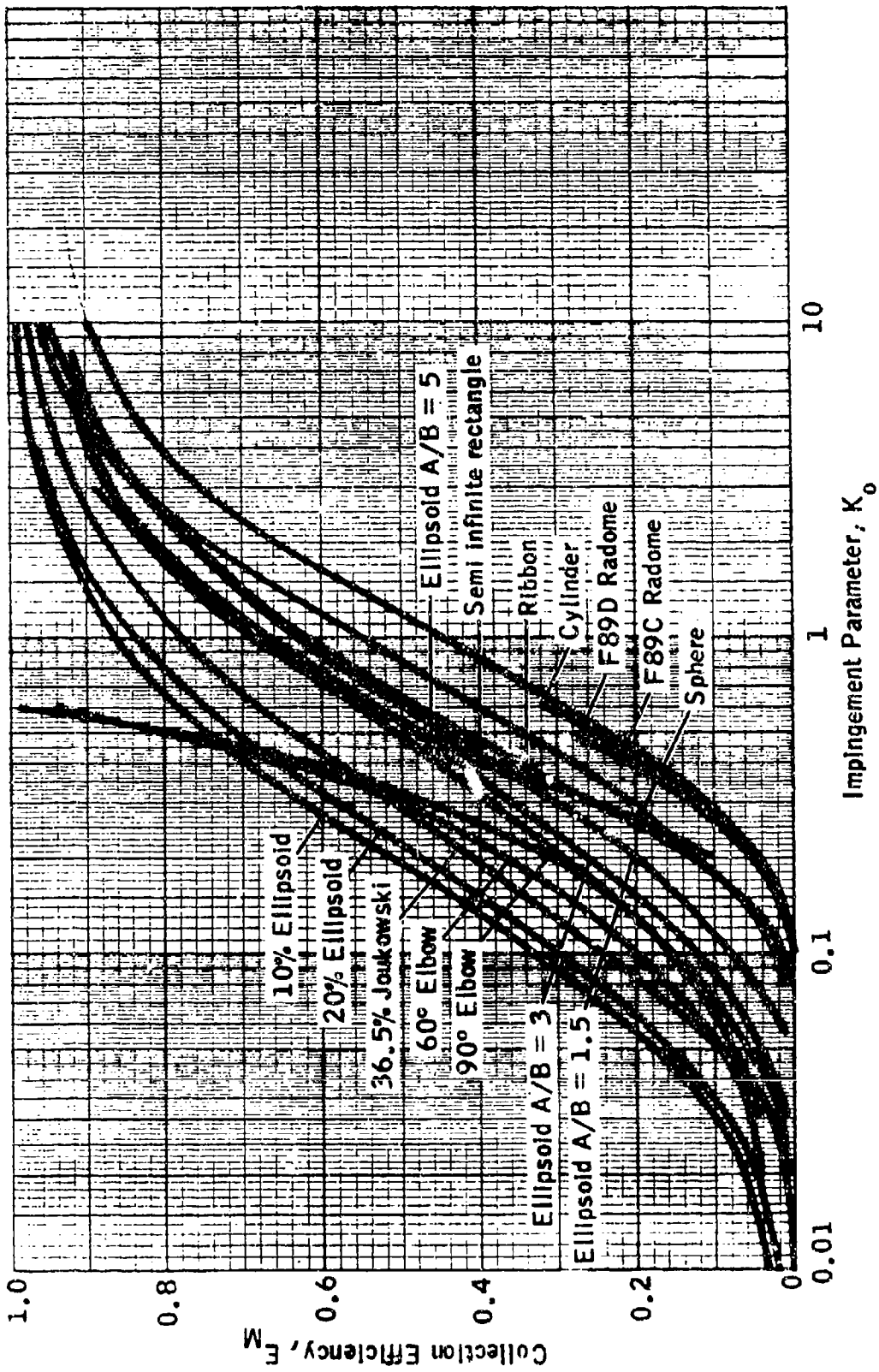
FIGURE 2-44. COLLECTION EFFICIENCY VERSUS K_o FOR GEOMETRIC BODIES - THEORETICAL DATA FOR 0° ANGLE OF ATTACK
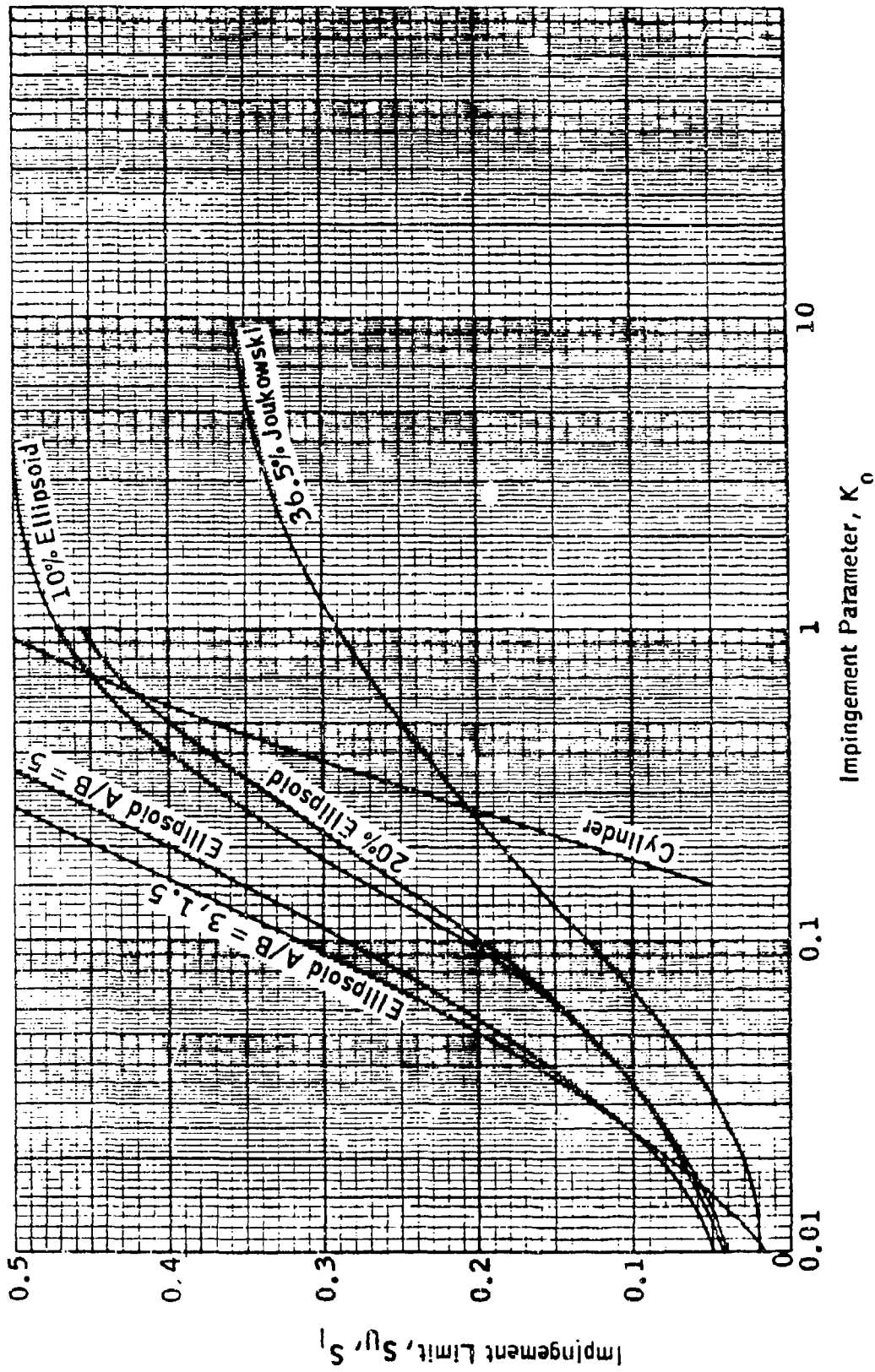
FIGURE 2-45. IMPINGEMENT LIMITS ON SEVERAL GEOMETRIC SHAPES AT 0° ANGLE OF ATTACK (THEORETICAL DATA)
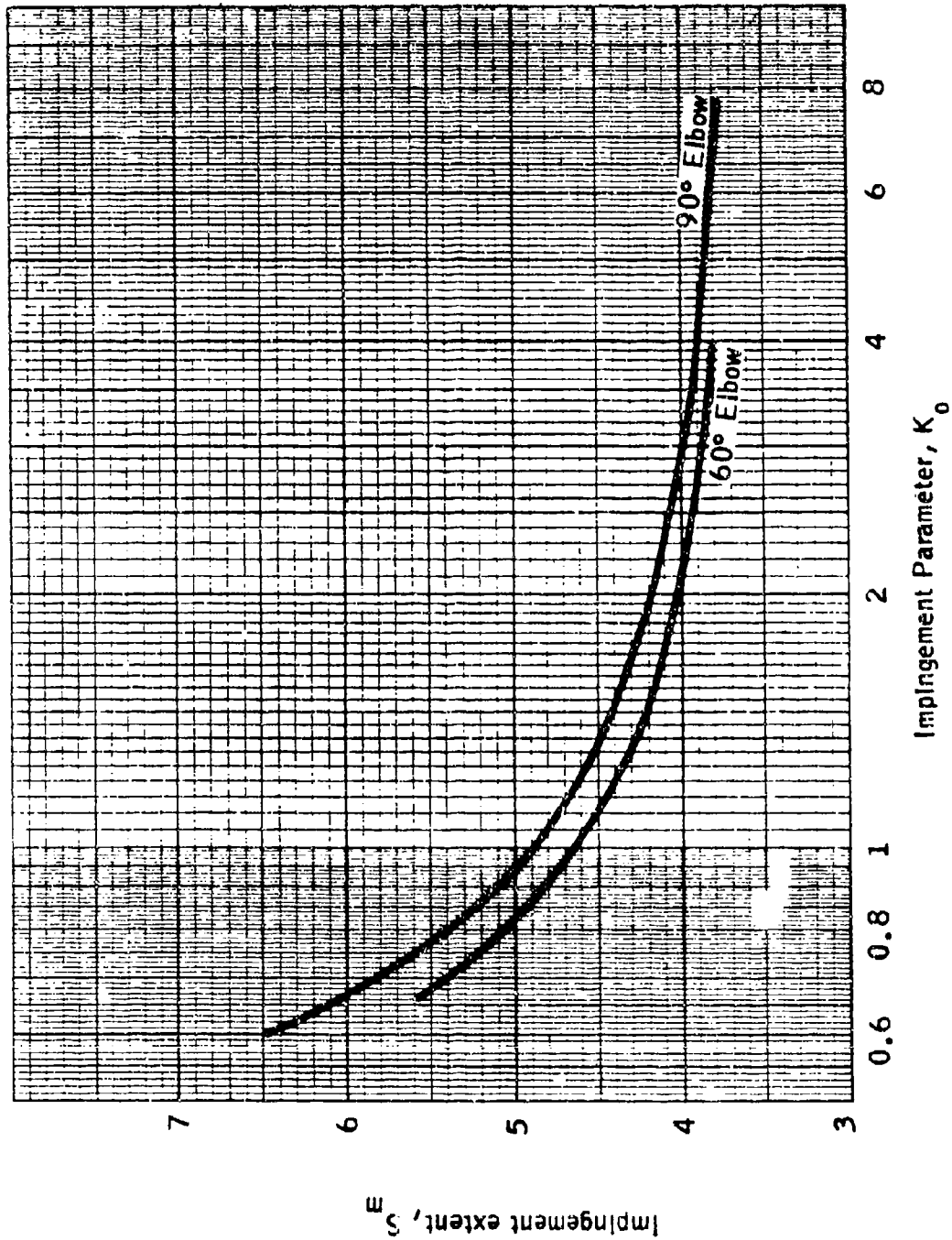
FIGURE 2-46. MAXIMUM EXTENT OF DROPLET IMPINGEMENT INSIDE 60° AND 90° ELBOWS (FROM NACA TN 2999 AND 3770)

NACA 0012   Radius of curvature: 1.58 % of chord   Thickness: 12% of chord

NACA 23015   Radius of curvature: 2.48 % of chord   Thickness: 15% of chord
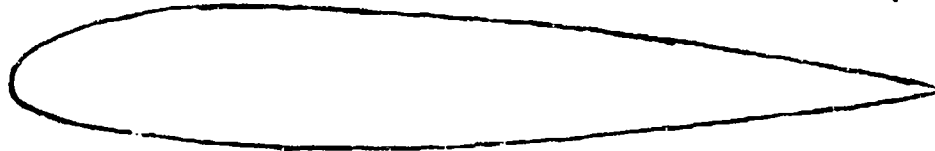
NACA 63-415   Radius of curvature: 1.594 % of chord   Thickness: 15% of chord
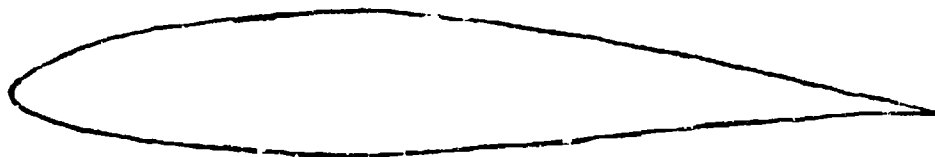
NACA 64-109   Radius of curvature: 0.579 % of chord   Thickness: 9% of chord
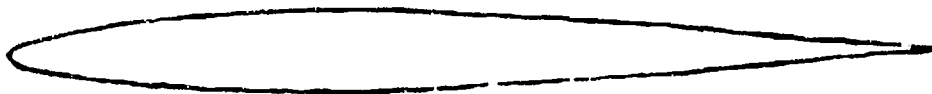
NASA LS(1)-0417   Radius of curvature: 2.0243 % of chord   Thickness: 17% of chord

NACA MS(1)-0313   Radius of curvature: 1.5928 % of chord   Thickness: 13% of chord

FIGURE 2-47.   AIRFOIL PROFILES FOR IMPINGEMENT PARAMETER PLOTS IN
               FIGURES 2-48 THROUGH 2-59

I 2-112
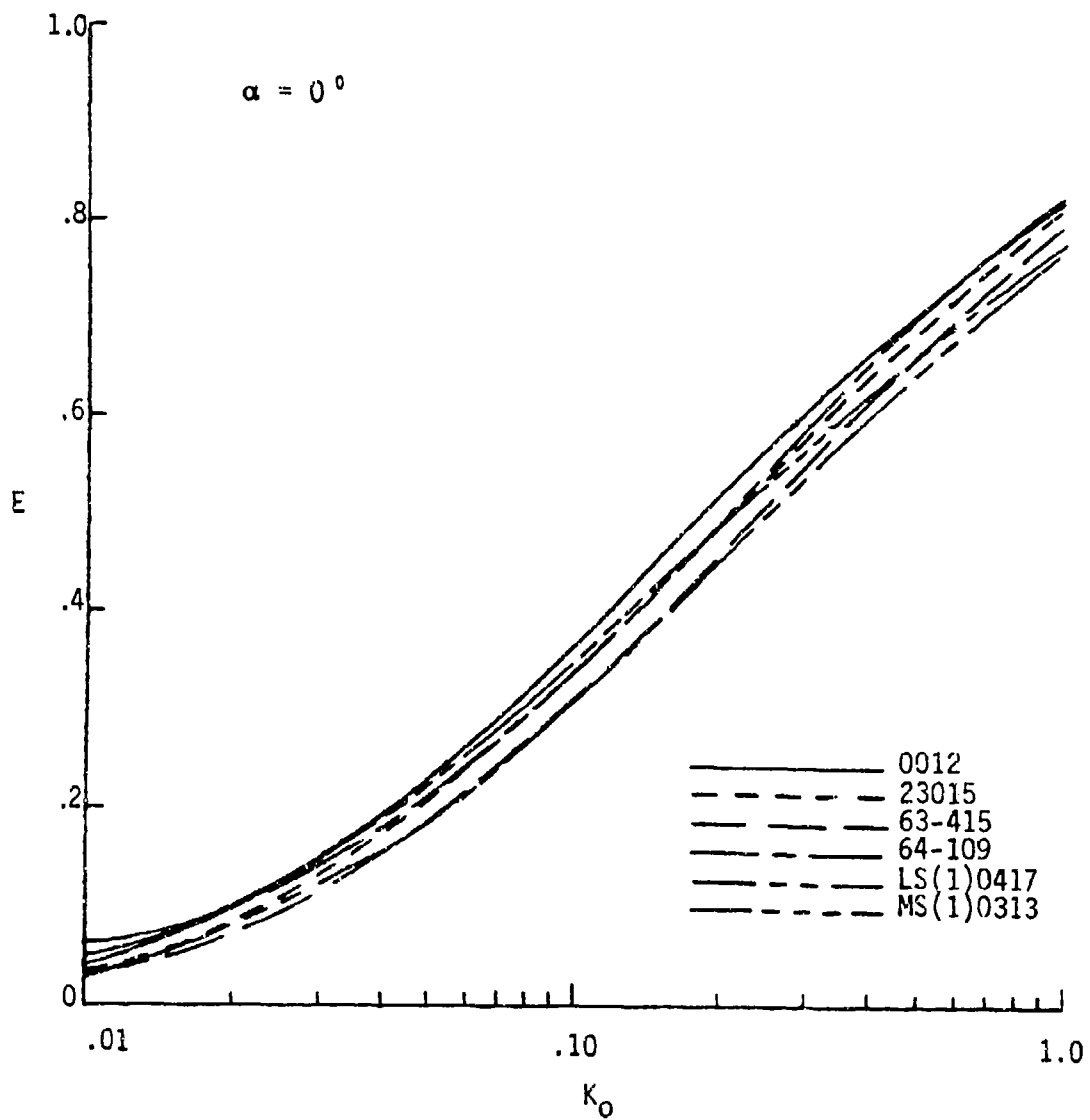
FIGURE 2-48. THEORETICAL DATA ON THE COLLECTION EFFICIENCY OF
SEVERAL AIRFOILS ($\alpha = 0°$)

I 2-113
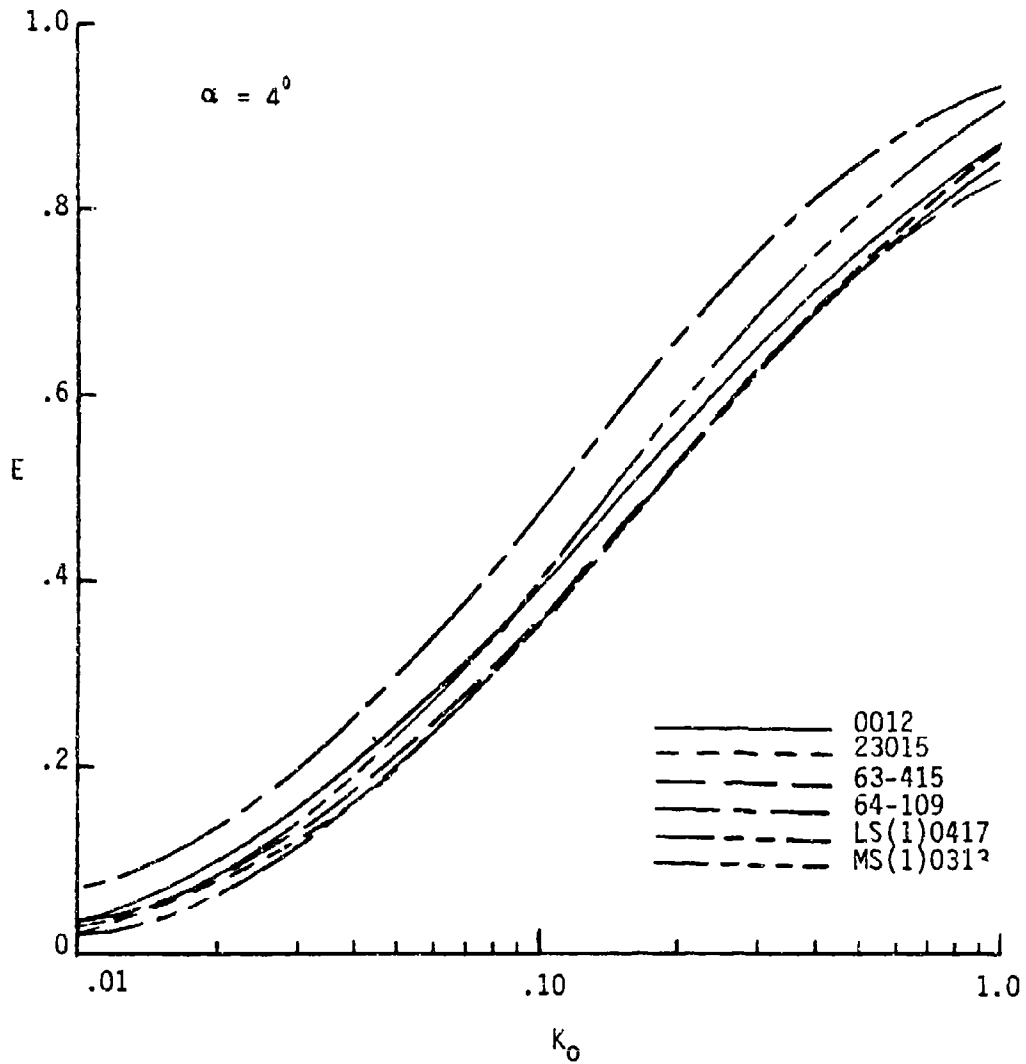
FIGURE 2-49.   THEORETICAL DATA ON THE COLLECTION EFFICIENCY OF
SEVERAL AIRFOILS ($\alpha = 4°$)
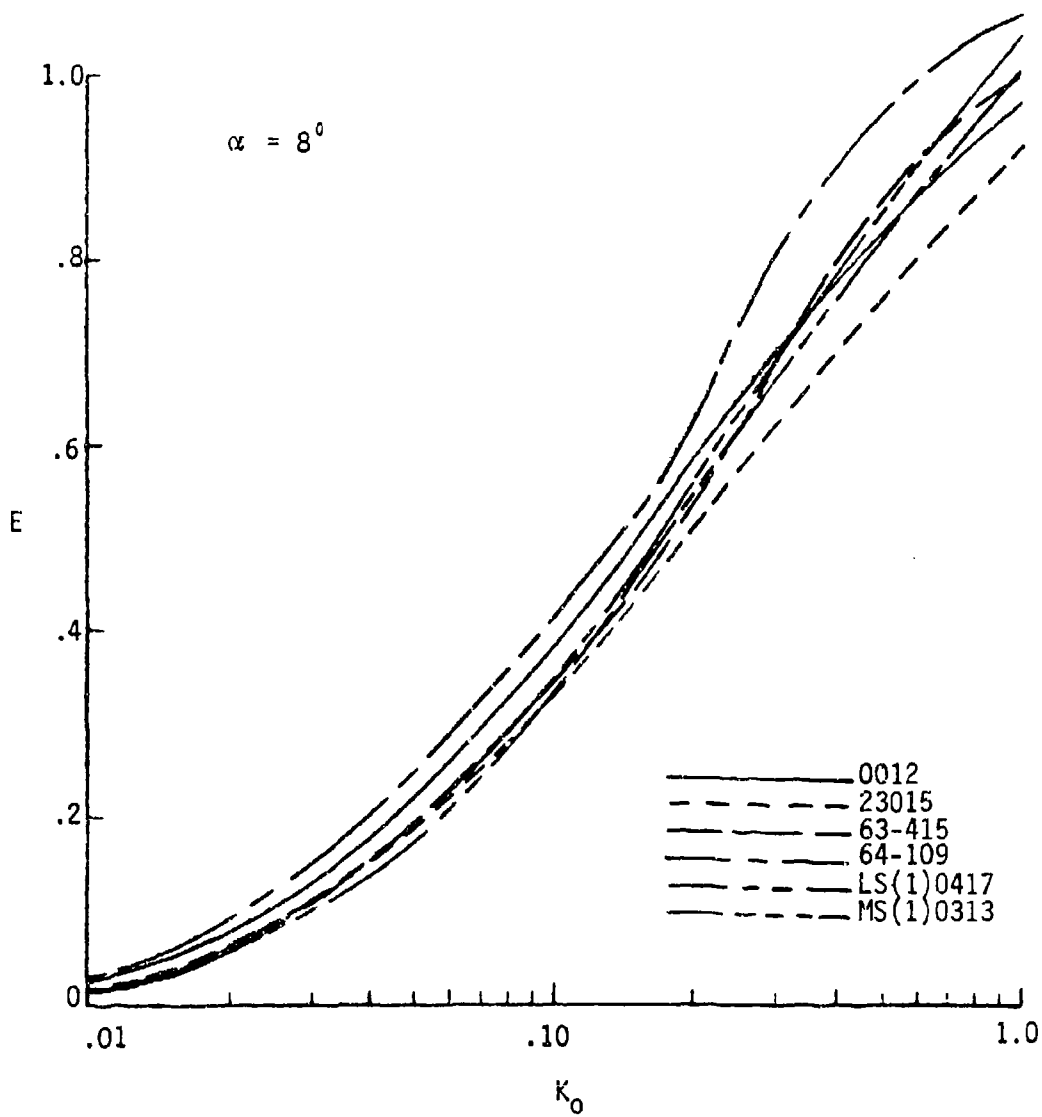
FIGURE 2-50.   THEORETICAL DATA ON THE COLLECTION EFFICIENCY OF
SEVERAL AIRFOILS ($\alpha = 8°$)

I 2-115
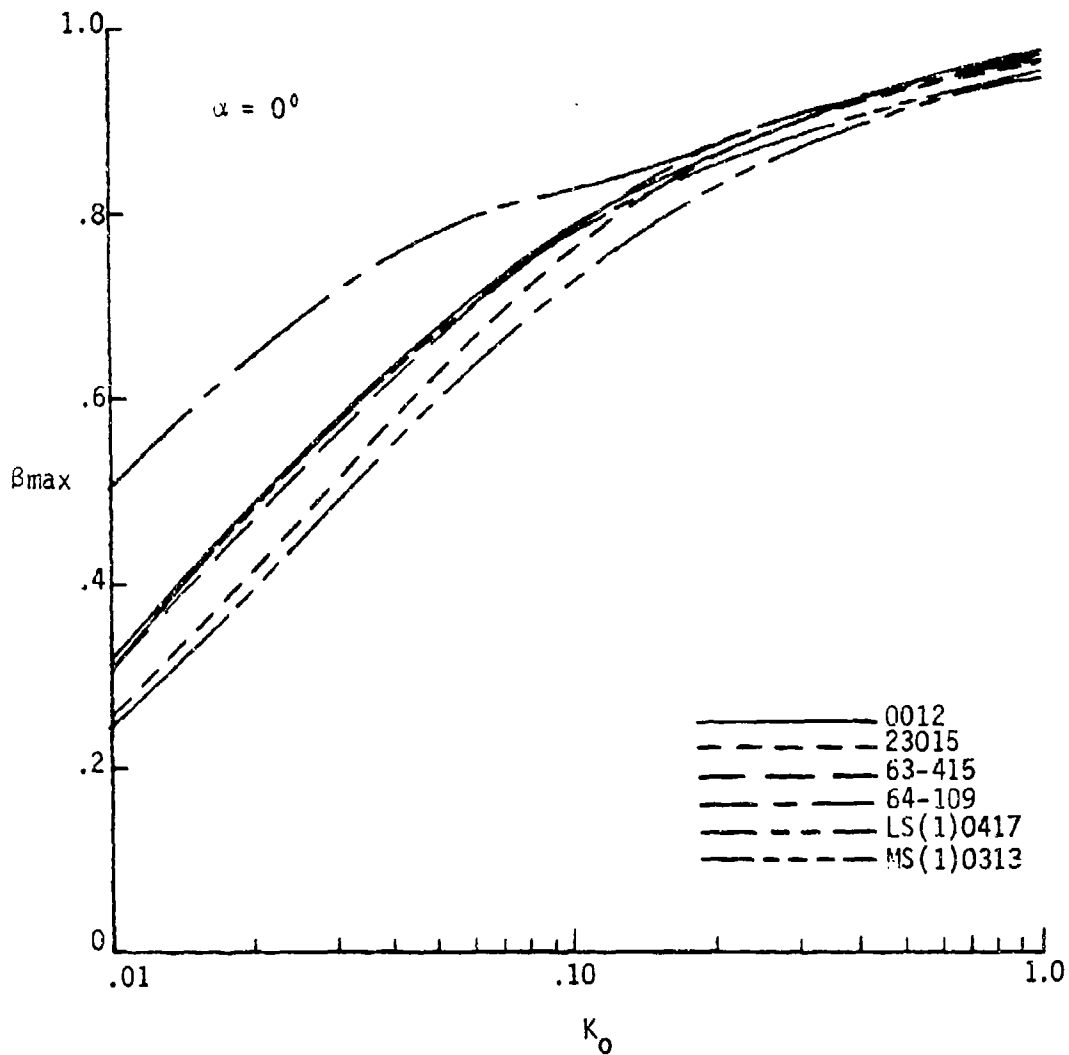
FIGURE 2-51. THEORETICAL DATA ON THE MAXIMUM IMPINGEMENT
EFFICIENCY OF SEVERAL AIRFOILS ($\alpha = 0°$)

I 2-116
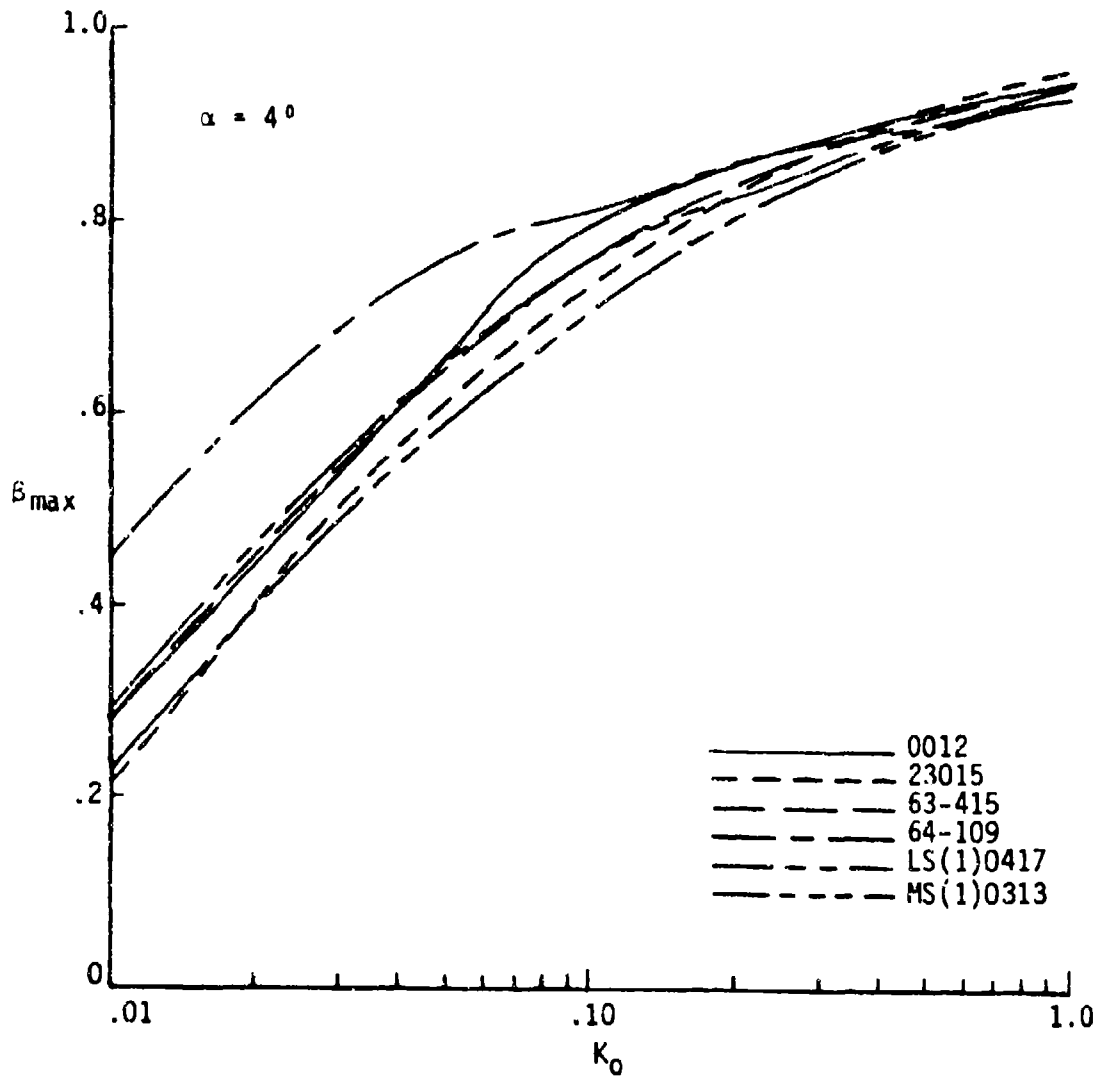
FIGURE 2-52. THEORETICAL DATA ON THE MAXIMUM IMPINGEMENT
EFFICIENCY OF SEVERAL AIRFOILS ($\alpha = 4°$)

I 2-117
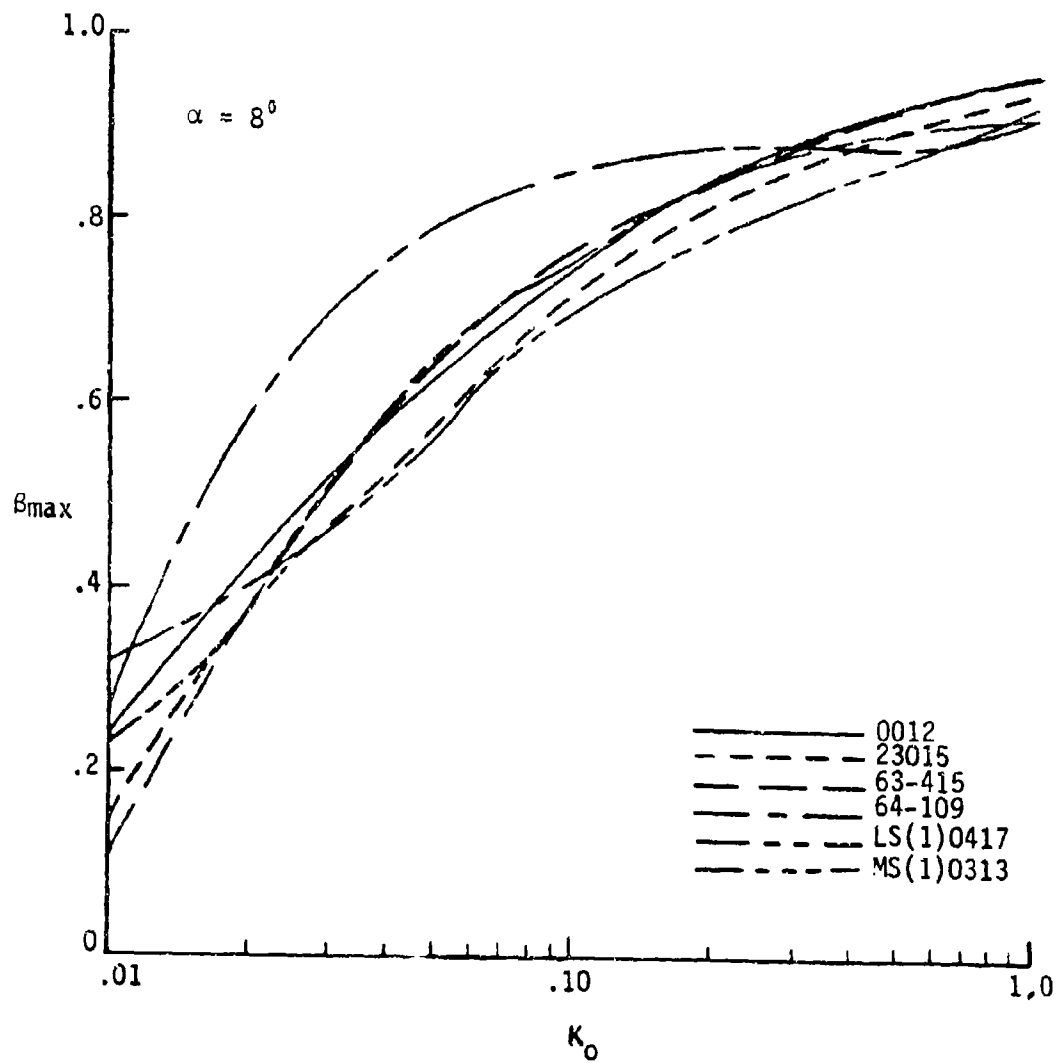
FIGURE 2-53.　THEORETICAL DATA ON THE MAXIMUM IMPINGEMENT
EFFICIENCY OF SEVERAL AIRFOILS (α = 8°)

I 2-118
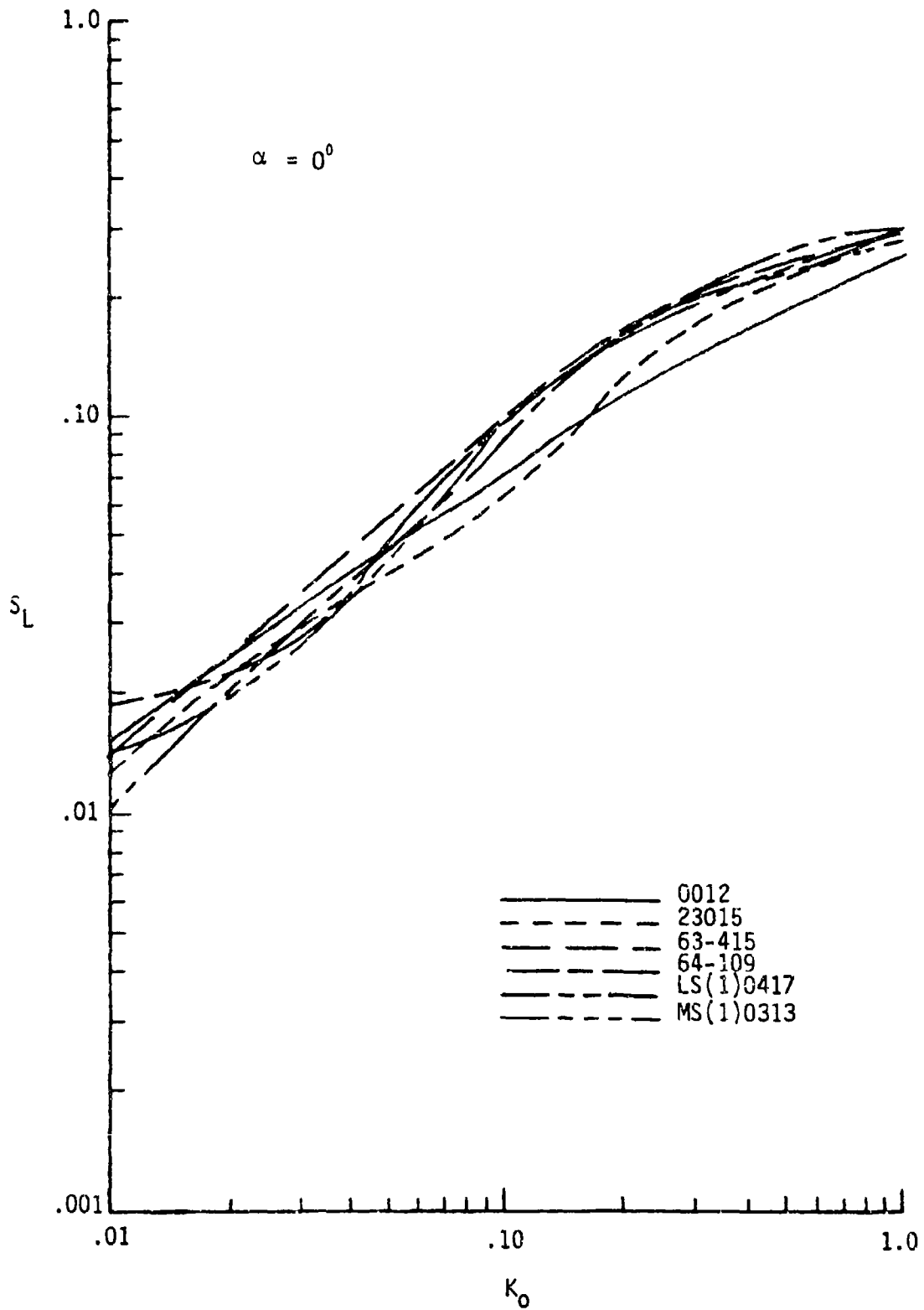
FIGURE 2-54. THEORET CAL DATA ON THE LOWER SURFACE IMPINGEMENT
LIMIT OF SEVERAL AIRFOILS ($\alpha = 0^\circ$)

I 2-119
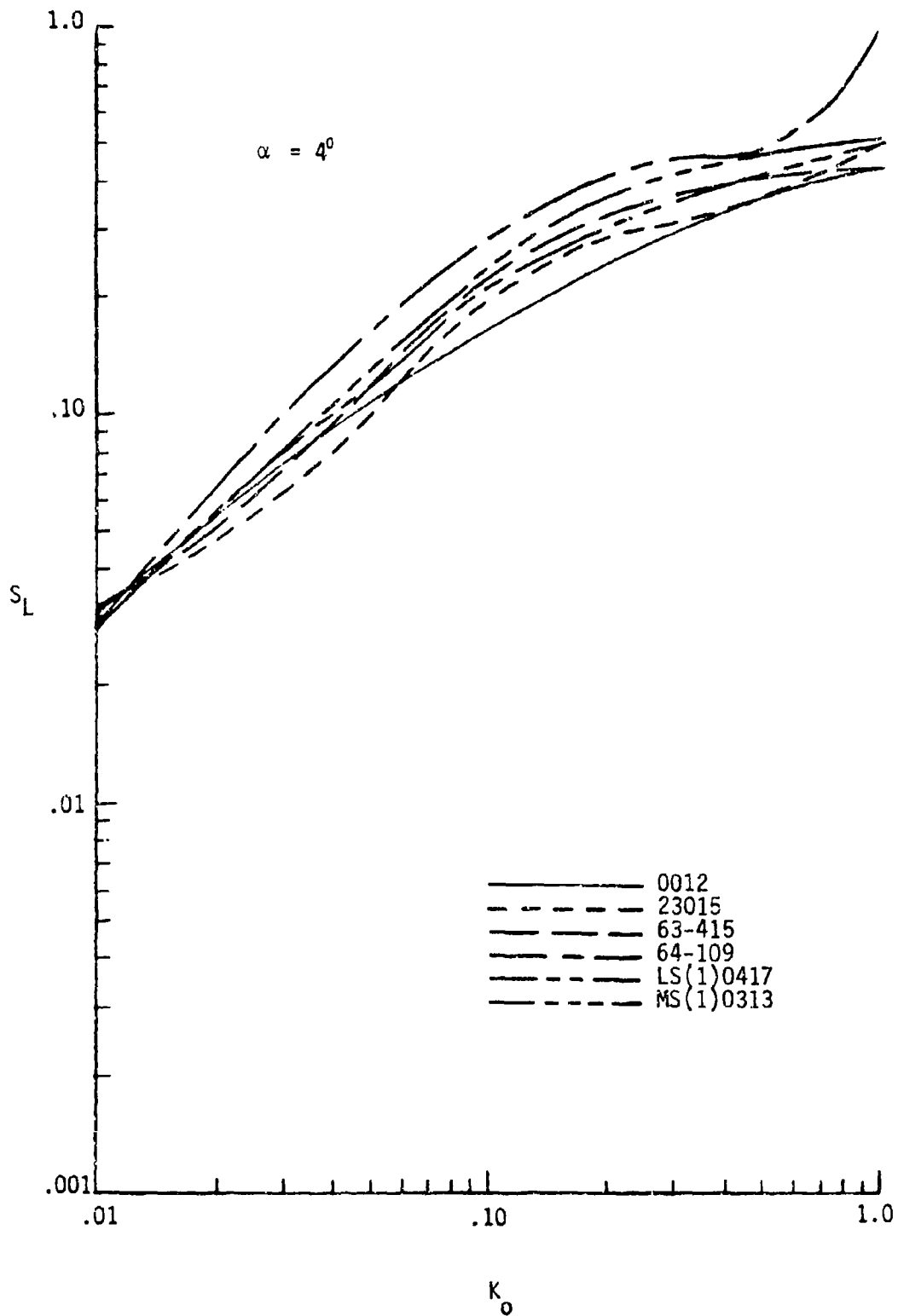
FIGURE 2-55. THEORETICAL DATA ON THE LOWER SURFACE IMPINGEMENT
LIMIT OF SEVERAL AIRFOILS (α = 4°)

I 2-120
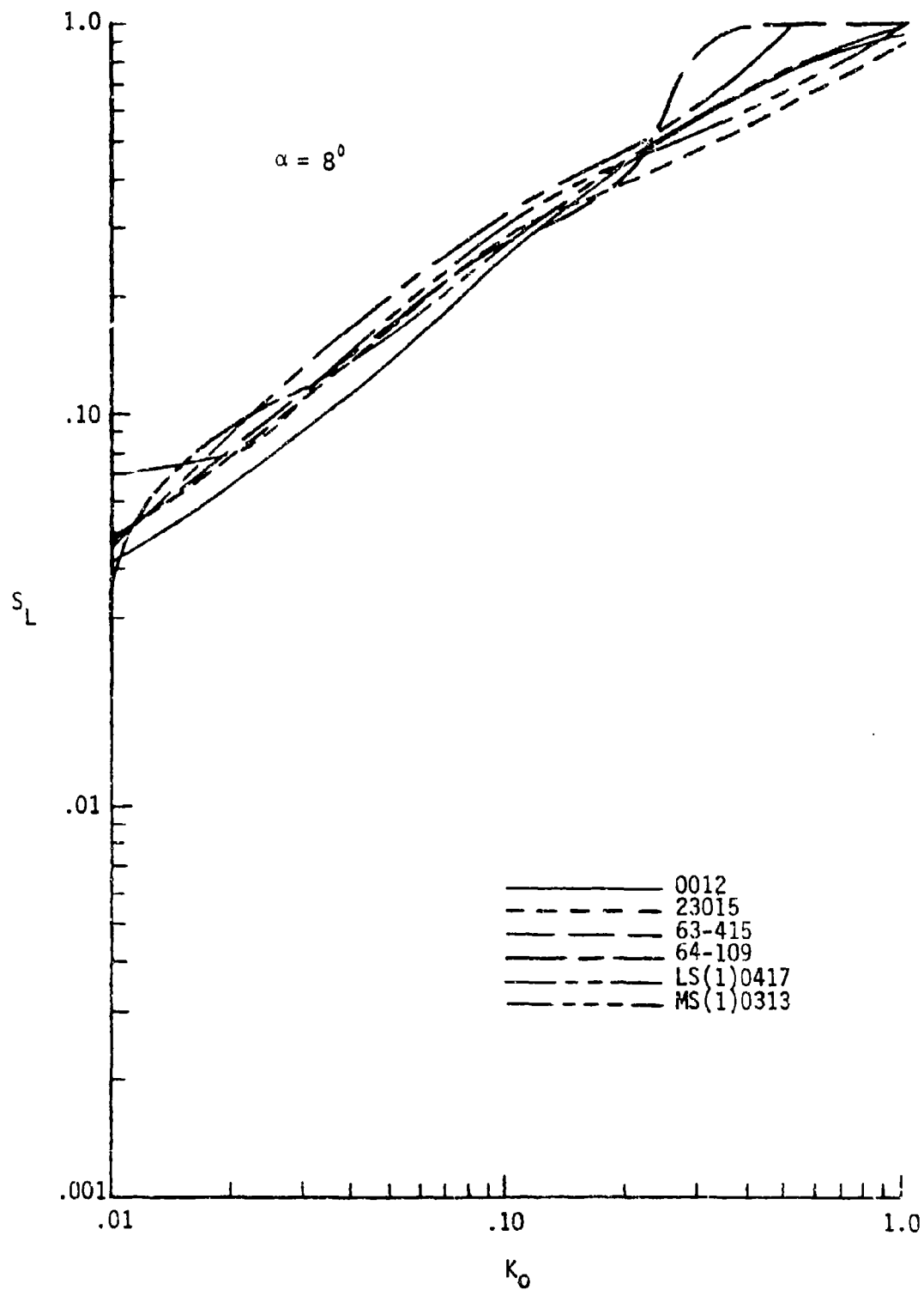
FIGURE 2-56.   THEORETICAL DATA ON THE LOWER SURFACE IMPINGEMENT
LIMIT OF SEVERAL AIRFOILS ($\alpha = 8°$)

I 2-121

$\alpha = 0^0$

S_U

K_O
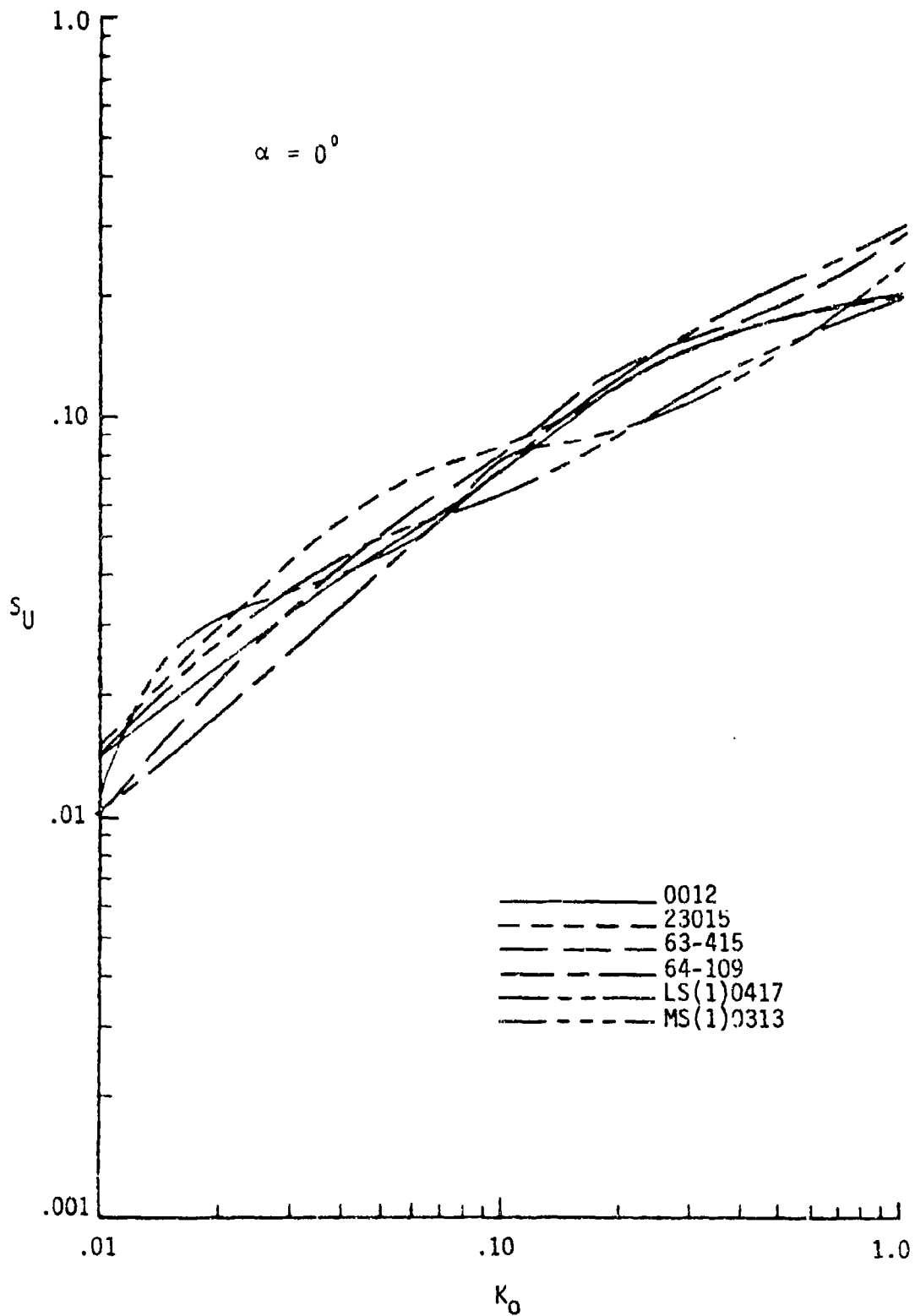
FIGURE 2-57. THEORETICAL DATA ON THE UPPER SURFACE IMPINGEMENT
LIMIT OF SEVERAL AIRFOILS ($\alpha = 0^\circ$)
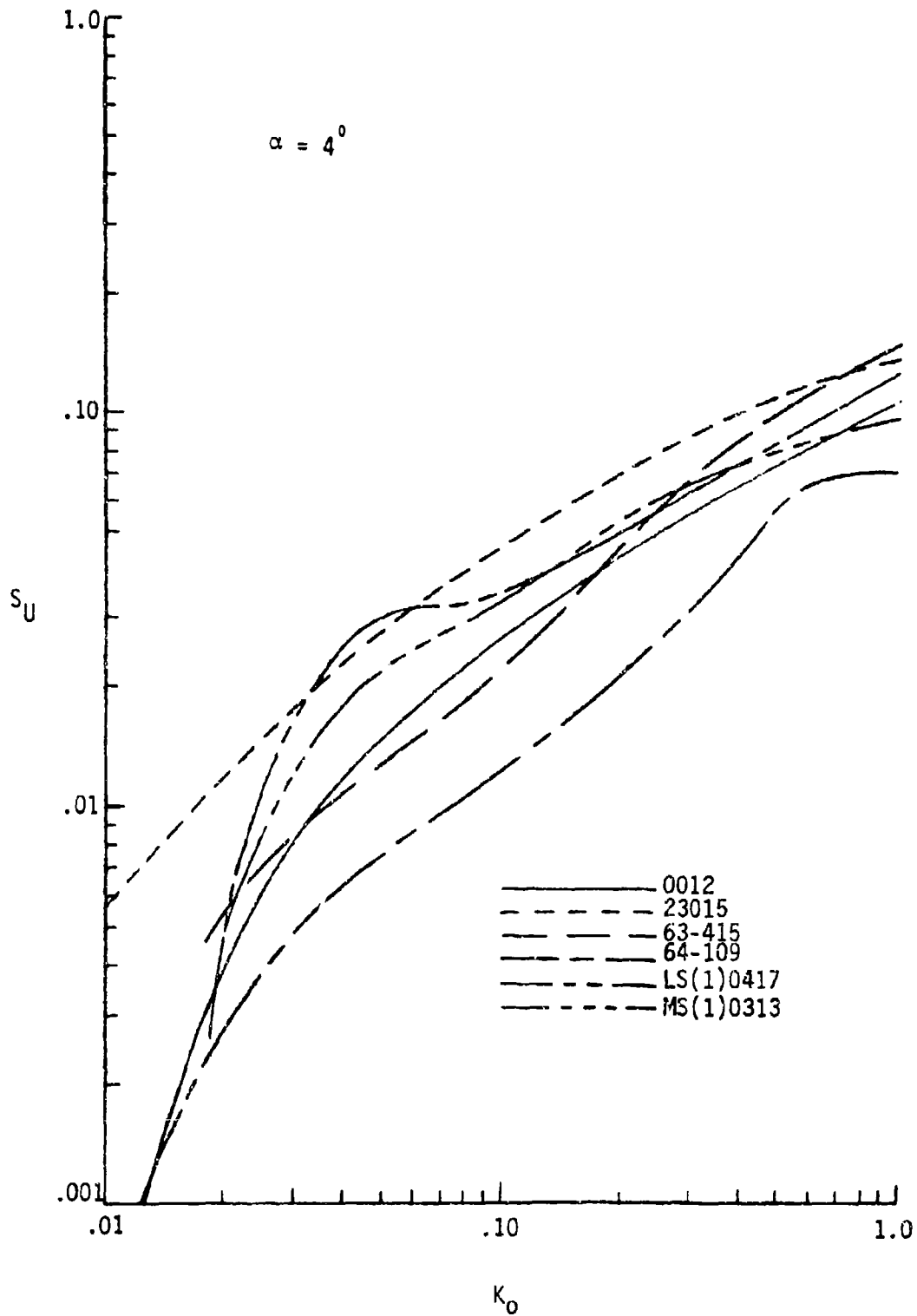
FIGURE 2-58.   THEORETICAL DATA ON THE UPPER SURFACE IMPINGEMENT
LIMIT OF SEVERAL AIRFOILS ($\alpha = 4°$)

I 2-123
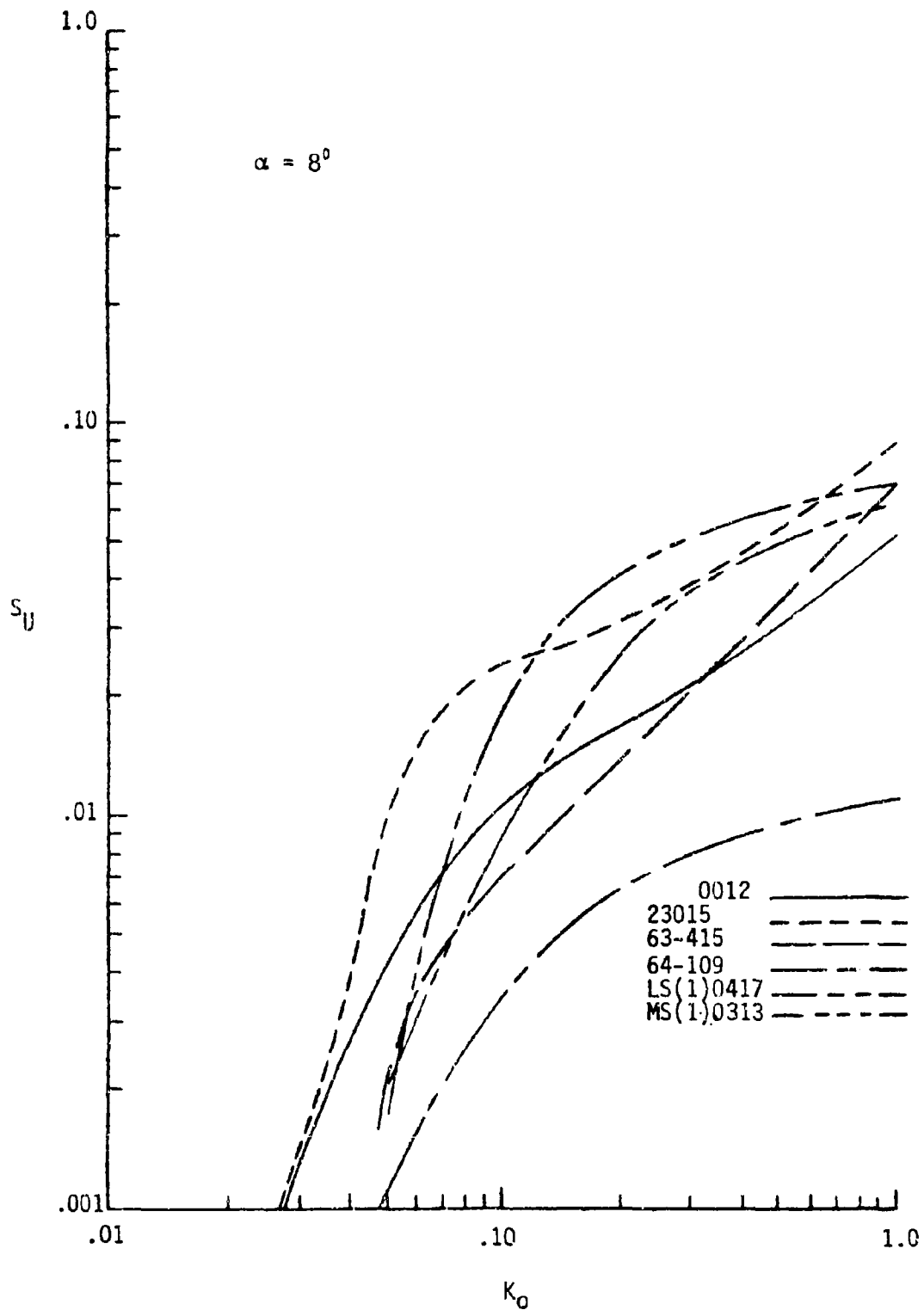
FIGURE 2-59.   THEORETICAL DATA ON THE UPPER SURFACE IMPINGEMENT
LIMIT OF SEVERAL AIRFOILS ($\alpha = 8°$)

I 2-124

NACA 23018   Radius of curvature: 3.56% of chord   Thickness: 18% of chord

Wortman
FX 67-K-170/17   Radius of curvature: 0.7604% of chord   Thickness: 17% of chord
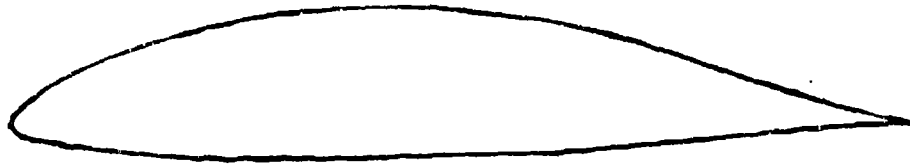
SC(2)-0714   Radius of curvature: 2.8012% of chord   Thickness: 14% of chord

FIGURE 2-60.   AIRFOIL PROFILES FOR IMPINGEMENT PARAMETER PLOTS
                IN FIGURES 2-61 THROUGH 2-63

I 2-125
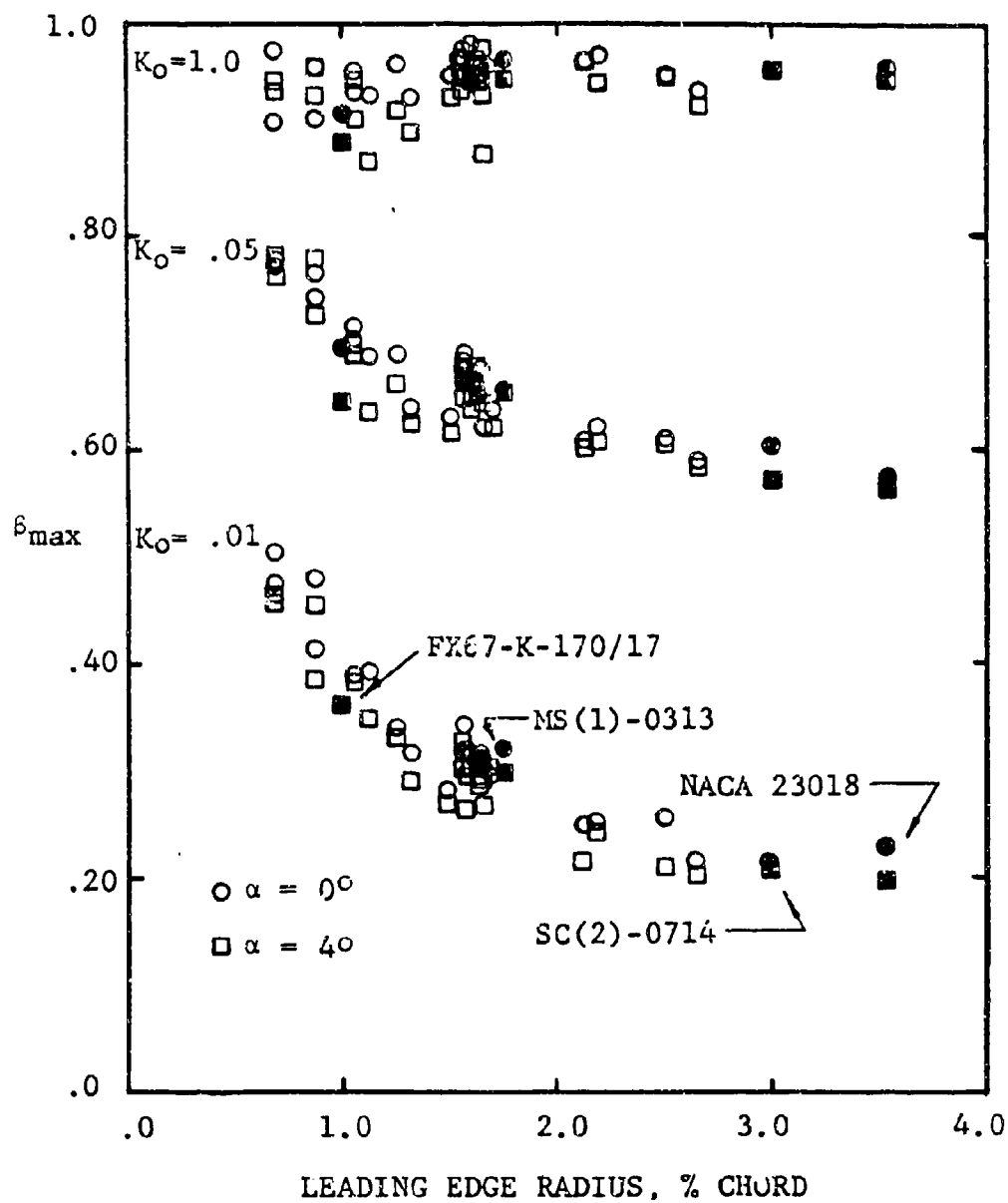
FIGURE 2-61.   MAXIMUM IMPINGEMENT EFFICIENCY FOR AIRFOILS
OF VARIOUS LEADING EDGE RADIUS

I 2-126
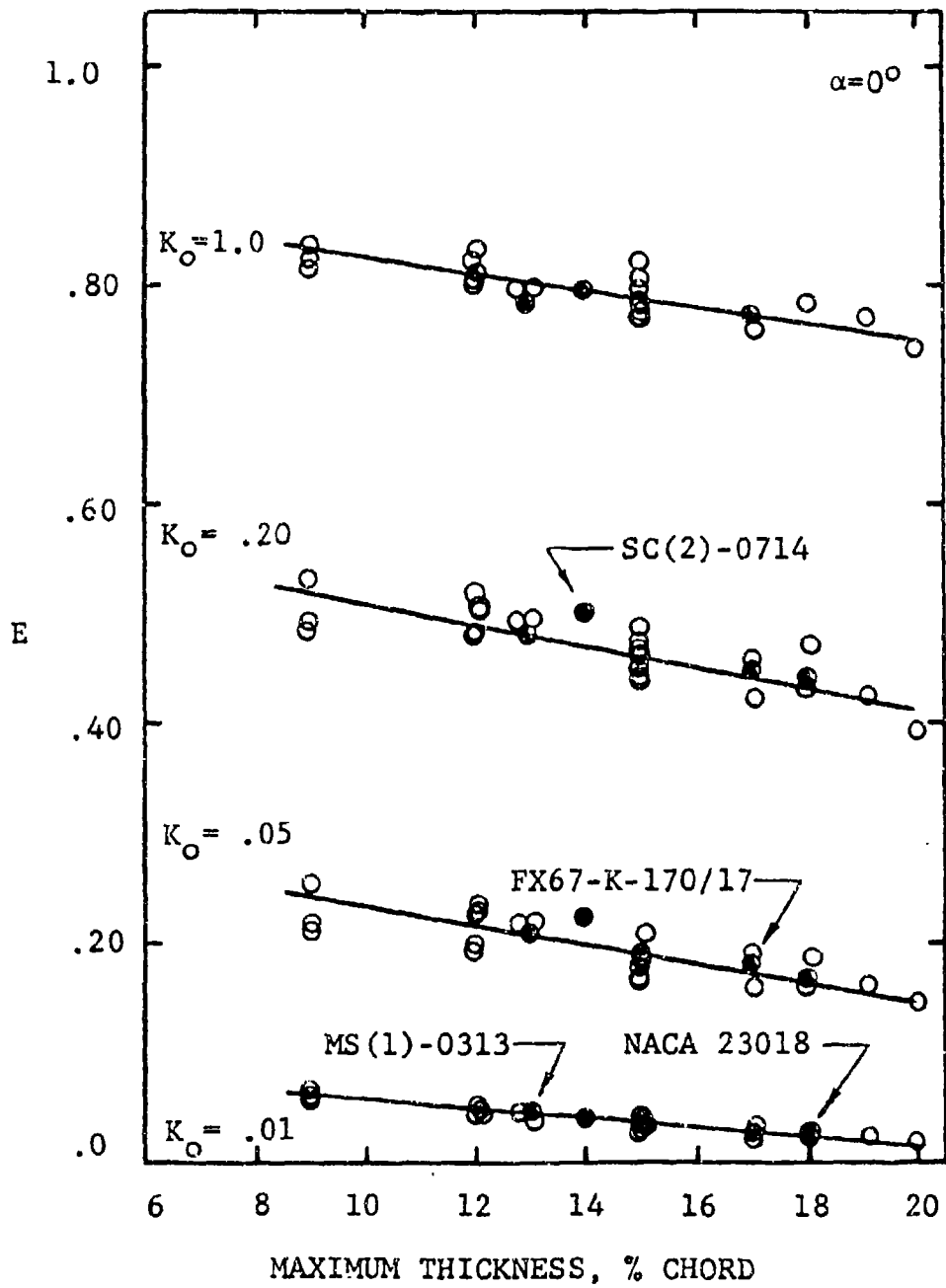
FIGURE 2-62.   COLLECTION EFFICIENCY FOR AIRFOILS AS A FUNCTION OF
MAXIMUM THICKNESS

I 2-127
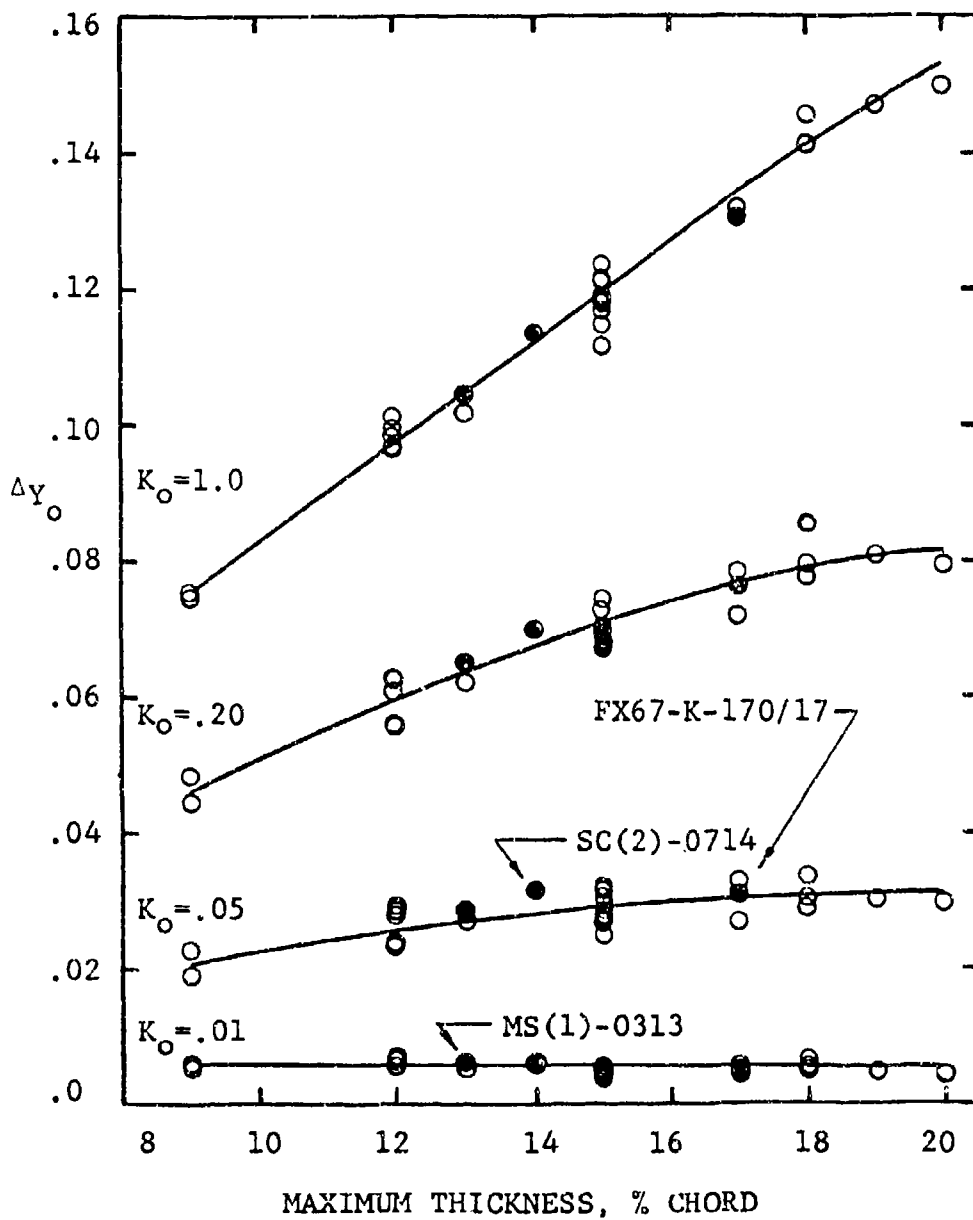
FIGURE 2-63. AMOUNT OF DROPLET IMPINGEMENT AS A FUNCTION OF
AIRFOIL MAXIMUM THICKNESS

I 2-128

↓ Leading edge   ↓ Leading edge
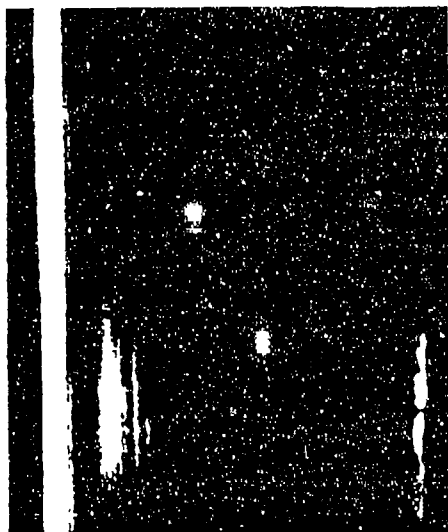
a. Angle of attack 0°, 0.5 gm/m^3,
    11 minutes, 0.16 lb./ft. span

b. Angle of attack 0°, 0.5 gm/m^3,
    12 minutes, 0.52 lb./ft. span

Upper surface   Lower surface

↓ Leading edge   ↓ Leading edge

c. Angle of attack 2.3°, 0.5 gm/m^3, 15 minutes, 0.22 lb./ft. span

FIGURE 2-64.   RIME ICE ACCRETIONS

I 2-129

Upper surface

Leading edge ↓   ↓ Leading edge

Lower surface

a.   Angle of Attack 2.3°, 0.5 gm/m^3, 18 minutes, 0.31 lb./ft. span

Upper surface

Leading edge ↓   ↓ Leading edge
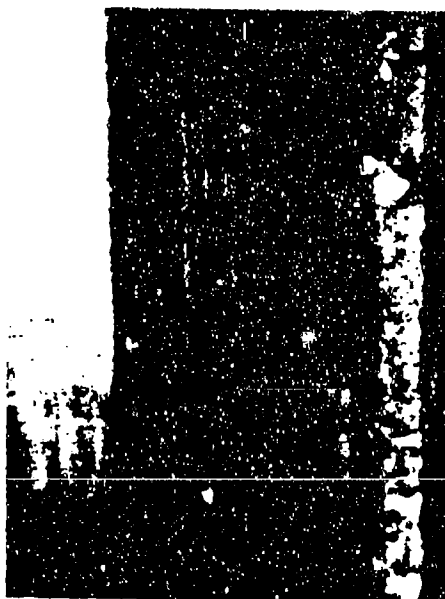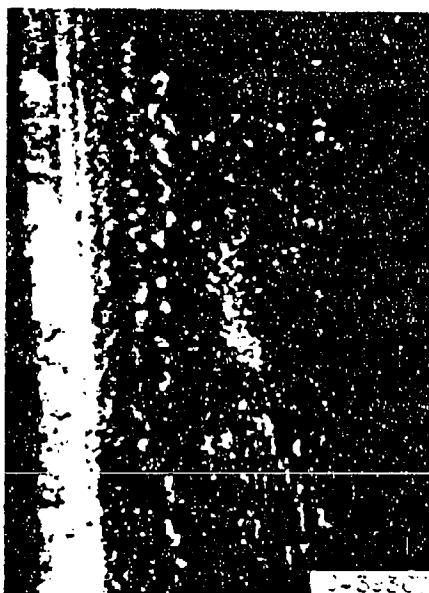
Lower surface

b.   Angle of attack 7.0, 1.0 gm/m^3, 10 minutes, 0.73 lb./ft. span

FIGURE 2-65a.   GLAZE ICE SHAPES

Leading edge ↓   ↓ Leading edge
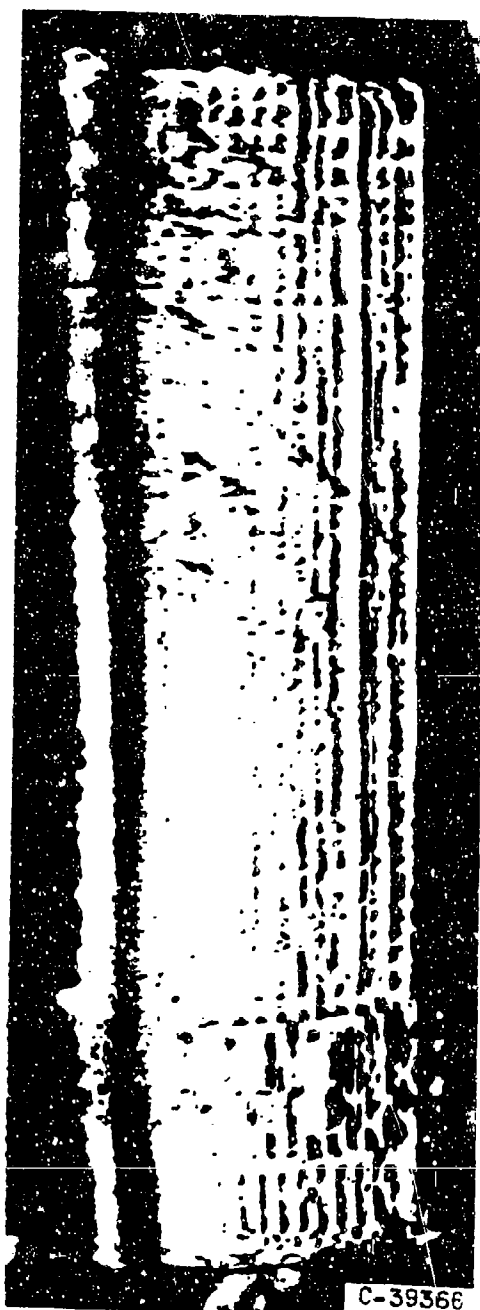
Upper Surface   Lower Surface

FIGURE 2-65b.   GLAZE ICE SHAPES

I 2-131

Rime Ice
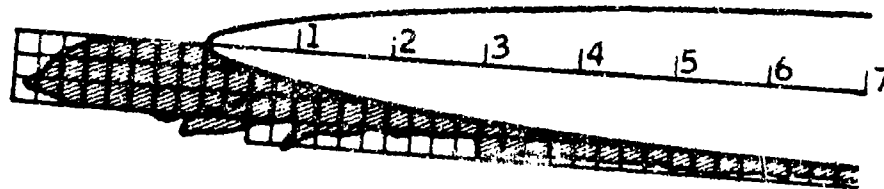
Air speed 275 mph, air total temperature 0°F, LWC 0.90gm/m^3, 15-micron droplet diameter, icing time 7 min., weight of ice 0.555 lb./ft. span, change in drag (ΔC_D) = 0.0061
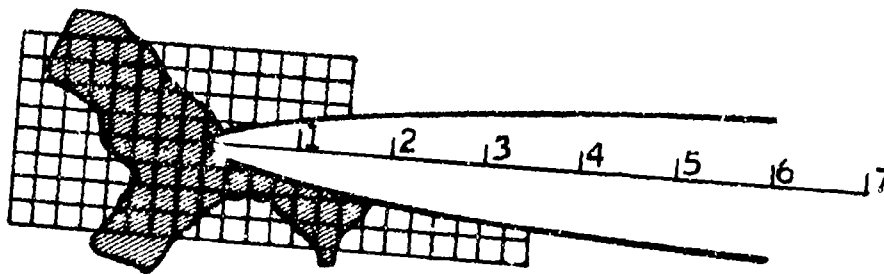
Glaze Ice

Air speed 275 mph, air total temperature 25°F, LWC 0.90gm/m^3, 15-micron droplet diameter, icing time 12 min., weight of ice 0.60 lb./ft. span, change in drag (ΔC_D) = 0.0370

Chord = 6 ft.
Scale = 1/2

FIGURE 2-66. TYPICAL RIME AND GLAZE ICE ACCRETIONS ON A 65A004 AIRFOIL AT 2° ANGLE OF ATTACK

FIGURE 2-67a.   GLAZE ICE SHAPES ON A SWEPT WING

I 2-133

FIGURE 2-67b.   CLOSE UP OF A LOBSTER ICE PLASTER

DRY GROWTH (RIME)

WET GROWTH (GLAZE)

BEAK ICE

ICE THICKNESS, †

DOUBLE–HORNED

ROUNDED GLAZE ICE
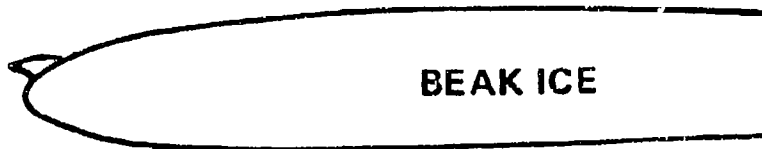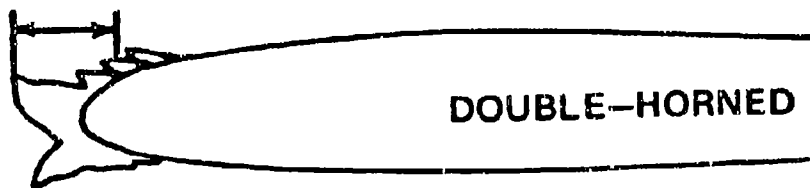
FIGURE 2-68. HIGH SPEED ICE SHAPES (REFERENCE 2-35)
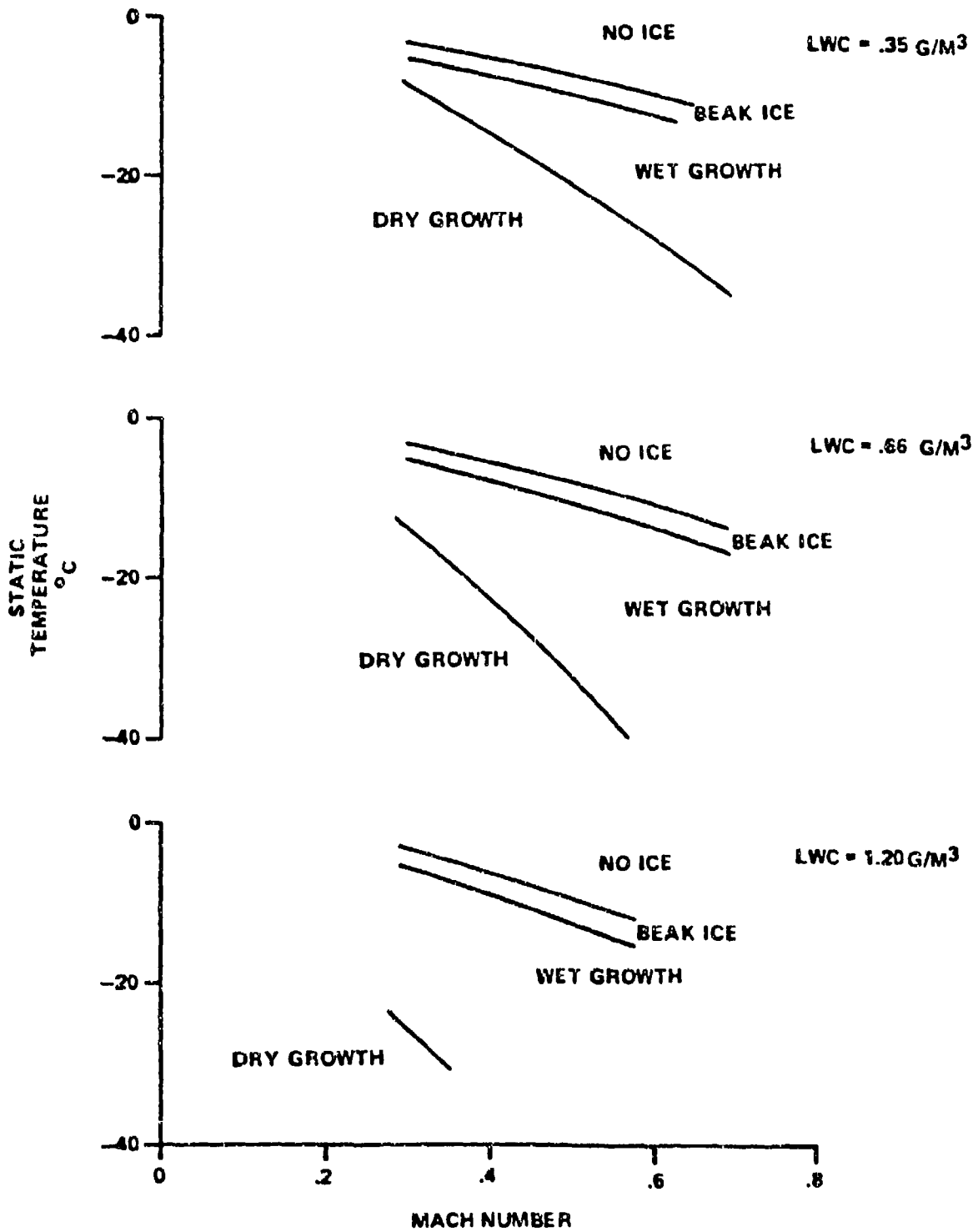
FIGURE 2-69. ICE BOUNDARIES AS A FUNCTION OF MACH NUMBER
(REFERENCE 2-35)

I 2-136

CASE	AIRSPEED, km/hr	TEMP., °C	LWC, g/m³	DVM μm
A,B,C	209	-8	2.1	20
D,E,F	209	-26	1.0	12

21 INCH CHORD 0012 AIRFOIL
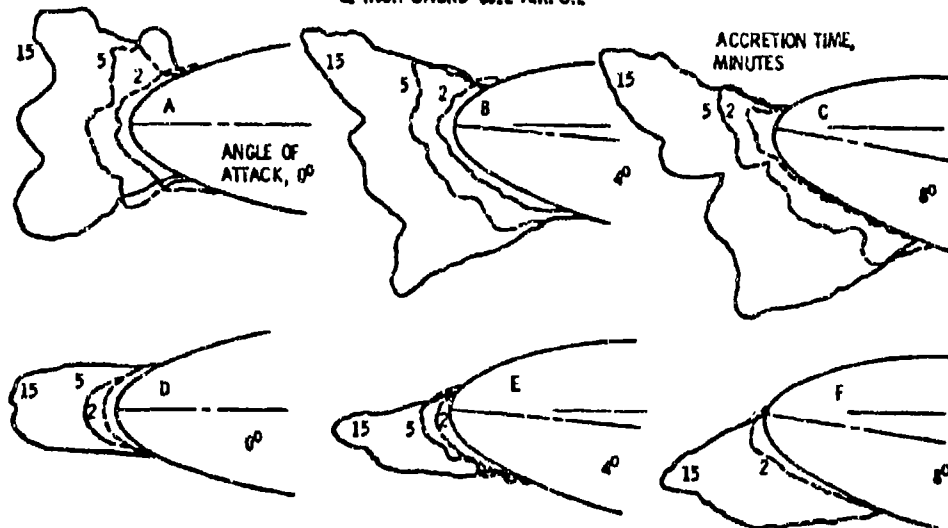
FIGURE 2-70.   EFFECT OF TIME AND ANGLE OF ATTACK ON THE ICE SHAPE
(REFERENCE 2-36)

○ AIRSPEED, 209 km/hr; LWC, 1.3 g/m³; TIME, 8 min.
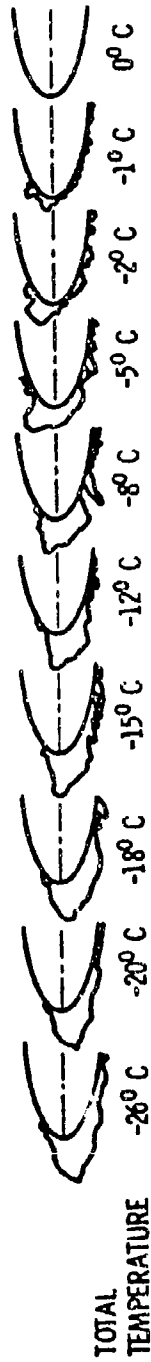
□ AIRSPEED, 338 km/hr; LWC, 1.05 g/m³; TIME, 6.2 min.
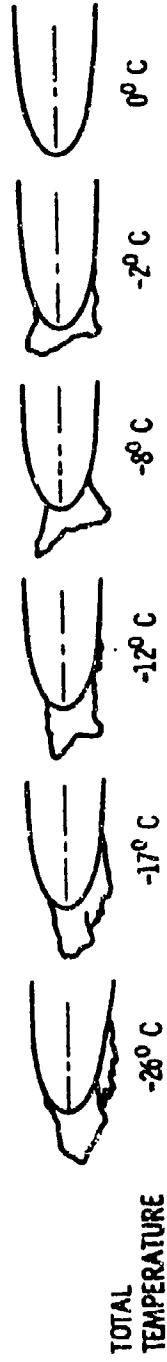
FIGURE 2-71. EFFECT OF TOTAL TEMPERATURE ON THE ICE SHAPE (REFERENCE 2-36)

DROP
SIZE,
DVM,
μm

- - - 14
— - — 20
——— 26
— - — 36

CASE A   B   C

D   E   F
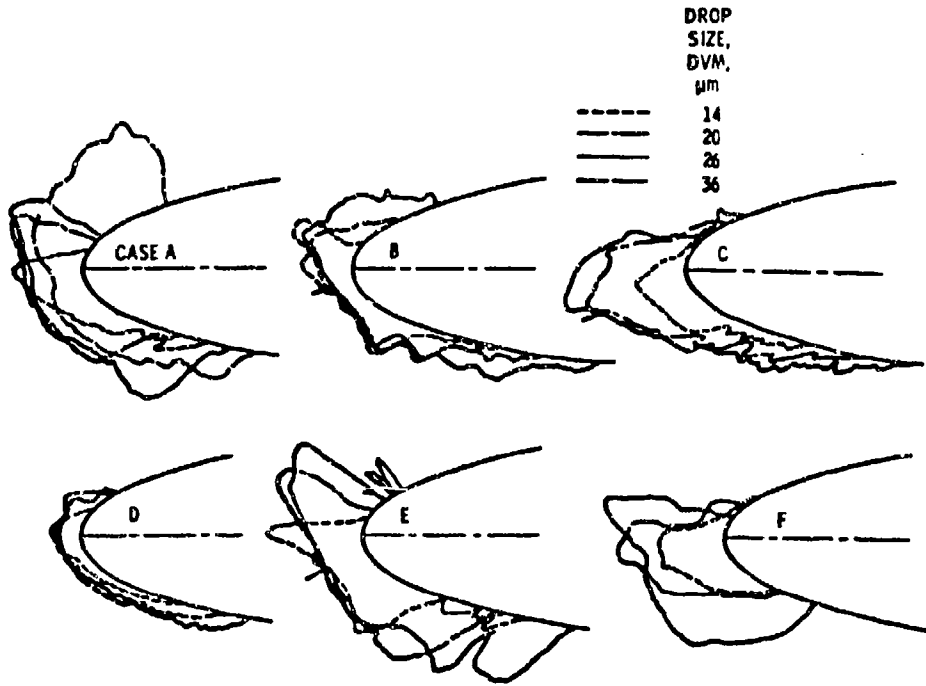
CASE	DATA SYMBOL	AIRSPEED, km/hr	TEMP., °C	LWC, g/m³	TIME, min
A	□	209	-8	1.3	8
B	○	209	-2	1.3	8
C	◇	209	-26	1.3	8
D	◊	209	-8	1.3	3
E	△	338	-8	1.05	6.2
F	⬠	209	-18	1.3	8

21 INCH CHORD 0012 AIRFOIL AT 4 DEGREE ANGLE

FIGURE 2-72.   EFFECT OF DROPLET SIZE ON THE ICE SHAPE
(REFERENCE 2-36)

I 2-139
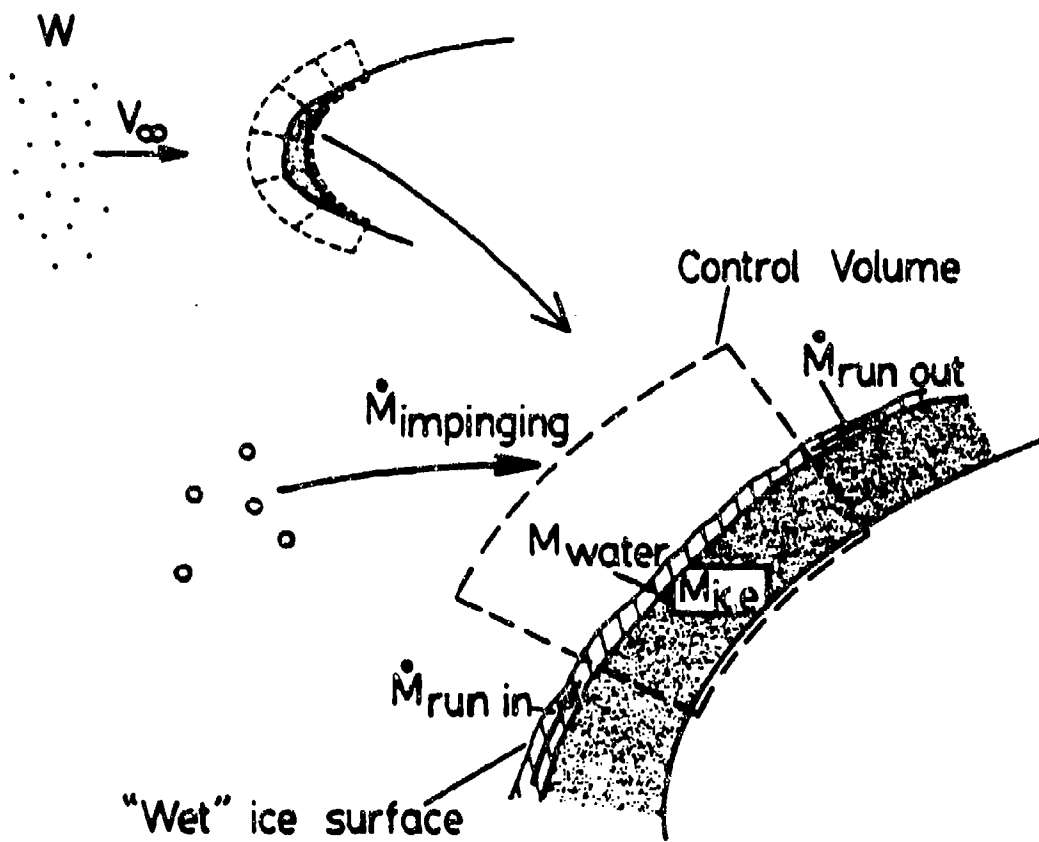
FIGURE 2-73.   CONTROL VOLUME MASS BALANCE FOR AN ICE SURFACE
(REFERENCE 2-43)
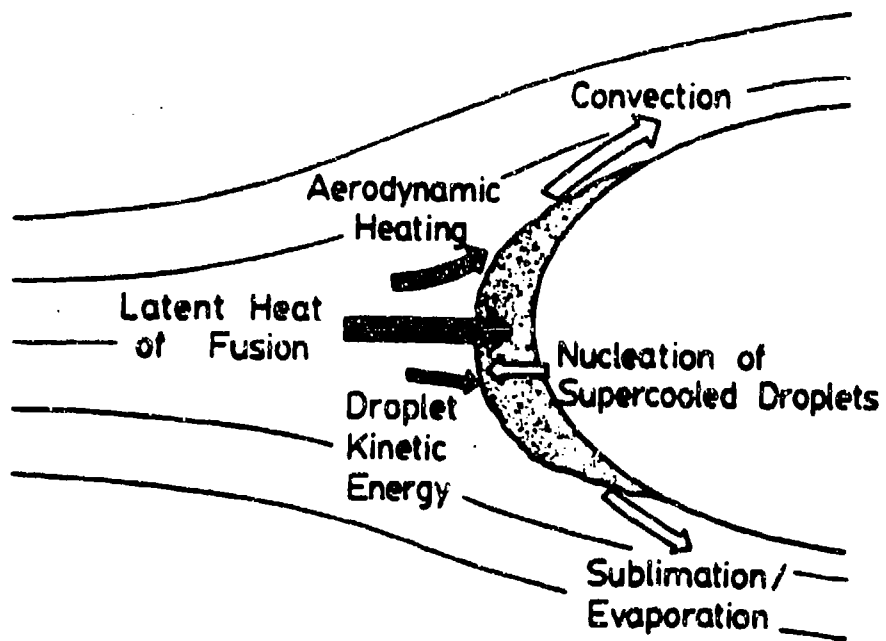
FIGURE 2-74. MODES OF ENERGY TRANSFER FOR AN ACCRETING ICE SURFACE
(REFERENCE 2-43)

I 2-141
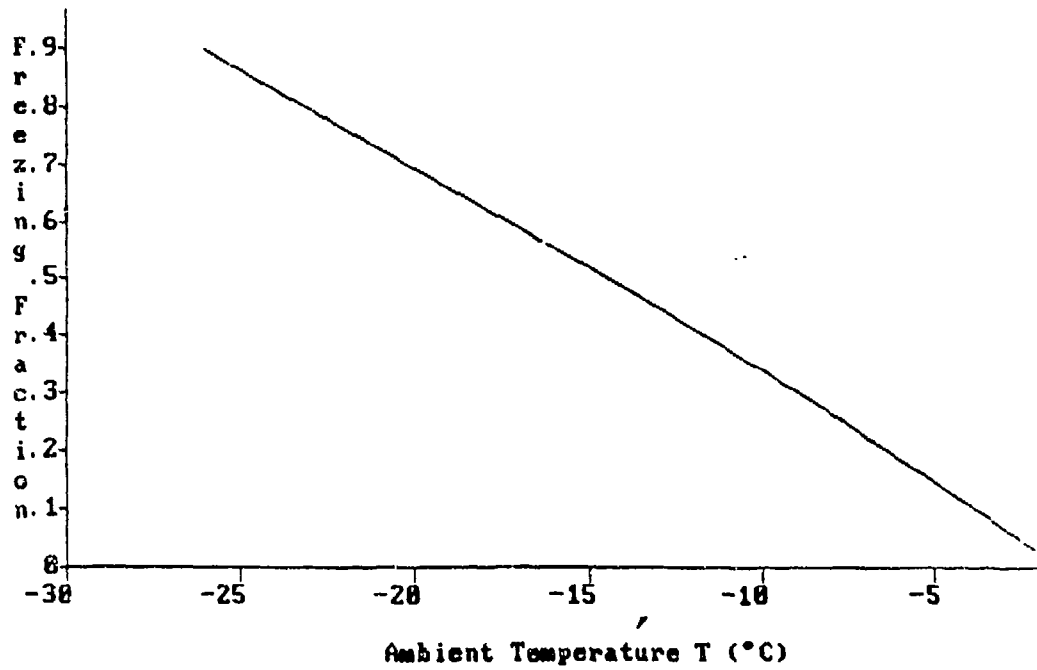
(a) LWC = .7 g/m^3, DROPLET DIAMETER δ = 20 μm, V_∞ = 70 m/s
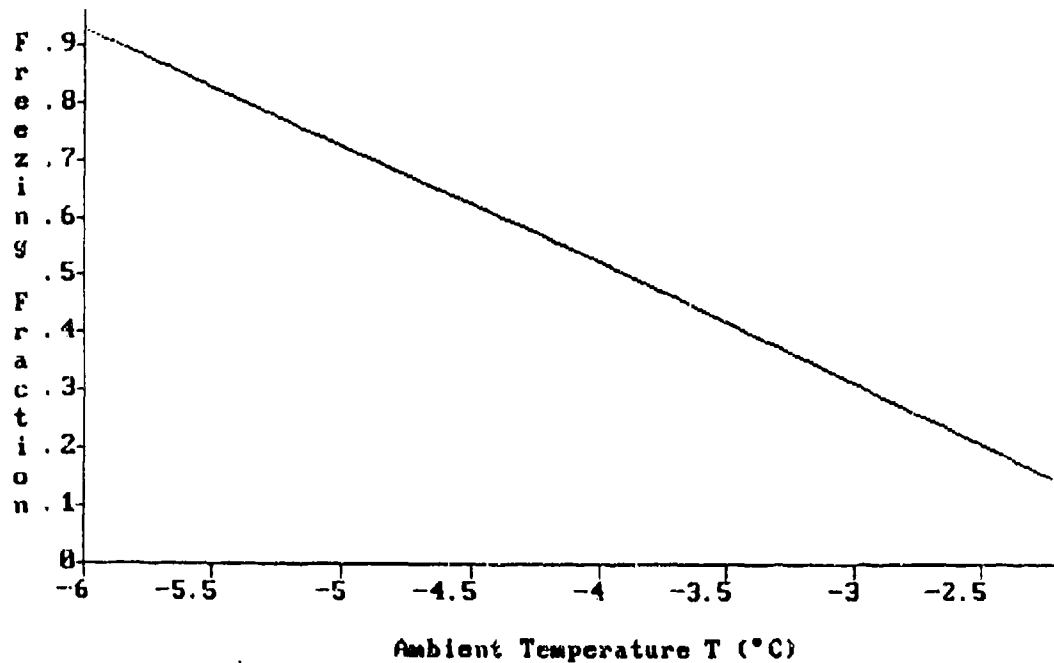
(b) LWC = .1 g/m^3, DROPLET DIAMETER δ = 20 μm, V_∞ = 70 m/s

FIGURE 2-75.   FREEZING FRACTION VS AMBIENT TEMPERATURE T_∞ FOR A
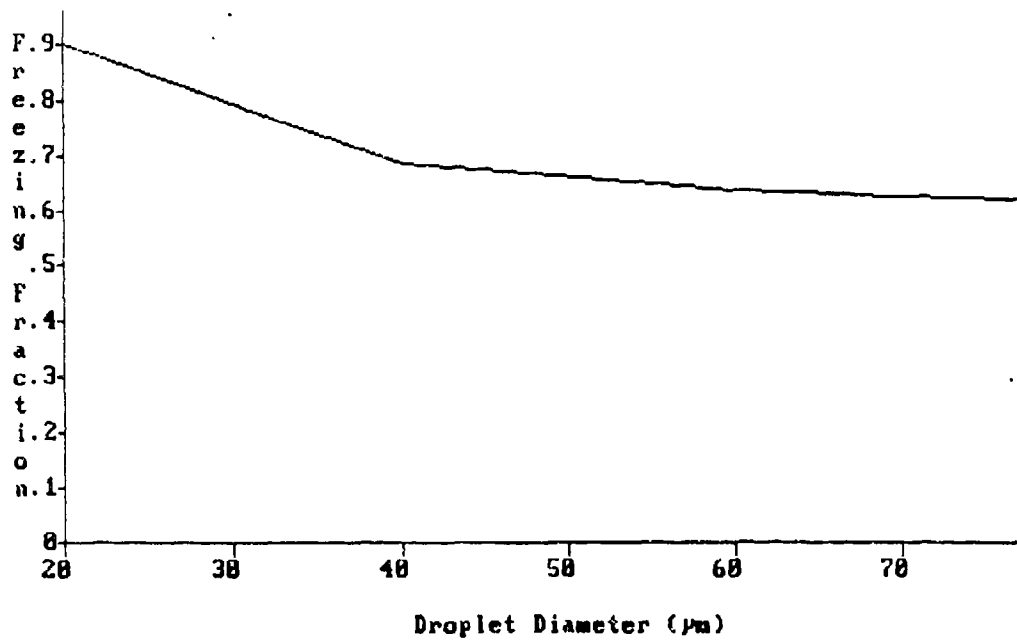CIRCULAR CYLINDER WITH DIAMETER 20 CM
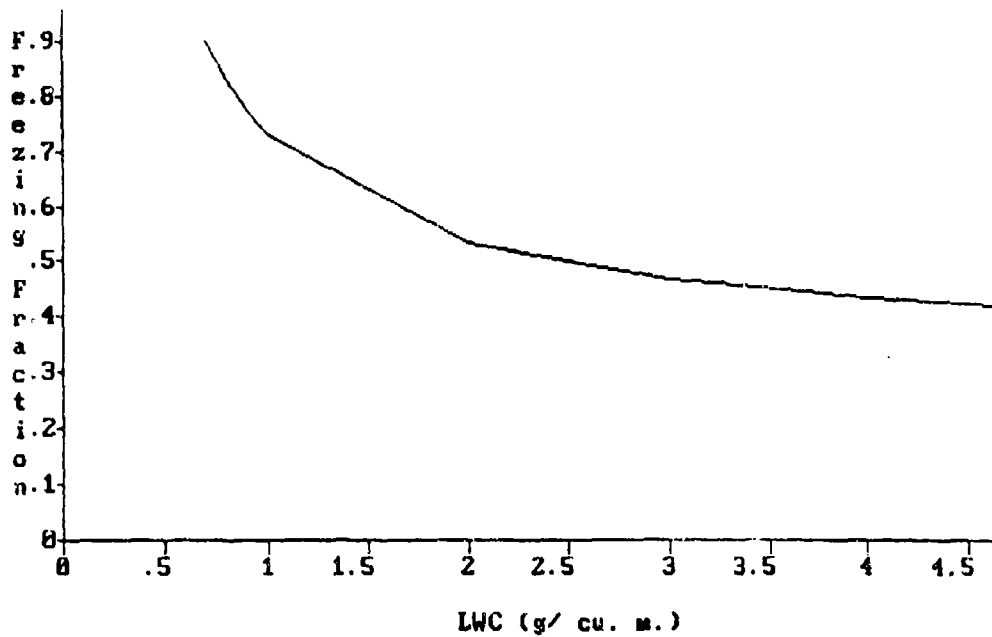
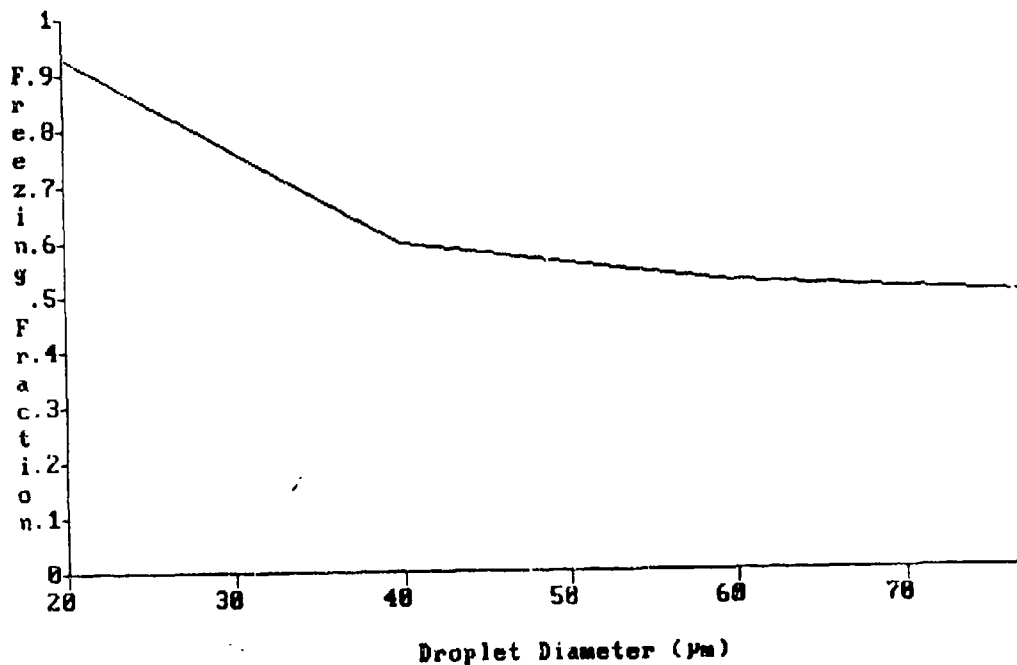(a) $T_\infty = -26$ °C, DROPLET DIAMETER $\delta = 20$ μm, $V_\infty = 70$ m/s
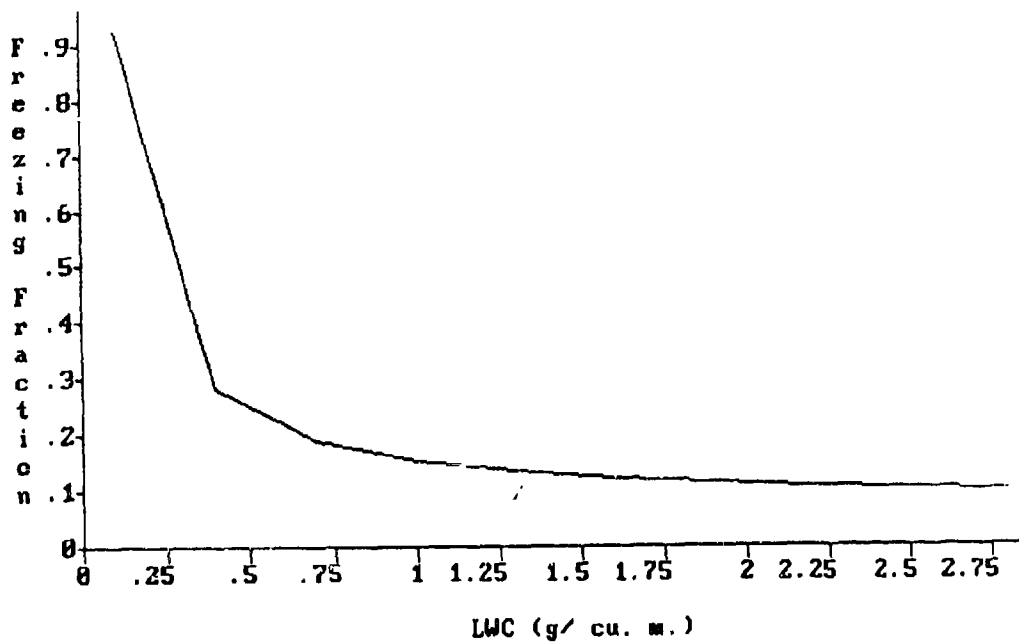
(b) $T_\infty = -6$ °C, DROPLET DIAMETER $\delta = 20$ μm, $V_\infty = 70$ m/s

FIGURE 2-76.   FREEZING FRACTION VS LWC FOR A CIRCULAR CYLINDER
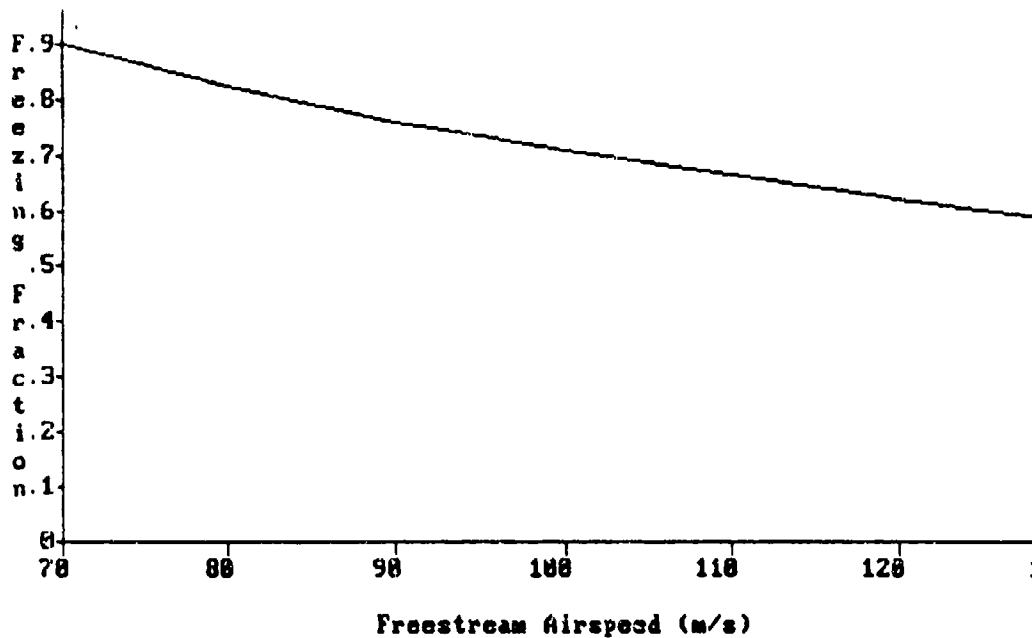   CIRCULAR CYLINDER WITH DIAMETER 20 CM

I 2-143

(a) $T_\infty = -26\ °C$, LWC = .7 g/m^3, $V_\infty = 70$ m/s

(b) $T_\infty = -6\ °C$, LWC = .1 g/m^3, $V_\infty = 70$ m/s

FIGURE 2-77.   FREEZING FRACTION VS DROPLET DIAMETER δ FOR A
                CIRCULAR CYLINDER WITH DIAMETER 20 CM
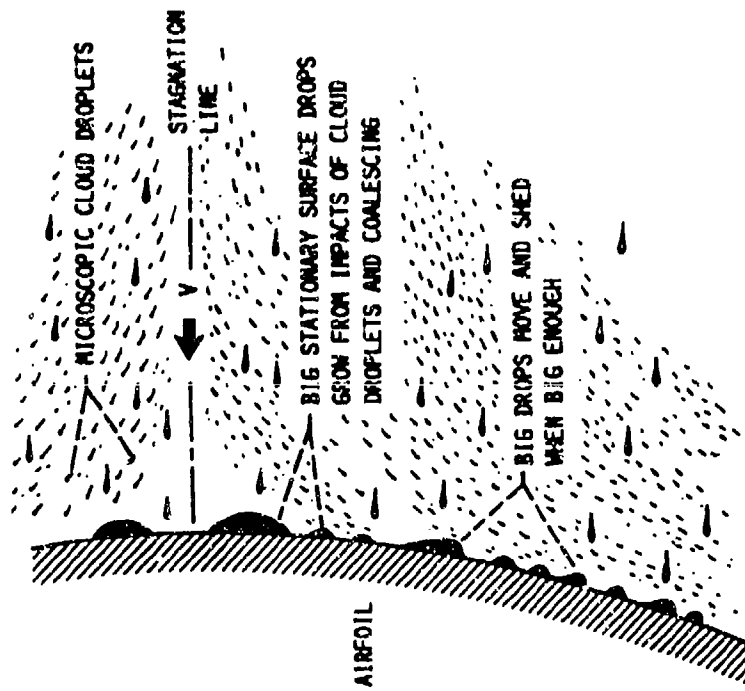
(a) $T_\infty = -26$ °C, LWC = .7 g/m^3, DROPLET DIAMETER $\delta = 20$ µm
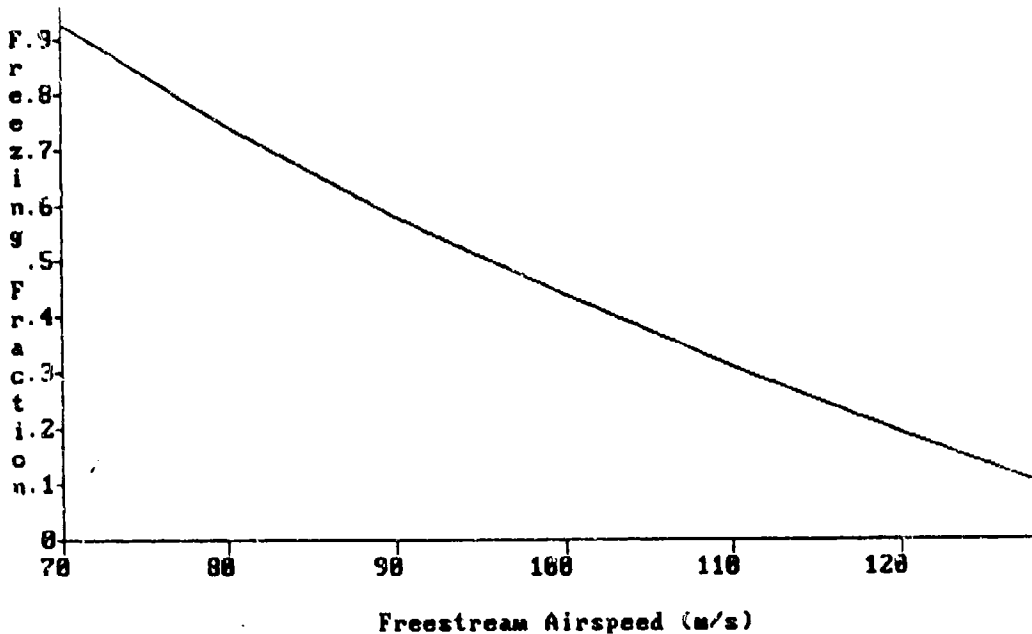
(b) $T_\infty = -6$ °C, LWC = .1 g/m^3, DROPLET DIAMETER $\delta = 20$ µm

FIGURE 2-78. FREEZING FRACTION VS. FREESTREAM AIRSPEED V_∞ FOR A
CIRCULAR CYLINDER WITH DIAMETER 20 CM

I 2-145
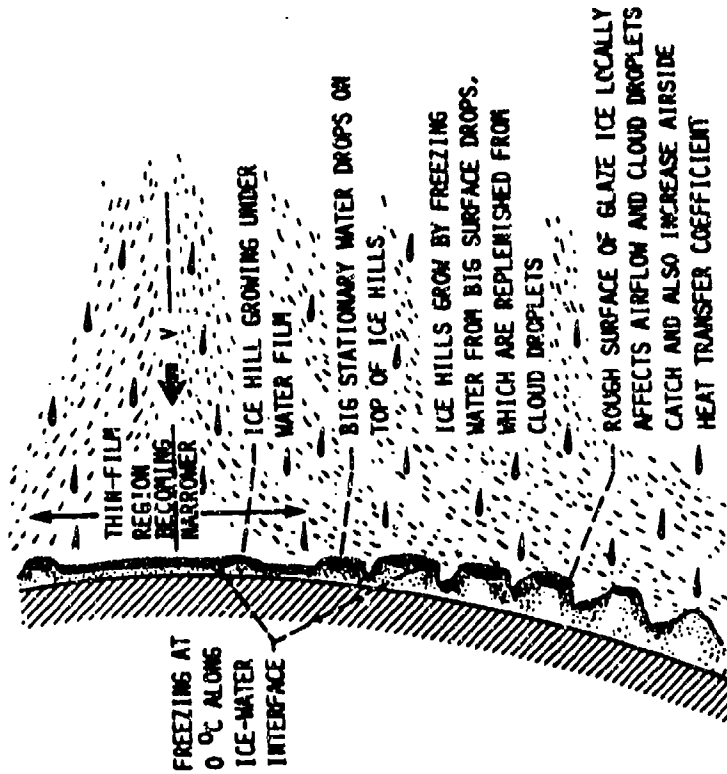
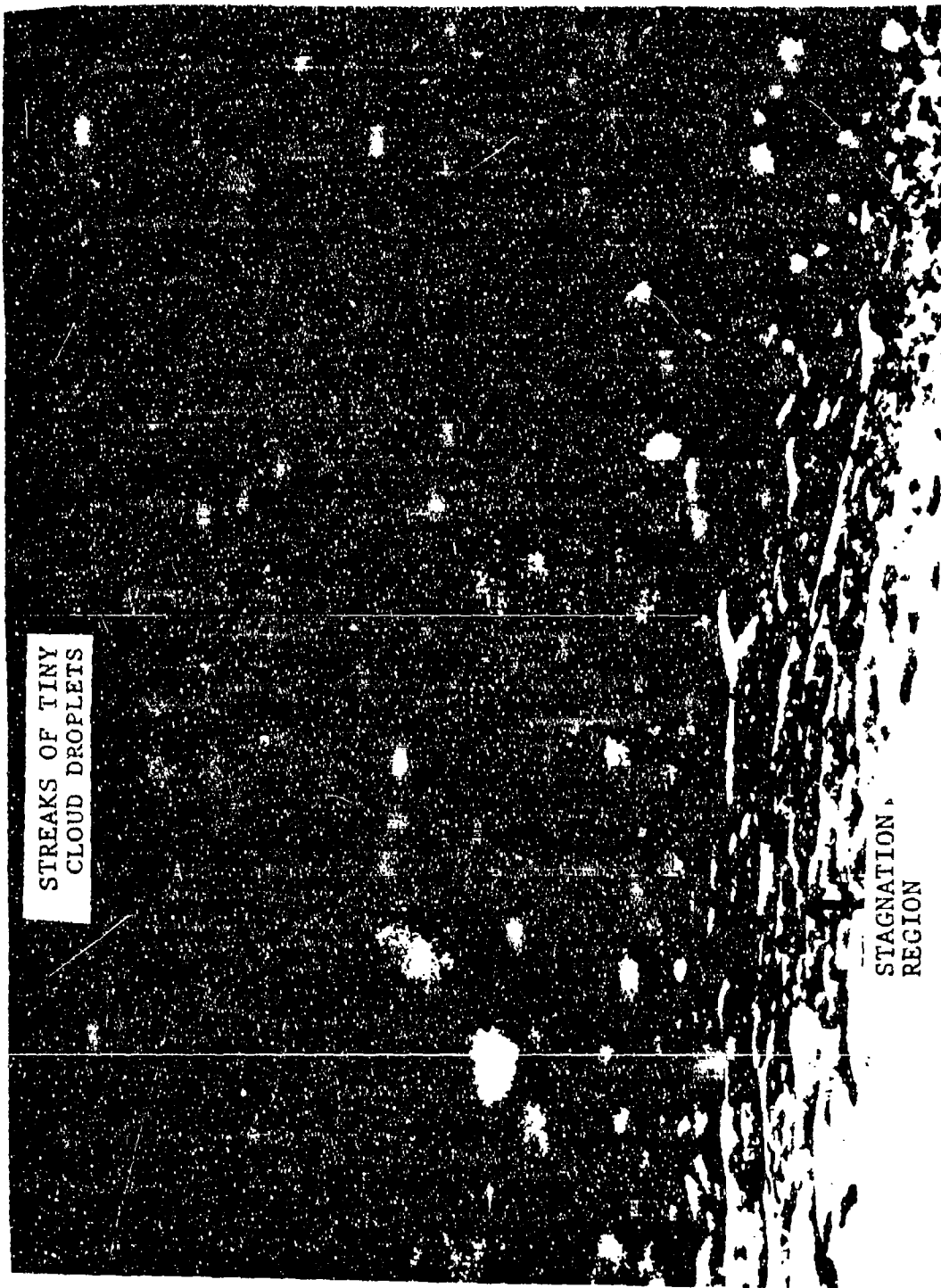FIGURE 2-79. PROPOSED NEW ICING MODEL FOR ICING PROCESS (REFERENCE 2-53)

STREAKS OF TINY
CLOUD DROPLETS

STAGNATION
REGION

FIGURE 2-80a. CLOSE UP PHOTOGRAPH OF COALESCING DROPLETS

FIGURE 2-80b. CLOSE UP PHOTOGRAPH OF FROZEN DROPLETS

FIGURE 2-81. ICE SHAPE TYPES AS A FUNCTION OF SPEED AND AMBIENT
TEMPERATURE FOR A LIQUID WATER CONTENT OF 0.2 G/M³
(REFERENCE 2-49)

I 2-149
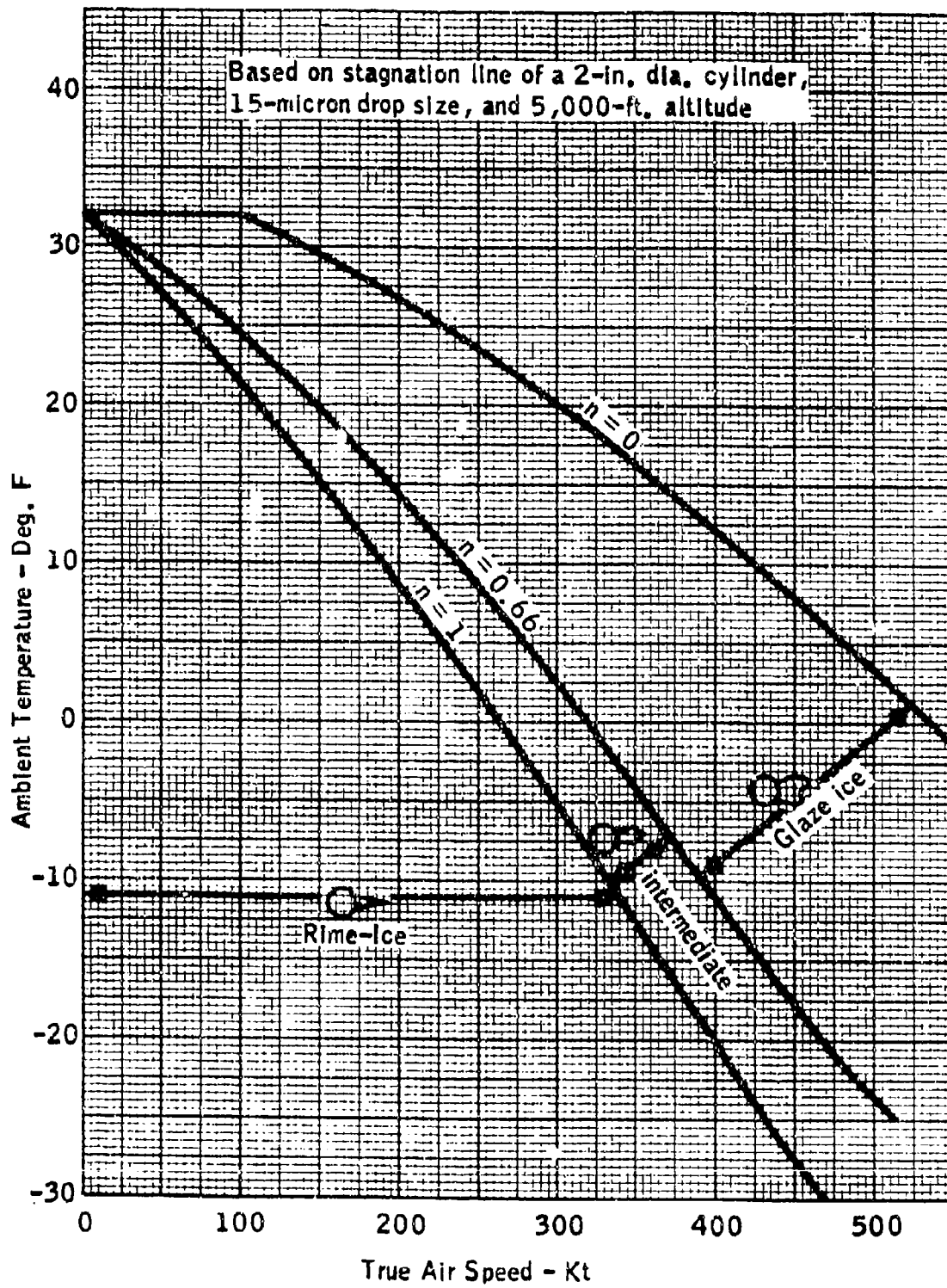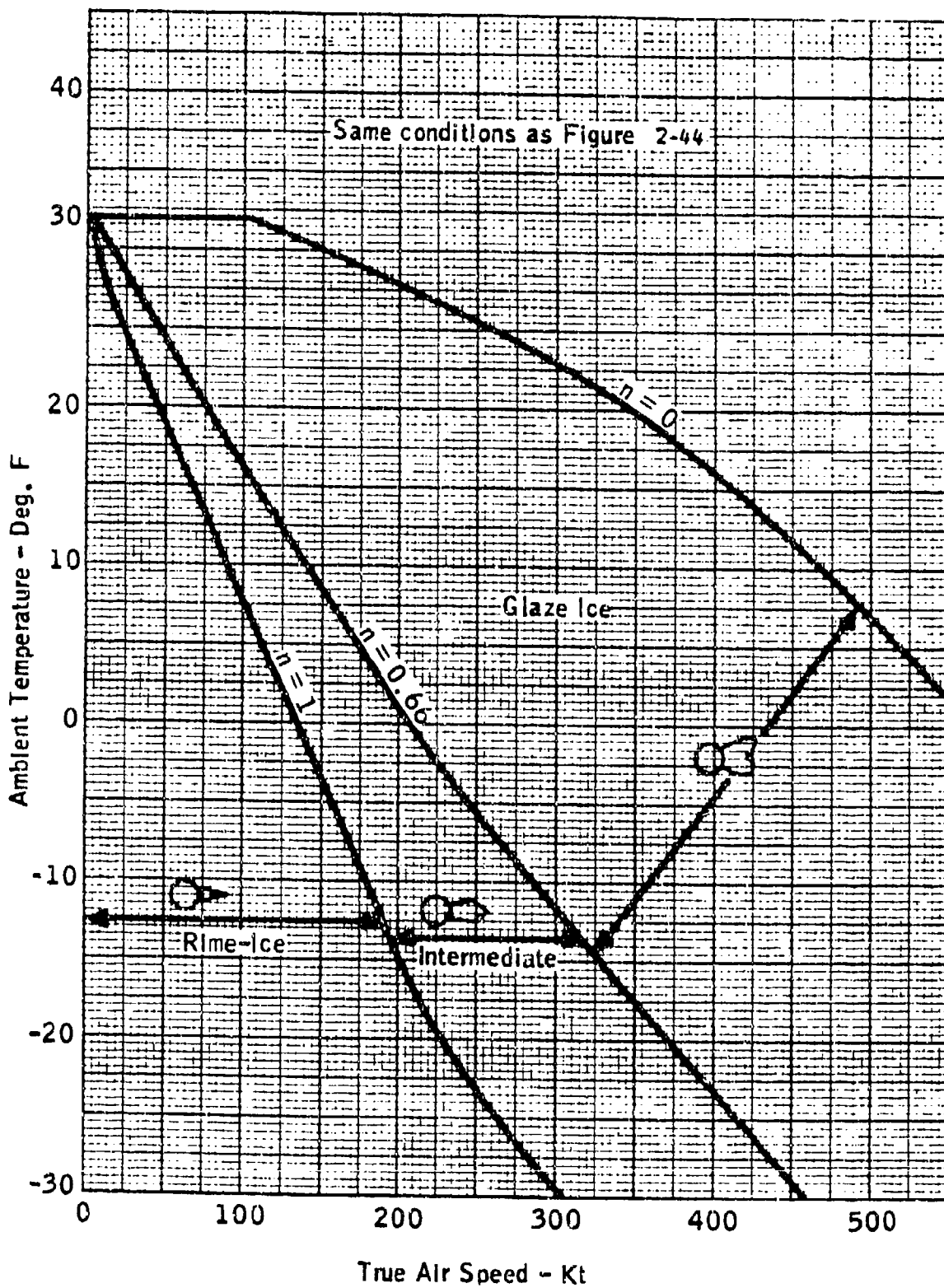
FIGURE 2-82. ICE SHAPE TYPES AS A FUNCTION OF SPEED AND AMBIENT TEMPERATURE FOR A LIQUID WATER CONTENT OF 0.5 G/M³ (REFERENCE 2-49)

I 2-150
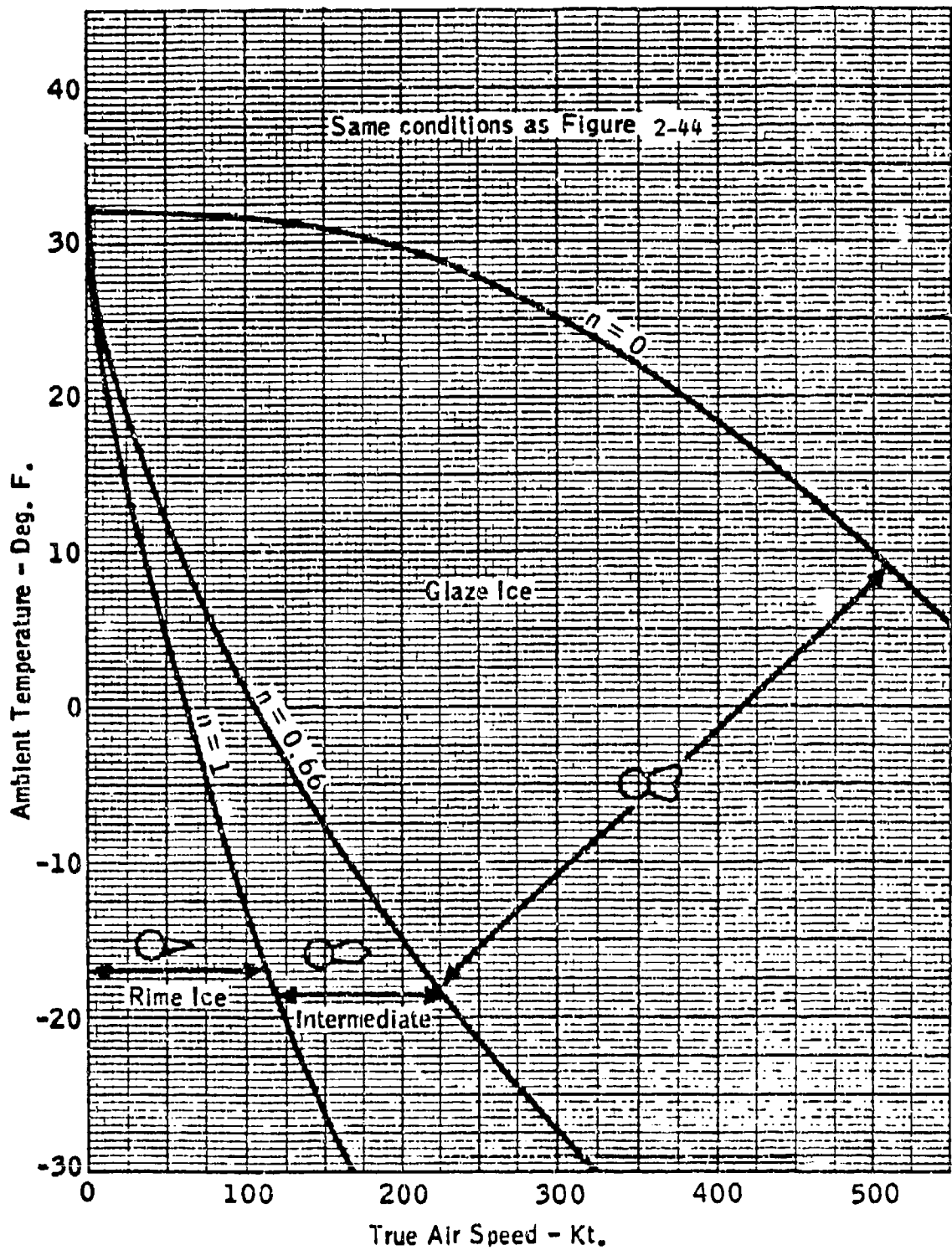
FIGURE 2-83.   ICE SHAPE TYPES AS A FUNCTION OF SPEED AND AMBIENT
              TEMPERATURE FOR A LIQUID WATER CONTENT OF 1.0 G/M^3
              (REFERENCE 2-49)

I 2-151
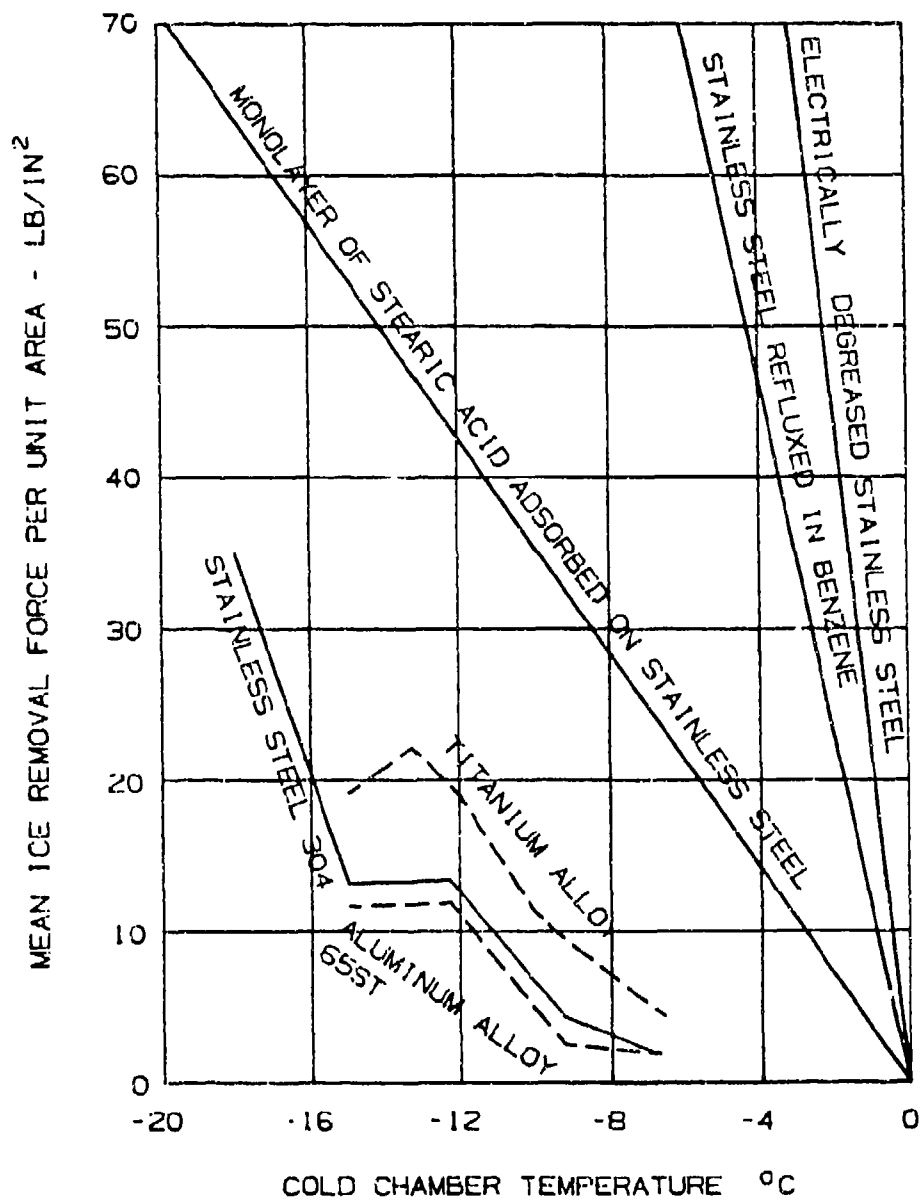
FIGURE 2-84. VARIATION OF ICE REMOVAL FORCE WITH TEMPERATURE

I 2-152

SHEAR STRESS VS. DROPLET MOMENTUM

(12F TO 18F)

Shear Stress(PSI) : 175E-11: Momentum +493

AVE. SCATTER ±13%

SHEAR STRESS (PSI)

V×D××3, FT××4/SEC ×10××10
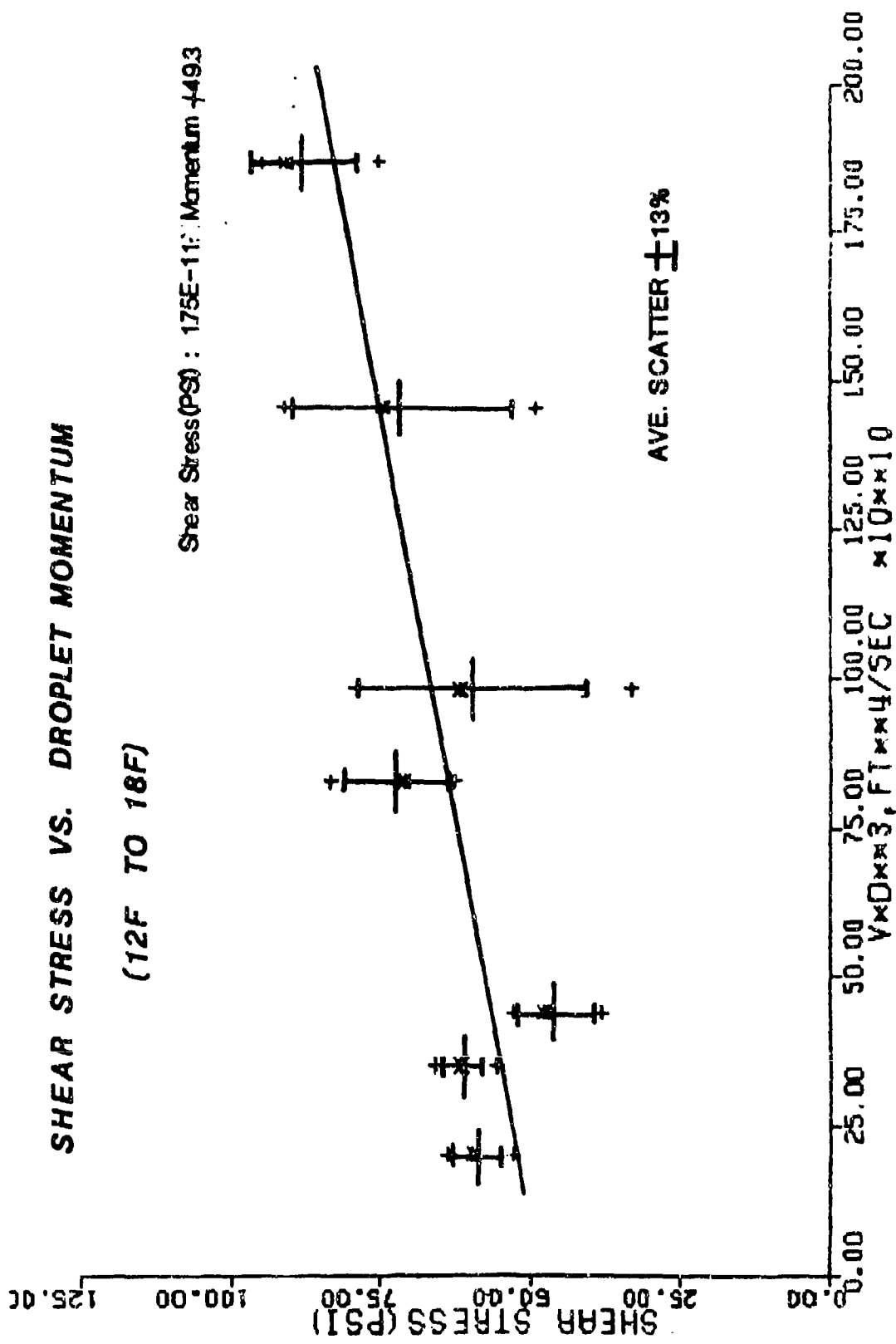
FIGURE 2-85. STATISTICAL PLOT OF ADHESIVE SHEAR VS. DROPLET MOMENTUM (REFERENCE 2-64)
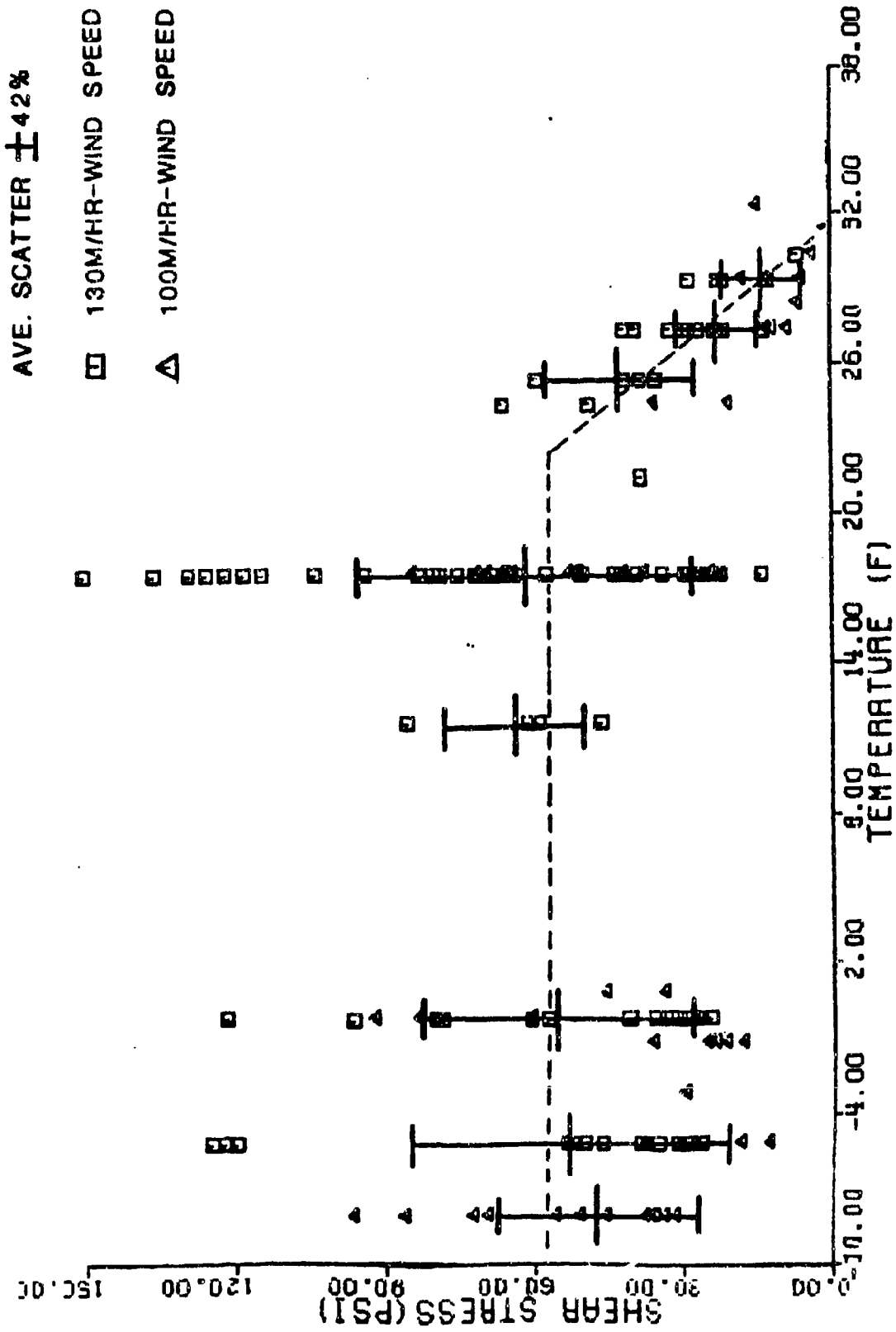
FIGURE 2-86. ADHESIVE SHEAR STRESS VS. INTERFACE TEMPERATURE (REFERENCE 2-64)
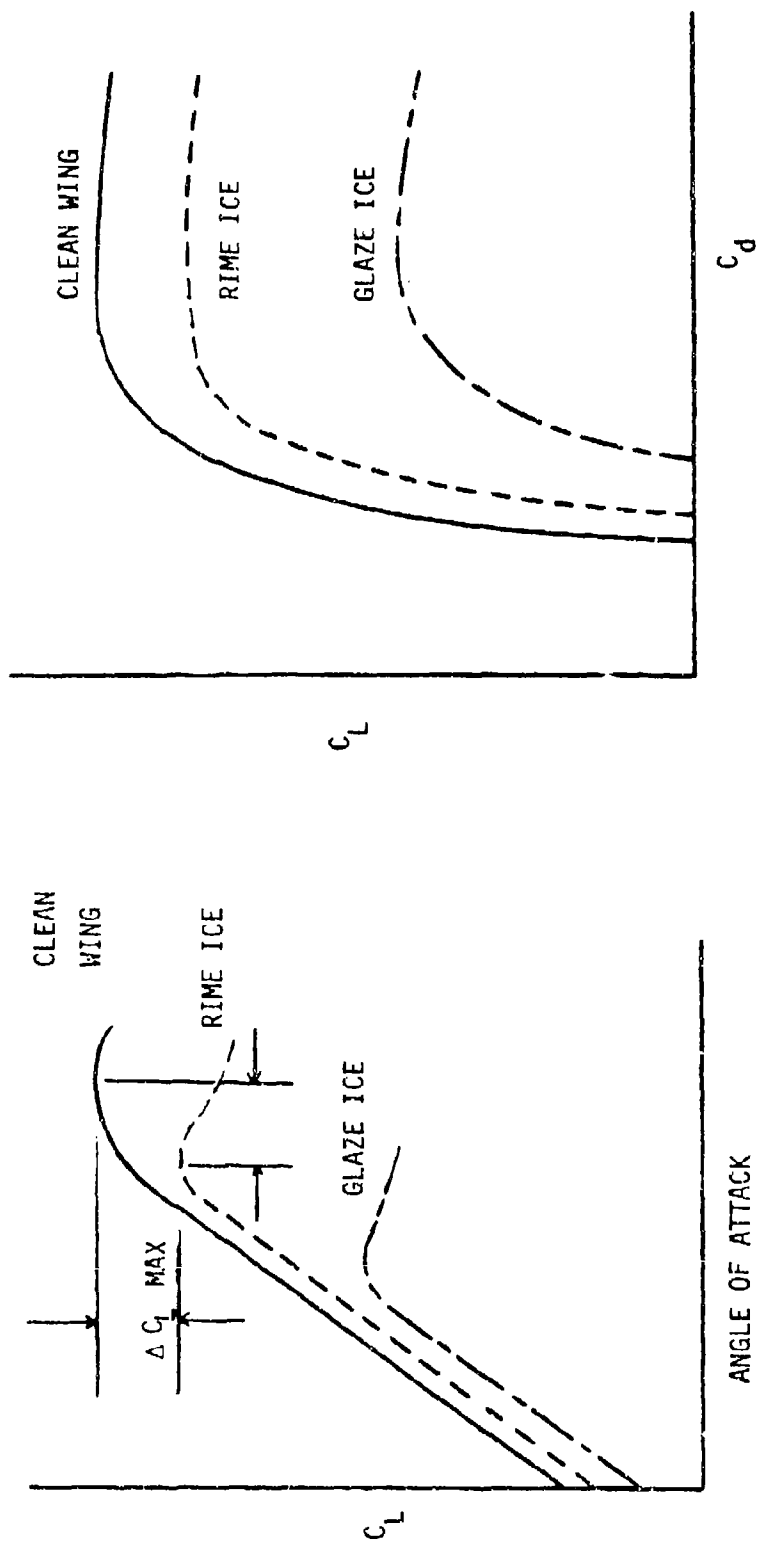
FIGURE 2-87. TYPICAL EFFECT OF ICE ACCRETION ON AIRFOIL PERFORMANCE
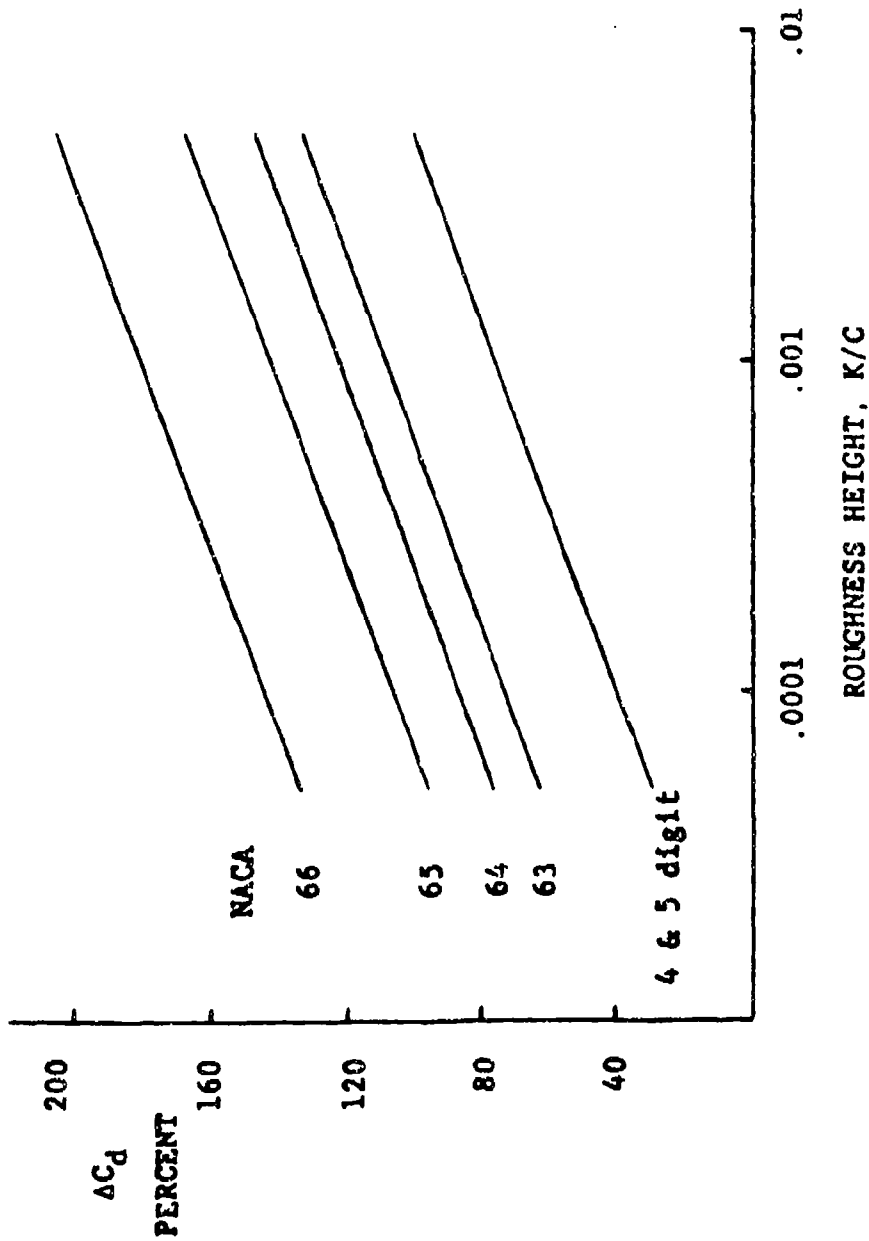
FIGURE 2-88. EFFECT OF ROUGHNESS HEIGHT ON DRAG FOR SEVERAL AIRFOIL CLASSES.

I 2-156
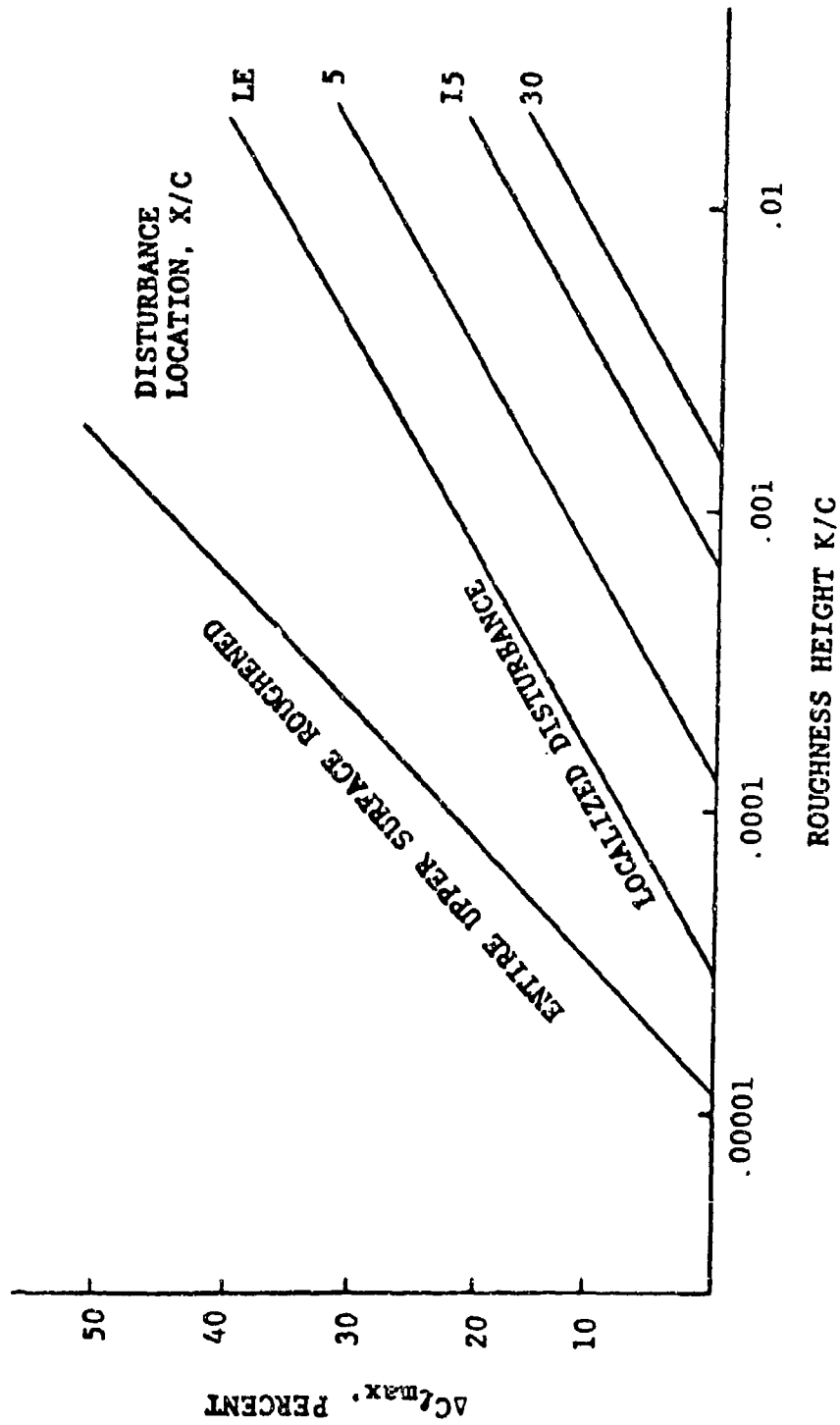
FIGURE 2-89. REDUCTION OF MAXIMUM LIFT COEFFICIENT DUE TO WING SURFACE ROUGHNESS

NACA 0012 AIRFOIL WITH 5 MIN GLAZE ICE

$\alpha = 3.85^{o}$ Re $= 1.5 \times 10^{6}$ M $= 0.12$

——— DIVIDING STREAMLINE

– – – STAGNATION STREAMLINE

0.10   0.20

X/c
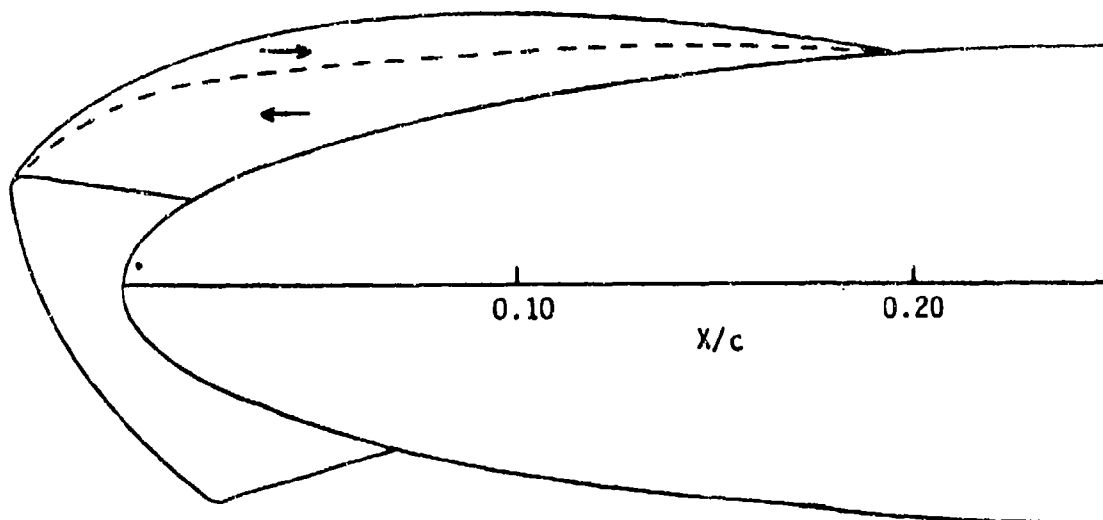
FIGURE 2-90.   MEASURED SEPARATION BUBBLE ON A NACA 0012 AIRFOIL
WITH A SIMULATED FIVE MINUTE GLAZE ICE SHAPE
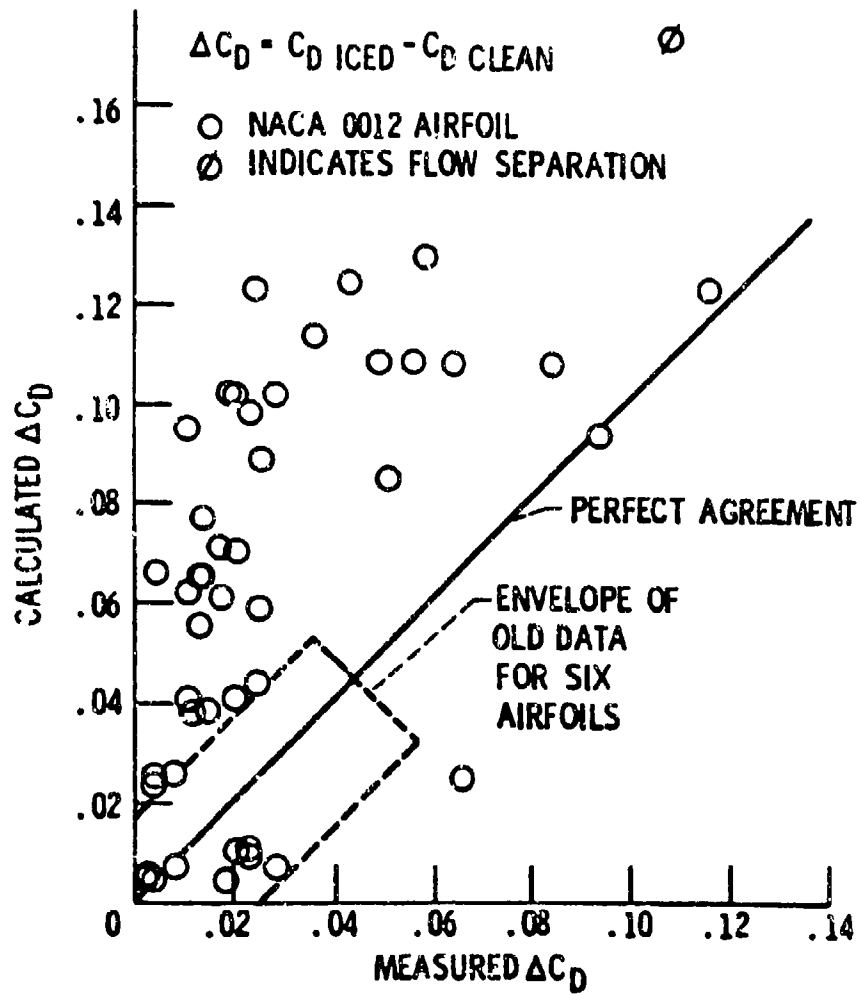
FIGURE 2-91. COMPARISON OF GRAY'S CORRELATION WITH MEASURED
INCREASE IN DRAG COEFFICIENT (REFERENCE 2-36)

I 2-159
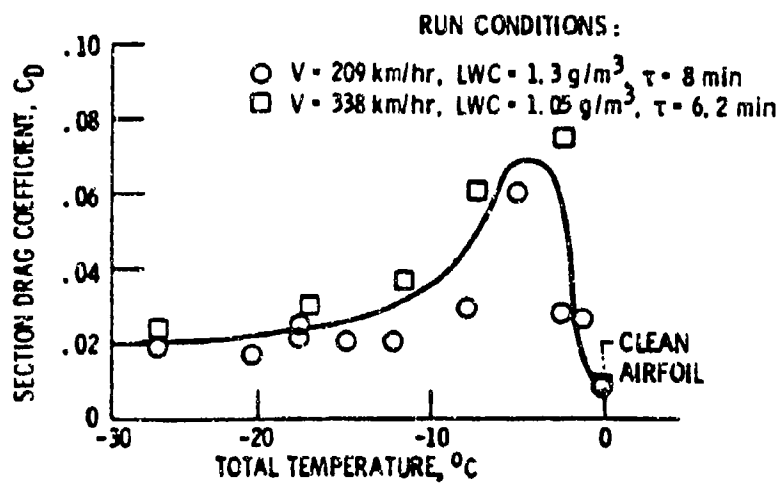
FIGURE 2-92. EFFECT OF TOTAL TEMPERATURE ON AIRFOIL DRAG
(REFERENCE 2-36)

I 2-160
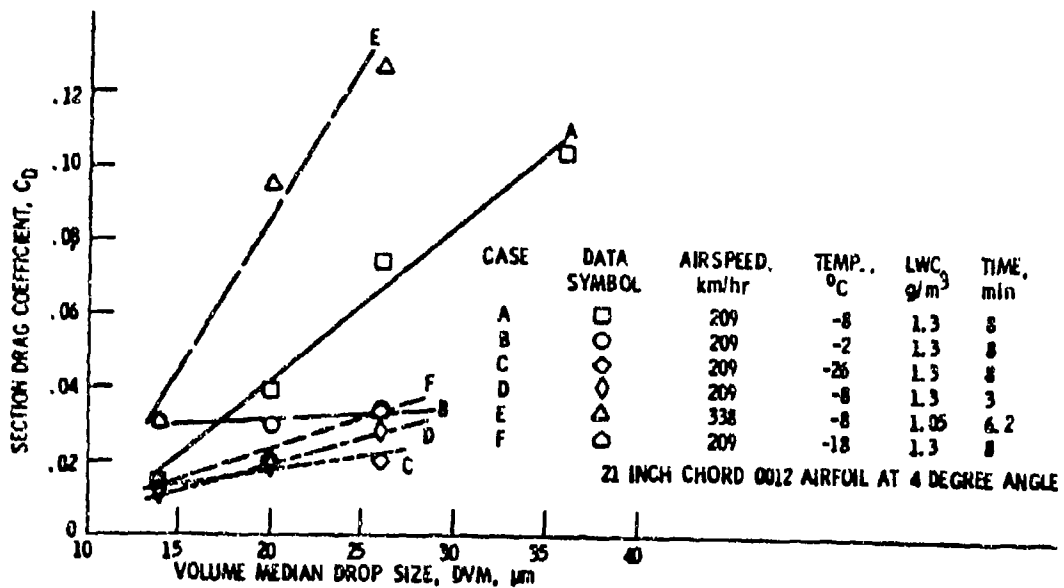
FIGURE 2-93.   EFFECT OF DROPLET SIZE ON AIRFOIL DRAG
              (REFERENCE 2-36)

I 2-161
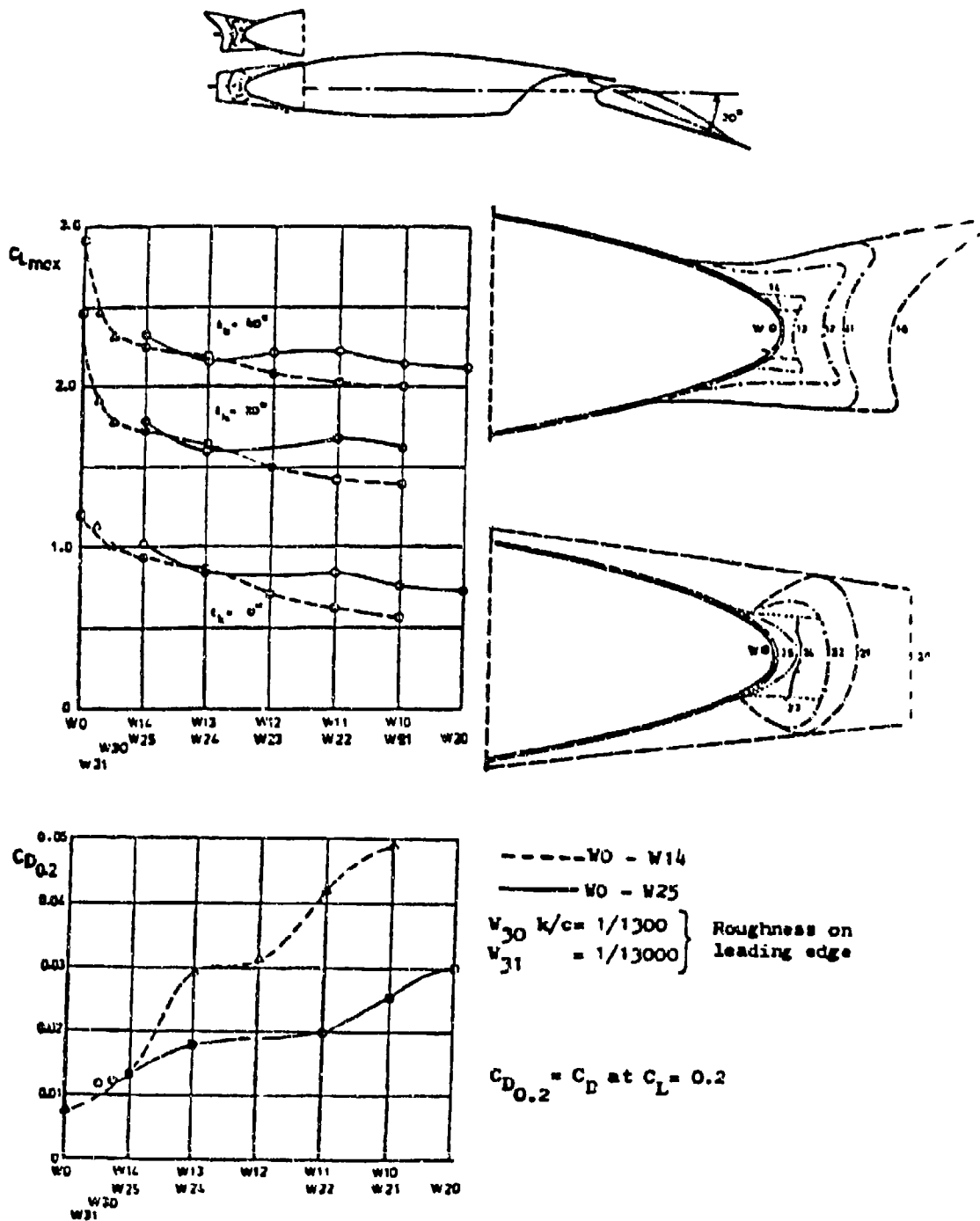
FIGURE 2-94.   EFFECT OF SIMULATED LARGE ICE SHAPES ON MAXIMUM LIFT
AND CRUISE DRAG OF NACA 65A215
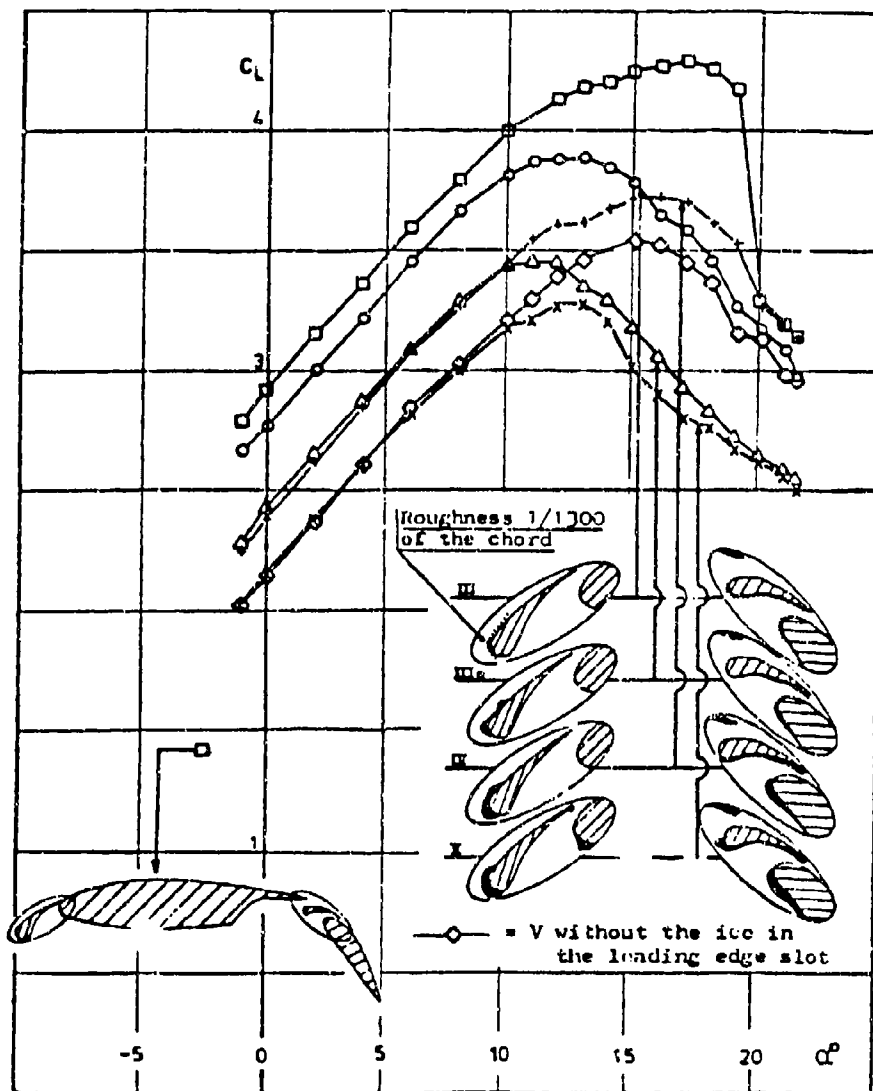
FIGURE 2-95. EFFECT OF ICE SHAPES ON LIFT CURVE OF NACA 65A215
WITH FLAPS AND SLATS EXTENDED
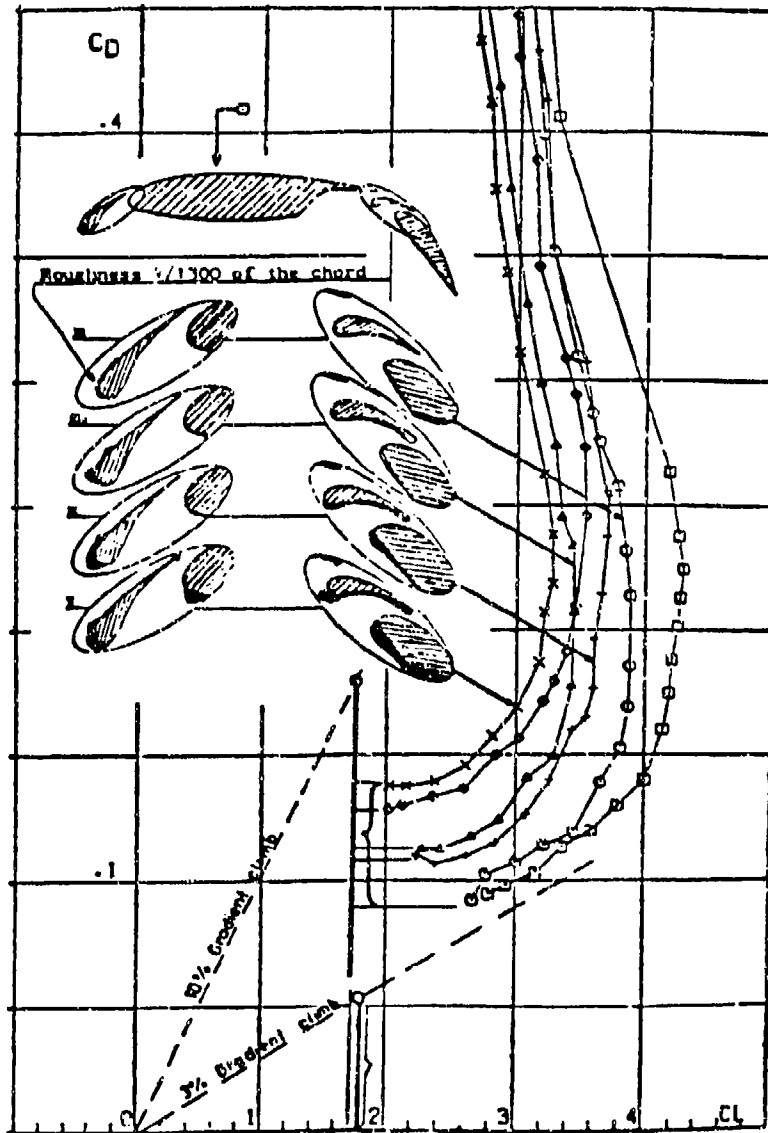
FIGURE 2-96. EFFECTS OF ICE SHAPES ON DRAG OF NACA 65A215
WITH FLAPS AND SLATS EXTENDED
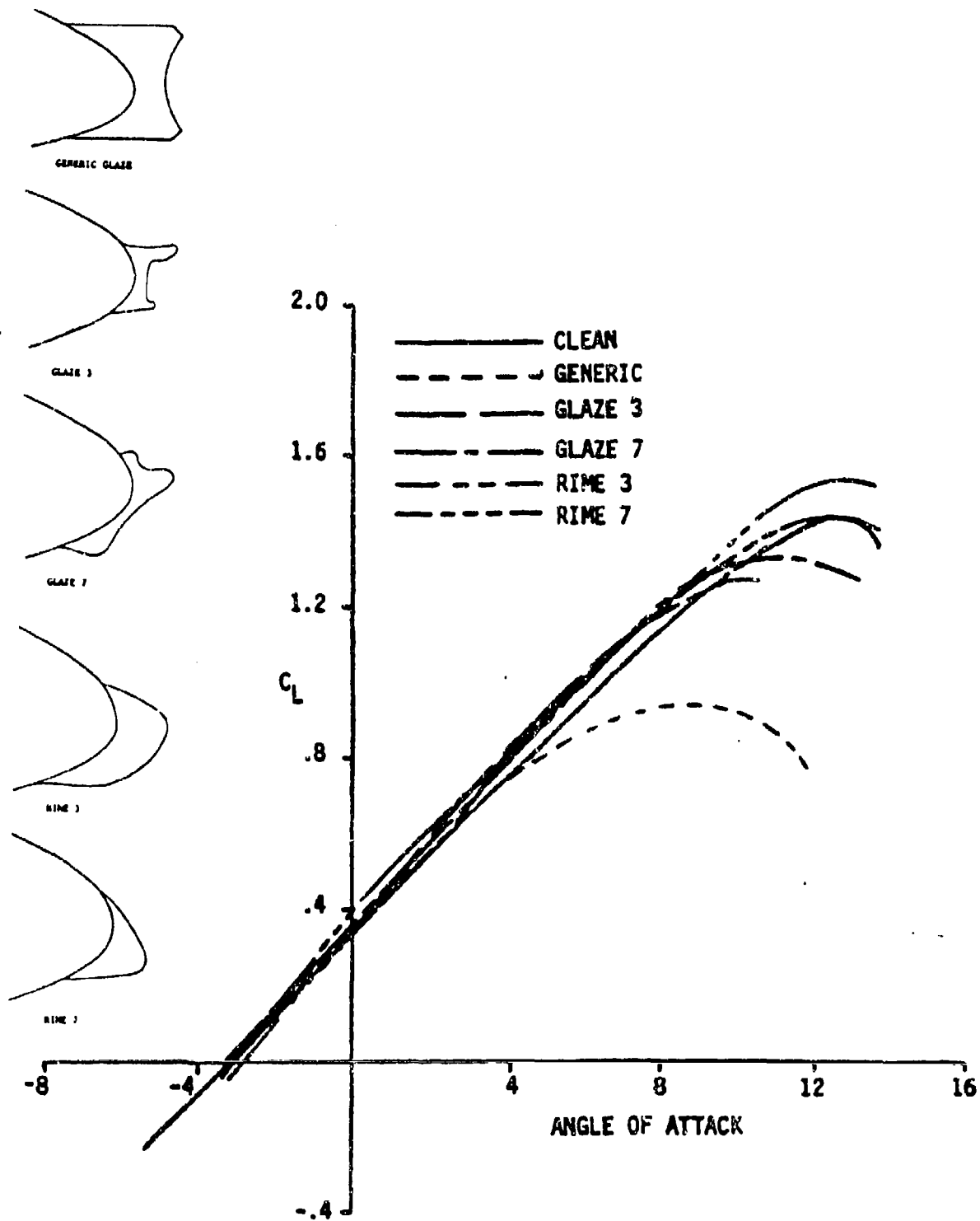
FIGURE 2-97.   EFFECT OF ICE SHAPES ON THE LIFT OF A
              NACA 63A415 AIRFOIL
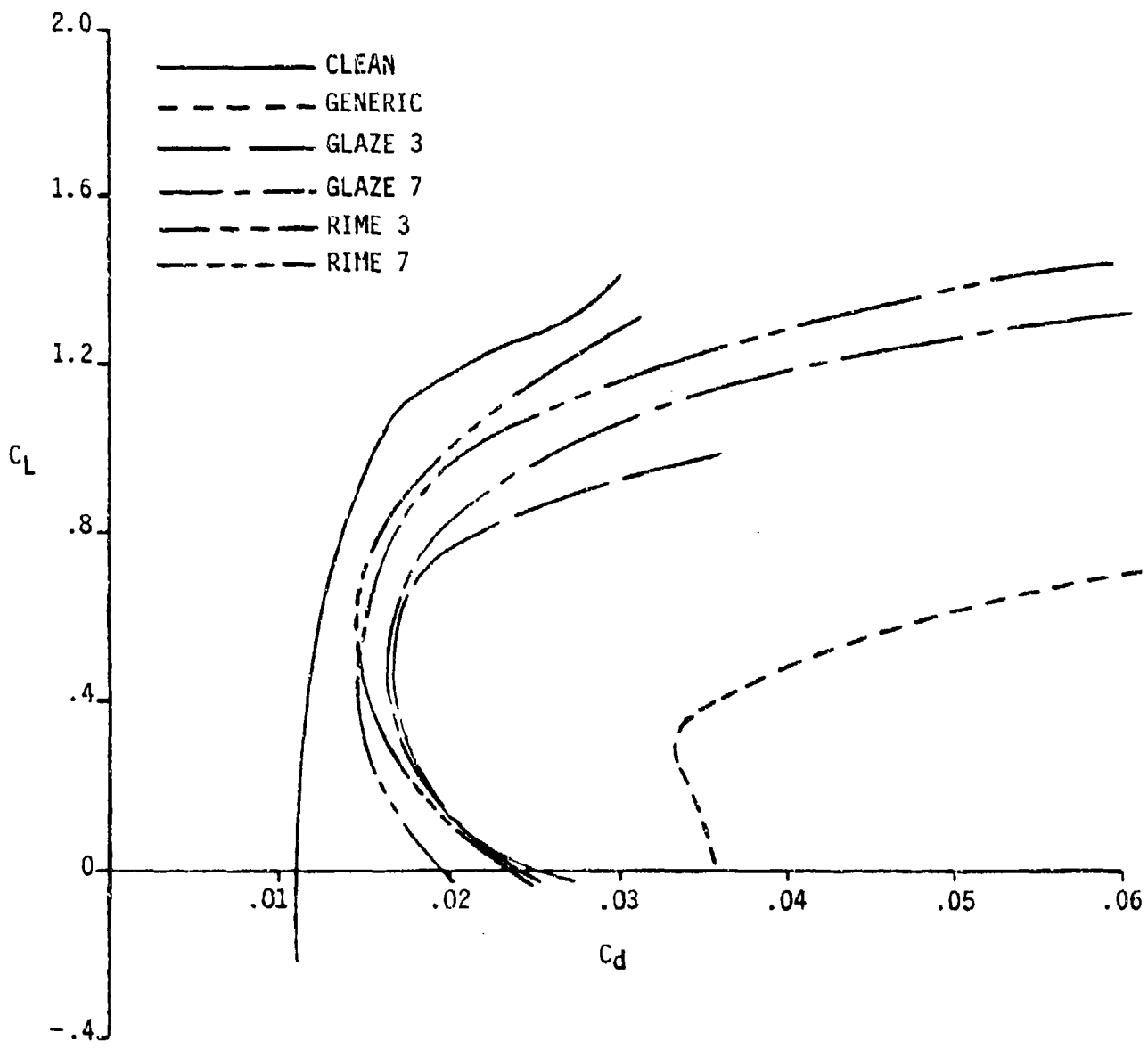
FIGURE 2-98. EFFECT OF ICE SHAPES ON THE DRAG OF A
NACA 63A415 AIRFOIL
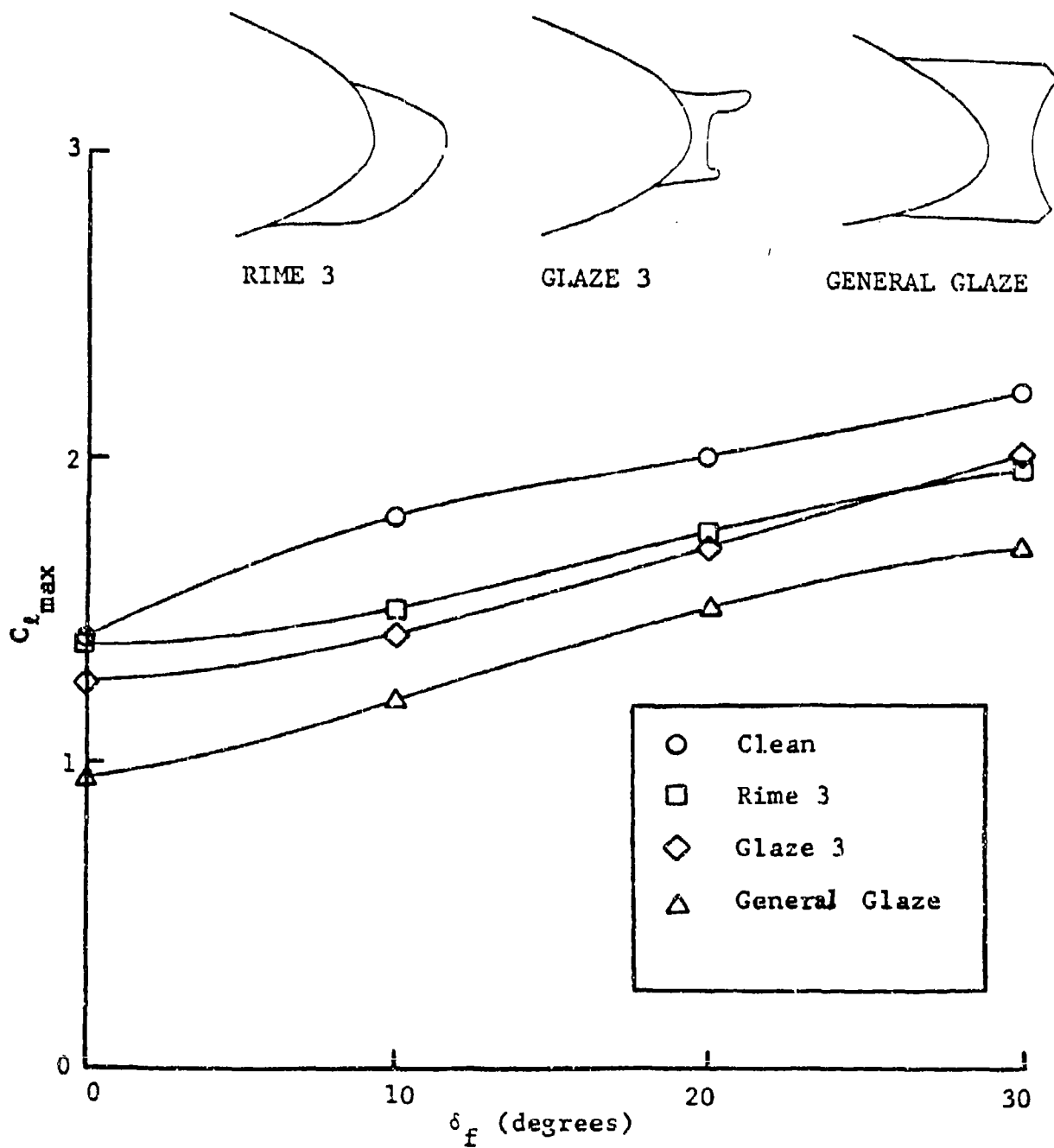
FIGURE 2-99. EFFECT OF FLAP DEFLECTION ON THE MAXIMUM LIFT OF A
NACA 63A415 AIRFOIL WITH ICE

I 2-167

(a) CRUISE WING.

(b) FLAPS 1.

(c) FLAPS 5.

(d) FLAPS 15.
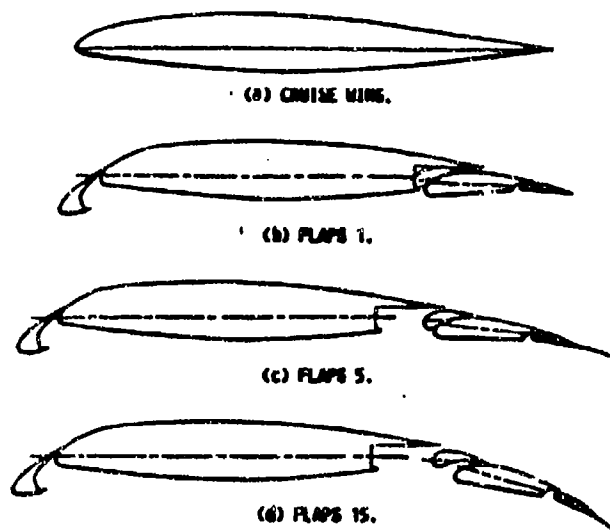
FIGURE 2-100.   MULTI-ELEMENT AIRFOIL CONFIGURATIONS EMPLOYED
DURING ICE ACCRETION TESTS (REFERENCE 2-76)
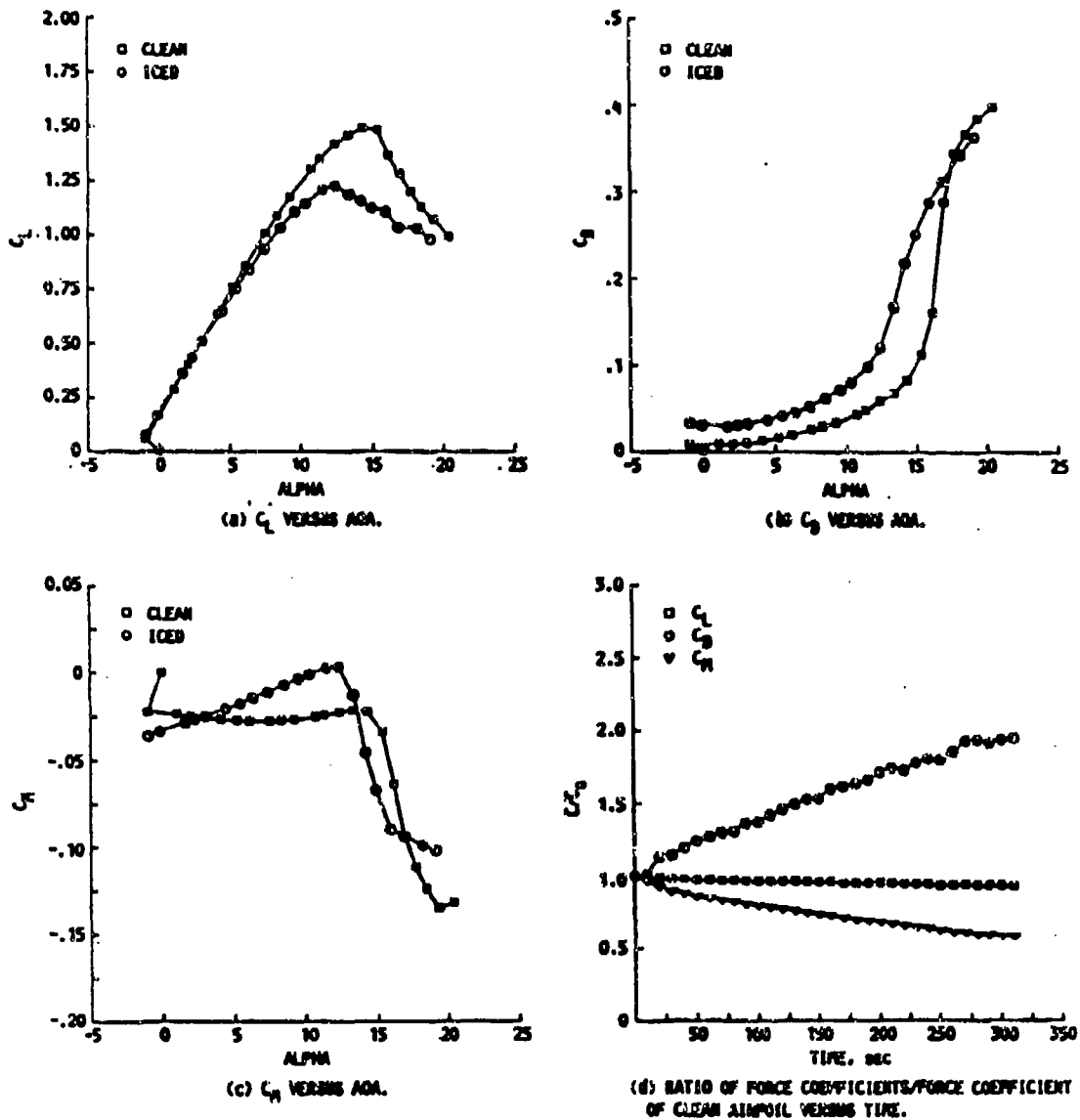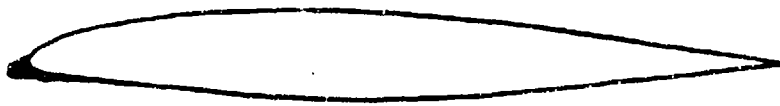
FIGURE 2-101.   ICE SHAPE TRACING AND FORCE BALANCE MEASUREMENTS FOR
FIVE MINUTE ICING ENCOUNTER WITH T = 10 °F, LWC =
1.13 G/M³, MVD = 17 μm, V = 158 FT/S AND α = 5°
FOR CRUISE CONFIGURATION (REFERENCE 2-76)
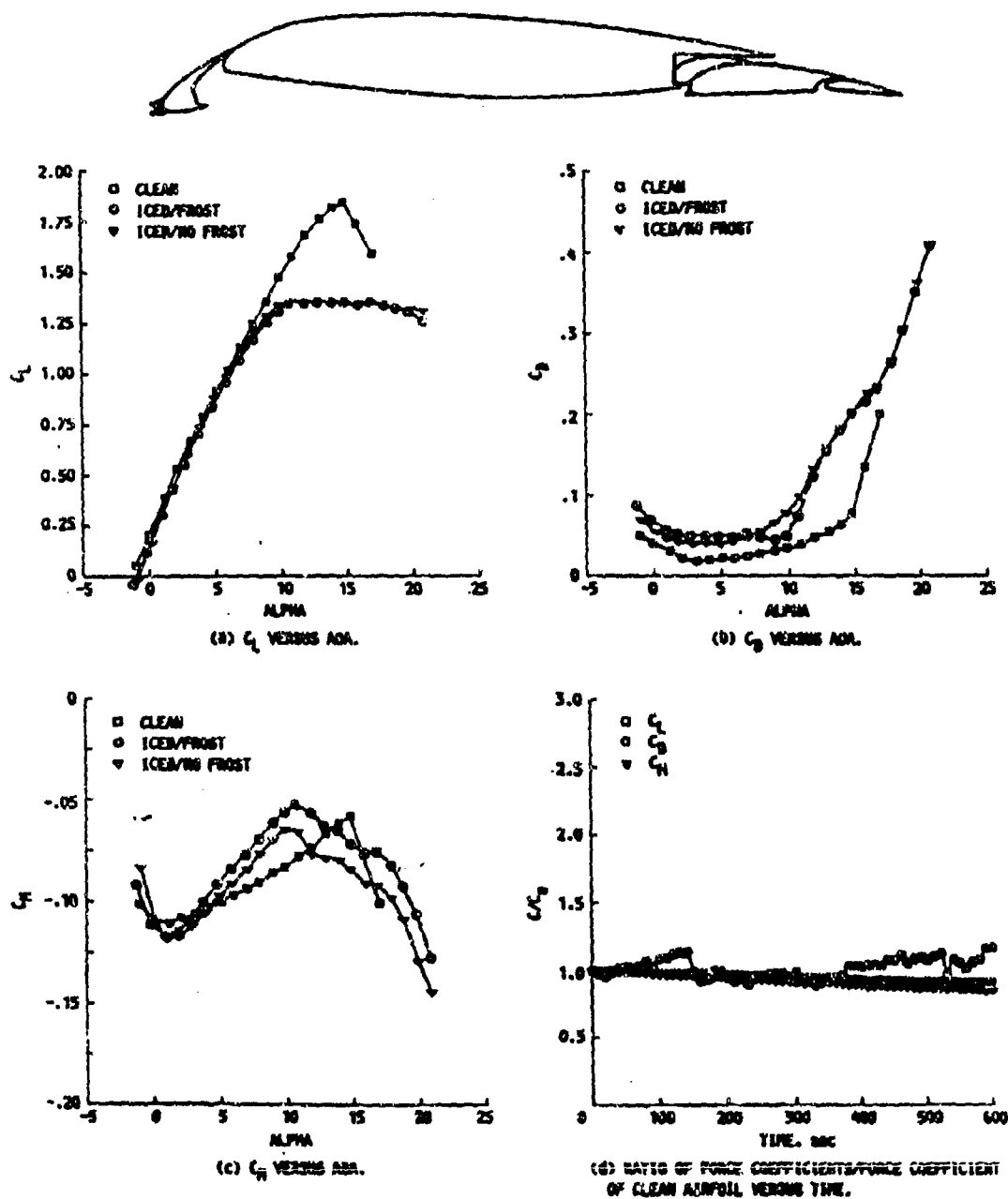
FIGURE 2-102. ICE SHAPE TRACING AND FORCE BALANCE MEASUREMENTS FOR
TEN MINUTE ICING ENCOUNTER WITH T = 26 °F, LWC =
.92, G/M³, MVD = 14.4 μm, V = 159 FT/S AND α = 5°
FOR 1° FLAP CONFIGURATION (REFERENCE 2-76)
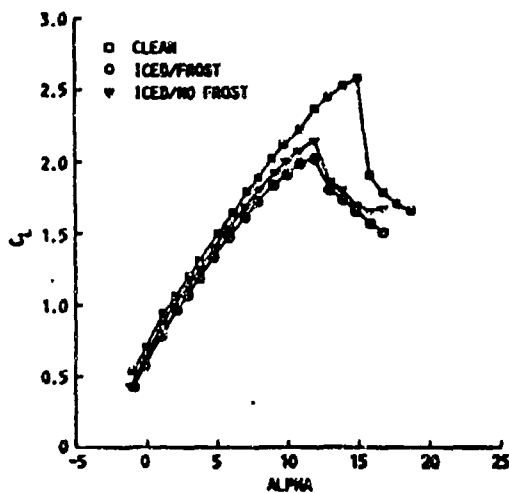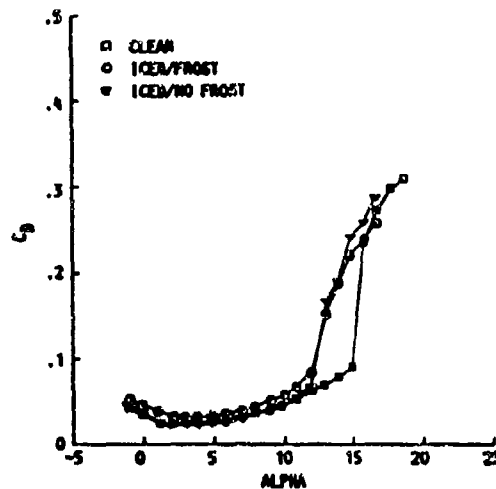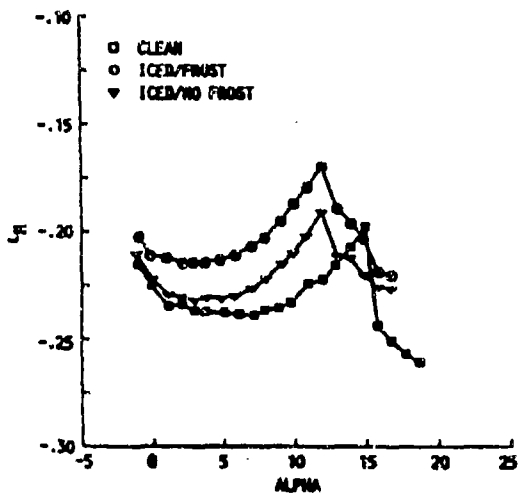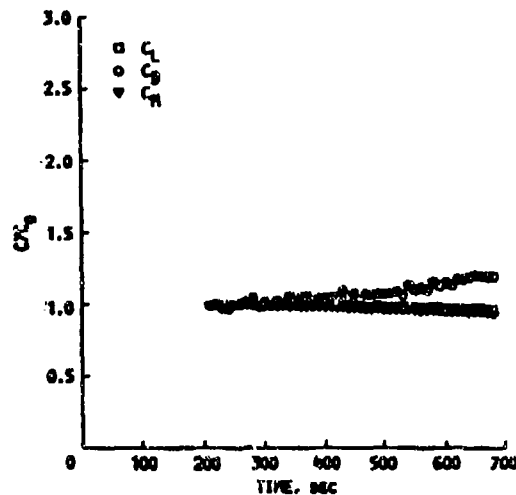
I 2-170

FIGURE 2-103. ICE SHAPE TRACING AND FORCE BALANCE MEASUREMENTS FOR
ELEVEN MINUTE ICING ENCOUNTER WITH T = 25 °F, LWC =
.46 G/M³, MVD = 12 μm, V = 158 FT/S AND α = 5°
FOR 5° FLAP CONFIGURATION (REFERENCE 2-76)

I 2-171
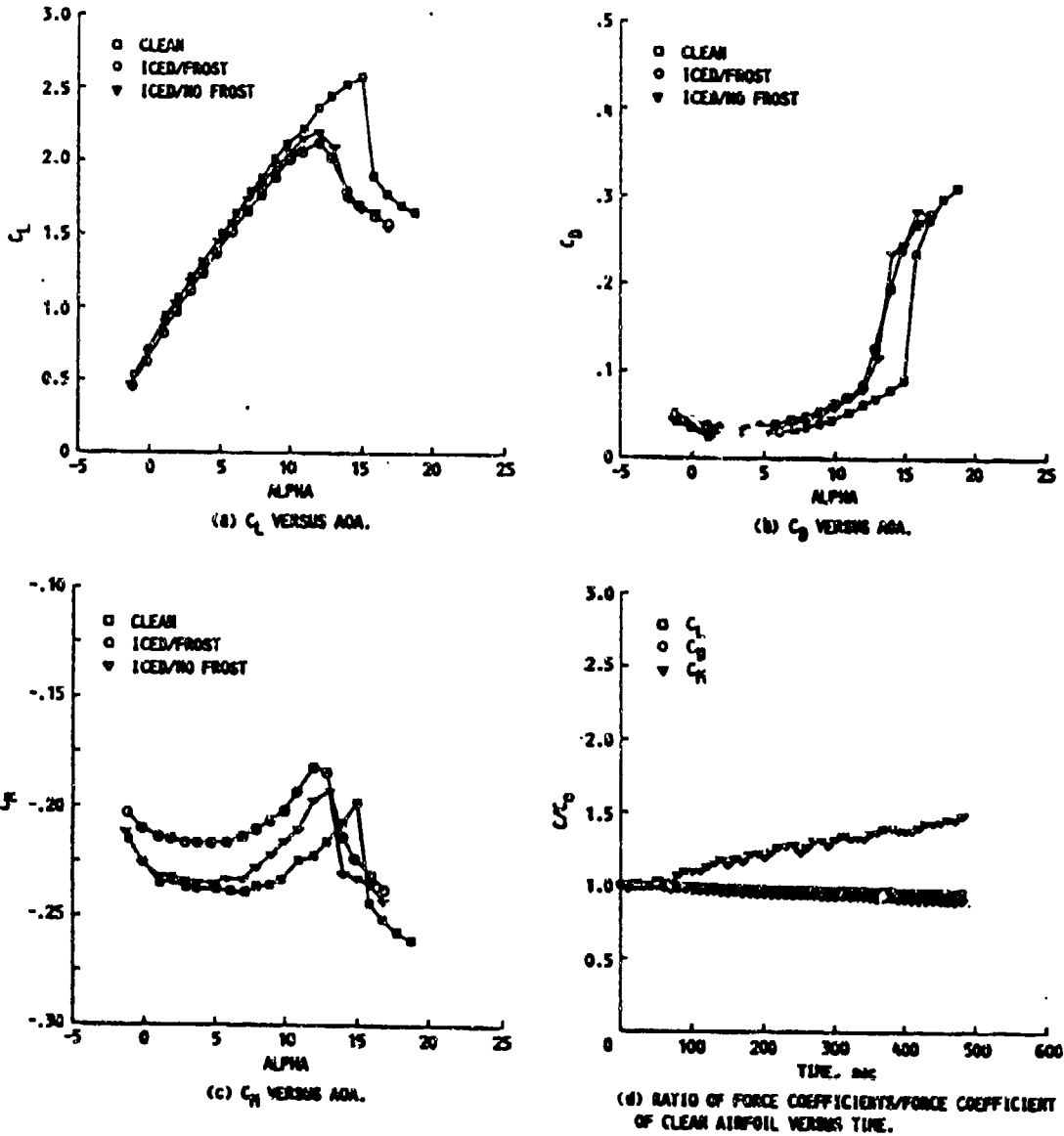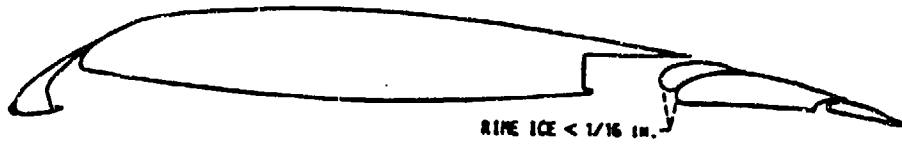
FIGURE 2-104.   ICE SHAPE TRACING AND FORCE BALANCE MEASUREMENTS FOR
                EIGHT MINUTE ICING ENCOUNTER WITH T = 17 °F, LWC =
                .42 G/M³, MVD = 13.4 µm, V = 158 FT/S AND α = 5°
                FOR 5° FLAP CONFIGURATION (REFERENCE 2-76)
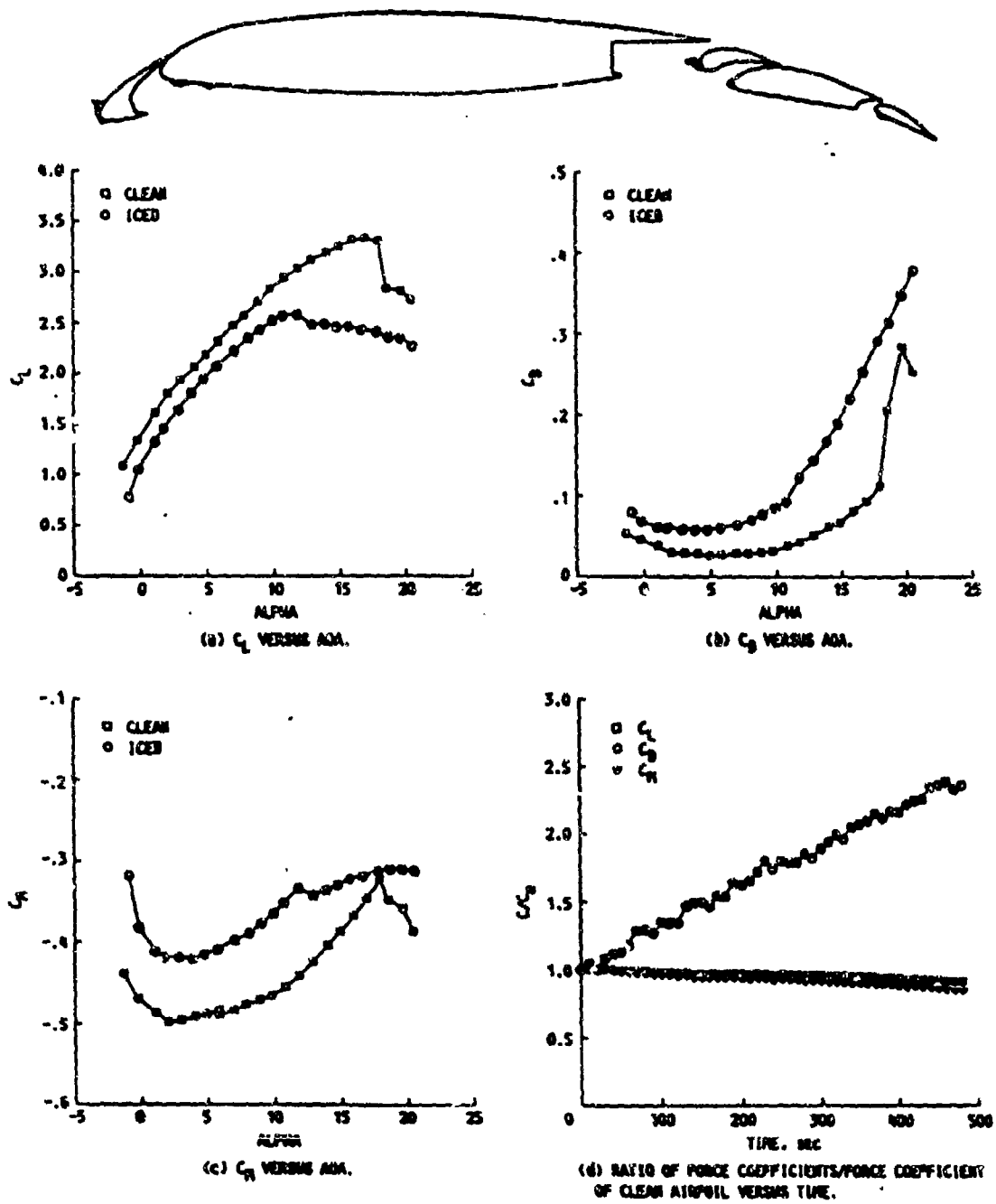
FIGURE 2-105. ICE SHAPE TRACING AND FORCE BALANCE MEASUREMENTS FOR EIGHT MINUTE ICING ENCOUNTER WITH T = 28 °F, LWC = .92 G/M³, MVD = 14.4 μm, V = 158 FT/S AND α = 5° FOR 15° FLAP CONFIGURATION (REFERENCE 2-76)

I 2-173
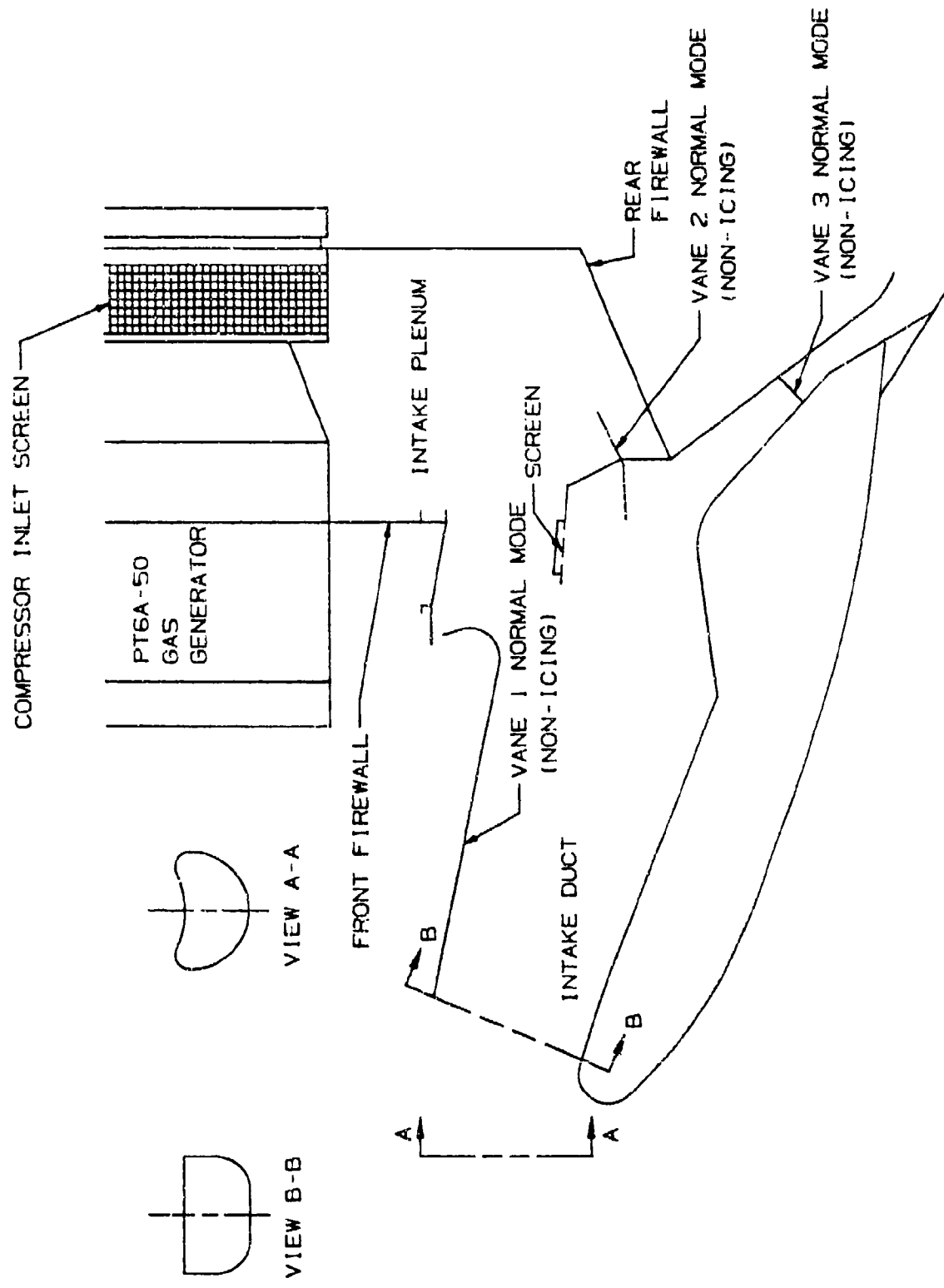
FIGURE 2-106a. PT6A-50 ANTI-ICING CONFIGURATION INERTIAL SEPARATION SYSTEM

COMPRESSOR INLET SCREEN

PT6A-50
GAS
GENERATOR

INTAKE PLENUM

REAR
FIREWALL

VANE 2 ICING MODE

VANE 3 ICING MODE

SCREEN

FRONT FIREWALL

VANE 1 ICING MODE

INTAKE DUCT

VIEW B-B   VIEW C-C   VIEW A-A

A

B

C

C

B

A
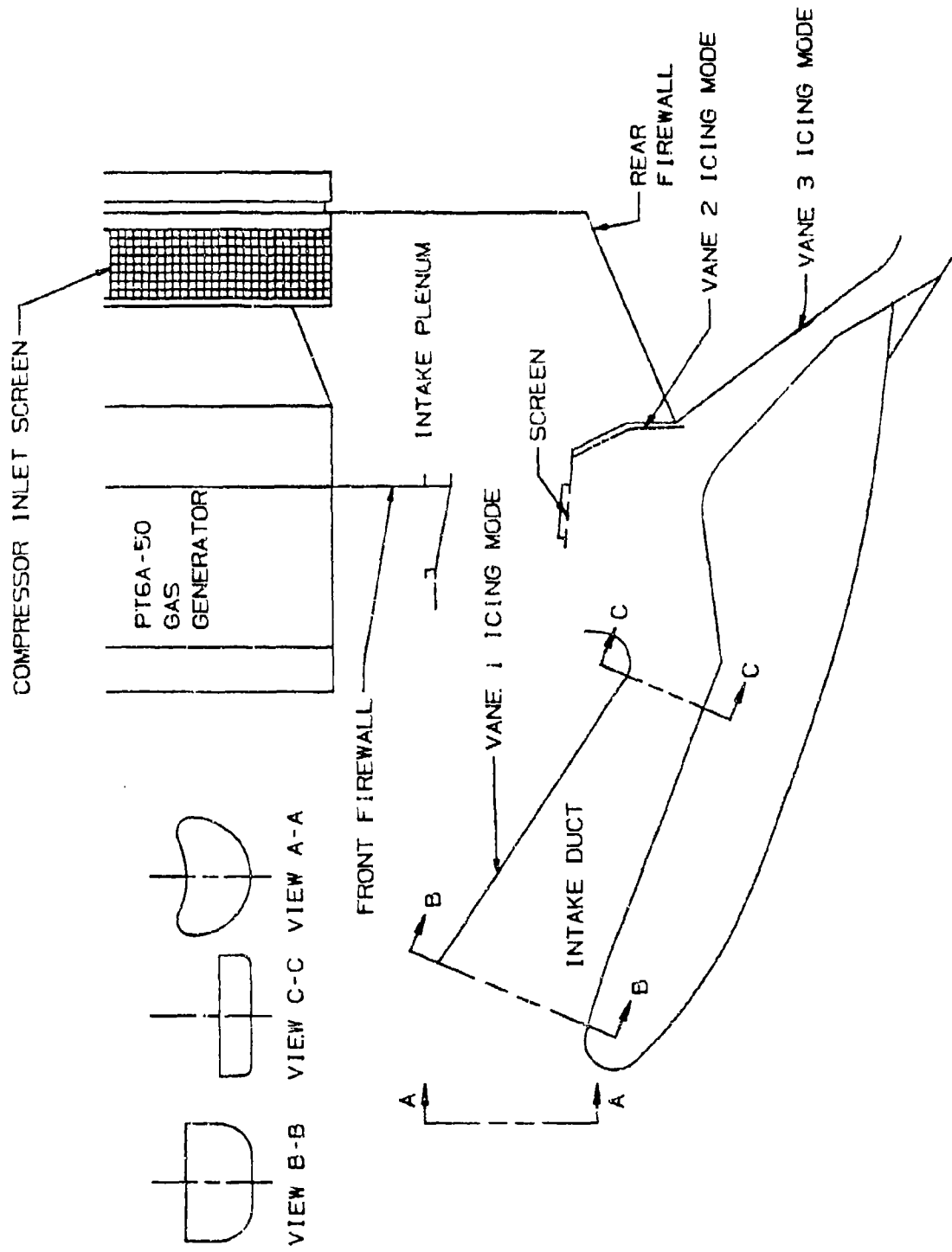
FIGURE 2-106b. PT6A-50 ANTI-ICING CONFIGURATION INERTIAL SEPARATION SYSTEM
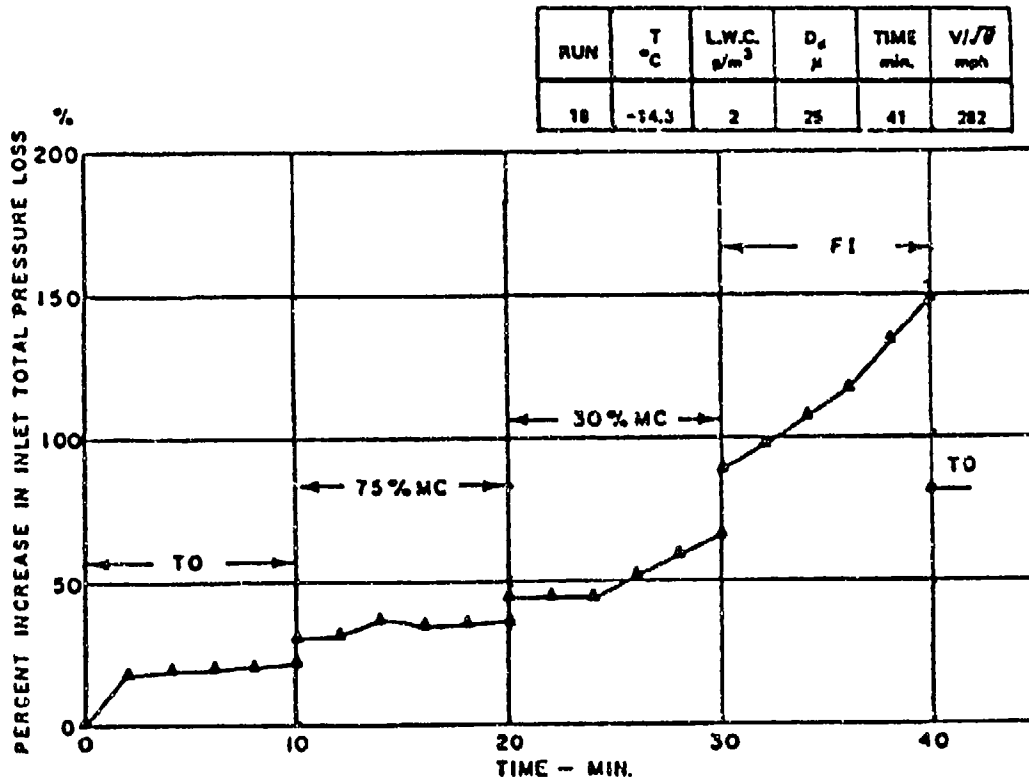
FIGURE 2-107. PERCENT INCREASE IN PRESSURE LOSS VERSUS TIME - CERTIFICATION TEST 1
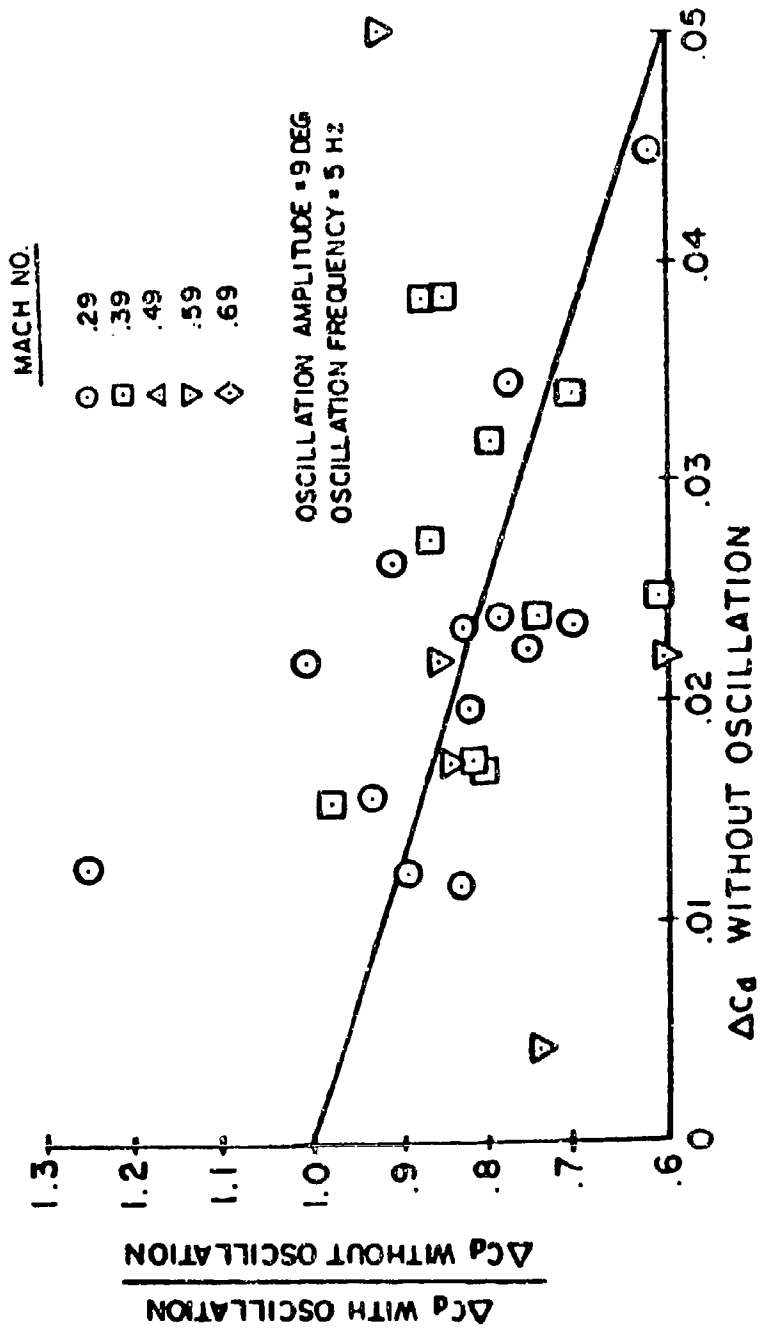
FIGURE 2-108. EFFECT OF AIRFOIL OSCILLATION ON DRAG COEFFICIENT
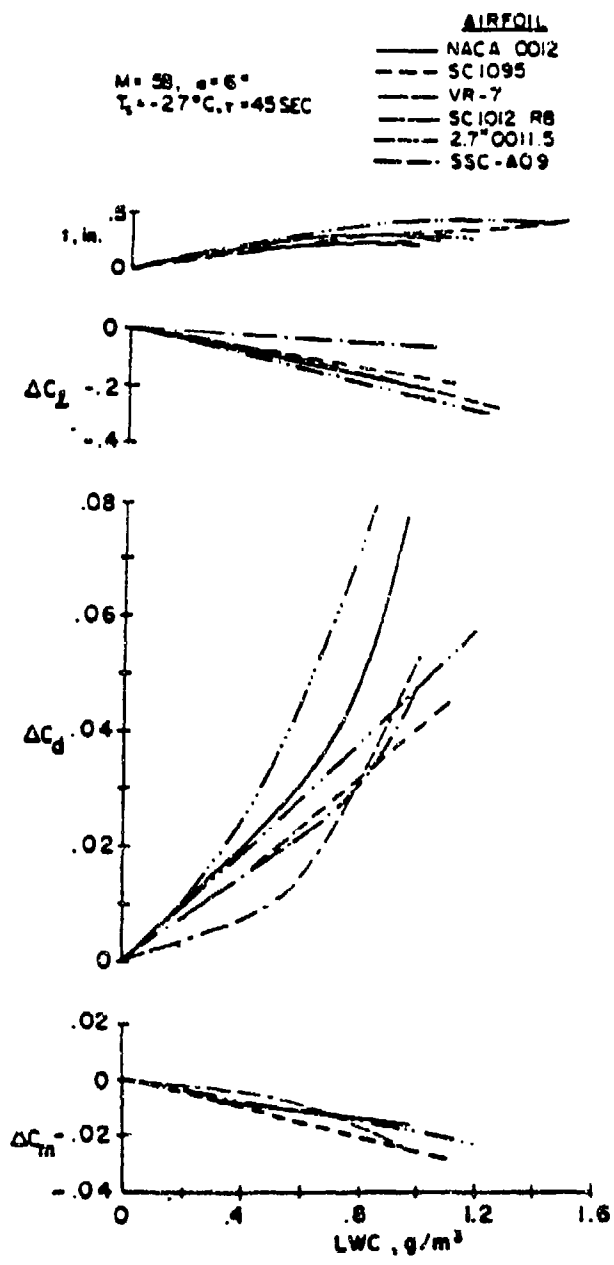
FIGURE 2-109. EFFECT OF LIQUID WATER CONTENT ON ROTOR AIRFOIL
PERFORMANCE
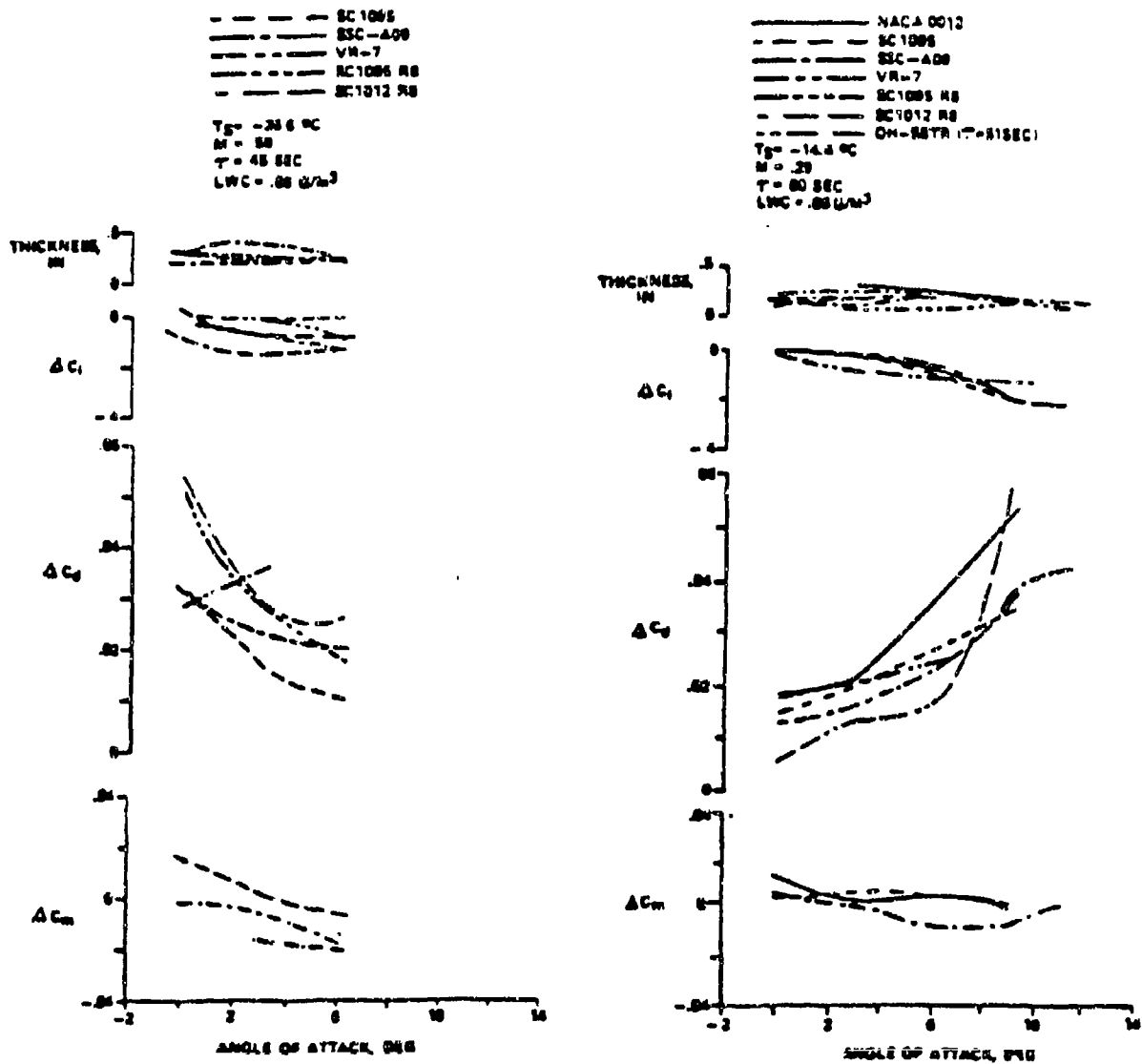
FIGURE 2-110. ROTOR AIRFOIL PERFORMANCE DUE TO ICE ACCRETION AT TWO MACH NUMBERS
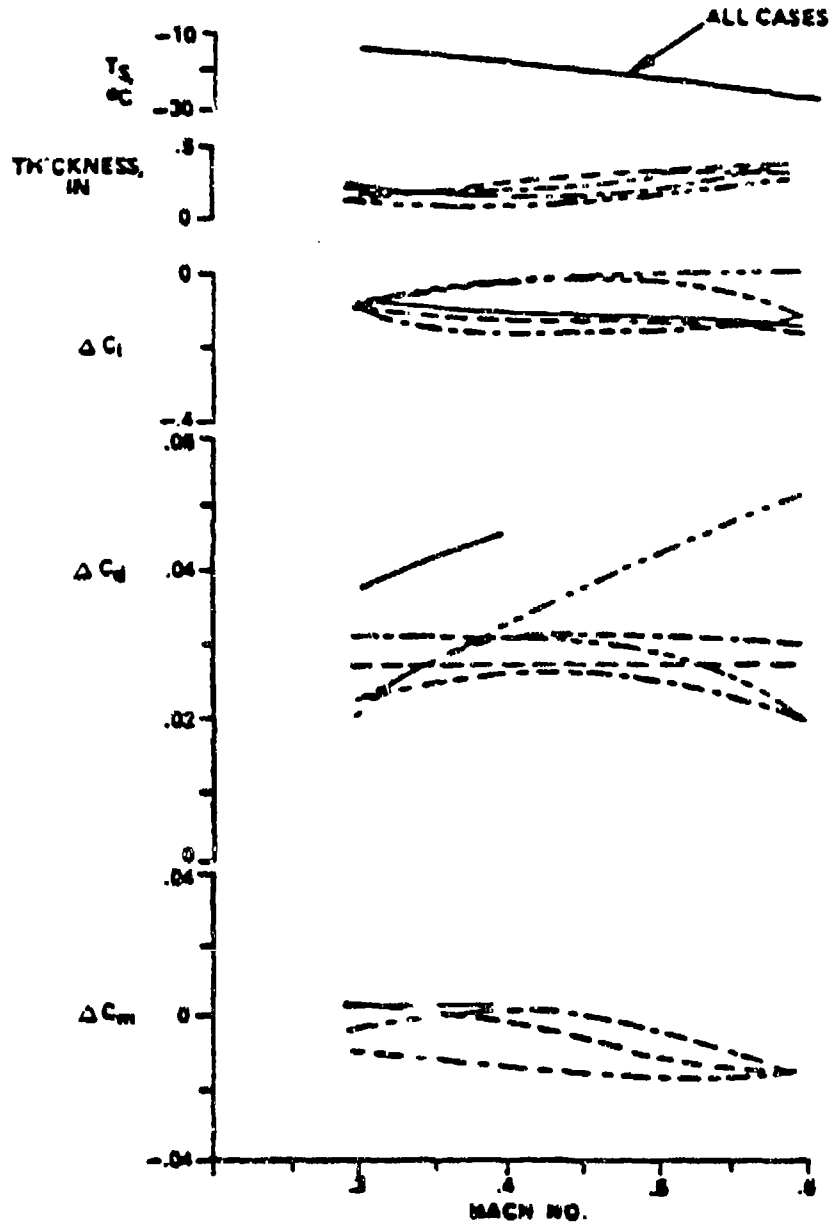
FIGURE 2-111. EFFECT OF MACH NUMBER ON ROTOR AIRFOIL PERFORMANCE

I 2-130
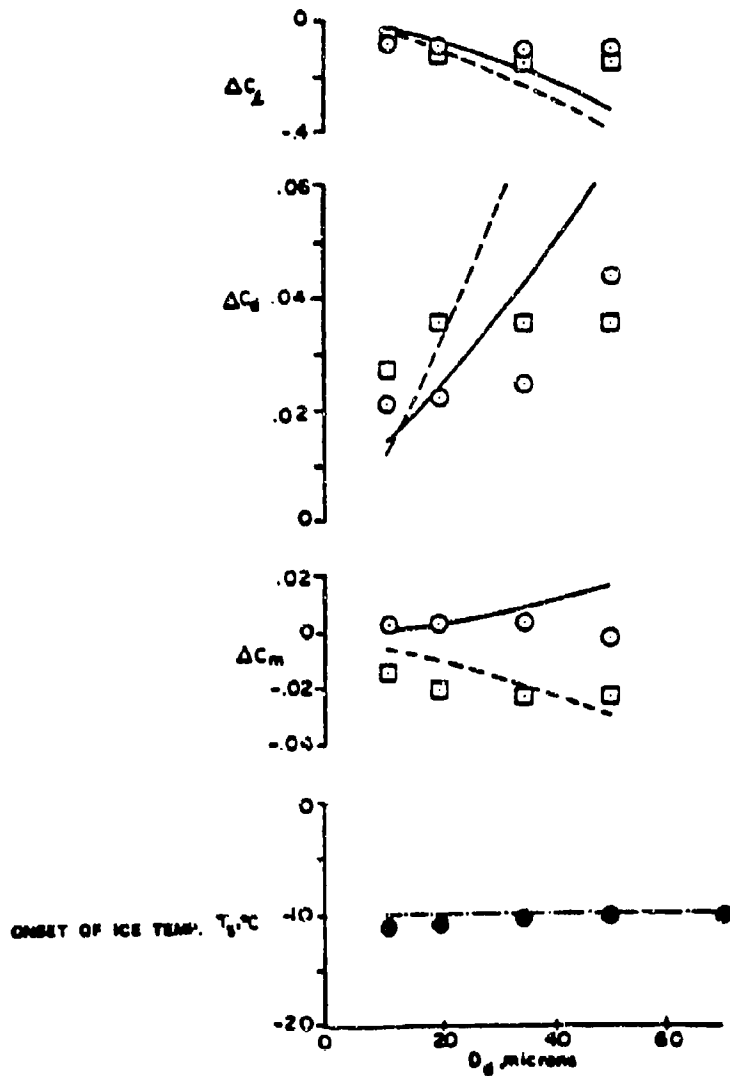
FIGURE 2-112. EFFECT OF DROPLET DIAMETER ON ROTOR AIRFOIL
PERFORMANCE
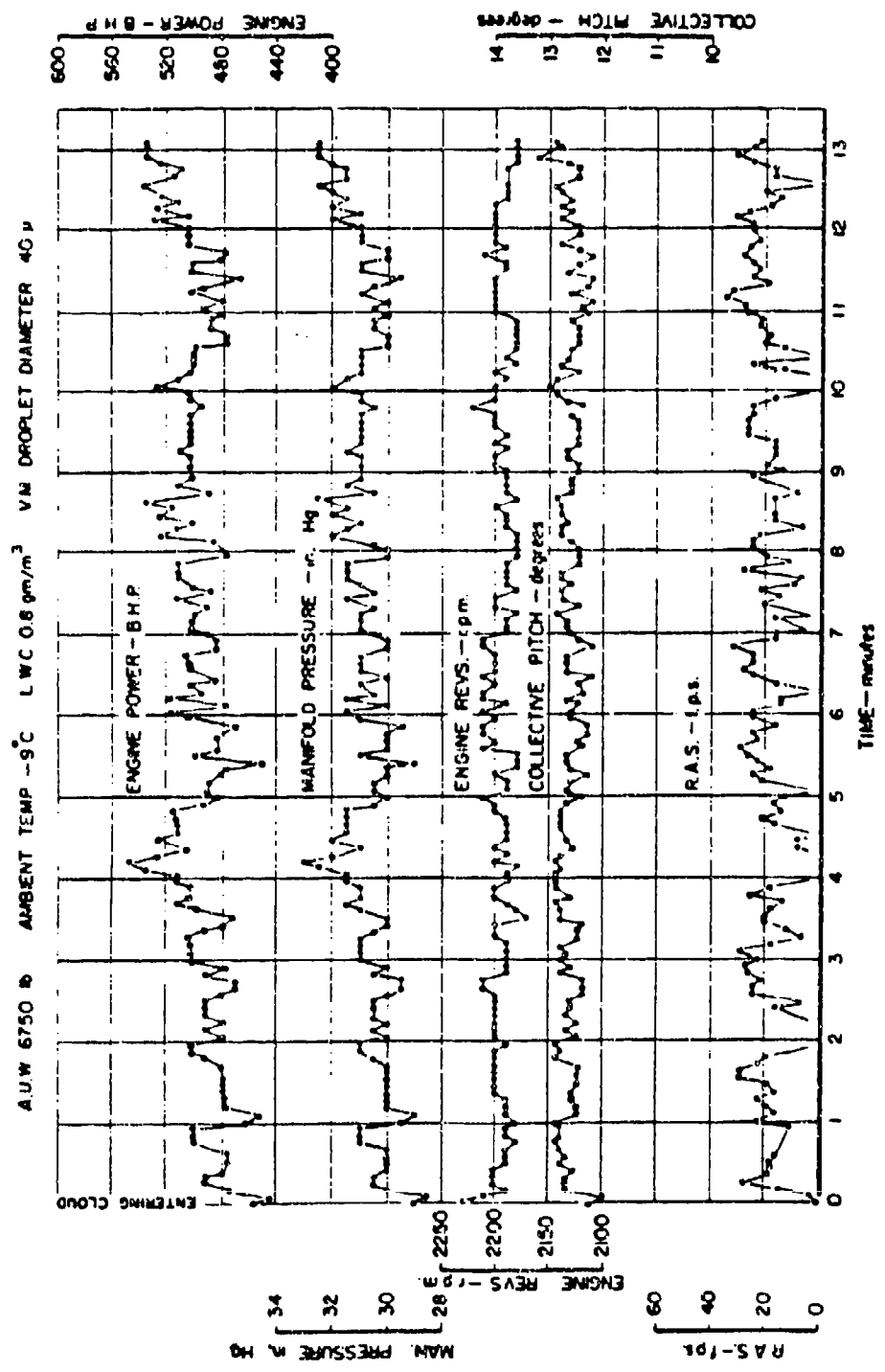
FIGURE 2-113. MEASURED FLIGHT PARAMETERS FOR A SIKORSKY HO4S-2 HELICOPTER
IN ICING CONDITIONS
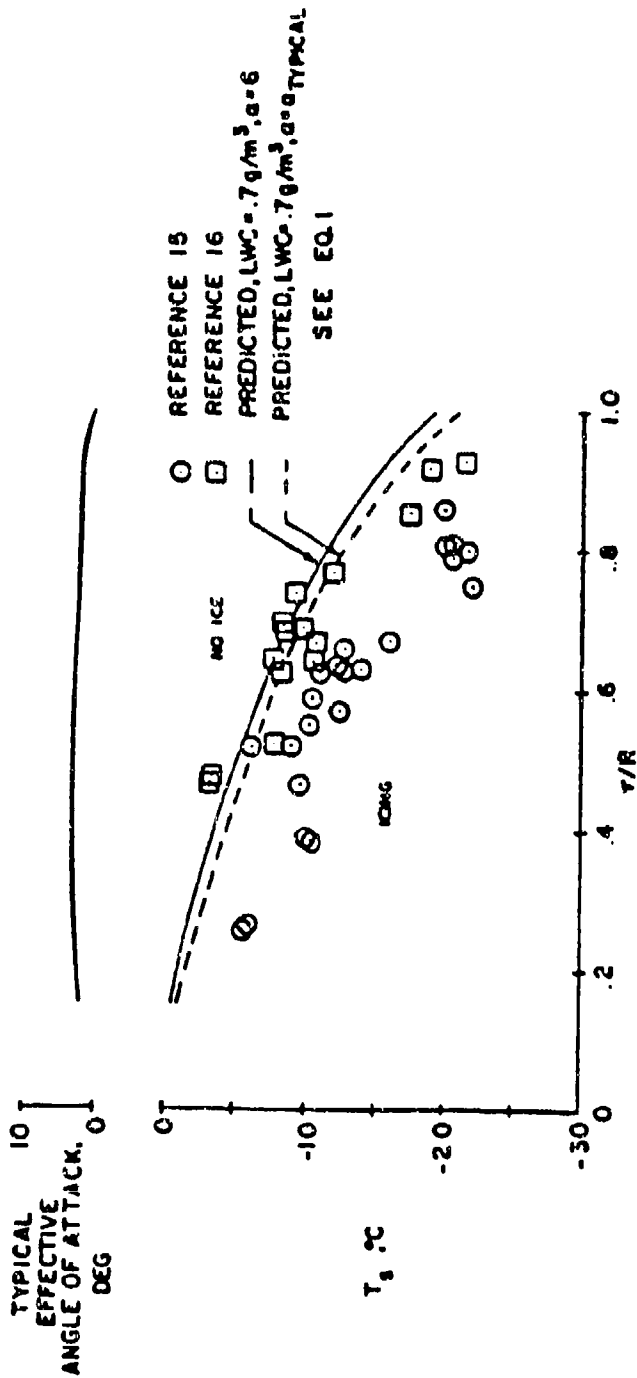
FIGURE 2-114. ICING EXTENT FOR THE JCH-1H HELICOPTER
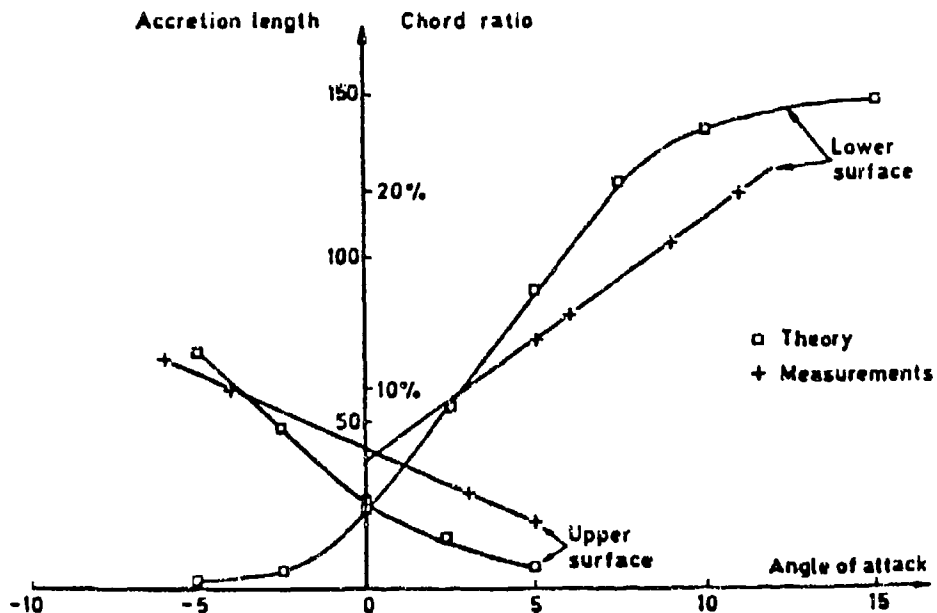
Extent of the Wetted Surface as a Function
of Angle of Attack

FIGURE 2-115a.   CHORDWISE EXTENT OF ICING AS A FUNCTION OF ANGLE OF
ATTACK
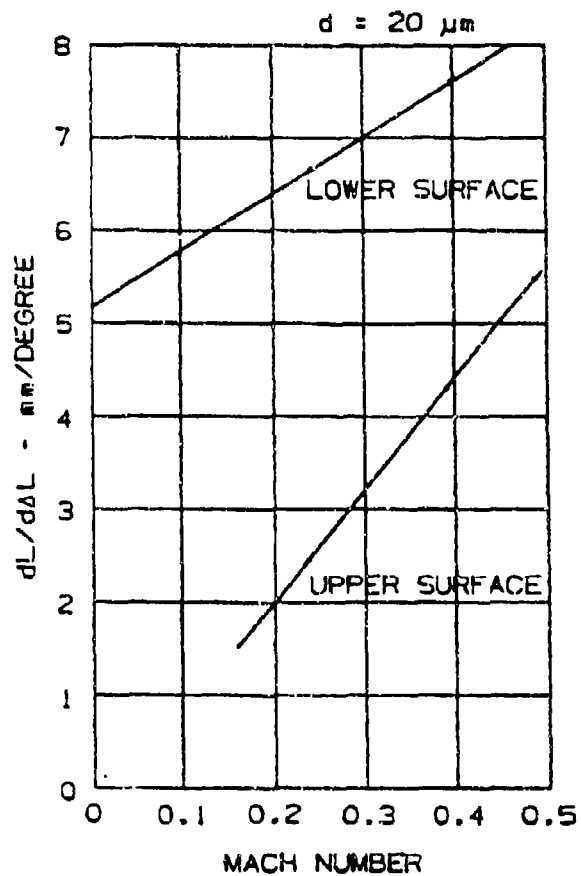
Variation in Wetted Area at Angle of Attack,
as a Function of Speed

FIGURE 2-115b. CHORDWISE EXTENT OF ICE AS A FUNCTION OF MACH
NUMBER

I 2-185
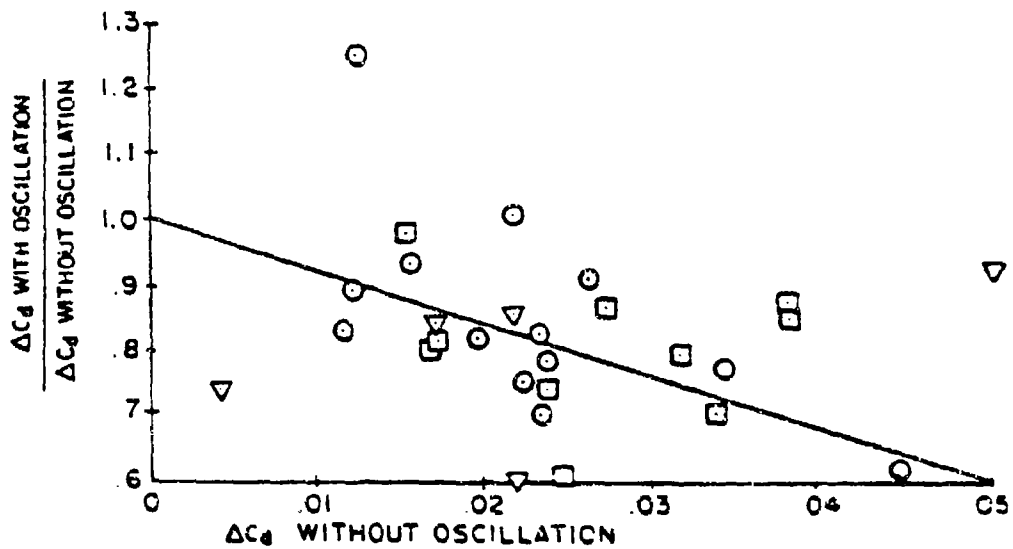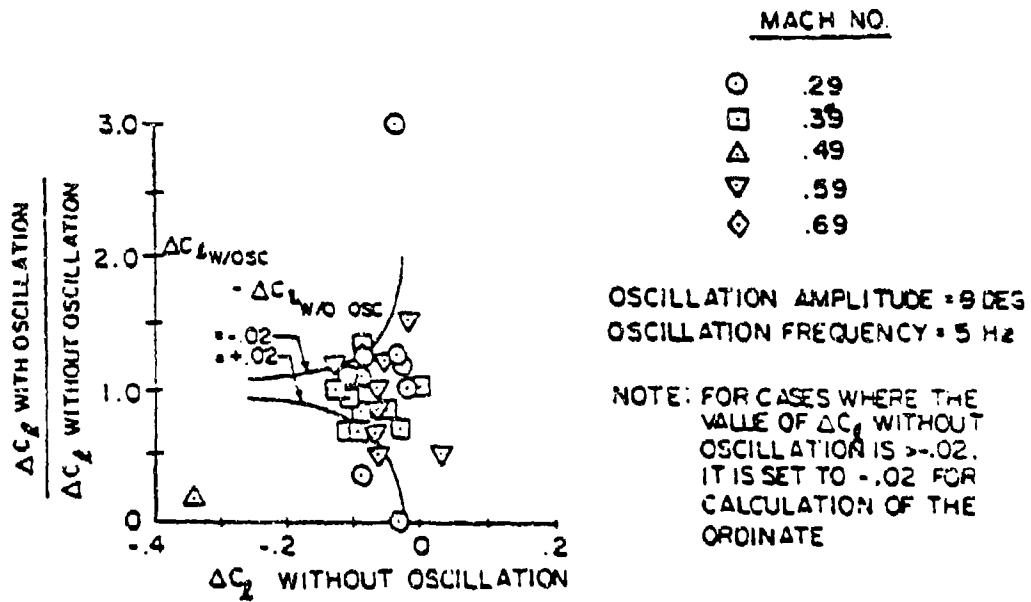
FIGURE 2-116a. EFFECT OF AIRFOIL OSCILLATION AND ANGLE OF ATTACK
CHANGES ON FORCE COEFFICIENTS
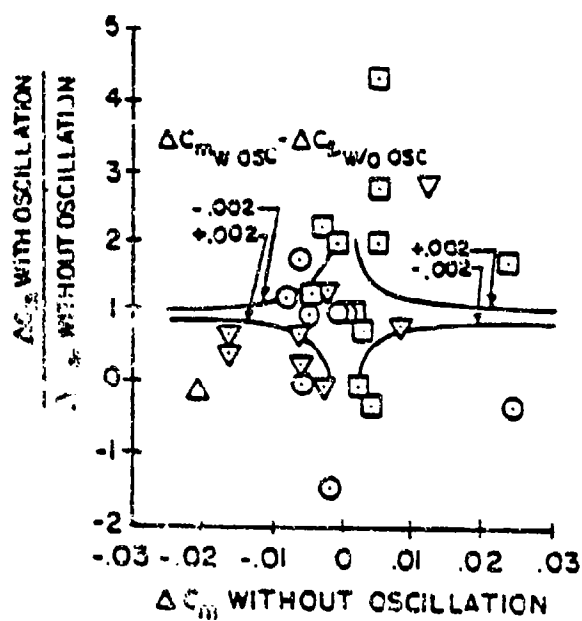
FIGURE 2-216b. EFFECT OF AIRFOIL OSCILLATION AND ANGLE OF ATTACK
CHANGES ON MOMENT COEFFICIENTS

FIGURE 2-117. EFFECT OF ICE IMITATORS ON LIFT AND HINGE MOMENT
CURVES OF A TYPICAL TAILPLANE

I 2-188
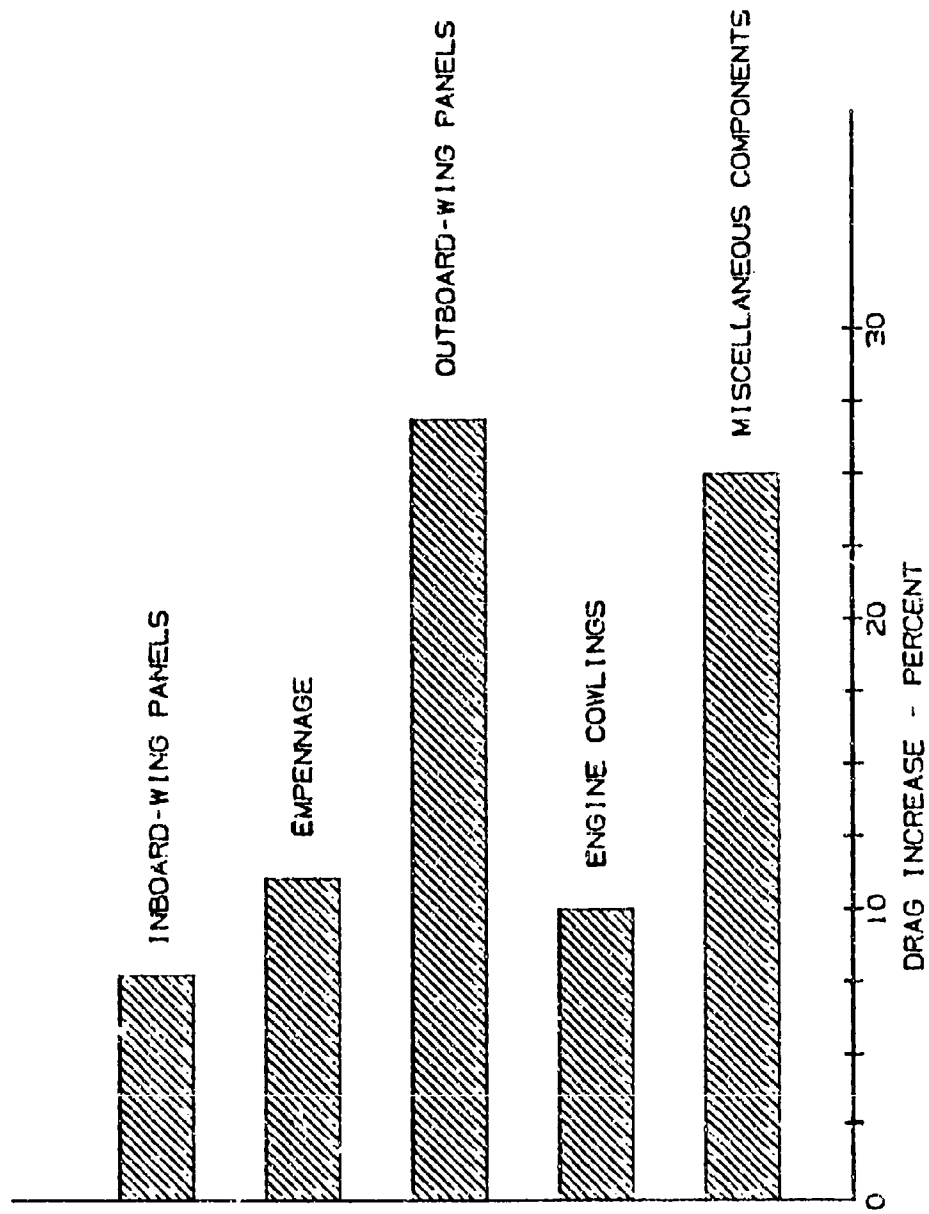
FIGURE 2-118. PERCENT OF DRAG INCREASE DUE TO VARIOUS AIRCRAFT COMPONENTS
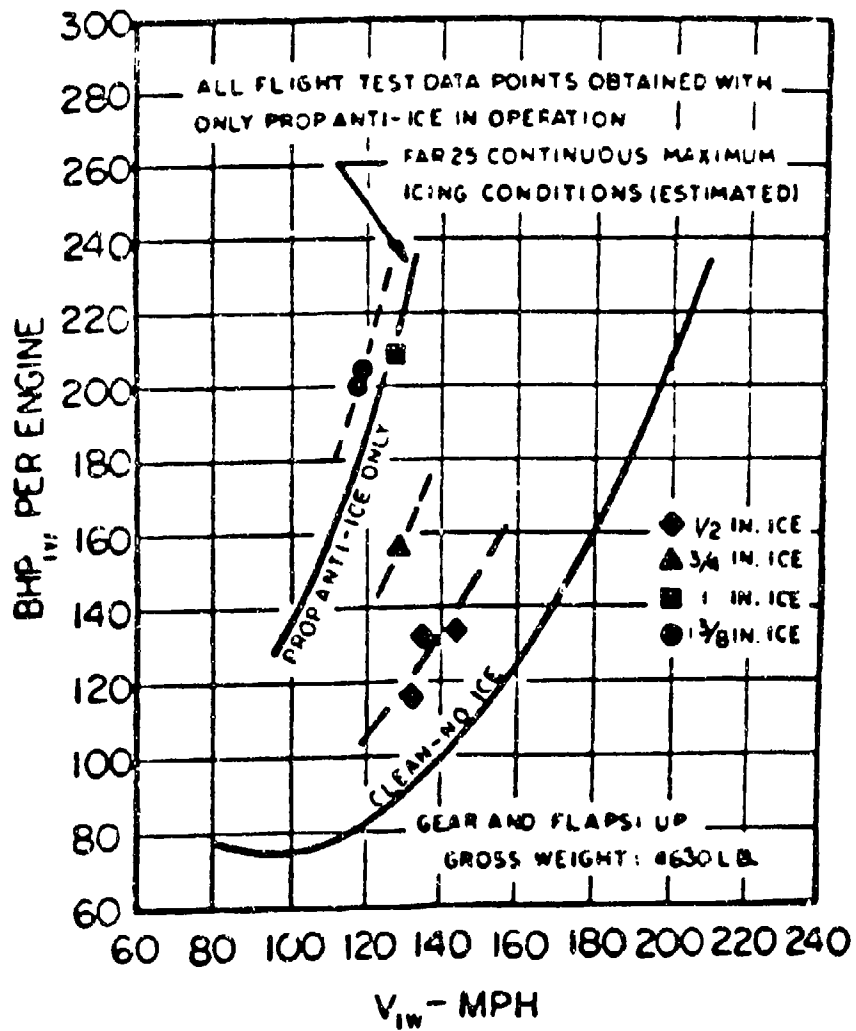
FIGURE 2-119. CORRELATION BETWEEN FLIGHT TEST AND ESTIMATED ICING
CRUISE PERFORMANCE DECREMENTS FOR SUPER SKYMASTER

I 2-190
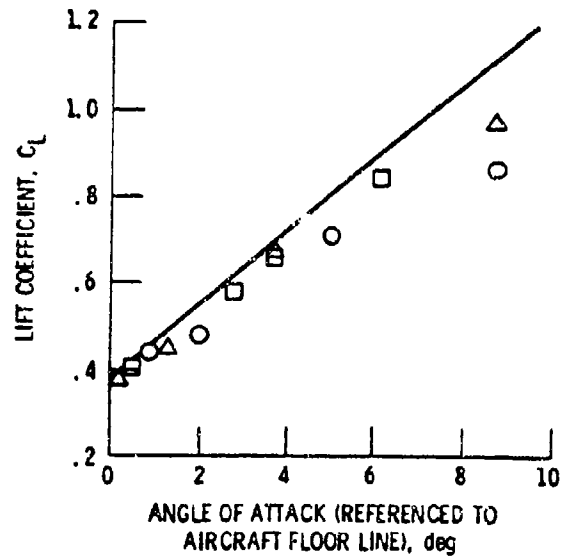
(a) Variation of aircraft C_L versus α.
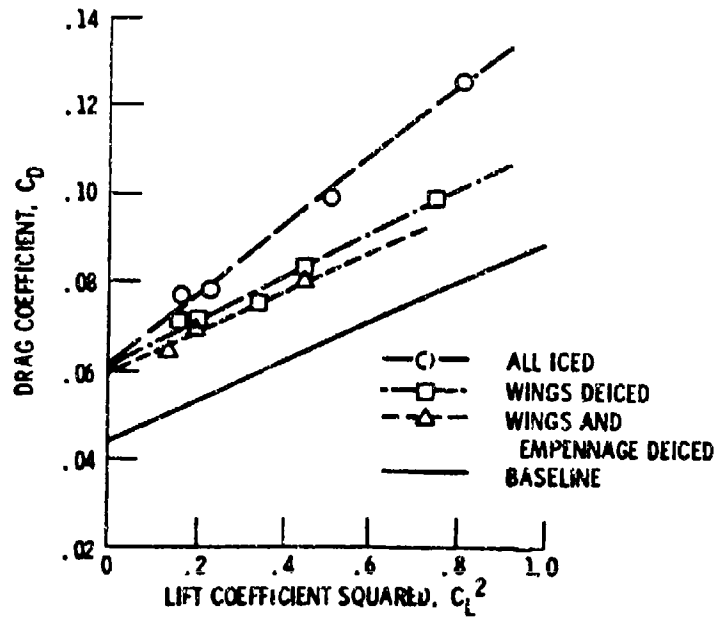
(b) Shift in aircraft drag polar.

FIGURE 2-120.   EFFECT OF GLAZE ICING ON AIRCRAFT LIFT CURVE AND
DRAG POLAR AS COMPARED TO THE UN-ICED BASELINES.
$\delta_r = 0$.
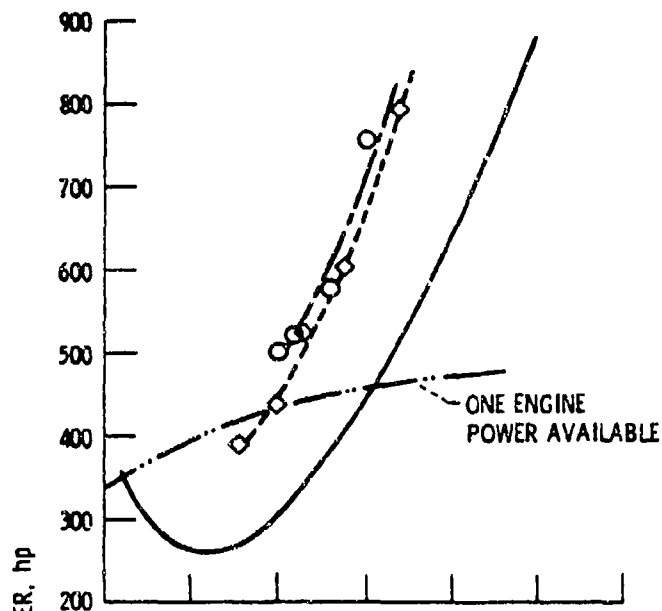
(a) Flight test data corrected to standard day, sea level, and standard weight conditions.
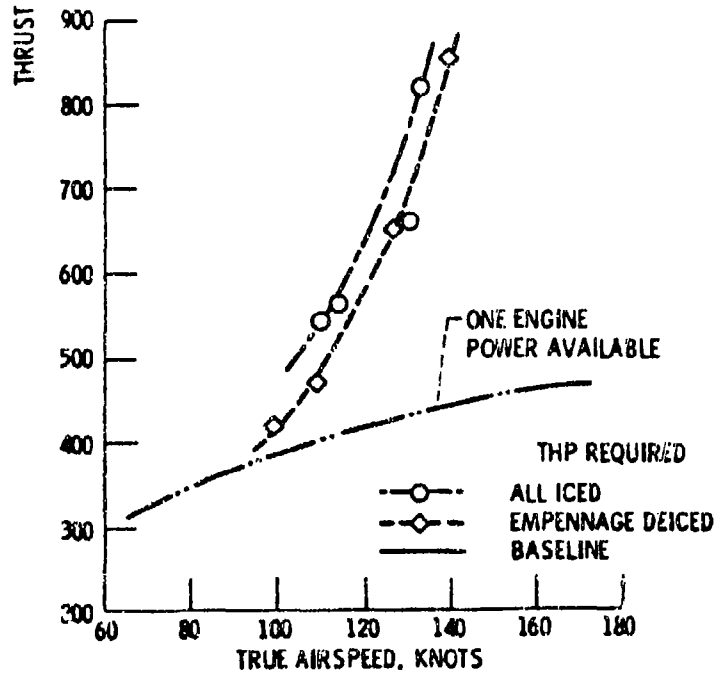
(b) Test conditions at 6000 ft. Flight test data corrected to standard weight only.

FIGURE 2-121. EFFECT OF HEAVY GLAZE ICING ON THRUST HORSEPOWER REQUIRED RELATIVE TO CALCULATED ONE-ENGINE THRUST HORSEPOWER AVAILABLE. $\delta_F = 0$.

CHAPTER I
SECTION 3.0
ATMOSPHERIC DESIGN CRITERIA

CHAPTER I - FLIGHT IN ICING
CONTENTS
SECTION 3.0 ATMOSPHERIC DESIGN CRITERIA

LIST OF TABLES

LIST OF FIGURES

SYMBOLS AND ABBREVIATIONS

Symbol	Description
AGL	Above Ground Level
$^{\circ}C$	Degrees Celsius
cm	Centimeters
$^{\circ}F$	Degrees Fahrenheit
FAA	Federal Aviation Administration
FAR	Federal Aviation Regulation
g/m^3	Grams per cubic meter
JAR	Joint Airworthiness Regulation
km	Kilometer
LWC	Liquid Water Content
m	Meters
MVD	Median Volumetric Diameter
NACA	National Advisory Committee for Aeronautics
NASA	National Aeronautics and Space Administration
n mi	Nautical mile
μm	Microns (micro meter)
PA	Pressure Altitude

GLOSSARY

AGL - Above ground level

adiabatic expansion - A process in which no heat is transferred and the mass has a decrease in temperature.

anti-icing - Prevention of ice from forming on aircraft surfaces.

bleed air - Small extraction of hot air from turbine engine compressor.

cumuliform clouds - A cloud species characterized by vertical development with dome-shaped tops and separated by clear spaces.

de-icing - Removal of ice that has formed on aircraft surfaces.

engine induction system - All systems which provide air to an engine, i.e., for a turbine engine the inlet lip, guide vanes, spinner, etc.

liquid water content (LWC) - The total mass of water contained in all the liquid cloud droplets within a unit volume of cloud. Units of LWC are usually grams of water per cubic meter of air (g/m^3).

median volume diameter (MVD) - The droplet diameter which divides the total water volume present in the droplet distribution in half; i.e., half the water volume will be in larger drops and half the volume in smaller drops. The value is obtained by actual drop size measurements.

nucleation - In meteorology, the initiation of either of the phase changes from water vapor to liquid water, or from liquid water to ice.

stratiform clouds - A cloud species characterized by a flattened appearance and spread out in an extensive horizontal layer.

I.3.0 ATMOSPHERIC DESIGN CRITERIA

I.3.1 INTRODUCTION

This section of the Icing Handbook discusses the FAA, military, and some foreign design criteria derived from the icing atmosphere data discussed in Section 1.0. Aircraft design must follow regulatory requirements as well as atmospheric criteria. The basis for most of the information in this section is the FAA report "Engineering Summary of Airframe Icing Technical Data", ADS-4, (reference 3-1), and Federal Aviation Regulations, Part 25, Appendix C (reference 3-2). Atmospheric criteria in these documents and in the European Joint Airworthiness Requirements (JAR 25) (reference 3-3) are based on NACA reports of the late 1940's and early 1950's (reference 3-4 to 3-18). A general specification development tree is shown in figure 3-1 listing report numbers and dates. No new information is contained in this tree but it provides an overview of the development of the specification. Data presented in these NACA reports has served for a number of years. A good critique of this old data and the FAR 25, Appendix C data can be found in reference 3-19. Recently (references 3-20 and 3-21) further atmospheric data has been collected and analyzed that add to this body of knowledge. This latter addition is directed towards the atmosphere below 10,000 feet (3048 meters) AGL which influences primarily light single engine aircraft and helicopter operation. It also adds to the environmental definition for large aircraft and military aircraft operating below normal cruise altitude, especially in unexpected or prolonged holding patterns.

Design requirements are discussed in this section along with some applicable regulatory requirements. The system design engineer must account for at least the following:

a. Determine the aircraft mission
b. Obtain pertinent atmospheric data for the mission envelope
c. Estimate the worst case icing conditions for that aircraft mission.
d. Know the aircraft design limitations - physical and economic
e. Interweave the atmospheric and regulatory data together with the design and economic limitations to obtain an optimum design.

The intent of this section is to aid the design engineer in the process of interweaving the atmospheric and regulatory data.

I.3.2 DESIGN ICING ENVELOPE

3.2.1 Transport Category Aircraft

The icing environment for transport category aircraft is defined by FAR Part 25 Appendix C (figures 3-2, 3-3). The design criteria is described in terms of cloud liquid water content (LWC), cloud median volume droplet diameter (MVD), ambient temperature, altitude, horizontal cloud extent, and cloud type. Cloud types being stratiform (layer) clouds for continuous maximum conditions and cumuliform (vertical) clouds for intermittent maximum conditions. The reason for the differentiation is discussed in Section I.1.0.

3.2.2 Small Aircraft

Due to icing system cost considerations, small aircraft are much less likely than transport category aircraft to apply for icing certification. Nevertheless, small aircraft, which operate under FAR Part 23 rules (reference 3-22), must meet the same icing design criteria as transport category aircraft (FAR Part 25, Appendix C). Differences in the design of ice protection equipment between small and transport category aircraft result from differences in their mission envelopes. Some small aircraft, especially single engine propeller driven types, are relatively slow with maximum flight altitudes in the vicinity of 10,000 feet (3 km) ASL. Lest the designer get the idea that the relatively low liquid water content of stratiform clouds are conservative as far as icing is concerned, a look at the end product is needed. Measurements show that the largest liquid water contents in stratiform clouds are to be found below 10,000 feet in the wintertime. Figure 3-10 gives a relative value for ice accretion as related to the horizontal extent of the encounter. Therefore the small aircraft, due to their slow speeds and low operating altitudes, would be subject to considerable icing exposures during wintertime IFR flight. This can create as high or higher demand on an icing system as for transport category aircraft. This only serves to point out that many different factors should be considered in the design of ice protection systems.

3.2.2.1 Typical Values Considered

Tables 3-1 and 3-2 lists values which have been considered in evaluating different types of systems. These values should not be considered the only design points since the extremes of the icing envelopes must be considered as well as the type of system. For instance, a large LWC at a relatively high temperature may have more effect on a thermal system because of the large amount of energy required to elevate the mass of water to above freezing than would a lower LWC at a much colder temperature because of the mass of water involved.

LWC values resulting from a probability analysis of Pacific coast cumulus cloud data is compared to the Intermittent Maximum design conditions in table 3-3 (reference 3-1). A similar comparison for stratus clouds and Continuous Maximum design conditions is given in table 3-4 (reference 3-1). These comparisons show that the FAR Part 25 criteria tend to be slightly conservative.

3.2.3 Rotorcraft

Recent advances in rotorcraft systems have made all-weather operations feasible. The icing environment for rotorcraft is defined by FAR Part 29. Many operators require, or at least desire, that their all-weather flight envelope includes a capability for flight into known (or forecast) icing conditions. This will also impact requirements on the flight operating procedures in the Flight

Manual, and the Minimum Equipment List. The objective of icing certification and qualification is to verify that, throughout the approved envelope, the helicopter can operate safely in icing conditions expected to be encountered in service. The envelope requirements vary with operator and qualifying agency. Most design and qualification envelopes are based on the 99.9 percentile of exceedance probability conditions set forth by the FAA in FAR Part 29 (FAR Part 25) Appendix C (reference 3-23) or in Advisory Circular (AC) 29-2 (reference 3-24). The FAA may accept limited certification with respect to pilot controllable variables such as altitude and airspeed, but has not accepted limitations that involve other parameters such as liquid water content and ambient temperature because of the difficulty in accurately forecasting weather conditions and the difficulty of finding viable, operationally acceptable escape routes when limitations are exceeded. Other agencies, especially the United States military, have specified temperature and liquid water content limitations for qualification of rotorcraft without ice protection systems and for aircraft that are equipped with ice protection systems. For example, the US Army UH-60A BLACK HAWK, which has a bleed air engine inlet anti-ice system and an electro-thermal rotor deice system, is qualified for flight in super-cooled 20 micron droplet clouds with liquid water contents that do not exceed 1.0 grams per cubic meter and temperatures that are not below -4 $^{\circ}$F (-20 $^{\circ}$C). Earlier versions of the UH-60A were not equipped with blade de-icing systems. For these helicopters an envelope limited to liquid water contents of 0.3 grams per cubic meter has been recommended. Similarly the Marine CH-53E helicopter, which does not have blade de-icing capability, has received a recommendation that it be cleared for flight in icing conditions up to 0.5 grams per cubic meter, with flight at temperatures below 14 $^{\circ}$F (-10 $^{\circ}$C) limited to operational necessities only. Bell 214ST and Sikorsky S-61N helicopters have been granted limited CAA clearances for North Sea operations, where an escape route to the warmer ocean surface is available. For these aircraft the maximum liquid water content is 0.20 and the minimum temperature is 23 $^{\circ}$F (-5 $^{\circ}$C). A release to fly the RAF HC-Mk1 Chinook in icing at temperatures above 21 $^{\circ}$F (-6 $^{\circ}$C) (liquid water content = .56 grams per cubic meter) was recommended.

At this time, the design icing envelopes do not consider potentially more severe icing conditions: freezing rain, freezing drizzle, mixed conditions (a combination of ice crystals and super-cooled droplets), sleet, and hail. Criteria for certification and qualification in the above atmospheric conditions have not been established. Engine induction systems may be qualified for snow operation, therefore qualifying the rotorcraft for flight in falling or blowing snow and blowing snow regulation of FAR Part 29.1093 and guidance information referenced in paragraph 532 of Advisory Circular 29-2, Change 2.

Many helicopter components and ice protection systems are subjected to qualification for flight within specified design envelopes. However, it must be recognized that the critical design condition will vary from one helicopter design to another, and from one component to another. For example, critical temperatures for the design and evaluation of rotor system icing may range from -4 to 10°F (-20 to -12 $^{\circ}$C) due to varing kinetic heating under different deice system operating procedures. The

engine inlets, protuberances, empennage and fuselage will incur more serious ice accretion at warmer icing temperatures within the design envelope.

FAA certification rules differ for rotors and engines. Criteria that are peculiar to engines are discussed later in this section. Rotorcraft may be certified to the FAR Part 29, Appendix C envelope, as the AS322 Super Puma was in 1984, or to an altitude-limited envelope. The actual icing envelope may be restricted to the pressure altitude for which certification is requested, but approval of a maximum altitude less than 10,000 feet (3048 meters) is discouraged. Figures 3-11 and 3-12 summarize the original FAA 10,000-foot altitude limited continuous and intermittent icing envelopes. These limited envelopes have a maximum liquid water content of 1.5 grams per cubic meter. For an electro-thermal deice system- equipped helicopter, the limitation reduces the portion of the icing envelope when the system will be electrically saturated as discussed in Section III 2.2.3. Change 2 of AC 29-2 (reference 3-24) sanctions the use of a new characterization of the icing environment below an altitude of 10,000 feet (3048 meters). This envelope, shown in figure 3-13, eliminates the distinction between continuous and intermittent icing and uses cloud extent to define the duration of the icing exposure. The concept is that there is not much difference in LWC's between stratiform clouds (continuous) and the bases of convective (intermittent) clouds. One of the more significant differences between this envelope and the figure 3-11 and 3-12 envelopes is the higher (1.74 vs 1.5 grams per cubic meter) maximum liquid water content that results from a single observation at a temperature of 21 °F (-6 °C). This higher liquid water content will increase the time that electro-thermal systems may become electrically saturated. The new characterization also reduces the median volume droplet diameter to as low as three microns (figure 3-13). Water catch rates have generally been determined using the inertias of 20 micron droplets and impingement limits determined from the trajectories of 40 to 50 micron droplets. The complete range of applicable droplet sizes should be considered to establish the most severe icing condition for a particular component.

The rotorcraft should be capable of holding for 30 minutes in continuous icing with a fully functional ice protection system at the most critical weight, center of gravity, and altitude. For those aircraft certified to the envelope of figure 3-12, this requirement is met for liquid water contents up to a maximum of 0.8 grams per cubic meter at the most critical weight, center of gravity, and altitude.

The basic U.S. military envelope (references 3-25, 3-40) has a maximum liquid water content of one gram per cubic meter and a minimum temperature of -4 °F (-20 °C) as shown in figure 3-14. The UK Royal Air Force is currently evaluating the HC-Mk1 Chinook to the design conditions of table 3-5, which provides for continuous and periodic maximum operation down to an ambient temperature of -4 °F (-20 °C).

The FAA engine certification rules for rotorcraft differ from rotor certification rules, especially for aircraft not intended for flight into forecast icing. Engine induction system icing protection is required even if the flight manual prohibits flight into known atmospheric icing conditions. For this case a concept of limited exposure associated with escape from inadvertant ice encounters may be used. Under this concept, the rotorcraft is assumed to fly directly through the icing environment, and

I 3-4

the exposure time can be calculated knowing the cloud horizontal extent and aircraft flight speed. When an induction system has been qualified to a lesser rule than that required for full certification, the engine induction system must be re-evaluated. Design of an engine induction system for continuous operation in icing is desirable in the beginning to avoid requalification if full certification is later requested. Flight idle engine operating conditions tend to be more critical to operation and, therefore, the design must be adequate for low speed and minimum power flight regimes. The engine induction system may be certified for operation in snow at the discretion of the manufacturer.

3.2.4 Military Specifications

Several military specifications contain requirements applicable to the design of ice protections systems on military aircraft. The pertinent specification is cited in the following discussions on Airframe, Engines, and Transparent Areas.

3.2.4.1 Airframe

Anti-icing systems for military aircraft are based on the requirements of Mil-A-9482 (reference 3-25) and Mil-E-87145 (reference 3-40). The parameters in Mil-A-9482 are listed in table 3-1, and are similar to the FAA requirements for a maximum continuous icing atmosphere. The parameters in Mil-E-87145 are similar to FAR Part 25 Appendix C.

If the operating speed on a military aircraft is great enough the aircraft need not be equipped with anti-icing systems (figure 3-15). For military aircraft the power required for high speed provides an excess of available power at low speeds where icing would normally occur during loiter and descent which are very limited in duration. For commercial aircraft the descent may involve holding at a relatively low altitude where icing is present.

3.2.4.2 Engines

Turbine engine anti-icing systems for the military are designed to the requirements of MIL-E-5007 (reference 3-26) and Mil-E-87231 (reference 3-41). Two specific conditions in Mil-E-5007, quite similar to the conditions for maximum intermittent, are itemized in this specification for the design and testing of running wet systems (table 3-1):

Condition	LWC g/m^3	Temp $^{\circ}F(^{\circ}C)$	MVD μm
Cond. I	1.0	-4(-20)	15
Cond. II	2.0	23(-5)	25

3.2.4.3 TRANSPARENT AREAS

Ice protection systems for transparent areas on military aircraft are based on the requirements of Mil-T-5842B (reference 3-42).

3.2.5 Foreign Requirements
3.2.5.1 JAR's

The foreign requirements have been consolidated to a large extent in the Joint Airworthiness Requirement (reference 3-3) abbreviated as JAR. The format, including the paragraph numbering system, is identical to the United States Federal Aviation Regulation (FAR 25) (reference 3-2). The icing requirements are stated in paragraph JAR 25.1419 to be designed per Appendix C which is identical to FAR 25 Appendix C (reference 3-2).

These requirements serve as a basis for each country's certification. However, each maintains their own sovereign rights and quite varied deviations are seen from these general requirements. The countries utilizing JAR's are generally the Western European Countries.

3.2.5.2 British

British Civil Airworthiness Regulations (BCAR) (D4-7 and D5-5) (reference 3-27) specify a droplet size of 20 microns for the stratiform clouds (continuous maximum icing condition) as compared to the 15 micron as specified by FAR 25 and JAR 25 Appendix C. The British also list conditions for ice crystals and/or mixtures of liquid water and ice crystals as shown in table 3-6. Also contained in the British regulation is a section on hail which is quoted as follo

Hailstone Characteristics:
a) Maximum size - 5 cm (2.0 in) diameter
b) Specific gravity - 0.9
c) Encountered throughout the altitude range 0 to 12,000m (40,000 ft.) for a horizontal distance of 1 km (0.5 n mi)
d) The number of stones encountered is assumed. as $20/m2 (2.0/ft^2)$ of frontal area or 1.0 stones, whichever is greater.

The British specification for powerplant operation list a combination of intermittent and continuous maximum envelope for 30 minutes with a one-half mile at approximately double the LWC of the "intermittent" condition as shown in table 3-7 and figure 3-16.

3.2.5.3 Union of Soviet Socialist Republic

The USSR requirements are similar to the British and United States except at temperatures above and below 14 °F (-10 °C) the LWC is higher (figure 3-17 and 3-18). The USSR regulation (reference

3-28, 3-29) also specifies an average droplet size of 16 μm as compared to the British volume median drop size of 20 μm and the United States volume median of 15 μm. Since, for a given temperature, the LWC is slightly higher, the Russian requirements will be more severe. (figure 3-19)

I.3.3 OTHER FREEZING CONDITIONS

3.3.1 Snow

Snow is not usually a problem as far as icing on aircraft is concerned, since the particles are dry and do not adhere to the surfaces. However, it can be a problem for heated engine inlets (See the discussion in Section 1.3 and that under Ice Crystals Section 3.3.2). No quantified design criteria are available for snow, but table 3-8 is included to show the encounter frequency of snow in addition to other types of encounters.

3.3.2 Ice Crystals

Ice crystals by themselves do not generally contribute to airplane icing problems. However special attention should be paid to areas of engine inlets with rough or curved ducts and/or any flow reversal problems. Ice crystals can accumulate in these areas and dislodge as a mass to create choking and engine damage problems. A mixed condition, that is a condition where both ice crystals and supercooled droplets exist, probably constitutes the worst condition for engine and intake icing. The only ice crystal concentration standards available are given in table 3-9 as compiled by the National Research Council of Canada (reference 3-30).

3.3.3 Frost

Frost can be a sleeping killer since it may accumulate in quite heavy amounts over a clear night due to the effects of nocturnal radiation. (See discussion in Section 1.6.) Frost on upper surface of wings can disrupt airflow due to the roughness of the surface, causing the flow separation thus creating a higher stall speed.

Although no design criteria exist for frost, some regulations, FAR 135.227 (reference 3-31), state that parts of the aircraft; namely, rotorblades, propellers, windshields, powerplant, or flight instruments must be clear of frost, and frost adhering to any lifting surface must be "polished to make it smooth". This criteria allows the operator to fly with frost but alerts him to the fact that a performance penalty is expected, (reference 3-32) i.e., stall speed will be higher. Overall it is a recommended policy to NOT attempt takeoff with frost on any lifting surfaces.

3.3.4 Freezing Rain

The only freezing rain criteria available are presented in table 3-2. Freezing rain can cause problems in areas where icing may not normally be a problem such as static ports, fuel and/or air conditioning vents, exposed control horns, and exposed control cables. Some of the consideration in dealing with freezing rain is the visualization of larger quantities of water that may run back into

otherwise inaccessible locations and freeze. These may be harmless, except for the added weight, or may be deadly if the accumulation causes a significant decrease in aerodynamic performance or causes a control surface to bind.

The frequency of freezing rain must be deduced from ground level observations reported in reference 3-33 (since no flight data other than those of table 3-8 can be found). The time frequency of rainfall rate is shown in figure 3-20 for rain and freezing rain/snow, plotted against the parameter of annual precipitation/number of days with precipitation. For rain and freezing rain and snow combined, the maximum frequency is 3.15 per cent for 0.06 in./hr. and 1.8 per cent for 0.12 in./hr. The corresponding maximum frequencies for freezing rain and snow (combined) are 0.47 per cent (for 0.06 in./hr.) and 0.015 per cent (for 0.12 in./hr.). From this data it can be seen that the suggested data of reference 3-4 (based on 0.1 in./hr.) represents a realistic value for design purposes.

3.3.5 Mixed Conditions

Mixed conditions may mean any combination of liquid, ice and snow (i.e., liquid/ice, snow/ice, or liquid/snow/ice). The ratio of liquid to ice, based on total LWC has been reported to range from 25 percent at 32 °F (0 °C) to 50 percent at -4 °F (-20 °C) (references 3-34 and 3-35).

Mixed conditions are basically unstable and do not occur frequently (See discussion Section 1.7). The effects of mixed conditions must be considered during design to minimize accretion and other problems associated with snow and/or ice, especially at the higher levels of supercooled LWC (1.0 g/m^3 or greater) which forms the classic "severe" icing environment. No design criteria exist for mixed conditions but some guidance can be found in tables 3-8 and 3-9.

1.3.4 ICE ACCRETION PROBABILITIES

The probability of accumulating a specific amount of ice is of special interest for parts of an aircraft that do not have icing protection. The data of figure 3-21 shows that a maximum accretion, on a 1/8 inch diameter probe during climbout and descent is 0.4 in., whereas for continuous icing the maximum amounts are 3.5 to 5 in., depending on the data source. (The 0.4-in. maximum during climb and descent was based on data from jet fighter aircraft. For aircraft with lower rates of climb and descent, the maximum value may be higher. Values of ice accretion for specific rates of climb and probabilities are shown in reference 3-7). These values are based on the rate of accretion on a 1/8-in. diameter probe (icing rate meter) which would have a collection efficiency of nearly 100 per cent regardless of airspeed or drop size. For aircraft of larger size with a greater leading edge radius, the maximum ice accretion thickness may be substantially less due to a smaller collection efficiency.

Rate of ice formation and ice shape are affected by many factors, including LWC, drop size, air speed, temperature, body size and shape. Nevertheless, the data of figure 3-22 does indicate the order of magnitude that might be anticipated for various levels of probabilities. Methods of predicting ice size and shape are reported in detail in Section 2.

At a combination of higher speed, ambient temperature and LWC, there is a limiting temperature above which the water will not freeze completely, but will run off. This is shown in figure 3-22. As the ambient temperature exceeds the given curves, water will freeze only partly or not at all, and calculations of ice accretion must consider this factor. (Further discussion of this subject is contained in Section 2.0).

3.4.1 Low-Altitude Icing Data

Most of the data presented in the previous section is based on altitudes in the range of approximately 3,000 to 24,000 ft (914 to 7315 meters). Concern has been expressed as to the severity of low-altitude icing, particularly with respect to light aircraft that might operate in the low-altitude regime. Data were obtained from William Lewis of the NASA Lewis Research Center on low-altitude icing (reference 3-36). These data (figure 3-23) and adiabatic lifting theory show that the liquid water content is reduced at low altitude. In terms of height above the ground, maximum values for 1,000, 3,000, and 5,000 ft. (305, 914, and 1524 meters) are 0.24, 0.65, and 0.8 g/m^3 respectively. Thus, design use of the liquid water contents for normal operational altitudes will produce systems that are more than adequate for very low altitude operation. Freezing rain at low altitudes can be a problem also.

Little data are available on the statistical frequency of icing encounters for areas other than the continental USA and certain areas of the North Atlantic and Pacific Oceans. One approach to the problem is outlined in a report by R.W. Jailer (reference 3-37) in which icing probabilities for the northern hemisphere are predicted by means of frequency data on low pressure areas and freezing level altitudes. The assumption is made that the frequency of clouds and below freezing temperature is proportional to the icing frequency. For January, it may be seen that the frequency varies from 0.01 (southeast USA) to 0.05 (Great Lakes area) for the continental USA. Values up to 0.07 are seen in the Aleutian Islands area.

3.4.2 High-Altitude Icing Data

The data presented in Section 1.0 covers several hundred icing encounters, but are obtained primarily from aircraft having operational ceilings of about 22,000 ft (6706 meters). The advent of turbine powered aircraft with high-altitude capabilities has raised the question of whether the temperature – altitude icing envelopes established previously are adequate. A considerable number of reports (reference 3-38) of icing encounters were collected by Boeing from operation of B-52 type bombers, KS-135 tanker aircraft, and 707 commercial jet transports. These are plotted in figure 3-24. Also included in figure 3-24 are the icing envelopes based on the NACA data (references 3-4 - to 3-18 and 3-39) used for the FAA commercial transport criteria). Data from NACA TN 4314, (reference 3-17) which was obtained from icing encounters during climb and descent by a jet interceptor squadron, is also included.

From the data presented, it may be seen that icing encounters above 24,000 ft. (7315 meters) are rare, as are icing encounters below -22 °F (-30 °C). It does appear that the temperature range of the icing envelopes could be increased by about 10 °F at the higher altitudes.

With one exception, the high-altitude icing encounters are reported as "light" icing; this is in agreement with previous data showing reduced LWC with lower temperature.

Two data points are found at temperatures well below -40 °F (-40 °C); however, the notation with the Boeing data (reference 3-38) states that the temperatures were probably measured in dry air after the icing encounter. (Temperature in clouds may be several degrees warmer than the adjacent air.) Existence of water in supercooled droplet form at temperatures below -40 °F (-40 °C) is very unlikely.

Based on the data available, it appears that high-altitude icing is infrequent and when encountered is not likely to be of a severe nature. An aircraft having ice protection systems designed to cope with the icing conditions defined in Section 3.2 will probably have no difficulties when icing is encountered at high altitudes. Exceptions to this statement may occur where extreme conditions are deliberately sought, as in the USAF "Project Rough Rider." For routine commercial and military operation, the statements are considered applicable.

I.3.5 REFERENCES

3-1 Bowden, D. T., et al, "Engineering Summary of Airframe Icing Technical Data," FAA-TR-ADS-4, 1964.

3-2 "Airworthiness Standards: Transport Category Airplanes," U.S. Department of Transportation, Federal Aviation Administration, Federal Aviation Regulations, FAR Part 25, Washington, D.C., 1985.

3-3 "Joint Airworthiness Requirements JAR-25 Large Aeroplanes," (published by British CAA), 1980.

3-4 Jones, A.R. and Lewis, William, "Recommended Values of Meteorological Factors to be Considered in the Design of Aircraft Ice-Prevention Equipment, NACA TN 1855, March 1959.

3-5 Hoecker, Jr., and Lewis, William, "Observations of Icing Conditions Encountered in Flight During 1948, NACA TN 1904, 1949.

3-6 Bergrun, Norman R. and Lewis, William, "A Probability Analysis of the Meteorological Factors Conducive to Aircraft Icing in the United States," NACA TN 2738, 1952.

3-7 Perkins, Porter J., "Icing Frequencies Experienced During Climb and Descent by Fighter-Interceptor Aircraft," NACA TN 4314, July 1958.

3-8 Lewis, William, "Icing Zones in a Warm Front System with General Precipitation," NACA TN 1392, 1947.

3-9 Lewis, William, "A Flight Investigation of the Meteorological Conditions Conducive to the Formation of Ice on Airplanes," NACA TN 1393, 1947.

3-10 Lewis, William, Kline, D. B., and Steinmetz, C. P., "A Further Investigation of the Meteorological Conditions Conducive to Aircraft Icing," NACA TN 1424, 1947. 3-11 Kline, Dwight B., "Investigation of Meteorological Conditions Associated with Aircraft Icing in Layer-Type Clouds for 1947-48 Winter," NACA TN 1793, 1949.

3-12 Hacker, P. T. and Dorsch, R. G., "A Summary of Meteorological Conditions Associated with Aircraft Icing and a Proposed Method of Selecting Design Criterions for Ice-Protection Equipment," NACA TN 2569, 1951.

3-13 Kline, Dwight B. and Walker, Joseph A., "Meteorological Analysis of Icing Conditions Encountered in Low Altitude Stratiform Clouds," NACA TN 2306, 1951.

3-14 Perkins, P. J., Lewis, William, and Mulholland, D. R., "Statistical Study of Aircraft Icing Probabilities at the 700 and 500 Millibar Levels Over Ocean Area in the Northern Hemisphere," NACA TN 3984, 1957.

3-15 Perkins, Porter J., "Preliminary Survey of Icing Conditions Measured During Routine Transcontinental Airline Operation," NACA RM E52J06, 1952.

3-16 Perkins, Porter J., "Statistical Survey of Icing Data Measured in Scheduled Airline Flights over the United States and Canada from November 1951 to June 1952," NACA RM E55F28a, 1955.

3-17 Neel, Carr B., "A Heated-Wire, Liquid-Water Content Instrument and Results of Initial Flight Tests in Icing Conditions," NACA RM A54I23, 1955.

3-18 Perkins, Porter J., "Summary of Statistical Icing Cloud Data Measured Over United States and North Atlantic, Pacific, and Arctic Oceans During Routine Aircraft Operations," NASA Memo 1-19-59L, 1959.

3-19 Lewis, W., "Review of Icing Criteria," in Aircraft Ice Protection. Report of Symposium of April 28-30, 1969, DOT/FAA Flight Standards Service, Washington, D.C., 1969.

3-20 Masters, C. O., "A New Characterization of Supercooled Clouds Below 10,000 Feet AGL," DOT/FAA/CT-83/22.

3-21 Jeck, R. K., "A New Data Base of Supercooled Cloud Variables for Altitudes up to 10,000 Feet AGL and the Implications for Low Altitude Aircraft Icing," OOT/FAA/CT-83/21.

3-22 "Airworthiness Standards: Normal Category Airplanes," U.S. Department of Transportation, Federal Aviation Administration, Federal Aviation Regulations, FAR Part 23, Washington, D.C., 1986.

3-23 "Airworthiness Standards: Transport Category Rotorcraft," U.S. Department of Transportation, Federal Aviation Administration, Federal Aviation Regulations, FAR Part 29, Washington, D.C., 1986.

3-24 "Certification of Transport Category Rotorcraft," U.S. Department of Transportation, Federal Aviation Administration, Advisory Circular, AC 29-02, May 1983 (Revised 11/84 and 5/85).

3-25   Anti-Icing Equipment for Aircraft Heated System Type. MIL-A-9482 Amendment 2, dated 1 April 1981.

3-26   "Military Specification - Engine, Aircraft, Turbojet, General Specification," MIL-E-5007D, 1973.

3-27   British Civil Airworthiness Requirements, Subsections D4-7 and D5-5, March 16, 1959.

3-28   Borovich, A., et al, "Cloud Physics," 1961, English translation OTS-63-11141.

3-29   Trunov, 0., "Icing of Aircraft and the Means of Preventing It," 1965 English translation, FTD-MT-65-490.

3-30   United Kingdom Ministry of Aviation, Aviation Publication 970 (Leaflets 714/2 and 714/3).

3-31   "Air Taxi Operators and Commercial Operators," U.S. Department of Transportation, Federal Aviation Administration, Federal Aviation Regulations, FAR Part 135, 1986.

3-32   Dietenberger, M. A., "A Model For Nocturnal Frost Formation On A Wing Section," NASA CR 3733, Oct 1983.

3-33   "Handbook of Geophysics," U.S. Air Force, the MacMillan Co., New York, (Chapter 6), 1960.

3-34   Peterson, A. A., et al, "Helicopter Icing Review," NASA FAA CT 80-210.

3-35   Don, T. C., "Helicopter Icing Symposium." AD-A 067981, dated 11-1-78.

3-36   Lewis, W., Unpublished Letter, NASA Lewis Research Center, April 14, 1963.

3-37   Jailer, R. W., "Evaluation of Northern Hemisphere Icing Probabilities," WADC TN 55-225.

3-38   Rock, E. The Boeing Company, Renton, Washington, Letter No. 6-7731-69, April 29,1963.

3-39   Lewis, W., "Icing Properties of Noncyclonic Winter Stratus Clouds," NACA TN 1391, 1947.

3-40   "Military Specification - Environmental Control, Airborne." MIL-E-87145, 21 February 1980.

3-41   "Military Specification - Engines, Aircraft, Turbojet and Turbofan," MIL-E-87231, 30 September 1985.

3-42   "Transparent Areas on Aircraft Surfaces (Windshields and Canopies), Rain Removing and Washing Systems for, Defrosting, De-Icing, Defogging, General Specification for," MIL-T-5842B(AS), 29 March 1945.

TABLE 3-1. GENERAL ICING DESIGN PARAMETERS

	Distance Miles	LWC g/m^3	Temp °F (°C)	MVD Microns
Evaporative A/I System (Commercial) Military - Mil-A-9482 (Reference 3-25)		0.43 0.50	15 (-9) 15 (-9)	20 20
De-Ice Systems Running Wet A/I Systems		0.23	0 (-18)	20
Turbine Engines and Engine Inlets - Running Wet Ice Crystals/Ice and LW	3 30min/30sec	1.7 1-8	-4 (-20)	20
Military Engines MIL-E-5007D (Reference 3-26) Cond I Cond II		1 2	-4 (-20) 23 (-5)	15 25
Freezing Rain - Exposed items other, airframe - controls, static ports, etc. (Reference 3-4)	100	0.15	25 to 32 (-4 to 0)	1000
Range in Values for Stratus Clouds	20-200	0.1-0.8	-40 to 32 (-40 to 0)	10-40
Continuous Max for Cumulus Clouds	2-6	0.2-2.5	-40 to 32 (-40 to 0)	10-40
Impingement Limit Calculation	---	---	---	40

TABLE 3-2. RECOMMENDED VALUES OF METEOROLOGICAL FACTORS FOR CONSIDERATION
IN THE DESIGN OF AIRCRAFT ICE PREVENTION EQUIPMENT

(Based on NACA TN 1855 (Reference 3-4); Maximum Instantaneous Class Deleted)

Class	Air Temp. °F (°C)	Liquid Water Content g/m^3	Drop Diameter Microns	Pressure Altitude 1,000 Ft.	Remarks
II-M Intermittent, Maximum	32 (0)	2.5		10-15	
	14	2.2		10-20	Horizontal extent-
	- 4	1.7		12-30	3 miles
	-22	1.0	20	15-30	Characteristic - High
	-40 (-40)	0.2		15-30	liquid water content
	32 (0)	1.3		8-15	Applicable to: Any
	14	1.0		8-20	critical component of
	- 4	0.8	30	10-30	the airplane where ice
	-22	0.5		15-30	accretion, even though
	-40 (-40)	0.1		15-30	slight and of short duration, could not be tolerated
	32 (0)	0.4		8-15	Example: Induction
	14	0.3		8-20	system (particularly
	- 4	0.2	50	10-30	turbine engine inlets)
	-22	0.1		15-30	
	-40 (-40)	0.1		15-30	
II-N Intermittent, Normal	32 (0)	0.8	20	8-12	
	14	0.6	20	8-15	
	- 4	0.4	18	12-20	
	-22	0.1	15	15-25	
	-40 (-40)	0.1	13	15-25	

TABLE 3-2
(Cont'd.)

Class	Air Temp. °F (°C)	Liquid Water Content g/m³	Drop Diameter Microns	Pressure Altitude 1,000 Ft. (1,000 m)	Remarks
III-M Continuous Maximum	32 (0) 14(-10) - 4(-20) -22(-30) -40(-40)	0.8 0.6 0.3 0.2 0.05	15	3-22 (1-7)	Horizontal extent – Continuous Characteristic: Moderate to low liquid water content for an indefinite period
	32 (0) 14(-10) - 4(-20) -22(-30) -40(-40)	0.5 0.3 0.15 0.10 0.03	25	3-22 (1-7)	Applicable to: All components of the air-plane; i.e., every part of the airplane should be examined with the question - "Will this part be affected seriously by accretions during continuous flight in icing conditions?"
	32 (0) 14(-10) - 4(-20) -22(-30) -40(-40)	0.15 0.10 0.06 0.04 0.01	40	3-22 (1-7)	Example: Wing and tail surfaces
III-N Continuous Normal	32 (0) 14(-10) - 4(-20) -22(-30)	0.3 0.2 0.1 0.1	15	3-22 (1-7)	
IV-M Freezing Rain	25-32 (-4 to 0)	0.15	1,000	0-5 (0-2)	Horizontal extent: 100 mi. Characteristic: Very large drops at near-freezing temperatures and low values of liquid water content Applicable to: Compo-nents of the airplane for which no protec-tion would be supplied. Example: Fuselage static pressure air-speed vents

Note: Based on 0.10 in./hr. rainfall rain

TABLE 3-3. COMPARISON OF VALUES OF LIQUID WATER CONTENT FOR PACIFIC COAST CUMULUS CLOUDS, WITH CORRESPONDING VALUES FOR INTERMITTENT MAXIMUM CONDITIONS

Temperature °F (°C)		Drop Diameter Microns	Liquid Water Content (g/m³)	
			TN 1855 (Reference 3-4) Recommended Design Values	TN 2738 (Reference 3-6) Probability Analysis [P_e=.001]
32	(0)	20	2.5	2.46
32	(0)	30	1.3	1.50
32	(0)	50	0.4	0.42
14	(-10)	20	2.2	2.30
14	(-10)	30	1.0	1.35
14	(-10)	50	0.3	0.37
- 4	(-20)	20	1.7	1.45
- 4	(-20)	30	0.8	0.70
- 4	(-20)	50	0.2	0.15
-22	(-30)	20	1.0	0.37
-22	(-30)	30	0.5	0.15
-22	(-30)	50	0.1	0
-40	(-40)	20	0.2	0
-40	(-40)	30	0.1	0
-40	(-40)	50	0.1	0

TABLE 3-4. COMPARISON OF WEIGHTED AVERAGE VALUES OF LIQUID WATER CONTENT FOR STRATUS CLOUDS, WITH CORRESPONDING VALUES FOR CONTINUOUS MAXIMUM CONDITIONS

Temperature °F (°C)	Drop Diameter Microns	Liquid Water Content (g/m³)	
		TN 1855 (Reference 3-4) Recommended Design Values	TN 2738 (Reference 3-6) Probability Analysis [P_e=.001]
32 (0)	15	0.80	0.77
32 (0)	25	0.50	0.49
32 (0)	40	0.15	0.20
14 (-10)	15	0.60	0.50
14 (-10)	25	0.30	0.28
14 (-10)	40	0.10	0.08
- 4 (-20)	15	0.30	0.17
- 4 (-20)	25	0.15	0.09
- 4 (-20)	40	0.06	0.02
-22 (-30)	15	0.20	0.02
-22 (-30)	25	0.10	0.01
-22 (-30)	40	0.04	0.003
-40 (-40)	15	0.05	0
-40 (-40)	25	0.03	0
-40 (-40)	40	0.01	0

TABLE 3-5. UK CIVIL DESIGN ATMOSPHERIC CONDITIONS
FOR FLIGHT IN SUPERCOOLED CLOUDS (Reference 3-27)

Condition	Air Temperature °F (°C)	Liquid Water g/m³	Horizontal Extent (KM)	Droplet Size MVD (Microns)	Altitude Range (Ft)
I Continuous Maximum Icing	41 (+5) 32 (0) 14 (-10) -4 (-20)	0.90 0.80 0.60 0.30	Continuous	20	4,000 to 10,000
II Periodic Maximum Icing	41 (+5) 32 (0) 14 (-10) -4 (-20)	1.35 1.20 0.90 0.45	6 KM every 100 KM of Condition I	20	4,000 to 10,000

TABLE 3-6. UK CIVIL DESIGN ATMOSPHERIC CONDITIONS
FOR FLIGHT IN ICE CRYSTAL CLOUDS (Reference 3-27)

Air Temp. °F (°C)	Altitude Range (m X 10³)	Altitude Range (ft X 10³)	Max. Ice Crystal Content (g/m³)	Horizontal Extent (n mile)	Horizontal Extent (km)	Mean Particle Diameter (mm)
32°(0) to -4°(-20)	3.0-9.0	10.0-30.0	8.0 5.0 2.0 1.0	0.5 2.5 50.0 300.0	1.0 5.0 100.0 500.0	1
-4°(-20) to -40°(-40)	4.5-12.0	15.0-40.0	5.0 2.0 1.0 0.5	2.5 10.0 50.0 300.0	5.0 20.0 100.0 500.0	

TABLE 3-7. UK CIVIL AIRWORTHINESS REQUIREMENTS
FOR POWER PLANT (Reference 3-27)

Instantaneous Maximum

Temperature °F (°C)	LWC - g/m³	Drop Diameter Microns	Altitude Feet	Horizontal Extent Nautical Miles
32° (0) 14° (-10) -4° (-20) -22° (-30) -40° (-40)	5.0 4.0 3.0 2.0 0.5	20 20 20 20 20	10,000 - 20,000 10,000 - 27,500 15,000 - 30,000 15,000 - 35,000 15,000 - 40,000	Continuous for 1/2 mile

**TABLE 3-8. FREQUENCY OF ENCOUNTER WITH VARIOUS TYPES OF
METEOROLOGICAL CONDITIONS DURING THE 1948 OPERATION**

Condition	No. of min. condition	Per cent of total flight time	Per cent of total time in continuous or intermittent visible moisture
Clear Air	6,523	61.1	---
Liquid cloud			
Continuous	209	2.0	5.0
Intermittent			
Clear air predominant	509	4.7	12.1
About one-half clear	368	3.5	8.9
Cloud predominant	325	3.0	7.8
Subtotal, liquid	1,406	13.2	33.8
Mixed snow and liquid cloud			
Liquid predominant			
Continuous	180	1.7	4.3
Intermittent	384	3.6	9.2
Snow predominant			
Continuous	310	2.9	7.5
Intermittent	108	1.0	2.6
Subtotal, mixed	982	9.2	23.6
Snow			
Continuous	1,122	10.5	27.0
Intermittent	228	2.1	5.5
Subtotal, snow	1,350	12.6	32.5
Rain	335	3.1	8.1
Rain and snow	30	0.3	0.7
Freezing rain	13	0.1	0.3
Freezing rain and liquid cloud	41	0.4	1.0
Subtotal, rain	419	3.9	10.1
Total	10,680	100.0	100.0

Source: (Reference 3-15)

TABLE 3-9. ICE CRYSTAL CONCENTRATION STANDARDS
(SUPPLIED BY THE NATIONAL RESEARCH COUNCIL OF CANADA [REFERENCE 3-30])

Ambient Temperature °F (°C)	Altitude 1,000 Ft	Maximum Total Concentration (ice crystals plus LWC) g/m³	Maximum Concentration in Liquid Form g/m³	Extent Nautical Miles
32 to -4(0 to -20)	10 to 30	8	1	0.5
		5	1	3
		2	1	50
		1	0.5	Indef.
-4 to -40(-20 to -40)	15 to 40	5	0	3
		2	0	
		1	0	
		0.5	0	Indef.
-40 to -76(-40 to -60)	20 to 45	2	0	3
		1	0	10
		0.25	0	Indef.
-76 to -112(-60 to -80)	30 to 60	1	0	3
		0.50	0	10
		0.10	0	Indef.

Thirty minutes exposure is considered for the "indefinite" extent.

NOTES   (Reference 3-30)

1. In the present state of knowledge, it is not possible to say how much of the "total free water contents" tabulated exist in the form of water and how much as ice crystals, because supercooled water has been shown to exist at temperatures down to -40 °F (-40 °C). Furthermore the percentage of ice crystals and water may vary considerably in any one cloud.

2. From present information it appears that the worst condition for engine and intake icing in mixed water/ice crystals occurs when there is a small quantity of water present.

3. The following assumptions may reasonably be made for design purposes:

    a. Below -40 °F (-20 °C) all the water present may be assumed to be in the form of ice crystals.

    b. Of the total free water shown in the 32 °F to -4 °F (0 °C to -20 °C) range, not more than 1 g/m³ should be taken as water and the remainder as ice crystals, except where the total water content is shown as 1 g/m³, when half should be considered as water and half ice crystals.

    c. When the extent of the condition is shown as "indefinite," it is acceptable to show that the airplane functions satisfactorily during 30 minutes continuous exposure to the conditions.

FAR PART 25

↓

SUBPART E - POWERPLANT

↓

PARA. 25.1093 INDUCTION SYSTEM
DE-ICNG AND ANTI-ICING PROVISIONS

↓

APPENDIX C

CAM 4b
PARA 4b.1 (b) (7)
CONTINUOUS MAXIMUM ICING
AND (8) INTERMITTENT
MAXIMUM ICING

↓

CONTINUOUS MAXIMUM ICING
INTERMITTENT MAXIMUM ICING

| LIQUID WATER CONTENT, MEAN EFFECTIVE DROPLET DIA., AMB. TEMP. | ALTITUDE AMB. TEMP. | LIQUID WATER CONTENT FACTOR CLOUD HORIZONTAL EXTENT |

| SOURCE NACA TN 1855 | SOURCE NACA TN 2569 | SOURCE NACA TN 2738 |

| NACA TN 1393 NACA TN 1424 | | NACA TN'S 1393 1424 1793 1904 2306 |

| NACA TN 1391 | NACA TN 1392 |

FIGURE 3-1.   DERIVATION OF FAR ICING STANDARDS (REFERENCE 3-12)

Continuous maximum (stratiform clouds) atmospheric icing conditions. Pressure altitude range: sea level–22,000 feet; maximum vertical extent: 6500 feet; horizontal extent: standard distance of 17.4 nautical miles.
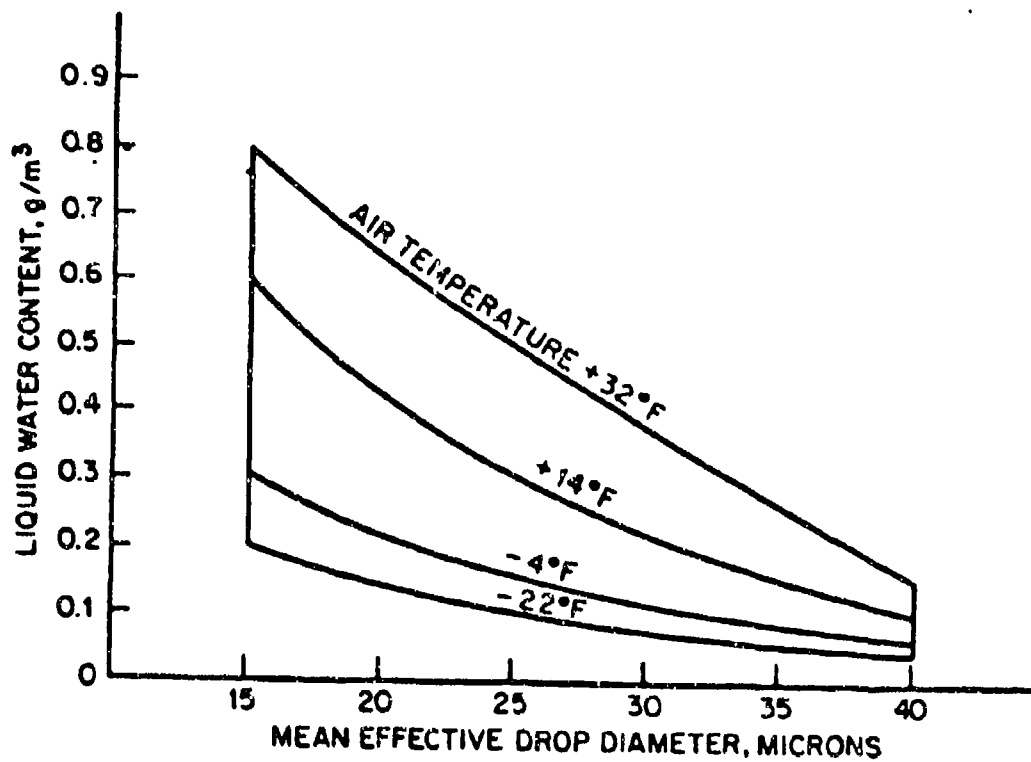
FIGURE 3-2.   FAR 25 ATMOSPHERIC ICING DESIGN CONDITIONS - STRATIFORM CLOUDS
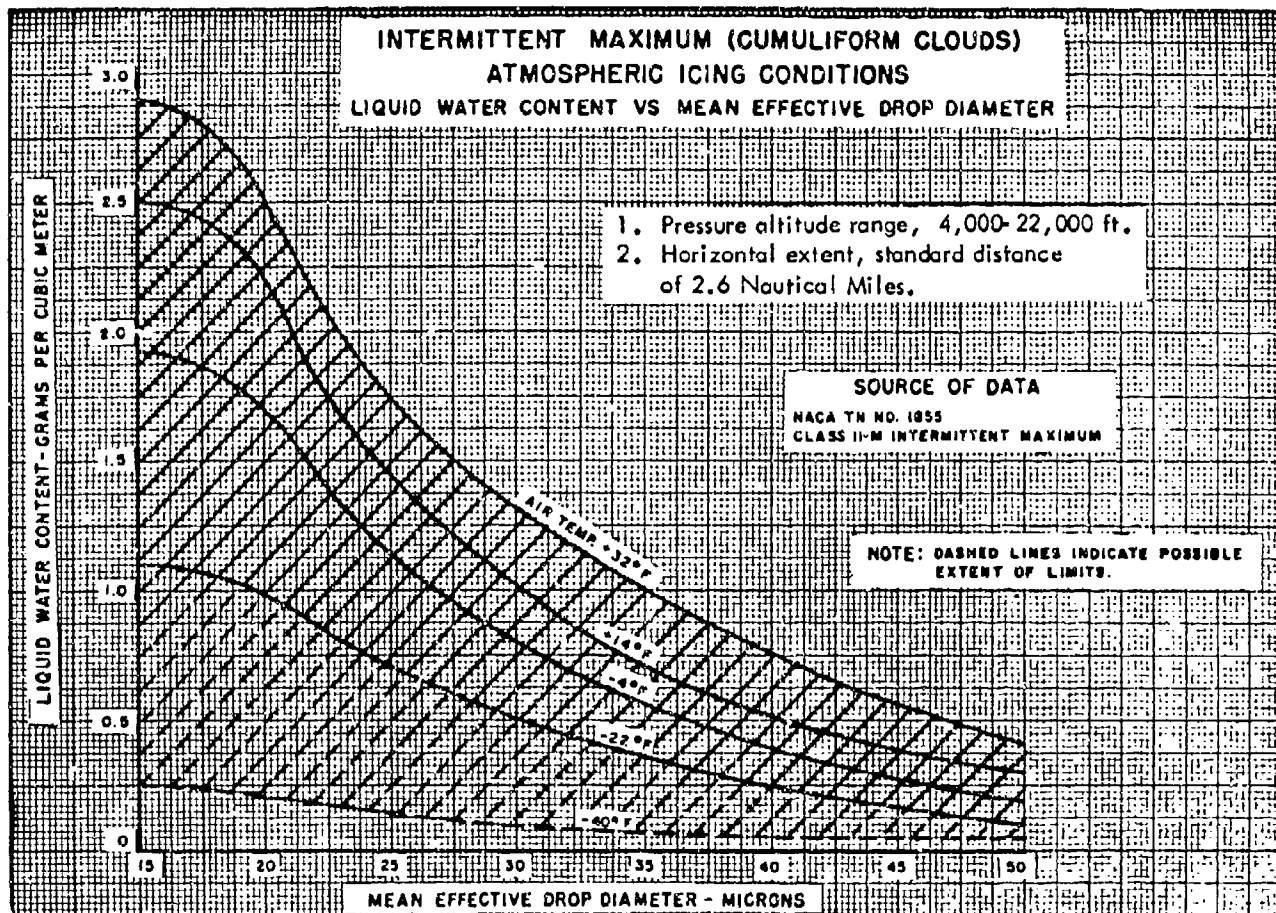
FIGURE 3-3. FAR 25 ATMOSPHERIC ICING DESIGN CONDITIONS
— CUMULIFORM CLOUDS

Source of data:
(Reference 3-12)

Ambient temperature – Deg. F

Pressure altitude – 1,000 Ft.
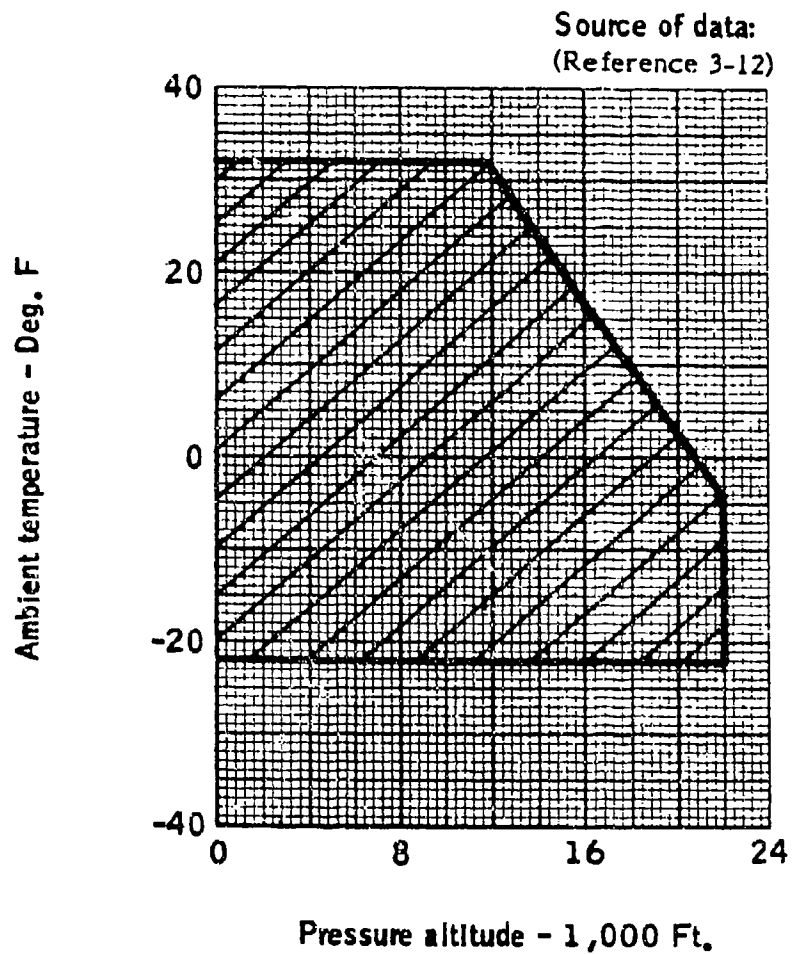
FIGURE 3-4. CONTINUOUS MAXIMUM ATMOSPHERIC ICING CONDITIONS – STRATIFORM
CLOUDS. AMBIENT TEMPERATURE VERSUS PRESSURE ALTITUDE (REFERENCE 3-2)

I 3-24
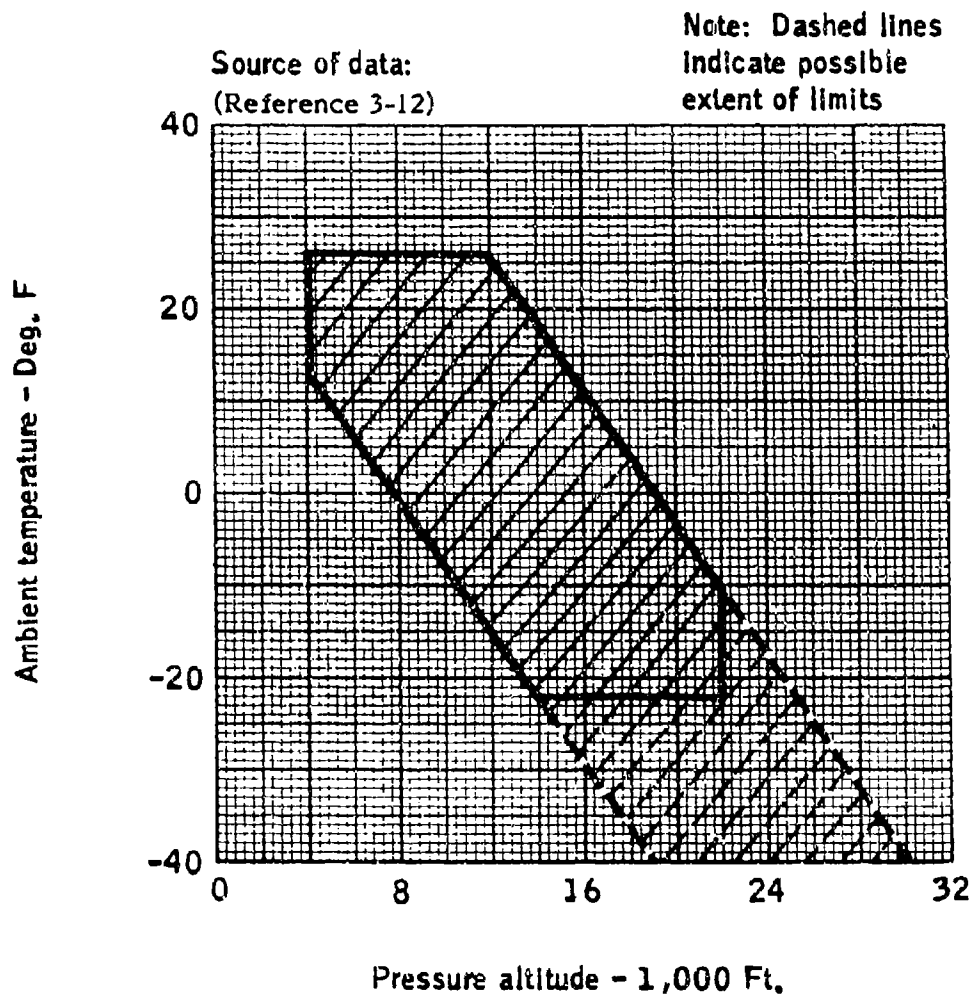
FIGURE 3-5. INTERMITTENT MAXIMUM ATMOSPHERIC ICING CONDITIONS – CUMULIFORM CLOUDS. AMBIENT TEMPERATURE VERSUS PRESSURE ALTITUDE (REFERENCE 3-2)

I 3-25
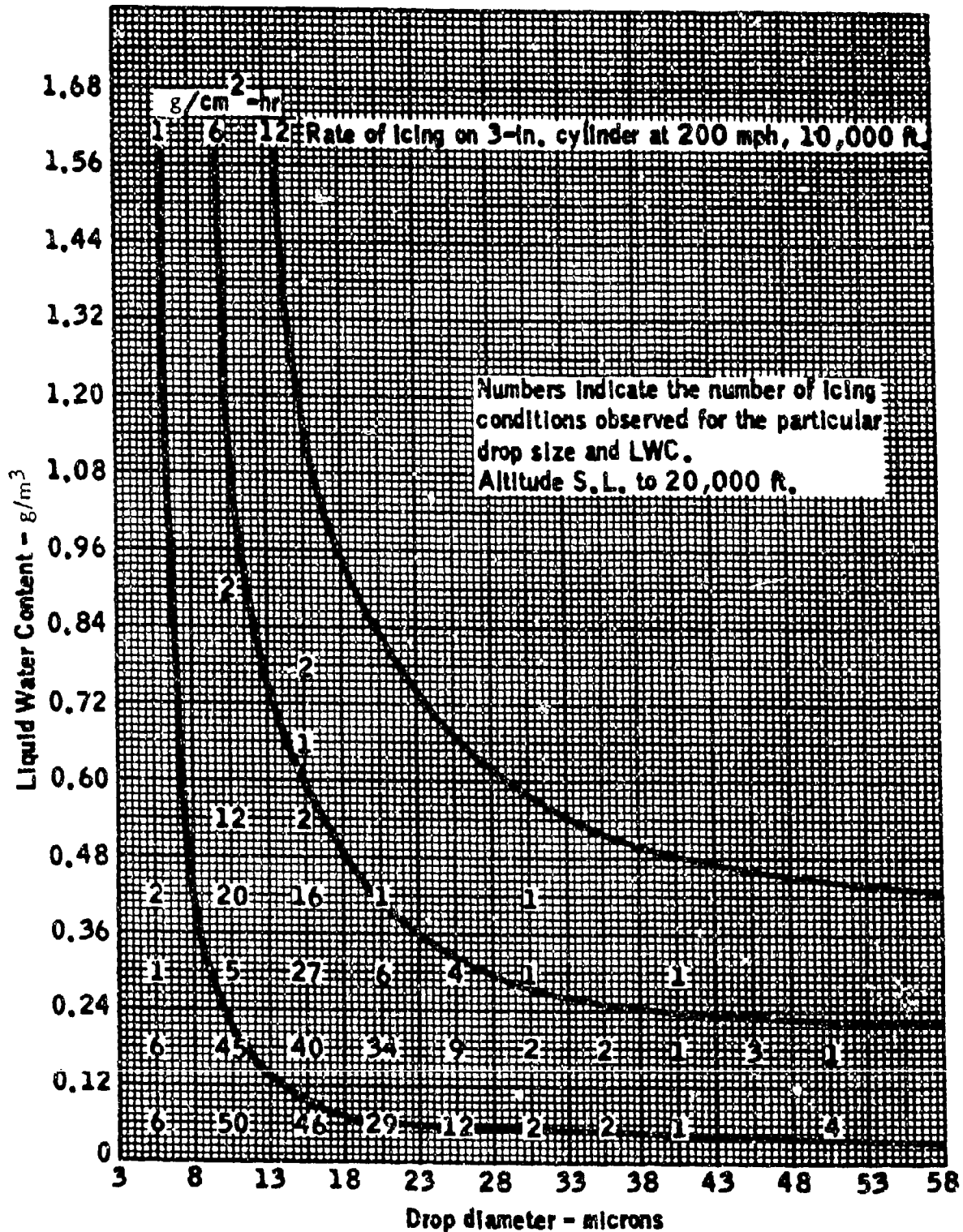
FIGURE 3-6. STRATIFORM CLOUDS - LAYER TYPE, LWC VERSUS DROP DIAMETER

(REFERENCE 3-12)

I 3-26
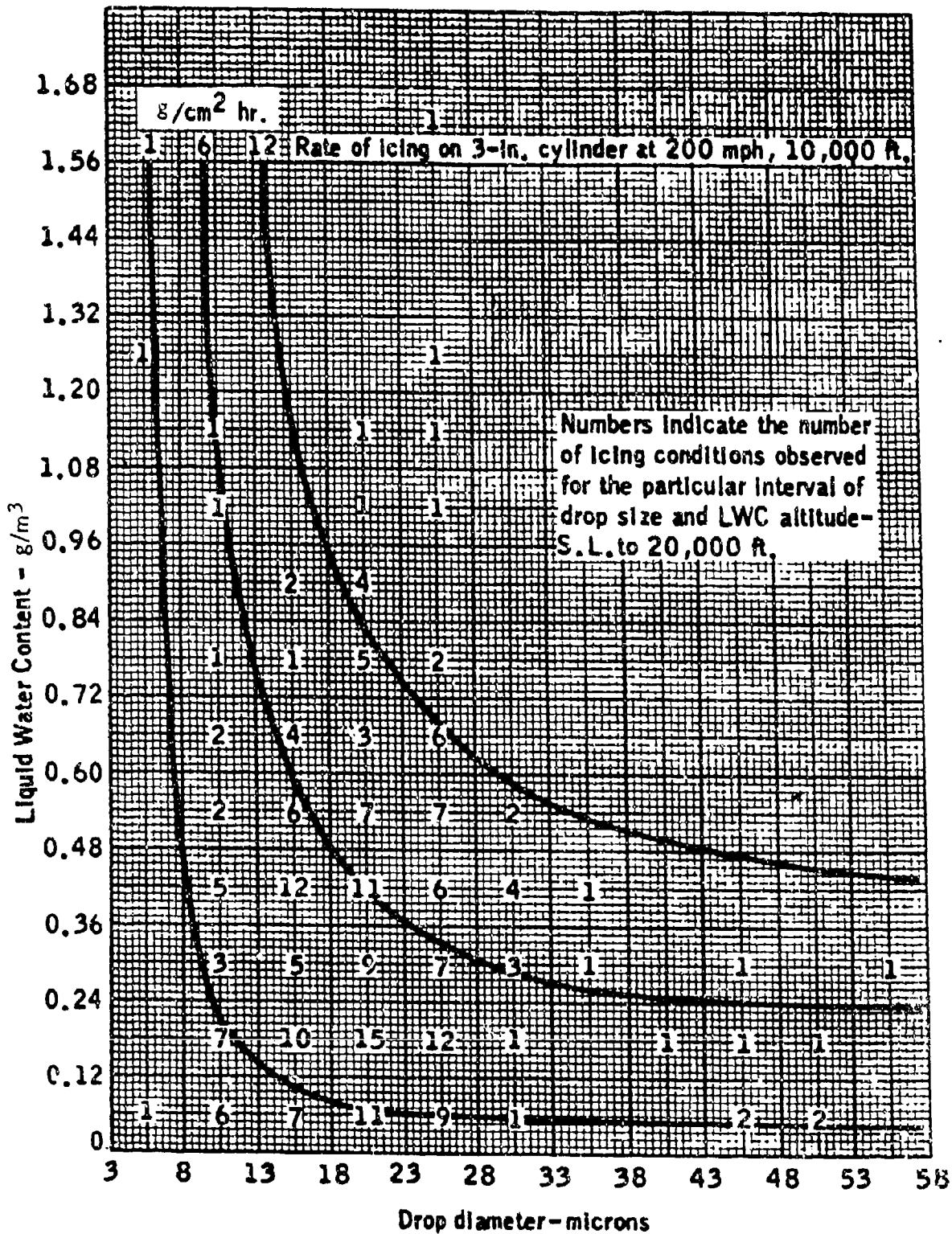
FIGURE 3-7. CUMULIFORM CLOUDS - LWC VERSUS DROP DIAMETER (REFERENCE 3-12)
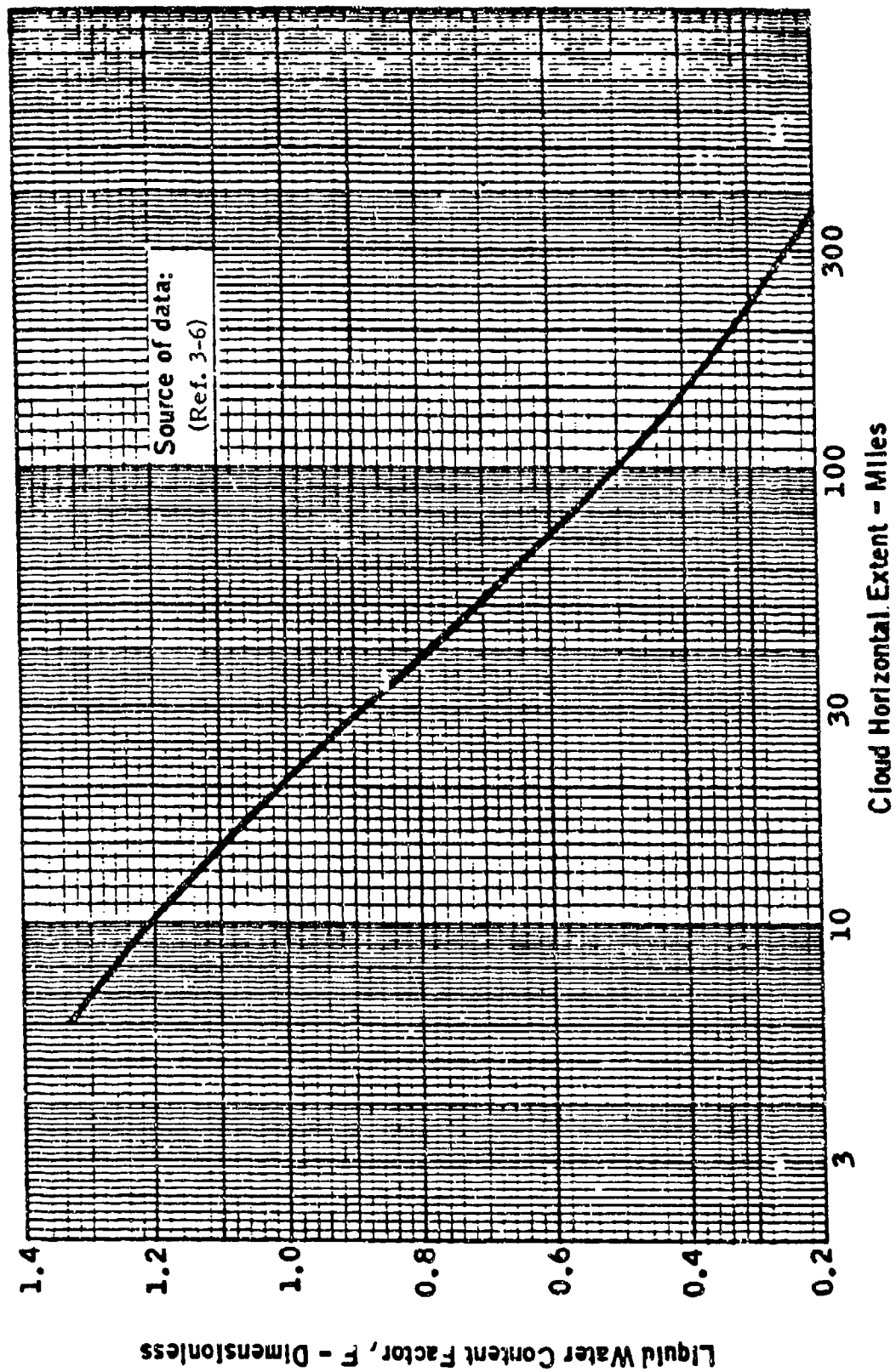
FIGURE 3-8. CONTINUOUS MAXIMUM ATMOSPHERIC ICING CONDITIONS - STRATIFORM CLOUDS. LWC FACTOR VERSUS CLOUD HORIZONTAL DISTANCE EXTENT (REFERENCE 3-2)
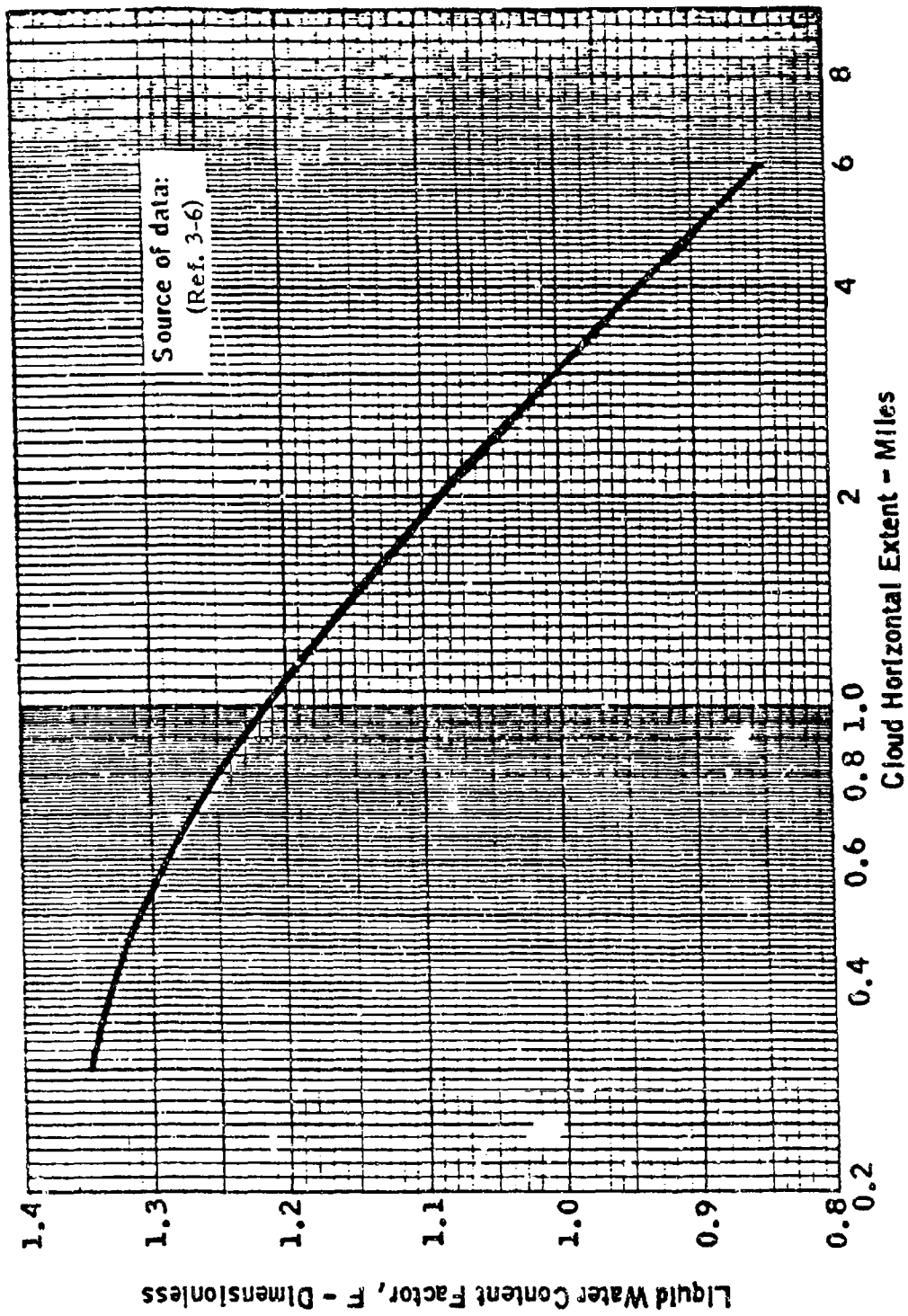
FIGURE 3-9. INTERMITTENT MAXIMUM ATMOSPHERIC ICING CONDITIONS - CUMULIFORM CLOUDS. VARIATION OF LWC FACTOR WITH CLOUD HORIZONTAL DISTANCE EXTENT (REFERENCE 3-2)
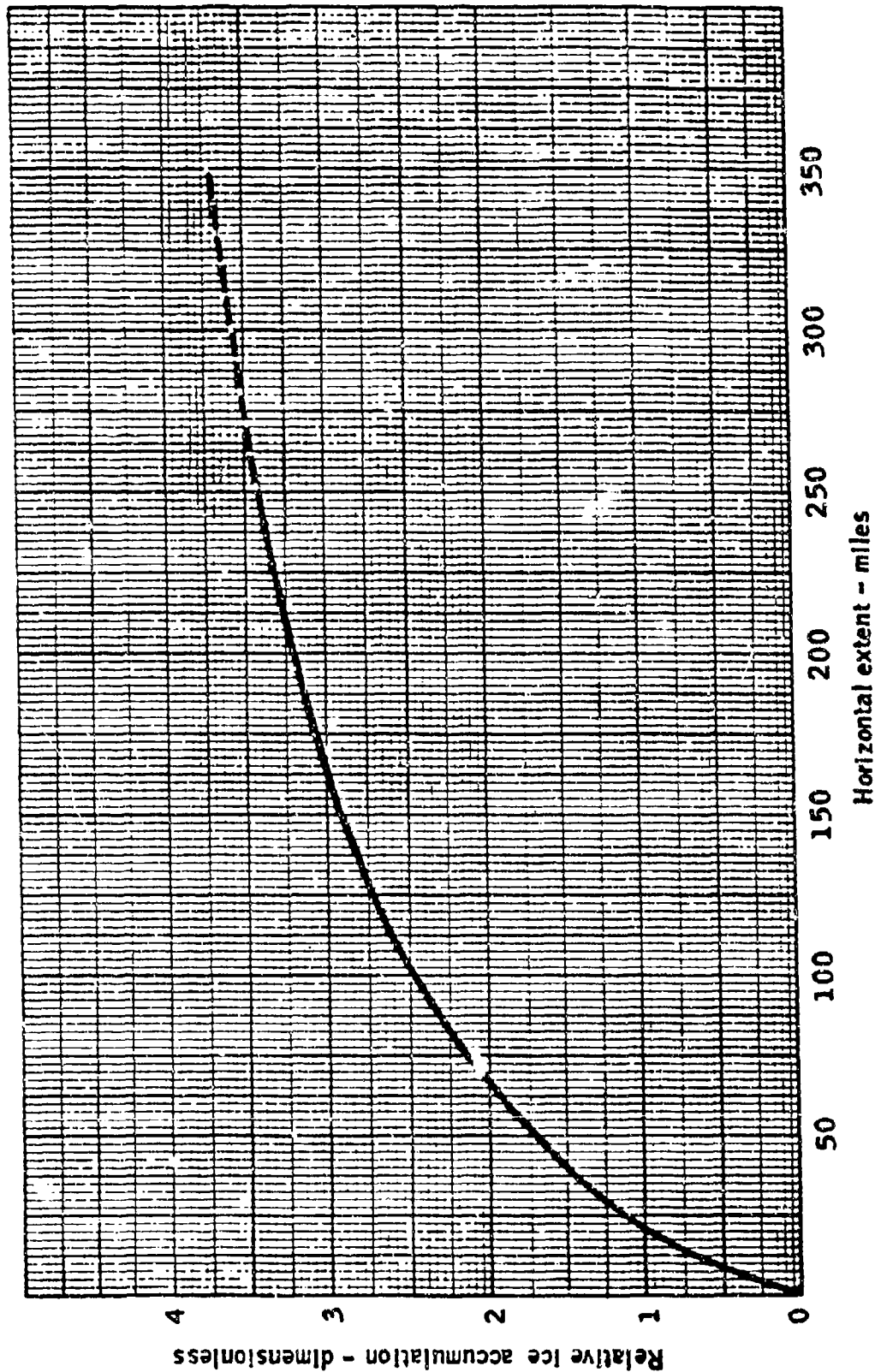
FIGURE 3-10. PLOT OF RELATIVE AMOUNT OF ICE ACCUMULATION FOR VARIOUS FLIGHT DISTANCES IN CONTINUOUS MAXIMUM ICING (BASED UPON A 20-MILE STANDARD DISTANCE AND THE DATA OF REFERENCE 3-36)

MAXIMUM AND MIMIMUM ICING TEMPERATURES ARE A FUNCTION OF
ALTITUDE AS FOLLOWS:

PRESS. ALT. (FEET)	MAX. AMB. TEMP. (DEGREES C)	MIN. AMB. TEMP. (DEGREES C)
0	0.0	-17.8
2000	0.0	-20.6
4000	0.0	-23.3
6000	0.0	-23.3
8000	0.0	-23.3
10000	-3.9	-23.3
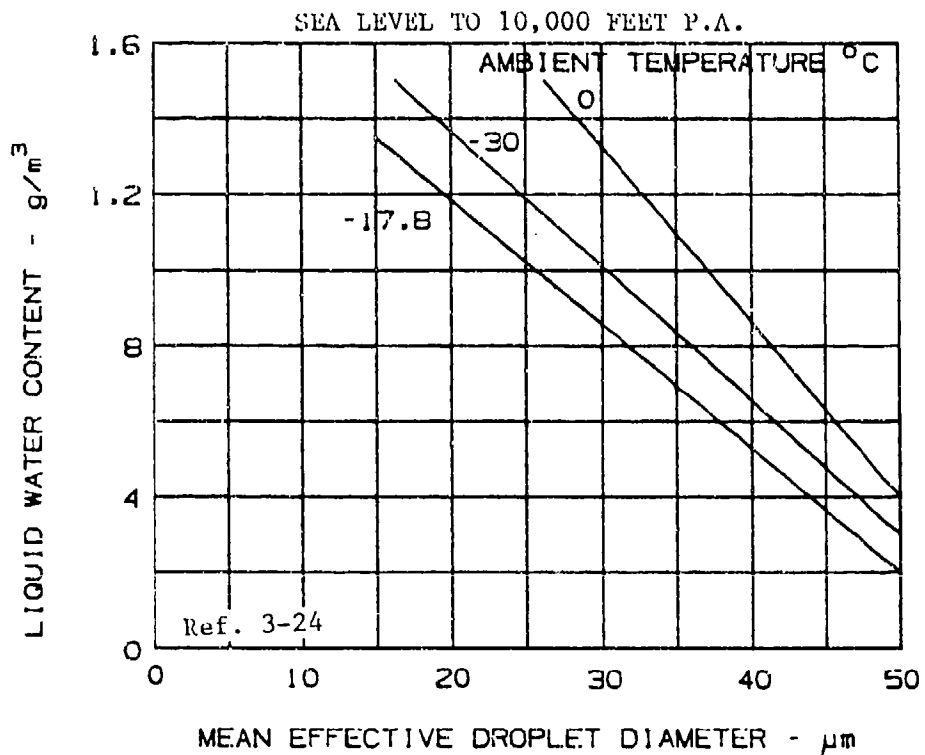
FIGURE 3-11. FAA ALTITUDE LIMITED ENVELOPE FOR INTERMITTENT ICING CONDITIONS

MAXIMUM AND MINIMUM ICING TEMPERATURES ARE A FUNCTION
OF ALTITUDE AS FOLLOWS:

PRESS. ALT. (FEET)	MAX. AMB. TEMP. (DEGREES C)	MIN. AMB. TEMP. (DEGREES C)
0	NO ICING BELOW 4,000 FEET	
2000		
4000	0.0	-10.0
6000	0.0	-13.9
8000	0.0	-17.8
10000	0.0	-17.8
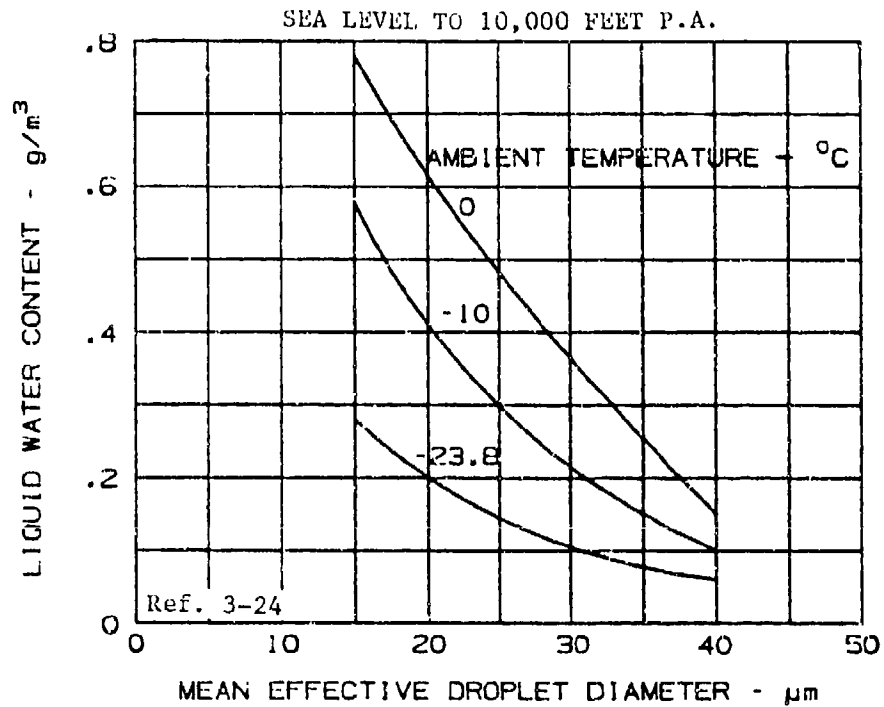
FIGURE 3-12.   FAA ALTITUDE LIMITED ENVELOPE FOR CONTINOUS ICING CONDITIONS
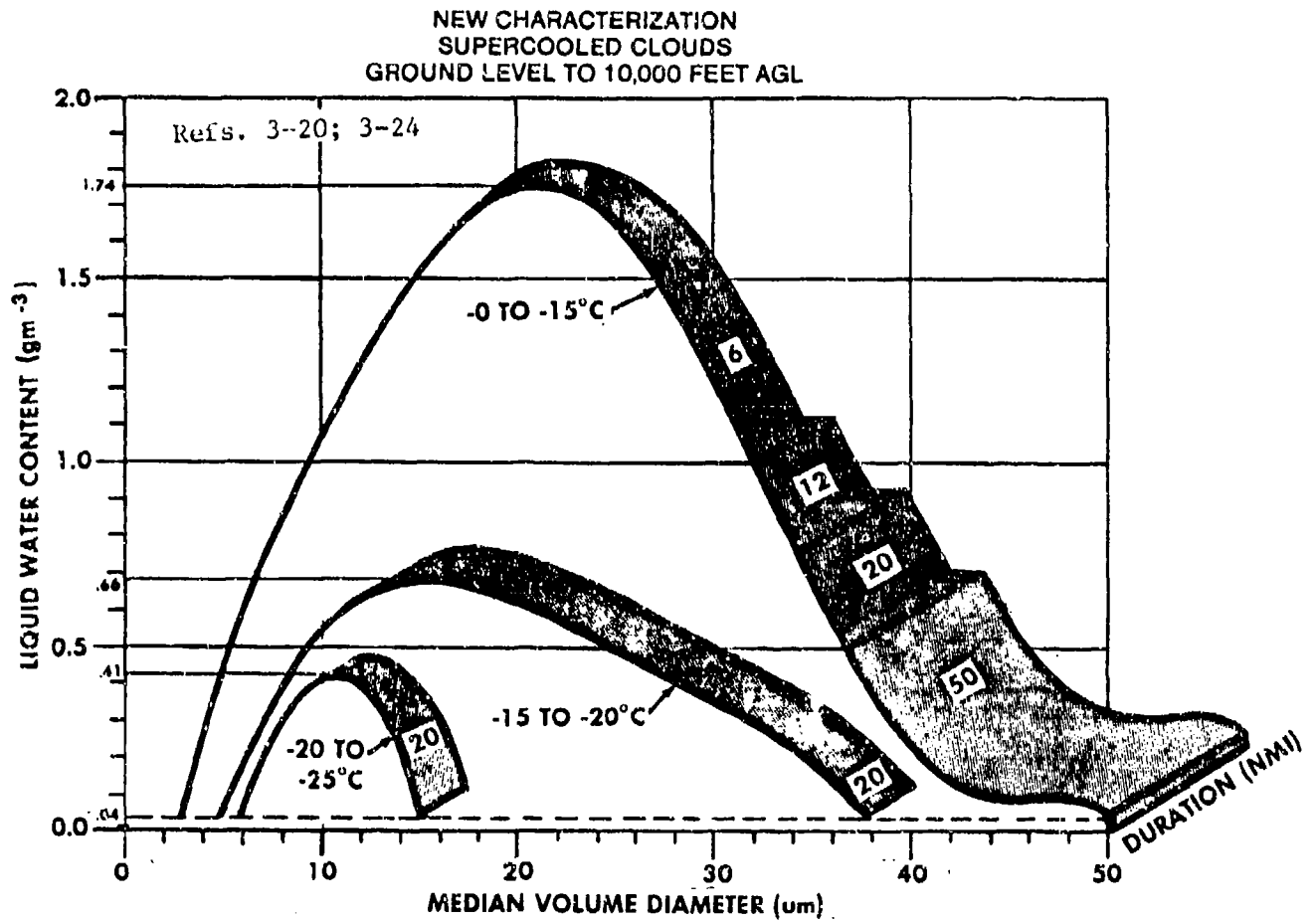
FIGURE 3-13. FAA ALTITUDE LIMITED CHARACTERIZATION FOR SUPERCOOLED CLOUDS

MEDIAN VOLUME DROPLET DIAMETER - 20 MICRONS

Refs. 3-25; 3-40
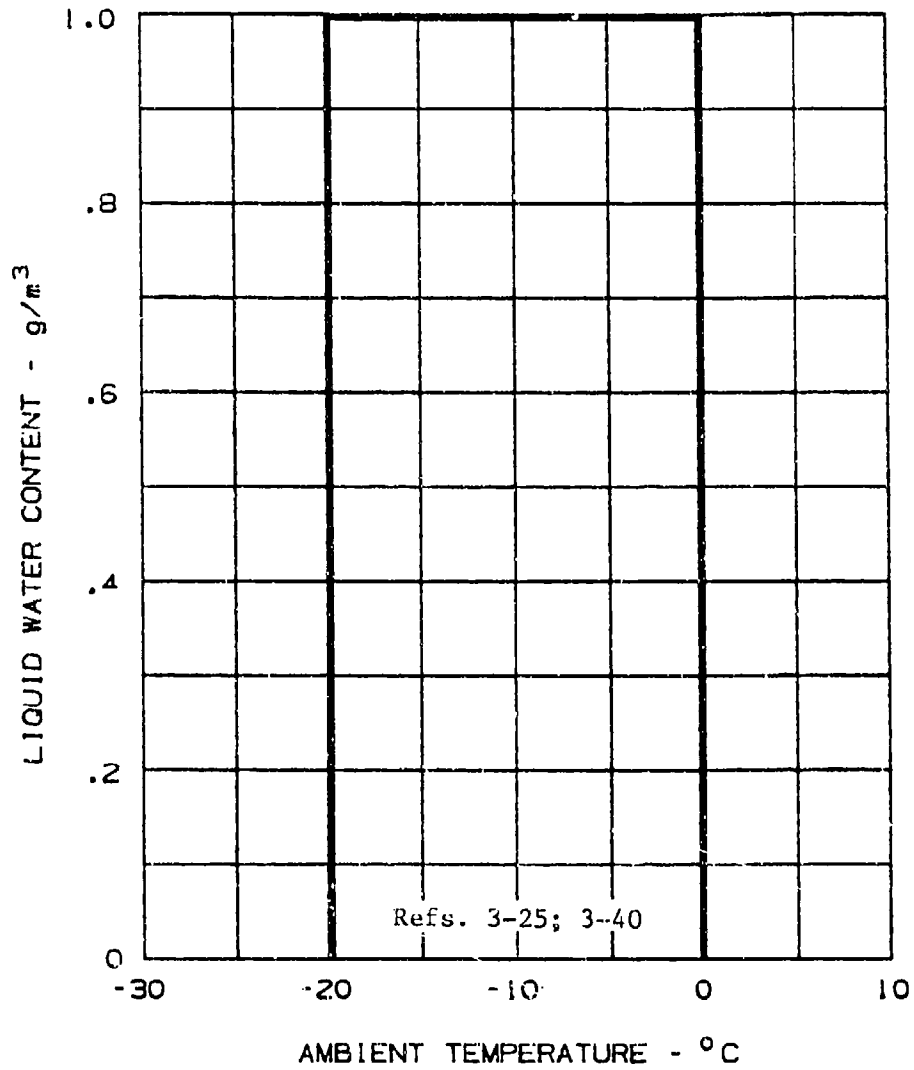
FIGURE 3-14. US MILITARY ENVELOPE OF ICING LIQUID WATER CONTENT
VERSUS OUTSIDE AIR TEMPERATURE
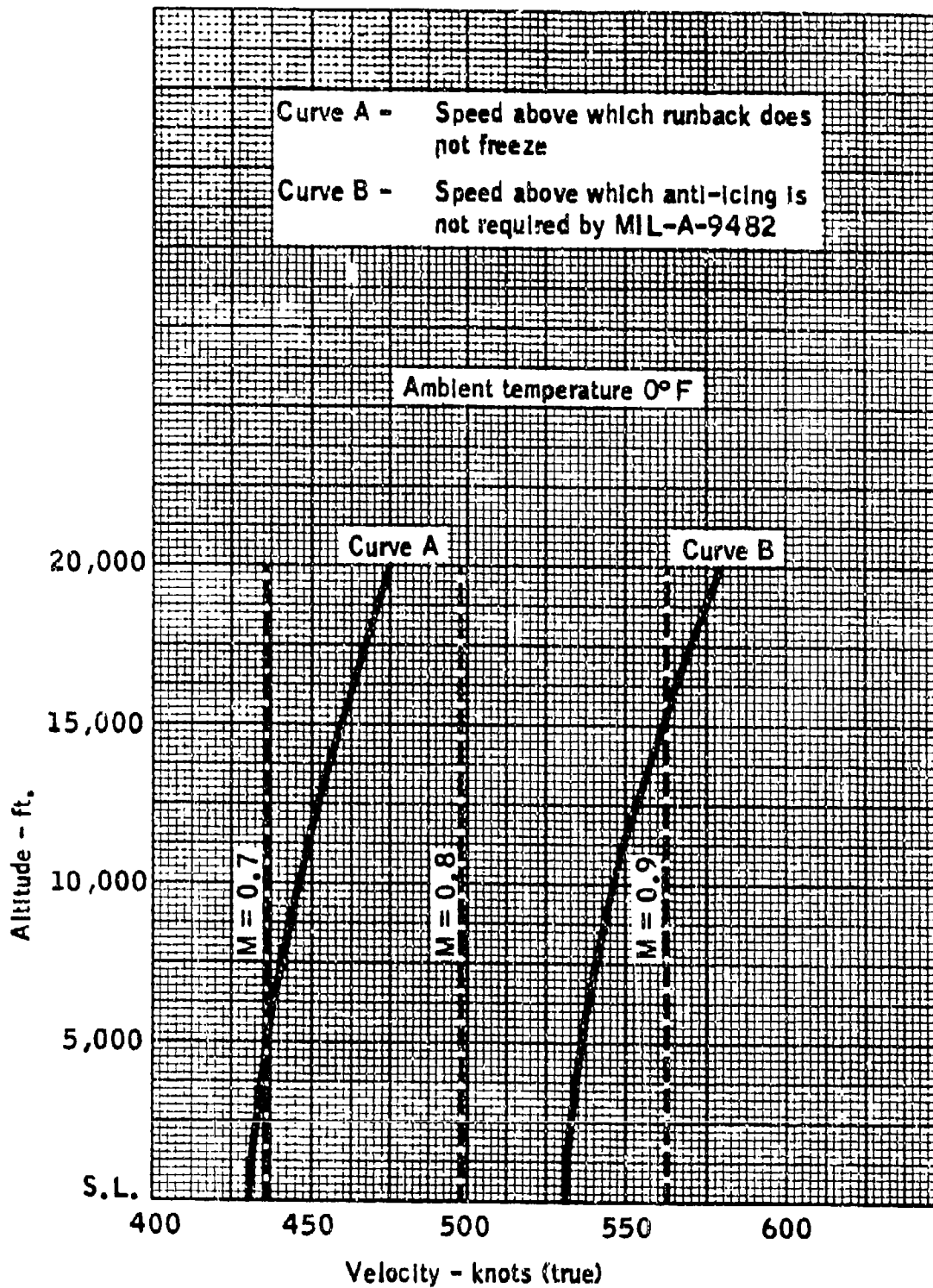
FIGURE 3-15.   EFFECT OF SPEED UPON REQUIREMENTS FOR ANTI-ICING
(REFERENCE 3-23)

I 3-35
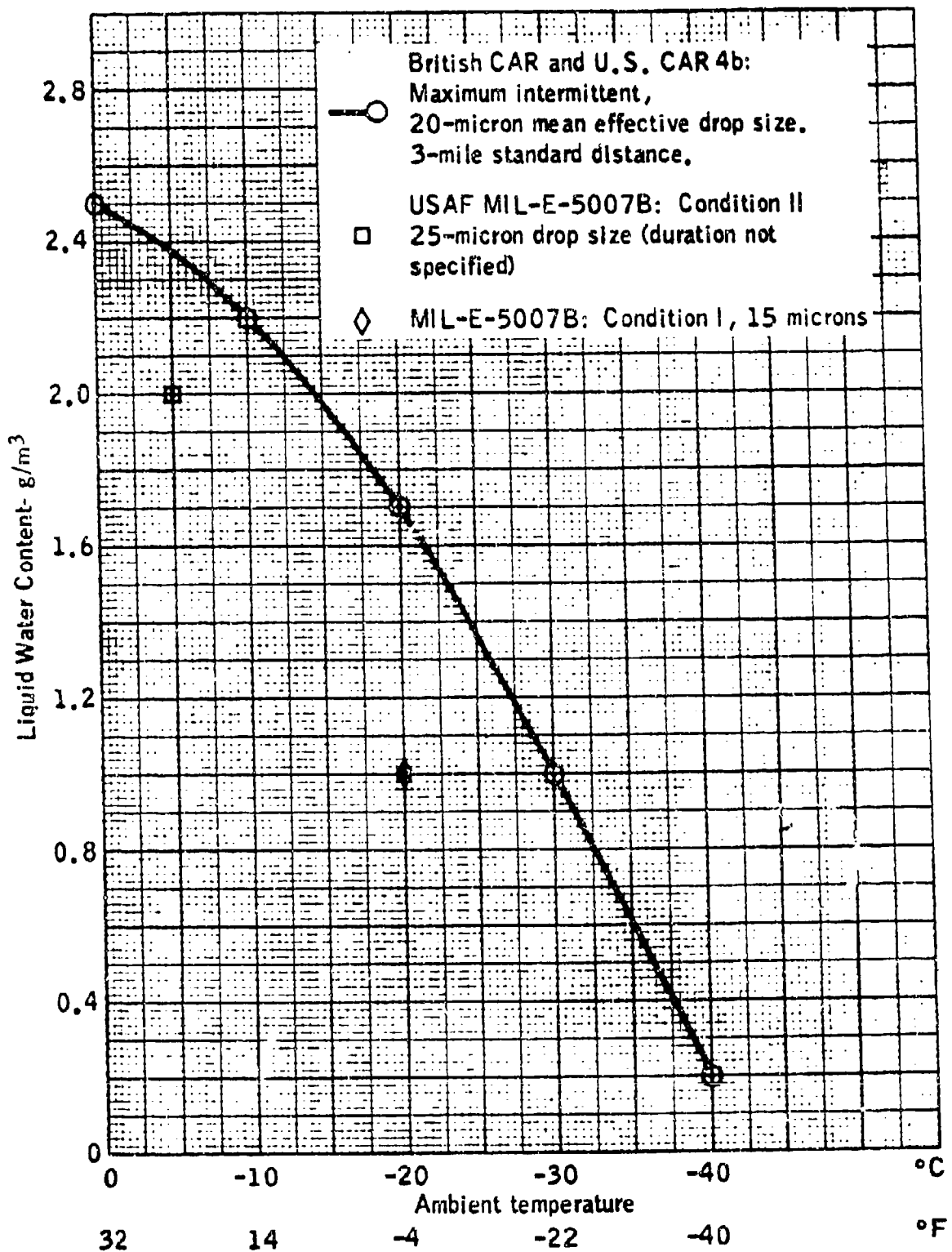
FIGURE 3-16.   BRITISH AND US STANDARD FOR INTERMITTENT ICING
(REFERENCE 3-2, `-24, 3-31)
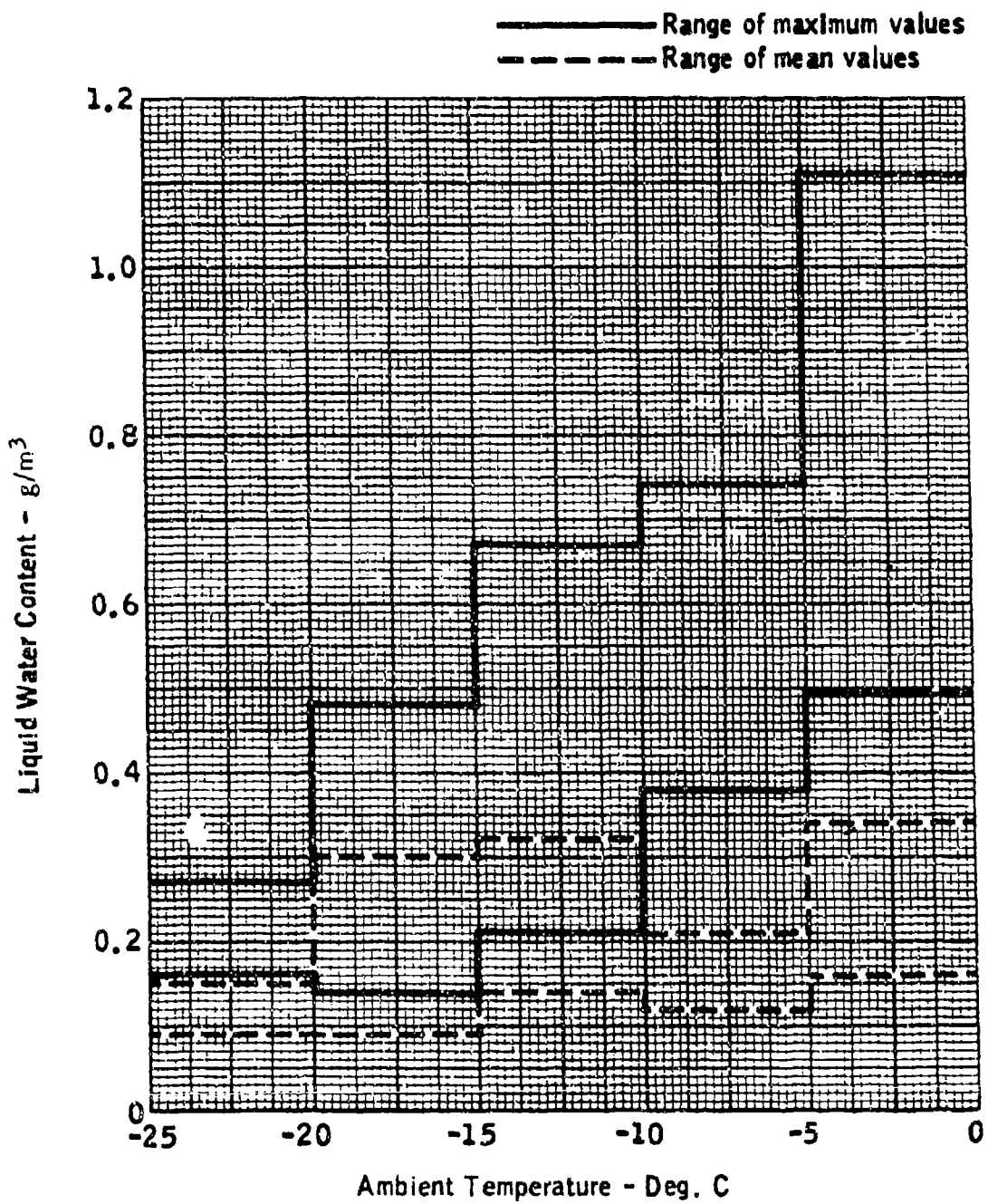
FIGURE 3-17. MAXIMUM AND MEAN LWC MEASURED IN THE USSR FOR STRATUS
TYPE CLOUDS (REFERENCE 3-29)

I 3-37
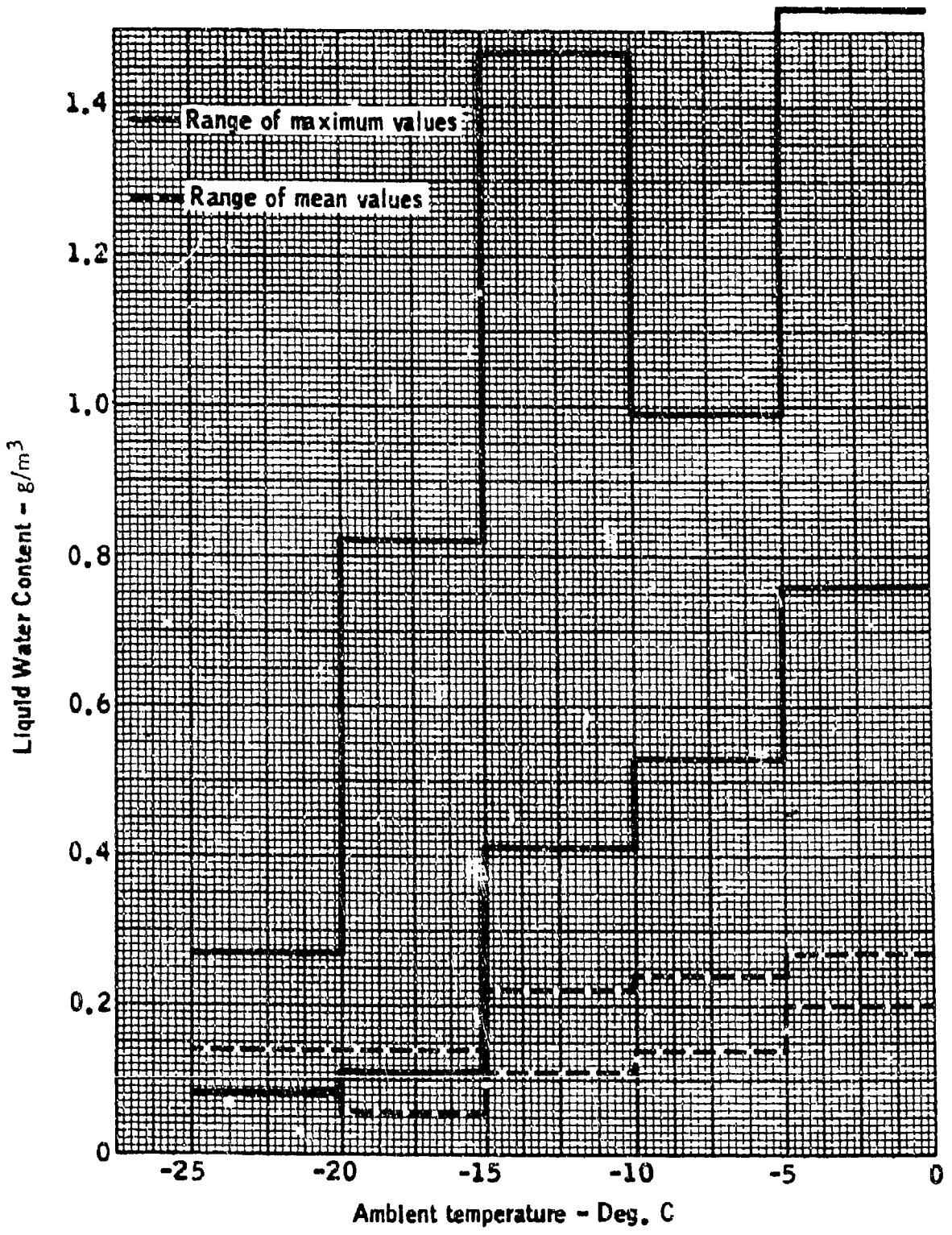
FIGURE 3-18. MAXIMUM AND MEAN LWC MEASURED IN THE USSR FOR CUMULUS
TYPE CLOUDS (REFERENCE 3-29)

I 3-38
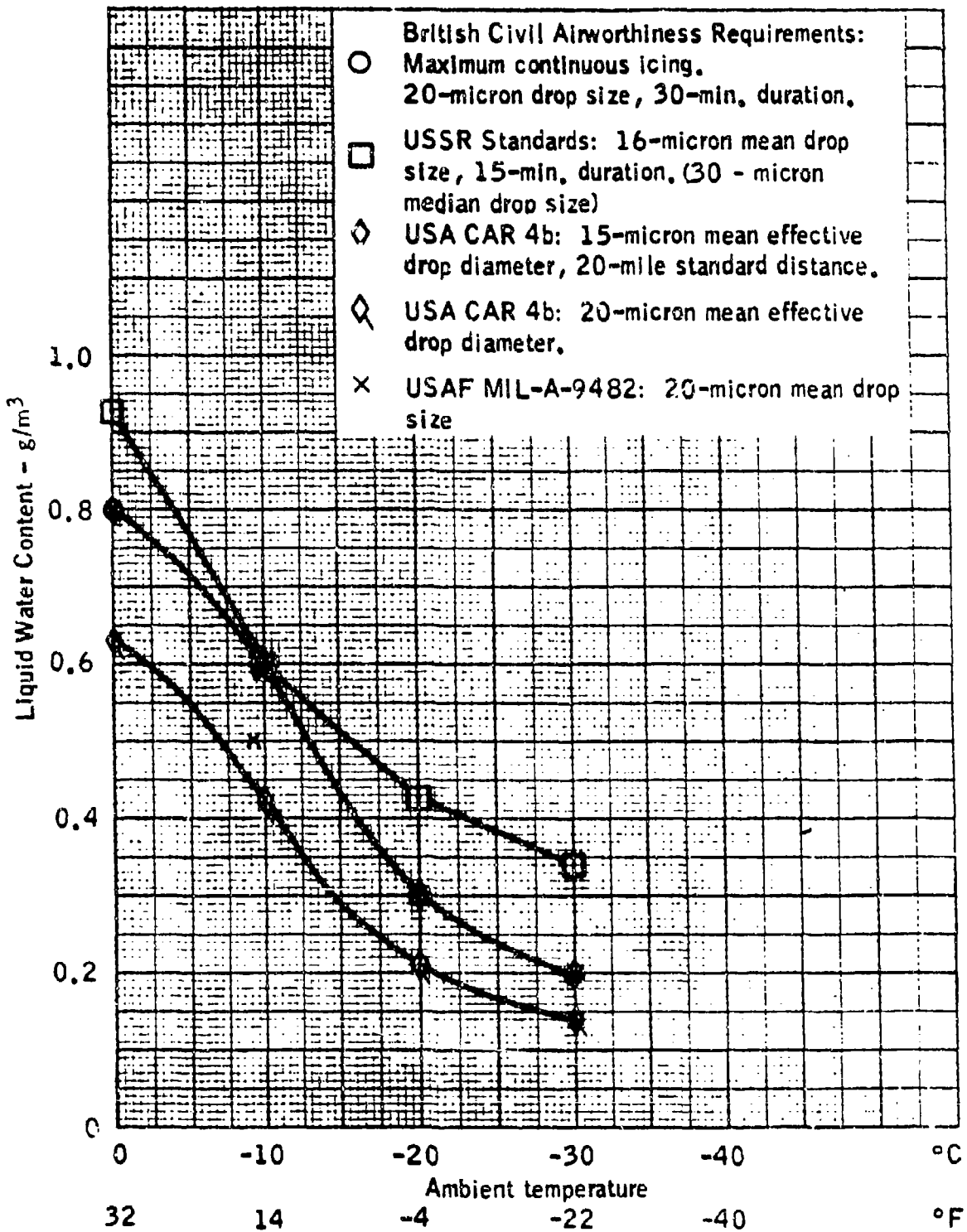
FIGURE 3-19. COMPARISON OF US, BRITISH, AND USSR TRANSPORT
STANDARDS FOR CONTINUOUS ICING (REFERENCE 3-2,3-23,3-31)

I 3-39
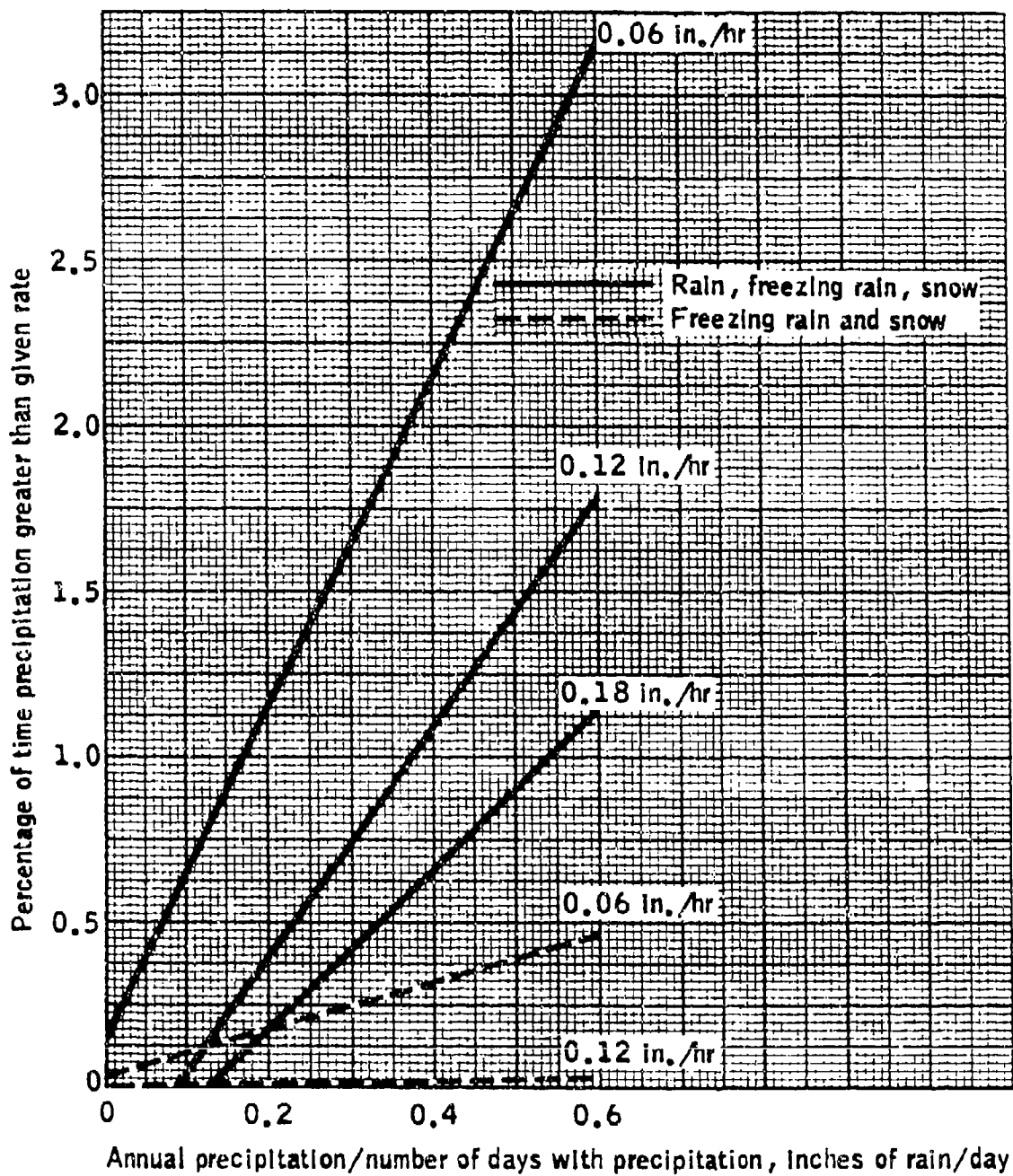
FIGURE 3-20. FREQUENCY RATES FOR RAIN, FREEZING RAIN AND SNOW
(REFERENCE 3-34)
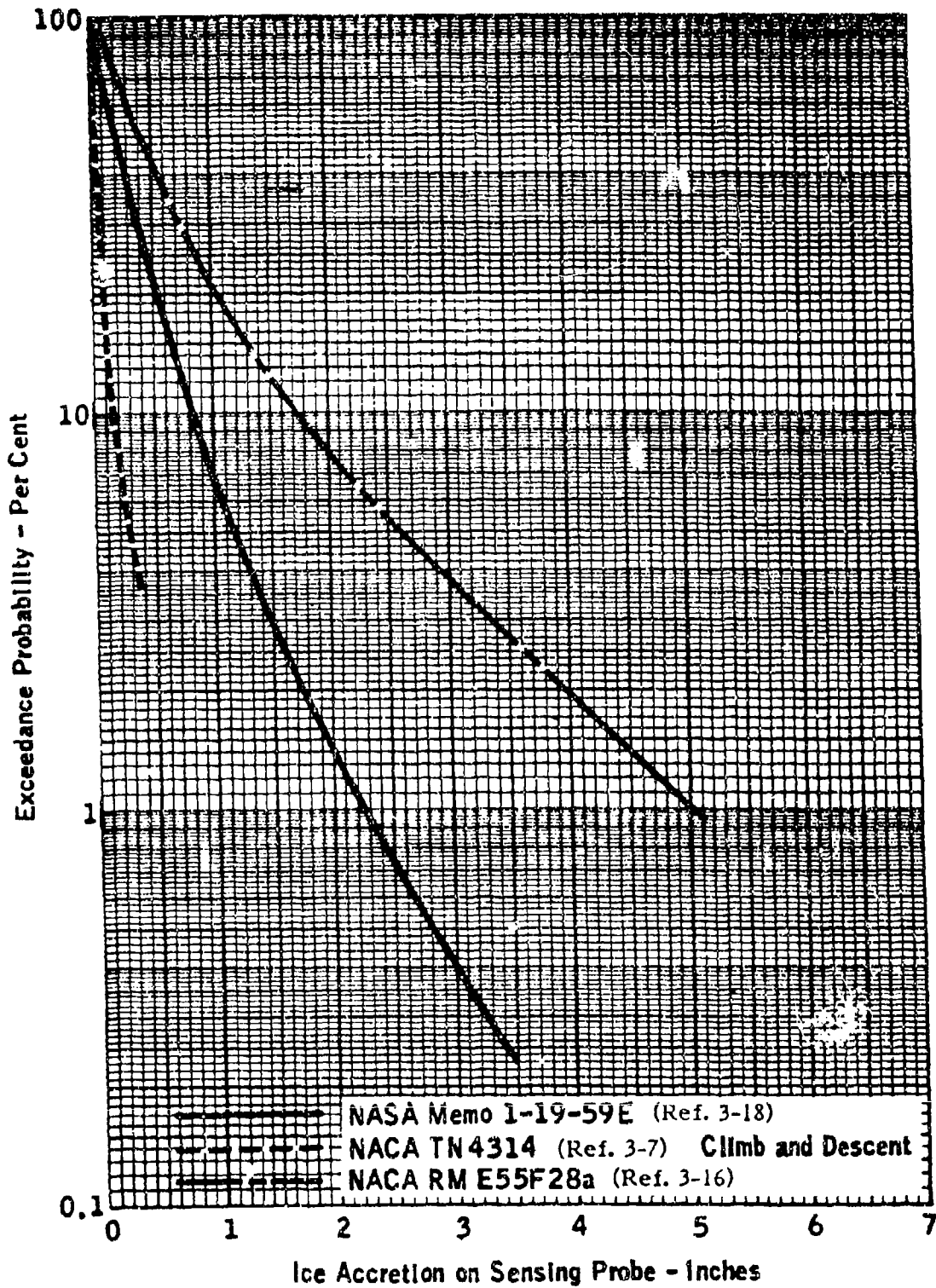
FIGURE 3-21. ICE ACCRETION PROBABILITIES (BASED UPON 1/8-IN DIAMETER PROBE) (REFERENCE 3-7, 3-16, 3-18)
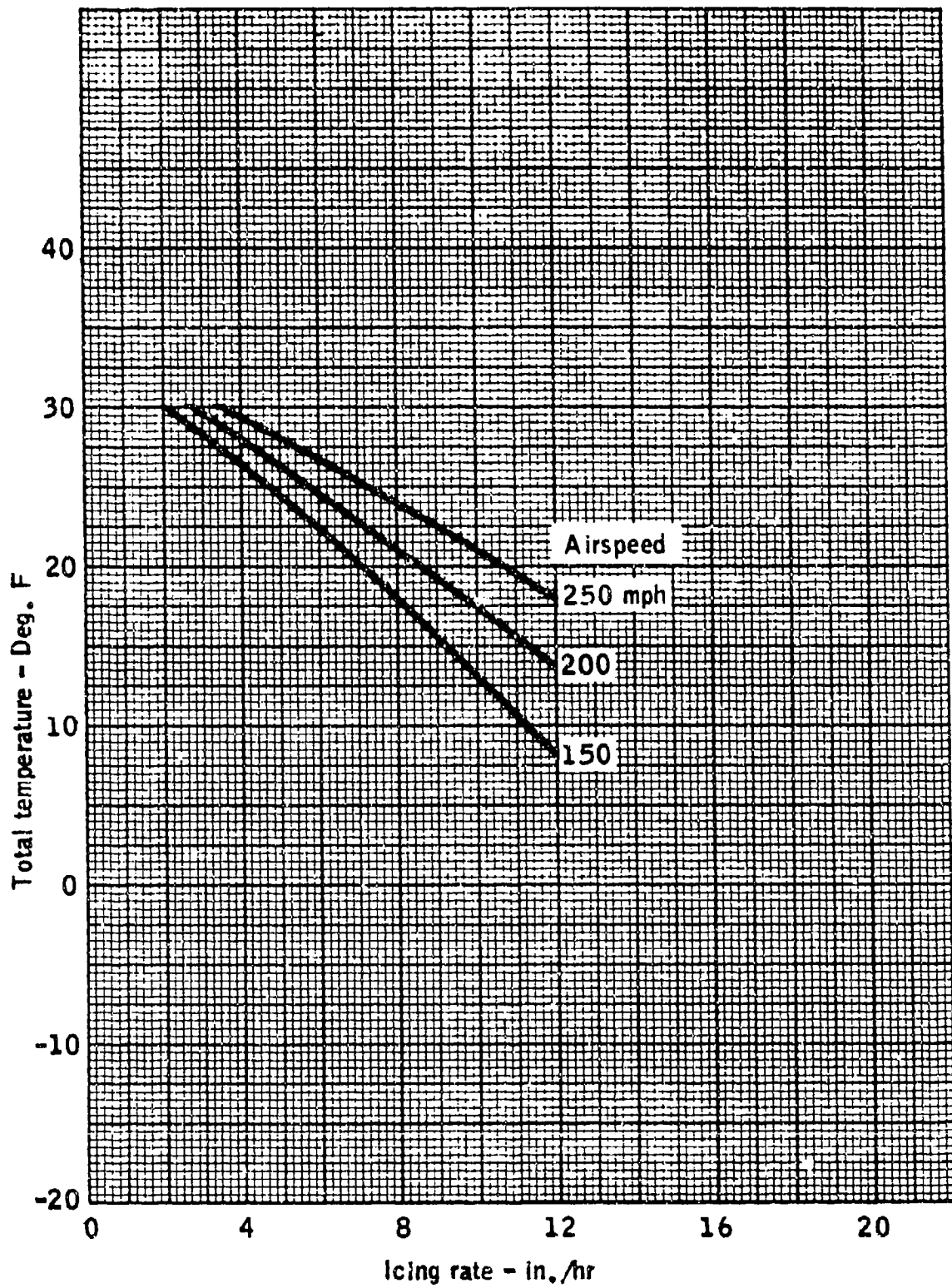
FIGURE 3-22.   LIMITING CURVES FOR ONSET OF WATER RUNOFF (FOR 1/8-IN
              PROBE) (REFERENCE 3-18)
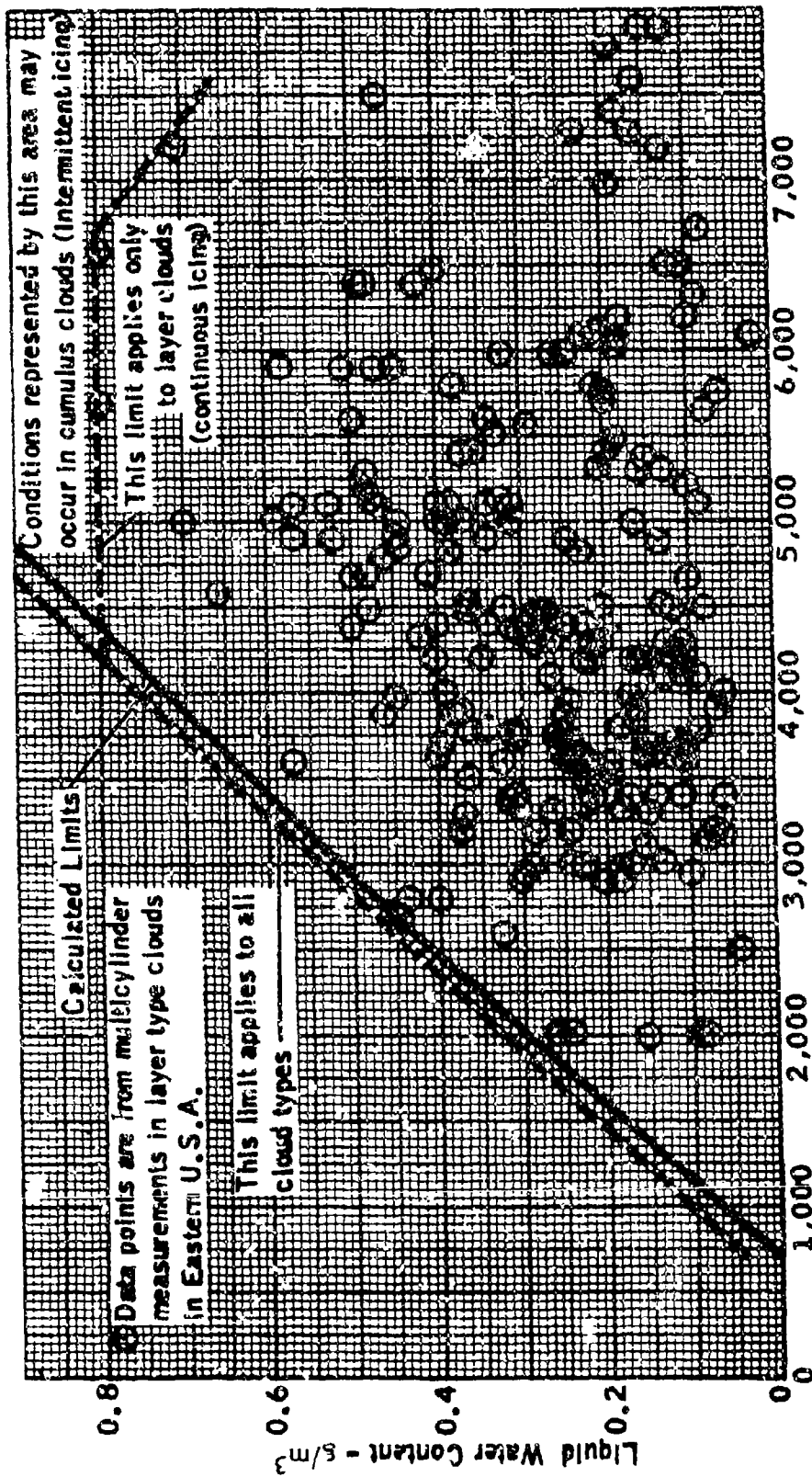
FIGURE 3-23. CLOUD LWC LIMITS AT LOW ALTITUDES (REFERENCE 3-36)
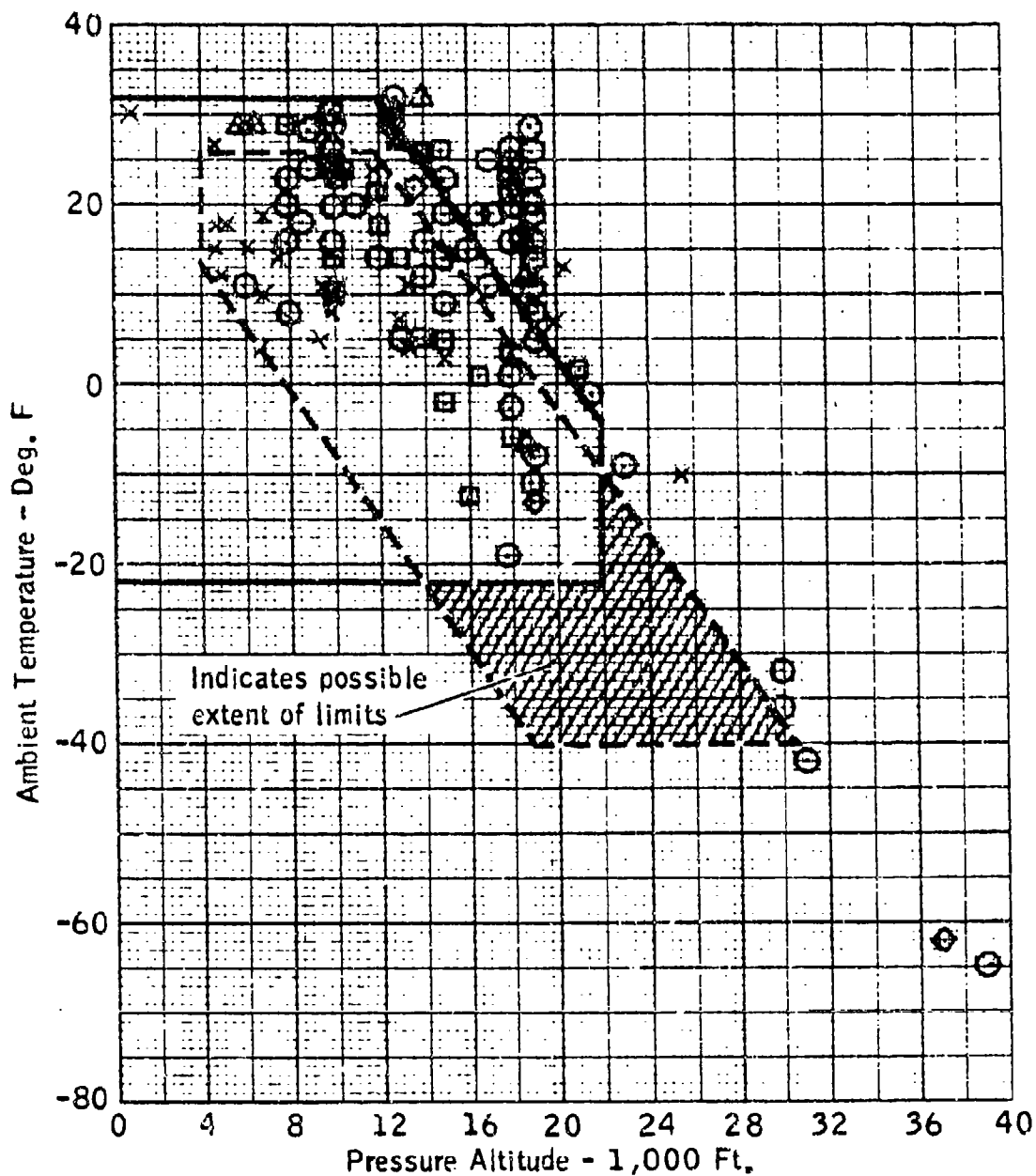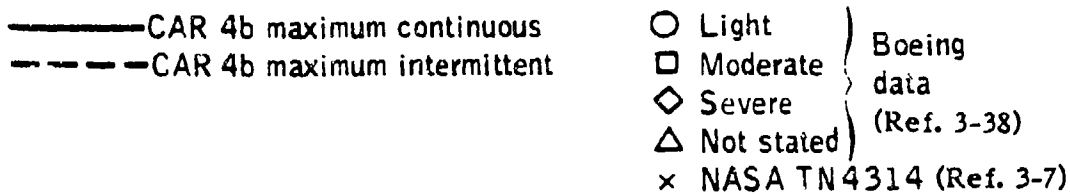
FIGURE 3-24.   COMPARISON OF FAR 25, APPENDIX C, ICING ENVELOPES
WITH REPORTED ENCOUNTERS (REFERENCE 3-38)

CHAPTER II
ICE DETECTION AND MEASUREMENT
SECTION 1.0 - ICE DETECTION
SECTION 2.0 - ICING MEASUREMENT INSTRUMENTS

CHAPTER II
SECTION 1.0
ICE DETECTION

CHAPTER II - ICE DETECTION AND MEASUREMENT
CONTENTS
SECTION II.1.0 ICE DETECTION

LIST OF FIGURES

SYMBOLS AND ABBREVIATIONS

Symbol	Description
c	speed of sound in ice, m/s
C	temperature in degrees Celsius
cm	centimeter
CRT	Cathode Ray Tube
D	ice thickness, millimeters
E	Young's modulus
F	temperature in degrees Fahrenheit
g	gram
hr	hour
Hz	frequency, cycles per second
km	kilometer
LWC	Liquid Water Content, g/m^3
m	meter
mm	millimeter
MTBF	Mean Time Between Failure
OAT	Outside Air Temperature
Rho	density
T	time, seconds
UFR	Undetected Failure Rate
u	Poisson's ratio

GLOSSARY

liquid water content (LWC) - The total mass of water contained in all the liquid cloud droplets within a unit volume of cloud. Units of LWC are usually grams of water per cubic meter of air (g/m^3).

median effective diameter (MED) - The droplet diameter which divides the total water volume present in the droplet distribution in half; i.e., half the water volume will be in larger drops and half the volume in smaller drops. The value is computed from assumed drop size distributions.

median volumetric diameter (MVD) - The droplet diameter which divides the total water volume present in the droplet distribution in half; i.e., half the water volume will be in larger drops and half the volume in smaller drops. The value is obtained by computation from actual drop size measurements.

micron(μm) - One millionth of a meter.

II.1.0 ICE DETECTION

II.1.1 INTRODUCTION

The detection of the onset of an icing condition is necessary to alert the flight crew to activate ice protection systems or to evade the icing condition so that the detrimental effects of ice accretion on aircraft flight safety and performance can be minimized or prevented. Ice detection instruments are available in several types including those which detect ice and provide a visual display in the cockpit and those that automatically activate ice protection systems. Currently, most ice detectors are only certified for use as an advisory backup system to visual crew monitoring of icing conditions. Certification of ice detection systems as primary systems has significant implications on the design and reliability of these systems.

The pilot techniques to avoid icing during flight are old and well known (reference 1-1). Obviously the Outside Air Temperature (OAT) must be near or below the freezing point and there must be some liquid water in the environment. A basic knowledge of the kinds of clouds and their characteristics, such as extent and probable water content, is all that is necessary. Generally a pilot can see the presence of ice by noting its growth on objects such as wiper blades, windshields, or thin probes in easy view. At night, a light is helpful in observing ice formation; however, pilot workload usually prevents attention to visual monitoring means.

In this section, ice detection methods are described with discussion of their characteristics, performance, and reliability.

II.1.2 VISUAL DETECTION

It may be possible for the pilot to visually detect the presence of icing by noting its formation on such unheated surfaces as wiper blades, portions of the windshield, or various probes within easy view. Observing the wing leading edges for ice buildup is also recommended; however, the leading edges are not always visible from the cockpit area, particulary at night and on swept wing or rotary wing aircraft. At night, a light should be used to observe ice formation. A simple and effective method of improving visual ice detection on fixed wing aircraft is to mount a four to six inch (10.2 to 15.2 cm) rod of 1/8 to 1/4 inch (0.32 to 0.64 cm) diameter on the fuselage in a position where the pilot can easily observe ice formation (the rod should be long enough to extend outside the air and water droplet boundary layers). The OAT probe in many light airplanes already serves in this capacity.

II.1.3 COMMERCIALLY AVAILABLE DETECTORS

I.3.1 Types Available

Ice detectors are available in several types which either detect the presence of ice or the presence of water. For the latter, an indication of the ambient air temperature is necessary to determine that

an icing condition exists. Detectors which sense the presence of ice provide indication that an icing condition exists and, in some cases, can be utilized to determine icing severity or rate. In the following paragraphs, detector types are discussed in terms of the principle of operation, present use, advantages, and disadvantages.

1.3.2 Hot Wire Ice Detectors

Hot wire ice detectors work on the principle that the transformation from ice to liquid water takes place at a constant temperature. Typically, the detector has a thermally sensitive nickel or nickel-alloy wire wound on a mandril that is exposed to the airstream. The wire is subjected to a periodic current pulse which causes the wire to heat up. If there is no ice on the wire, the resistivity will change linearly with time as the wire heats up. If ice has accreted, the wire temperature will remain constant at the melting point of ice. After all the ice is converted to water, the wire resistivity will again increase. The resistance plateau at the ice melting point is electronically sensed and an ice signal generated by the electronics. When ice is detected, the probe is deiced by an internal cartridge heater. The probe is then allowed to cool down and the sensor is again ready to accrete ice.

Typically, this type detector can detect accretions as small as 0.005 inches (0.13 mm), but due to its design technology, cannot distinguish ice thickness on the probe. An example of a hot wire ice detector for fuselage mounting is shown in (figure 1-1). Another version is available for engine inlet mounting.

1.3.3 Vibrating Probe Ice Detectors

Vibrating probe detectors work on the principle of an axially vibrating rod or probe whose natural frequency is known. The probe forms the sensor portion and is typically mounted on an aerodynamic strut. As ice accretes on the probe, the natural resonant frequency decreases. At a specified frequency shift, which is related to the ice mass on the probe, an output signal is generated and probe heaters are energized to remove the ice. The heater is then de-energized, the probe cools down, and is again ready to accrete ice. Icing severity is determined by measuring the overall cycle rate with respect to time. Cycle time is the combination of actual ice accretion time plus recovery time. Recovery time is the time the ice detector heaters are on plus the time for the sensing element to reach a temperature suitable for accreting ice. Typical heater-on-times are 5 seconds. Overall recovery time tends to vary with LWC and temperature, but is largely a function of velocity. Overall cycle times range from 75-125 seconds for trace icing to 10-20 seconds for heavy icing, depending upon ambient temperature and velocity (reference 1-2).

The ice detection and measurement capability of the vibrating probe ranges up to 2 g/m^3 and ice thickness from 0.01 to over 0.10 inches (0.25 to over 2.5 mm). Accuracy of this type detector in measuring icing severity is within ±15%. An example of a non-aspirated vibrating probe ice detector is shown in figure 1-2. An aspirated version of this type ice detector (figure 1-3) is available for rotorcraft application.

Another type of vibrating sensor designed to detect ice is the "vibrating diaphragm" ice detector. This sensor works on the principle of a diaphram (or disc) exposed to icing such that when ice accretes on the diaphram surface its stiffness increases causing the natural frequency to increase. Water or contaminants lower the natural frequency due to increased mass. The diaphram is forced into oscillation by a piezoelectric material. A second disc senses frequency changes, while the conditioning electronics measure the changes in frequency which is proportional to the accreted ice thickness. The sensing diaphram of this instrument is mounted flush with the surface to be protected. The sensor may be configured as a conventional finger probe or in a contoured non-intrusive design flush with an aircraft surface. The sensor, with integrated electronics, is typically small with a surface diameter down to 0.25 inches (0.64 cm). The operating temperature range is from -320 °F (-196 °C) to +392 °F (+200 °C). The achievable measurement accuracy for clear ice is expected to be ±0.05 mm. An example of this type sensor is shown in figure 1-4.

1.3.4 Pressure Array Detectors

These devices sense a decrease in ram air pressure whenever ice accretes over a row of holes drilled into the leading edge of a small strut. One type is in wide use on the Navy P-3 patrol aircraft (figure 1-5). This is a fuselage mounted device with a 3 1/2-inch strut. It has seven small holes about 1/32-inch in diameter located in-line near the tip, and one 1/4-inch diameter hole located about one third of the way in. A differential pressure sensor monitors the ram pressure difference between the large hole and the set of small holes. In the absence of any ice accretion the ram pressure is balanced and independent of the airspeed. Any ice accumulation on the strut will block the small holes first, and the resulting unbalance in ram pressure can be used to activate a warning light. At some threshold value of the pressure difference, an internal heater is temporarily energized to melt the ice accreted on the strut.

1.3.5 Obstruction Type Ice Detectors

1.3.5.1 Light Beam Interruption Ice Detectors

Light beam interruption ice detectors (reference 1-3) operate on the principle that ice accreted on a probe occludes a light beam (normally infrared) crossing the central area of the probe at an oblique angle with a light sensitive receiver placed on the opposite side. The degree of occlusion is determined by the amount of ice on the probe. When the light occlusion reaches a predetermined level, representing maximum permitted ice thickness, a heating cycle is initiated to remove ice from the low thermal inertia probe. The time taken to accrete ice between two predefined levels is used as a measure of the icing rate from which liquid water content can be calculated. These units have been aspirated to assist in detecting ice for helicopters. This type device is sensitive to as little as 0.005 inches (0.13 mm) of ice but cannot determine thickness of ice (reference 1-3). An example of a type of light beam interruption ice detector is shown in figure 1-6.

1.3.5.2 Beta Beam Interruption Ice Detectors

A beta beam interruption detector works in a similar manner to the light beam type device. The main disadvantage of the beta beam detector is that a radioactive source is required, usually Strontium 90. This detector is capable of detecting as little as 0.015 inches (0.38 mm) of ice thickness.

1.3.5.3 Rotating Disk Ice Detectors

The rotating disk ice detector is an obstruction type instrument where a disk is exposed perpendicular to the airstream. Ice accreting on the rotating disk is shaved off by a scraper; the torque required to remove the ice is used to activate a warning system. An alternative ice detector form is the rotating cylinder type ice detector which operates on the same principle as the rotating disk.

1.3.6 Pulse Echo Ice Detectors

The pulse-echo ice detector operates on the principle of using pulsed ultrasonic waves to measure ice thickness over a small transducer mounted flush with an aircraft surface (references 1-4 and 1-5). This system produces a real-time ice thickness signal wherein ice accretion rate may be determined by electronically differentiating ice thickness with respect to time.

In operation an ultrasonic transducer containing a piezoelectric element emits a pulse (2-10 MHz) which travels through the ice in a direction parallel to the transducer emitting axis. When the pulse reaches the ice/air interface it is reflected back into the ice layer. This "echo" returns to the aircraft surface where it is detected by the transducer which now acts as a receiver figures 1-7 and 1-8). The velocity of the pulse-echo signal through the ice (approximately 3800 m/s) is determined by the ice density and elastic constants. By measuring elapsed time the ice thickness, D, may be calculated from the formula $D = (CT_{p-e})/2$ where C is the pulse-echo signal velocity in ice (speed of sound in ice) and T_{p-e} the elapsed time between the pulse emission and echo signal return.

The pulse produced by the ultrasonic transducer is a short-duration compression wave (longitudinal wave). The velocity at which such a compression wave propagates through a solid medium is theoretically predicted (reference 1-4) to be

$$C = \left[\frac{E(1 - \upsilon)}{\rho(1 + \upsilon)(1 - 2\upsilon)} \right]^{1/2}$$

where E is the Young's modulus for the medium, u the Poisson's ratio, and p the density of the medium. Thus, the pulse-echo signal propagates through a solid medium at a constant velocity that depends only on the density and elastic constants of the medium.

Attenuation of the received echo signal can be divided into three components: absorption and scattering within the ice, and reflection at the ice/air interface. Absorption occurs as part of the wave vibrational energy and is stored as heat by the ice molecules and then lost through irreversible heat transfer within the ice layer. Scattering is caused by any inclusion within the ice such as air bubbles.

The third factor affecting the received echo signal strength is the ice/air interface shape itself. While almost 100% of the incident wave energy is reflected by the ice/air interface, the interface shape determines the reflected wave propagation direction(s). Rough ice surfaces will reflect the incident wave diffusely, while ice surfaces not parallel to the transducer face will cause the echo signal to propagate at an angle to the transducer emitter axis. In both cases the echo intensity received by the transducer will be diminished over that received from a uniform ice thickness with a flat, parallel ice/air surface.

Rough and/or concave ice surfaces, characteristic of rime and glaze ice formations, scatter the incident ultrasonic pulse. This reduces the echo signal strength received by the transducer. However, the echo signal is not completely obscured, therefore the pulse-echo time can be measured for ice shapes typically encountered during icing condition flight. The operational accuracy achievable depends primarily on the transducer specifications (frequency and element diameter) and the transducer location. An accuracy of ±0.02 inches (±0.5mm) has been obtained for ice thickness measurement of 0.04 to 1.2 inches (1 to 30 mm) (reference 1-4). The ultrasonic pulse-echo technique also allows the presence or absence of liquid water on the iced surface to be uniquely determined by examining the echo signal time variations received from the ice surface (reference 1-6).

An array of ultrasonic transducers (figure 1-8) has been employed on an airfoil to measure in-flight ice accretions. The ultrasonic thickness measurement accuracy of ice accretion, in this application, was found to be within ±0.5 mm of mechanical and stereo photograph measurements. (reference 1-6.)

The transducer is nonintrusive, small, and light weight. It mounts flush with the surface on which ice accretions are to be measured. A cockpit display unit can provide the pilot with an automatic "icing encountered" alert and indicate icing severity as well as providing ice protection system control.

At the present time, the pulse-echo ice detection system is in the experimental stage of development and is not being manufactured.

1.3.7 Microwave Ice Detectors

The microwave ice detecting system (figure 1-9) measures both icing rate and accumulated ice thickness (reference 1-7). This type system consists of three major components:

    a.   A microwave transducer

    b.   A data transmitter located near the transducer

    c.   A cockpit-mounted microprocessor and display

The microwave transducer consists of a resonant surface waveguide embedded flush in the surface on which ice accretes. The waveguide is constructed of dielectric material (polyethylene) having almost the same dielectric properties as ice. When ice accretes on the surface, the ice behaves as though it were part of the surface waveguide, effectively thickening it, causing its resonant frequency to shift downward in proportion to the thickness of the ice layer. The frequency shift is

electronically related to ice thickness by means of a preestablished empirical equation stored in the computer. Ice growth with time is stored in the computer from which icing rate is obtained by differentiating ice thickness with respect to time. Icing rate change is also computed from the second derivative of ice thickness with time. A light is used to indicate an increasing icing rate.

The microwave detection system is very sensitive to thin ice layers. Typically it will respond to an ice thickness less than 0.05 inches (0.13 mm). The system has a dynamic range that is limited by the size of the surface waveguide. Present units have ranges up to 0.9 inches (2.3 cm). For applications where large dynamic ranges are not the primary goal. such as for rotorcraft blades, the transducer size can be reduced to as small as 0.25 inches (0.64 cm).

II.1.4 INDICATOR OPTIONS

1.4.1 Fixed Wing Aircraft

There are several methods to indicate icing conditions to pilots. The most used method in a non Cathode Ray Tube (CRT) type cockpit is a "Master Caution Light" in conjunction with another warning light to annunciate an icing encounter to the pilot. This method is often used where the ice protection system controls must be manually energized. Other systems which automatically energize ice protection systems merely report the presence of ice via a panel light or in some cases not at all. The latter is often the case where the ice protection systems on the aircraft have little or no effect on the aircraft's power availability and/or mission performance.

In a cockpit where most of the system monitoring is done by computer and CRT readouts, a typed phrase such as ENGINE ICING or AIRPLANE ICING is used to alert the crew to an icing encounter. Again the ice protection system may or may not be automatically triggered by the ice warning output signal.

A FAIL signal is available on some ice detector units, especially those which utilize a microcomputer in their circuitry. A fail output can most effectively be used if such an output can be tied into a maintenance log aboard the aircraft. The fail signal circuit should be designed to reliably output a fail signal anytime the ice detection unit is not capable of outputting an ice warning signal during an icing encounter. In addition, the fail output circuitry should be designed such that it will not generate a false icing signal during a fail situation. There may be some exceptions to this rule, such as a heater failure, which does not affect the unit's capability to correctly detect an icing encounter.

1.4.2 Rotary Wing Aircraft

The general provisions stated above for fixed wing aircraft apply as well to the rotary wing aircraft. However, rotary wing aircraft have special requirements for icing indication. All-weather rotary wing aircraft require a system for removing the ice from the rotor blades. Generally, this is done by thermal methods. The blades, being thin, can be damaged by too much heat. However, ice

will not be shed if too little heat is applied. Thus the rate of ice accretion and the OAT are usually required to properly determine the amount of heat needed to deice the blades. The use of an ice detector only may not be sufficient to determine the rate of ice accretion. The cloud LWC that the aircraft is passing through must also be determined. The ice accretion rate output signal from the measuring instrument is normally fed into a blade deice controller unit which will integrate the OAT with the icing severity to control the rotor blade heaters. The system may be designed for manual control in the event of an ice detector failure. The use of a fail signal in a rotary wing aircraft is extremely important since the aircraft may be highly dependent on the icing rate detector for sustained flight in icing conditions.

II.1.5 RELIABILITY CONSIDERATIONS

Actual reported reliability experience for the vibrating probe type ice detector (Section 1.3.3) has been in excess of 8,000 flight hours mean time between removals. This is based on the use of this type of ice detector on the Lockheed L-1011 aircraft over a ten year period. In addition, the vibrating probe type ice detector has been used by the military, both foreign and domestic, for over fifteen years. In general, the reported reliability assessment by these military users have indicated a high degree of confidence in this type of ice detector. The other types of commercially available ice detectors do not have a sufficient data base by which any reasonable reliability assessment can be made at this time.

Another reliability consideration for ice detectors when used in a critical ice protection scenario is the Undetected Failure Rate (UFR). The UFR is the MTBF of undetectable failures within an ice detector that would cause no ice warning output in an icing atmosphere. This UFR, from a user viewpoint, must be sufficiently small to assure safe operation of the aircraft for a reasonable time period after an ice detector system has been pre-flight checked for proper performance. A suggested UFR would be 10-9 failures per flight hour based on a 10 hour or less flight. This is based on FAR 25.1309 for acceptable reliability performance of other flight critical systems.

The reliability of individual ice detector probe designs is, however, beyond the scope of this discussion. The end user and detector manufacturer must assess the practicality of the individual design for such aspects as design ruggedness, temperatures to which the probe may be subjected, and other conditions that may affect reliability.

II.1.7 REFERENCES

1-1   Perkins, Porter J., "Coping With In-Flight Icing," Sverdrup Technology, Inc., Presented at the 29th Corporate Aviation Seminar, Montreal, Canada, April 1-3, 1984.

1-2   Jensen, David and Wahlstrand, Noel, "Icing Rate Indicator System, "Rosemount Engineering Company Report No.26919B, February 1969.

1-3   "Specification 951469A - Mk 12B Ice Detector Unit IDU-3B," Leigh Instrument Limited, Ontario, Canada, September 1983.

1-4   Hansman, R.J. and Kirby, M.S., "Measurement of Ice Accretion Using Ultra-sonic Pulse-Echo Techniques," AIAA Journal of Aircraft, Volume 22, Number 6, June 1985, pp. 530-535.

1-5   Deom, A.A.and Garnier, J.C., "Detection and Measurement of Ice Accretion on a Profile by an Ultrasonic Nethod," AIAA-87-O179, AIAA 25th Aerospace Sciences Meeting, January 12-15, 1987, Reno, Nevada.

1-6   Hansman, R.J.and Kirby, M.S., "In-Flight Measurement of Ice Growth on an Airfoil Using an Array of Ultrasonic Transducers," AIAA-87-O187, AIAA 25th Aerospace Sciences Meeting, January 12-15, 1987, Reno, Nevada.

1-7   Magenheim, Bertram and Rocks, James K., "Development and Test of a Microwave Ice Accretion Measurement Instrument (MIAMI)," NASA CR 3598, 1982.

BLANK PAGE
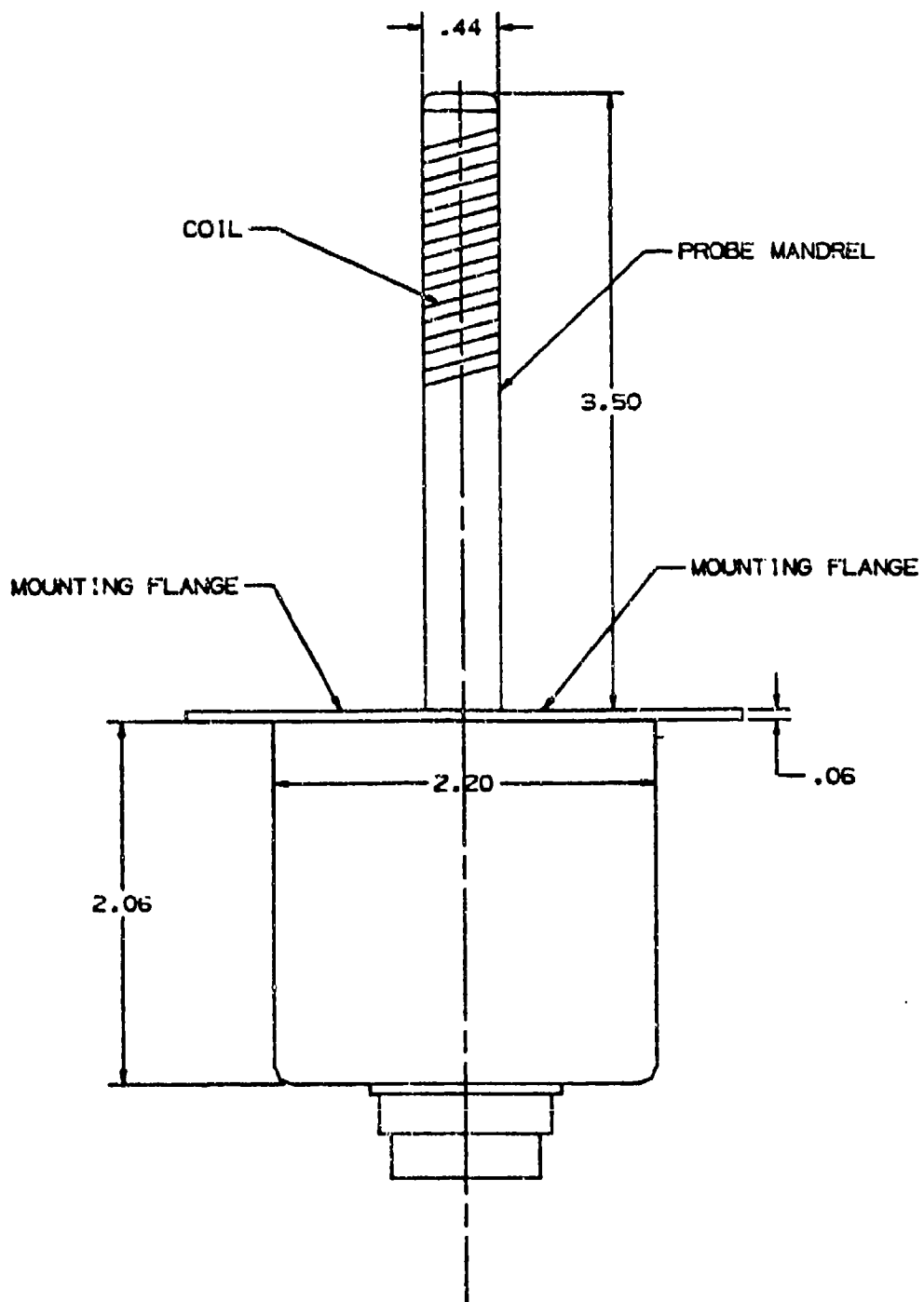
FIGURE 1-1. HOT WIRE ICE DETECTOR

MOUNTING FLANGE 4.50 IN DIA.

4.00 DIA.

.80

.25

STRUT AIRFOIL

STRUT BASE

2.00

.20

.16

3.00

3.77
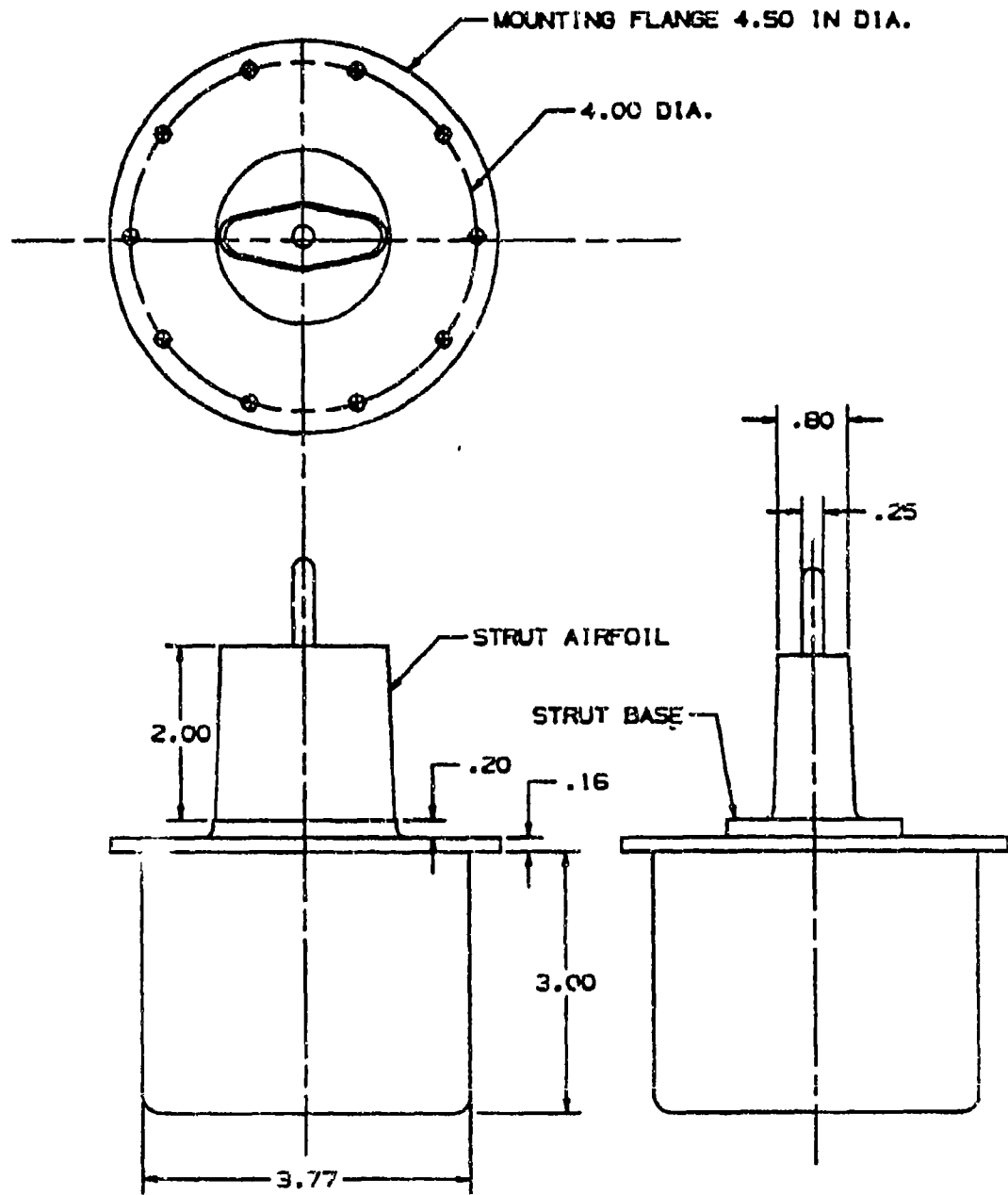
FIGURE 1-2. VIBRATING PROBE ICE DETECTOR-FUSELAGE MOUNT
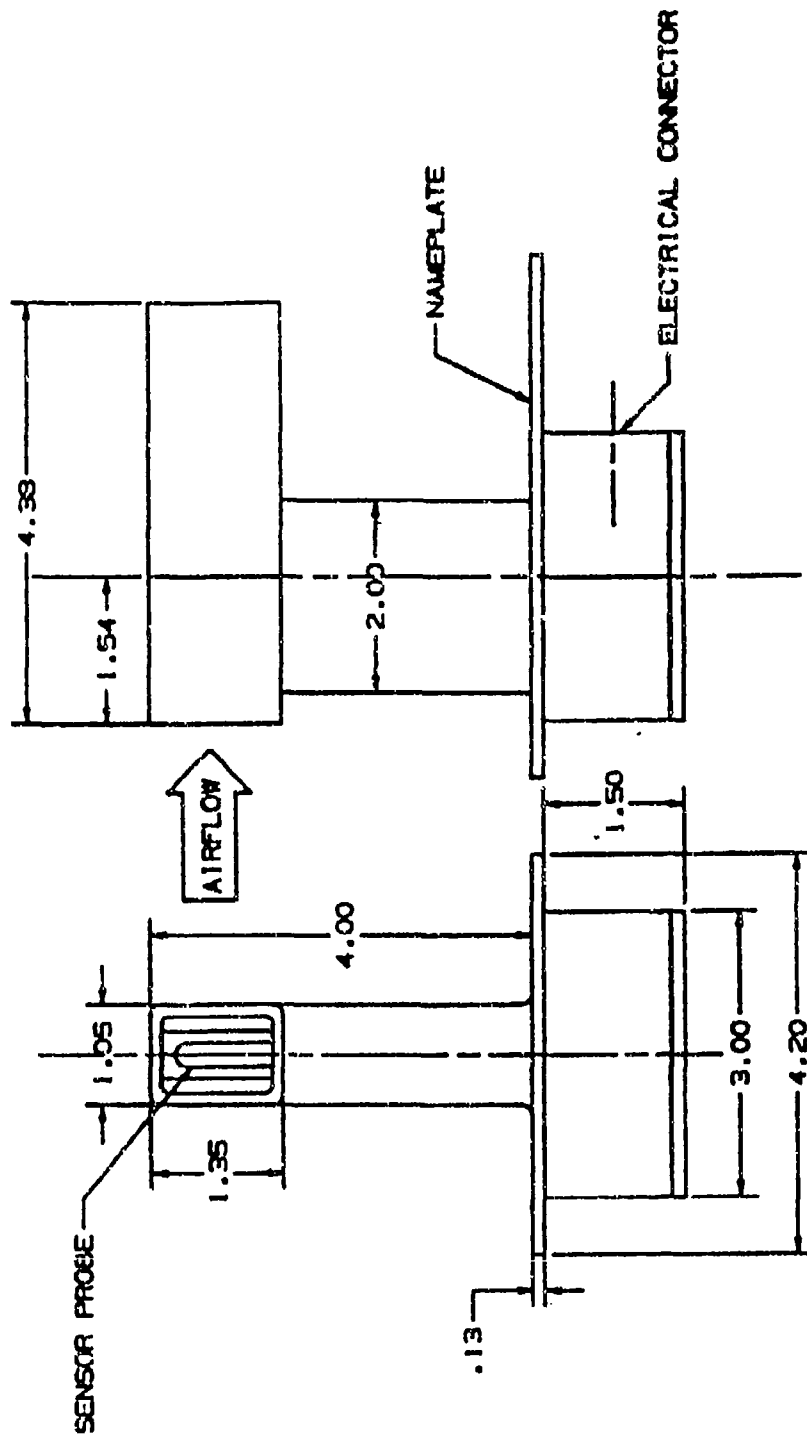
FIGURE 1-3. VIBRATING PROBE ICE DETECTOR-ASPIRATED
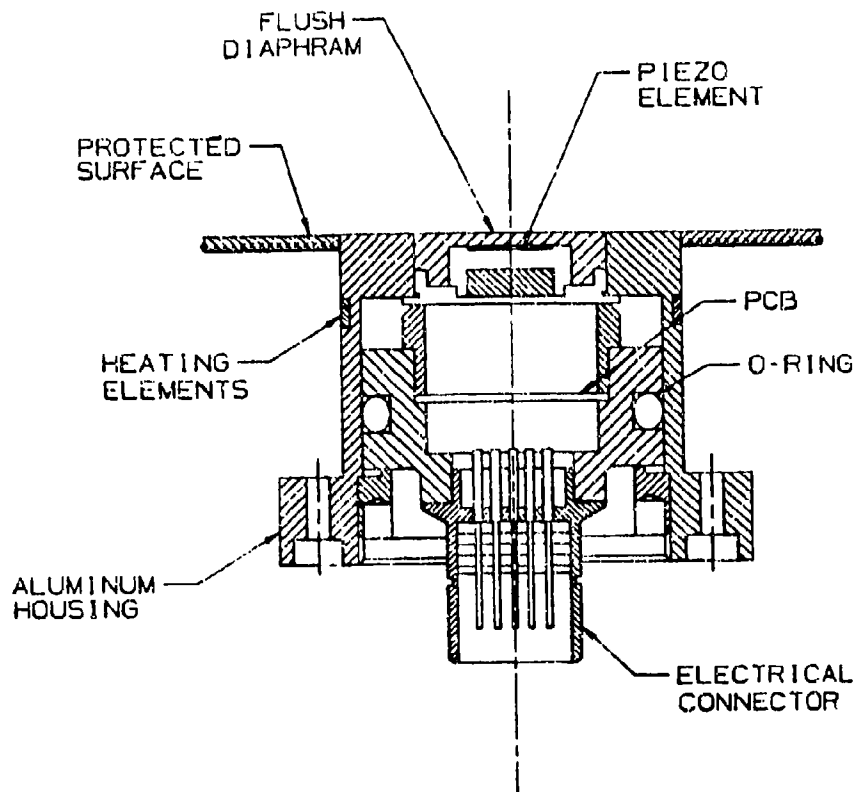
FIGURE 1-4. VIBRATING DIAPHRAGM ICE DETECTOR
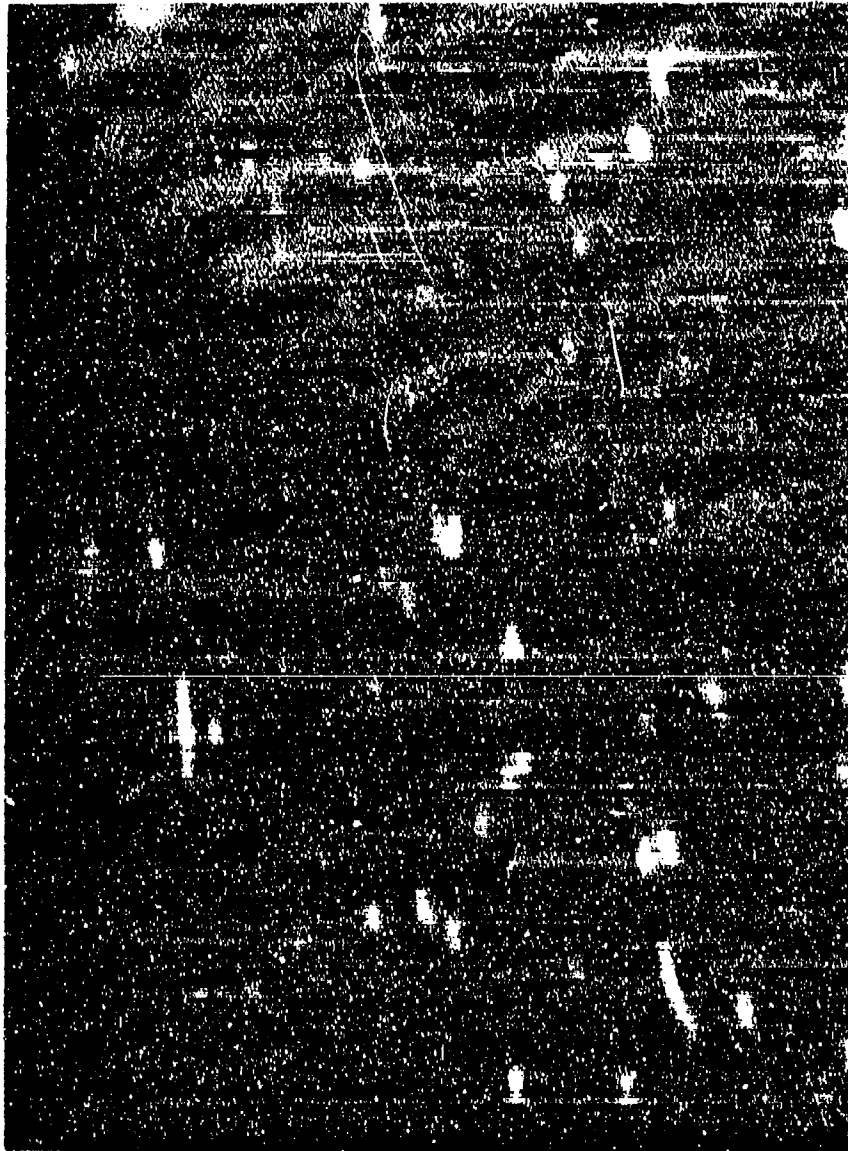
FIGURE 1-5 PRESSURE ARRAY PROBE
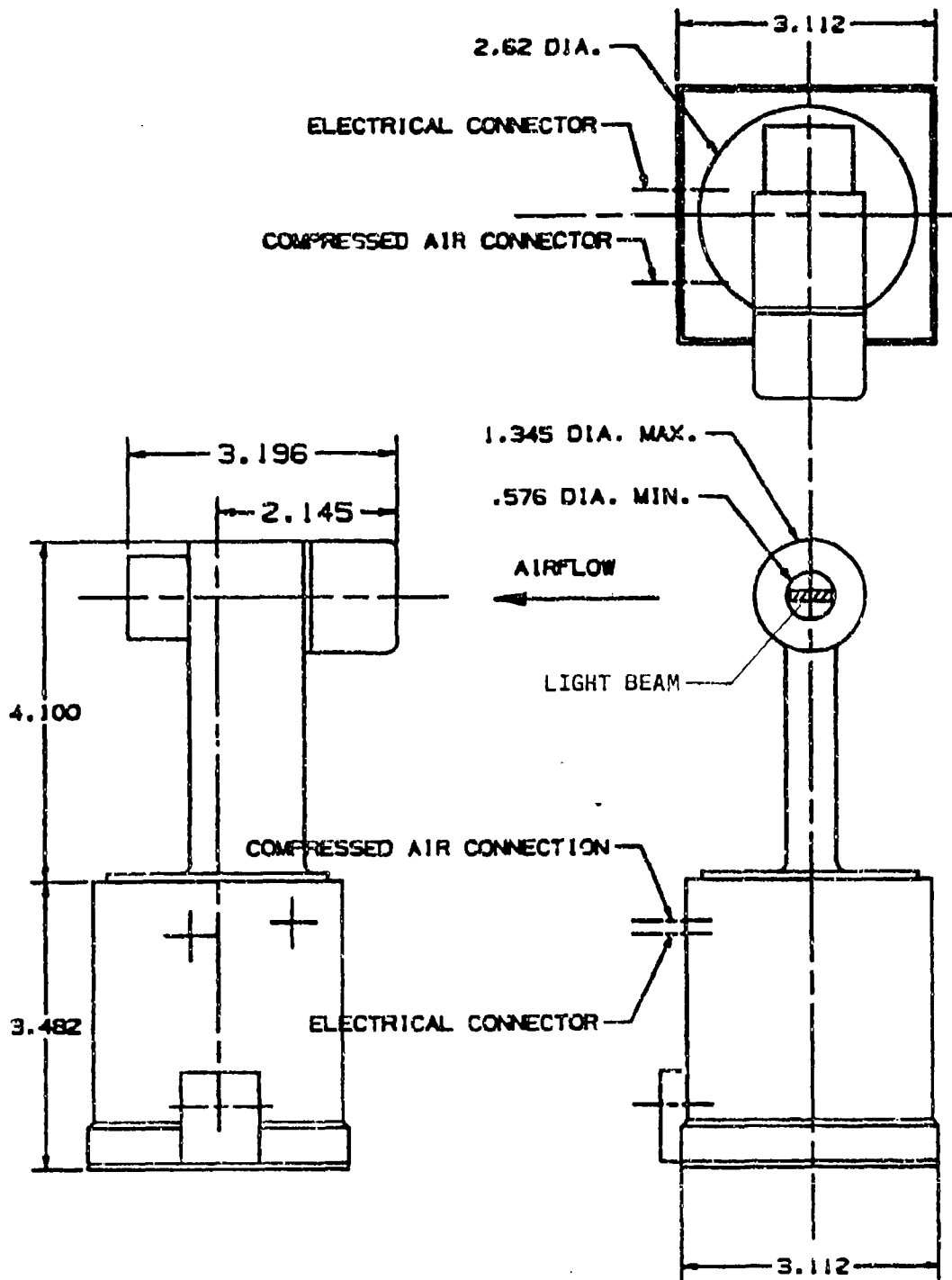
FIGURE 1-6 LIGHT BEAM INTERRUPTION ICE DETECTOR

$$D = CT/2$$
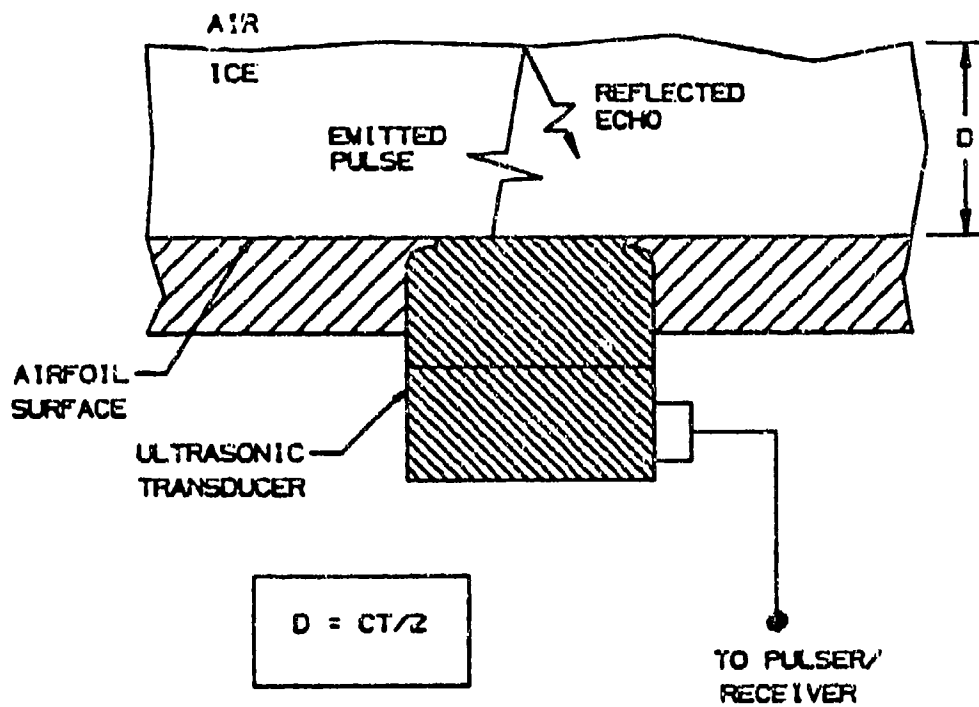
FIGURE 1-7 **PULSE-ECHO ICE DETECTOR**
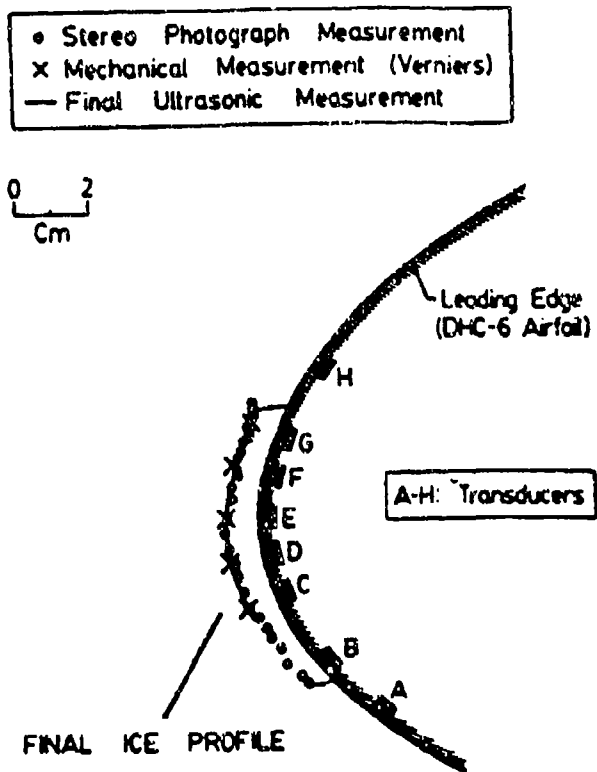
FIGURE 1-8   PULSE-ECHO TRANSDUCER ARRAY ON WING LEADING EDGE (REFERENCE 1-9)

TRANSDUCER
(PROTECTED
BY A
POLYURATHANE
OR
POLYETHELENE
EROSION
SHIELD)
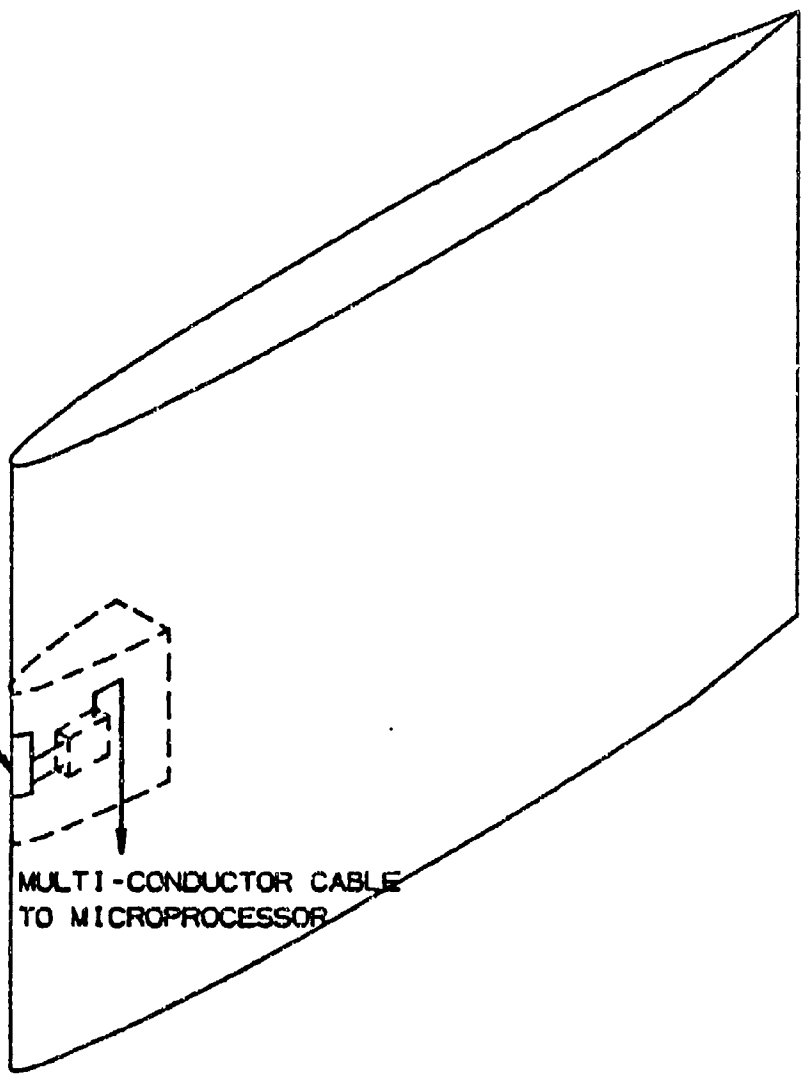
MULTI-CONDUCTOR CABLE
TO MICROPROCESSOR

FIGURE 1-9   MICROWAVE ICE DETECTOR

II 1-18

CHAPTER II
SECTION 2.0
ICING MEASUREMENT INSTRUMENTS

CHAPTER II
CONTENTS
SECTION 2.0 ICING MEASUREMENT INSTRUMENTS

CONTENTS (CONTINUED)

LIST OF FIGURES

SYMBOLS AND ABBREVIATIONS

Symbol	Description
A.C.	Alternating current
ASSP	Axial Scattering Spectrometer Probe
c	speed of sound in ice, m/s
C	temperature in degrees Celsius
CSIRO	Commonwealth Scientific and Industrial Research Organization (of Australia)
cm	centimeter
D	ice thickness, millimeters
D.C.	Direct Current
DOF	Depth of Field
E	Young's modulus
F	temperature in degrees Fahrenheit
FSSP	Forward Scattering Spectrometer Probe
g	gram
hr	hour
Hz,f	frequency
IRU	Integrated Rate Unit
J-W	Johnson - Williams
km	kilometer
K',K"	Scaling constants
LWC	Liquid Water Content, g/m^3
m	meter
mm	millimeter
n	number of program cycles per 67 Hz change
MVD	Median Volumetric Diameter
OAP	Optical Array Probe
OAT	Outside Air Temperature
q	Dynamic Pressure
RSS	Root Sum Square
s	second
μ	micron
V	Freestream Airspeed

GLOSSARY

liquid water content (LWC) - The total mass of water contained in all the liquid cloud droplets within a unit volume of cloud. Units of LWC are usually grams of water per cubic meter of air (g/m^3).

median effective diameter (MED) - The droplet diameter which divides the total water volume present in the droplet distribution in half; i.e., half the water volume will be in larger drops and half the volume in smaller drops. The value is obtained by computation from an assumed drop size distribution.

median volumetric diameter (MVD) - The droplet diameter which divides the total water volume present in the droplet distribution in half; i.e., half the water volume will be in larger drops and half the volume in smaller drops. The value is obtained by computation from actual drop size measurements.

micron (μm) - One milli ...h of a meter.

2.0 ICING MEASUREMENT INSTRUMENTS

II.2.1 INTRODUCTION

The measurement of the icing cloud for Liquid Water Content (LWC) and cloud droplet sizes is necessary (Federal Aviation Regulation 25.1419) to document the icing conditions existing during tests conducted in the laboratory, in icing tunnel spray rigs, airborne tankers, or in natural icing conditions. The measure of cloud droplet sizes and distribution provides a means to determine droplet Median Volumetric Diameter (MVD), as well as LWC. During normal aircraft operations, the measure of LWC can be employed to determine icing condition severity or intensity.

Icing measurement instruments are discussed in the following paragraphs including those used to measure LWC in flight or in the laboratory and cloud droplet measuring instruments intended for engineering test use.

II.2.2 ICING MEASUREMENT INSTRUMENTS AVAILABLE

2.2.1 Liquid Water Content Instruments

Instruments used to measure icing cloud liquid water content (LWC) are available in several types. Some of these may be used for normal aircraft operations or for engineering test purposes. Others a e primarily suited for laboratory use such as in the icing wind tunnel, ground and airborne spray tanker testing, research and development, and certification flight testing in natural icing conditions. The most commonly employed LWC instruments are the hot wire probe, the vibrating probe, the light interruption sensor, the blade, and rotating multi-cylinders. Each of these type instruments is discussed in the following paragraphs. Calibration techniques and problems are discussed in Section II.2.3, data correction in Section II.2.4, and precision and accuracy in Section II.2.5.

2.2.1.1 Hot Wire LWC Instruments

A variety of instruments have been devised to measure cloud LWC, but since the mid 1950's heated wire probes have been the most widely used. The two most common types of hot wire LWC instruments are known as the J-W and the CSIRO type meters.

The Johnson-Williams (J-W) type LWC meter (figure 2-1) is based on the principle that droplets hitting and evaporating from a heated wire, cool the wire. This wire, whose resistance is a function of temperature, is mounted perpendicular to the air flow. A second wire, mounted parallel to the air flow and not subjected to droplet impingement, is used for temperature compensation with altitude.

The electrical circuit that measures the resistance change is similar to a Wheatstone bridge circuit where the sensor wire represents one leg of the bridge while the compensation wire is the other leg. The circuit becomes unbalanced when one leg's resistance is different from the other's.

Thus, the effect of ambient temperature cooling the wires will not cause an imbalance because both wires cool at the same rate. (While droplets strike the sensing wire and cool it, the compensating wire is not effected).

Typical performance range of the J-W LWC meter is up to 3 g/m^3 in the low setting and 0 to 6 g/m^3 in the high setting. The true airspeed may vary from approximately 80 to 200 miles per hour (129 to 322 km/hr) (reference 2-1).

The CSIRO is another commonly used hot wire LWC meter (figure 2-2). The sensing element of this instrument is a coil of copper wire approximately 1.67 inches long by 0.71 inches diameter (4.25 cm long by 1.8 mm in diameter) (sizes vary for different models). The quantity of electric current used to maintain the coil at a constant temperature is measured. Droplets which strike the wire coil cause cooling; the increase in power needed to offset the cooling due to evaporation is calibrated in terms of liquid water content.

To eliminate axial cooling, two slave coils are connected at opposite ends of the sensing coil. The slave coils are maintained at the same temperature as the sensing coil to keep heat from being conducted out of the sensing coil ends. The effect of dry air cooling the sensing wire must also be considered. The manufacturer recommends making measurements, prior to cloud measurements, to determine the cooling effect of the dry air. The difference between readings in the cloud and in dry air is used to determine the liquid water content.

Typical performance range of the CSIRO LWC meter is 0 to 3 g/m^3. True airspeed ranges from approximately 140 to 230 miles per hour (225 to 370 km/hr) (reference 2-2).

2.2.1.2 Vibrating Probe Instrument

The vibrating probe operates on the principle of an axially vibrating probe whose natural frequency is known, as was discussed in Section 1.3.3. A tubular probe, manufactured from a magnetostrictive alloy, is mounted in an aspirated housing at its midpoint, exposing half of the tube to the airstream (figure 2-3). Since the probe is made of magnetostrictive materials, it will expand and relax under the influence of a varying magnetic field. A permanent magnet provides a constant magnetic bias through the tube. The field is modulated by a drive coil surrounding the lower half of the tube. A magnetostrictive oscillator circuit is completed with a feedback coil and operational amplifier. The axial movement of the tube, resulting from the activation of the drive coil, induces a current in the feedback coil. The feedback coil drives the operational amplifier which provides a signal to the drive coil. The circuit's rate of oscillation is determined by the natural resonant frequency of the sensor tube, which is tuned to 40,000 Hz.

In icing conditions, when ice accretes on the sensing probe, the resonant frequency of the probe decreases, due to the added mass of the ice, at a rate of 67 Hz for each 0.010 inch thickness of ice. The LWC can then be calculated from the frequency rate of change (reference 2-3):

$$LWC = \frac{K' \frac{df}{dt}}{V} \qquad (2\text{-}1)$$

Where df/dt = rate of change in frequency, V = airflow velocity across the probe, K' = scaling constant.

The frequency is measured once each program cycle by a microcomputer (approximately 5 times per second). At the beginning of each program cycle, the computer is gated on to count the cycle periods. At the end of the cycle, the computer compares the number of periods counted with the number of periods corresponding to a 67 Hz -frequency change. The differential expression df/dt can then be reduced to 67/0.2n where n is the number of program cycles required to observe a 67 Hz change. The LWC can be calculated as an inverse function of n.

$$LWC = \frac{K'' \, V}{n} \qquad (2\text{-}2)$$

Where n = number of program cycles per 67 Hz change, v = velocity across the probe, K'' = scaling constant.

This process continues until the total ice accumulation on the probe exceeds 0.060 inches or no further accumulation is observed. Internal probe heaters are then activated, the accreted ice is melted, then the process is restarted.

LWC calculations occur after each incremental 67 Hz frequency change. Each calculated value is stored in memory and averaged with several previous readings. This average is then made available with several previous readings. Following aircraft emergence from an icing condition, the LWC signal will decay to 0 within 60 seconds.

Typical performance range for this instrument is 0.05 to 3 g/m^3 and 10 to 50 microns MVD. True airspeed ranges from approximately 20 to 230 miles per hour (30 to 370 km/hr) (reference 2-3).

2.2.1.3 Light Beam Interruption Instrument

The light beam ice accretion and LWC instrument operates on the principle of ice accumulating on a probe which occludes a light beam. During operation, the detector head draws in ambient air by means of an ejector tube (figure 2-4). During icing conditions, ice accretes on the sensor probe at a rate proportional to the liquid water content (LWC) of the ambient air. The ice accreted on the probe occludes an infrared light beam crossing the central area of the probe at an oblique angle. The degree of occlusion is determined by the amount of ice on the probe. When light occlusion reaches a predetermined level, representing maximum permitted ice thickness, a heating cycle is initiated to remove ice from the low thermal inertia probe. When the accumulated ice melts, the original light path is restored then the heating cycle is terminated to permit ice

accretion to resume. The time taken to accrete ice between two predefined levels is used as a measure of the icing rate from which LWC can be calculated (reference 2-4). The system contains a microprocessor to process the information received from the photo detector via an analog-to-digital converter.

Typical performance range for this instrument is 0 to 2 g/m^3 LWC and 10-40 microns MVD from 0 to 15,000 feet (0 to 4572 meters) altitude. True airspeed ranges from 0 to 230 miles per hour (0 to 370 km/hr). The unit will operate at higher airspeeds provided the temperature of the aspirating compressed air is increased (reference 2-4).

2.2.1.4 Blade

The blade LWC measuring device (figure 2-5) is an old technique used primarily in the icing wind tunnel. This device is simply an object approximately 0.12 inches thick by 0.75 inches wide and 10 inches long (0.3 cm thick by 1.9 cm wide by 25 cm long, although other sizes can be used) that is made from aluminum bar stock. In operation, the blade is run out from behind a shielded position into the airstream for a nominal 30 seconds to expose the thin edge to the icing cloud. The thickness of accreted ice on the blade leading edge is then measured with a micrometer followed by calculation of LWC by accounting for the collection efficiency (reference 2-5).

2.2.1.5 Rotating Multi-Cylinders

The rotating multi-cylinder, one of the oldest ice accretion and LWC instruments in use today (figure 2-6), is another manually operated instrument. A typical multi-cylinder consists of five cylinders with varied diameters ranging from 0.5 inch to 4.5 inches, which are stacked (one atop the other with transition pieces) to make the cylinder array. In operation, the array of cylinders is run out from a shielded position for an appropriate period of time into the icing cloud then withdrawn. The LWC is determined from the weight of ice accreted on each cylinder according to the procedure of reference 2-6. After the LWC is determined, one of several standard drop size distribution is assumed, based on the relative amounts of ice collected on each of the various-sized cylinders. A MED (Median Effective Diameter) is then computed.

2.2.2 Droplet Sizing Instruments

Icing cloud droplet sizing instruments are needed for the accurate determination of droplet size distributions in icing research, ice protection system development, and in certification testing (reference 2-5). In earlier times (1940's and 1950's) manually operated instruments such as the oil slide and rotating multi-cylinders were used to measure or infer dropsize distributions. At present, a number of modern automated instruments are in wide use to measure droplet size.

2.2.2.1 Optical Array Probe (OAP)

This probe is another single particle size spectrometer sensitive to droplets intermediate in size between typical cloud droplets (1-50 microns) and precipitation particles (larger than about 0.3 mm). Nominal size ranges are usually about 20 to 200 microns or 30 to 300 microns.

The OAP makes use of a row of 16 or more miniature photodiodes to detect the shadows of these larger droplets as they pass through a small segment of a narrow laser beam. The number of photodiodes occluded by each shadow is a measure of the shadow width and therefore of the droplet diameter. As with the FSSP, the droplet "counts" are stored in 15 size "bins" which together span the range of diameters detectable by the probe. Digital readout is available at selectable rates up to about 10 per second and again, LWC or other quantities may be computed from the recorded size distributions.

Most cloud droplets are smaller than about 50 microns, so the OAP is useful mostly for small, drizzle-sized droplets. Otherwise not much is seen except possibly in the first one or two size bins. For this reason the FSSP is generally used as the principal (if not the only) dropsize probe on board.

2.2.2.2 Axial Scattering Spectrometer Probe (ASSP)

The Axial Scattering Spectrometer Probe (ASSP) was a predecessor of the Forward Scattering Spectrometer Probe (FSSP - see next section) and is no longer used.

2.2.2.3 Forward Scattering Spectrometer Probe (FSSP)

Beginning in 1973, a new type of automated, electro-optical, cloud particle size spectrometer became commercially available from Particle Measuring Systems (PMS), Inc., of Boulder, Colorado. The original model was called the Axially Scattering Spectrometer Probe (ASSP). This was soon followed by an alternate model called the Forward Scattering Spectrometer Probe, which is more commonly in use today. Both models are based on the principle of forward scattering of light from individual cloud droplets passing through a narrow, illuminating beam. The intensity of the light scattered by a droplet is proportional to the square of the droplet diameter, i.e., to the droplet size. An optical detector senses the flash of light from each droplet and generates a voltage pulse proportional to the droplet size. A 15-channel pulse height analyzer then sorts these pulses into one of 15 corresponding size intervals. These 15 size intervals typically span a total size range of about 3 to 45 microns in droplet diameter. The "counts" in the intervals are stored for periodic output to a digital recording medium. From the recorded size distributions one can easily compute the droplet number density (droplets per cubic centimeter of cloud along the flight path), the LWC, and other dropsize dependent quantities.

The FSSP and other PMS probes have become standard equipment for cloud physics research in the field. The principal advantages are good resolution of droplet sizes, high data rates (continuous sampling during the flight with accumulated droplet size spectra recorded every second, or faster), and direct computer compatibility.

II.2.3 CALIBRATION TECHNIQUES AND PROBLEMS

The vibrating probes, interrupted light beams, icing blades, and rotating cylinders are all normally calibrated in an icing wind tunnel where the airspeed, LWC, temperature, and median droplet size can be varied in a controlled manner. Comparisons of tunnel LWC with measured ice accretions on the probes provide calibrations within the accuracy of the tunnel calibration itself.

2.3.1 LWC Instruments

2.3.1.1 Hot Wire LWC Instruments (J-W and CSIRO)

The J-W LWC instrument (figure 2-1) is a heated wire device whose performance is approximated using a heat balance equation. The amount of heat supplied to the wire is balanced by convection, conduction, and radiation losses to the ambient air plus the heat required to evaporate impinging water droplets. The heat balance (reference 2-2), assuming negligible radiative or conductive losses, is described by

$$ P = ldvw[L + c(T_w \quad T_a)] + \pi lk(T_w - T_a) Nu \qquad (2-3) $$

where

p = total power required to heat the sensing wire

l = length of wire

d = diameter of wire

v = cloud velocity relative to wire

w = LWC

L = latent heat of water

c = specific heat of water

T_w = wire temperature

T_a = air temperature

k = thermal conductivity of air

Nu = Nusselt number for heat transfer from water to air (Nu is defined as the ratio of the film heat transfer coefficient to the thermal conductivity times the sensor diameter).

The sensing wire is composed of a material with a positive temperature coefficient of resistance such that cooling will cause its resistance to decrease. From equation (2-3) and the known temperature resistance characteristics of the wire, the LWC can be calculated after measuring the power, airspeed, altitude, and air temperature. An alternating current Wheatstone-bridge, with the sensor resistance as one leg, is used to measure resistance changes. To compensate for the dry air heat losses another leg of the bridge is formed by a second

"compensation" wire of the same composition as the sensor but exposed lengthwise to the airstream to shield it from passing water droplets.

The J-W instrument underestimates the mass of water droplets greater than 30 μm, possibly as a result of breakup on the sensing wire before evaporation. In addition, the J-W does not appear to respond well to LWC less than 0.05 g/m^3 (reference 2-2). Sources of uncertainty in the J-W measurements stem from observed out-of-cloud baseline drifting, inadequate compensation by the compensating wire, and improper grounding techniques in the sensing head and associated electronics. In addition, questionable construction techniques affect the measurement accuracy (reference 2-2).

The baseline out-of-cloud values measured by the J-W have been observed to drift even when environmental conditions remain constant. This drifting is characteristic of A.C. bridge measuring circuitry when a well-regulated voltage reference is not used. The baseline will also shift with airspeed, temperature, and altitude changes as the compensation wire is only partially successful in compensating for these effects. The magnitude of error introduced by this drift is approximately 10% on the average, although its unpredictability makes evaluation difficult, especially since the amount of drift is probe dependent.

The usual method of J-W calibration consists of replacing the sensing head with a dummy head which, according to the manufacturer, provides the same resistance load as the sensing wire under a specified LWC at the minimum design airspeed of the instrument. This dummy head calibration check provides valuable information concerning the status of the electronics, but this is not sufficient in itself. The major problem presented by this type calibration is the assumption that the resistance of the calibration resistors remains constant during power application. The typical power consumption of these resistors in on the order of 15-20 watts, with accompanying rises in temperature. The full scale values during calibration can drift 20-30%. A notable exception to this occurred during calibrations in an icing wind tunnel where good ventilation and a cool environment minimized temperature rises in the dummy head. The sensor head also needs to be checked periodically since the head, exposed to the elements, could become damaged. At this time, the only reliable method for complete calibration of the J-W is in an icing wind tunnel with well calibrated characteristics.

A study by Strapp and Schemenauer (reference 2-1) showed that 73% of the probes tested in the Ottawa wind tunnel agreed to within 20% of the tunnel values when using the calibration obtained with dummy heads.

Their study also showed several probes which demonstrated a marked dependence on tunnel airspeed and temperature as well. An additional problem with several of the probes was a buildup of ice on the compensation wire fastening post which caused a large fluctuation of indicated LWC. This condition prevailed at a temperature of -15°C and 172 miles per hour (77 m/s) airspeed.

In summary, the accuracy of the J-W measurements is a function of the particular probe used. Without completely testing a sensor in a well calibrated icing wind tunnel and if the only calibration

is that of the manufacturer's dummy head, the LWC values may only be accurate to 20%. However, if the sensing head is thoroughly evaluated and calibrated, the overall accuracy should be better than 20% (reference 2-1).

The CSIRO probe consists of a heated wire element constructed from a hollow metal cylinder closely wound with a single layer of insulated copper wire (figure 2-2). The resistance of the element is used in a feedback loop to maintain the temperature of the sensor constant. Axial heat losses are minimized in this probe through the use of slave coils on either side of the main sensing coil. With the current flowing through these coils duplicating that from the main coil, the axial temperature gradient is significantly reduced. both the J-W and the CSIRO probe use the same heat balance equation (2-3) for deriving the LWC; however, as equation (2-3) assumes a knowledge of the wire temperature, the CSIRO response is more accurately predicted since it is designed as a constant temperature probe whereas the J-W probe is not. The J-W probe uses a separate wire to compensate for environmental changes; the CSIRO probe uses calculated value, improved by calibration, to measure the power consumed in dry air.

King, et al (reference 2-10) conducted an extensive evaluation of the CSIRO probe which showed that the accuracy of the measured LWC is dependent on the accurate prediction of the heat losses in non-cloudy air. The dry air term (reference 2-2) is given by

$$P_{dry} = \pi lk(T_w - T_a) \ A \ Re^x \tag{2-4}$$

where the Nusselt number has been expressed as a function Re^x of the Reynold's number, defined as

$$Re = \frac{\rho \ VD}{\mu} \tag{2-5}$$

and

μ = is the viscosity of air

T_w = wire temperature

T_a = air temperature

D = sensor diameter

l = sensor length

V = air velocity

A = coefficient determined in either a wind tunnel or on the aircraft

x = coefficient determined in either a wind tunnel or on the aircraft

k = thermal conductivity of air

ρ = is the density of air

The diameter of the sensing wire presents a blockage to the flow, thus the probe's collection efficiency should be examined. As the probe will not collect any droplets smaller than 2 μm it will miss 20% of the 10 μm droplets; however, the contribution to the LWC from droplets smaller than 10 μm is minimal for most cloud types.

The CSIRO LWC probe is calibrated in a wind tunnel. The procedure involves placing the instrument in a dry air wind tunnel to simulate varying airspeed (aircraft velocities are used). Plots of voltage and power versus velocity establish the value of the calibration constants. A theoretical expression relating LWC to these constants is used to derive the final meter calibration (equation 2-4). The accuracy of this method has been established in independent wet wind tunnel tests (reference 2-10). In summary, the CSIRO probe accuracy is generally better that 5% at 1.0 g/m^3, based upon analysis of the probe's operating characteristics. Overall, the CSIRO probe is superior to that of the J-W probe in many key aspects except for the more fragile nature of the CSIRO sensing element which tends to break more easily.

2.3.1.2 Vibrating Probe Instrument

A vibrating probe ice detector and LWC instrument is designed to extend through the airflow boundary layer wherein a strut or mast supports the sensing element in this position. In general, it has been found that the best areas for mounting the probe consider the following:

  a.   Locate out of any boundary layer.
  b.   Locate away from areas of stagnated flow.
  c.   Locate away from areas of flow separation.
  d.   Locate away from areas where droplet centrification might occur.

The normal calibration technique for the vibrating probe is an experimental test in an icing wind tunnel of known calibration where the airspeed, LWC, and median droplet size can be varied in a controlled manner. Comparison of tunnel LWC to measured ice on the probe can provide calibration curves within the limits of accuracy of the particular icing tunnel employed. The probe manufacturer usually will provide the user with calibration data for the particular instrument.

2.3.1.3 Light Beam Interruption Instrument

The light beam interruption type of LWC instrument operates on the principle discussed in Section 2.2.1.3. In this system, dry bleed air from the engine is passed through the detector housing into the throat or aspirator of the tubular probe housing. The bleed air is then discharged through an annular ring at the front of the aspirator section. This bleed air entrains a flow of ambient air containing supercooled droplets. Ice is formed on a probe within the aspirator when water droplets impinge on the probe. When ice buildup measures 0.005 inches, it obstructs the light path of a photo-electric cell and triggers the start of a timing circuit. This timing is stopped when the ice reaches a thickness of 0.01 inches to permit the probe to be automatically deiced. The time elapsed

during icing is then converted into a measure of LWC. The rate of ice accretion (cycle time) is interpreted as icing severity (reference 2-4).

The normal calibration technique for the light beam interruption type instrument is experimental test in an icing wind tunnel where the airspeed, LWC, and median droplet size can be varied in a controlled manner. The icing rate is primarily a function of droplet collection efficiency on the probe. Comparison of tunnel LWC and icing cycle time for the light interruption instrument can provide calibration curves within the limits of accuracy of the particular icing tunnel employed.

2.3.1.4 Blade

The manually operated and deiced blade is an old device used to measure liquid water content. The unit is normally mounted behind a shield and run out into the airstream for a short period of time (30 seconds) to accrete ice. It is then withdrawn to permit the thickness of accreted ice, on the thin leading edge, to be measured with a micrometer. The LWC is then calculated after accounting for the collection efficiency. The blade design and the procedure used to determine LWC may be found in reference 2-11.

The normal calibration technique for the blade employs an icing wind tunnel where the airspeed, LWC, and median droplet size can be varied in a controlled manner. Comparison of tunnel LWC to measured ice on the blade can provide calibration curves within the limits of accuracy of the particular icing tunnel employed.

2.3.1.5 Rotating Multi-Cylinders

The rotating multi-cylinder is another manually operated instrument. The cylinder array is normally stowed in a shielded position and run out into the airstream for a short period of time to accrete ice and then withdrawn. The LWC and droplet size is determined by measuring the mass of ice accreted on each of the five cylinders according to references 2-12 and 2-13.

The normal calibration technique for the rotating multi-cylinder array is experimental test in an icing wind tunnel where the airspeed, LWC, and median droplet size can be varied in a controlled manner. Comparison of tunnel LWC and measured ice on the cylinder array can be used to obtain calibration curves within the limits of accuracy of the particular icing tunnel employed.

2.3.2 Droplet Sizing Instruments

2.3.2.1 Optical Array Probe (OAP)

Two methods of calibration are commonly used for the Optical Array Probe. The first and least accurate is to check the overall magnification of the optics. A clear plastic ruler or a wire of a known diameter is placed in the center of the laser beam. The image of the ruler or wire is formed on the diode array and is then measured with a ruler. The ratio of image size to true size is the

magnification. If the magnification is incorrect, the zoom lens can be adjusted to bring it into closer agreement with the manufacturer's specification (reference 2-7). A second method of calibration uses glass beads or particles of known diameter. The instrument is mounted vertically so that the probe arms are on top. The particles are then poured through the laser beam. The data system will show a narrow distribution of particle sizes centered about the bin which contains the particle size used. If the distribution is centered about a smaller bin, the magnification should be increased, or decreased if it is centered about a larger bin. The process of pouring beads and adjusting the magnification should continue until the distribution is centered about the correct bin (reference 2-7).

Mapping the OAP should involve a detailed mapping of the sample area where the purpose is to determine the instrument response as a function of particle speed and trajectory. To accomplish this, a number of factors must be strictly controlled. Particle size must match the OAP range. Trajectory must be able to direct the particle through any part of the laser beam with 2 degrees of freedom. Particle speed should be in the 225 miles per hour (100 m/s) range. The number of particles per unit time should be within an accuracy of 1 percent (reference 2-7).

Various kinds of particles can be used to make the mapping. These are discussed in the following:

(1) Particles produced by a water droplet generator are desirable because they have the same index of refraction as cloud droplets.

(2) Glass particles are widely used. If they are blown through a nozzle under high pressure, high velocities are obtainable. For an instrument like the OAP, the difference between the index of refraction of glass versus water is unimportant.

(3) Latex spheres pumped through a closed loop flow cell offer similar problems as glass beads. Although the number density can be somewhat controlled, their trajectory through the laser beam is virtually random.

(4) Chrome disks etched on a glass substrate are one of the newest methods of sample area mapping. For the OAP this device, called a reticle, offers a scattering signature similar to a water droplet. One of the major advantages of this method is the absolute control over particle size and number. The greatest drawback is the mechanical problem of spinning the reticle so the disks pass through the laser beam at high velocities.

See reference 2-7 for detailed description of OAP calibration procedures.

2.3.2.2 Forward Scattering Spectrometer Probe (FSSP)

Calibration of the FSSP is usually an indirect process wherein a calibration curve based on Mie theory is plotted predicting FSSP response to glass beads (reference 2-9). Glass beads of known sizes are then blown through the instrument establishing the relationship between the theoretical and experimental calibration. The experimental curve is much smoother than the theoretical one. Next, the FSSP response to water droplets is theoretically predicted, by knowing the relationship

between the experimental and theoretical curves for glass, the theoretical curve for water can be modified to give the predicted water droplet calibration.

The FSSP manufacturer's manual provides plots showing how the FSSP should respond to various size glass beads. This allows the user to check the instrument calibration from time to time by blowing glass beads through the laser beam and comparing the FSSP's present response with the factory calibration. The instrument manufacturer will provide a nozzle for these tests which fits in the flow straightening tube (figure 2-8) and is used to direct glass beads through the beam. A vacuum source and glass beads must be provided by the user. The data acquisition system records the bead size distribution as they accelerate through the laser beam. The peak of this distribution should fall in the same size bin as indicated by the manufacturer's calibration plot. The glass bead method is inconvenient for use in the field, however, because in addition to the special equipment required, the FSSP must be dismounted from the aircraft and brought indoors.

A simpler method may be used for routine calibration checks in the field (reference 2-21). Fine nylon strands stretched across a rigid frame serve as a repeatable simulation of fixed diameter droplets. The fibers produce an optical signal of fixed, repeatable amplitude each time the fiber is passed through the laser beam in the FSSP. Correspondingly, counts will build up in one of the 15 size bins. This same bin should respond each time the check is performed. Counts accumulating in a different bin would indicate a change in calibration by that amount. These checks can be performed easily and quickly with the FSSP in place on the aircraft.

II.2.4 DATA CORRECTION

It is assumed here that the probes or sensors are properly installed on the aircraft or in the icing tunnel, are operated correctly, and are in calibration during use. The only data correction concerns are then limited to:

a)   avoidable systematic errors (such as baseline drift with the J-W LWC meter) that may routinely occur during flight.

b)   limited measuring ranges, such as dropsize range for the hotwire probes and for the droplet size spectrometers.

c)   probe saturation, such as excessive droplet rate for the optical particle counters or excessive cycling rate for the vibrating probe sensors,

d)   ice accumulation on the LWC probes or optical particle counters v ere it interferes with the airflow or the optical path.

Regarding this last item, it must be realized that many of these non-ice accreting probes are used as much, if not more, in warm cloud research than in cold clouds. Although the probes are usually provided vith imt dded heaters where practicable, there may be some cold cloud situations where ice will t ild up on parts of the sensors that cannot be adequately warmed.

The above mentioned problems often result in important but subtle effects on the data. It may take an alert observer to note that conditions are right for problems to occur, and an experienced

eye to notice the effects in the data. Experience has shown that is it very helpful in this regard to have more than one sensor on board that can measure the same, or a related variable. For example, a decrease in droplet count that is not corroborated by the J-W LWC can be the tipoff to a problem with the droplet counter.

In general it is a good idea to have the research cloud physics instrumentation supervised and operated by a researcher or technician who is experienced in calibrating and servicing them as well as using them in the field.

2.4.1 LWC Instruments

2.4.1.1 Hot Wire LWC Instruments (J-W and CSIRO)

The main operational problem, especially with the J-W meter, is baseline drift during flight. The recorded output from the meter is usually a 0-3 volt signal proportional to the momentarily indicated LWC. In clear air the output voltage, or baseline signal, should be zero. Often the baseline voltage will be slightly positive or negative after a long transit through clouds, especially if the outside air temperature has changed (due to a change in flight level, for example) during the transit. This baseline drift can often increase (or decrease) the apparent LWC by as much as a few tenths of a gram per cubic meter by the end of the transit.

The correction for this effect may be performed manually from the chart recordings, or by computer if the data were recorded digitally. The exact amount of drift may be unknown for any point along the transit, but the usual procedure is to assume a linear increase (or decrease) along the transit. Any cloud-free gaps along the way will help track this drift, because the baseline voltage then corresponds to zero LWC in these gaps. The final adjustment consists of simply subtracting (or adding) the interpolated amount of baseline drift from the indicated LWC at points of interest along the transit.

Another operational problem may be icing of the inlet rim of the sensing tube. Although the strut is usually heated, ice may sometimes build up on the rim anyway. Ice accumulations can disturb the airflow through the tube, resulting in a suspicious reduction in the indicated LWC. There is no way to correct for this error, but the operator should stay alert for the possibility so the data can be disregarded as erroneous.

2.4.1.2 Vibrating Probe Instrument

The main problem in using these devices as a research probe for LWC is that their duty cycle decreases markedly as the LWC (ice accretion) increases. The duty cycle refers to the time interval when the probe is in the sensing mode and is generating an output voltage proportional to the ice thickness. This duty cycle alternates with a heating cycle which melts off the ice after a preselected amount has accumulated. The heating cycle requires a fixed amount of time, usually about seven seconds or more, for the probe to heat up and then cool down to the ambient

temperature again. This constitutes a "dead time" during which the probe is not available for use. For LWC's less than a few tenths of a gram per cubic meter, the dead time is a small or tolerable fraction of the time in cloud. At greater amounts of L 'C the ice may accumulate so rapidly that the heating cycle is nearly always on. The result is, in effect, a saturation of the probe such that it becomes useless for any quantitative measure of LWC or ice thickness during periods of elevated LWC. Unfortunately, these are often the most interesting icing encounters too. The probe remains a good indicator of relative icing rate, or "severity", due to the high rate of heating cycles, but there is no way to correct for an accurate value of LWC.

2.4.1.3 Light Beam Interruption Instrument

At the time of this writing, no information was available on data correction techniques for the light beam interruption LWC instrument.

2.4.1.4 Blade

There are no data correction techniques for the blade instrument. The ice accreted on the blade over a short period of time is measured with a micrometer. The LWC is calculated by accounting for the collection efficiency by the procedure given in reference 2-11.

2.4.1.5 Rotating Multi-Cylinders

The main operational problem is to account for cloud gaps that occur while the cylinders are exposed to the air stream. Because the cylinders are deployed for an extended time (typically one minute or more) the accumulated ice can only be interpreted as an average accumulation over the exposure interval. The total duration of clear air spaces in or between the clouds must be subtracted from the exposure time (or distance) to obtain a true average LWC for the cloudy portion alone. In order to keep track of the clear spaces, one of the other continuously operating cloud sensors must be used along with a time synchronized, recorded output.

Errors due to water runoff or blowoff (incomplete freezing) when the total temperature is above about -5 C are probably uncorrectable. These and other errors associated with weighing the cylinders, inferring dropsize distributions, dealing with large indicated MED's, etc., are described in the original NACA literature (reference 2-12).

2.4.2 Droplet Sizing Instruments

2.4.2.1 Optical Array Probe (OAP)

These probes generally undercount the number of droplets in the first three size intervals. Therefore, one correction involves boosting the apparent counts by an experimentally determined factor for each interval. The owners manual supplies this information.

The only other correction that may be needed is to account for the presence of ice particles in snowy areas or in glaciated clouds. The OAP cannot distinguish between particle shapes, and it blindly indicates apparent size based solely on the width of the particle shadow. Therefore, users of the data must be kept aware of when the flight was in ice particles so that the latter are not mistaken for droplets on the OAP.

2.4.2.2 Forward Scattering Spectrometer Probe (FSSP)

The main operating errors with the FSSP arise from saturation in dense clouds, false size spectra from ice particles, ice accretion in the vicinity of the optics, and fogging of the optics.

Saturation occurs when droplets pass through the laser beam at a rate too fast for the electronics to respond to all of them. This can happen at high airspeeds and/or in clouds with high droplet concentrations (i.e., more than about 500 per cm^3). The result is an indicated number density that is too low due to a combination of "dead time" losses and coincidence errors. Except for the earliest models, the FSSP's generally monitor the particle rate, or "activity" and the dead time. These variables are recorded along with the droplet size data and may be used to routinely generate corrections to the number density. A typical correction scheme is the equation

$$N_c = N_1(1 - KA) \tag{2-6}$$

where:

Nc is the corrected number density

N_1 is the uncorrected number density

A is the "activity"

K is an experimentally determined constant, usually about 0.7

This correction and other aspects of the calibration are thoroughly described in references 2-17, 2-18, and 2-19.

Ice crystals will produce an apparent size distribution but it will not be a correct one. Most of the time a given cloud parcel is either all droplets or all ice particles. Ice particles generally number no more than a few per cubic centimeter, so only if the cloud is all ice particles will there be a noticeable signature in the FSSP results. Reflections off the facets of the ice particles send counts more or less evenly distributed into all 15 of the FSSP size intervals. The presence of an ice particle cloud is recognizable by this flat size spectrum rather than one that is peaked somewhere in the 5 to 20 micron range as is the case for droplet clouds. The relatively low concentration of ice particles also results in a number density no more than about 20 per cm^3 as indicated by the FSSP. There is no way to correct for the presence of ice particles, but these characteristics of the recorded size spectrum serve to tip off the analyst that ice particles, rather than cloud droplets, were present at the time.

Ice accretion near the optical ports can sometimes occur even though the FSSP is heated in that area. The result may be a blocked laser beam or distorted air flow.

Fogging of the optics can also happen temporarily when the aircraft descends into clouds or humid air after flying at high altitudes where the FSSP has been cold soaked at low temperatures.

Both the fogging and the ice accretion generally result in a marked reduction in droplet counts when visual observation or other instruments indicate that the droplet count should be much higher. There is no possible correction for these situations. The aircraft must descend to warmer temperatures long enough to melt the ice or to evaporate the moisture off the optics.

II.2.5 PRECISION AND ACCURACY

2.5.1 LWC Instruments

2.5.1.1 Hot Wire LWC Instruments (J-W and CSIRO)

The J-W instrument underestimates droplet mass for droplets greater than 30 μm (reference 2-1) possibly as a result of breakup on the sensing wire before evaporation. Also, the J-W does not appear to respond well to LWC less than 0.05 g/m^3. Sources of uncertainty in the J-W measurements stem from observed out-of-cloud baseline drifting, inadequate compensation by the compensation wire, and improper grounding techniques in the sensing head and associated electronics. In addition, questionable construction techniques affect the measurement accuracy.

The sensor and compensation wire resistances range from 40-60 milliohms. Attempting to pass information at this level is generally difficult and very sensitive to other spurious resistance changes in the system. The combination of bonding techniques with soft solder and silver solder produce resistance changes under differing conditions but are difficult to assess quantitatively. The connector contact resistances are especially susceptible to changes with time due to corrosion and oxidation. These resistance changes are major source of error since the J-W uses the connector shell as its electrical signal return through the aircraft frame. As contact resistance increases, the sensitivity of the instrument decreases which causes an error in the gain factor. As a result the LWC measurements under these conditions will appear lower than the actual values.

The baseline, out-of-cloud values measured by the J-W have been observed to drift even when environmental conditions remain constant. This drifting is characteristic of A.C. bridge circuitry when a well-regulated voltage reference is not used. The baseline will also shift with airspeed, temperature, and altitude changes as the compensation wire is only partially successful in compensating for these effects. The magnitude of error introduced by this drift is approximately 10%, on the average, although its unpredictability makes evaluation difficult particularly because the degree of drift is probe dependent.

In summary, the accuracy of the J-W probe measurements is a function of the particular probe used. Without completely testing a sensor in an icing wind tunnel, the only calibration is that of the

manufacturer's dummy head. Thus the LWC values may be in error by 20%. However, if the sensing head is thoroughly evaluated and calibrated, the overall accuracy should be within 20%. The CSIRO probe consists of a heated wire element closely wound with a single layer of insulated copper wire. The element resistance is used in a feedback loop to maintain the temperature of the sensor constant. Axial heat losses are minimized through the use of slave coils on either side of the main sensing coil. With the current flowing through these coils duplicating that from the main coil, the axial temperature gradient is significantly reduced.

An extensive evaluation of the CSIRO probe (reference 2-10) showed that the accuracy of the measured LWC is dependent on the accurate prediction of the heat losses in non-cloudy air. King (reference 2-20) has estimated the inaccuracy of the CSIRO probe to be less than 5% at 1.0 g/m^3, based upon an analysis of the probe's operating characteristics.

2.5.1.2 Vibrating Probe LWC Instrument

The vibrating probe instrument electronics detect changes in the resonant frequency of a small vibrating sensor tube as ice acretes on the surface. Current versions of this instrument automatically deice after a given ice buildup. Recent comparison tests of several LWC instruments (reference 2-5) indicated a LWC repeatability of ±13% (1 standard deviation) with an average error of -11% for the vibrating probe when tested in an icing wind tunnel. These tests were conducted at low enough temperatures to avoid water run-off thermal errors. All tests were run over a range of airspeed, LWC, and median droplet sizes.

2.5.1.3 Light Beam Interruption Instrument

At the time of this writing no information was available concerning the precision and accuracy of the light beam interruption type LWC instrument.

2.5.1.4 Blade

The blade LWC instrument (figure 2-5) was similarly tested in an icing wind tunnel (reference 2-5) over the same range of conditions as the vibrating probe as discussed in Section 2.5.1.2. LWC repeatability for the Blade in these tests was ±19% (1 standard deviation) with an average error of -3%.

2.5.1.5 Rotating Multi-Cylinders

The rotating multi-cylinder instrument, made of five cylinders in a stacked array with diameters ranging from 0.32 cm to 11.0 cm, was similarly tested in an icing wind tunnel (reference 2-5) over the same range of conditions as for the vibrating probe and the blade. LWC repeatability for the rotating cylinder in these tests was ±15% (1 standard deviation) with an average error of -11%.

2.5.2 Droplet Sizing Instruments

2.5.2.1 Optical Array Probe (OAP)

The OAP instrument is available in different sizing ranges (e.g., the OAP-200X with a sizing range of 10 to 300 μm and the OAP-260X with a sizing range of 10 to 600 μm). The OAP shown in figure 2-7 in a simplified schematic uses a low power HeNe laser and cylindrical optics to form a beam with an elliptical profile. This laser beam is passed through the sampling region and an objective lens to illuminate a linear photodiode array 16, 32, or 64 elements long. Particles passing through the beam obscure a portion of the beam thereby forming a shadow which is imaged by the objective lens (at some preset magnification) onto the diode array. The measured size of the particle is represented as a discrete number of photodiodes shadowed. Shadows from particles which traverse at axial or z positions, displaced from the object plane, are then out-of-focus at the diode array plane. As a result a problem with determining the correct size of an out-of-focus object is introduced. The axial extent of the region where particles are sufficiently in focus is termed the depth-of-field (DOF). The particle sampling window is an approximately rectangular section of the laser beam situated in the y-z plane. The axial (z) extent of the window is effectively the DOF with the height somewhat less than, but of the order of, the diode array length. Therefore a depth-of-field correction must be performed by the instrument to account for the strong sampling bias in favor of large particles.

For the OAP, the DOF varies as the square of the particle diameter, but is limited at the high end by the physical distance of 61 mm between probe arms (not shown in figure 2-7). The effective array width dependence reflects the fact that a large particle has a smaller acceptance window where it can cross the array image and not cover one of the end diodes. The instrument logic rejects particles which shadow an end diode because a correct size measurement could not be made.

The OAP was calibrated utilizing particle diameters ranging from 80 to 455 μm (reference 2-7). The best fit calibration constant was determined to be 0.96. The typical full-width response broadening, at one standard deviation, was about two channels (20 μm). Thus, the OAP sized particles were found to be 4% low relative to independent measurements of the particle image diameters. Measurements of the DOF agreed well with predictions and the manufacturer's specifications.

2.5.2.2 Forward Scattering Spectrometer Probe (FSSP)

Scattering probes use a velocity averaging circuit to reject particles which pass near the beam edges. This scheme is implemented by maintaining an electronically derived running average of the particle's transit time through the laser beam. If a particle's transit time exceeds the average it is accepted; if shorter, it is assumed that the particle passed too close to the beam edge and is rejected as it might otherwise be undersized. Additional details of this operation may be found in ref. 2-9.

The measurement accuracy of these instruments is a function of the optical resolution and the response characteristics of the electronics. The manufacturer estimates the sizing resolution to be 10% as a result of the variations in the light intensity across the length and width of the beam. These

variations also cause initially monodispersed spectra to be artificially broadened. Systematic oversizing of cloud droplets will occur when particles are coincident in the beam. Assuming a random distribution of particles, the probability of coincident events varies from 1% for 100 droplets/cm^3, to 12% at 500 cm^{-3} and 30% at a concentration of 1000 cm^{-3}. These probabilities are statistically derived using a Poisson distribution after assuming typical values for airspeed (80 m/s) and sample area (depth-of-field, 3 mm; beam diameter, 0.2 mm). The oversizing due to coincidence cannot be quantized; however, the general effect will be to broaden the spectra toward larger sizes (references 2-17 and 2-19).

Particles will be measured as less that their actual size if they pass through the beam faster than the response time of the electronics. Laboratory tests have indicated that this effect is not significant until airspeeds exceed 100 m/s, at which point the particle is undersized by about 2 μm. The cumulative effect of beam inhomogeneities, particle coincidence, and response time is to broaden the measured droplet distribution. The average amount of broadening is estimated to be 3-4 μm, from the observed standard deviation of monodisperse glass bead samples. This was obtained by comparing the indicated particle distribution with the actual distribution of the glass beads determined by a microscope (references 2-17 and 2-19).

Errors in sizing also arise when calibrating the probe with glass beads. The procedure is to pass glass beads of known size through the instrument then adjust the indicated size(s) to account for differences in the index of refraction between glass and water as described by Pinnick (reference 2-9). The adjustment procedure introduces uncertainty because of multiple values of the Mie scattering function, especially for sizes less than 15 μm diameter. The maximum error introduced by this uncertainty is approximately 10 percent.

Errors in determining the depth-of-field and beam diameter affect the accuracy of concentration measurements. The electronic definition of the DOF is not precise therefore it cannot be determined to less than 10%. As the beam diameter is also difficult to measure, an error of less than 10% should not be expected. An additional uncertainty is introduced by the velocity-averaging circuit. In theory an average of 62% of the particles passing within the DOF should meet the velocity acceptance criteria. Empirical data from several instruments tested shows that approximately 50% are accepted. The velocity accepted fraction is thus the same as the beam fraction through which particles may pass and be accepted by the velocity averaging circuit.

In summary, the FSSP instrument exhibits the following accuracy as a function of the source of error (reference 2-2):

Concentration

      DOF - within 10%

      Beam diameter - within 10%

      Beam fraction variability - 40-10%

      Activity losses - 10-100%

      RSS - 17%

Size

      Laser inhomogeneity - 10%

      Electronic response time and coincident particles - 10%

      Calibration - 10%

      RSS - 17%

Spectral Shape (as measured in standard deviation)

      Same error sources as in measurement of size - ± 4 μm

LWC

      Combined sources of size and concentration measurement errors - 34%*

(*Accuracy when beam fraction and activity corrections have been made.)

II.2.6 REFERENCES

2-1 Strapp, J.W. and Schemenauer, R.S., "Calibrations of Johnson-Williams Liquid Water Content Meters in High-Speed Icing Tunnel," Journal of Applied Meteorology, Volume 21, Number 1, January 1982, pp. 98-108.

2-2 Baumgardner, D., "An Analysis and Comparison of Five Water Droplet Measuring Instruments," Journal of Applied Meteorology, Volume 22, 1983, pp. 891-910.

2-3 Jensen, David and Wahlstrand, Noel, "Icing Rate Indicator System," Rosemount Engineering Company, Report No. 26919B, February 1969.

2-4 "Specification 951469A - Mk 12B Ice Detector Unit IDU-3B," Leigh Instrument Limited, Ontario, Canada, September 1983.

2-5 Olsen, W., Takeuchi, D., and Adams, K., "Experimental Comparison of Icing Cloud Instruments," NASA TM 83340, AIAA-83-0026, AIAA 21st Aerospace Sciences Conference, Reno, Nevada, January 10-13, 1983.

2-6 Brun, R., Lewis, W., Perkins, P., and Serifini, J., "Impingement of Cloud Droplets on a Cylinder and Procedure for Measuring Liquid Water Content and Droplet Sizes in Supercooled Clouds by Rotating Cylinder Method," NACA Report 1215, 1955.

2-7   Hovenac, E.A., Hirleman, E.D., and Ide, R.F., "Calibration and Sample Volume Characterization of PMS Optical Array Probes," Presented at the International Conference on Liquid Atomization and Spray Systems (ICLASS 85)," London, England, July 1985.

2-8   Cerni, T.A., "Determination of the Size and Concentration of Cloud Drops with an FSSP," Journal of Climate and Applied Meteorology, Volume 22, Number 8, August 1983, pp. 1346-1355.

2-9   Pinnick, R.G., Garvey, D.M., and Duncan, L.D., "Calibration of Knollenberg FSSP Light-Scattering Counters for Measurement of Cloud Droplets," Journal of Applied Meteorology, Volume 20, 1981, pp. 1049-1057.

2-10 King, W.D., Dye, J.E., Strapp, J.W., Baumgardner, D., and Huffman, D., "Icing Tunnel Tests on the CSIRO Liquid Water Probe," Journal of Atmospheric and Oceanic Technology, 1985.

2-11 Stallabrass, J.R., "An Appraisal of the Single Rotating Cylinder Method of Liquid Water Content Measurement," NRC Report LTR-LT-92, 1978.

2-12 Brun, R., Lewis, W., Perkins, P., and Scarafini, J., "Impingement of Cloud Droplets on a Cylinder and Procedure for Measuring Liquid Water Content and Droplet Sizes in Supercooled Clouds by Rotating Cylinder Method," NACA Report 1215, 1955.

2-13 Howell, William E., "Comparison of Three Multi-Cylinder Meters and Critique of Multi-Cylinder Method," NACA TN 2708, 1952.

2-14 Hovenac, Edward A., "Calibration of Droplet Sizing and Liquid Water Content Instruments: Survey and Analysis," NASA CR 175099, DOT/FAA/CT-86/19, May 1986.

2-15 Norment, H.G., Quea.y, A.G., and Shaw, R.J., "Three-Dimensional Trajectory Analysis of Two Drop Sizing Instruments: PMS OAP and PMS FSSP," AIAA-87-0180, Presented at the AIAA 25th Aerospace Sciences Meeting, Reno, NV, January 12-15, 1987.

2-16 "Cloud Particle Measurement Symposium - Summaries and Abstracts," U.S. National Center for Atmospheric Research, Boulder, Colorado, September 1982.

2-17 Baumgardner, D., Strapp, W., and Dye, J.E., "Evaluation of the Forward Scattering Spectrometer Probe Part II: Corrections for Coincidence and Dead-Time Losses," Journal of Atmospheric and Oceanic Technology, Volume 2, December 1985, pp. 626-632.

2-18 Cerni, R.A., and Cooper, W.A., "Sizing of Cloud Droplets with an FSSP," Cloud Particle Measurement Symposium; Summaries and Abstracts, D. Baumgardner and J.E. Dye, eds., NCAR/TN-199+PROC, National Center for Atmospheric Research, 1982, pp. 20-26.

2-19 Dye, J.E. and Baumgardner, D., "Evaluation of the Forward Scattering Spectrometer Probe Part I: Electronic and Optical Studies," Journal of Atmospheric and Oceanic Technology, Volume 11, December 1984, pp. 329-344.

2-20 King, W.D., et al, "Icing Wind Tunnel Tests on the CSIRO Liquid Water Probe," Journal of Atmospheric and Oceanic Technology, Volume 2, September 1985, pp. 340-352.

2-21 Jeck, R.K., "Calibration and Testing of Optical, Single Particle, Size Spectrometers with Monofilament Fibers as Substitute Particles," Applied Optics, Volume 19, 1980, pp. 657-659.
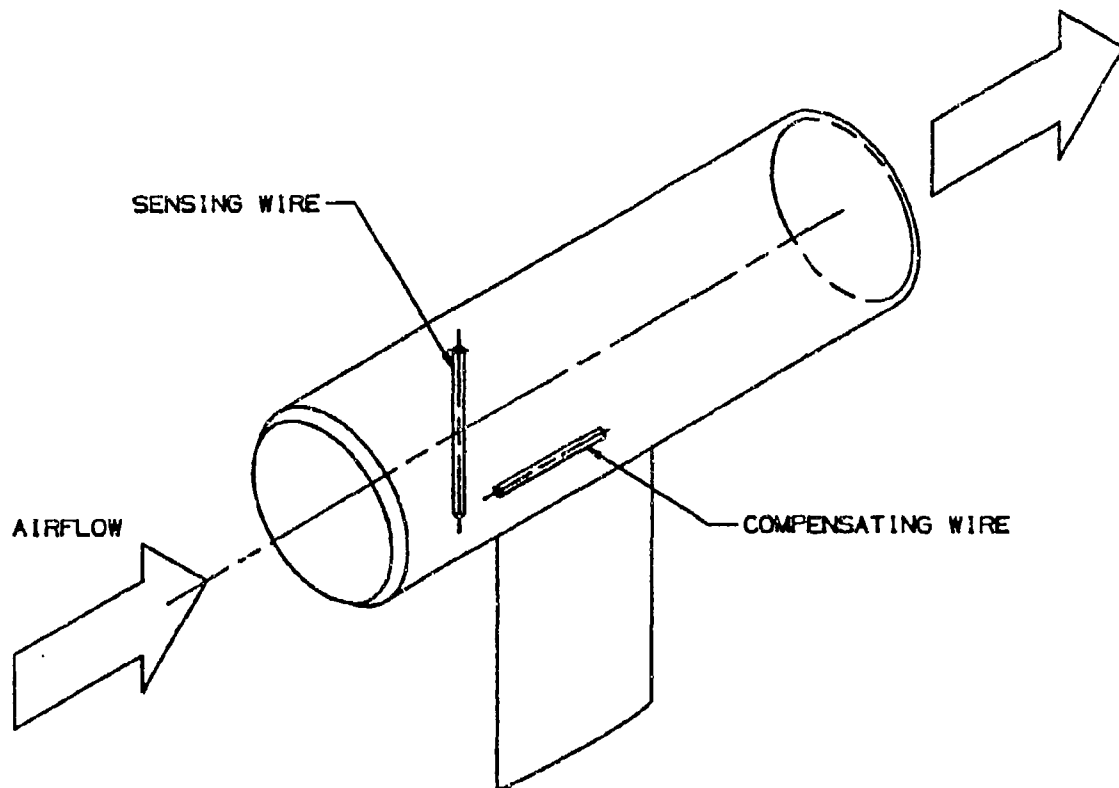
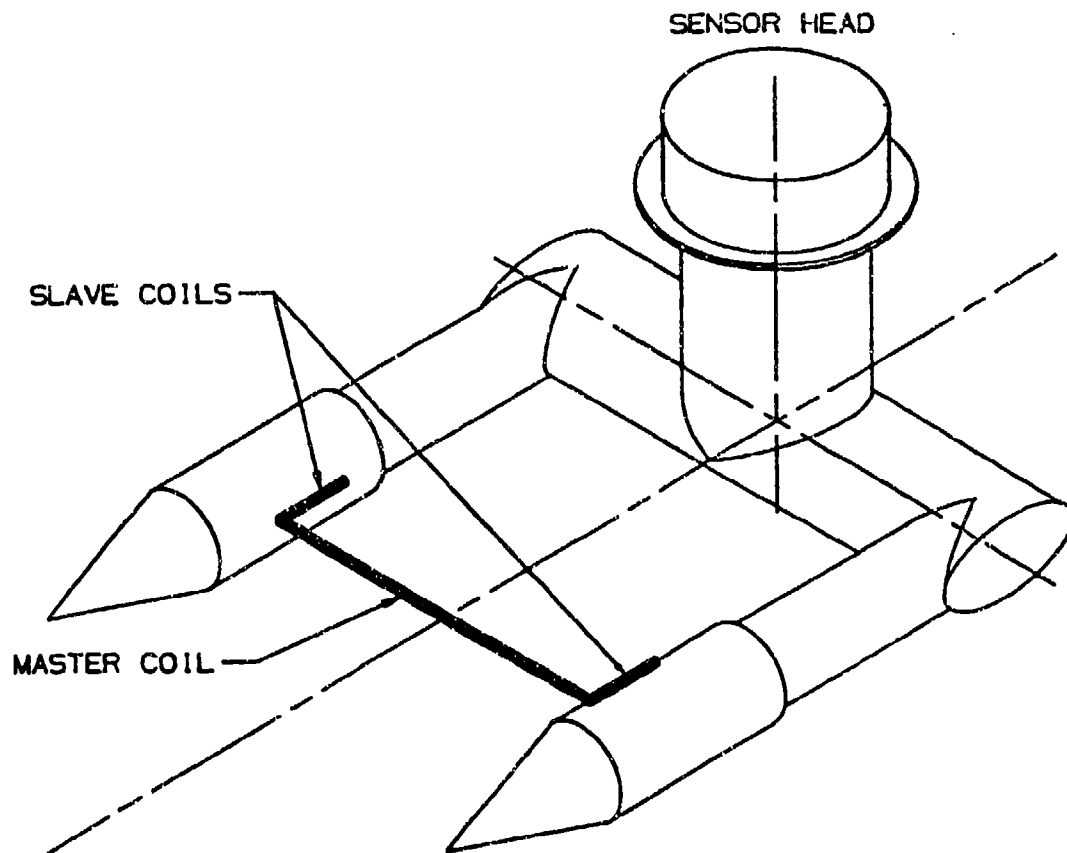FIGURE 2-1. HOT WIRE LIQUID WATER CONTENT METER (J-W)
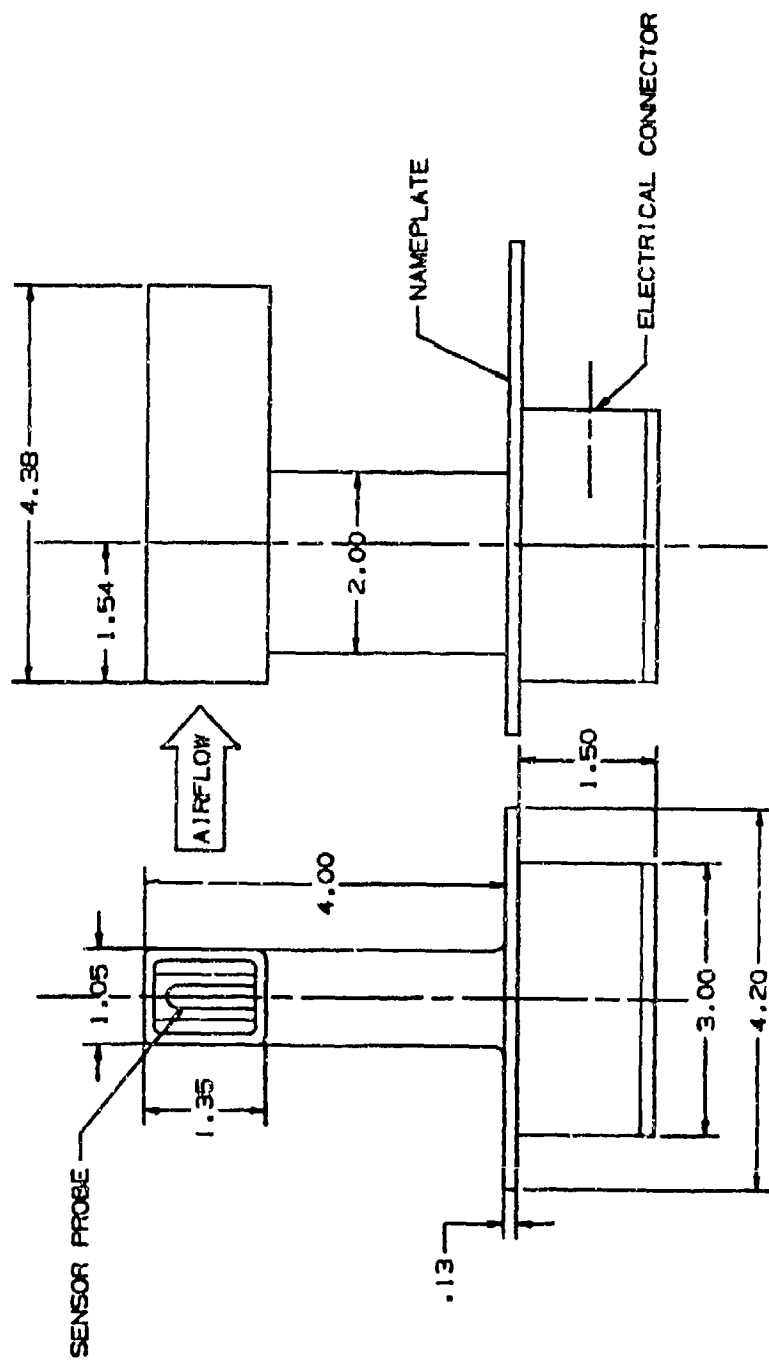
FIGURE 2-2. HOT WIRE LIQUID WATER CONTENT METER (CSIRO)
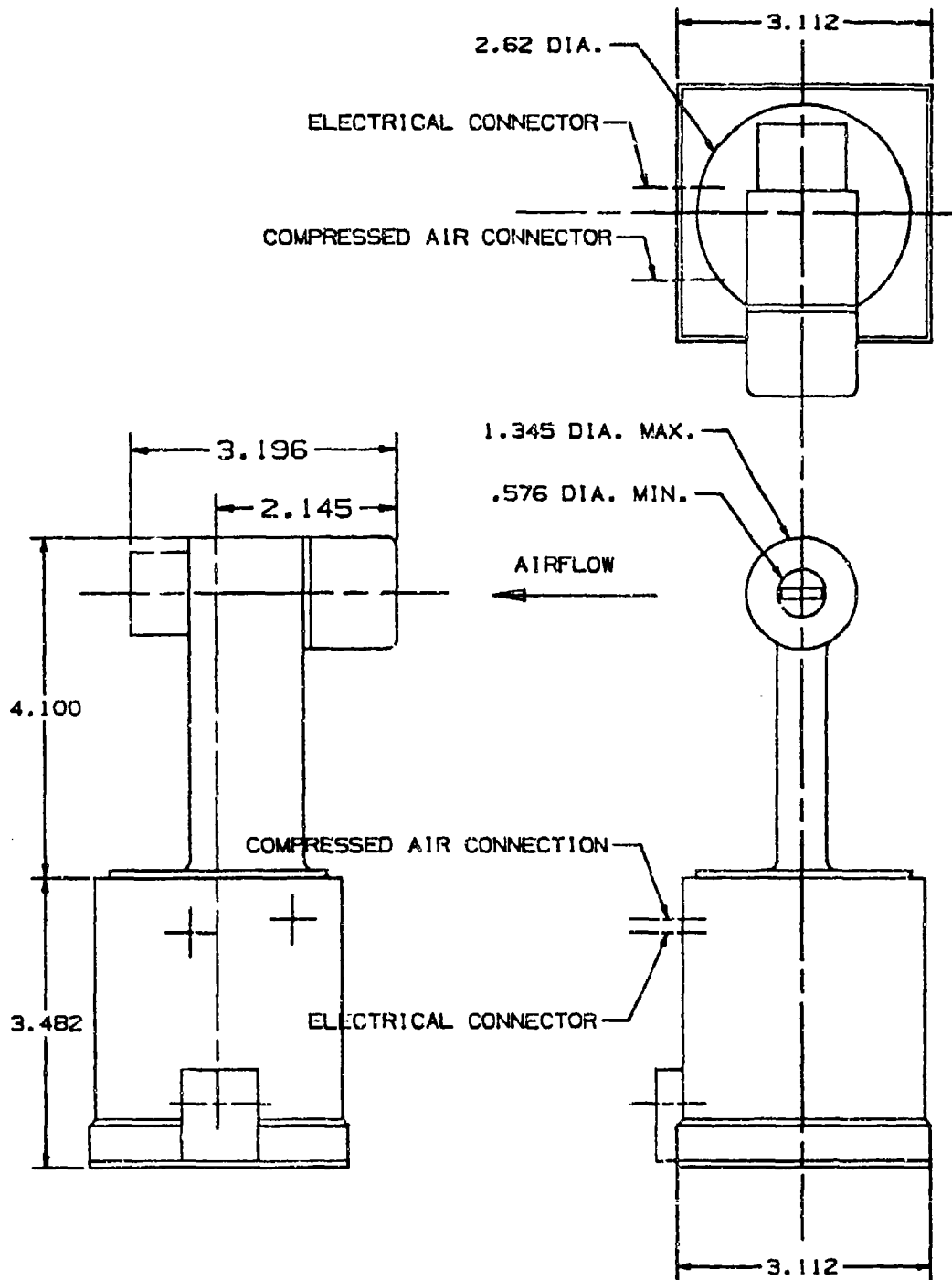
FIGURE 2-3. VIBRATING PROBE LWC INSTRUMENT

FIGURE 2-4. LIGHT BEAM INTERRUPTION LWC INSTRUMENT

.750 (1.9 CM)

.120
(0.3 CM)

AIRFLOW
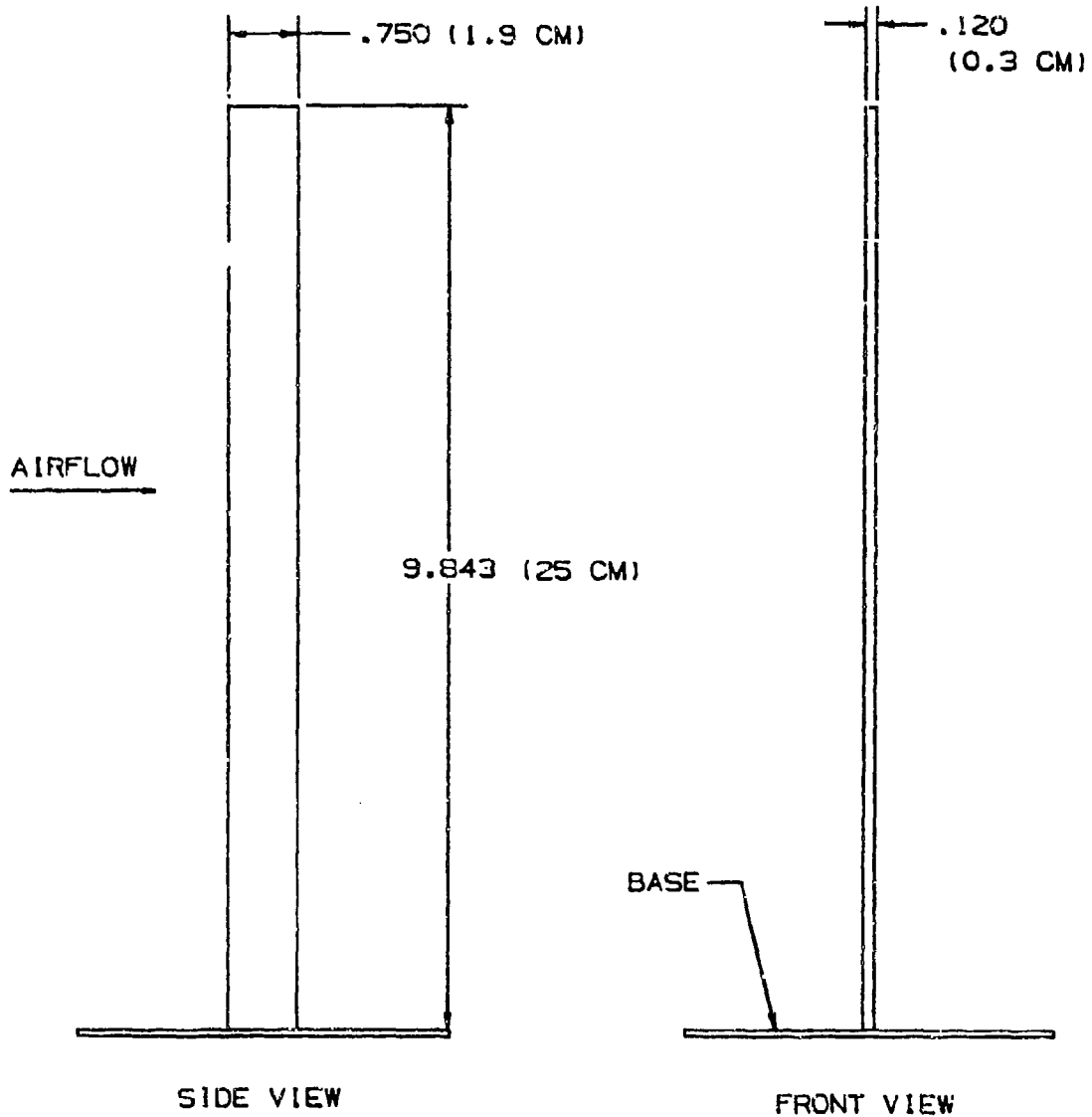
9.843 (25 CM)

BASE

SIDE VIEW
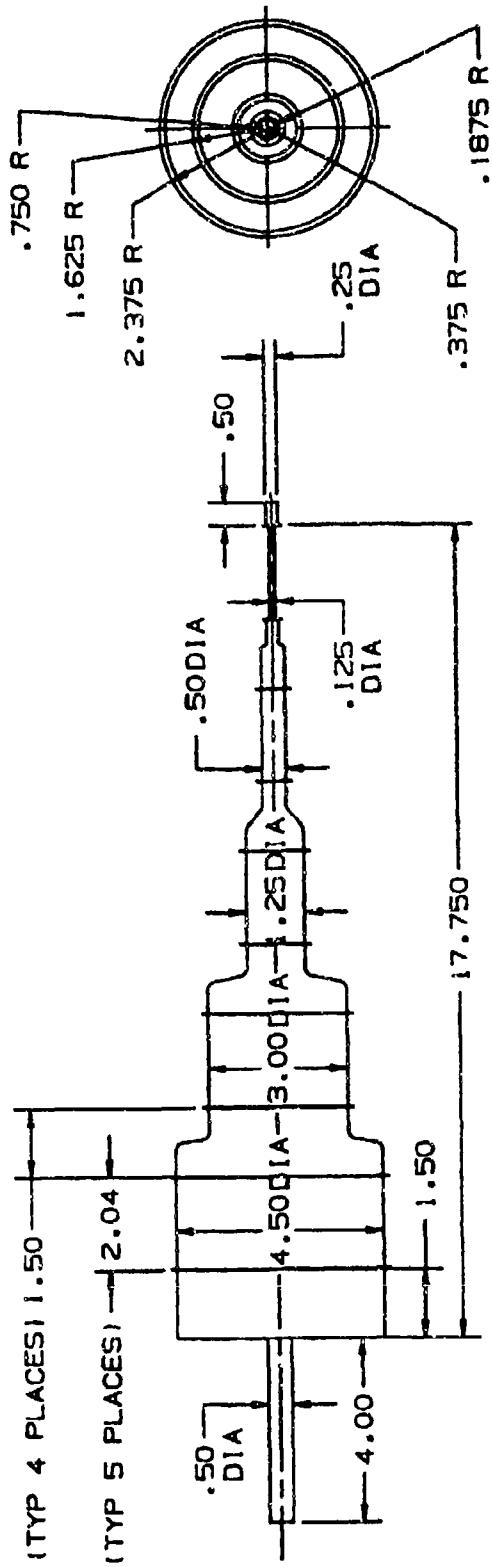
FRONT VIEW

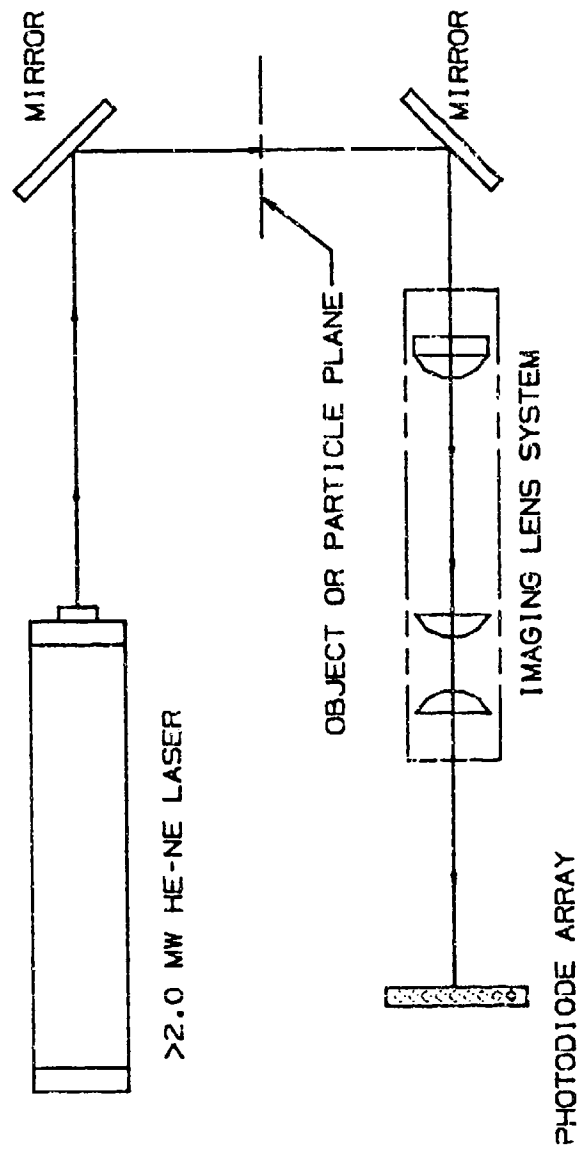FIGURE 2-5.   BLADE LWC INSTRUMENT

FIGURE 2-6. ROTATING MULTI-CYLINDER INSTRUMENT

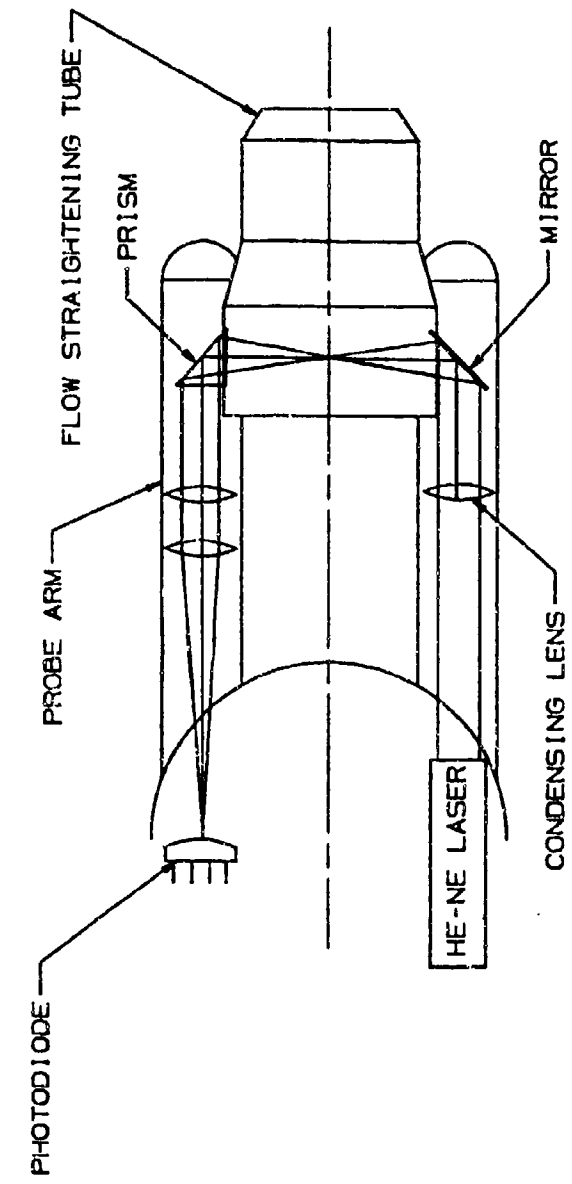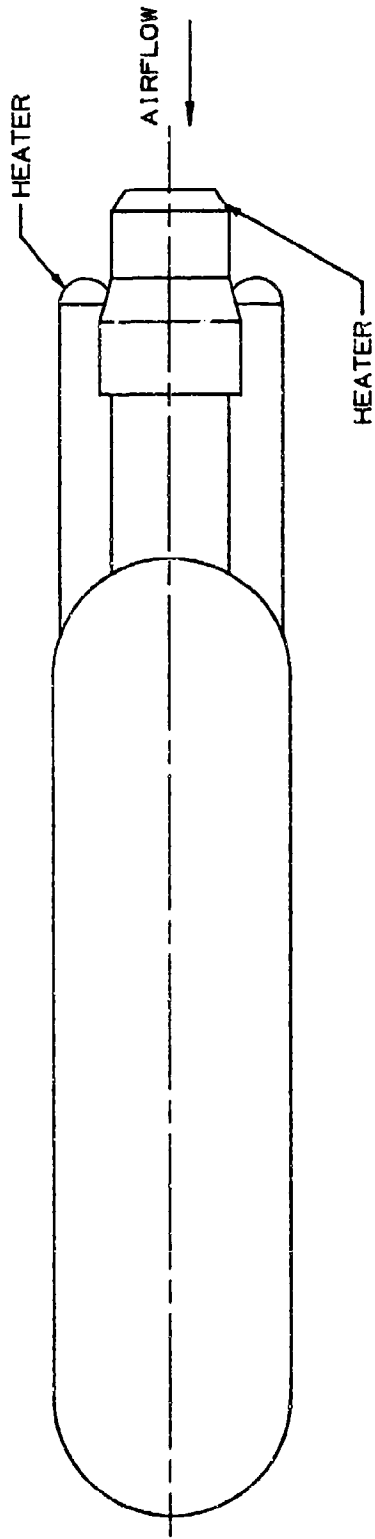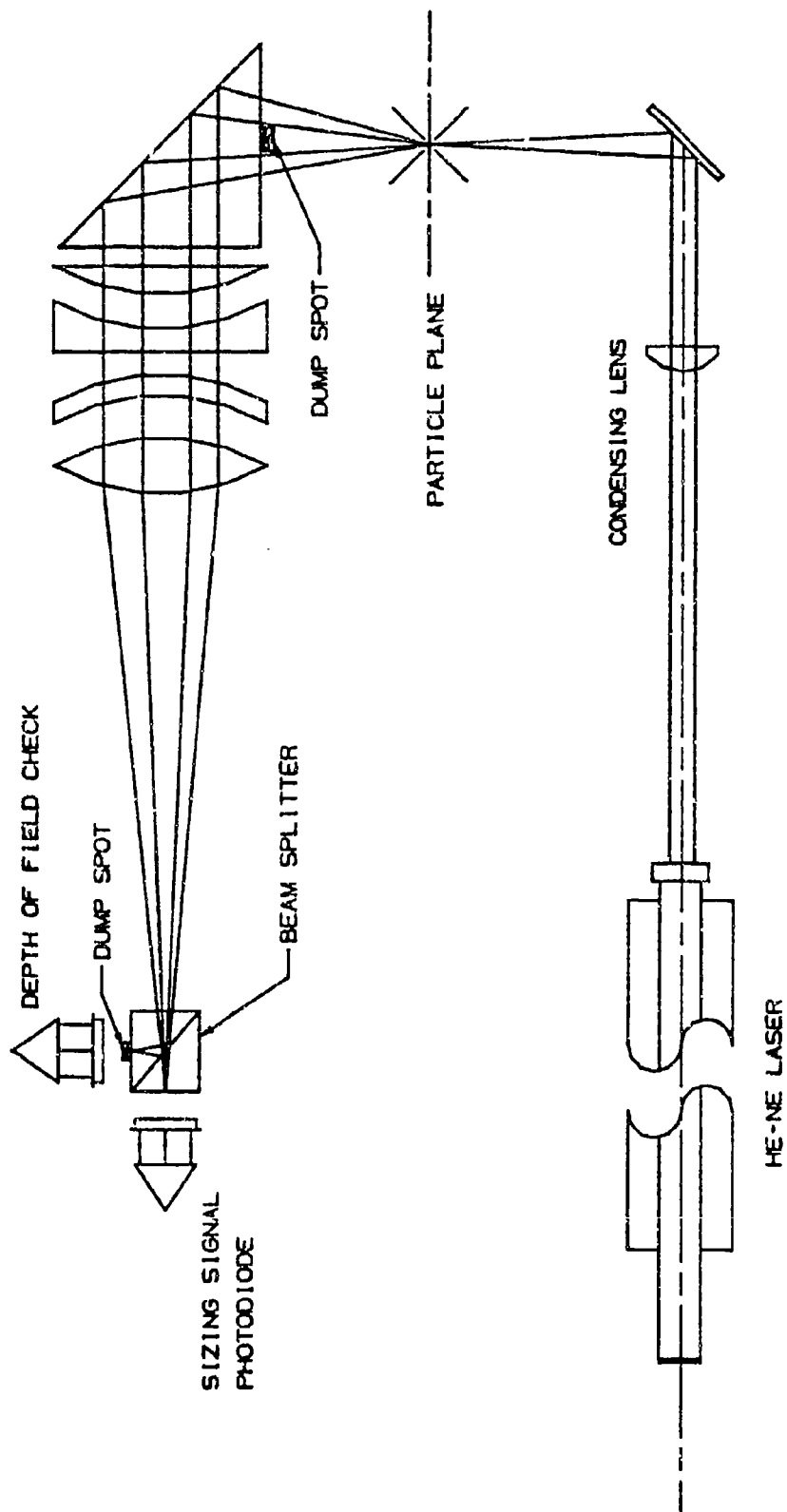FIGURE 2-7. OPTICAL COMPONENTS OF OPTICAL ARRAY PROBE (OAP)

FIGURE 2-8. FORWARD SCATTERING SPECTROMETER PROBE (FSSP)

FIGURE 2-9. OPTICAL COMPONENTS IN FSSP

Labels within figure: DEPTH OF FIELD CHECK, DUMP SPOT, DUMP SPOT, BEAM SPLITTER, SIZING SIGNAL PHOTODIODE, PARTICLE PLANE, CONDENSING LENS, HE-NE LASER